Antonio Benayas
Eva Hemmer
Guosong Hong
Daniel Jaque *Editors*

Near Infrared-Emitting Nanoparticles for Biomedical Applications

Springer

Near Infrared-Emitting Nanoparticles for Biomedical Applications

Antonio Benayas • Eva Hemmer
Guosong Hong • Daniel Jaque
Editors

Near Infrared-Emitting Nanoparticles for Biomedical Applications

Springer

Editors
Antonio Benayas
Department of Physics and CICECO – Aveiro Institute of Materials
University of Aveiro
Aveiro, Portugal

Guosong Hong
Department of Materials Science and Engineering
Wu Tsai Neurosciences Institute
Stanford University
Stanford, CA, USA

Eva Hemmer
Department of Chemistry and Biomolecular Sciences
University of Ottawa
Ottawa, ON, Canada

Daniel Jaque
Physics of Materials Department
Universidad Autónoma de Madrid
Madrid, Spain

ISBN 978-3-030-32035-5 ISBN 978-3-030-32036-2 (eBook)
https://doi.org/10.1007/978-3-030-32036-2

This Springer imprint is published by the registered company Springer Nature Switzerland AG.
The registered company address is: Gewerbestrasse 11, 6330 Cham, Switzerland

Preface and Summary

All imaging methods rely on either endogenous contrast from biological tissue, such as non-contrast X-ray computed tomography (CT) and functional magnetic resonance imaging (fMRI), or externally introduced contrast agents such as contrast-enhanced CT, positron emission tomography (PET), and single-photon emission computed tomography (SPECT). Despite their great success in clinical imaging, major limitations of these mature imaging methods include intrinsically limited spatial resolutions (MRI and PET), reconstruction-dependent poor temporal resolution (CT, MRI, PET, and SPECT), adverse effects due to hazardous ionizing radiation (CT, PET, and SPECT), and lack of both exogenous and endogenous probes for molecular or functional imaging. In addition to all these drawbacks, MRI, PET, SPECT, and CT are far from being cost-effective techniques. This is a drawback in developed countries as it increases the budget of health systems, but it is dramatic in non-developed countries where these techniques are not available.

In contrast to all these "conventional imaging techniques," in vivo fluorescence imaging is not limited by these aforementioned challenges, but instead offers diffraction-limited high spatial resolution and real-time dynamics image acquisition, as well as a wide selection of functional and molecular markers for revealing rich information from fluorescence imaging. In addition, in its basic version, fluorescence imager can be considered as a cheap instrument. It is, basically, constituted by a excitation light source (lamp or diode laser), a set of optical filters to remove background, and a fluorescence camera for image acquisition. The experimental simplicity of a fluorescence imager makes it economically affordable. Indeed, the cost of fluorescence imagers (already commercially available for preclinical studies) is orders of magnitude lower than those of imaging techniques already working at the clinical level. This would make possible its implantation in a large number of preclinical units with affordable costs. In addition, optical radiation used as excitation source is nonionizing so that it is potentially innocuous. As some of the other techniques, fluorescence imaging also requires the use of a biocompatible probe to enhance the brightness, contrast, and resolution of the bioimaging. Fortunately, numerous biocompatible materials (such as organic molecules and

inorganic nanocrystals) can act as fluorescence probes so that somehow the use of harmful probes (such as radioactive traces) is not necessary.

The simplicity and high acquisition speed of fluorescence imagers have enamored the users of preclinical units. We can say that fluorescence imaging is among the most popular imaging techniques for research units working in animal models. The translation of fluorescence imaging into the clinics is still far from being a reality. One of the biggest issues avoiding the transaction into the clinics of fluorescence imaging is the limited tissue penetration depth due to scattering and absorption of fluorescence photons in biological tissue. To address this challenge, in the past decade this field has witnessed rapid development with a lot of interest focused on biomedical imaging, optical biosensing, and imaging-guided therapies in the near infrared (NIR) spectral region. The NIR spectral region, which is broadly defined as the wavelength range from 700 nm to 3 μm in the electromagnetic spectrum, has been demonstrated with the following advantages for the *golden beneficial trifecta* for in vivo imaging:

– Superior penetration depth.
– Greater optical contrast, that is, better-resolved images.
– Higher signal-to-noise ratio (lower autofluorescence background).

The physical mechanisms behind the above listed NIR spectral range beneficial assets are quite intermingled, regarding their implementation in the biomedical arena. We found lower absorption coefficient shown at those NIR wavelengths by the biological tissues. The fact constitutes clear advantages in "two ways" for light-related biomedical purposes, as it benefits the transmission through tissues of both inbound (excitation) and outbound (emission) photons. Secondly, we are considering ballistic photons here. Then, the scattering they undergo because of interacting with optically dense matter—namely, the different kinds of biological tissues—is considerably lower for longer wavelength light (i.e., NIR). Finally, autofluorescence—i.e., undesired light emission from the tissue itself—is both less excited by and produced at NIR wavelengths.

Authored by distinguished researchers from four different continents, the 13 chapters of this book cover very distinct aspects of near infrared-emitting nanoparticles for biomedical applications, obviously with special emphasis on fluorescence imaging where the near infrared nanoparticles act as contrast agents. Throughout the rest of this introductory chapter, the editorial team offers an overview of how the chapters relate to the topic and the thematic transitions between them.

The chapter by *Marcos-Vidal/Vaquero/Ripoll* drives the reader through the light–matter interaction specifics, giving a broad insight regarding the physics of light propagation in optically dense tissues, much needed for an opening piece within a book of this interdisciplinary character. For all those ones not entirely familiar with the current landscape of fluorescence imaging, this chapter perfectly frames the physics rationale behind the current trends of shifting optical excitation and signal of the contrast agents (nanoprobes) to the near infrared.

Here, it is worth highlighting the comprehensive and thorough explanation given about the specifics of both *absorption* (accounting for the radiation that is dissipated

without re-emission of light) and *scattering* (or re-emission of incident light) in Sect. 1.1. Regarding the latter phenomenon, the authors have managed to elegantly describe the Mie theory for non-physicist audiences, by way of authoritative and concise definitions without excessive mathematical apparatus. Then, the core sections on *light propagation in biological tissues* and *properties of light in the NIR range* (broke down by different biological compounds/types of tissues) provide the basics to understand the rationale behind the spectral range objects of special attention as the scope of the whole book targets.

The narrative follows by the piece by *del Rosal/Thomas/Mahadevan-Jansen/Stoddart* that is entirely devoted to *autofluorescence*. As in any other measurement process, signal-to-noise ratio (SNR) optimization is the most important criterion to assess the procedural and usefulness. Therefore, the optical background generated by the intrinsic fluorescence of several different biomolecules must be the subject of specific and careful analysis.

The chapter goes beyond the widely accepted framework of accounting for a much generalized autofluorescence presence throughout the visible (VIS) wavelengths. In fact, the different sections tackle the NIR autofluorescence—more scarcely described in the literature—reviewing the involved molecules and their spectral emission ranges. Moreover, particular areas of interest where fluorescence imaging has established as a battle-hardened useful technique, such as surgical oncology, are discussed. For clarity of purpose, it must be noted that throughout the chapter autofluorescence is openly considered not just as an inconvenience or difficulty to bypass/eliminate for high-contrast imaging, but as a source of advantageous and utile knowledge for in vivo detection of malignances and diseases.

Thus, we really believe that once the readership has taken and understood the first two chapters, the rationale behind the shift towards contrast agents emitting at NIR wavelengths, increasingly happening during the last decade, is justified in a conceptually rigorous way. Whether approaching the matter from the research community interested in fluorescence bioimaging or coming from other domains, the plethora of beneficial effects of NIR light is factually set, ranging from deeper through tissue penetration to better optical resolution.

Having started the book with two chapters providing the reader insights into the physical characteristics of NIR light and its interaction with matter, the following chapter shifts gears paying attention to biological and chemical facets. Seeking in vitro and in vivo applications of nanomaterials, their *surface functionalization* is indispensable. This is as it endows the nanoprobes with the necessary biocompatibility, colloidal stability in biological environments, or targeting capabilities.

Addressing this aspect of fundamental importance for any bioprobes, the chapter by *Hirsch* offers a critical look at the currently known methods for surface modification and functionalization of NIR-emitting nanoparticles for biomedical applications. The author stresses the importance of carefully carried out and well-characterized surface functionalization, especially for biomedical applications, where the surface ligand choice has great impact on the nano-bio interaction, thus, ultimately the performance of the bioprobes.

General principles of surface modification are explained; advantages and disadvantages of various strategies are discussed. Several examples are given to illustrate these various approaches, wherein the focus is mainly set on rare earth-doped nanoparticles (RENPs). Thus, this chapter does not only provide insight into the state-of-the-art surface chemistry and remaining challenges that still need to be tackled by the research community, but also invites the reader to the first journey discovering the manifold application potential of NIR luminescent bioprobes.

For the next thematic block within our opus, the connecting wire between the distinct grouped chapters is the contrast between different types of NIR-emitting nanomaterials although abundantly carefully chosen examples of applications and preclinical developments are supplied. It opens with the work of *Tan/Chen* focusing on the latest and most insightful advances of in vivo imaging, achieved by way of *rare earth-doped nanoparticles (RENPs)* as fluorescence contrast agents.

Most researchers know about the RENPs through the upconverting emission (one emitted photon of higher energy for each bunch ≥ 2 absorbed photons of lower energy) that has produced a gamut of interesting research outcome within different areas of knowledge, in particular the biomedical arena. Yet, this chapter also forcefully presents downshifting RENPs, where much more efficient NIR emission is obtained. In particular, through very illustrative examples, the authors make the case for the *time-gating* imaging technique, as a playing field where RENPs can outperform other competitors. This methodological approach relies on the long time scale of the emission lifetime from chosen fluorophores, lasting much longer than the short-lived autofluorescence.

Moreover, the chapter constitutes an honest account of the current limitations and shortcomings of RENPs as well. Low light absorption that decisively affects the emission brightness of them is the key challenge to tackle, for RENPs decisively occupying their place at the table of the fluorescence contrast agent with credible clinical potential.

Moving further into longer wavelengths in the NIR spectrum, the chapter of *Du/Wan/Dai* summarizes the latest advances in the development of fluorophores in the *second near infrared window* (NIR-II window) from 1000 to 1700 nm. With the first demonstration of in vivo NIR-II fluorescence imaging in rodents a decade ago, the Dai group has pioneered in the synthesis and application of a wide palette of NIR-II fluorophores, ranging from single-walled carbon nanotubes (SWCNTs), quantum dots (QDs), semiconducting polymers to small organic molecules. In this chapter, the authors have offered a timely overview including latest efforts from Dai and coworkers towards the realization of "ideal" fluorophores for NIR-II imaging with high fluorescence quantum yield, further red-shifted emission wavelength, and favorable pharmacokinetics.

The past decade of in vivo NIR-II fluorescence imaging can be roughly divided into two phases, both of which have been significantly contributed by the pioneering research of the Dai group. In the first phase from 2009 to 2014, nanomaterials with NIR-II fluorescence and good biocompatibility were demonstrated as promising contrast agents with greater tissue penetration depth and crisper contrast/resolution of imaging than their counterparts in the shorter wavelength, NIR-I window.

One remaining challenge of materials used for imaging during this first phase comes from the suboptimal pharmacokinetics of SWCNTs and QDs due to their relatively large size and difficulty of biodegradation. This remaining challenge is one of the key motivations of many recent advances reviewed in this chapter, which provides a good summary of the second phase of NIR-II fluorescence imaging research from 2014 to now with a focus on the emergence of many small organic molecule-based NIR-II fluorophores such as CH1055 and IR-E1. These water-soluble NIR-II fluorescent molecules exhibit outstanding pharmacokinetics with rapid renal clearance, opening up great opportunity for clinical translations. Optimization of the molecular structure as well as exploitation of supramolecular interactions has led to increased fluorescence quantum efficiency of these NIR-II fluorophores. Besides these advances, further extension of the emission wavelengths using rare-earth and small-bandgap III-V semiconducting nanoparticles is another focus of this chapter.

The following two chapters discuss carbon-based NIR emitters for biomedical applications in more detail. The chapter by *Jena/Cupo/Heller* sets the focus on *SWCNTs*, while the subsequent work by *de Medeiros/Naccache* provides a comprehensive review on various *carbon-based nanomaterials*, their synthesis and application in biomedicine.

The major advantages of *SWCNTs as NIR bioprobes* include the intrinsic multiplexed optical sensing ability, coupled with the novel biodistribution capability due to the small size and aspect ratio. In light of this, multiple examples are known to demonstrate the excellent performance of SWCNTs for NIR-based bioimaging. Furthermore, *Jena/Cupo/Heller* introduce to the reader some aspects that deserve specific attention, not only by the nanotube community but also by other researchers working in the field of (anisotropic) bioprobes. More precisely, the need for the development of novel characterization techniques is stressed, particularly to accurately analyze individual nanotubes.

Hence, this chapter includes an introduction to the technique of *hyperspectral imaging* that originally stems from the fields of astronomy and satellite-based remote sensing, but that is recently attracting increasing attention by the nano-bio community. The beauty of these techniques consists in the possibility to simultaneously collect a large variety in spectral as well as spatial information, whereas samples can be studied on a surface, in fixed tissues and in cells. This allows not only to study the optical properties of individual SWCNTs, but also to observe kinetic bioprocesses or to assess their capabilities to act as luminescent sensors, for example, biomolecules related to a specific disease.

While the reader will find an impressive list of achievements with respect to NIR-based biomedical applications of SWCNTs and their study by hyperspectral imaging, the authors do not hold back remaining issues and current challenges that have to be addressed to further advance this field and to develop the next *tools for basic research and translational biomedicine*.

The chapter by *De Medeiros/Naccache* presents the larger realm of carbon nanomaterials. Besides carbon nanotubes (CNTs), this chapter includes a detailed review on carbon dots (CDs) and graphene dots (GDs). The in-depth description and

evaluation of various synthesis techniques towards these materials will particularly suit the reader with a strong interest for materials synthesis.

As in the case of CNTs presented by several authors, GDs and CDs have also been reported as promising candidates for biomedical applications, including in vivo bioimaging in the first NIR biological window. Interestingly, this chapter provides several examples for biomedical applications beyond NIR bioimaging, namely in sensing. Indeed, it is summarized that many biomolecules, metals, and cations can be identified by the carbon-based nanomaterials. This holds promises towards innovative multimodal bioprobes.

With respect to remaining challenges, while carbon-based nanomaterials (in particular CDs and GDs) are generally considered advantageous over other materials due to their low toxicity, the authors point out that further studies regarding the toxicity and biodistribution are still required. Other questions remain unanswered when it comes to the mechanisms of interaction between cells, tissues, and carbon-based nanomaterials, and—on a more fundamental note—the mechanisms of fluorescence, the role of the surface, and the interaction between these nanomaterials and biomolecules. Yet, as the authors conclude their chapter (being in line with other contributions to this book)—"Carbon nanomaterials hold an immense potential and a bright future that we believe will change the entire biomedical landscape and will result in the development of novel diagnostic and imaging tools for the most challenging problems in nanomedicine."—we can only agree with such statement, and we are looking forward to future developments in the domain of carbon-based NIR probes.

As a final contribution within the second block of the book—which we can label as the more materials-based part of it although always compatible with describing exciting applications, the chapter by *Viana/Richard/Castaing/Glais/Pellerin/Liu/Chanéac* discusses the NIR-persistent luminescent nanoparticles from a broad perspective. Persistent luminescence constitutes an attractive and physically peculiar phenomenon, based on materials that are able to store optical energy and release it gradually by photon emission.

The chapter digs into the physics behind that intriguing behavior. Furthermore, the narrative didactically connects such knowledge with the two possible materials' engineering routes to produce persistent luminescence materials:

- Relying on intrinsic defects, optimizing traps by compositional variation and thermal annealing.
- Optimization of the traps by co-doping.

The case study of $ZnGa_2O_4$:Cr is developed in detail regarding an outstanding platform for NIR-persistent luminescence, analyzing the physics of its persistent luminescence emission. Thermoluminescence, as a distinctive feature of the system is also described, is the most commonly used technique to demystify the traps number and their depths. Application-wise, the topics of biocompatibility and long-term in vivo imaging are covered in the final part of the chapter. Overall, the description on this not yet well-known approach to imaging will undoubtedly enlighten the

research community, especially those not quite familiar with lanthanide-doped materials.

Although portraying a title carrying a materials flavor, the chapter from *Ortgies/Martin* stands alone, halfway between thematic blocks in this book. It is, indeed, the most methodologically oriented insight of the whole compendium work, towards autofluorescence-free imaging (or minimizing autofluorescence, as it constitutes an undesirable background).

Strategies to filter autofluorescence from the image are explained first, establishing a clear filtering domain difference among them. On the one hand, *spectral filtering* relies on using fluorophores emitting at longer NIR wavelengths than the spectral region where autofluorescence mostly occurs (see *del Rosal/Thomas/Mahadevan-Jansen/Stoddart* chapter). On the other hand, the *time-domain filtering* points out towards the *time-gating techniques*. Those are based on using fluorophores that present fluorescence lifetimes orders of magnitude longer (μs to ms) than the lifetimes of the molecules causing the autofluorescence (usually in the range of ns). The signal-to-noise ratio increases very quickly with the delay time, even if the long-lifetime fluorophore is present at a concentration a million-fold lower than the fluorophores causing the autofluorescence. It represents a refreshing and fascinating example how RENPs with lower brightness in the NIR—actually "lower" when compared with quantum dots or dyes—comes to the forefront of the stage for time-gating, as their much longer lifetimes allow them to play a leading role, by not requiring top-notch expensive electronics.

The second insightful block within the chapter is devoted to routes avoiding the excitation of the molecules responsible for the autofluorescence, i.e., using fluorophores that do not require in-body excitation. The discussion on those strategies, persistent luminescence, allows the reader to benefit from the comparison between this chapter and previous one by *Viana/Richard/Castaing/Glais/Pellerin/Liu/Chanéac*, about the very same topic tackled from a broader materials' perspective. Different alternatives are: chemiluminescence, which is the emission of light as the result of a chemical reaction, and bioluminescence, which involves a number of biochemical and enzymatic reactions. As no light excitation is required for either of the two, background signal arising from autofluorescence does not exist, and high sensitivity and signal-to-noise ratios can be achieved.

The chapter is nicely wrapped up with a thorough comparative analysis among the different described techniques, together with a comprehensive list of the quantum yield values found in literature for different NIR-emitting nanoparticles families.

With a toolbox of NIR-II fluorescent agents available to scientists, the following two chapters by *Bardhan/Belcher* and *Chen/Zhang/Li/Wang* take an important step further to tackle *pressing biomedical challenges* with the help of in vivo NIR-II fluorescence imaging. The ultimate goal of NIR-II fluorophore-based biomedical imaging is to develop more precise diagnostics and more efficacious therapies that will be applied in clinical practice. These two chapters are laudable for bridging tool development and translation-oriented applications.

The chapter by *Bardhan/Belcher* offers a very comprehensive and authoritative overview of the applications of polymer-functionalized NIR-II emitters for *cancer theranostics* and *treatment of bacterial infections*. The authors have covered a broad range of NIR fluorophores from organic dyes to inorganic nanoparticles with a focus on SWCNTs and a wide variety of polymer-based functionalization strategies with a highlight on bioinspired, bacteriophage-assisted surface coating. In addition to the breadth of coverage, the discussion has gone into a great depth in the context of preclinical studies and clinical trials, offering a unique perspective facilitating the timely translation from bench to bedside.

The chapter by *Chen/Zhang/Li/Wang* chooses a specific type of NIR-II fluorophore, silver sulfide (Ag_2S) QDs, for discussion of its usefulness in the application of *in vivo stem cell tracking*. As in the case of most NIR-II fluorescent materials, successful in vivo studies and potential clinical translations of Ag_2S QDs necessitate carefully designed surface functionalization, which is discussed in conjunction with these nanoparticles' in vivo behavior such as pharmacokinetics, toxicology, and molecular specificity. A few selected examples of stem cell labeling and tracking studies are reviewed, including stem cell transplantation for liver therapy and cutaneous regeneration.

Moving from specific materials classes back to the larger variety of NIR-emitting bioprobes, *Jin/Nomura* discuss the potential of NIR emitters for their specific application in *in vivo mouse brain imaging*.

Again, NIR light that matches the second biological window is demonstrated to be the preferred excitation and emission light when seeking non-invasive fluorescence imaging of brain. Operating in the NIR-II window, autofluorescence, absorption, and scattering by scalp and skull can be reduced while otherwise significantly affecting the signal-to-background ratios of the fluorescence images.

It may appear to the reader that SWCNTs are at the forefront of in vivo optical bioimaging; *Jin/Nomura* also describe recent achievements based on these NIR emitters. Yet, as we can learn from this chapter, the choice is not limited to SWCNTs: Ag_2S QDs, PbS QDs, and rare earth-doped nanoparticles are discussed as alternative NIR nanoprobes for intravital imaging in the second NIR window. In addition, the reader will learn about the still young field of next-generation organic dye-based NIR nanoprobes capable of emitting at wavelengths over 1000 nm. Besides, some attention is devoted to the technical description of in vivo mouse imaging platforms, which will become handy to those aiming for their own experimental work and will hopefully stimulate the development of systems suitable for humans, a challenge that remains unaddressed to date.

Besides fluorescence imaging applications in the NIR, from the first few chapters we know that the interaction between NIR light and certain nanomaterials also lead to strong absorption of photons and efficient local generation of heat. Most readers are familiar with the photothermal effect and biomedical applications based thereon of plasmonic nanoparticles comprising gold and silver. Thus, the chapter by *Marciniak/Kniec/Elzbieciak/Bednarkiewicz* provides a different perspective by focusing on non-plasmonic photothermal materials that can be activated by NIR light, ranging from carbon nanomaterials (graphene oxide, SWCNTs, etc.), rare-

earth nanoparticles, polymers, silicon nanoparticles, titanium oxide nanoparticles to iron oxide nanoparticles. This—last but not least—chapter provides a broad survey of the current state-of-the-art development of non-plasmonic NIR photothermal agents and their applications from cancer ablation to neural activation. It is noteworthy that given the natural occurrence of heat-sensitive ion channels (such as TRPV-1) in the central nervous system, photothermal activation of these endogenous ion channels may provide a unique pathway for modulating neural activity and treating neurological diseases, calling for future advances in more efficient photothermal agents in the NIR window.

Aveiro, Portugal — Antonio Benayas
Ottawa, ON, Canada — Eva Hemmer
Stanford, CA, USA — Guosong Hong
Madrid, Spain — Daniel Jaque

Acknowledgements

A. Benayas thanks the European Commission as this project has received funding from the European Union's Horizon 2020 research and innovation program under the Marie Skłodowska Curie grant agreement no. 709270 "TEMPTATION."

Contents

Chapter 1
Optical Properties of Tissues in the Near Infrared: Their Relevance for Optical Bioimaging

Asier Marcos-Vidal, Juan José Vaquero, and Jorge Ripoll

1.1 Optical Properties of Tissues: Physical Origin and Statistical Approach

> Color: a phenomenon of light (such as red, brown, pink, or gray) or visual perception that enables one to differentiate otherwise identical objects—Merriam-Webster dictionary.

The phenomena of color surround us during our everyday life. From a visual point of view, color is just a component of light; however, it is associated with an electromagnetic perturbation propagating in space and interacting in several ways with matter. These perturbations are due to electromagnetic waves that oscillate at different frequencies, measured in Hz, with a certain associated wavelength λ, measured in nanometers (nm). Now, color can be redefined as the response or interpretation of the brain to each of these frequency components of light. This description of color reveals that it is not an intrinsic property of matter itself, but a result of its interaction with the electromagnetic radiation from the visible portion of the spectrum.

The human visual system allows to detect a wide range of stimuli; however, as happens with other senses, its sensitivity is restricted to a very narrow range of wavelengths. Infrared light (IR) is a region within the spectrum located above the red color—in terms of the wavelength—and invisible to naked eyes. This portion of the spectrum is very wide, much more than the visible (see Fig. 1.1), and is where several phenomena in nature such as heat emission take place. However, in

A. Marcos-Vidal (✉) · J. J. Vaquero · J. Ripoll (✉)
Departamento de Bioingeniería e Ingeniería Aeroespacial, Universidad Carlos III de Madrid, Madrid, Spain

Unidad de Medicina y Cirugía Experimental, Instituto para la Investigación Biomédica del Hospital Gregorio Marañón, Madrid, Spain
e-mail: asmarcos@ing.uc3m.es; jjvaquer@ing.uc3m.es; jripoll@ing.uc3m.es

A. Benayas et al. (eds.), *Near Infrared-Emitting Nanoparticles for Biomedical Applications*, https://doi.org/10.1007/978-3-030-32036-2_1

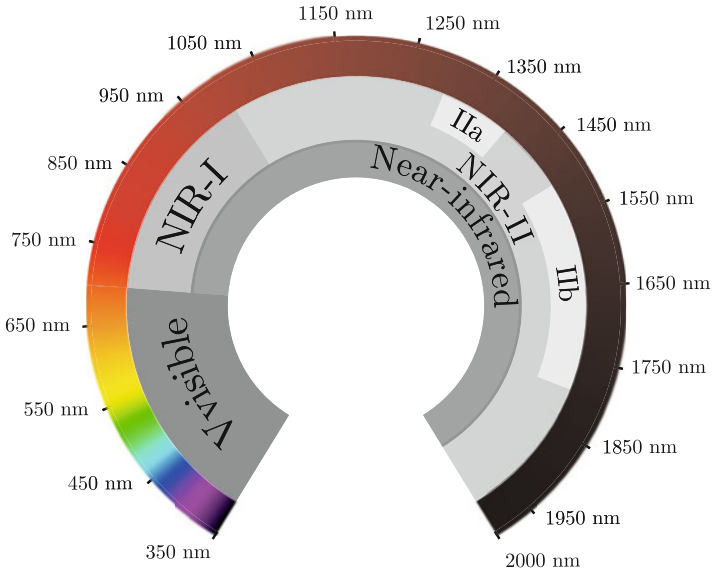

Fig. 1.1 Spectrum of visible and near infrared light with the most common imaging subwindows

biomedical imaging we are interested only in a small portion of this region, from 700 to 2000 nm, that we name the near infrared (NIR). The boundaries of the NIR are given by the high absorption that light presents in most of the IR spectrum.

The study of the interactions that occur between light and matter allows to understand the mechanisms of multiple phenomena that take place in nature. In fact, some light-based diagnosis techniques exploit this knowledge to obtain meaningful information from the body. Few of them are as simple as looking into the ear with an otoscope, seeking red areas that would reveal irritation or infections, while others require complex mathematical models or instrumentation to measure biomedical parameters or even retrieve structural information from inside the body [18].

The limitations of optical imaging techniques stem from phenomena of light propagation, so the optimal design of the optical devices relies on their comprehensive knowledge and understanding. In the following sections of this chapter, the basic interactions of light and matter will be described, then the optical properties of light in the NIR will be introduced, to finally evaluate how do they affect image quality in terms of resolution and penetration into tissues. Given the complexity of propagation theory, this text will not present a rigorous derivation of the equations presented. Readers looking for a detailed mathematical approach are encouraged to consult more specialized publications [4, 15, 20].

1.1.1 Basic Interactions Between Light and Matter

The propagation of light through tissues is a very complex phenomenon and is still a subject under study nowadays. The two main interactions that characterize it are absorption and scattering. Before going in depth into their physical meaning, it is very important to understand that energy exchanges with the medium occur within an energetic balance, having fundamental laws that must be preserved.

The fact that light is of electromagnetic nature ties it to one of the most elementary theorems in physics: energy conservation. Whatever happens during propagation, energy must be preserved. This property is the starting point to derive the equations that describe the flux of light through tissues.

The general equation of the theorem of energy conservation derived from the Poynting's theorem and has the expression:

$$\frac{\partial W}{\partial t} + \frac{dP_{abs}}{dV} + \nabla \cdot S = 0 \tag{1.1}$$

The first term describes the variation of energy density with time, the second the absorbed power, and the third the energy exchange with the medium due to incoming and outgoing energy.

The Poynting's vector describes the energy flow of an electromagnetic wave as the cross product of the electric and the magnetic fields and is directly related to what we can actually measure with the instrumentation.

This expression must always hold in the far-field—distances of several wavelengths—and, in the case of light, the particularization in terms of the statistical approximation of the optical properties of the medium will lead to the radiative transfer equation (RTE), which is the main equation for energy transport that accounts for scattering, absorption, and emission in a statistical manner. The detailed derivation of the RTE is out of the scope of this chapter; however, we will try to give a general idea of the meaning behind it.

Keeping in mind the theorem of energy conservation (Eq. 1.1), we will start now describing the main interactions that occur in tissues: absorption and scattering.

From a macroscopic point of view, absorption can be described as the energy dissipation that is produced during the interaction of an electromagnetic wave with matter. However, this process is rather more complex if studied from a particle point of view.

At room temperature, by default electrons from a particle, be it an atom or a molecule, can be found in a ground energetic state. Here we must point out that in the ground state (see Fig. 1.2, where it is defined as singlet state S_0), its electronic configuration is in the lowest available energy state given the conditions of the environment. When the incident light reaches the particle, the molecule or atom will be taken to an excited state, as long as the incident energy is enough to reach it. This means that electrons will be promoted to higher energy orbitals. Now, the molecule will tend to return back into the ground state by releasing the absorbed energy. This relaxation can occur in several ways, giving different results depending on the transition path and the excited state reached after the process.

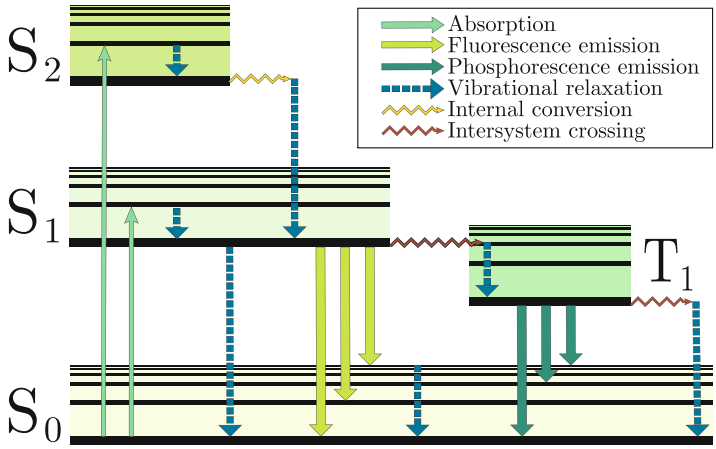

Fig. 1.2 Perrin–Jablonski diagram of the de-excitation pathways of a particle

The levels and sublevels of excitation that a particle can reach depend on the relative orientation of electron spins and the nature of the orbitals. These levels can be of two types: singlet S_1, S_2 and triplet T_1 state. Singlet states mean that all spins are paired—up/down—having a multiplicity of $M = 2S + 1 = 1$. A triplet state, on the other hand, has two spins in the same state, thus reaching a multiplicity of $2S+1 = 3$. The most common situation is that the particle reaches a singlet state. In this case, during de-excitation, the energy can be liberated following two energetic paths. Energy can be delivered into the system in form of heat due to vibrational relaxation or it can be released through fluorescence emission. In the latter, the emitted electromagnetic radiation will be of lower energy—longer wavelength—since some energy is lost in the process.

Alternatively, during de-excitation the particle can turn into a triplet state through intersystem crossing. Since it is a lower energy state, the particle can then easily relax to the ground state either through internal conversion or through what we call phosphorescence which has very long lifetimes, due to the fact that a triplet–singlet ($T_1 \rightarrow S_0$) transition is in principle forbidden due to Hund's rule.

It is important to point out that processes of fluorescence have lifetimes in the order of tens to hundreds of nanoseconds. However, phosphorescence can be a much slower process, having a delay that can go from fractions of a second up to a few seconds, minutes, or even hours. All these processes and paths of excitation and de-excitation are depicted in Jablonski diagrams as in Fig. 1.2.

Absorption accounts for the radiation that is dissipated without re-emission of light. For a single particle, it can be estimated by measuring the amount of power loss due to its interaction with an incident electromagnetic wave. The ratio of incident energy $|\langle \mathbf{S}^{(inc)} \rangle|$ [W] and absorbed power $\overline{P_{abs}}$ [W/cm^2] defines the absorption cross section σ_a.

$$\sigma_a = \frac{\overline{P_{abs}}}{|\langle \mathbf{S}^{(inc)} \rangle|}, \qquad \left(\mathrm{cm}^2\right) \tag{1.2}$$

The absorption cross section of a particle represents the effective cross section compared to its geometrical cross section in area units. This value represents only the absorption for a single particle, while, in bioimaging, it is much more useful to calculate the equivalent for a statistical ensemble of N particles per unit volume V, represented by the absorption coefficient μ_a:

$$\mu_a = \rho \sigma_a, \qquad \left(\mathrm{cm}^{-1}\right) \tag{1.3}$$

where

$$\rho = \frac{N}{V}, \qquad (\text{particles}/\,\mathrm{cm}^3) \tag{1.4}$$

Absorption is the main limiting property in terms of how deep light can penetrate in tissues, since it removes energy of the incident wavelength as light propagates within the medium. Absorption attenuates the incident light, converting it into either vibrations of the medium—heat—through non-radiative processes, or emission of light of different wavelengths through radiative processes (fluorescence, phosphorescence, and in specific cases of shorter wavelengths of emission, upconversion).

The re-emission of the incident radiation is known as scattering and practical cases of light propagation theory with in-vivo applications, only light re-emitted with the same frequency is considered. In this case, the phenomenon is specifically termed elastic scattering. In addition to the arrangement of the particles, the amount of scattering of a medium depends also on the size, shape, and spatial distribution of these scatterers.

In Mie theory [17], the probability for an incident wave of being scattered into a certain direction depends on the relative size of the particle with respect to the incident wavelength. When particles in the medium are smaller, light is scattered as an outgoing spherical wave. This solution to the Mie theory is known as Rayleigh scattering. When there is a slight index of refraction mismatch, such as between cells and the surrounding extracellular medium, as the size of the particle increases the scattered radiation deviates from that of an outgoing spherical wave, peaking in the forward scattering direction.

The scattering cross section σ_s quantifies the scattering efficiency of a particle. This can be obtained by calculating the ratio between the scattered power $\overline{P_{sc}}$ and the incident energy. However, given the directional dependence of scattering, it can be also estimated as the integral of the scattering amplitude $|f\left(\hat{\mathbf{s}}, \hat{\mathbf{s}}_0\right)|$ over all angles. The scattering amplitude accounts for the contribution of the scattered wave to a certain direction $\hat{\mathbf{s}}$, given an incident direction $\hat{\mathbf{s}}_0$. Hence, the scattering cross section gives information about the probability of light of being scattered, no matter the direction, and is defined as:

$$\sigma_s = \frac{\overline{P_{sc}}}{|\langle \mathbf{S}^{(inc)} | \rangle|} = \int_{(4\pi)} |f\left(\hat{\mathbf{s}}, \hat{\mathbf{s}}_0\right)|^2 d\Omega, \qquad \left(\mathrm{cm}^2\right) \tag{1.5}$$

The scattering coefficient μ_s can be estimated similarly to the absorption coefficient for a known density of particles in the medium.

$$\mu_s = \rho \sigma_s \qquad \left(\mathrm{cm}^{-1}\right) \tag{1.6}$$

In biological tissues, cells can be considered as the main scatterers. As they are quite transparent and their average size is usually greater than the wavelengths used for imaging, the angular distribution of the scattered light becomes highly anisotropic mainly due to the small index of refraction mismatch between different tissue components. Therefore, the description of scattering in tissues must account for this effect. The anisotropy factor g represents the average cosine of the angle between the incident wave and the scattered. This unitless parameter takes values from -1 to 1, being -1 fully backward scattering and 1 only forward. A particle with perfect isotropic scattering would have a value of 0. In terms of scattering, and neglecting absorption, this coefficient informs about how much transparent is the medium.

The anisotropy factor is included in the model through the reduced scattering coefficient, with the expression:

$$\mu_s' = (1 - g)\, \mu_s \qquad \left(\mathrm{cm}^{-1}\right) \tag{1.7}$$

As an example, a highly scattering medium with a scattering coefficient of $110\,\mathrm{cm}^{-1}$ can decrease its effective scattering through the reduced scattering coefficient if its anisotropy is 0.9–1.10 cm^{-1}. Usually, biological tissues have very high scattering anisotropy, taking values that range from $g = 0.8$ to $g = 0.9$ [16].

The scattering coefficient follows a negative power law with respect to the wavelength, thus decreasing as wavelength increases. This dependence is monotonic, due to the small size of the particles with respect to the wavelengths considered.

The dependence of the angular distribution of scattering on the relative size between the wavelength and the particles makes the scattering coefficient value to follow a negative power law with respect to the wavelength, thus for tissues decreases as wavelength increases with monotonic dependence.

It is important to remark that the statistical definition of the optical properties in terms of their relative cross sections and particle densities is valid for biological tissues only because the variations on the properties within the medium are assumed to be very smooth. Also, the constant movement of cells (motility) induces a self-averaging effect to the local light intensity. This property cancels any effect coming from constructive or destructive interference in the case of using coherent illumination.

Before moving into the physics of light propagation, two more important coefficients must be defined using the quantities of scattering, absorption, and anisotropy. The transport coefficient μ_{tr}' accounts for scattering and absorption together. This

important parameter is especially relevant when modeling propagation using Beer–Lambert's law (in absence or negligible scattering) as will be seen in the following sections.

$$\mu'_{tr} = \mu'_s + \mu_a = (1-g)\,\mu_s + \mu_a \qquad \left(\mathrm{cm}^{-1}\right) \tag{1.8}$$

A direct consequence of the definition of the transport coefficient is the transport mean free path (tmfp, l^*_{tr}), also called transport length. This parameter is key to determine the degree of diffusiveness of light because it represents the mean distance that light must travel in the medium in order to become totally isotropic in propagation and hence lose its original directionality. This term is defined as the inverse of the transport coefficient:

$$l^*_{tr} = \frac{1}{\mu'_{tr}} = \frac{1}{\mu'_s + \mu_a} \qquad (\mathrm{cm}) \tag{1.9}$$

1.2 Light Propagation in Biological Tissues

Once the optical properties of tissues have been defined, we will try to understand how light propagates through tissues. In turbid media, propagation is modeled by the diffusion approximation of the diffusion equation. The derivation of this expression is beyond the purposes of this chapter, and therefore, we will only give an overview of the steps to reach it, explaining the purpose of each of them.

The path towards deriving the diffusion equation from radiative transfer theory [15] begins by recovering the equation of energy conservation and rewriting it to include the absorption and scattering coefficients that we described in the previous section. For that, the energy must be expressed in terms of the specific intensity $I(\mathbf{r}, \hat{\mathbf{s}})$ [W/cm$^2 sr$]. This quantity represents the average flow of energy at a point $\mathbf{r}$ in a certain direction $\hat{\mathbf{s}}$. It is calculated through the integration of the discrete interaction of every incident wave—Poynting's vector—with the scatterers and absorbers within a small volume. This is equivalent to estimating the average Poynting's vector within this small volume in a certain direction.

When the equation for energy conservation is expressed in terms of the specific intensity, we obtain the RTE, which models the energy flow in a medium through the evaluation of its intensity in a certain direction in small volumes with homogeneous optical properties. The expression for a system where a certain amount of energy $\epsilon(\mathbf{r}, \hat{\mathbf{s}})$ [W/s cm^3] is introduced by a source is represented by the RTE:

$$\frac{1}{c_0}\frac{\partial}{\partial t} I(\mathbf{r}, \hat{\mathbf{s}}) + \hat{\mathbf{s}} \cdot \nabla I(\mathbf{r}, \hat{\mathbf{s}}) + \mu_t I(\mathbf{r}, \hat{\mathbf{s}}) - \mu_t \int_{(4\pi)} I(\mathbf{r}, \hat{\mathbf{s}}') p(\hat{\mathbf{s}}, \hat{\mathbf{s}}') d\Omega' = \epsilon(\mathbf{r}, \hat{\mathbf{s}}) \tag{1.10}$$

Then, if the directional information is integrated, an equivalent expression to the RTE will be reached (see Eq. 1.11), however this time in terms of the average intensity $U(\mathbf{r})$ and the flux $\mathbf{J}(\mathbf{r})$ for each position. Here, it is important to remember that the average energy for every point is calculated using the average intensity within small volumes of the medium. This time, the result of the integral over the energy introduced into the system is the source term $S_o(\mathbf{r})$ [cm^3].

$$\frac{1}{c_0}\frac{\partial}{\partial t}U(\mathbf{r}) + \nabla \cdot \mathbf{J}(\mathbf{r}) + \mu_t U(\mathbf{r}) - \mu_s U(\mathbf{r}) = S_0(\mathbf{r}) \tag{1.11}$$

The terms in Eq. (1.11) represent each of these quantities:

- The first term represents the variation of the average intensity at **r** with time.
- The second term describes the energy flux coming and leaving the volume.
- The next term accounts for the losses due to absorption and scattering. The latter here refers to the amount of energy that is scattered out of the volume considered at **r** and hence is accounted as loses.
- The last term is also referred to scattering, but in this case is describing the energy that is coming into the volume scattered by the areas surrounding. Therefore, this term has a negative sign in the equation.

The RTE can model nearly any situation regarding light propagation. Before particularizing it for diffusion, it is interesting to analyze the case in which the contributions from scattering can be neglected. Here, the medium would have a very small scattering coefficient, and hence the term that accounts for contributions from adjacent volumes can be eliminated from the expression. Assuming also no external sources and constant illumination, the equation would become:

$$\nabla \cdot \mathbf{J}(\mathbf{r}) + \mu_t U(\mathbf{r}) = 0 \tag{1.12}$$

This expression represents the modified Beer–Lambert's law for light propagation. Here, the variation of the flux of energy—which represents the fluctuation of energy density in a volume—is only caused by attenuation of the average intensity in terms of the transport coefficient (Fig. 1.3). The solution to this expression is simply an exponentially decaying intensity without any spatial change in the spatial distribution of the intensity in propagation.

The diffusion approximation aims to simplify the RTE by adding some conditions and assumptions that will help to reach an analytic solution. Through these approximations, we will obtain an expression for the average intensity U that represents the light distribution in diffusive media. Here, we will mention the most important ones, explaining their limitations and consequences in the solution of the light propagation equation.

The diffusion equation is based on Fick's law. These establish that the flux of energy flows from high concentration regions to others with lower concentration, creating a gradient of energy that depends on a constant termed the diffusion coefficient, D. This parameter is usually expressed in terms of the properties of

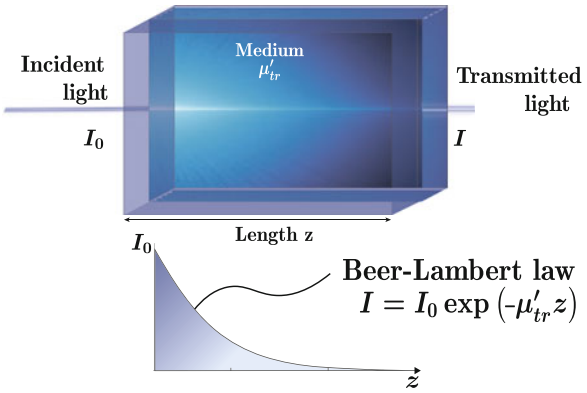

Fig. 1.3 Representation of the Beer–Lambert's law. Light transmitted in a scattering-free medium has an exponentially decaying intensity without any variation in its spatial distribution along the propagation axis

the medium and regulates the amount of energy flow. The expression for the flux $\mathbf{J}$ in terms of the gradient of the average intensity becomes:

$$\mathbf{J}(\mathbf{r}, t) = -D\nabla U(\mathbf{r}, t) \tag{1.13}$$

Before introducing the main approximation that will help to find an expression for the specific intensity, it is important to point out that in diffusion theory, light intensity flowing in the medium is divided into two components [15]:

- *Reduced intensity*, I_{ri}: ballistic contribution of light that still has high directionality.
- *Diffuse intensity* I_d: corresponds to light that has already being scattered several times and therefore has lost its initial directionality and whose flux follows Fick's law (see Eq. 1.13).

At the vicinity of the source, most of the contribution to the intensity will be from the reduced component. However, after several scattering events, it will lose completely its original direction of propagation, being its energy gradually transferred to the diffuse intensity. At a point $\mathbf{r}$ in the medium, the intensity will be a combination of these two components. Equivalently, this step has attached the definition of the corresponding average reduced and diffuse intensities, U_{ri} and U_d, and fluxes $\mathbf{J}_{ri}$ and $\mathbf{J}_d$.

In order to reach the solution of the diffusion problem, an estimation for the diffuse intensity must be introduced (since the reduced is given by the source, following Beer–Lambert's law). The definition of the angular distribution of the specific intensity is the main approximation within the diffusion approximation. It assumes that the diffuse component of the intensity can be modeled as the combination of the contributions of a uniform average intensity and a flux pointing in a certain direction (see Fig. 1.4). Mathematically, it corresponds to the first-order spherical harmonic expansion, leading to the following expression:

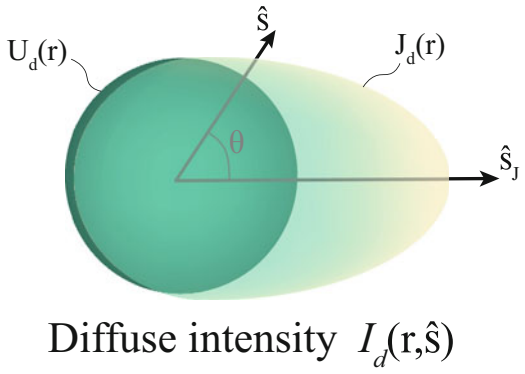

Fig. 1.4 Approximation of the diffuse intensity as a first-order spherical harmonic. The illustration depicts the angular dependence of the diffuse intensity

$$I_d\left(\mathbf{r},\hat{\mathbf{s}}\right)=\frac{U_d\left(\mathbf{r}\right)}{4\pi}+\frac{3}{4\pi}\mathbf{J}_d(\mathbf{r})\cdot\hat{\mathbf{s}} \tag{1.14}$$

This approximation incorporates essential information from the distribution of the diffuse specific intensity and allows to find an expression for the diffusion coefficient. If the definition for the diffuse intensity is introduced into the RTE and then again integrating over all angles to obtain the expression for the flux $\mathbf{J}_d$ can be found:

$$\mathbf{J}_d=-\frac{1}{3\left(\mu_s'+\mu_a\right)}\nabla U_d\left(\mathbf{r},t\right) \tag{1.15}$$

This expression is Fick's law from which the diffusion coefficient can be easily extracted:

$$D=\frac{1}{3\left(\mu_s'+\mu_a\right)}\qquad(\text{cm}) \tag{1.16}$$

The last step to finally reach the diffusion approximation is to introduce the expression for the diffuse flux into the equation for energy conservation (Eq. 1.11), which yields:

$$\frac{1}{c_0}\frac{\partial}{\partial t}U_d\left(\mathbf{r},t\right)+\mu_a U_d\left(\mathbf{r},t\right)-D\nabla^2 U_d\left(\mathbf{r},t\right)=\mu_s' U_{ri}\left(\mathbf{r},t\right) \tag{1.17}$$

In this equation, the only contribution to the reduced intensity, the ballistic component of light, comes from the source. It is very interesting to notice that if constant illumination is assumed—no temporal variation—the diffusion equation can be rewritten as a Helmholtz equation, using the relationship:

$$k_0^2=-\frac{\mu_a}{D} \tag{1.18}$$

The expression now becomes:

$$\left(\nabla^2 + k_0^2\right) U(\mathbf{r}) = -\frac{\mu_s'}{D} U_{ri}(\mathbf{r}, t) \tag{1.19}$$

This change allows to transform it into an inhomogeneous differential equation whose solution to a point source is:

$$U(\mathbf{r}) = \mathbf{S}_0 \frac{\exp(ik_0\mathbf{r})}{4\pi D\mathbf{r}} \tag{1.20}$$

The expression above represents the intensity distribution for a point source propagating in a diffusive medium.

1.3 Properties of Light in the Near Infrared

The previous section presented a description of the physics that characterize the propagation of light in tissues. The optical properties are not constant along the spectrum, taking different values for scattering and absorption depending on the chromophores, particle sizes and shapes present in the tissues, and the incident wavelength. In this section, we aim to describe the scattering and absorption spectra in the visible and NIR for the components of the tissues that have the greatest impact on imaging: blood, water, and skin. The study of the behavior of light at different wavelengths will help to understand why NIR light is so advantageous for imaging and the considerations that must be taken when designing optical systems.

1.3.1 Blood

Blood is the main absorber in tissues due to the strong presence of hemoglobin, which is the vehicle for oxygen transport. This chromophore constitutes up to 97% of red blood cells composition which conform approximately 50% of the whole blood's volume. The other half are white cells, platelets, and mainly plasma, which is nearly transparent due to its elevated content of water. There are some differences between the absorption efficacy of oxygenated and deoxygenated blood, being the first redder and therefore slightly more absorbent in the region within 600 and 700 nm. These properties enable several measurements of biomedical parameters such as blood oxygen saturation just by playing with the intensities that pass through a finger at different wavelengths.

In the NIR, both oxygenated and deoxygenated blood have a minimum in their absorption curve (see Fig. 1.5), becoming nearly two orders of magnitude more transparent than in the visible regime. Since blood is one of the main absorbers

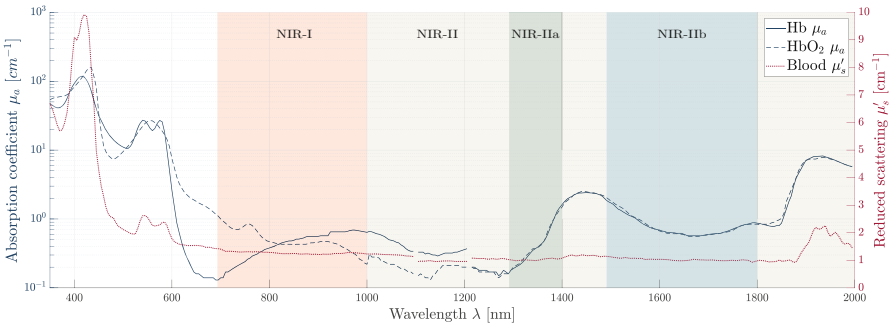

Fig. 1.5 Spectra of absorption and scattering of blood and water absorption. In the near infrared blood presents reduced scattering and less absorption compared to the visible region. Note that the absorption for oxygenated blood (HbO_2) in the range from 600 to 800 nm is much lower than deoxygenated giving it its characteristic dark red color. Data interpolated from [5]

in the body, and given its strong presence in tissues, light in the NIR can penetrate much deeper than in the visible range. Moreover, the scattering coefficient decreases monotonically for longer wavelengths, increasing notably the transport mean free path of light in the NIR [5].

1.3.2 Water

Since 60% of human body weight is water—on average—it must be carefully taken into account for imaging. Its absorption spectrum reveals high transparency in the visible wavelengths, increasing significantly in the infrared. In fact, in the NIR, it can be up to two orders of magnitude more absorbent.

The water absorption coefficient curve has a sharp transition in the NIR, having a peak at 1400 nm that limits the penetration depth of light for this window. This maximum splits the II-NIR window into the a and b regions. So far, during the design of the optimal working wavelength of an imaging system, this peak used to be avoided, using frequencies of the spectrum below or above (see Fig. 1.6). However, recent studies suggest that image contrast and penetration depth can be maximized at those wavelengths of greatest water absorption [6, 26].

1.3.3 Skin

Optical imaging techniques that aim to measure deep into tissues must traverse the skin. Its main chromophore is melanin, which is in charge of protecting the body against ultraviolet radiation by absorbing the harmful radiation and releasing

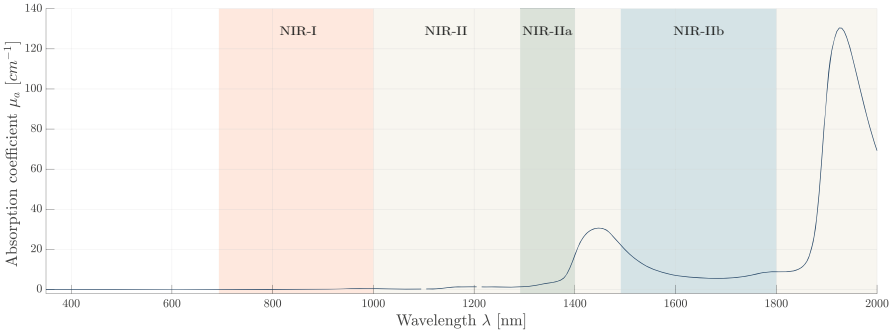

Fig. 1.6 Absorption spectrum of water. Attenuation increases in the near infrared. The absorption peaks are used to determine the imaging windows. Data interpolated from Steve Jacques and Scott Prahl's website, http://omlc.org/spectra

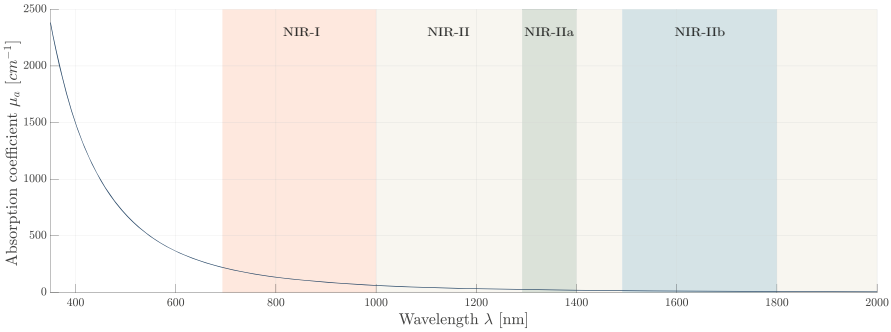

Fig. 1.7 Absorption spectrum of melanin. Data generated using Steve Jacques and Scott Prahl's website, http://omlc.org/spectra

it through vibrational relaxation as heat. Thus, skin absorption is very high between 300 and 400 nm (see Fig. 1.7).

The absorption coefficient of skin depends on the type and density of melanin that predominates, which gives a specific color depending on the subject. In general, experimental measurements of its optical properties reveal that at longer wavelengths than 400 nm absorption decreases, having a minimum region between the I and II-a near infrared windows. In the II-b, the increase of absorbance of water reduces the skin's transmittance slightly.

In terms of depth of penetration, the best region to measure through skin is between 1000 and 1300 nm; however, as the scattering coefficient decreases for longer wavelengths, imaging in the II-b region is still favorable [3].

1.3.4 Tissue Autofluorescence

Tissues by default have endogenous fluorescent components, each with different absorption and emission properties and lifetimes. In fluorescence imaging modalities, the excitation light can also activate these molecules, creating an "endogenous" background intensity in the images that decreases the signal-to-noise ratio, the sensitivity, and the fluorescent probe specificity. This is especially critical for the cases where the fluorophore is located deep in the tissues and nearly no excitation illumination can reach it. In this scenario, increasing the exposure time of the sensor will also amplify the background intensity.

Light in the NIR, especially in the II window, presents two advantages regarding tissue autofluorescence. Firstly, the tissue autofluorescence is much lower than in the visible and I-NIR. This is especially relevant for the II-a and b windows of the spectrum, where the autofluorescence intensity is almost negligible [24]. Secondly, the increased depth of penetration and reduced scattering allows the excitation of the target fluorophore with more intensity and accuracy (due to lower scattering). In the I-NIR window, a significant contribution to autofluorescence can still be found in melanin, inner organs and, in the specific case of mice, in the intestines mainly due to the presence of alfalfa [8]. This particular case may be significantly improved by switching to an alfalfa-free diet.

1.4 Imaging in the II Near Infrared Window

As has been presented during the previous sections, imaging in the NIR has several advantages over the visible spectrum. Given the broad range of wavelengths it comprises, several NIR subwindows have been defined according to the optical properties of tissues. Recently, the latest detection instruments allowed imaging in the II-NIR window, which has the most advantageous optical properties.

In general, most of the tissues present lower absorption and scattering rates in the II-NIR window and, in addition to the reduced autofluorescence, they contribute to an optimal scenario for fluorescence imaging. Techniques suffering from limited efficiency on the excitation of the fluorophore due to scattering such as light-sheet fluorescence microscopy [19] can take advantage of NIR wavelengths to create planes of light that allow to scan through larger samples. Moreover, fluorophores with emissions in the II-a and II-b windows offer better possibilities in terms of contrast and resolution at depths up to several centimeters [9, 13]. However, the number of fluorophores effective in this range is still very limited, specially those with tested biocompatibility [14]. Lately, some groups have started to explore the possibilities of commercially available NIR dyes, such as the FDA-approved indocyanine green (ICG) for imaging in the II-NIR window [7]. Finally, other techniques such as optical projection tomography (OPT) can notably improve their performance in terms of resolution and sample sizes using low scattering wavelengths [1, 12, 23].

Although the optical properties in the II-NIR region seem to be ideal, there is still much to do regarding the characterization of the propagation of light at these new imaging windows. The reduction in scattering increases the ballistic contribution of light (what was termed reduced intensity in Eq. 1.17), but the contribution of diffuse light still needs to be accounted for. Indeed, some approximations need to be revisited since the diffusion approximation on its own is not enough to properly model light propagation in this regime.

When propagating in very low scattering media, the contribution from the reduced intensity is higher than the expected by the diffusion equation [30]. This is the case of NIR light, where the transport length is much greater, hence measurements will be taken at distances where light has not become yet totally diffusive (or that still maintains some of its original directionality). When the transport mean free path increases, the transition from the ballistic to the diffusion regime takes place within up to several centimeters inside tissue (instead of millimeters as in the case of visible light), therefore the region with a high contribution of the reduced intensity is higher.

Under these conditions, one of the main approximations in the diffusion equation, the angular distribution of light based on a single angular component, might not be adequate. There are works using higher orders of spherical harmonic expansions to model the diffuse intensity, named the P_n approximation [2]. Others try to find the distance in terms of the transport length where the transition from ballistic to diffusion propagation takes place [29]. The study of the propagation of NIR light still has many unresolved issues. Currently the most common approach is to simulate the propagation using Monte Carlo methods [28] and then try to refine the diffusion model [10, 22, 25] or the RTE [27] to make them reproduce the results. Further investigations are needed to appropriately characterize the propagation in the NIR and improve the reconstruction methods.

1.5 Consequences of Near Infrared Light Propagation in Image Quality and Resolution

The previous sections of this chapter described the basics of light propagation in biomedical tissues. Additionally, the optical properties of tissues in the NIR and their consequences in diffusion theory were explained. This section aims to present from a practical point of view the consequences that the physics behind light propagation has when imaging in turbid media such as tissues. We will discuss the concept of resolution, how the properties of the medium affect it, and how light diffusion reduces image resolution as we image further from the objects studied.

The solution to the diffusion equation is an exponentially decaying outgoing spherical wave. Light emitted by an isotropic source, which could be a fluorescent bead, would propagate as displayed in Fig. 1.8. The Monte Carlo simulation propagates light in a medium with low scattering, where diffusion is expected to

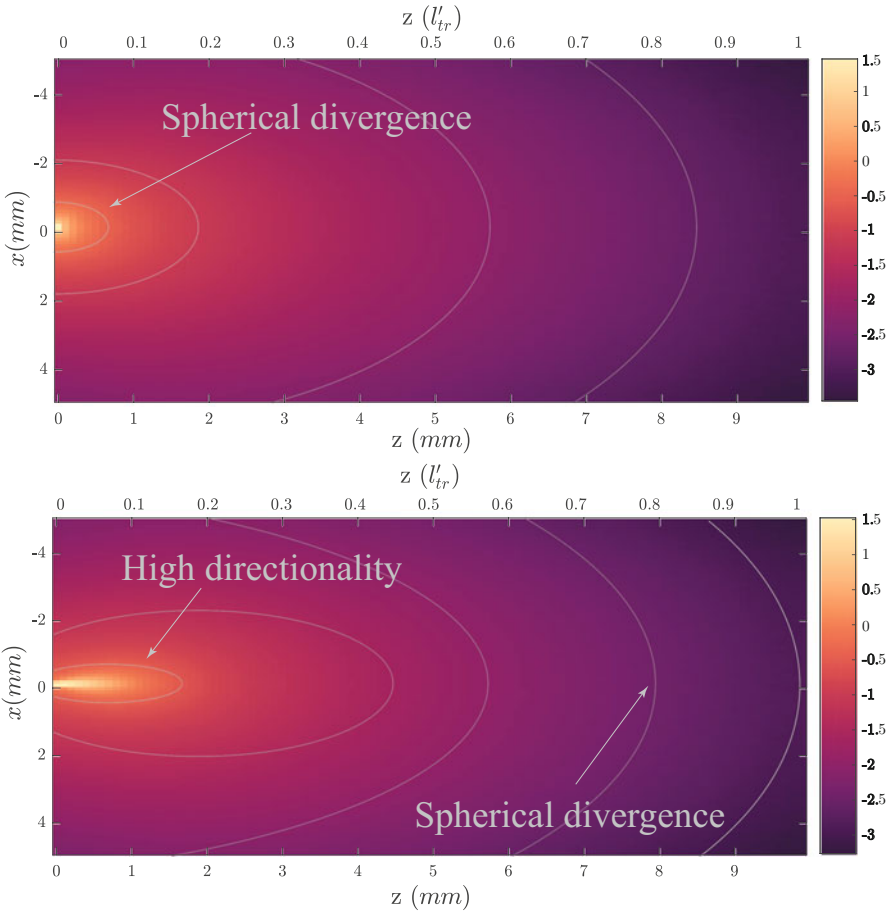

Fig. 1.8 Monte Carlo simulations using the MCX package [11] of an isotropic source (top) and a collimated Gaussian beam (bottom) propagating in a medium with optical properties: $\mu_a = 0.025\,\mathrm{cm}^{-1}$, $\mu_s' = 1\,\mathrm{cm}^{-1}$

hold at large distances from the source (approx. 1 cm, the inverse of the transport mean free path) only. If the source is collimated (see Fig. 1.8, bottom), as in the case of a laser beam, the effect of diffusion is much clearer from a visual point of view. Light has high directionality when entering the medium, but after traveling a very short distance, it loses it completely. Soon it starts propagating as a spherical wave centered inside the medium at a depth equivalent to one transport mean free path, as described by the solution of the diffusion equation. Although the simulations were performed using a relatively low scattering medium, it is easy to notice how directionality is nearly lost after just a few mm. In the case of a high scattering medium, this distance could have been lower than a millimeter. The quick loss of intensity also illustrates how difficult is to reach deep tissues. Even with low

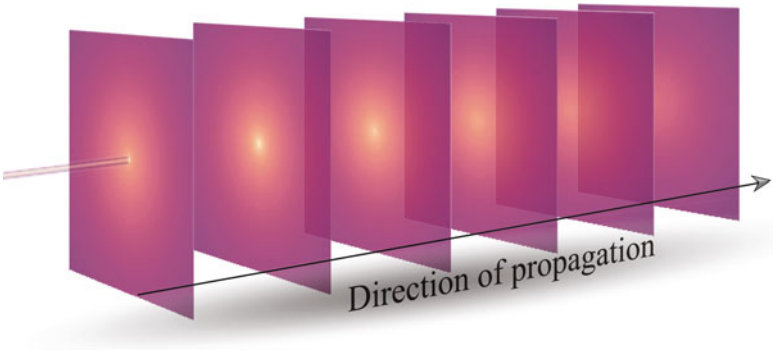

Fig. 1.9 Illustration of the propagation of a collimated source through an infinite medium with optical properties: $\mu_a = 0.025\,\mathrm{cm}^{-1}$, $\mu_s' = 1\,\mathrm{cm}^{-1}$. Images generated using simulations performed with Monte Carlo MCX package [11]

absorption, scattering would spread the light everywhere, inevitably reducing the intensity in the direction of propagation and leading to a uniform distribution of light in the distance (Fig. 1.9).

Light diffusion also reduces the amount of information that light carries from the sample. To describe this effect, we need first to introduce the concept of spatial resolution. This key parameter in the evaluation of the performance of any imaging system quantifies its actual resolving power. Formally, it can be defined as the ability to separate images of two neighboring object points.

In signal processing and engineering, a spatial frequency refers to the number of cycles of a sinusoidal per unit length. In the context to imaging, it can be said that high frequencies contain the information of fine details and sharp edges. The connection between spatial frequencies and resolution arises from the fact that the resolution limit of an image is the highest spatial frequency that can be resolved. Diffusion attenuates all frequencies, but this attenuation increases exponentially for higher spatial frequencies [21].

The response in the frequency domain in diffuse imaging can be predicted by the transfer function. This function describes how much each spatial frequency K is attenuated due to the effect of propagation. The convolution between an incident field and the transfer function of the medium allows to estimate the intensity distribution at a certain plane z. The resolution limit at a certain distance can be obtained from the transfer function by measuring the full width half maximum (FWHM). This parameter is obtained by measuring the width of the lobe where the intensity falls to the half of its maximum value. Figure 1.10 shows how the bandwidth decreases with distance while, at the same time, there is a global attenuation of the intensity for the entire frequency spectrum. This means that there is a quick loss of energy components in high frequency, thus acting as a low pass filter which narrows as we propagate deeper into the medium

The main effect of low pass filtering an image is a loss of details, making it blurry. Figure 1.11 gives an intuitive idea of these effects. After propagating a few millimeters, the smaller structures—high frequencies components—are nearly invisible.

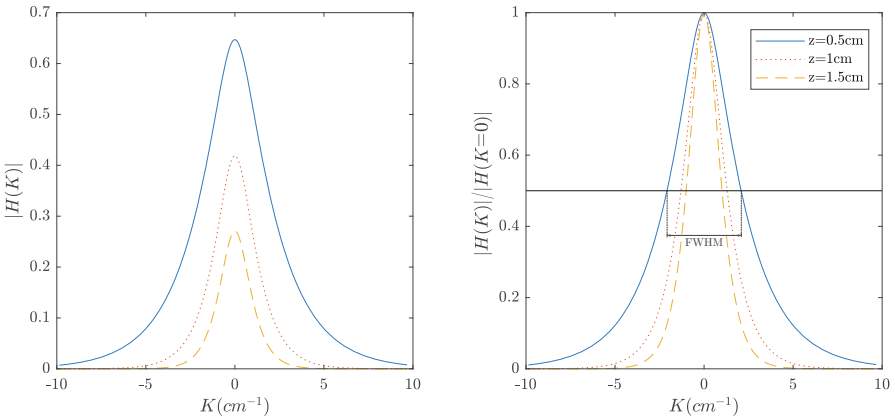

Fig. 1.10 Example values of the transfer function in a diffusive medium with optical properties $\mu_a = 0.025\,\mathrm{cm}^{-1}$, $\mu_s' = 10\,\mathrm{cm}^{-1}$. Right plot shows the values of the left plot normalized to the $K = 0$ value

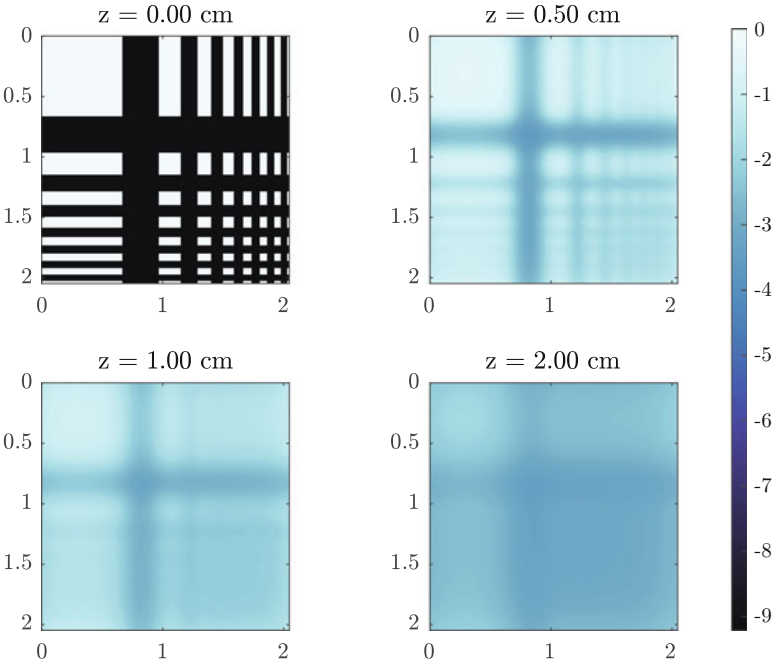

Fig. 1.11 Simulation of the propagation of a pattern using the transfer function of a diffusive media with optical properties: $\mu_a = 0.025\,\mathrm{cm}^{-1}$, $\mu_s' = 10\,\mathrm{cm}^{-1}$. Intensities normalized with respect to $z = 0\,\mathrm{cm}$

The loss of resolution affects also to the larger—low-frequency components—which will become indistinguishable too after traveling slightly further in the medium. Also, the general intensity of the image decreases with propagation.

The consequences of light diffusion on quality are unavoidable; however, a reduced scattering and absorption medium can increase distance light may propagate without significant loss of resolution, reducing the spectral losses in the first millimeters and allowing a higher depth of penetration. This is the biggest advantage of using NIR light for imaging and the main reason for the high interest shown by the scientific community. Nowadays, the recent appearance of new NIR cameras sensitive to IIa and IIb windows, and the development of novel fluorescent probes in this range offer to researchers the possibility to take advantage of all the benefits that NIR light can bring into imaging.

References

1. Arranz A, Dong D, Zhu S, Savakis C, Tian J, Ripoll J (2015) In-vivo optical tomography of small scattering specimens: time-lapse 3D imaging of the head eversion process in Drosophila melanogaster. Sci Rep 4(1):7325
2. Arridge SR, Schotland JC (2009) Optical tomography: forward and inverse problems. Inverse Prob 25(12):123010
3. Bashkatov AN, Genina EA, Kochubey VI, Tuchin VV (2005) Optical properties of human skin, subcutaneous and mucous tissues in the wavelength range from 400 to 2000 nm. J Phys D Appl Phys 38(15):2543–2555
4. Born M, Wolf E, Bhatia AB, Clemmow PC, Gabor D, Stokes AR, Taylor AM, Wayman PA, Wilcock WL (1999) Principles of optics. Cambridge University Press, Cambridge
5. Bosschaart N, Edelman GJ, Aalders MCG, van Leeuwen TG, Faber DJ (2014) A literature review and novel theoretical approach on the optical properties of whole blood. Lasers Med Sci 29(2):453–479
6. Carr JA, Aellen M, Franke D, So PTC, Bruns OT, Bawendi MG (2018) Absorption by water increases fluorescence image contrast of biological tissue in the shortwave infrared. Proc Natl Acad Sci 115(37):9080–9085
7. Carr JA, Franke D, Caram JR, Perkinson CF, Saif M, Askoxylakis V, Datta M, Fukumura D, Jain RK, Bawendi MG, Bruns OT (2018) Shortwave infrared fluorescence imaging with the clinically approved near-infrared dye indocyanine green. Proc Natl Acad Sci 115(17):4465–4470
8. Del Rosal B, Villa I, Jaque D, Sanz-Rodríguez F (2016) In vivo autofluorescence in the biological windows: the role of pigmentation. J Biophoton 9(10):1059–1067
9. Diao S, Blackburn JL, Hong G, Antaris AL, Chang J, Wu JZ, Zhang B, Cheng K, Kuo CJ, Dai H (2015) Fluorescence imaging in vivo at wavelengths beyond 1500 nm. Angew Chem Int Ed 54(49):14758–14762
10. Durduran T, Yodh AG, Chance B (1997) Does the photon-diffusion coefficient depend on absorption? J Opt Soc Am A Opt Image Sci Vis 14(12):3358–3365
11. Fang Q, Boas DA (2009) Monte Carlo simulation of photon migration in 3D turbid media accelerated by graphics processing units. Opt Exp 17(22):20178
12. Fieramonti L, Bassi A, Foglia EA, Pistocchi A, D'Andrea C, Valentini G, Cubeddu R, de Silvestri S, Cerullo G, Cotelli F (2012) Time-gated optical projection tomography allows visualization of adult zebrafish internal structures. PLoS One 7(11):1–7

13. Hong G, Diao S, Chang J, Antaris AL, Chen C, Zhang B, Zhao S, Atochin DN, Huang PL, Andreasson KI, Kuo CJ, Dai H (2014) Through-skull fluorescence imaging of the brain in a new near-infrared window. Nat Photon 8(9):723–730
14. Hong G, Antaris AL, Dai H (2017) Near-infrared fluorophores for biomedical imaging. Nat Biomed Eng 1(1):0010
15. Ishimaru A (1978) Wave propagation and scattering in random media. Elsevier, New York
16. Jacques SL (2013) Optical properties of biological tissues: a review. Phys Med Biol 58(11):R37–R61
17. Mie G (1908) Beiträge zur Optik trüber Medien, speziell kolloidaler Metallösungen. Ann Phys 330(3):377–445
18. Ntziachristos V, Ripoll J, Weissleder R (2002) Would near-infrared fluorescence signals propagate through large human organs for clinical studies? Opt Lett 27(5):333
19. Olarte OE, Andilla J, Gualda EJ, Loza-Alvarez P (2018) Light-sheet microscopy: a tutorial. Adv Opt Photon 10(1):111
20. Ripoll J (2012) Principles of diffuse light propagation: light propagation in tissues with applications in biology and medicine. World Scientific, Singapore
21. Ripoll J, Nieto-Vesperinas M, Carminati R (1999) Spatial resolution of diffuse photon density waves. J Opt Soc Am A 16(6):1466
22. Ripoll J, Yessayan D, Zacharakis G, Ntziachristos V (2005) Experimental determination of photon propagation in highly absorbing and scattering media. J Opt Soc Am A Opt Image Sci Vis 22(3):546–551
23. Ripoll J, Meyer H, Garofalakis A (2009) In vivo optical tomography: from diffusion to ballistic. Opt Mater 31(7):1082–1085
24. Smith AM, Mancini MC, Nie S (2009) Bioimaging: second window for in vivo imaging. Nat Nanotechnol 4(11):710–711
25. Spott T, Svaasand LO (2000) Collimated light sources in the diffusion approximation. Appl Opt 39(34):6453–6465
26. Tanzid M, Hogan NJ, Sobhani A, Robatjazi H, Pediredla AK, Samaniego A, Veeraraghavan A, Halas NJ (2016) Absorption-induced image resolution enhancement in scattering media. ACS Photon 3(10):1787–1793
27. Tarvainen T, Vauhkonen M, Kolehmainen V (2005) Coupled radiative transfer equation and diffusion approximation model for photon migration in turbid medium with low-scattering and non-scattering. Phys Med Biol 4913(20):4913–4930
28. Wang L, Jacques SL, Zheng L (1995) MCML – Monte Carlo modeling of light transport in multi-layered tissues. Comput Methods Prog Biomed 47(2):131–146
29. Yaroshevsky A, Glasser Z, Granot E, Sternklar S (2011) Transition from the ballistic to the diffusive regime in a turbid medium. Opt Lett 36(8):1395
30. Yoo KM, Liu F, Alfano RR (1990) When does the diffusion approximation fail to describe photon transport in random media? Phys Rev Lett 64(22):2647–2650

Chapter 2
NIR Autofluorescence: Molecular Origins and Emerging Clinical Applications

Blanca del Rosal, Giju Thomas, Anita Mahadevan-Jansen, and Paul R. Stoddart

2.1 Introduction

Fluorescence imaging is a well-established technique in biomedical research, enabling visualization of subcellular structures and molecular processes through selective labeling with fluorescent contrast agents [1]. Although fluorescence imaging is a mainstay of cell and tissue imaging, it has only had a minor impact in the broader field of biomedical research, for example, in small animal models or in the clinical field. This is a consequence of the limitations of the majority of the fluorophores used for cellular imaging, as they require UV/visible light for optical excitation and they emit in the visible. The large attenuation of light by tissues in these spectral ranges makes imaging at tissue depths beyond a few hundred microns impossible, thus preventing the application of fluorescence for minimally invasive in vivo bioimaging. Although clearing techniques have been developed to reduce the opacity of biological tissues to light, these are not applicable in live animals [2]. However, the attenuation of light is substantially reduced at longer wavelengths, effectively expanding the applicability of fluorescence imaging to deep tissues in living organisms. The negligible absorption of biological tissues in the near infrared (NIR) spectral ranges known as biological windows (NIR-I, 650–950 nm; NIR-II,

B. del Rosal (✉)
Centre for Micro-Photonics, Swinburne University of Technology, Hawthorn, VIC, Australia
e-mail: bdelrosalrabes@swin.edu.au

G. Thomas · A. Mahadevan-Jansen
Vanderbilt Biophotonics Center, Vanderbilt University, Nashville, TN, USA

Department of Biomedical Engineering, Vanderbilt University, Nashville, TN, USA

P. R. Stoddart
ARC Training Centre in Biodevices, Swinburne University of Technology, Hawthorn, VIC, Australia

A. Benayas et al. (eds.), *Near Infrared-Emitting Nanoparticles for Biomedical Applications*, https://doi.org/10.1007/978-3-030-32036-2_2

1000–1700 nm) and the monotonic decrease in scattering for longer wavelengths enable imaging in vivo with micrometric spatial resolution at tissue depths up to a few centimeters [3–5]. Compared to imaging techniques already established at the clinical level, NIR fluorescence imaging offers two clear advantages: the low cost and versatility of the required equipment and the possibility of imaging in real time while avoiding major concerns from a biosafety standpoint [6]. This has generated substantial research efforts to implement in vivo fluorescence imaging in preclinical research and at the clinical level [7].

The development of NIR fluorescence as an in vivo imaging technique has come hand in hand with progress in two key areas: NIR detector technology and material synthesis techniques. The lack of cost-effective cameras capable of imaging in NIR-II contributed to the slow development of NIR bioimaging until recently. The systems developed for preclinical in vivo fluorescence imaging are equipped with Si detectors, whose sensitivity falls off dramatically beyond 900 nm, rendering them useless for NIR-II imaging. Cameras capable of imaging in the 1000–1700 nm spectral range employ InGaAs sensors, which used to rely on liquid nitrogen cooling to lower the thermal noise to acceptable levels. This increased their price point and made them impractical for broader applications in bioimaging. However, the development of newer InGaAs sensors capable of low noise imaging at higher temperatures (about −80 °C, achievable with thermoelectric cooling) has made affordable NIR cameras accessible to researchers working in the bioimaging field.

The lack of suitable NIR-II cameras until recently explains why no fluorophores were designed to operate in this spectral range. As reviewed in detail by Hong et al. in 2016, most NIR contrast agents developed for bioimaging applications, including small-molecule dyes, NIR fluorescent proteins, and a great variety of inorganic nanoparticles (NPs), operate in NIR-I [8]. The only NIR fluorophores (methylene blue, MB, and indocyanine green, ICG) that have received FDA approval for clinical application so far also absorb and emit within this spectral range. However, research has shown that NIR-II imaging is superior to NIR-I in terms of spatial resolution, penetration depth, and signal-to-noise ratio [9, 10]. NIR-II imaging was demonstrated in vivo with different inorganic NPs (carbon nanostructures, lanthanide-doped NPs, and quantum dots) well before any dyes with emission bands in this spectral range were available. Inorganic NPs offer some advantages with respect to organic fluorophores, including a higher photochemical stability and a lower tendency to aggregate. The possibility of tuning the emission wavelength and lifetime of inorganic NPs enables multiplexed imaging both in the wavelength and time domains, thus enabling visualization of multiple structures simultaneously [11–13]. Despite their usefulness for preclinical research, concerns due to their possible accumulation in the organism and subsequent long-term toxicity will likely complicate their application at the clinical level. However, the recent development of dyes offering NIR-II contrast—which is also achievable with clinically approved, NIR-I-emitting ICG—suggests that the applicability of NIR fluorescence imaging will not be limited to research for much longer [14–16].

One of the major limitations of fluorescence microscopy for cell and tissue imaging lies in the intrinsic fluorescence of some biomolecules present in

biological tissues. This can reduce the signal-to-noise ratio of the resulting images and complicate or even prevent the identification of extrinsic fluorophores [17]. Autofluorescence is the major source of background noise in fluorescence microscopy images and is hard to avoid due to the large variety of biomolecules that contribute to the overall autofluorescence signal [18]. This results in broad autofluorescence spectra (typically spanning several hundreds of nanometers) which vary greatly between tissues and complicate the design of a general solution for autofluorescence-free imaging. Current techniques for improving the signal-to-noise ratio with no image processing are impractical, as they need to be tailored to each specific application, requiring an optimized filter set for a given fluorophore and/or treatment of the sample to eliminate a certain source of autofluorescence [19, 20]. Image processing techniques based on background subtraction are therefore the commonplace approach for maximizing the signal-to-noise ratio in fluorescence images in the visible [21, 22].

As occurs in the visible, autofluorescence constitutes the major source of background noise for NIR imaging in vivo. However, NIR autofluorescence is by no means as well studied as it is in the visible: despite many authors observing an intense autofluorescence in small animal imaging experiments, its molecular origins are often unclear. The spectroscopic properties of some known NIR intrinsic fluorophores are still not fully characterized, particularly in NIR-II. While much attention is dedicated to reducing autofluorescence background "noise," the tissue dependence of autofluorescence can convey useful diagnostic information about the tissue status [23]. This chapter addresses both of these aspects of the autofluorescence phenomenon.

In the following sections, we will deal with the major contributors to autofluorescence of biological tissues in the NIR and discuss why they constitute an issue when performing in vivo fluorescence imaging (Sect. 2.2). Despite NIR autofluorescence constituting the main source of background noise when imaging external contrast agents, it also provides valuable information about the molecular components present in a tissue, which will be described in Sect. 2.3. As will be discussed in Sect. 2.4, this has enabled the design of diagnostic strategies based on NIR autofluorescence, which are attracting increasing attention on account of their non-invasiveness and ease of implementation.

2.2 NIR Autofluorescence as a Problem

There is relatively little available information about NIR autofluorescence, largely because of the same lack of contrast agents and imaging systems that prevented significant progress with in vivo NIR imaging until recently. Early reports on NIR small animal imaging observed a substantial decrease in autofluorescence for NIR excitation and emission wavelengths when compared to different ranges within the visible, as shown in Fig. 2.1a [24]. This reduced autofluorescence complements the improved penetration of NIR light into tissues to enable low noise in vivo

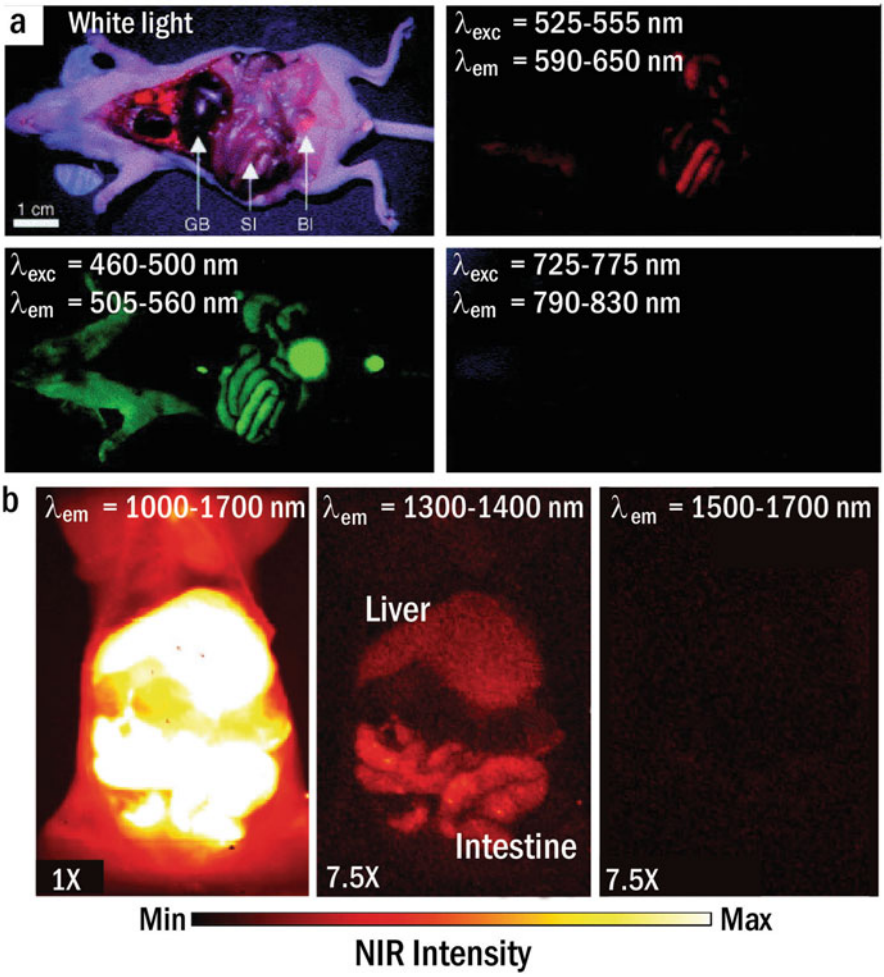

Fig. 2.1 In vivo autofluorescence. (**a**) Fluorescence images obtained in different spectral ranges in the visible and NIR-I for a mouse with its abdominal organs exposed. The excitation power density was set to 2 mW/cm^2 in all cases. Adapted with permission [24]. Copyright 2003, Elsevier. (**b**) Fluorescence images obtained under 808 nm excitation for a mouse with its abdominal organs exposed. Adapted with permission [32]. Copyright 2015, Elsevier

fluorescence imaging at increased tissue depths compared to visible wavelengths. Despite these images leading to the idea that the biological windows are intrinsically autofluorescence-free, that is overly optimistic: the irradiation power density used to obtain the images in Fig. 2.1a was only 2 mW/cm^2. This is two orders of magnitude lower than the typical irradiation power densities used in NIR small animal imaging, which usually approach the maximum permissible exposure thresholds. In the NIR, these thresholds depend on the wavelength (the longer the wavelength, the higher the

tolerable exposure) and lie between 0.2 and 1 W/cm^2 for wavelengths in the 700–1050 nm range [25]. Under these higher intensity irradiations, NIR autofluorescence can still be a problem, preventing accurate isolation of the emission generated by NIR contrast agents for in vivo experiments. As shown in the NIR images in Fig. 2.1b, autofluorescence is present even in NIR-II [26]. It does, however, decrease for longer wavelengths, becoming negligible in the 1500–1700 nm spectral range (often labeled as NIR-IIb or NIR-III). As a reduced signal-to-noise ratio due to the presence of autofluorescence can lead to misinterpretation of biodistribution studies of NIR fluorophores and limit the potential clinical applicability of NIR fluorescence imaging [27], developing strategies for minimizing the autofluorescence background has been a priority in the NIR bioimaging research field [28–33].

The complexity of biological tissues and the intrinsic challenges associated with in vivo imaging at large penetration depths complicate the extraction of information about autofluorescence in living organisms [34]. The overall autofluorescence signal registered by the imaging system will be composed of the contributions of several endogenous fluorophores located at different tissue depths. The spectral shape and intensity of this signal will depend on the type and concentration of these fluorophores, but the interaction between the light (both the excitation light and the emitted autofluorescence) and the tissues cannot be neglected either. Thus, the depth at which the endogenous fluorophores are located and the optical properties of the tissues the light has to penetrate through will influence the overall autofluorescence emission. This indicates that the in vivo autofluorescence background will vary greatly depending on the targeted tissue and the experimental conditions. Moreover, individual variations in tissue thickness, fluorophore concentration and distribution grant that no two in vivo imaging experiments display identical autofluorescence profiles, as has been experimentally observed [35–38].

Despite its variability and complexity, strategies that take advantage of the common features of endogenous fluorophores have enabled autofluorescence-free in vivo imaging. These approaches rely on NIR contrast agents whose fluorescence emission is significantly different from autofluorescence, spectrally or temporally, and experimental setups capable of filtering out the autofluorescence background [28]. However, the need to eliminate the autofluorescence background to achieve high contrast in vivo images and the possibility of doing so by choosing an adequate experimental approach has to date resulted in very few reports dealing with the causes of NIR autofluorescence at the molecular level, as we will detail in the following section.

2.3 NIR Autofluorescence Sources

Whereas many molecules in cells and tissues display fluorescence in the UV/visible range, only a few intrinsic fluorophores emitting in the NIR under NIR excitation have been identified. The spectroscopy of visible-emitting intrinsic fluorophores

has been thoroughly characterized, thanks to the widespread use of fluorescence microscopy in biomedical research. This has enabled the development of imaging strategies to minimize the background noise and autofluorescence-based methods for diagnostic and analytical applications [39–41].

2.3.1 Autofluorescence in the Visible

Multiple endogenous fluorophores contribute to the intrinsic fluorescence of cells and tissues in the visible range. As most of them do not constitute a source of background noise in NIR imaging, we will not give a detailed description of their properties, which can be found in several previous works [17, 42, 43]. In animal cells, flavins and pyridine nucleotides are two major contributors to visible autofluorescence, displaying emission bands close to 500 nm upon UV excitation. The autofluorescence of these molecules, heavily involved in cellular energy metabolism, depends on their oxidation state and binding to other molecules, so that tissue metabolic status can be evaluated by monitoring their emission [44, 45]. Other fluorescent compounds in animal cells include aromatic amino acids (tryptophan, tyrosine, and phenylalanine) and lipopigments, which are by-products of lipid oxidation. The former emit at around 400 nm under UV excitation, while lipopigments are optimally excited at 340–390 nm and present their emission peak close to 600 nm [46]. Accumulation of lipopigments in the cytoplasm is linked not only to aging, but also to multiple pathologies (retinal degeneration or atherosclerosis, for instance), so detection of these components via fluorescence can be used for diagnostic applications [47–49]. The extracellular matrix contributes to visible autofluorescence even more so than intracellular components due to the relatively high quantum yield of collagen and elastin. The fluorescence of these structural proteins displays multiple excitations and emission peaks spanning the visible range and seems to be associated with crosslink formation, which makes it relevant for disease diagnostics [50].

Fluorescence of all these biological components arises from transitions between singlet states, thus presenting characteristic short decay times (in the nanosecond range) [51]. The emission lifetimes of intrinsic fluorophores has been characterized in detail due to the development of fluorescence lifetime microscopy as a powerful tool capable of monitoring biochemical processes in living cells [52].

2.3.2 In Vivo Autofluorescence in the NIR: Plant Sources

Plant tissues present autofluorescence in a broad spectral range due to emission from a diverse group of phytochemicals, including flavonoids, lignin, carotenes, anthocyanins, and chlorophyll [53]. Among them, chlorophyll is the most widely studied fluorescent compound, as its visible/NIR-I fluorescence allows non-invasive

assessment of photosynthesis in living plants [54, 55]. Green plants present two variants of this chromophore, chlorophyll *a* and chlorophyll *b*, which present similar excitation bands in the blue and far-red, and emission bands that extend from the far-red into NIR-I. However, due to non-radiative energy transfer processes from chlorophyll *b* to chlorophyll *a*, the latter is the main contributor to plant fluorescence [56]. Chlorophyll *a* presents excitation maxima at 485 nm and 655 nm, while its emission band is centered at 682 nm and displays a shoulder peak at 740 nm that extends well into NIR-I as shown in Fig. 2.2a [57]. As it originates from allowed transitions between excited singlet states and the ground state (see the inset in Fig. 2.2a), the fluorescence of chlorophyll has a very fast time decay (in the order of nanoseconds) [58, 59]. Chlorophyll also presents longer lifetime (in the milliseconds range) phosphorescence bands that peak at around 950 nm and arise from spin-forbidden transitions from energy triplet states to the singlet ground state [60]. The extremely low quantum yield of these transitions (10^4–10^6

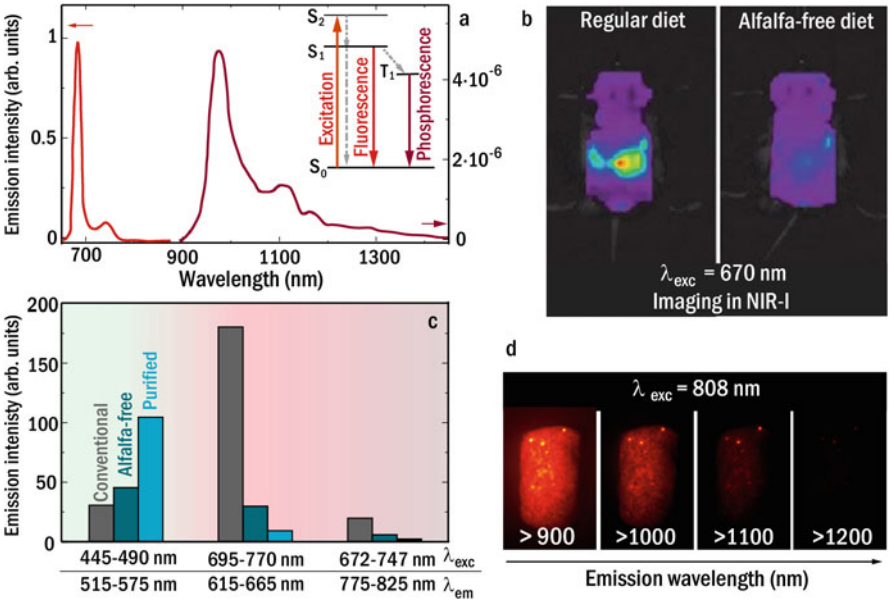

Fig. 2.2 Chlorophyll photoluminescence (**a**) Chlorophyll *a* fluorescence (left) and phosphorescence (right) spectra obtained at low temperature (77 K) upon excitation at 660 nm. The phosphorescence intensity, as labeled on the right axis, is expressed with respect to the normalized fluorescence intensity indicated in the left axis. The inset represents a simplified chlorophyll energy level diagram. The dashed lines correspond to non-radiative internal energy conversion processes. Adapted with permission [61]. Copyright 2014, American Chemical Society. (**b**) In vivo NIR emission of mice fed a conventional or an alfalfa-free diet for 4 weeks prior to image acquisition. Reproduced with permission [62]. Copyright 2007, Springer Nature. (**c**) Fluorescence of conventional, alfalfa-free, and purified food pellets in the green, far-red, and NIR-I. Data extracted from reference 35. (**d**) Fluorescence of conventional food pellets in different spectral ranges under 808 nm excitation. Reproduced with permission [63]

times lower than that of fluorescence) makes the contribution of phosphorescence to the overall chlorophyll emission minimal: the red tail of the fluorescence band is up to 100 times more intense than phosphorescence [61]. Therefore, chlorophyll fluorescence—and not phosphorescence—is most likely the origin of any detectable chlorophyll NIR emission.

Plant autofluorescence might initially seem irrelevant when dealing with animal imaging. However, the presence of fluorescent vegetable components in laboratory rodent diets is one of the major causes of NIR autofluorescence in small animal imaging experiments. This has been known since the 1980s, when Weagle et al. identified chlorophyll as the main culprit of the autofluorescence background they observed when studying the biosynthesis and clearance of porphyrins in nude mice after administration of a porphyrin precursor [64]. The stomach mucosa, analyzed ex vivo, the undigested contents of the stomach, and the food pellets the mice had been fed all presented the same spectral features (a band centered at 674 nm) as the in vivo autofluorescence background. An ethanol extraction of the food pellets pinpointed the cause of the autofluorescence to the alfalfa contained in the food and, more specifically, to the degradation products of chlorophyll *a* (pheophytin *a* and pheophorbide *a*). The close similarity of the spectroscopic features of these chlorophyll by-products made it impossible to determine whether it was one or both of them causing the autofluorescence background. Further experiments corroborated this association between in vivo autofluorescence and the cereal components of rodent chow [65] and eventually led to the development and subsequent commercialization of "fluorescence-free" products, which do not include chlorophyll-containing unrefined vegetable products in their formulation [66]. Mice given alfalfa-free dietary formulations present a lowered digestive tract NIR-I autofluorescence upon NIR-I excitation (see Fig. 2.2b), as first demonstrated by Troy et al. in 2004 and confirmed by other authors [62, 67]. Subsequent studies comparing in vivo NIR-I autofluorescence in mice fed conventional, alfalfa-free, or purified diets (composed of casein, cornstarch, sugar, oil, vitamins, and minerals) concluded that the latter produced the least intense background, as shown in Fig. 2.2c [68]. However, no dietary intervention achieved a complete elimination of autofluorescence in the digestive tract, suggesting the contribution of components other than chlorophyll to food autofluorescence, although no specific fluorophores have been identified. Technical notes of commercial preclinical imaging systems emphasize the need to use alfalfa-free or purified diets, which come at a higher cost than conventional variants, to avoid substantial interference of chlorophyll fluorescence when imaging in NIR-I [69, 70].

Chlorophyll fluorescence has not been systematically characterized in NIR-II, although food-related autofluorescence is still an issue for small animal imaging in this spectral range [27, 30]. Conventional rodent food pellets contribute a non-negligible fluorescence emission for wavelengths up to 1200 nm, as shown in Fig. 2.2d. To the best of our knowledge, no research so far has addressed the effects of alfalfa-free or purified diets on in vivo autofluorescence in NIR-II, as the development of contrast agents emitting beyond 1200 nm allows this background to be avoided without applying specific dietary strategies.

2.3.3 *In Vivo Skin Autofluorescence in the NIR*

Besides food-related autofluorescence, skin pigmentation is the major source of background noise for in vivo NIR imaging. The first studies on skin autofluorescence, carried out in the 1990s, focused on ultraviolet and visible wavelengths. In these spectral ranges, aromatic amino acids (tyrosine and tryptophan) and structural proteins (collagen) are responsible for the intrinsic fluorescence of skin [71–73]. The extremely weak emission of melanins at these wavelengths, on the other hand, led some authors to mistakenly consider them non-fluorescent pigments [72, 74–76].

Several chemically distinct variants of melanins are present in living organisms. The most abundant are eumelanin (black pigment responsible for dark pigmentation) and pheomelanin (yellow-brown pigment present, for instance, in light skin). Melanins display atypical absorption spectra for an organic chromophore: their characteristic broadband, featureless, absorbance curves are similar to those of semiconductors (see Fig. 2.3a) [77]. Both eumelanin and pheomelanin display a monotonic decrease in the absorbance for increasing wavelengths, although the former shows a higher absorbance [78]. The fluorescence of eumelanin (which has been characterized in greater detail than pheomelanin) also presents some atypical features, including a dependence of the emission peak and bandwidth on the excitation wavelength [79]. In the visible range, increasing the excitation wavelength results in a redshift and a broadening of the emission band of eumelanin while also reducing the emission intensity. The radiative quantum yield of eumelanin, which is well below 1%, also depends on the excitation wavelength, as demonstrated in the 250–500 nm spectral range [80]. All of these studies indicate that there is a large molecular heterogeneity in eumelanin, meaning there is not a single eumelanin chromophore but many chemically distinct species [81].

Melanin spectroscopy has not been systematically studied in the spectral ranges of interest for in vivo imaging, despite the evidence that pigmentation-related autofluorescence contributes to background noise even in NIR-II. NIR melanin fluorescence was first studied in detail for wavelengths within the first biological window (NIR-I) by Huang et al. [82]. With excitation at 785 nm, they observed that the NIR-I emission of both synthetic and natural melanins (as shown in Fig. 2.3b) increased for longer wavelengths, with two discrete peaks at 880 and 895 nm previously identified as Raman scattering [83]. The autofluorescence spectra of black skin appendages from different species (human hair, feline fur, and chicken feathers) all presented very similar characteristics and differed from their white counterparts. The emission spectra of white skin appendages, characterized by a lower content of eumelanins, decreased for increasing wavelengths [82]. The spectroscopy of melanins in NIR-II is completely unexplored so far. However, pigmentation-dependent autofluorescence can contribute significant background noise to in vivo small animal imaging experiments in this wavelength range unless they are carried out in nude mice, as shown in Fig. 2.3c. This figure shows the NIR autofluorescence in two wavelength ranges (900–1700 nm, corresponding to the full detection range of an InGaAs camera, and 1200–1700 nm) for five strains of

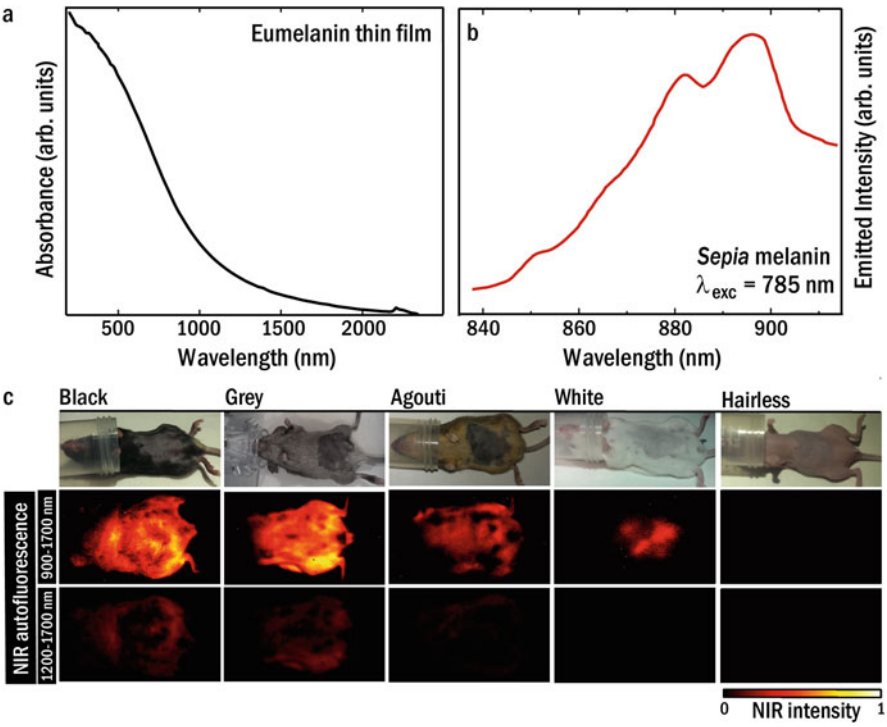

Fig. 2.3 NIR melanin autofluorescence. (**a**) UV/visible/NIR absorption spectra of a eumelanin thin film. Adapted with permission [79]. Copyright 2005, Elsevier. (**b**) In vitro NIR-I emission spectrum obtained for a sample of *Sepia Officinalis* melanin under 785 nm excitation. Adapted with permission [82]. Copyright 2014, SPIE. (**c**) In vivo NIR fluorescence images obtained for mice strains with different skin pigmentations under 808 nm laser light excitation (0.2 W/cm^2). Fluorescence images are shown for two spectral ranges (900–1700 nm and 1200–1700 nm), highlighting the reduction in fluorescence for longer wavelengths. Adapted with permission [84]. Copyright 2015, Wiley-VCH

mice with distinct pigmentation. The intense autofluorescence background present for mice with darker pigmentation decreases if the detection range is restricted to longer wavelengths, as skin autofluorescence decreases sharply between 900 and 1200 nm.

This reduction in melanin emission intensity with increasing wavelengths (which also occurs in food-related autofluorescence) enables imaging with minimal background noise by selecting contrast agents that emit well into the NIR-II range. Alternatively, techniques where long-lifetime fluorophores are coupled with time-gated imaging systems have also enabled autofluorescence-free imaging in the broader detection range (900–1700 nm) [30].

2.3.4 Other Sources of In Vivo NIR Autofluorescence

Food components, particularly chlorophyll, and skin pigmentation, as described in the previous subsections, are responsible for most of the autofluorescence background observed in NIR fluorescence imaging of small animals. However, NIR autofluorescence observed both in vivo and ex vivo in different organs, including the kidneys, spleen, and liver, cannot be attributed to either source [84]. The authors have considered that this emission arises from the emission tail of some visible-emitting fluorophores, particularly ceroids, lipofuscins, and endogenous porphyrins [8, 40]. Furthermore, it has been hypothesized that inflammation in tissue could lead to oxidative stress resulting in cross-linking and dimerization in proteins [85], which in turn could also generate endogenous NIR fluorophores. However, no studies so far have focused on finding the molecular causes or characterizing the spectroscopic features of this NIR emission.

2.4 NIR Autofluorescence as a Solution: Applications

NIR autofluorescence in tissues can cause interference during label-free image acquisition or while imaging with an exogenously administered NIR contrast agent. However, NIR autofluorescence can provide valuable information about the molecular components present in a tissue. As a result, tissue NIR autofluorescence is being explored for a range of biomedical applications, including surgical guidance and diagnostics for cancer, monitoring ophthalmic diseases, intraoperative identification of parathyroid glands, or tracking atherosclerotic plaques in coronary artery diseases.

2.4.1 Surgical Guidance and Diagnostics in Cancer

Over the past few decades, it has been well documented that fluorescence spectroscopy and/or imaging can be a valuable tool in the field of clinical and surgical oncology [17, 40, 86, 87]. The popularity of fluorescence spectroscopy/imaging stems from its ability to perform simple, non-invasive, real-time assessment of the tissues in a cost-effective manner. The majority of the fluorescence-based research for oncological applications has relied on emission from endogenous fluorophores, where excitation wavelengths typically range from 250 to 550 nm [88]. However, the limited penetration depth of these wavelengths in tissues has proven to be a major deterrent for oncological applications, as fluorescence can be measured only from superficial tissue layers. While NIR-excitable contrast agents have been explored for deep tissue imaging, the feasibility of that approach depends on the pharmacokinetics and cost of the exogenous contrast agent.

While NIR autofluorescence has been attributed to several fluorophores, as discussed in Sect. 2.2, the diagnostic potential of NIR autofluorescence was only discovered relatively recently. Zhang et al. serendipitously observed that the background signal during Raman measurement—NIR autofluorescence—was notably different for a normal human breast tissue as compared to a cancerous one [89]. That reported finding was subsequently investigated by Demos et al., who observed that the NIR autofluorescence intensity over the 700–1000 nm spectral range was distinctive for cancerous and non-cancerous regions across several organs and tissues, including breast, liver, kidneys, pancreas, prostate, and bladder [88, 90].

Since then, researchers have tried to exploit the potential of NIR autofluorescence for oncological applications in various organs. While evaluating the scope of NIR autofluorescence for differentiating breast cancer from adjacent tissues, Demos et al. observed that cancerous breast tissue exhibited a 1.3 to 2.6 times stronger NIR autofluorescence than normal fatty or fibrous tissue when the tissues were excited at 532 or 633 nm [91]. Fournier et al. tested whether this NIR optical property could be utilized for discriminating between benign and malignant breast tumors in a rat model [92]. The results indicated that the tumor-to-normal (T/N) ratio of NIR autofluorescence intensity diverged the most between benign and malignant tumors at 670 nm excitation with emission being collected at 800 nm. By assigning a threshold with T/N ratio > 1 as malignant and T/N ratio < 1 as benign, this technique was able to differentiate between the two classes of tumors with 76% sensitivity and 75% specificity.

Due to melanin being a potent NIR fluorophore, the feasibility of using NIR autofluorescence for skin cancer diagnostics has been examined, particularly for pigmented skin lesions. Studies have shown that melanomas tend to have higher NIR autofluorescence than healthy skin and basal cell carcinomas (non-pigmented) [93–96]. Diagnostic accuracies as high as 97.3% were reported when NIR autofluorescence was combined with other modalities such as Raman spectroscopy and/or visible fluorescence spectroscopy [97]. In contrast to breast and skin cancers, studies have reported lower NIR intensity in tumors in the kidneys and urinary bladder, as compared to the normal tissue regions. In the study by Demos et al., the cancerous areas appeared darker than the adjacent normal tissue in NIR autofluorescence images acquired in the 700–1000 nm spectral region [98]. Similarly, Lieber et al. observed that at 785 nm excitation, normal kidney tissues generated an emission peak at 830 nm, while Wilm's tumor specimens had a reduced intensity at 830 nm and the emission peak shifted below 810 nm [99]. These findings were consistent with the works of Jacobson et al., who additionally observed that while urinary bladder tumors typically had lower NIR autofluorescence than the normal regions, advanced tumors with signs of necrosis could exhibit elevated NIR autofluorescence relative to its surroundings [100].

A similar trend of reduced NIR autofluorescence intensity in diseased/cancerous tissues (see Fig. 2.4a) has been noted from gastrointestinal malignancies in the colon and stomach, as well as in rare tumors such as soft tissue sarcomas [101–104]. These findings, however, are in contrast with organs like liver and pancreas as reported earlier by Demos et al. [88]. These differences may stem from (i) variability of

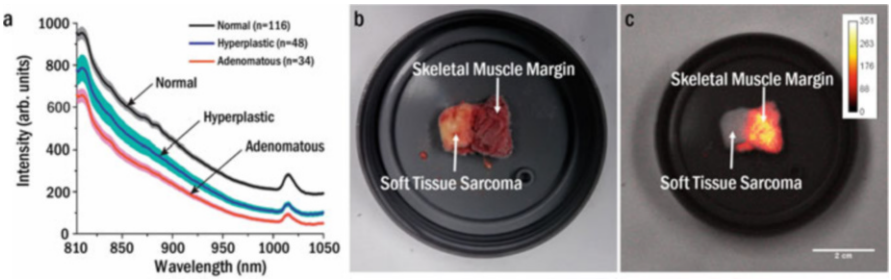

Fig. 2.4 NIR autofluorescence applied to cancer diagnostics and surgical guidance. (**a**) In vivo mean NIR autofluorescence spectra of normal colon, hyperplastic, and adenomatous polyps. The shaded areas in the NIR autofluorescence spectra represent the respective standard errors. Adapted with permission [103]. Copyright 2011, Elsevier. (**b**) Visible color image of a soft tissue sarcoma tumor margin ex vivo. (**c**) Corresponding NIR autofluorescence image of the soft tissue sarcoma tumor margin overlaid on a white light image. Note the presence of higher NIR autofluorescence in the skeletal muscle margin as compared to the soft tissue sarcoma. (Fig. 2.4b and c *courtesy of Dr. John Q. Nguyen, PhD—Massachusetts General Hospital, Boston, USA*)

endogenous fluorophores across organs, (ii) changes in scattering and absorption properties of the organs owing to compositional differences, (iii) variation in the cancer subtypes that were studied, and (iv) choice of the excitation wavelength and the corresponding wavelength range of the emission signal.

2.4.2 Monitoring Ophthalmological Diseases

To track specific ophthalmologic diseases, the clinician typically examines the fundus of the eye with an ophthalmoscope using white light. The ocular fundus, which is comprised of the retina, optic disc, macula, fovea, and posterior pole, contains several fluorophores such as lipofuscin, melanin, collagen, elastin, and luteal pigments (lutein and zeaxanthin) [105, 106]. Therefore, visualizing autofluorescence of the ocular fundus has emerged as a valuable technique for monitoring ophthalmological diseases on the basis of naturally or pathologically occurring fluorophores. Traditional fundus autofluorescence imaging is performed using scanning laser ophthalmoscopy (SLO) collecting the 500–800 nm emission obtained under blue light excitation (wavelength = 488 nm) [107]. This generates a fluorescence image based on the spatial distribution of lipofuscin and other fluorophores in the fundus [106].

The presence of NIR autofluorescence in the eye appears to have been unknown until Piccolino et al. observed “pre-injection fluorescence” in the fundus as seen in Fig. 2.5, with an absorption peak at 805 nm and an emission peak at 835 nm, prior to indocyanine green (ICG) angiography [108]. The authors hypothesized that this NIR autofluorescence in the fundus could be due to a combination of hemoglobin degradation by-products (porphyrins), lipofuscin deposits, and/or melanin. This

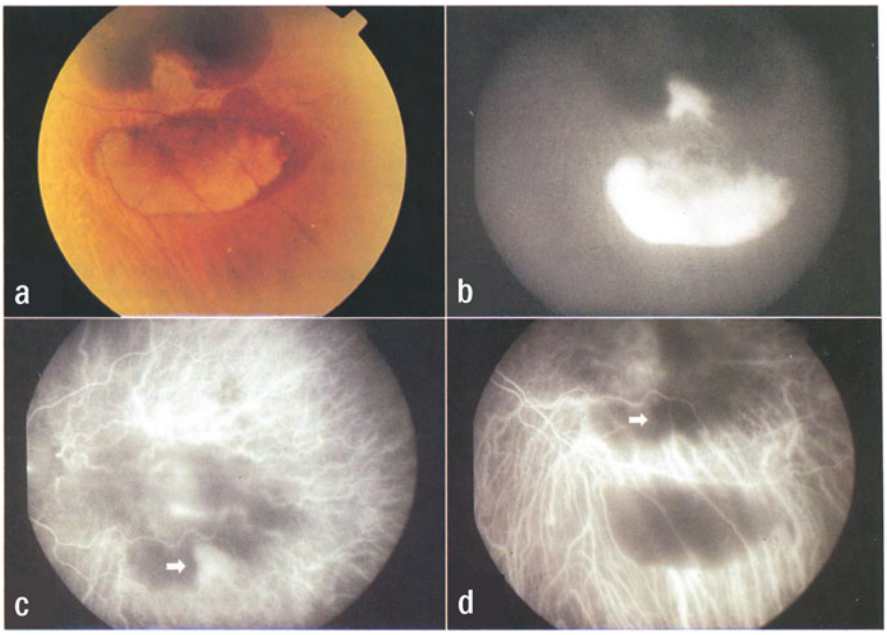

Fig. 2.5 NIR autofluorescence observed in the retina. (**a**) A disciform macular lesion with large subretinal hemorrhage observed with white light. (**b**) NIR autofluorescence observed in the grayish portion of the hemorrhage prior to injection with ICG. Background NIR fluorescence was still present for the lesion during (**c**) the early phase and (**d**) the middle phase of the ICG photograph, as indicated by the arrows. Adapted with permission [108]. Copyright 1995, Elsevier

was further investigated by Keilhauer et al., whose results indicated that the NIR autofluorescence could be arising primarily from ocular melanin in the retinal pigment epithelium (RPE) layer and, to some degree, from pigments in the choroid and iris, while Weinberger et al. postulated that the phenomenon was indeed "true" NIR autofluorescence—possibly originating from melanin and/or lipofuscin [109, 110]. The source of fundus NIR autofluorescence was eventually traced down to melanosomes in the RPE layers with no significant contribution from lipofuscin when investigated in mice retina by Gibbs et al. [111]

In the original study by Piccolino, NIR autofluorescence was observed in only 40.8% of the examined patients and was found to correlate with old subretinal hemorrhages (see Fig. 2.5b), lipofuscin-like deposits, pigmented choroidal neovascular membranes, and serous retinal detachments (older by several months to years) [108]. This prompted several researchers to tap into the potential of NIR autofluorescence as an optical biomarker for evaluating ophthalmologic diseases. Various studies have now explored the feasibility of using NIR autofluorescence to track early disease or degeneration in the RPE layer across a spectrum of ophthalmologic diseases. These include central serous chorioretinopathy, age-related macular degeneration, idiopathic choroidal neovascularization, Stargardt disease (juvenile macu-

lar degeneration), chloroquine retinopathy, Bietti's crystalline dystrophy, Vogt–Koyanagi–Harada disease, Best's disease, retinitis pigmentosa, choroidal nevi, optic nerve pit maculopathy, pseudoxanthoma elasticum, and congenital achromatopsia [107, 112–119].

As described earlier, while ocular melanin is mainly responsible for NIR autofluorescence in the fundus (> 800 nm), lipofuscin is the predominant fluorophore involved in traditional autofluorescence of the fundus (500–800 nm). Therefore, the observed pattern and distribution of NIR autofluorescence may not match with that visualized during traditional fundus autofluorescence imaging [118]. Moreover, the NIR autofluorescence signal from the fundus is generally weak and about 60–100 times less intense than the traditional fundus autofluorescence signal [107]. Since both forms of autofluorescence imaging provide different, but valuable information regarding the stage/progression of retinal disease, NIR autofluorescence imaging can be utilized as a complementary technique alongside traditional autofluorescence imaging during fundus examination. Combining both imaging modalities can be beneficial for clinicians and researchers in terms of understanding and monitoring degenerative changes that occur in ophthalmic diseases.

2.4.3 Intra-Operative Parathyroid Gland Identification

Parathyroid glands are small organs that are pivotal for calcium regulation in our body and tend to be located in close proximity to the thyroid gland. Identifying parathyroid glands during neck surgeries can be a major challenge, as their size is comparable to a lentil or grain of rice, and they are often misidentified as a piece of fat, lymph node, or a thyroid nodule. Subsequently a healthy parathyroid gland could accidentally be excised or damaged during a thyroid surgery (thyroidectomy), leading to undesired side effects associated with hypocalcemia (low blood calcium) [120]. In contrast, failing to identify and remove diseased parathyroid glands as in primary hyperparathyroidism can lead to persistent hypercalcemia despite the surgery [121]. Although conventional imaging modalities such as ultrasound, sestamibi scans, and computed tomography (CT) can help to visualize parathyroid glands preoperatively with varying success [122, 123], this may still not correlate with what surgeons observe intraoperatively. In addition, these techniques can only detect diseased parathyroid glands while failing to localize normal/healthy ones. Therefore, most surgeons still rely on visual assessment for identifying parathyroid glands during neck surgery, which leads to varied accuracy depending on surgical experience [121, 124].

Thus the biomedical imaging community has focused on developing non-invasive optical modalities to intraoperatively differentiate parathyroid glands from adjacent neck structures. Methods such as optical coherence tomography [125–127], diffuse reflectance spectroscopy [128], and imaging with contrast agents [129–131] have met with limited success. However, investigating the use of Raman spectroscopy for detecting parathyroid glands, Paras et al. observed a distinctive

phenomenon where the raw Raman signal acquired from canine, swine, and in vitro human parathyroid tissue saturated the detector, whereas the signal for fat, lymph node, and thyroid tissues did not [132]. Consequently, it was realized that parathyroid glands exhibit stronger NIR autofluorescence than other neck tissues and this phenomenon can be exploited for in vivo identification of both normal and diseased parathyroid glands in real time without requiring any exogenous contrast agents [133, 134]. When investigated over a larger sample set of 137 patients, this technique was consistently reliable in identifying parathyroid glands and achieved 97% accuracy [135].

Subsequent work has shown that NIR imaging localizes parathyroid autofluorescence with 100% accuracy over the entire surgical field of view [137, 138]. Several research groups have therefore investigated the feasibility of surgeons using commercial NIR imaging cameras intraoperatively to visualize and identify parathyroid glands in relation to adjacent neck structures on a remote display monitor (see Fig. 2.6) [136, 139–148]. Although these studies achieved high accuracy in parathyroid identification, NIR imaging disrupts the surgical work-flow due to the sensitivity of NIR detectors to ambient lights, which cannot be kept on during NIR imaging. In line with this limitation, Thomas et al. recently evaluated a clinical prototype called the "PTeye" for real-time parathyroid identification using NIR autofluorescence, where the device was made user-friendly for easy interpretation by surgeons and could also work in the presence of ambient room lights [149].

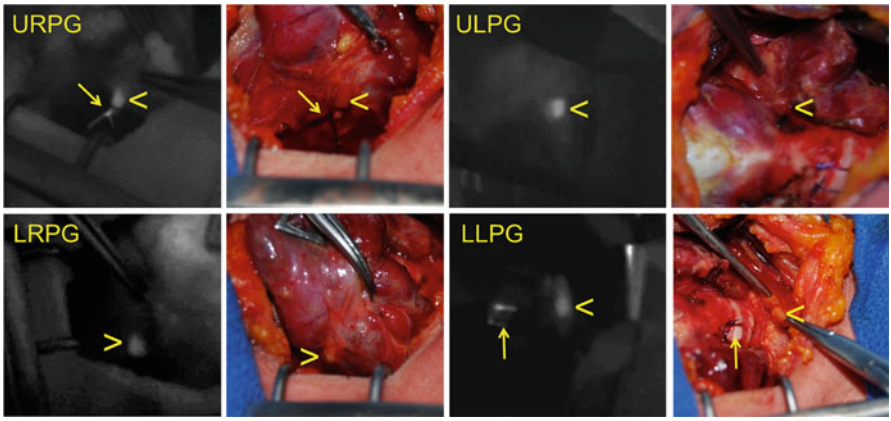

Fig. 2.6 NIR autofluorescence observed in the parathyroid gland (PG). Intraoperative NIR imaging and the corresponding white light view of the PG of the same patient. URPG—upper right parathyroid gland, ULPG—upper left parathyroid gland, LRPG—lower right parathyroid gland, LLPG—lower left parathyroid gland. Arrowhead marks the parathyroid gland, arrow points to a suture [136]. Copyright 2016, Springer Nature

2.4.4 *Imaging Atherosclerotic Plaque in Coronary Artery Disease*

Coronary artery disease (CAD) currently remains the frontrunner for patient mortality in the USA and could become the leading cause of death worldwide by 2020 [150]. CAD tends to develop when the coronary arteries that perfuse the heart become diseased and develop blockages, predominantly due to a combination of inflammatory processes and atherosclerotic plaque deposits. To develop better treatment strategies and improve outcomes in CAD patients researchers are now focused on non-invasively tracking the progression of CAD by characterizing the causative agent—atherosclerotic plaques—in vivo with various imaging modalities.

Among several imaging techniques, intravascular ultrasound and optical coherence tomography (OCT) have been used to characterize the structure of atherosclerotic plaques in blood vessels, achieving an axial resolution as small as 10 μm in the case of OCT [151, 152]. However, these imaging modalities cannot monitor compositional changes in atherosclerotic plaques, such as the presence of necrosis or the amount of lipid content, whereas these factors are vital for understanding the ongoing pathogenesis that underlies CAD. As a result, NIR fluorescence spectroscopy based on ICG or other contrast agents was explored as a single optical modality or in combination with OCT for characterizing plaque composition [153–155].

However, in a subsequent report by Gardecki et al., it was found that necrotic cores in atherosclerotic plaque emitted strong NIR autofluorescence when performing Raman spectral acquisitions on human aortic atherosclerotic plaques ex vivo [157]. Based on this unexpected finding, the same group investigated the potential for NIR autofluorescence spectroscopy to differentiate between necrotic and non-necrotic plaques, as the former are considered a higher risk factor [158]. For this study, ex vivo aortic plaques were first excited at 633 nm using a fiber-based system and NIR autofluorescence was collected in the 680–900 nm range. The results indicated that necrotic plaques have a significantly higher mean NIR autofluorescence signal than the non-necrotic lesions. In addition, a multimodal system with a fully functional catheter measuring 0.87 mm was designed in the same study for acquiring combined OCT-NIR autofluorescence images from cadaveric specimens of human coronary arteries. The scope for this multimodal approach was further investigated across coronary arteries of 12 patients in vivo, with strong NIR autofluorescence being detected from plaques that had morphological features associated with high risk, i.e., lipid-containing plaques, plaque erosion/rupture, and thrombus rupture (see Fig. 2.7) [156]. As validation of these results, another study of high-risk atherosclerotic plaques has reported the presence of NIR autofluorescence for early identification and therapeutic intervention in patients with high-risk plaques [159].

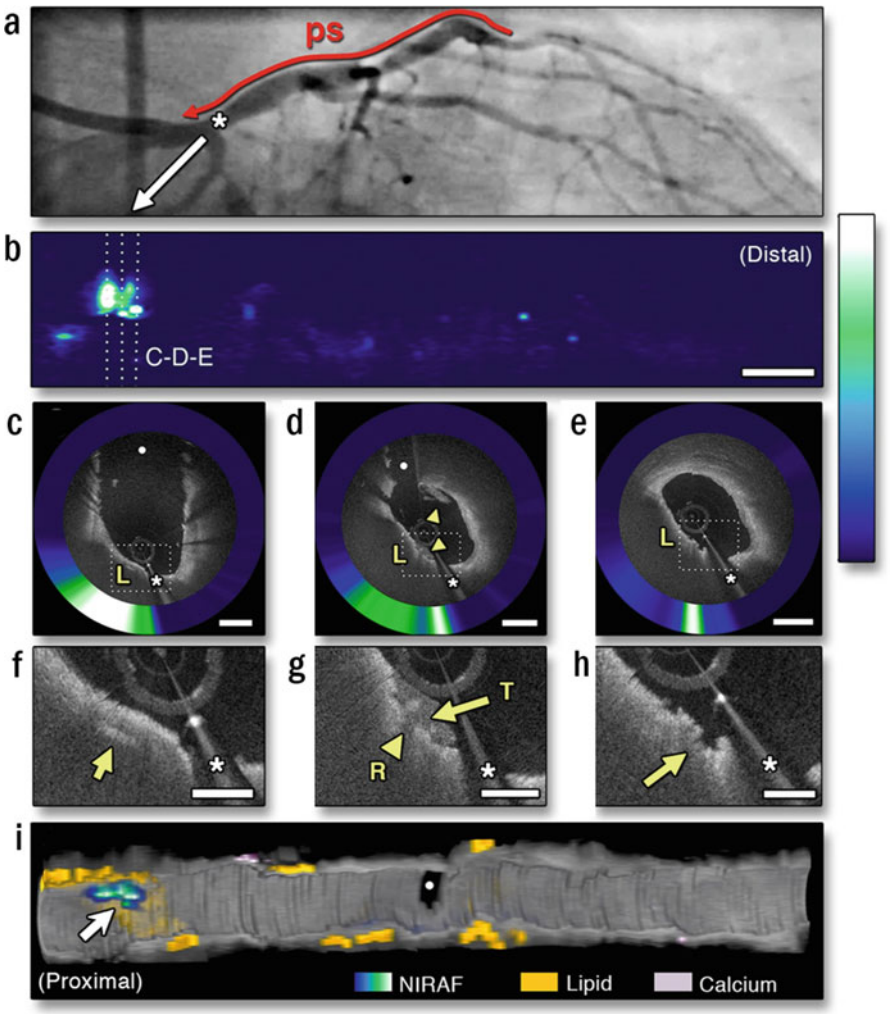

Fig. 2.7 NIR autofluorescence visualized in vivo across a diseased coronary artery in combination with OCT. (**a**) Coronary angiogram of the left anterior descending coronary artery (LAD). (**b**) Two-dimensional NIR autofluorescence map showing a focal region of elevated emission in the ostial LAD. (**c–e**) OCT-NIR autofluorescence cross sections from sites in (**b**) with elevated NIR autofluorescence, revealing subclinical fibrous cap rupture of a thin-cap fibroatheroma. Magnification of a cholesterol crystal (arrow) below the cap, colocalized with high NIR autofluorescence **(f)** and magnified views of the rupture site (**g, h**). In (**g**), the rupture site (arrowhead) is covered by a small white luminal thrombus (arrow), and the arrow in (**h**) points to the site of the thin-cap rupture, demonstrating colocalized and very high focal NIR autofluorescence signal. (**i**) Three-dimensional cutaway rendering showing that the highest NIR autofluorescence spot appears focally within a large lipid pool (arrow), and the remaining portion of the vessel shows diffuse disease that was negative for NIR autofluorescence. Scale bars on OCT images and magnifications are equal to 1 mm and 0.5 mm, respectively; scale bar in (B) is equal to 5 mm. (*) Indicates a guidewire shadow. *ps* = pullback segment of catheter; *L* = lipid; *R* = rupture site; *T* = thrombus; *TCFA* = thin-cap fibroatheroma. Adapted with permission [156]. Copyright 2016, Elsevier

2.5 Conclusion and Future Perspectives

The development of NIR contrast agents and technological advances in NIR instrumentation, particularly the increased availability of detectors in the NIR-II spectral range (1000–1700 nm), has expanded the applicability of fluorescence imaging to deep tissues in small animal models. This is a consequence of biological tissues being relatively transparent to NIR radiation, as only a few biomolecules absorb light in this spectral range, and scattering decreases at longer wavelengths. The NIR emission of these molecules is responsible for the autofluorescence background observed in NIR fluorescence images in vivo. Research on NIR imaging in vivo has focused on developing experimental strategies for minimizing this background by taking advantage of the spectroscopic features of autofluorescence, such as the fast time decay and decreasing intensity at longer wavelengths. Less attention has been paid to identifying the sources of autofluorescence: in the case of small animal imaging, the only fluorophores that have been systematically studied are chlorophyll (present in small animals through their diet) and melanin. However, other endogenous pigments, such as lipofuscins and porphyrins, display NIR emission under NIR excitation and thus contribute to in vivo autofluorescence. An improved understanding of the broader family of endogenous NIR fluorophores may help to manage the associated background noise in imaging applications.

Although autofluorescence is frequently regarded as a nuisance that needs to be eliminated for high contrast bioimaging, in some cases it provides useful information that can be applied for tissue diagnostics in vivo. NIR autofluorescence can help to identify cancerous masses, diagnose retinal pathologies, or discriminate between stable and unstable atherosclerotic plaques. This can be achieved in a truly minimally invasive manner, as relying on NIR autofluorescence removes the need for exogenous contrast agents and maximizes the imaging penetration depth. To take advantage of the full potential of NIR autofluorescence in this respect, it is again essential to gain a better understanding of the endogenous NIR fluorophores in tissue. This, in turn, is likely to support fundamental research in biochemistry and promote further expansion of NIR autofluorescence into clinical applications.

References

1. Stephens DJ, Allan VJ (2003) Light microscopy techniques for live cell imaging. Science 300(5616):82–86
2. Susaki Etsuo A, Ueda Hiroki R (2016) Whole-body and whole-organ clearing and imaging techniques with single-cell resolution: toward organism-level systems biology in mammals. Cell Chem Biol 23(1):137–157
3. Smith AM, Mancini MC, Nie S (2009) Second window for *in vivo* imaging. Nat Nanotechnol 4(11):710–711
4. Weissleder R (2001) A clearer vision for in vivo imaging. Nat Biotechnol 19(4):316–317
5. Lim YT, Kim S, Nakayama A, Stott NE, Bawendi MG, Frangioni JV (2003) Selection of quantum dot wavelengths for biomedical assays and imaging. Mol Imaging 2(1):50–64

6. Weissleder R, Pittet MJ (2008) Imaging in the era of molecular oncology. Nature 452(7187):580–589
7. Sevick-Muraca E (2012) Translation of near-infrared fluorescence imaging technologies: emerging clinical applications. Annu Rev Med 63:217–231
8. Hong G, Antaris AL, Dai H (2017) Near infrared fluorophores for biomedical imaging. Nat Biomed Eng 1:0010
9. Hong G, Diao S, Chang J, Antaris AL, Chen C, Zhang B, Zhao S, Atochin DN, Huang PL, Andreasson KI, Kuo CJ, Dai H (2014) Through-skull fluorescence imaging of the brain in a new near-infrared window. Nat Photonics 8:723
10. Hong G, Lee JC, Jha A, Diao S, Nakayama KH, Hou L, Doyle TC, Robinson JT, Antaris AL, Dai H, Cooke JP, Huang NF (2014) Near infrared II fluorescence for imaging hindlimb vessel regeneration with dynamic tissue perfusion measurement. Circ Cardiovasc Imaging 7(3):517–525
11. Ortgies DH, Tan M, Ximendes EC, del Rosal B, Hu J, Xu L, Wang X, Martín Rodríguez E, Jacinto C, Fernandez N, Chen G, Jaque D (2018) Lifetime-encoded infrared-emitting nanoparticles for in vivo multiplexed imaging. ACS Nano 12(5):4362–4368
12. Fan Y, Wang P, Lu Y, Wang R, Zhou L, Zheng X, Li X, Piper JA, Zhang F (2018) Lifetime-engineered NIR-II nanoparticles unlock multiplexed in vivo imaging. Nat Nanotechnol 13:941–946
13. Bruns OT, Bischof TS, Harris DK, Franke D, Shi Y, Riedemann L, Bartelt A, Jaworski FB, Carr JA, Rowlands CJ (2017) Next-generation in vivo optical imaging with short-wave infrared quantum dots. Nat Biomed Eng 1:0056
14. Carr JA, Franke D, Caram JR, Perkinson CF, Saif M, Askoxylakis V, Datta M, Fukumura D, Jain RK, Bawendi MG (2018) Shortwave infrared fluorescence imaging with the clinically approved near-infrared dye indocyanine green. Proc Natl Acad Sci USA 115(17):4465–4470
15. Antaris AL, Chen H, Cheng K, Sun Y, Hong G, Qu C, Diao S, Deng Z, Hu X, Zhang B (2016) A small-molecule dye for NIR-II imaging. Nat Mater 15(2):235
16. Wan H, Yue J, Zhu S, Uno T, Zhang X, Yang Q, Yu K, Hong G, Wang J, Li L (2018) A bright organic NIR-II nanofluorophore for three-dimensional imaging into biological tissues. Nat Commun 9(1):1171
17. Richards-Kortum R, Sevick-Muraca E (1996) Quantitative optical spectroscopy for tissue diagnosis. Annu Rev Phys Chem 47(1):555–606
18. Chorvat D Jr, Chorvatova A (2009) Multi-wavelength fluorescence lifetime spectroscopy: a new approach to the study of endogenous fluorescence in living cells and tissues. Laser Phys Lett 6(3):175–193
19. Billinton N, Knight AW (2001) Seeing the wood through the trees: a review of techniques for distinguishing green fluorescent protein from endogenous autofluorescence. Anal Biochem 291(2):175–197
20. Neumann M, Gabel D (2002) Simple method for reduction of autofluorescence in fluorescence microscopy. J Histochem Cytochem 50(3):437–439
21. Szöllösi J, Lockett SJ, Balázs M, Waldman FM (1995) Autofluorescence correction for fluorescence in situ hybridization. Cytometry 20(4):356–361
22. Leavesley SJ, Annamdevula N, Boni J, Stocker S, Grant K, Troyanovsky B, Rich TC, Alvarez DF (2012) Hyperspectral imaging microscopy for identification and quantitative analysis of fluorescently-labeled cells in highly autofluorescent tissue. J Biophotonics 5(1):67–84
23. Croce AC, Bottiroli G (2014) Autofluorescence spectroscopy and imaging: a tool for biomedical research and diagnosis. Eur J Histochem 58(4):2461
24. Frangioni JV (2003) In vivo near-infrared fluorescence imaging. Curr Opin Chem Biol 7(5):626–634
25. Institute ANS (2000) American national standard for safe use of laser. Laser Institute of America, Orlando, FL
26. Diao S, Blackburn JL, Hong G, Antaris AL, Chang J, Wu JZ, Zhang B, Cheng K, Kuo CJ, Dai H (2015) Fluorescence imaging in vivo at wavelengths beyond 1500 nm. Angew Chem 127(49):14971–14975

27. Villa I, Vedda A, Cantarelli I, Pedroni M, Piccinelli F, Bettinelli M, Speghini A, Quintanilla M, Vetrone F, Rocha U, Jacinto C, Carrasco E, Rodríguez F, Juarranz Á, del Rosal B, Ortgies D, Gonzalez P, Solé J, García D (2015) 1.3 μm emitting SrF_2:Nd^{3+} nanoparticles for high contrast in vivo imaging in the second biological window. Nano Res 8(2):649–665
28. del Rosal B, Benayas A (2018) Strategies to overcome autofluorescence in nanoprobe-driven in vivo fluorescence imaging. Small Methods 2(9):1800075
29. Wang J, Ma Q, Hu X-X, Liu H, Zheng W, Chen X, Yuan Q, Tan W (2017) Autofluorescence-free targeted tumor imaging based on luminous nanoparticles with composition-dependent size and persistent luminescence. ACS Nano 11(8):8010–8017
30. del Rosal B, Ortgies DH, Fernández N, Sanz-Rodríguez F, Jaque D, Rodríguez EM (2016) Overcoming autofluorescence: long-lifetime infrared nanoparticles for time-gated in vivo imaging. Adv Mater 28(46):10188–10193
31. Park C-K, Cho H (2015) Improvement in tracing quantum dot-conjugated nanospheres for in vivo imaging by eliminating food autofluorescence. J Nanomater 16(1):289
32. Diao S, Hong G, Antaris AL, Blackburn JL, Cheng K, Cheng Z, Dai H (2015) Biological imaging without autofluorescence in the second near-infrared region. Nano Res 8(9):3027–3034
33. Bouccara S, Fragola A, Giovanelli E, Sitbon G, Lequeux N, Pons T, Loriette V (2014) Time-gated cell imaging using long lifetime near-infrared-emitting quantum dots for autofluorescence rejection. J Biomed Opt 19(5):051208
34. Koch M, Symvoulidis P, Ntziachristos V (2018) Tackling standardization in fluorescence molecular imaging. Nat Photonics 12:505–515
35. Davies MA, Hogan MP (2001) Body-site variation of skin autofluorescence. Appl Spectrosc 55(11):1489–1494
36. Delori F, Greenberg JP, Woods RL, Fischer J, Duncker T, Sparrow J, Smith RT (2011) Quantitative measurements of autofluorescence with the scanning laser ophthalmoscope. Invest Ophthalmol Vis Sci 52(13):9379–9390
37. Stanciu CE, Philpott MK, Bustamante EE, Kwon YJ, Ehrhardt CJ (2016) Analysis of red autofluorescence (650–670nm) in epidermal cell populations and its potential for distinguishing contributors to 'touch' biological samples. F1000Res 5:180
38. Fryen A, Glanz H, Lohmann W, Dreyer T, Bohle RM (1997) Significance of autofluorescence for the optical demarcation of field cancerisation in the upper aerodigestive tract. Acta Otolaryngol 117(2):316–319
39. Christensen J, Nørgaard L, Bro R, Engelsen SB (2006) Multivariate autofluorescence of intact food systems. Chem Rev 106(6):1979–1994
40. Yuanlong Y, Yanming Y, Fuming L, Yufen L, Paozhong M (1987) Characteristic autofluorescence for cancer diagnosis and its origin. Lasers Surg Med 7(6):528–532
41. Koenig K, Schneckenburger H (1994) Laser-induced autofluorescence for medical diagnosis. J Fluoresc 4(1):17–40
42. Monici M (2005) Cell and tissue autofluorescence research and diagnostic applications. Biotechnol Annu Rev 11:227–256
43. Wolfbeis OS (1985) The fluorescence of organic natural products. In: Molecular luminescence spectroscopy methods and applications. Wiley, New York, pp 167–370
44. Huang S, Heikal AA, Webb WW (2002) Two-photon fluorescence spectroscopy and microscopy of NAD(P)H and flavoprotein. Biophys J 82(5):2811–2825
45. Quinn KP, Sridharan GV, Hayden RS, Kaplan DL, Lee K, Georgakoudi I (2013) Quantitative metabolic imaging using endogenous fluorescence to detect stem cell differentiation. Sci Rep 3:3432
46. Lakowicz JR (2006) Protein fluorescence. In: Principles of fluorescence spectroscopy. Springer, Boston, pp 529–575
47. Patková J, Vojtíšek M, Tůma J, Vožeh F, Knotková J, Šantorová P, Wilhelm J (2012) Evaluation of lipofuscin-like pigments as an index of lead-induced oxidative damage in the brain. Exp Toxicol Pathol 64(1–2):51–56

48. Verbunt RJ, Fitzmaurice MA, Kramer JR, Ratliff NB, Kittrell C, Taroni P, Cothren RM, Baraga J, Feld M (1992) Characterization of ultraviolet laser-induced autofluorescence of ceroid deposits and other structures in atherosclerotic plaques as a potential diagnostic for laser angiosurgery. Am Heart J 123(1):208–216
49. Nandakumar N, Buzney S, Weiter JJ (2012) Lipofuscin and the principles of fundus autofluorescence: a review. In: Seminars in ophthalmology, vol 5–6. Taylor & Francis, Boca Raton, pp 197–201
50. Richards-Kortum R, Rava R, Baraga J, Fitzmaurice M, Kramer J, Feld M (1990) Survey of the UV and visible spectroscopic properties of normal and atherosclerotic human artery using fluorescence EEMS. In: Pratesi R (ed) Optronic techniques in diagnostic and therapeutic medicine. Springer Science & Business Media, Boston, pp 129–138
51. Berezin MY, Achilefu S (2010) Fluorescence lifetime measurements and biological imaging. Chem Rev 110(5):2641–2684
52. Bastiaens PIH, Squire A (1999) Fluorescence lifetime imaging microscopy: spatial resolution of biochemical processes in the cell. Trends Cell Biol 9(2):48–52
53. García-Plazaola JI, Fernández-Marín B, Duke SO, Hernández A, López-Arbeloa F, Becerril JM (2015) Autofluorescence: biological functions and technical applications. Plant Sci 236:136–145
54. Maxwell K, Johnson GN (2000) Chlorophyll fluorescence—a practical guide. J Exp Bot 51(345):659–668
55. Schreiber U, Bilger W, Neubauer C (1995) Chlorophyll fluorescence as a nonintrusive indicator for rapid assessment of in vivo photosynthesis. In: Ecophysiology of photosynthesis. Springer, Berlin, Heidelberg, pp 49–70
56. Ustin SL, Gitelson AA, Jacquemoud S, Schaepman M, Asner GP, Gamon JA, Zarco-Tejada P (2009) Retrieval of foliar information about plant pigment systems from high resolution spectroscopy. Remote Sens Environ 113:S67–S77
57. Krause GH, Weis E (1984) Chlorophyll fluorescence as a tool in plant physiology. Photosynth Res 5(2):139–157
58. Krause G, Weis E (1991) Chlorophyll fluorescence and photosynthesis: the basics. Annu Rev Plant Biol 42(1):313–349
59. Schmuck G, Moya I (1994) Time-resolved chlorophyll fluorescence spectra of intact leaves. Remote Sens Environ 47(1):72–76
60. Krasnovsky A, Kovalev YV (2014) Spectral and kinetic parameters of phosphorescence of triplet chlorophyll a in the photosynthetic apparatus of plants. Biochem Mosc 79(4):349–361
61. Hartzler DA, Niedzwiedzki DM, Bryant DA, Blankenship RE, Pushkar Y, Savikhin S (2014) Triplet excited state energies and phosphorescence spectra of (bacterio) chlorophylls. J Phys Chem B 118(26):7221–7232
62. Bhaumik S, DePuy J, Klimash J (2007) Strategies to minimize background autofluorescence in live mice during noninvasive fluorescence optical imaging. Lab Anim 36(8):40
63. del Rosal Rabes B (2017) Nanomateriales para terapia e imagen en el infrarrojo. Dissertation, Universidad Autónoma de Madrid
64. Weagle G, Paterson PE, Kennedy J, Pottier R (1988) The nature of the chromophore responsible for naturally occurring fluorescence in mouse skin. J Photochem Photobiol B 2(3):313–320
65. Konig K, Kienle A, Boehncke W-H, Kaufmann R, Ruck A, Meier T, Steiner R (1994) Photodynamic tumor therapy and on-line fluorescence spectroscopy after ALA administration using 633-nm light as therapeutic and fluorescence excitation radiation. Opt Eng 33(9):2945
66. Holmes H, Kennedy J, Pottier R, Rossi F, Weagle G (1995) A recipe for the preparation of a rodent food that eliminates chlorophyll-based tissue fluorescence. J Photochem Photobiol B 29(2):199
67. Troy T, Jekic-McMullen D, Sambucetti L, Rice B (2004) Quantitative comparison of the sensitivity of detection of fluorescent and bioluminescent reporters in animal models. Mol Imaging 3(1):9–23

68. Inoue Y, Izawa K, Kiryu S, Tojo A, Ohtomo K (2008) Diet and abdominal autofluorescence detected by in vivo fluorescence imaging of living mice. Mol Imaging 7(1):7290
69. Tseng J-C, Vasquez K, Peterson JD, Hopkinton M (2015) Optical imaging on the IVIS SpectrumCT system: general and technical considerations for 2D and 3D imaging. Technical note, pre-clinical in vivo imaging PerkinElmer, Inc, Waltham, MA
70. In vivo animal imaging diet considerations (2008) Application Note for Pearl Imager. LICOR Biosciences
71. Zeng H, MacAulay C, Palcic B, McLean DI (1995) Spectroscopic and microscopic characteristics of human skin autofluorescence emission. Photochem Photobiol 61(6):639–645
72. Kollias N, Zonios G, Stamatas GN (2002) Fluorescence spectroscopy of skin. Vib Spectrosc 28(1):17–23
73. Gillies R, Zonios G, Anderson RR, Kollias N (2000) Fluorescence excitation spectroscopy provides information about human skin in vivo. J Invest Dermatol 115(4):704–707
74. Kozikowski S, Wolfram L, Alfano R (1984) Fluorescence spectroscopy of eumelanins. IEEE J Quantum Electron 20(12):1379–1382
75. Gallas JM, Eisner M (1987) Fluorescence of melanin-dependence upon excitation wavelength and concentration. Photochem Photobiol 45(5):595–600
76. Elleder M, Borovanský J (2001) Autofluorescence of melanins induced by ultraviolet radiation and near ultraviolet light. A histochemical and biochemical study. Histochem J 33(5):273–281
77. Meredith P, Sarna T (2006) The physical and chemical properties of eumelanin. Pigment Cell Res 19(6):572–594
78. Zonios G, Dimou A, Bassukas I, Galaris D, Tsolakidis A, Kaxiras E (2008) Melanin absorption spectroscopy: new method for noninvasive skin investigation and melanoma detection. J Biomed Opt 13(1):014017
79. Capozzi V, Perna G, Gallone A, Biagi P, Carmone P, Fratello A, Guida G, Zanna P, Cicero R (2005) Raman and optical spectroscopy of eumelanin films. J Mol Struct 744:717–721
80. Nighswander-Rempel SP, Riesz J, Gilmore J, Meredith P (2005) A quantum yield map for synthetic eumelanin. J Chem Phys 123(19):194901
81. d'Ischia M, Napolitano A, Pezzella A, Meredith P, Sarna T (2009) Chemical and structural diversity in eumelanins: unexplored bio-optoelectronic materials. Angew Chem Int Ed 48(22):3914–3921
82. Huang Z, Zeng H, Hamzavi I, Alajlan A, Tan E, McLean DI, Lui H (2006) Cutaneous melanin exhibiting fluorescence emission under near-infrared light excitation. J Biomed Opt 11(3):034010
83. Huang Z, Lui H, Chen X, Alajlan A, McLean DI, Zeng H (2004) Raman spectroscopy of in vivo cutaneous melanin. J Biomed Opt 9(6):1198–1205
84. del Rosal B, Villa I, Jaque D, Sanz-Rodríguez F (2016) In vivo autofluorescence in the biological windows: the role of pigmentation. J Biophotonics 9(10):1059–1067
85. Malencik D, Anderson S (2003) Dityrosine as a product of oxidative stress and fluorescent probe. Amino Acids 25(3–4):233–247
86. Ramanujam N (2000) Fluorescence spectroscopy of neoplastic and non-neoplastic tissues. Neoplasia 2(1–2):89–117
87. Wagnieres GA, Star WM, Wilson BC (1998) In vivo fluorescence spectroscopy and imaging for oncological applications. Photochem Photobiol 68(5):603–632
88. Demos SG, Gandour-Edwards R, Ramsamooj R, de Vere WR (2004) Near infrared autofluorescence imaging for detection of cancer. J Biomed Opt 9(3):587–593
89. Zhang G, Demos S, Alfano R (1999) Far-red and NIR spectral wing emission from tissues under 532 and 632 nm photo-excitation. Lasers Life Sci 9(1):1–16
90. Demos SG, Staggs MC, Gandour-Edwards R, Ramsamooj R, de Vere White R (2002) Tissue imaging for cancer detection using NIR autofluorescence. In: Optical biopsy IV, 2002. International Society for Optics and Photonics, pp 31–35

91. Demos SG, Bold R, White RV, Ramsamooj R (2005) Investigation of near-infrared autofluorescence imaging for the detection of breast cancer. IEEE J Sel Top Quantum Electron 11(4):791–798
92. Fournier LS, Lucidi V, Berejnoi K, Miller T, Demos SG, Brasch RC (2006) In-vivo NIR autofluorescence imaging of rat mammary tumors. Opt Express 14(15):6713–6723
93. Han X, Lui H, McLean DI, Zeng H (2009) Near infrared autofluorescence imaging of cutaneous melanins and human skin in vivo. J Biomed Opt 14(2):024017
94. Wang S, Zhao J, Lui H, He Q, Zeng H (2013) In vivo near-infrared autofluorescence imaging of pigmented skin lesions: methods, technical improvements and preliminary clinical results. Skin Res Technol 19(1):20–26
95. Khristoforova YA, Bratchenko IA, Artemyev DN, Myakinin OO, Kozlov SV, Moryatov AA, Zakharov VP (2015) Method of autofluorescence diagnostics of skin neoplasms in the near infrared region. J Biomed Photonics Eng 1(3)
96. Khristoforova Y, Bratchenko I, Artemyev D, Myakinin O, Moryatov A, Kozlov S, Zakharov VP (2016) NIR autofluorescence skin tumor diagnostics. In: Laser Optics (LO), 2016 International Conference. IEEE, pp S2–17
97. Bratchenko IA, Artemyev DN, Myakinin OO, Khristoforova YA, Moryatov AA, Kozlov SV, Zakharov VP (2017) Combined Raman and autofluorescence ex vivo diagnostics of skin cancer in near-infrared and visible regions. J Biomed Opt 22(2):027005
98. Demos SG, Gandour-Edwards R, Ramsamooj R, de Vere WR (2004) Spectroscopic detection of bladder cancer using near-infrared imaging techniques. J Biomed Opt 9(4):767–712
99. Lieber CA, Kabeer MH (2010) Characterization of pediatric Wilms' tumor using Raman and fluorescence spectroscopies. J Pediatr Surg 45(3):549–554
100. Jacobson MC, deVere White RW, Demos SG (2012) In vivo testing of a prototype system providing simultaneous white light and near infrared autofluorescence image acquisition for detection of bladder cancer. J Biomed Opt 17(3):036011
101. Bergholt MS, Zheng W, Lin K, Ho KY, Teh M, Yeoh KG, So JBY, Huang Z (2011) Combining near-infrared-excited autofluorescence and Raman spectroscopy improves in vivo diagnosis of gastric cancer. Biosens Bioelectron 26(10):4104–4110
102. Shao X, Zheng W, Huang Z (2011) In vivo diagnosis of colonic precancer and cancer using near-infrared autofluorescence spectroscopy and biochemical modeling. J Biomed Opt 16(6):067005
103. Shao X, Zheng W, Huang Z (2011) Near infrared autofluorescence spectroscopy for in vivo identification of hyperplastic and adenomatous polyps in the colon. Biosens Bioelectron 30(1):118–122
104. Nguyen JQ, Gowani Z, O'Connor M, Pence I, Holt G, Mahadevan-Jansen A (2015) Near infrared autofluorescence spectroscopy of in vivo soft tissue sarcomas. Opt Lett 40(23):5498–5501
105. Fleckenstein M, Schmitz-Valckenberg S, Holz F (2010) Fundus autofluorescence imaging in clinical use. Rev Ophthalmol, August Issue
106. Landrum JT, Bone RA (2001) Lutein, zeaxanthin, and the macular pigment. Arch Biochem Biophys 385(1):28–40
107. Skondra D, Papakostas TD, Hunter R, Vavvas DG (2012) Near infrared autofluorescence imaging of retinal diseases. In: Seminars in ophthalmology, vol 5–6. Taylor & Francis, Boca Raton, pp 202–208
108. Piccolino FC, Borgia L, Zinicola E, Iester M, Torrielli S (1996) Pre-injection fluorescence in indocyanine green angiography. Ophthalmology 103(11):1837–1845
109. Keilhauer CN, Delori FC (2006) Near infrared autofluorescence imaging of the fundus: visualization of ocular melanin. Invest Ophthalmol Vis Sci 47(8):3556–3564
110. Weinberger AW, Lappas A, Kirschkamp T, Mazinani BA, Huth JK, Mohammadi B, Walter P (2006) Fundus near infrared fluorescence correlates with fundus near infrared reflectance. Invest Ophthalmol Vis Sci 47(7):3098–3108

111. Gibbs D, Cideciyan AV, Jacobson SG, Williams DS (2009) Retinal pigment epithelium defects in humans and mice with mutations in MYO7A: imaging melanosome-specific autofluorescence. Invest Ophthalmol Vis Sci 50(9):4386–4393
112. Ayata A, Tatlipinar S, Kar T, Unal M, Ersanli D, Bilge AH (2008) Near infrared and short-wavelength autofluorescence imaging in central serous chorioretinopathy. Br J Ophthalmol 93(1):79–82
113. Kellner U, Kellner S, Weinitz S (2010) Fundus autofluorescence (488 nm) and near-infrared autofluorescence (787 nm) visualize different retinal pigment epithelium alterations in patients with age-related macular degeneration. Retina 30(1):6–15
114. Pilotto E, Vujosevic S, Melis R, Convento E, Sportiello P, Alemany-Rubio E, Segalina S, Midena E (2011) Short wavelength fundus autofluorescence versus near-infrared fundus autofluorescence, with microperimetric correspondence, in patients with geographic atrophy due to age-related macular degeneration. Br J Ophthalmol 95(8):1140–1144
115. Schmitz-Valckenberg S, Lara D, Nizari S, Normando EM, Guo L, Wegener AR, Tufail A, Fitzke FW, Holz FG, Cordeiro MF (2010) Localisation and significance of in vivo near-infrared autofluorescent signal in retinal imaging. Br J Ophthalmol 95(8):1134–1139
116. Sparrow JR, Marsiglia M, Allikmets R, Tsang S, Lee W, Duncker T, Zernant J (2015) Flecks in recessive Stargardt disease: short-wavelength autofluorescence, near-infrared autofluorescence, and optical coherence tomography. Invest Ophthalmol Vis Sci 56(8):5029–5039
117. Koizumi H, Maruyama K, Kinoshita S (2010) Blue light and near-infrared fundus autofluorescence in acute Vogt–Koyanagi–Harada disease. Br J Ophthalmol 94:1499–1505
118. Keilhauer CN, Delori FC (2010) Near infrared autofluorescence imaging. In: Holz FG, Spaide R (eds) Medical retina: focus on retinal imaging. Springer, Berlin, Heidelberg, pp 69–76
119. Ayata A, Tatlıpınar S, Ünal M, Erşanlı D, Bilge AH (2008) Autofluorescence and OCT features of Bietti's crystalline dystrophy. Br J Ophthalmol 92(5):718–720
120. Applewhite MK, White MG, Xiong M, Pasternak JD, Abdulrasool L, Ogawa L, Suh I, Gosnell JE, Kaplan EL, Duh Q-Y, Angelos P, Shen WT, Grogan RH (2016) Incidence, risk factors, and clinical outcomes of incidental parathyroidectomy during thyroid surgery. Ann Surg Oncol 23(13):4310–4315
121. Chen H, Wang TS, Yen TW, Doffek K, Krzywda E, Schaefer S, Sippel RS, Wilson SD (2010) Operative failures after parathyroidectomy for hyperparathyroidism: the influence of surgical volume. Ann Surg 252(4):691–695
122. Ahuja AT, Wong KT, Ching ASC, Fung MK, Lau JYW, Yuen EHY, King AD (2004) Imaging for primary hyperparathyroidism—what beginners should know. Clin Radiol 59(11):967–976
123. Mohebati A, Shaha AR (2012) Imaging techniques in parathyroid surgery for primary hyperparathyroidism. Am J Otolaryngol 33(4):457–468
124. Sosa JA, Bowman HM, Tielsch JM, Powe NR, Gordon TA, Udelsman R (1998) The importance of surgeon experience for clinical and economic outcomes from thyroidectomy. Ann Surg 228(3):320–330
125. Sommerey S, Al Arabi N, Ladurner R, Chiapponi C, Stepp H, Hallfeldt KK, Gallwas JK (2015) Intraoperative optical coherence tomography imaging to identify parathyroid glands. Surg Endosc 29(9):2698–2704
126. Ladurner R, Hallfeldt KK, Al Arabi N, Stepp H, Mueller S, Gallwas JK (2013) Optical coherence tomography as a method to identify parathyroid glands. Lasers Surg Med 45(10):654–659
127. Conti de Freitas LC, Phelan E, Liu L, Gardecki J, Namati E, Warger WC, Tearney GJ, Randolph GW (2014) Optical coherence tomography imaging during thyroid and parathyroid surgery: a novel system of tissue identification and differentiation to obviate tissue resection and frozen section. Head Neck 36(9):1329–1334
128. Schols RM, Bouvy ND, Wieringa FP, Alic L, Stassen LPS (2013) Diffuse optical reflectance spectrometry in thyroid and parathyroid surgery. In: 21st International Congress of the European Association for Endoscopic Surgery, Vienna

129. Tummers QR, Schepers A, Hamming JF, Kievit J, Frangioni JV, van de Velde CJ, Vahrmeijer AL (2015) Intraoperative guidance in parathyroid surgery using near-infrared fluorescence imaging and low-dose methylene blue. Surgery 158(5):1323–1330
130. Antakia R, Gayet P, Guillermet S, Stephenson TJ, Brown NJ, Harrison BJ, Balasubramanian SP (2014) Near infrared fluorescence imaging of rabbit thyroid and parathyroid glands. J Surg Res 192(2):480–486
131. Hyun H, Park MH, Owens EA, Wada H, Henary M, Handgraaf HJM, Vahrmeijer AL, Frangioni JV, Choi HS (2015) Structure-inherent targeting of near-infrared fluorophores for parathyroid and thyroid gland imaging. Nat Med 21(2):192–197
132. Paras CA (2012) A novel optical approach to the intraoperative detection of parathyroid glands Thesis, Vanderbilt University
133. Paras C, Keller M, White L, Phay J, Mahadevan-Jansen A (2011) Near infrared autofluorescence for the detection of parathyroid glands. J Biomed Opt 16(6):067012
134. McWade MA, Paras C, White LM, Phay JE, Mahadevan-Jansen A, Broome JT (2013) A novel optical approach to intraoperative detection of parathyroid glands. Surgery 154(6):1371–1377
135. McWade MA, Sanders ME, Broome JT, Solórzano CC, Mahadevan-Jansen A (2016) Establishing the clinical utility of autofluorescence spectroscopy for parathyroid detection. Surgery 159(1):193–203
136. De Leeuw F, Breuskin I, Abbaci M, Casiraghi O, Mirghani H, Ben Lakhdar A, Laplace-Builhé C, Hartl D (2016) Intraoperative near-infrared imaging for parathyroid gland identification by auto-fluorescence: a feasibility study. World J Surg 40(9):2131–2138
137. McWade MA, Paras C, White LM, Phay JE, Solórzano CC, Broome JT, Mahadevan-Jansen A (2014) Label-free intraoperative parathyroid localization with near-infrared autofluorescence imaging. J Clin Endocrinol Metab 99(12):4574–4580
138. McWade M, Pence IJ, Paras C, Mahadevan-Jansen A (2015) Imaging system design for surgical guidance with near-infrared autofluorescence. In: Advanced biomedical and clinical diagnostic and surgical guidance systems XIII. International Society for Optics and Photonics, p 931303
139. Falco J, Dip F, Quadri P, de la Fuente M, Rosenthal R (2016) Cutting edge in thyroid surgery: autofluorescence of parathyroid glands. J Am Coll Surg 223(2):374–380
140. Ladurner R, Sommerey S, Arabi NA, Hallfeldt KKJ, Stepp H, Gallwas JKS (2017) Intraoperative near-infrared autofluorescence imaging of parathyroid glands. Surg Endosc 31(8):3140–3145
141. Benmiloud F, Rebaudet S, Varoquaux A, Penaranda G, Bannier M, Denizot A (2018) Impact of autofluorescence-based identification of parathyroids during total thyroidectomy on postoperative hypocalcemia: a before and after controlled study. Surgery 163(1):23–30
142. Chotalia R, Bloxham R, McIntyre C, Tolley N, Palazzo F (2017) Can near infrared autofluorescent imaging prevent inadvertent parathyroidectomy? A pilot study. Eur J Surg Oncol 43(12):2385
143. Kahramangil B, Berber E (2017) The use of near-infrared fluorescence imaging in endocrine surgical procedures. J Surg Oncol 115(7):848–855
144. Kim SW, Lee HS, Lee KD (2017) Intraoperative real-time localization of parathyroid gland with near infrared fluorescence imaging. Gland Surg 6(5):516
145. Ladurner R, Al Arabi N, Guendogar U, Hallfeldt K, Stepp H, Gallwas J (2017) Near infrared autofluorescence imaging to detect parathyroid glands in thyroid surgery. Ann R Coll Surg Engl 100(1):1–4
146. Shinden Y, Nakajo A, Arima H, Tanoue K, Hirata M, Kijima Y, Maemura K, Natsugoe S (2017) Intraoperative identification of the parathyroid gland with a fluorescence detection system. World J Surg 41(6):1506–1512
147. Alesina P, Meier B, Hinrichs J, Mohmand W, Walz M (2018) Enhanced visualization of parathyroid glands during video-assisted neck surgery. Langenbeck's Arch Surg 403(3):395–401

148. Kim Y, Kim SW, Lee KD, Y-c A (2018) Real-time localization of the parathyroid gland in surgical field using raspberry pi during thyroidectomy: a preliminary report. Biomed Opt Express 9(7):3391–3398
149. Thomas G, McWade MA, Paras C, Mannoh EA, Sanders ME, White LM, Broome JT, Phay JE, Baregamian N, Solorzano CC (2018) Developing a clinical prototype to guide surgeons for intraoperative label-free identification of parathyroid glands in real-time. Thyroid 28(11):1517–1531
150. Antman EM, Hand M, Armstrong PW, Bates ER, Green LA, Halasyamani LK, Hochman JS, Krumholz HM, Lamas GA, Mullany CJ (2008) 2007 focused update of the ACC/AHA 2004 guidelines for the management of patients with ST-elevation myocardial infarction. Circulation 117(2):296–329
151. Koskinas KC, Ughi GJ, Windecker S, Tearney GJ, Räber L (2016) Intracoronary imaging of coronary atherosclerosis: validation for diagnosis, prognosis and treatment. Eur Heart J 37(6):524–535
152. Tearney GJ, Yabushita H, Houser SL, Aretz HT, Jang I-K, Schlendorf KH, Kauffman CR, Shishkov M, Halpern EF, Bouma BE (2003) Quantification of macrophage content in atherosclerotic plaques by optical coherence tomography. Circulation 107(1):113–119
153. Calfon MA, Rosenthal A, Mallas G, Mauskapf A, Nudelman RN, Ntziachristos V, Jaffer FA (2011) In vivo near infrared fluorescence (NIRF) intravascular molecular imaging of inflammatory plaque, a multimodal approach to imaging of atherosclerosis. J Vis Exp 54:e2257
154. Vinegoni C, Botnaru I, Aikawa E, Calfon MA, Iwamoto Y, Folco EJ, Ntziachristos V, Weissleder R, Libby P, Jaffer FA (2011) Indocyanine green enables near-infrared fluorescence imaging of lipid-rich, inflamed atherosclerotic plaques. Sci Transl Med 3(84):84ra45–84ra45
155. Lee S, Lee MW, Cho HS, Song JW, Nam HS, Oh DJ, Park K, Oh W-Y, Yoo H, Kim JW (2014) Fully integrated high-speed intravascular optical coherence tomography/near-infrared fluorescence structural/molecular imaging in vivo using a clinically available near-infrared fluorescence–emitting indocyanine green to detect inflamed lipid-rich atheromata in coronary-sized vessels. Circ Cardiovasc Interv 7(4):560–569
156. Ughi GJ, Wang H, Gerbaud E, Gardecki JA, Fard AM, Hamidi E, Vacas-Jacques P, Rosenberg M, Jaffer FA, Tearney GJ (2016) Clinical characterization of coronary atherosclerosis with dual-modality OCT and near-infrared autofluorescence imaging. JACC Cardiovasc Imaging 9(11):1304–1314
157. Gardecki JA, Chau AH, Tearney GJ (2009) Report on ex vivo Raman database studies. Prescient Medical Inc. and The General Hospital Corporation, Boston
158. Wang H, Gardecki JA, Ughi GJ, Jacques PV, Hamidi E, Tearney GJ (2015) Ex vivo catheter-based imaging of coronary atherosclerosis using multimodality OCT and NIRAF excited at 633 nm. Biomed Opt Express 6(4):1363–1375
159. Htun NM, Chen YC, Lim B, Schiller T, Maghzal GJ, Huang AL, Elgass KD, Rivera J, Schneider HG, Wood BR, Stocker R, Peter K (2017) Near infrared autofluorescence induced by intraplaque hemorrhage and heme degradation as marker for high-risk atherosclerotic plaques. Nat Commun 8(1):75

Chapter 3
Surface Modification of Near Infrared-Emitting Nanoparticles for Biomedical Applications

Thomas Hirsch

3.1 Introduction

Near infrared-emitting nanoparticles (NIR-NPs), excitable in a biologically silent wavelength regime are highly attractive for biomedical applications for several reasons: (a) photoexcitation in the near infrared (NIR) region does not trigger the luminescence of biological matter, which minimizes background fluorescence to almost zero; (b) higher penetration depth of the excitation light is enabled; (c) emitted light in the infrared (IR) can also penetrate tissues without showing any phototoxicity. For these reasons, NIR-emitting probes are needed, which are chemically stable and display low cytotoxicity. These outstanding features are found, for instance, in lanthanide-doped nanoparticles (Ln-NPs) [1, 2, 3]. These kinds of nanomaterials will come along with other benefits like narrow emission bands, large Stokes-shift, or upconversion ability [4]. Furthermore, they can be excited by cheap, low-power continuous wave lasers, and these probes do not suffer from blinking or photobleaching. The typical excitation wavelengths used for upconversion (800 or 980 nm) are within the so-called first optical window. Lanthanide-doped nanoparticles are known for low cytotoxicity [5], enabling them for various applications including photodynamic therapy [6, 7], drug delivery [8, 9, 10], bioimaging [11, 12, 13], nanothermometry [14], sensing [15, 16] of parameters such as pH values [17] or oxygen [18], and in immunoassays [19]. Most examples in bioimaging report on the upconversion (anti-Stokes emission) properties of lanthanide-doped nanoparticles, mainly attributed to the fact that the visual range of the spectrum is easy to analyze and well covered by instruments. This is also the reason why many examples for the surface chemistry presented in

T. Hirsch (✉)
Institute of Analytical Chemistry, Chemo- and Biosensors, University of Regensburg, Regensburg, Germany
e-mail: thomas.hirsch@ur.de

A. Benayas et al. (eds.), *Near Infrared-Emitting Nanoparticles for Biomedical Applications*, https://doi.org/10.1007/978-3-030-32036-2_3

this chapter deal with applications based on the anti-Stokes emission. Nevertheless, all of these materials will also show classical emission at lower energies compared to the excitation wavelength. Therefore all of the surface modification strategies presented in upconversion nanoparticles are also valid upon bioimaging in the NIR range. Many efforts have been made in the last years to design and synthesize Ln-NPs of controlled size, shape, and composition. Bottom-up strategies such as co-precipitation, thermal decomposition, and solvothermal syntheses turned out to result in small and monodisperse nanoparticles but yet possessing bright upconversion luminescence [20]. The main focus on research deals with understanding of the complex photophysics and improving the intrinsically low quantum yields [21, 22]. A well-designed core–shell architecture even allows the synthesis of upconversion nanoparticles with quantum yields close to that of the bulk material [23]. The chemical stability of the most efficient fluoride host materials like $NaYF_4$, especially in low particle concentrations or under flow-conditions, seems to be critical. A rapid dissolution of such particles in aqueous systems has been reported [24, 25, 26]. To fully exploit lanthanide-doped nanoparticles in biological applications, the surface functionalization remains a crucial step: (1) the surface ligands need to provide colloidal stability under physiological conditions; (2) the luminescence properties should not be negatively affected in terms of surface quenching; (3) chemical stability to overcome dissolution effects should be provided; and (4) functionalities for targeting or receptors for diagnosis or drugs for delivery should be introduced. Especially for bioimaging applications, the choice of the surface ligand is crucial as it determines the nanoparticle behavior in biological systems, e.g., in terms of their surface charge, layer tightness, or hydrophilicity [27]. Colloidal stability under physiological conditions is very important for in vitro and especially for in vivo applications of nanoparticles. Usually a zeta potential of around ± 30 mV is known to warrant colloidal stability due to electrostatic repulsion. But charged surfaces (positive > negative) have a higher binding affinity to biomolecules resulting in a biomolecular corona [28]. Here, it is preferable that no biomolecular corona is formed around the nanoparticle. Otherwise, surface functionalities will be buried by the proteins and transport and targeting will be hindered. The most common procedure for the preparation of stealth surfaces is the functionalization with polymeric ethylene glycol (PEGylation) since it provides stabilization due to steric repulsion and a low attachment of biomolecules [29]. However, PEGylation yields particles aggregating at high salt concentrations and having huge hydrodynamic diameter making renal clearance impossible [30]. A more recent approach is the formation of zwitterionic and highly hydrophilic surfaces with amphiphilic molecules [31]. These particles are known to be highly biocompatible and have a long blood circulation time, but the synthesis of neutral and zwitterionic surfaces with colloidal stability is still challenging [32].

3.2 Strategies for Surface Modification

The main intention in surface modification is dedicated to the transfer of hydrophobic NPs, as obtained from most bottom-up synthesis protocols, into hydrophilic particles, dispersible in aqueous systems [33]. The most common strategies are: (1) chemical modification of the surface ligand; (2) attaching polymers or amphiphilic molecules as additional bi- or multilayer coating; (3) growing of a silica coating to use the standard surface chemistry as established for many other particle systems; and (4) exchange of the hydrophobic ligand by a hydrophilic one (Fig. 3.1). All these strategies are summarized in detail in a review by Muhr et al. [34].

The first method, the direct chemical modification of oleate or oleylamine, the most common capping present at the particle surface right after the synthesis, by oxidation of the –C=C– bond can be achieved by agents like the Lemieux–von Rudloff reagent [35], ozone [36], or 3-chloroperoxybenzoic acid [37]. Water-dispersibility will be provided by the resulting carboxylic groups. This method is less common as these reactions are not very easy to handle, e.g., for the use of ozone, a generator is needed. Often there is also a lack of information on the exact stoichiometry of surface ligands and oxidizing agents. Additionally, the oxidizing agents need to be soluble in the organic media. With the number of ligands getting oxidized the stability of the particles in the solvent gets minimized. This makes it difficult to end up with a full oxidation of all ligands originally present at the surface.

Other techniques, not replacing the original surface capping, overcome some of these drawbacks. The formation of a bilayer at the particle surface makes use

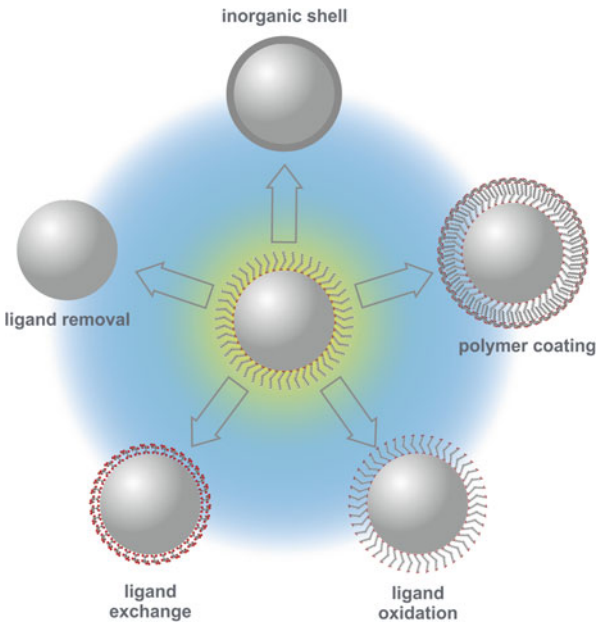

Fig. 3.1 Different strategies for surface modification of NIR-NPs to achieve dispersibility in water comprising the attachment of additional layers in terms of inorganic shells or polymer coatings, the direct modification of the native ligand by ligand oxidation or the ligand exchange, which can be either a complete replacement of the ligand prior attachment of a new surface capping or a two-step ligand exchange via stabilizing agents

of the van der Waals interaction between the hydrophobic part of an amphiphilic molecule. This interaction is weak and little is known on the stability of such layers under biological circumstances. It is known that in biological membranes the lipids can either be exchanged, or other lipophilic molecules can be inserted into the membrane. Such possibilities need to be taken into account when applying particles with this type of surface modification in biological systems. On the other hand, amphiphilic molecules are available in large variations offering a toolbox for tuning surface properties in terms of different charges or different binding groups for further functionalization. With alternating charges, it is also possible to assemble a layer-by-layer coating, which is attractive when the particle surface needs to be shielded. In general, such a strategy to use a hydrophobic barrier by bi- or multilayer is straightforward when the inorganic host material of the particle needs to be prevented from the access of water molecules in order to avoid its dissolution, or to minimize non-radiative deactivation of the luminescence by quenching due to –OH vibrations. Particles with amphiphilic molecules at the surface generally display good colloidal stability in aqueous solution. By the use of phospholipids functionalities such as biotin, folate, or maleimide can be introduced enabling easy coupling of bioreceptors or drugs for theranostic applications. Biocompatibility can be enhanced by the use of phospholipids consisting of poly(ethylene glycol) (PEG) units [38, 39]. Surface modifications by phospholipids with functionalized head groups and PEG spacers are easy to apply, but time consuming in synthesis and therefore costly if commercially available. A straightforward example is shown by the group of Prasad. They designed bilayer coated particles with PEG-phospholipids with outstanding stability in vitro at 37 °C for 24 h and only 25% loss of particle integrity when dispersed in cell growth medium containing 10% fetal bovine serum (Fig. 3.2) [40].

A cheaper version of amphiphiles are detergents such as Tween 80, cetyltrimethylammonium, dodecyltrimethylammonium, dodecyl sulfate, and the tert-octylphenyl ether of poly(ethylene glycol) which render nanoparticles water dispersible [41], but often lead to lower biocompatibility. The critical part when using amphiphilic molecules for surface modification is the right choice of their concentration to prevent the formation of either empty micelles or such including more than one nanoparticle. Extrusion steps can help in sizing of the micelles, but an optimization is necessary for every type and size of particles as simple up- or downscaling will not be successful. Another possibility is not to use amphiphilic molecules but amphiphilic polymers, e.g., poly(maleic anhydride-*alt*-1-octadecene) [42, 43]. The advantage is given by the presence of multiple alkyl chains per molecule and weak chelating effects stabilizing the surface coating against ligand detachment. Particles coated with poly(maleic anhydride-*alt*-1-octadecene) display good temporal stability over a wide pH range from 3 to 13, which can be further increased by crosslinking within the layer by a reaction of the anhydride groups with bis(hexamethylene)triamine [44].

Quite popular is the growth of additional shells consisting of oxides or noble metals on Ln-NPs. These techniques take advantage of the availability of already established protocols for further surface functionalization, which can be easily

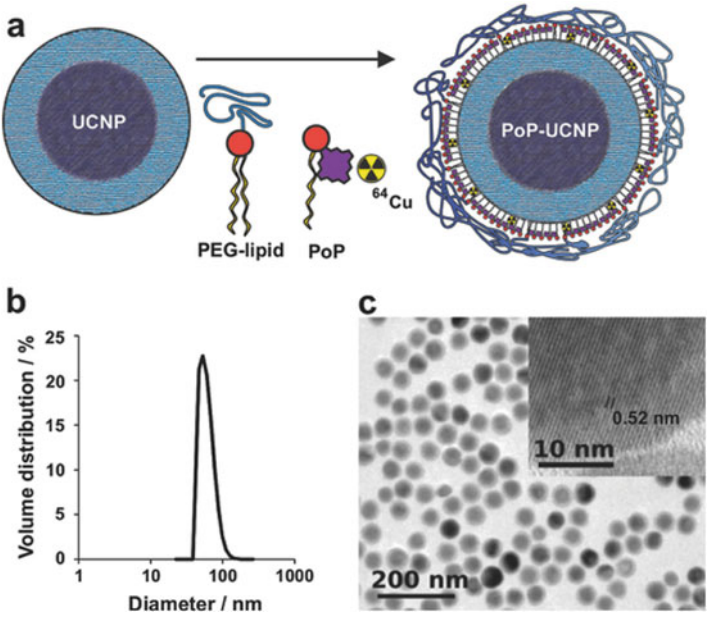

Fig. 3.2 Scheme of porphyrin-phospholipid-coated upconversion nanoparticles (PoP-UCNPs) for hexamodal imaging (**a**). Size distribution obtained from light scattering (**b**) and electron micrographs (**c**) of PoP-UCNPs. Image reprinted from Ref. [40] with permission Copyright © 2015, John Wiley and Sons

adapted, such as silane chemistry for silica shells or thiol chemistry on gold shells [45, 46]. Other reasons to go for this strategy are the introduction of additional features like catalytic effects by TiO_2 shells [47], plasmonic modulation of the luminescence properties by gold or silver shells [48], the encapsulation of dyes, drugs, or other molecules in mesoporous silica shells [49]. Silica shells are created by surfactant-assisted growth of silica precursors. The Stöber method or the reverse microemulsion method allows the coating of both, hydrophilic and hydrophobic nanoparticles [50]. Silica coatings are characterized by good dispersibility in water and low cytotoxicity [51]. To end up in uniform particle size distributions with a defined thickness of the silica shell can be very tricky due to a lot of parameters, which play a crucial role during the synthesis, e.g., there is a strong dependency on the concentration ratio of the silica precursor and the surfactant, which is needed in the first step [52, 53]. On the other hand, it is possible to obtain particles with an extremely thin silica shell in the range of 1 to 2 nm thickness, which is beneficial for application utilizing a distance dependent energy transfer from or to the particle by any surface bound molecule [54]. The zeta potential of particles encapsulated by a silica shell is usually slightly negative at neutral pH, which leads to aggregation or precipitation within several hours [55, 56]. If stability over a longer time scale is needed, it is recommended to immediately silanize the surface with surface ligands

providing additional charged groups in solvents at the desired pH value [57]. The poor temporal stability in aqueous solutions of silica modified particles can also become an obstacle during purification steps. Often it gets extremely difficult or almost impossible to disperse such particles after a centrifugation step or to form a clear solution due to the presence of larger agglomerates. A direct functionalization minimizes the tendency for agglomeration by applying modified silanizing agents directly after the coating of Ln-NPs with SiO_2 without any purification step in between. Even more elegant is to use functional organosilanes already during the polymerization process forming the silica shell. For both methods, most commonly used are organosilanes such as aminopropyl-trimethoxysilanes [58], aminopropyl-triethoxysilanes [59], N-[3-(trimethoxysilyl)-propyl]-ethylenediamine [60], or carboxyethylsilanetriol [37]. Silica shells are also of interest for designing composite materials with multimodality. The incorporation of a NIR dye into a silica shell grown on upconversion nanoparticles enabled a probe suitable for NIR imaging and photothermal therapy (Fig. 3.3) [61].

A similar concept can be used for drug delivery, e.g., as demonstrated by the entrapment of doxorubicin into mesoporous silica shells of upconversion nanoparticles [8]. This concept can easily be adapted to other nanoparticles.

An extremely versatile method for surface modification of NIR-NPs is the replacement of the hydrophobic surface capping by a new hydrophilic ligand. Here, two principles are known, the one which displaces one ligand by another in one step and the other removing the ligand before adding a new capping agent in a

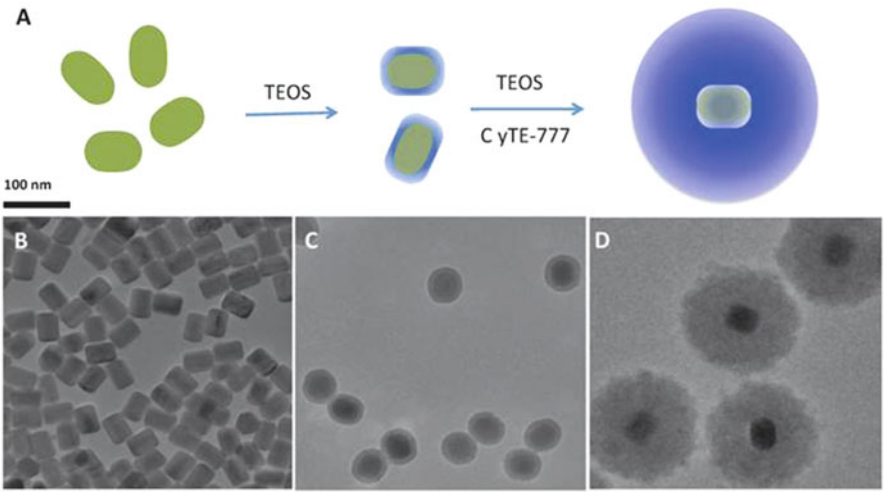

Fig. 3.3 (**a**) Synthetic scheme and (**b-d**) Transmission electron microscopy images (**b**, upconverting nanoparticles (UCNPs); **c**, UCNP@SiO_2 core/shell nanoparticles; **d**, UCNP@SiO_2/Dye nano-composites) of NIR excitable lanthanide-doped nanoparticles modified with a silica shell made from tetraethyl orthosilicate (TEOS) with an incorporated carbocyanine dye (CyTE-777) used for photothermal treatment. Figure reproduced from Ref. [61]

two-step process. The first method requires that the new surface ligand coordinates more efficiently to the particle than the ligand, which should be replaced. Second, for a phase transfer into hydrophilic media the new ligand needs also to be more polar in comparison to the original surface capping. To find such ligands is the most difficult part as the protocol for the replacement is quite simple. Typically, oleate-capped nanoparticles are stirred in the presence of an excess of the new ligand for several hours up to several days, at moderate temperature [62]. The more time is needed, the higher is the risk that the particles tend to agglomerate during the ligand replacement. Therefore, no general protocol can be given but an individual optimization of particle to ligand to solvent ratio as well as stirring time and temperature is needed. This can become quite time-consuming as a full characterization of the surface coverage in terms of composition as well as surface loading always is challenging demanding several complementary techniques. Heterobifunctional ligands consisting of poly(ethylene glycol) with a thiol function on one side and an amino or carboxylic group at the opposite end offer further coupling of biomolecules to the nanoparticles. The poly(ethylene glycol) is described as an oxophilic polydentate ligand binding to lanthanide ions at the particle surface [63]. Zhang et al. have reported a ligand exchange with 2-bromo-2-methylpropionic acid and a polymerization of this surface modification with oligo(ethylene glycol) methacrylate to end up with particles colloidal stable in phosphate buffer [64]. This is outstanding as phosphate is known for a strong coordination to the nanoparticles consisting of lanthanides, which can lead to a ligand exchange with time, accompanied by a loss of colloidal stability. Even surface coatings of mixed chemical compositions can be realized by ligand exchange methods as shown by the construction of multimodal nanoparticles with capabilities for multimodal bioimaging in terms of luminescence, magnetic resonance (MR), and radioactivity. The authors describe a simultaneous ion and ligand exchange for lanthanide-based NIR-NPs. At the particle surface, lanthanide ions have been exchanged by Gd^{3+} enabling MR and fluoride ions have been exchanged by the radio nuclide $^{18}F^{-}$. For targeting of cancers, the surface capping oleylamine was exchanged for a mixture of folic acid, oleic acid, and aminocaproic acid [65]. These particles preferably bind to the folate receptor protein, which is commonly expressed at the surface of many human cancer cells.

In contrast to the simultaneous ligand exchange, the two-step ligand exchange generates an intermediate particle system that can be either ligand-free or stabilized by ions such as the BF_4^{-} [66]. This has several advantages as it enables a better control for the stripping of the native ligand as well as for the attachment of the new ligand. Additionally, nanoparticles with BF_4^{-} modification can be stored in a solvent like DMF for months without any tendency for agglomeration. This strategy of a two-step ligand exchange by the use of nitrosyl tetrafluoroborate ($NOBF_4$) was introduced by the group of Murray [66] and can be used for many kinds of inorganic nanoparticles coated by ligands such as oleate or oleylamine. The ligand gets stripped off in a first step and will be replaced by BF_4^{-} ions. The role of the nitrosyl ion is not fully understood so far. A mechanism is discussed, where it forms HNO_2 in the presence of traces of water, which will initiate the stripping of the

ligands off the particle surface [66]. This idea is underpinned by the fact that other tetrafluoroborates such as the so-called Meerwein salt (Et_3OBF_4) are much less effective or do even not work at all. The BF_4^--stabilized particles can be easily purified by centrifugation without tending to agglomerate and this stabilizing ligand can be replaced by almost any ligand with an affinity to the particle surface. It is reported that NIR-NPs, capped with O-phospho-L-threonine, PEG-phosphate, or alendronate ligands, will provide a long-term colloidal stability at close to neutral surface charge at physiological pH [67]. Furthermore, particles with such surface modifications show great resistance to protein corona formation, when dispersed in serum. A protein corona changes on the one hand the identity of the nanoparticle, meaning that targeting ligands are not freely available, and on the other hand, it induces a fast clearance by the reticuloendothelial system and thus a reduced blood circulation time [32] (Fig. 3.4).

Capobianco et al. made use of hydrochloric acid to strip off the hydrophobic ligands in order to generate ligand-free particles which are already water dispersible [68]. This fast and simple method is very useful in biofunctionalization as demonstrated with a functionalization by heparin for bioimaging and cellular targeting [69]. However only little information is known in the colloidal stability of the ligand-free particles in aqueous solutions. It is expected that the particles will minimize their surface energy by agglomeration without any capping agents; therefore, it is expected that those particles cannot be stored for long time.

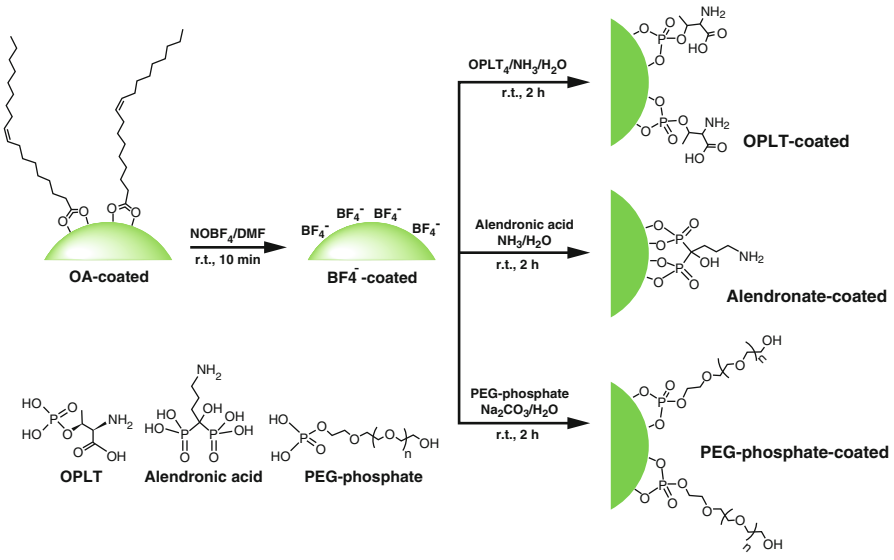

Fig. 3.4 Scheme of a two-step ligand exchange via $NOBF_4$ to obtain colloidal stable lanthanide-doped nanoparticles. The ligands O-phospho-L-threonine (OPLT), PEG-phosphate, or alendronate successfully prevent the formation of a protein corona. Reproduced from Ref. [67] with permission from The Royal Society of Chemistry

3.3 Conclusion and Challenges in Surface Modification

In summary, a great arsenal of different strategies has been established to engineer the particles surface enabling colloidal stability and functionalities in terms of targeting, drug delivery or to improve the luminescence properties by either plasmonic enhancement or efficient blocking of non-radiative deactivation by solvent molecules. Nevertheless, one might ask the question why there is only one inorganic NIR probe, the Cornell Dots™, approved by the FDA so far [70]? Also surprising is the fact that nanoprobes in general fail when it comes to targeting. A literature survey from the past 10 years on tumor targeting with nanoparticles revealed that only 0.7% in median are found to be delivered to a tumor [71]. Toxicity, biodistribution, retention time, clearance, and physiological and chemical interactions are the key parameters and all of them are directly linked to the surface properties. To bring NIR-NPs to practical medical applications a lot of attention needs to be paid to these parameters, starting by establishing reproducible protocols for surface characterization on a nanoscale validated by an excellent surface characterization. Many reports suffer from details on surface coverage of the ligands or do not report on colloidal properties in physiological media [72]. A phase transfer from organic to aqueous solutions can not only be achieved when the particle is completely covered by a new ligand. Yet, incomplete surface coverage will be prone to access of salts and proteins present in complex biological media and can lead to a fast degradation of the engineered surface chemistry under such circumstances. Therefore, main challenges include a better control of a homogeneous surface coating and more reproducible methods for surface loading and/or modification. Despite these challenges, NIR-NPs are considered to represent very promising materials for biomedical applications as evidenced by the rapid growth of outstanding articles covering this field of research.

References

1. Lingeshwar Reddy K, Balaji R, Kumar A, Krishnan V (2018) Lanthanide doped near infrared active upconversion nanophosphors: fundamental concepts, synthesis strategies, and technological applications. Small 26:1801304
2. Xu J, Gulzar A, Yang P, Bi H, Yang D, Gai S, He F, Lin J, Xing B, Jin D (2019) Recent advances in near-infrared emitting lanthanide-doped nanoconstructs: mechanism, design and application for bioimaging. Coord Chem Rev 381:104–134
3. Jalani G, Tam V, Vetrone F, Cerruti M (2018) Seeing, targeting and delivering with upconverting nanoparticles. J Am Chem Soc 140(35):10923–10931
4. Zheng W, Huang P, Tu D, Ma E, Zhu H, Chen X (2015) Lanthanide-doped upconversion nano-bioprobes: electronic structures, optical properties, and biodetection. Chem Soc Rev 44(6):1379–1415
5. Zhou JC, Yang ZL, Dong W, Tang RJ, Sun LD, Yan CH (2011) Bioimaging and toxicity assessments of near-infrared upconversion luminescent $NaYF_4$:Yb,Tm nanocrystals. Biomaterials 32(34):9059–9067

6. Qian HS, Guo HC, Ho PC, Mahendran R, Zhang Y (2009) Mesoporous-Silica-coated up-conversion fluorescent nanoparticles for photodynamic therapy. Small 5(20):2285–2290
7. Buchner M, García Calavia P, Muhr V, Kröninger A, Baeumner AJ, Hirsch T, Russell DA, Marín MJ (2018) Photosensitiser functionalised luminescent upconverting nanoparticles for efficient photodynamic therapy of breast cancer cells. Photochem Photobiol Sci 110:2795
8. Liu J, Bu W, Pan L, Shi J (2013) NIR-triggered anticancer drug delivery by upconverting nanoparticles with integrated azobenzene-modified mesoporous silica. Angewandte Chemie Int Ed 125(16):4471–4475
9. Shen J, Zhao L, Han G (2013) Lanthanide-doped upconverting luminescent nanoparticle platforms for optical imaging-guided drug delivery and therapy. Adv Drug Deliv Rev 65(5):744–755
10. Jalani G, Tam V, Vetrone F, Cerruti M (2018) Seeing, targeting and delivering with upconverting nanoparticles. J Am Chem Soc 140(35):10923–10931
11. Prodi L, Rampazzo E, Rastrelli F, Speghini A, Zaccheroni N (2015) Imaging agents based on lanthanide doped nanoparticles. Chem Soc Rev 44(14):4922–4952
12. Xu S, Huang S, He Q, Wang L (2015) Upconversion nanophosphores for bioimaging. TrAC Trends Anal Chem 66:72–79
13. Dong H, Du SR, Zheng XY, Lyu GM, Sun LD, Li LD, Zhang PZ, Zhang C, Yan CH (2015) Lanthanide nanoparticles: from design toward bioimaging and therapy. Chem Rev 115(19):10725–10815
14. Quintanilla M, Benayas A, Naccache R, Vetrone F (2015) Luminescent nanothermometry with lanthanide-doped nanoparticles. In: Thermometry at the nanoscale. The Royal Society of Chemistry, Oxfordshire, pp 124–166
15. Gorris HH, Resch-Genger U (2017) Perspectives and challenges of photon-upconversion nanoparticles-part II: bioanalytical applications. Anal Bioanal Chem 409(25):5875–5890
16. Zhang Z, Shikha S, Liu J, Zhang J, Mei Q, Zhang Y (2018) Upconversion nanoprobes: recent advances in sensing applications. Anal Chem
17. Arppe R, Näreoja T, Nylund S, Mattsson L, Koho S, Rosenholm JM, Soukka T, Schäferling M (2014) Photon upconversion sensitized nanoprobes for sensing and imaging of pH. Nanoscale 6(12):6837–6843
18. Achatz DE, Meier RJ, Fischer LH, Wolfbeis OS (2011) Luminescent sensing of oxygen using a quenchable probe and upconverting nanoparticles. Angewandte Chemie Int Ed 123(1):274–277
19. Wang M, Hou W, Mi CC, Wang WX, Xu ZR, Teng HH, Mao CB, Xu SK (2009) Immunoassay of goat antihuman immunoglobulin G antibody based on luminescence resonance energy transfer between near-infrared responsive $NaYF_4$:Yb,Er upconversion fluorescent nanoparticles and gold nanoparticles. Anal Chem 81(21):8783–8789
20. Chen G, Qiu H, Prasad PN, Chen X (2014) Upconversion nanoparticles: design, nanochemistry, and applications in theranostics. Chem Rev 114:5161–5214
21. Wisser MD, Fischer S, Siefe C, Alivisatos AP, Salleo A, Dionne JA (2018) Improving quantum yield of Upconverting nanoparticles in aqueous media via emission sensitization. Nano Lett 18(4):2689–2695
22. Wiesholler LM, Hirsch T (2018) Strategies for the design of bright upconversion nanoparticles for bioanalytical applications. Opt Mater 80:253–264
23. Homann C, Krukewitt L, Frenzel F, Grauel B, Würth C, Resch-Genger U, Haase M (2018) $NaYF_4$:Yb,Er/$NaYF_4$ core/shell nanocrystals with high upconversion luminescence quantum yield. Angewandte Chemie Int Ed 57:8765–8769
24. Dukhno O, Przybilla F, Muhr V, Buchner M, Hirsch T, Mély Y (2018) Time-dependent luminescence loss for individual upconversion nanoparticles upon dilution in aqueous solution. Nanoscale 10(34):15904–15910
25. Plohl O, Kraft M, Kovač J, Belec B, Ponikvar-Svet M, Würth C, Lisjak D, Resch-Genger U (2017) Optically detected degradation of $NaYF_4$:Yb,Tm-based upconversion nanoparticles in phosphate buffered saline solution. Langmuir 33(2):553–560

26. Lahtinen S, Lyytikäinen A, Päkkilä H, Hömppi E, Perälä N, Lastusaari M, Soukka T (2016) Disintegration of hexagonal $NaYF_4$:Yb^{3+},Er^{3+} upconverting nanoparticles in aqueous media: the role of fluoride in solubility equilibrium. J Phys Chem C 121(1):656–665
27. Kim ST, Saha K, Kim C, Rotello VM (2013) The role of surface functionality in determining nanoparticle cytotoxicity. Acc Chem Res 46(3):681–691
28. Del Pino P, Pelaz B, Zhang Q, Maffre P, Nienhaus GU, Parak WJ (2014) Protein corona formation around nanoparticles–from the past to the future. Mater Horizons 1(3):301–313
29. Generalova AN, Rocheva VV, Nechaev AV, Khochenkov DA, Sholina NV, Semchishen VA, Zubov VP, Koroleva AV, Chichkov BN, Khaydukov EV (2016) PEG-modified upconversion nanoparticles for in vivo optical imaging of tumors. RSC Adv 6(36):30089–30097
30. García KP, Zarschler K, Barbaro L, Barreto JA, O'Malley W, Spiccia L, Stephan H, Graham B (2014) Zwitterionic-coated "stealth" nanoparticles for biomedical applications: recent advances in countering biomolecular corona formation and uptake by the mononuclear phagocyte system. Small 10(13):2516–2529
31. Nsubuga A, Zarschler K, Sgarzi M, Graham B, Stephan H, Joshi T (2018) Towards Utilising Photocrosslinking of Polydiacetylenes for the preparation of "stealth" Upconverting nanoparticles. Angew Chem Int Ed 130(49):16268–16272
32. Jin Q, Deng Y, Chen X, Ji J (2019) Rational Design of Cancer Nanomedicine for simultaneous stealth surface and enhanced cellular uptake. ACS Nano 13(2):954–977
33. Erathodiyil N, Ying JY (2011) Functionalization of inorganic nanoparticles for bioimaging applications. Acc Chem Res 44(10):925–935
34. Muhr V, Wilhelm S, Hirsch T, Wolfbeis OS (2014) Upconversion nanoparticles: from hydrophobic to hydrophilic surfaces. Acc Chem Res 47(12):3481–3493
35. Chen Z, Chen H, Hu H, Yu M, Li F, Zhang Q, Zhou Z, Yi T, Huang C (2008) Versatile synthesis strategy for carboxylic acid−functionalized upconverting nanophosphors as biological labels. J Am Chem Soc 130(10):3023–3029
36. Zhou HP, Xu CH, Sun W, Yan CH (2009) Clean and flexible modification strategy for carboxyl/aldehyde-functionalized upconversion nanoparticles and their optical applications. Adv Funct Mater 19(24):3892–3900
37. Hu H, Yu M, Li F, Chen Z, Gao X, Xiong L, Huang C (2008) Facile epoxidation strategy for producing amphiphilic up-converting rare-earth nanophosphors as biological labels. Chem Mater 20(22):7003–7009
38. Park YI, Kim JH, Lee KT, Jeon KS, Na HB, Yu JH, Kim HM, Lee N, Choi SH, Baik SI, Kim H (2009) Nonblinking and nonbleaching upconverting nanoparticles as an optical imaging nanoprobe and T1 magnetic resonance imaging contrast agent. Adv Mater 21(44):4467–4471
39. Nam SH, Bae YM, Park YI, Kim JH, Kim HM, Choi JS, Lee KT, Hyeon T, Suh YD (2011) Long-term real-time tracking of lanthanide ion doped upconverting nanoparticles in living cells. Angew Chem 123(27):6217–6221
40. Rieffel J, Chen F, Kim J, Chen G, Shao W, Shao S, Chitgupi U, Hernandez R, Graves SA, Nickles RJ, Prasad PN, Kim C, Cai W, Lovell JF (2015) Hexamodal imaging with Porphyrin-phospholipid-coated upconversion nanoparticles. Adv Mater 27(10):1785–1790
41. Liang S, Zhang X, Wu Z, Liu Y, Zhang H, Sun H, Sun H, Yang B (2012) Decoration of up-converting $NaYF_4$:Yb,Er(Tm) nanoparticles with surfactant bilayer. A versatile strategy to perform oil-to-water phase transfer and subsequently surface silication. CrystEngComm 14(10):3484–3489
42. Pellegrino T, Manna L, Kudera S, Liedl T, Koktysh D, Rogach AL, Keller S, Rädler J, Natile G, Parak WJ (2004) Hydrophobic nanocrystals coated with an amphiphilic polymer shell: a general route to water soluble nanocrystals. Nano Lett 4(4):703–707
43. Wang C, Tao H, Cheng L, Liu Z (2011) Near-infrared light induced in vivo photodynamic therapy of cancer based on upconversion nanoparticles. Biomaterials 32(26):6145–6154
44. Jiang G, Pichaandi J, Johnson NJ, Burke RD, Van Veggel FC (2012) An effective polymer cross-linking strategy to obtain stable dispersions of upconverting $NaYF_4$ nanoparticles in buffers and biological growth media for biolabeling applications. Langmuir 28(6):3239–3247

45. Brühwiler D (2010) Postsynthetic functionalization of mesoporous silica. Nanoscale 2(6):887–892
46. Sperling RA, Parak WJ (2010) Surface modification, functionalization and bioconjugation of colloidal inorganic nanoparticles. Philos Trans R Soc A Math Phys Eng Sci 368(1915):1333–1383
47. Xu Z, Quintanilla M, Vetrone F, Govorov AO, Chaker M, Ma D (2015) Harvesting lost photons: plasmon and upconversion enhanced broadband photocatalytic activity in core@shell microspheres based on lanthanide-doped $NaYF_4$, TiO_2, and Au. Adv Funct Mater 25(20):2950–2960
48. Runowski M, Goderski S, Paczesny J, Ksiezopolska-Gocalska M, Ekner-Grzyb A, Grzyb T, Rybka JD, Giersig M, Lis S (2016) Preparation of biocompatible, luminescent-plasmonic core/shell nanomaterials based on lanthanide and gold nanoparticles exhibiting SERS effects. J Phys Chem C 120(41):23788–23798
49. Liu J, Bu W, Pan L, Shi J (2013) NIR-triggered anticancer drug delivery by upconverting nanoparticles with integrated azobenzene-modified mesoporous silica. Angew Chem 125(16):4471–4475
50. Li C, Ma C, Wang F, Xi Z, Wang Z, Deng Y, He N (2012) Preparation and biomedical applications of core–shell silica/magnetic nanoparticle composites. J Nanosci Nanotechnol 12(4):2964–2972
51. Jalil RA, Zhang Y (2008) Biocompatibility of silica coated $NaYF_4$ upconversion fluorescent nanocrystals. Biomaterials 29(30):4122–4128
52. Liz-Marzán LM, Giersig M, Mulvaney P (1996) Synthesis of nanosized gold−silica core−shell particles. Langmuir 12(18):4329–4335
53. Caruso F (2001) Nanoengineering of particle surfaces. Adv Mater 13(1):11–22
54. Liu F, Zhao Q, You H, Wang Z (2013) Synthesis of stable carboxy-terminated $NaYF_4$:Yb^{3+},Er^{3+}@SiO_2 nanoparticles with ultrathin shell for biolabeling applications. Nanoscale 5(3):1047–1053
55. Wang M, Mi C, Zhang Y, Liu J, Li F, Mao C, Xu S (2009) NIR-responsive silica-coated $NaYbF_4$: Er/Tm/Ho upconversion fluorescent nanoparticles with tunable emission colors and their applications in immunolabeling and fluorescent imaging of cancer cells. J Phys Chem C 113(44):19021–19027
56. Idris NM, Gnanasammandhan MK, Zhang J, Ho PC, Mahendran R, Zhang Y (2012) In vivo photodynamic therapy using upconversion nanoparticles as remote-controlled nanotransducers. Nat Med 18(10):1580
57. Bagwe RP, Hilliard LR, Tan W (2006) Surface modification of silica nanoparticles to reduce aggregation and nonspecific binding. Langmuir 22(9):4357–4362
58. Wang M, Mi CC, Wang WX, Liu CH, Wu YF, Xu ZR, Mao CB, Xu SK (2009) Immunolabeling and NIR-excited fluorescent imaging of HeLa cells by using $NaYF_4$:Yb,Er upconversion nanoparticles. ACS Nano 3(6):1580–1586
59. Hu H, Xiong L, Zhou J, Li F, Cao T, Huang C (2009) Multimodal-luminescence Core–Shell Nanocomposites for targeted imaging of tumor cells. Chem Eur J 15(14):3577–3584
60. Vuojola J, Riuttamäki T, Kulta E, Arppe R, Soukka T (2012) Fluorescence-quenching-based homogeneous caspase-3 activity assay using photon upconversion. Anal Chim Acta 725:67–73
61. Shan G, Weissleder R, Hilderbrand SA (2013) Upconverting organic dye doped core-shell nano-composites for dual-modality NIR imaging and photo-thermal therapy. Theranostics 3(4):267
62. Schäfer H, Ptacek P, Kömpe K, Haase M (2007) Lanthanide-doped $NaYF_4$ nanocrystals in aqueous solution displaying strong up-conversion emission. Chem Mater 19(6):1396–1400
63. Voliani V, González-Béjar M, Herranz-Pérez V, Duran-Moreno M, Signore G, Garcia-Verdugo JM, Pérez-Prieto J (2013) Orthogonal functionalisation of upconverting $NaYF_4$ nanocrystals. Chem Eur J 19(40):13538–13546
64. Zhang W, Peng B, Tian F, Qin W, Qian X (2013) Facile preparation of well-defined hydrophilic core–shell upconversion nanoparticles for selective cell membrane glycan labeling and cancer cell imaging. Anal Chem 86(1):482–489

65. Liu Q, Sun Y, Li C, Zhou J, Li C, Yang T, Zhang X, Yi T, Wu D, Li F (2011) ^{18}F-labeled magnetic-upconversion nanophosphors via rare-earth cation-assisted ligand assembly. ACS Nano 5(4):3146–3157
66. Dong A, Ye X, Chen J, Kang Y, Gordon T, Kikkawa JM, Murray CB (2010) A generalized ligand-exchange strategy enabling sequential surface functionalization of colloidal nanocrystals. J Am Chem Soc 133(4):998–1006
67. Nsubuga A, Sgarzi M, Zarschler K, Kubeil M, Hübner R, Steudtner R, Graham B, Joshi T, Stephan H (2018) Facile preparation of multifunctionalisable "stealth" upconverting nanoparticles for biomedical applications. Dalton Trans 104:139
68. Bogdan N, Vetrone F, Ozin GA, Capobianco JA (2011) Synthesis of ligand-free colloidally stable water dispersible brightly luminescent lanthanide-doped upconverting nanoparticles. Nano Lett 11(2):835–840
69. Bogdan N, Rodríguez EM, Sanz-Rodríguez F, de la Cruz MC, Juarranz Á, Jaque D, Solé JG, Capobianco JA (2012) Bio-functionalization of ligand-free upconverting lanthanide doped nanoparticles for bio-imaging and cell targeting. Nanoscale 4(12):3647–3650
70. Rampazzo E, Genovese D, Palomba F, Prodi L, Zaccheroni N (2018) NIR-fluorescent dye doped silica nanoparticles for in vivo imaging, sensing and theranostic. Methods Appl Fluoresc 6(2):022002
71. Wilhelm S, Tavares AJ, Dai Q, Ohta S, Audet J, Dvorak HF, Chan WC (2016) Analysis of nanoparticle delivery to tumours. Nat Rev Mater 1(5):16014
72. Mandl G, Cooper D, Hirsch T, Seuntjens J, Capobianco JA (2019) Perspective: lanthanide-doped upconverting nanoparticles. Methods Appl Fluoresc 7(1):012004

Chapter 4
Rare Earth-Doped Nanoparticles for Advanced In Vivo Near Infrared Imaging

Meiling Tan and Guanying Chen

4.1 Introduction

Fluorescence-based optical imaging has drawn increasing attention, as it enables high-contrast in vitro imaging at microscopic resolution and in vivo imaging at micrometer-scale resolution [1, 2]. For small animal imaging, light penetration depth and signal-to-noise ratio are two critical aspects that significantly affect imaging results. Light penetration depth is determined by the scattering and absorption of biological tissues at the wavelength of light, while signal-to-noise ratio is often dictated by background fluorescence (i.e., tissue autofluorescence) from endogenous fluorophores (hemoglobin, melanin, lipids, etc.) [3–6]. For probes with emission in the visible range (400–700 nm), light penetration depth is typically limited to be $\sim$ 1 mm due to the relatively strong absorption and scattering of visible photons [7, 8]. This reason also impairs the quality of acquired photographic images, resulting in low resolution and a decrease of signal-to-noise ratio. When shifting both the excitation and emission wavelengths to the first near infrared biological window (700–950 nm, NIR-I) [9–11], light penetration depth (also, imaging depth) can be increased to several millimeters, along with an improved imaging quality. Importantly, many works demonstrated that imaging quality could be largely further increased when using probes with emission band in the second near infrared window (1000–1700 nm, NIR-II). This is because light absorption and, in particular, light scattering from biological tissues are substantially reduced in NIR-II region compared to that in NIR-I window [7, 12, 13] (Fig. 4.1). Light

M. Tan · G. Chen (✉)
MIIT Key Laboratory of Critical Materials Technology for New Energy Conversion and Storage, School of Chemistry and Chemical Engineering and Key Laboratory of Micro-systems and Micro-structures, Ministry of Education, Harbin Institute of Technology, Harbin, People's Republic of China
e-mail: chenguanying@hit.edu.cn

A. Benayas et al. (eds.), *Near Infrared-Emitting Nanoparticles for Biomedical Applications*, https://doi.org/10.1007/978-3-030-32036-2_4

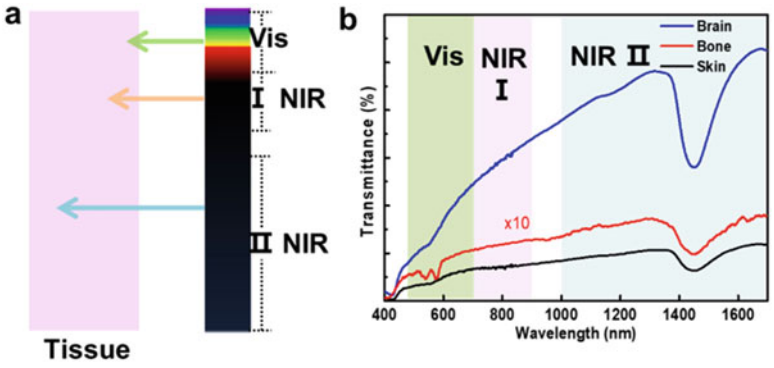

Fig. 4.1 (**a**) Schematic illustration of light penetration depth in tissue in the visible, NIR-I, and NIR-II windows. (**b**) The transmission of light at different wavelengths through a nude mouse skin, bone, and brain. Courtesy by Tymish Y. Ohulchanskyy at Shenzhen University

scattering in tissue can be scaled as $\sim \lambda^{-\alpha}$, where $\alpha = 0.22$–1.68 depends on biological tissues [14]. As a result, light with longer wavelengths is less scattered, thus resulting in better imaging depth and quality. Recently, a series of organic and inorganic materials have been proposed and applied for NIR-II in vivo imaging, such as single-walled carbon nanotubes (CNs), small molecules, quantum dots (QDs), and rare earth-doped nanoparticles (RENPs) [3, 15–18].

RENPs are an inorganic guest–host system with at least one dimension of less than 100 nm, where rare-earth ions are diluted as a guest in the host lattice of a dielectric material with appropriate phonon spectrum. Typically, chemically stable host material with low phonon cut-off energy, e.g., sodium yttrium fluoride ($NaYF_4$, 350 cm^{-1}) is a favorable rare-earth luminescence, because it minimizes non-radiative multiphonon-assisted deactivations at intermediate and emitting states [19]. Indeed, RENPs, among reported optical nanoprobes, hold promise for NIR bioimaging, because they can pliably convert NIR excitation light to emissions with either shorter wavelength (upconversion luminescence, UCL) or longer wavelength (downshifting luminescence, DCL). Compared with reported probes (QDs, organic dyes, and carbon nanotubes), RENPs have superior optical performance, such as sharp emission band, large anti-Stokes or Stokes shift, long lifetime, low biological toxicity, and low background autofluorescence [19, 20]. These merits make them attractive to be used as contrast agents to discern between delicate biological structures for disease diagnosis and intraoperative imaging-guided surgery. Typically, ytterbium (Yb^{3+}) or neodymium (Nd^{3+}) ions are doped in RENPs and used as sensitizers to absorb excitation light photons, thus allowing the excitation to be performed at either 980 nm (corresponding to the $^2F_{7/2} \rightarrow {}^2F_{5/2}$ transition of Yb^{3+} ions) or 800 nm (corresponding to the $^4I_{9/2} \rightarrow {}^4F_{5/2}$ transition of Nd^{3+} ions), where low-cost, high-power diode lasers are commercially available. Importantly, both wavelengths are located in NIR-I window, rendering optical imaging in deep tissues and at high resolution [8, 21–25].

Tissue autofluorescence remains substantial in the NIR range (in particular, 700–1000 nm, but decreased at longer wavelengths) even with NIR light excitation, blurring the obtained bioimaging images [26]. Luckily, RENPs often have long luminescence lifetime, making themselves attractive for the removal of autofluorescence background through time-gated imaging (TGI) technique. TGI is an established stroboscopic technique, which eliminates the autofluorescence by exploiting the long lifetime of emissions from optical probes ($\sim$ µs to ms) against the short lifetime ($\sim$ ns) of tissue autofluorescence. An appropriate time delay (longer than the lifetime of autofluorescence) between the excitation and detection allows a straightforward exclusion of the autofluorescence background, rendering high-contrast NIR in vivo imaging. Furthermore, the lifetime of RENPs with a given luminescence wavelength can be precisely engineered to produce a set of lifetime-encoded luminescent NPs. This provides new numerous possibilities for multiplexed lifetime imaging in the NIR range.

In this chapter, we present the use of two types of NIR-emitting RENPs for steady-state in vivo imaging: (1) upconversion nanoparticles (UCNPs) and (2) downshifting nanoparticles (DCNPs). We also describe the principle of TGI and the use of RENPs for high-contrast TGI optical imaging in NIR-II window. Moreover, multiplexed optical imaging using NIR-emitting RENPs with tunable lifetimes is further discussed.

4.2 NIR Emissions from RENPs

4.2.1 NIR Upconversion Luminescence

Upconversion refers to an anti-Stokes process in which two or more low energy photons are absorbed, and then combined to produce a higher energy photon. The typical upconversion process with NIR emission is from the Yb^{3+}-Tm^{3+} pair, which is excited at 980 nm and emits at 800 nm in NIR-I window. Yb^{3+} ion absorbs the 980 nm excitation, and then transfers its energy to a neighboring Tm^{3+} ion, promoting it to the $^3H_5$ state. After a non-radiative relaxation to the $^3F_4$ state, the Tm^{3+} ion at this state is further excited to the $^3F_{2,3}$ state, followed by phonon-assisted relaxations to the $^3H_4$ state, where the emission of 800 nm is produced by a radiative decay to the ground state (Fig. 4.2a). Despite the existence of other emission bands in the visible and ultraviolet range, in most cases, the emission of 800 nm dominates the whole UCL spectrum, especially in Yb^{3+}-enriched UCNPs. Indeed, it has been revealed that an elevation of Yb^{3+} ions doping concentration in fluoride nanocrystals usually results in higher UCL intensity at 800 nm [27, 28].

Beyond that, Er^{3+} ions can be used as sensitizers to absorb excitation energy at 1532 nm and then transfer their energy to activators, such as Yb^{3+}, Ho^{3+}, Tm^{3+}, Nd^{3+} ions, to produce UCL in NIR-II window (Fig. 4.2b). The absorption of excitation photons promotes Er^{3+} ions from the ground state to the $^3I_{13/2}$ state,

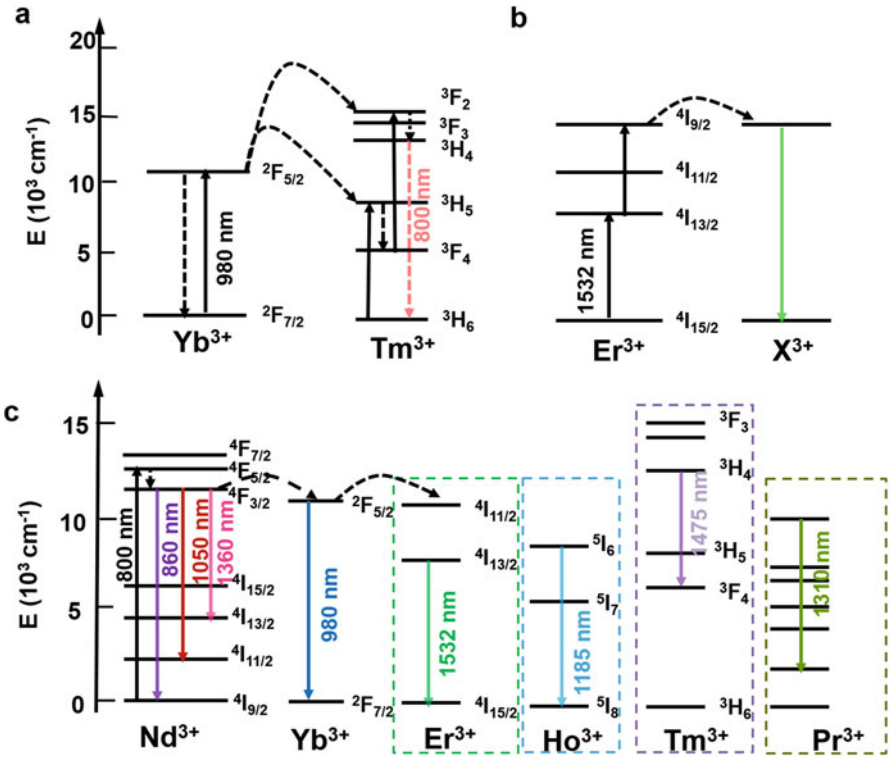

Fig. 4.2 Schematic illustration of simplified energy levels and energy transfer routes for NIR upconversion from (**a**) Yb^{3+}/Tm^{3+} ion pair under 980 nm excitation, and (**b**) Er^{3+}/X^{3+}(X = Yb, Ho, Tm) ion pair under 1532 nm excitation, and for (**c**) NIR downshifting luminescence from Nd^{3+}, Yb^{3+}, and other activators (Er^{3+}, Ho^{3+}, Tm^{3+}, Pr^{3+}) under 800 nm excitation

which can be further excited to the $^4I_{9/2}$ state via either absorption of another excitation photon or energy transfer from another Er^{3+} ion at the $^3I_{13/2}$ state. At the $^4I_{9/2}$ state, Er^{3+} ion can transfer its energy to surrounding activators to produce activator-defined NIR-II UCL. For example, an efficient NIR emission at 1180 nm from Ho^{3+} was observed from $NaErF_4$:Ho@$NaYF_4$ core/shell NPs under the excitation of 1532 nm [29]. This Er^{3+}-sensitized Ho^{3+} UCL emissions are suitable for NIR-II UCL imaging, as both excitation and emission wavelengths are located in the NIR-II windows. Note that this Er^{3+}-based sensitizing process can be modulated to enhance UCL through codoping with different types of rare-earth ions or modification of nanostructure [30].

4.2.2 NIR Downshifting Luminescence

In most circumstances, RENPs emit downshifting luminescence (DCL) at longer wavelengths, whereby the emission intensity depends linearly on the excitation power density. The existence of abundant energy levels of rare-earth ions in the NIR range provides many ways to realize both excitation and emission wavelengths in the NIR biological windows (Fig. 4.2b). Nd^{3+}-based RENPs are promising towards this regard, as Nd^{3+} ions have large absorption cross section at around 800 nm and can act as sensitizers to sensitize activators to produce tunable DCL. Generally, Nd^{3+}-sensitized RENPs can be divided into three types: (1) single Nd^{3+}-doped NPs. After promoting Nd^{3+} from the ground state to the $^4F_{5/2}$ state by 800 nm excitation, the Nd^{3+} ion can relax to the $^4F_{3/2}$ state, whereby the emissions of 860 nm, 1050 nm, and 1360 nm are generated, being assigned to the $^4F_{3/2} \rightarrow {}^4I_{9/2}$, $^4F_{3/2} \rightarrow {}^4I_{11/2}$, and $^4F_{3/2} \rightarrow {}^4I_{13/2}$ transitions, respectively. (2) Nd^{3+}/Yb^{3+}-codoped RENPs. The harvested energy by the $^4F_{5/2}$ state of Nd^{3+} ions under 800 nm excitation can be transferred to Yb^{3+} ions at an efficiency over 70%, thus generating the 1000 nm DCL from Yb^{3+} ions (the $^2F_{7/2} \rightarrow {}^2F_{5/2}$ transition). For Nd^{3+} /Yb^{3+} codoped system, the excitation wavelength is in NIR-I window, while the emission wavelength is in NIR-II window. (3) Nd^{3+}/Yb^{3+} and X^{3+} (X = Er, Ho, Tm, or Pr) doped RENPs. This type of NIR DCL can be achieved following the energy transfer route of $Nd^{3+} \rightarrow Yb^{3+} \rightarrow X^{3+}$. Nd^{3+} ions act as energy donor, while Yb^{3+} ions are used as energy bridge, exacting the energy from Nd^{3+} ions, and then transferring to the activator ion (Er^{3+}, Ho^{3+}, Tm^{3+}, or Pr^{3+}) to produce activator-defined DCL.

For the $Nd^{3+} \rightarrow Yb^{3+} \rightarrow X^{3+}$ system, the efficiency of DCL mainly depends on three parts: (1) the energy transfer efficiency between Nd^{3+} and Yb^{3+}, (2) the energy transfer efficiency from Yb^{3+} ions to the X^{3+} activator; (3) the non-radiative and upconverting losses at the emitting states of the X^{3+} activator. The reported DCL efficiency for different activators is ranked as $Er^{3+} > Ho^{3+} > Tm^{3+} > Pr^{3+}$. The system with Tm^{3+} or Pr^{3+} activators is less efficient, owing to the involvement of upconversion process for Tm^{3+} emitting state, and the existence of dense energy levels for Pr^{3+} that promotes non-radiative relaxations from the emitting state [3, 31, 32]. For the third type of RENPs, it should be noted that there exist efficient energy back-transfer processes from the X^{3+} activators to the ^4I_J manifolds of Nd^{3+}, thus resulting in luminescence quenching. To minimize this back energy transfer, the doping concentration of Nd^{3+} ions should be as less as 1%. However, the low concentration strongly limits the absorption at 800 nm, and thus the brightness of RENPs. To solve this problem, a spatial isolation of Nd^{3+} and X^{3+} activator using a core/shell or core/shell/shell structure is usually needed, which entails high Nd^{3+}doping content to 20 or 100%, thus increasing DCL intensity by orders of magnitude [29–31].

4.3 In Vivo NIR Imaging Using RENPs

4.3.1 Bioimaging Using NIR UCL

As mentioned before, Yb^{3+}/Tm^{3+}-coped UCNPs with emission at 800 nm and excitation at 980 nm are promising for high-contrast small animal imaging, as both excitation and emission wavelengths are located in the NIR biological windows in which light attenuation and scattering are significantly reduced. Moreover, tissue autofluorescence is absent in the emission detection range, as autofluorescence is supposed to have a longer wavelength than the excitation at 980 nm, if any. Towards this regard, high-contrast in vivo bioimaging was firstly reported in 2008 using NIR_{in}-NIR_{out} $NaYF_4$:20%Yb^{3+}/1%Tm^{3+} UCNPs [33]. This NIR_{in}-to-NIR_{out} upconversion process entails an observation of UCL in the liver of Balb-c mice after 2 hours intravenous injection with upconverting RENPs. The signal-to-background (SBR) ratio was determined to be about 10. This parameter, however, strongly depends on the efficiency of imaging contrast agents. A later report demonstrates an exceptionally high SBR ratio using core/shell (α-$NaYbF_4$:Tm^{3+})/CaF_2 UCNPs with a quantum yield as high as 0.6 ± 0.1% under imaging condition laser irradiation (0.3 W/cm^2) (Fig. 4.3a) [27]. The high Yb^{3+} ion content in this particle also increases the absorption at excitation of 980 nm and shortens the distance between Yb^{3+} and Tm^{3+} ions, thus favoring the emission brightness of Tm^{3+} ions at 800 nm. After intravenous injection of these water-soluble core/shell NPs for 2 hours, the whole-body imaging of a mouse can clearly show the shape of liver without excision, presenting a SBR ratio as high as 310. Interesting, the UCL from the Yb^{3+}-enriched core/shell NPs is able to be detected through a 3.2 cm biological tissue (pork tissue), with high contrast against the background (Fig. 4.3b, c).

Another example for UCL imaging in NIR-II window is to use Er^{3+}-sensitized UCNPs (i.e., $NaErF_4$:Ho^{3+}@ $NaYF_4$ core/shell nanocrystals) with both excitation and emission wavelengths located in NIR-II region [29]. In the described core/shell NPs, Er^{3+} ions perform as both sensitizer and activator ions, which absorb the 1530 nm excitation photon and then sensitize the neighboring Er^{3+} ions to produce the 980 nm emission, while the Ho^{3+} ions function as another type of emitters to generate UCL at 1180 nm, after accepting the energy transferred from adjacent Er^{3+} ions (Fig. 4.3d). Based on the ratio metric UCL (I_{980}/I_{1180}) of the Er^{3+}-sensitized UCNPs, H_2O_2 sensitive microneedle patch was prepared to allow dynamic inflammation sensing in vivo. As can be seen in Figs. 4.3e–h, the luminescence images of microneedle array were clear under the skin tissue, and the signal from single needle (200 × 200 μm) could be distinguished (Fig. 4.3e–h).

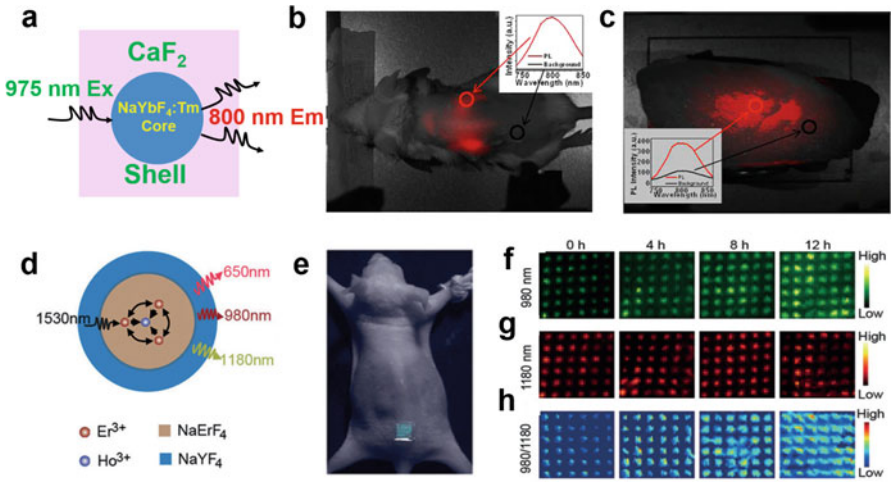

Fig. 4.3 (**a**) A schematic illustration of UCL from core/shell (α-$NaYbF_4$:Tm^{3+})/CaF_2 NPs under 980 nm excitation; (**b**) Whole-animal imaging of a BALB/c mouse injected with hyaluronic acid (HA)-coated (α-$NaYbF_4$:Tm^{3+})/CaF_2 core/shell nanoparticles; (**c**) Merged UCL/bright-field image of a cuvette containing the HA-coated core/shell UCNPs covered with a 3.25 cm thick pork tissue (Reproduced from Chen et al. 2012) [27]; (**d**) A schematic illustration of UCL from $NaErF_4$:Ho^{3+}@$NaYF_4$ core/shell NPs structure under 1532 nm excitation; (**e**) Photographic image of a mouse with microneedle-patch-injected UCNPs; UCL images of the microneedle-patch-treated mouse at (**f**) 980 nm, (**g**) 1180 nm, and (**h**) ratio metric (I_{980}/I_{1180}) channels taken at different time points after lipopolysaccharide-induced inflammation. Reproduced from Zhang et al. 2018 [29]

4.3.2 Bioimaging Using NIR-II Downshifting Luminescence

Recent results have shown that in vivo imaging with fluorophores emitting in the NIR-II window has significantly improved the signal-to-noise ratio, probes tissue at centimeter range of depth, and achieves micrometer-scale resolution at depths of millimeters. This associates with the low tissue autofluorescence, reduced photon scattering, and high penetration depth [14, 17]. Naczynski et al. synthesized a set of $NaYF_4$:Yb^{3+}/Ln^{3+}(Ln = Er, Ho, Tm, Pr) @$NaYF_4$ core/shell NPs with tunable emissions in NIR-II region under 980 nm excitation [3]. They demonstrated that these NPs were capable of resolving anatomical structures including organs, and blood vessels using video-rate imaging at micrometer resolution and millimeter depths (Fig. 4.4a, b). They also evaluated the disease tracking potential of NIR-II imaging by injecting RENPs into the nude mice model with developed melanoma xenografts (Fig. 4.4c). NPs emitting at two different NIR-II wavelengths (1532 nm from Er^{3+}-doped NPs and 1150 nm from Ho^{3+}-doped NPs) were separately injected into the same mouse with xenografted melanomas. Attaching corresponding separated optical filters to the camera, different wavelengths images were clearly observed with no crosstalk between these NPs (Fig. 4.4d). Importantly,

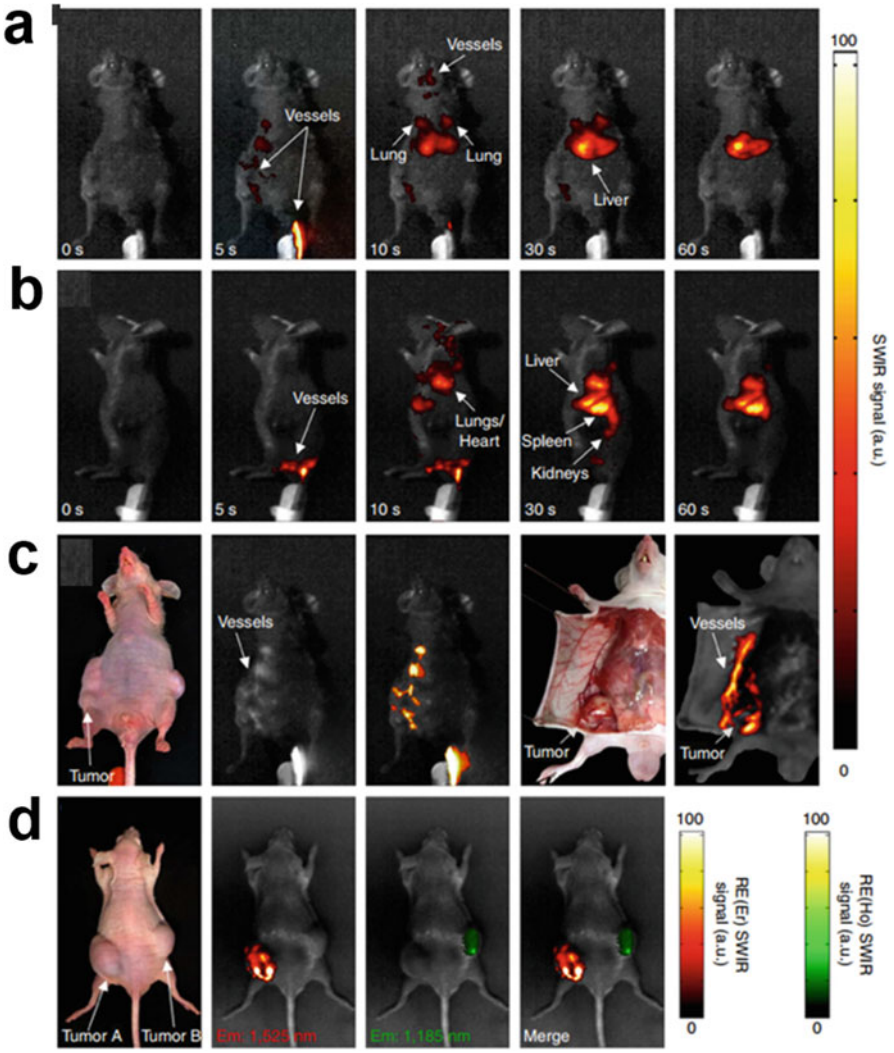

Fig. 4.4 Real-time, video-rate biodistribution imaging of intravenously injected REs captured in hairless mice using the imaging system prototype from both ventral (**a**) and left lateral (**b**) aspects. Nude mice bearing melanoma xenografts were intravenously injected with REs and imaged near surrounding tumor regions before dissection (**c**) from the ventral aspect. Proof-of-concept multiplexed SWIR imaging performed from the dorsal aspect in mouse xenografts (**d**) after Er- and Ho-doped rare-earth probes were separately injected into tumor sites on either flank of the animal. Representative images (n ¼ 3) are shown in all instances [3]. All imaging results were acquired using a prototype imaging systems consisting of a room temperature-cooled InGaAs camera operating at a typical exposure time of 50 ms, adjustable filter mounts, a collimated laser at 980 nm with an output power density of 0.14 Wcm^2, and a neoprene rubber imaging surface. Reproduced from Naczynski et al. 2013

these NIR-II-emitting NPs were able to be used for small cancer lesion detection and monitoring, showing superior unprecedented results.

However, there exists a potential harmful problem associated with the excitation wavelength (980 nm) of this work. It is known that, water molecules, which are abundant in the body, have large absorption efficient at 980 nm. As a result, overexposure of biological species to this excitation light could cause overheating of tissues, resulting in significant cell death and tissue damage. So it is of necessity to shift the excitation wavelength to more biocompatible excitation wavelengths without producing local heating effect. The overheating effect induced by 980 nm excitation could be largely mitigated using 808 nm laser excitation because the absorption coefficient of water at ~808 nm is small around 0.02 cm^{-1}, about 24 times lower than the value of 0.482 cm^{-1} at ~980 nm. The Nd^{3+} ions possess a high absorption cross section (~1.2×10^{-19} cm^2) at 808 nm which is one order of magnitude higher than that of Yb^{3+} ions (~ 1.8×10^{-20} cm^2). Moreover, it was shown that Nd^{3+} ions can transfer the absorbed energy to ytterbium (Yb^{3+}) at high efficiencies (more than 70%), providing possibilities to produce Nd^{3+}-based NIR-II-emitting NPs with 808 nm excitation.

Indeed, Nd^{3+}-based downshifting NPs have been proposed in vivo imaging in the NIR-II region. The early Nd^{3+}-based NPs for bioimaging are purely Nd^{3+}-doped NPs with excitation band centered at 800 nm and emission band centered at 860 nm, 1060 nm, 1340 nm, originating from different transitions from the excited level $^4F_{3/2}$ to different ^4I_J levels (consult Fig. 4.2). Core/shell $NaGdF_4$:3%Nd@$NaGdF_4$ NPs were reported to exhibit efficient NIR-to-NIR downshifting luminescence for bioimaging [34]. The thick $NaGdF_4$ shell (~ 2.5 nm) isolates the core nanoparticle from the surrounding quenchers, thus endowing NPs with absolute quantum yield as high as 40% in hexane and 20% for ligand-stripped ones in aqueous form. A high-contrast NIR luminescent image at 860 nm was obtained in a nude mouse with subcutaneous injection under regular lamp light excitation at 740 nm (Fig. 4.5 a, b, c). Note that the 740 nm light corresponds to the transition from the ground $^4I_{13/2}$ state to the $^4F_{7/2}$ state, instead of to the $^4F_{5/2}$ state for 800 nm excitation. Later, LaF_3:Nd^{3+} NIR-emitting NPs with excitation at 800 nm for bioimaging were reported by Jaque's group [35]. The emission band at 1050 nm from LaF_3:Nd^{3+} is the most intense peak, which lies in the NIR-II window. Therefore, the use of 1050 nm emission allows a high-contrast in vivo imaging with imaging depth as large as 1 cm. Recently, Nd^{3+}-enriched $LiLuF_4$:10%Nd@$LiLuF_4$ NPs were reported for bioimaging [36]. In addition to the high Nd^{3+} doping concentration that allows for efficient excitation light harvesting, the absolute quantum yield of these NPs was quantified to be as high as 32% without obvious luminescence concentration quenching. Because of efficient NIR-II emission at 1050 nm, the signal-to-noise ratio of the resulted image was quantified to be about 25.1, and the long-time biodistribution of these NPs could be allowed under ultralow power-density excitation (10 mW cm^{-2}) at 732 nm. In fact, various kinds of Nd^{3+}-doped NPs such as GdF_3:Nd^{3+}, KY_3F_{10}:Nd^{3+}, and SrF_2:Nd^{3+} NPs have been synthesized and applied for NIR bioimaging [37, 38], but most commonly under excitation at 808 nm.

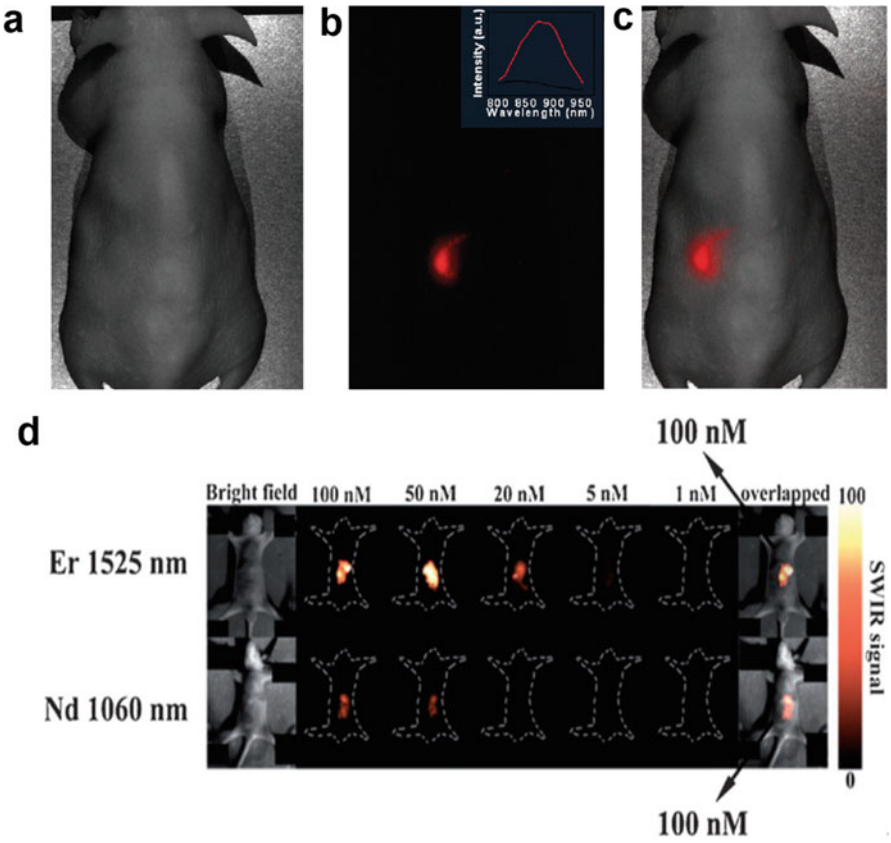

Fig. 4.5 In vivo whole-body image of a nude mouse subcutaneously injected with ligand-stripped ($NaGdF_4$:3% Nd^{3+})/$NaGdF_4$ nanocrystals: (**a**) bright-field image, (**b**) DCL image, and (**c**) superimposed image of a and b. The inset in Fig. 4.4b is the spectra of NIR DCL signal taken from the injection site, contrasted with a background signal taken from non-injected area (Reproduced from Chen et al. 2012) [34]. (**d**) Comparison of the NIR-II signals from $NaGdF_4$@Na(Gd,Yb)F_4:Er@$NaYF_4$:Yb @ $NaNdF_4$:Yb NPs (Er 1525 nm) and $NaGdF_4$:Nd/$NaGdF_4$(Nd 1060 nm) in the stomach of a nude mice with different NC concentrations. Reproduced from Wang et al. 2015 [11]

Besides the direct use of NIR-II emission from single Nd^{3+}-doped NPs for in vivo imaging, Nd^{3+}-sensitized NPs with emissions in NIR-II region have also been proposed. For example, $NaYF_4$:Nd^{3+}/Yb^{3+}@CaF_2 core/shell NPs were applied for steady-state bioimaging of mouse, which showed superior NIR emission at 1000 nm from Yb^{3+} ions sensitized by Nd^{3+} ions [39]. It is well known that in traditional Nd^{3+}-doped NPs, the concentration of Nd^{3+} ions is limited to less than 5% to avoid the luminescence concentration quenching effect [37, 40]. This prevents efficient harvesting of excitation light, and thus the NPs' brightness. In this system, an introduction of Yb^{3+} ions enables efficient transfer of harvested

photonic energy from Nd^{3+} to Yb^{3+} activators, before deactivation of Nd^{3+} ions at excited states via luminescence concentration quenching. As a result, the optimal Nd^{3+} ion concentration can reach as high as 60%, presenting an optimized formula of $NaYF_4$:7%Yb^{3+},60%Nd^{3+}@CaF_2 that produces intense Yb^{3+} NIR luminesce. These NPs were converted into aqueous form after stripping off the oleic acid ligand, which was coordinated to the surface during the synthesis period. After intravenously injecting ligand-stripped NPs into a mouse, the high spatial resolution imaging of blood vessel (~0.19 mm) was achieved with weak autofluorescence, clearly demonstrating that these NPs can be used as NIR optical contrast agents.

Nd^{3+}, Yb^{3+} and activators (Er^{3+}, Ho^{3+}, Tm^{3+}, Pr^{3+}) tri-doped NPs are also emerging for in vivo imaging in NIR-II window. In these RENPs, typically, a core/shell or core/shell/shell structure is vital to be used to entail an efficient emission of activators, because the structure not only can prevent unwanted energy transfer processes or interactions, but also can suppress surface quenching effect. Zhang's group reported the use of $NaGdF_4$@Na(Gd,Yb)F_4:Er^{3+} @$NaYF_4$:Yb^{3+} @$NaNdF_4$:Yb^{3+} core/multishell NPs for bioimaging with emission at 1532 nm and excitation at 800 nm [11]. In this system, Nd^{3+} ions doped in the third shell absorbs 800 nm excitation light, and then transfers to Yb^{3+} ions in the second shell, which act as energy bridge to migrate the energy further to the Yb^{3+} ions in the first shell, and finally to the Er^{3+} ions in the same first shell to produce the 1532 nm emission. Note that an inert $NaGdF_4$ NPs were employed as the starting core, instead of the direct use of Na(Gd,Yb)F_4:Er^{3+} NPs, for seed-mediated epitaxial growth, because variation of Yb^{3+}/Er^{3+} dopant ratio can change the final size of the core/multishell NPs. After coating with phospholipids, these water-soluble core multishells showed good biocompatibility and low toxicity. Moreover, these NPs are able to be detected in tissues at depth of up to 18 mm with a low detection threshold concentration (5 nM for the stomach of nude mice and 100 nM for the stomach of SD rats). Moreover, NIR-II DCL from $NaGdF_4$@Na(Gd,Yb)F_4:Er@$NaYF_4$:Yb @$NaNdF_4$:Yb NPs (Er 1525 nm) showed higher intensity than that from reported $NaGdF_4$:Nd/$NaGdF_4$(Nd 1060 nm) NPs in the stomach of a nude mice under 800 nm excitation (Fig. 4.5d). However, one has to bear in mind that the brightness of both types of NPs is different; as a result, such comparison cannot draw a conclusion that imaging at 1532 nm is better than at 1064 nm. More careful comparisons are needed to be further investigated. In addition, recently, ICG-sensitized $NaYF_4$:Yb^{3+}/X^{3+}@$NaYbF_4$@$NaYF_4$:Nd^{3+} (X = null, Er, Ho, Tm, or Pr) core/shell/shell NPs with a set of narrow-band emissions in NIR-II window were synthesized [41]. The ICG dye on the surface of NPs allows to strongly absorb 800 nm excitation, as it has absorption cross section about 1000–10,000 times higher than that of rare-earth ions. Subsequently, the ICG dyes can transfer the harvested photon energy to Nd^{3+} ions in the second shell, then to Yb^{3+} ions in the first shell, and then to Yb^{3+} ions in the core, and finally to the activators X^{3+} (X = null, Er, Ho, Tm) also in the core. The ICG sensitization not only improves the NIR-II emission intensity by fourfold, but also expands the excitation to a broad spectral range (700–860 nm), which facilitates their use in bioapplications. The NIR-II emission from

ICG-sensitized Er^{3+}-doped core/shell/shell nanocrystals allows clear observation of a sharp image through 9 mm thick chicken breast tissue, and emission signal detection through 22 mm thick tissue, yielding a better imaging profile than from typically used Yb^{3+}/Tm^{3+} codoped upconverting nanocrystals imaged in the NIR I region (700–950 nm). All in all, recent results indicate that Nd^{3+}-based NIR-II-emitting nanocrystals are suitable for high-contrast optical imaging in deep tissues.

4.4 Time-Gated Luminescence Imaging

The properties of a light wave can be assessed in various aspects, such as wavelength, polarization, intensity, and lifetime [42]. Each parameter could be used as a dimension to interrogate the properties of a given material. Luminescence lifetime is an average time that an excited luminescence material stays in its excited state, which usually is independent of the concentration of the probe and the excitation power density. Additionally, the lifetime of luminescence probes can be altered and distinguished by their different energy transfer rates to surrounding environment. Hence, optical probes with different lifetimes can be applied for time-resolved luminescence imaging to eliminate the nuisance of autofluorescence and to probe local environment change. Rare earth-doped NPs typically have long fluorescence lifetimes (in the order of 10^{-4} to 10^{-3} s), which lend themselves for time-gated optical imaging [43].

4.4.1 Principle of Time-Gated Imaging

Common luminescence imaging uses steady-state emission at a certain wavelength from imaging contrast agents. However, steady-state imaging is often accompanied by substantial tissue autofluorescence, thus significantly decreasing the signal to noise of acquired images. Time-gated luminescence technique is an effective approach to solve this problem, which exploits the long lifetime of emissions from optical probes ($\sim$ μs to ms) against the short lifetime ($\sim$ ns) of tissue autofluorescence. In a typical time-gated imaging experiment, a pulsed laser is usually used to excite the long lifetime probes. After the stoppage of pulse laser, a delay time (1–200 μs) is introduced to a camera before taking fluorescence images. This time delay is tailored to ensure complete removal of autofluorescence by postponing camera acquisition with a time longer than the lifetime of autofluorescence (several nanoseconds) (Fig. 4.6). Thus, only the long lifetime signal is able to fall into collection window, while the unwanted autofluorescence is ruled out completely. Therefore, the imaging contrast (or the signal-to-noise ratio) can be largely increased, especially for luminescence probes with inefficient emissions. Note that the signal-to-noise ratio depends on the delay time for camera

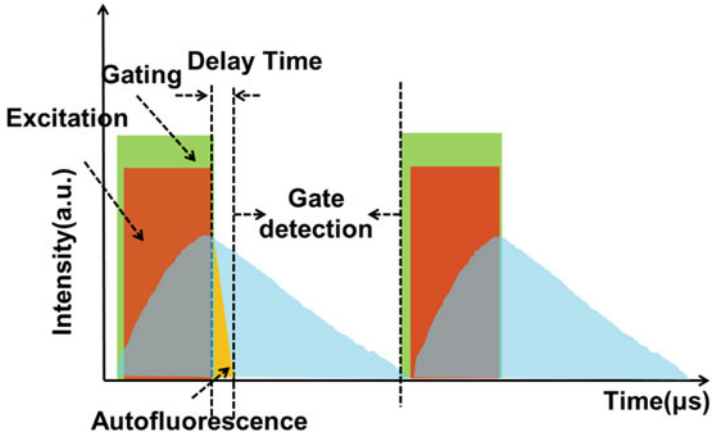

Fig. 4.6 A schematic depiction of the general principle of time-gated imaging technique. Periodic excitation is often provided from high repetition pulsed lasers or chopper-regulated light. Image acquisition is synchronized with the excitation but triggered at a certain delay time after the end of each laser pulse. The delay is usually long enough to allow a complete decay of autofluorescence

acquisition; if the delay time is too short, the autofluorescence cannot be removed completely; on the opposite, if the delay time is too long, it will lead to a collection of fewer luminescence photons. An appropriate time delay should be adopted to maximize the collected luminescence photons from probes, but minimize the ones from tissue autofluorescence. Reported pulse excitation sources include chopped continuous-wave (cw) Hg lamp light or laser light (He-Cd laser, argon-ion laser), or pulsed xenon flash lamp, switched ultraviolet (UV) light-emitting diode (LED), and NIR diode lasers [44]. The selection of pulse laser depends on the absorption of fluorescence probe. For example, to excite Tb^{3+}-doped complex with emissions at 540 nm, an ultraviolet light-emitting diode (UV LED) emitting at 300–340 nm is often employed, overlapping with the absorption of the complex [45]. To enable high efficiency detection, the laser pulse length should be as short as possible, while the period be long enough to allow the probe luminescence to decay completely. Alongside pulsed lasers, a rotating mechanical optical chopper can also be used with continuous-wave light to discriminate long-lived luminescence against rapidly decaying autofluorescence (time resolution typically on microseconds). The time resolution can be modified by changing the number of blades that impact the rotating speed. Charge-couple device (CCD) is the mostly widely device to convert the photon signals into digital images, which has a time response on nanoseconds. Therefore, the minimal time resolution for a time-gated system is usually determined by the decay edge of optically chopped light or pulsed laser sources.

4.4.2 *Time-Gated Imaging in NIR-II Window*

Time-gated imaging has long been investigated in the visible range, while its extension to NIR-II window was recently reported by Jaque's group in 2016, who demonstrated that micro-sized $NaGdF_4:Nd^{3+}$ particles can be successful for time-gated imaging under pulsed diode laser excitation at 808 nm [46]. Despite NIR excitation, tissue autofluorescence remains substantial, overlapping with 1060 nm emission band in NIR-II window. The lifetime of 1060 nm luminescence was determined to be about 90 ± 7 μs, much longer than that of autofluorescence (several nanoseconds). Indeed, it was found that an introduction of 1 μs delay time between the excitation and camera can completely remove autofluorescence from both mice diet and skin pigmentation (Fig. 4.7). Moreover, using this time-gated technique, a clear tracing of the biodistribution of subcutaneously injected or orally administered NPs was made possible; no interference from autofluorescence exists. This work opens up a new avenue for high-contrast, deep-penetrating, and high-resolution in vivo imaging in NIR-II window.

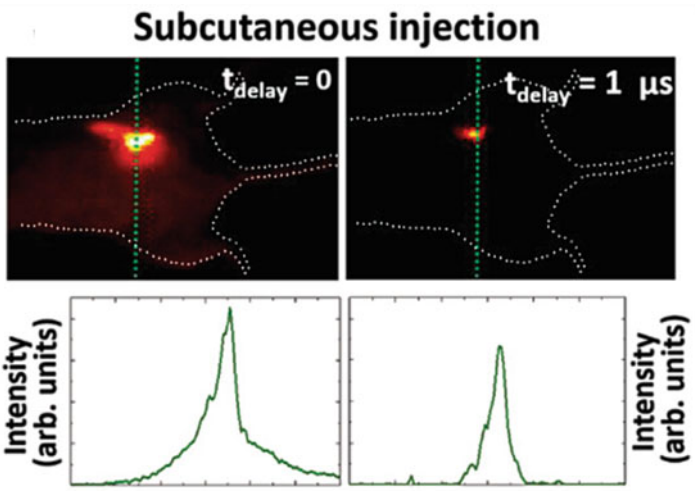

Fig. 4.7 In vivo fluorescence images collected for a C57BL/6 mouse subcutaneously injected with 100 μL of a dispersion of $NaGdF_4:Nd^{3+}$ NPs (10 mg mL^{-1}) using zero and 1 μs delay times between the camera and the end of excitation pulse. The bottom figure provides the emission intensity profiles taken along the dashed green lines in the infrared images above. Reproduced from del Rosal et al. 2016 [43]

4.4.3 *Multiplexing Imaging with Tunable Lifetimes*

Optical multiplexing imaging provides a rapid way to simultaneously detect several analytes or targets in sensing and bioimaging applications [47–49]. Usually, probes with distinct, non-overlapping emission bands are tagged with different antibodies, thus allowing cancer diagnosis through real-time observation of multiple targeted biological entities. Though carbon nanotubes, organic dyes, and semiconductor quantum dots have been proposed towards this regard, but their emission bands are either usually too broad to provide adequate number of detection channel or in the visible range that is not suitable for in vivo multiplexing. Besides emission wavelength or color, it is also possible to use other optical characteristics, such as lifetime, to distinguish different probes. Due to the nature of intra f-f transition of rare-earth luminescence, a major benefit of RENPs lifetime imaging is that it is independent of NPs concentration, which can be calibrated absolutely, in opposite to intensity measurements that are subject to imaging depth and tissue scattering properties. Recently, Jaque's and Chen's groups demonstrated that simple dopant engineering can lead to rare earth-doped NPs with tunable (0.1–1.5 ms) and medium-independent luminescence lifetimes. The combination of these lifetime-tunable NPs and time-gated technique enables to obtain multiplexed in vivo images for complex biodistribution of RENPs studies [50]. Specifically, the $NaYF_4$:Yb,Nd@CaF_2 core/shell NPs were synthesized, which emit at 980 nm (from Yb^{3+} ions) under 808 nm excitation. A change of Nd^{3+}-doped concentration affects the energy transfer efficiency between the Yb^{3+} and Nd^{3+} ions, thus tailoring the lifetime of emission. A mouse was administrated with two lifetime types of $NaYF_4$:Yb,Nd@CaF_2 core/shell NPs via oral or intravenous administration. The intensity-based in vivo image cannot discern the biodistribution of the two lifetime RENPs. However, in the lifetime-based image, longer lifetime NPs (intravenously administrated) can be seen to be accumulated at liver, which is consistent with the results reported in the literature. And the shorter lifetime NPs were shown to be accumulated at the stomach, which is consistent with the fact that these NPs are orally administrated. After excision of the mouse, the lifetime curves obtained at stomach and liver of mouse are indeed the same as that from the injected RENPs (Fig. 4.8). This work provided an example to design diagnostic tools for in vivo multiplexing imaging in time domain.

4.5 Conclusions

In this chapter, we describe the use of upconverting and downshifting RENPs for in vivo NIR imaging, including their advantages of emission in NIR-I and NIR-II windows for biological imaging and the use of time-gated technique for autofluorescence-free imaging and multiplexed lifetime imaging. Although RENPs for in vivo NIR imaging have attained exciting outcomes, there are still some challenges which need to be solved for practical applications:

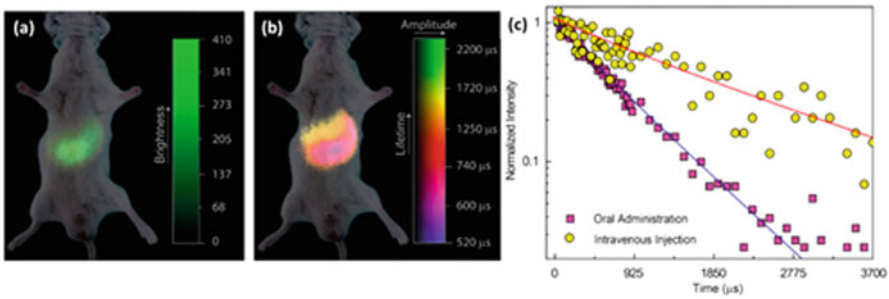

Fig. 4.8 In vivo multiplexed lifetime imaging: (**a**) Intensity-based infrared image of a mouse after oral and intravenous injection of $NaY_{0.9-x}Yb_{0.1}Nd_xF_4@CaF_2$ NPs with an Nd^{3+} content of x = 0.3 and 0.2, respectively. (**b**) Lifetime-based image of same mouse as in (**a**). The different location of the two types of NPs is evidenced. (**c**) Fluorescence decay curves obtained at two different locations corresponding to $NaYF_4$:Yb,Nd@CaF_2 core/shell NPs administrated orally and intravenously. Symbols are experimental data and solid lines are best exponential fits. Reproduced from Ortgies et al. 2018 [50]

1. The emission brightness remains a concern for RENPs, especially upconverting NPs. The reported luminescence quantum yield for downshifting NPs can reach ~ 30%, but less than 1% for upconverting NPs under imaging-related low-power excitation density (~ 0.1 W/cm^2). As such, various ways are suggested to be taken to enhance the emission brightness of RENPs, such as the use of core/shell structure for higher quantum yield and organic dye sensitization for enhanced light absorption.
2. For in vivo imaging, the original hydrophobic groups on RENPs should be taken place by a hydrophilic one to make them water dispersible. Aqueous dispersion NPs typically are reported to have more than two-folds decrease of emission intensity, since high phonon vibrations from the surface ligands or water molecules can substantially quench RE luminescence. For example, the hydroxyl group was demonstrated to efficiently quench the transition $^2F_{5/2} \rightarrow {}^2F_{5/2}$ of Yb^{3+} ions and $^4I_{13/2} \rightarrow {}^4I_{15/2}$ of Er^{3+} ions [51–53]. Thus, new suitable phase transfer or surface modification strategies are appealing to be developed without sacrificing emission intensity. Meanwhile, a high stability of water-soluble RENPs should also be achieved at the same time, which will benefit their circulation in the body.
3. Reported NIR small animal imaging results are non-targeted; targeted imaging or imaging-guided therapy of diseases is a natural next step, especially considering high-contrast and high-resolution images achieved so far.
4. Time-gated multiplexed imaging in NIR-II window is emerging as a new direction for in vivo biosensing, but based on single emission wavelength. Combination of different emission bands and tunable emission lifetimes can expand the number of detection channels. We envision that further development of NIR imaging with RENPs will eventually provide a set of useful tools for clinical diagnosis and therapy.

References

1. Leblond F, Davis SC, Valdã©S PA, Pogue BW (2010) Pre-clinical whole-body fluorescence imaging: review of instruments, methods and applications. J Photochem Photobiol B 98(1):77–94
2. Quek CH, Leong KW (2012) Near-infrared fluorescent nanoprobes for in vivo optical imaging. Nano 2(2):92–112
3. Naczynski DJ, Tan MC, Zevon M, Wall B, Kohl J, Kulesa A, Chen S, Roth CM, Riman RE, Moghe PV (2013) Rare-earth-doped biological composites as in vivo shortwave infrared reporters. Nat Commun 4(3):1345–1346
4. Bashkatov AN, Genina ÉA, Kochubey VI, Tuchin VV (2005) Optical properties of the subcutaneous adipose tissue in the spectral range 400–2500 nm. Opt Spectrosc 99(5):836–842
5. Frangioni JV (2003) In vivo near-infrared fluorescence imaging. Curr Opin Chem Biol 7(5):626–634
6. Zonios G, Bykowski J, Kollias N (2001) Skin melanin, hemoglobin, and light scattering properties can be quantitatively assessed in vivo using diffuse reflectance spectroscopy. J Investig Dermatol 117(6):1452–1457
7. Hong G, Robinson JT, Zhang Y, Diao S, Antaris AL, Wang Q, Dai H (2012) In vivo fluorescence imaging with Ag2S quantum dots in the second near-infrared region. Angew Chem 124(39):9956–9959
8. Weissleder R (2001) A clearer vision for in vivo imaging. Nat Biotechnol 19(4):316–317
9. Pansare V, Hejazi S, Faenza W, Prud'Homme RK (2012) Review of long-wavelength optical and NIR imaging materials: contrast agents, fluorophores and multifunctional Nano carriers. Chem Mater 24(5):812
10. Gao X, Cui Y, Levenson RM, Chung LW, Nie S (2004) In vivo cancer targeting and imaging with semiconductor quantum dots. Nat Biotechnol 22(8):969–976
11. Wang R, Li X, Zhou L, Zhang F (2015) Epitaxial seeded growth of rare-earth nanocrystals with efficient 800 nm near-infrared to 1525 nm short-wavelength infrared downconversion photoluminescence for in vivo bioimaging. Angew Chem Int Ed 53(45):12086–12090
12. Hong G, Lee JC, Robinson JT, Raaz U, Xie L, Huang NF, Cooke JP, Dai H (2012) Multifunctional in vivo vascular imaging using near-infrared II fluorescence. Nat Med 18(12):1841
13. Hong G, Zou Y, Antaris AL, Diao S, Wu D, Cheng K, Zhang X, Chen C, Liu B, He Y (2014) Ultrafast fluorescence imaging in vivo with conjugated polymer fluorophores in the second near-infrared window. Nat Commun 5:4206
14. Welsher K, Sherlock SP, Dai H (2011) Deep-tissue anatomical imaging of mice using carbon nanotube fluorophores in the second near-infrared window. Proc Natl Acad Sci U S A 108(22):8943
15. Hong G, Antaris AL, Dai H (2017) Near-infrared fluorophores for biomedical imaging. Nat Biomed Eng 1(1):0010
16. Zhang Y, Hong G, Chen G, Li F, Dai H, Wang Q (2016) Ag2S quantum dot: a bright and biocompatible fluorescent nanoprobe in the second near-infrared window. ACS Nano 12(2):464–464
17. Antaris AL, Chen H, Cheng K, Sun Y, Hong G, Qu C, Diao S, Deng Z, Hu X, Zhang B (2016) A small-molecule dye for NIR-II imaging. Nat Mater 15(2):235–242
18. Antaris AL, Chen H, Diao S, Ma Z, Zhang Z, Zhu S, Wang J, Lozano AX, Fan Q, Chew L (2017) A high quantum yield molecule-protein complex fluorophore for near-infrared II imaging. Nat Commun 8:15269
19. Ai X, Ho CJ, Aw J, Attia AB, Mu J, Wang Y, Wang X, Liu X, Chen H (2016) In vivo covalent cross-linking of photon-converted rare-earth nanostructures for tumour localization and theranostics. Nat Commun 7:10432
20. Xiaomin L, Fan Z, Dongyuan Z (2015) Lab on upconversion nanoparticles: optical properties and applications engineering via designed nanostructure. Chem Soc Rev 44(6):1346–1378

21. Byrnes KR, Waynant RW, Ilev IK, Wu X, Barna L, Smith K, Heckert R, Gerst H, Anders JJ (2005) Light promotes regeneration and functional recovery and alters the immune response after spinal cord injury. Lasers Surg Med 36(3):171–185
22. Sun LD, Wang YF, Yan CH (2014) Paradigms and challenges for bioapplication of rare earth upconversion luminescent nanoparticles: small size and tunable emission/excitation spectra. Acc Chem Res 47(4):1001–1009
23. Chen C, Li C, Shi Z (2016) Current advances in lanthanide-doped upconversion nanostructures for detection and bioapplication. Adv Sci 3(10):1600029
24. Smith AM, Mancini MC, Nie S (2009) Bioimaging: second window for in vivo imaging. Nat Nanotechnol 4(11):710–711
25. Wang YF, Liu GY, Sun LD, Xiao JW, Zhou JC, Yan CH (2013) Nd(3+)-sensitized upconversion nanophosphors: efficient in vivo bioimaging probes with minimized heating effect. ACS Nano 7(8):7200–7206
26. Del RB, Villa I, Jaque D, Sanz-Rodríguez F (2016) In vivo autofluorescence in the biological windows: the role of pigmentation. J Biophotonics 9(10):1059–1067
27. Chen G, Shen J, Ohulchanskyy TY, Patel NJ, Kutikov A, Li Z, Song J, Pandey RK, Agren H, Prasad PN (2012) (α-NaYbF4:tm(3+))/CaF2 core/shell nanoparticles with efficient near-infrared to near-infrared upconversion for high-contrast deep tissue bioimaging. ACS Nano 6(9):8280
28. Shen J, Chen G, Ohulchanskyy TY, Kesseli SJ, Buchholz S, Li Z, Prasad PN, Han G (2013) Upconversion: tunable near infrared to ultraviolet Upconversion luminescence enhancement in (α-NaYF4:Yb,tm)/CaF2 Core/Shell nanoparticles for in situ real-time recorded biocompatible Photoactivation (small 19/2013). Small 9(19):3212–3212
29. Zhang F, Liu L, Wang S, Zhao B, Pei P, Fan Y, Li X (2018) Er3+ sensitized 1530 nm to 1180 nm second near-infrared window upconversion nanocrystals for in vivo biosensing. Angew Chem Int Ed Engl 57(25):7518–7522
30. Cheng XW, Pan Y, Yuan Z, Wang XW, Su WH, Yin LS, Xie XJ, Huang L (2018) Er3+ sensitized photon upconversion nanocrystals. Adv Funct Mater 28(22)
31. Bausá LE (2005) An introduction to the optical spectroscopy of inorganic solids. Wiley, pp 199–234
32. Saders BV, Albaroudi L, Mei CT, Riman RE (2013) Rare-earth doped particles with tunable infrared emissions for biomedical imaging. Opt Mater Express 3(5):566–573
33. Nyk M, Kumar R, Ohulchanskyy TY, Bergey EJ, Prasad PN (2008) High contrast in vitro and in vivo photoluminescence bioimaging using near infrared to near infrared up-conversion in Tm3+ and Yb3+ doped fluoride nanophosphors. Nano Lett 8(11):3834
34. Chen G, Ohulchanskyy TY, Liu S, Law WC, Wu F, Swihart MT, Ågren H, Prasad PN (2012) Core/Shell NaGdF4:Nd3+/NaGdF4 Nanocrystals with efficient near-infrared to near-infrared downconversion photoluminescence for bioimaging applications. ACS Nano 6(4):2969
35. Rocha U, Kumar KU, Jacinto C, Villa I, Sanz-Rodríguez F, Juarranz A, Carrasco E, Veggel FCJMV, Bovero E (2014) Neodymium-doped LaF 3 nanoparticles for fluorescence bioimaging in the second biological window. Small 10(6):1141–1154
36. Qin QS, Zhang PZ, Sun LD, Shi S, Chen NX, Dong H, Zheng XY, Li LM, Yan CH (2017) Ultralow-power near-infrared excited neodymium-doped nanoparticles for long-term in vivo bioimaging. Nanoscale 9(14):4660–4664
37. Jiang X, Cao C, Feng W, Li F (2016) Nd3+-doped LiYF4 nanocrystals for bio-imaging in the second near-infrared window. J Mater Chem B 4(1):87–95
38. Rosal BD, Pérezdelgado A, Misiak M, Bednarkiewicz A, Vanetsev AS, Orlovskii Y, Jovanović DJ, Dramićanin MD, Rocha U, Kumar KU (2015) Neodymium-doped nanoparticles for infrared fluorescence bioimaging: the role of the host. J Appl Phys 118(14):143104
39. Cao C, Xue M, Zhu X, Yang P, Feng W, Li F (2017) Energy transfer highway in Nd(3+)-sensitized nanoparticles for efficient near-infrared bioimaging. ACS Appl Mater Interfaces 9(22):18540–18548

40. Villa I, Vedda A, Cantarelli IX, Pedroni M, Piccinelli F, Bettinelli M, Speghini A, Quintanilla M, Vetrone F, Rocha U (2015) 1.3 μm emitting SrF 2:Nd 3+ nanoparticles for high contrast in vivo imaging in the second biological window. Nano Res 8(2):649–665
41. Shao W, Chen GY, Kuzmin A, Kutscher HL, Pliss A, Ohulchanskyy TY, Prasad PN (2016) Tunable narrow band emissions from dye-sensitized Core/Shell/Shell nanocrystals in the second near-infrared biological window. J Am Chem Soc 138(50):16192–16195
42. Zhang KY, Qi Y, Wei H, Liu S, Qiang Z, Wei H (2018) Long-lived emissive probes for time-resolved photoluminescence bioimaging and biosensing. Chem Rev 118(4):1770–1839
43. Berezin MY, Achilefu S (2010) Fluorescence lifetime measurements and biological imaging. Chem Rev 110(5):2641–2684
44. Connally RE, Piper JA (2010) Time-gated luminescence microscopy. Ann N Y Acad Sci 1130(1):106–116
45. Jin D (2011) Demonstration of true-color high-contrast microorganism imaging for terbium bioprobes. Cytometry 79A(5):392–397
46. del Rosal B, Ortgies DH, Fernandez N, Sanz-Rodriguez F, Jaque D, Rodriguez EM (2016) Overcoming autofluorescence: long-lifetime infrared nanoparticles for time-gated in vivo imaging. Adv Mater 28(46):10188–10193
47. Abbasi AZ, Amin F, Niebling T, Friede S, Ochs M, Carregalromero S, Montenegro JM, Gil PR, Heimbrodt W, Parak WJ (2011) How colloidal nanoparticles could facilitate multiplexed measurements of different analytes with analyte-sensitive organic fluorophores. ACS Nano 5(1):21
48. Hoffmann K, Behnke T, Drescher D, Kneipp J, Reschgenger U (2013) Near-infrared-emitting nanoparticles for lifetime-based multiplexed analysis and imaging of living cells. ACS Nano 7(8):6674
49. Grabolle M, Kapusta P, Nann T, Shu X, Ziegler J, Reschgenger U (2009) Fluorescence lifetime multiplexing with nanocrystals and organic labels. Anal Chem 81(18):7807–7813
50. Ortgies DH, Tan M, Ximendes EC, Del BR, Hu J, Xu L, Wang X, Martín ER, Jacinto C, Fernandez N (2018) Lifetime-encoded infrared-emitting nanoparticles for in vivo multiplexed imaging. ACS Nano 12(5):4362–4368
51. Zhang L, Hu H (2002) The effect of OH − on IR emission of Nd 3+, Yb 3+ and Er 3+ doped tetraphosphate glasses. J Phys Chem Solids 63(4):575–579
52. Yan Y, Faber AJ, Waal HD (1995) Luminescence quenching by OH groups in highly Er-doped phosphate glasses. J Non-Cryst Solids 181(3):283–290
53. Arppe R, Hyppänen I, Perälä N, Peltomaa R, Kaiser M, Würth C, Christ S, Reschgenger U, Schäferling M, Soukka T (2015) Quenching of the upconversion luminescence of NaYF4:Yb3+,Er3+ and NaYF4:Yb3+,Tm3+ nanophosphors by water: the role of the sensitizer Yb3+ in non-radiative relaxation. Nanoscale 7(27):11746–11757

Chapter 5
Recent Advances in Development of NIR-II Fluorescent Agents

Haotian Du, Hao Wan, and Hongjie Dai

In vivo imaging is an emerging and promising technique to profile the internal status of biological systems, sparking much attention [1–4]. Among the various in vivo imaging modalities, fluorescence imaging, which is based on fluorescent dyes for visualization of biological processes or structures in living organisms, provides benefits of real-time image acquisition with high spatial resolution via non-radioactive optical systems [5, 6]. However, the imaging depth and spatial resolution for in vivo fluorescence imaging have been limited mainly due to photon scattering, absorption, and interference from autofluorescence of endogenous biological tissues. The past decade has witnessed rapid development of novel in vivo fluorescence imaging methods. Specifically, a newly developed fluorescence imaging approach that extends imaging wavelengths to the second near infrared window (NIR-II window, 1000–1700 nm) has received much interest. Compared to the visible (400–700 nm) and traditional near infrared window (NIR-I window, 700–900 nm), fluorescence imaging in the NIR-II window presents significant advances of improved penetration depth and higher spatial resolution, owing to reduced photon scattering, minimized tissue absorption, and negligible autofluorescence from endogenous molecules [7]. Defined as the "biological tissue transparency" window [8], fluorescence imaging in the NIR-II window opens up a wide range of opportunities from better understanding the underlying mechanisms of many physiological processes to opening unique potentials for clinical translation [9].

Since the first report of in vivo NIR-II fluorescence imaging [10], it has been constantly demonstrated that the quality of NIR-II imaging highly relies on

Haotian Du and Hao Wan contributed equally with all other contributors.

H. Du · H. Wan · H. Dai (✉)
Department of Chemistry, Stanford University, Stanford, CA, USA
e-mail: hdai@stanford.edu

A. Benayas et al. (eds.), *Near Infrared-Emitting Nanoparticles for Biomedical Applications*, https://doi.org/10.1007/978-3-030-32036-2_5

the rational design and optimization of fluorophores [11]. In particular, an ideal fluorophore suitable for in vivo NIR-II imaging should have high fluorescence quantum yield, red-shifted emission wavelength, and favorable pharmacokinetics. In this chapter, we discuss recent advances in the development of NIR-II fluorescent agents with remarkable improvements made on the aforementioned properties.

5.1 NIR-II Fluorophores with High Fluorescence Quantum Yields

Developing new fluorophores with high quantum yields (QYs) benefits NIR-II fluorescence imaging with greater tissue penetration, higher clarity, and faster dynamics by improving the signal-to-noise ratio (SNR) of imaging [12, 13]. Additionally, owing to a higher QY, the required dose of fluorophores can be reduced to achieve the same level of fluorescence intensity, thus mitigating potential toxicity concerns related to in vivo administration of the fluorophores. There has been research towards improving the QY of a broad range of NIR-II fluorophores, including small organic molecule dyes [14–16], inorganic quantum dots (QDs) [17–19], and rare-earth nanoparticles (RENPs) [20–22]. These latest developments have demonstrated significantly higher QYs in aqueous solution than single-walled carbon nanotubes (SWCNTs), which are the first NIR-II fluorescent agent used for in vivo imaging with a fluorescence QY of merely ~0.4% [10, 23] (measured against the reference of IR-26 with QY of ~0.5%, and same hereafter).

Compared with inorganic nanomaterials, small organic molecules benefit from more favorable pharmacokinetics and mitigated toxicity, thereby offering unique potentials for clinical translation of in vivo NIR-II fluorescence imaging. To date, a handful of organic NIR-II fluorophores has been developed for various applications. The construction of a large conjugated structure in organic molecules has been the major strategy to reduce the energy bandgap of the fluorophores and thus extend their emission wavelengths into the NIR-II window [24, 25]. More specifically, the donor–accepter–donor (D-A-D) architecture, in which strong electron-donating groups are built around strong electron acceptors through π-bridging moieties, creates a low bandgap between HOMO (highest occupied molecular orbital) and LUMO (lowest unoccupied molecular orbital), shifting the fluorescence emission into the NIR-II window [16, 26, 27]. However, large conjugated planar backbones tend to have strong intermolecular interactions with surrounding molecules, for which excited states of fluorophores could be easily attacked and quenched [16, 28]. The bright fluorescence from organic fluorophores is usually quenched to most extent after being transferred into an aqueous environment, resulting from the attack of water molecules and self-aggregation caused by hydrophobic interaction [29]. Therefore, building a hydrophobic environment around the acceptor where the LUMO of the conjugated molecule is mainly distributed would efficiently reduce non-radiative energy transfer and minimize the quenching effect, thus leading to a high QY in aqueous environment. In the following paragraphs, we discuss different strategies that have been applied so far to realize this goal.

The first strategy is the optimization of the molecular structure of the NIR-II fluorophore. The introduction of shielding units and engineering of the molecular structure of donor units have been demonstrated as efficient ways to protect fluorophores from quenching. The molecular backbone based on the structure of shielding unit–donor–acceptor–donor–shielding unit (S-D-A-D-S) was firstly introduced in the NIR-II fluorophore IR-FE [14]. The backbone adopted benzobisthiadiazole (BBTD) derivatives as the acceptor (A), 3,4-ethylenedioxy thiophene (EDOT) as the donor (D), and dialkyl fluorene as the shielding unit (S). Alkyl chains on fluorene stretch out of the plane of the conjugated backbone to shield the backbone from aggregation. Furthermore, polyethylene glycol (PEG) chains were conjugated to the hydrophobic backbone through click chemistry to impart the fluorophore with good water solubility and superior biocompatibility. With all these rational designs, a molecular fluorophore IR-FEP suitable for in vivo fluorescence imaging with a high QY of ~2.0% was obtained, much higher than the first reported organic fluorophore (CH1055-PEG) for NIR-II imaging (QY ~0.30%). On the other hand, engineering of the formulation of the donor moiety can further increase the QY of NIR-II fluorophores [15]. As an example, the NIR-II fluorophore IR-FTAP adopts two different types of donors, with octyl thiophene as the first donor and thiophene as the second donor, demonstrating a higher QY of ~5.3% in aqueous solution along with red-shifted emission wavelength. Specifically, thiophene was introduced as the second donor to further extend the conjugated structure, contributing to a red-shifted emission. Bulky and hydrophobic alkyl side chains on the first donor afforded larger distortion of conjugated backbone and less interaction with water molecules, thus maintaining the high QY of fluorophores upon water transfer. Benefiting from the bright NIR-II fluorophores, real-time fluorescence imaging of hind limb mouse blood vessels has been achieved with high spatial resolution and fast temporal dynamics for tracking the blood flow in the vessels.

Besides rational design of the molecular structure of NIR-II fluorophores, another strategy for minimizing non-radiative process and reducing the quenching effect is to encapsulate the fluorophore in an amphiphilic matrix. The hydrophobic part of the amphiphilic matrix creates a hydrophobic environment for the organic fluorophore molecules, repelling water molecules from fluorophore molecules to maintain the QY. Meanwhile, the hydrophilic chains on the amphiphilic matrix ensure the solubility of encapsulated fluorophores in aqueous solution and their biocompatibility. As a typical example, CH-4T with four sulfonic acid groups showed an unprecedented serum boosted QY when forming supramolecular assemblies with plasma proteins (Fig. 5.1a) [30]. The small molecular fluorophore produced ~50 fold brightness enhancement in fetal bovine serum (FBS) compared to that in water (Fig. 5.1b). Moreover, the QY can be further boosted by simply heating the mixture of fluorophore and FBS to 70 °C, termed CH-4T/FBS-HT (Fig. 5.1c). The significant enhancement of QY could be attributed to the hydrophobic pocket formed by protein molecules in serum which confines the conformation of the fluorophore molecules, and prevents the fluorophores from forming π–π stacked aggregates [31]. Through this way, less excited energy was dissipated through internal conversion via free rotating parts, thus resulting in a higher QY. By

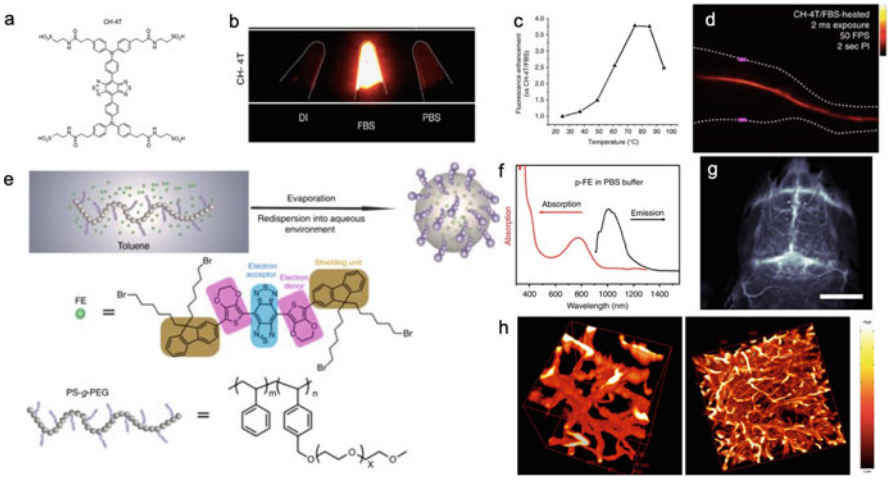

Fig. 5.1 High QY NIR-II imaging agents with supramolecular interaction. (**a**) Chemical structure of CH-4 T. (**b**) NIR-II fluorescence images of CH-4T in deionized water, FBS, and phosphate-buffered saline (PBS) at equal absorbance of OD 0.1 (Ex: 808 nm, Em: >1100 nm). (**c**) Plots summarizing fluorescence brightness after 10 min heating of CH-4T in FBS. (**d**) CH-4T/FBS-HT ultrafast imaging (50 fps) of integrated ROI region on the hind limb femoral artery. Color-bar range from low to high fluorescence intensity. (**e**) Scheme of p-FE synthesis and chemical structure of FE and PS-g-PEG. (**f**) Absorption and emission spectra (Ex: 808 nm) of p-FE in the PBS buffer. (**g**) Wide-field NIR-II epifluorescence imaging of the brain in a mouse injected with p-FE (Ex: 808 nm, Em: >1200 nm, 5 ms exposure time). Scale bar represents 6 mm. (**h**) 3D reconstruction of vasculatures in mouse brain obtained by NIR-II confocal imaging: a small-area scan (left side, 200 μm × 200 μm × 200 μm, x × y × z, step size: 1 μm along x, y, and z directions, galvo mirror scanning, scanning speed: 2 s/frame) and a large-area scan (right side, 400 μm × 400 μm × 400 μm, x × y × z, step size: 2 μm along x and y directions, 2.7 μm along z direction, stage scanning, scanning speed 450 s/frame) are shown [30, 32]

further optimization of the molar ratio of protein to fluorophore in the complex, the QY of protein–fluorophore complex can be enhanced to as high as ~11%. With this exceptionally bright complex, ultrafast NIR-II fluorescence imaging at a high speed of 50 frames per second (fps) was successfully realized to monitor the hemodynamics in real time (Fig. 5.1d). In addition, the bright protein–fluorophore complex successfully resolved individual cardiac cycles by measuring the NIR-II fluorescence intensity in the femoral artery. Furthermore, compared with clinically approved fluorophore indocyanine green (ICG) with fluorescence emission in the NIR-I window, lymph node imaging in the NIR-II window based on the protein–fluorophore complex demonstrated significantly improved imaging depth and resolution, clearly resolving the targets even at a depth of ~5 to 8 mm. Recently, an organic NIR-II fluorophore with an unprecedented QY of ~16.5% was achieved (Fig. 5.1e and f) [32]. Through encapsulation of the organic NIR-II dye (named "FE") into the hydrophobic interior of an amphiphilic polymer, poly (styrene-co-chloromethyl styrene)-graft-poly(ethylene glycol) (PS-g-PEG), a bright and

biocompatible nanofluorophore (named "p-FE") was successfully generated. The bright NIR-II emission in the >1100 nm spectrum from p-FE affords non-invasive in vivo imaging in real time, successfully tracking blood flow in mouse brain vessels (Fig. 5.1g). Excitingly, p-FE enables one-photon based, three-dimensional (3D) confocal imaging of cerebral vasculatures in fixed mouse brain tissue with a layer-by-layer imaging depth up to ~1.3 mm and sub-10 μm high spatial resolution, offering unprecedented insights for potential future applications of NIR-II imaging (Fig. 5.1h).

Inorganic nanoparticles-based NIR-II fluorophores, such as QDs and RENPs, have attracted much attention recently due to their excellent performance in fluorescence imaging. The high QY, superior photostability, and tunable narrow emission of these nanofluorophores make them ideal candidates for next-generation functional biomedical imaging with deep tissue penetration, high spatial resolution, fast temporal dynamics, and color multiplexity. However, despite the high brightness of these nanoparticles as synthesized in the organic solvents, their fluorescence is usually significantly quenched after transferring to water, severely hindering their in vivo imaging applications. Hydroxyl group (OH–) has been identified to be a main contributor for quenching these inorganic nanofluorophores because of its fundamental stretching vibration, which could lead to non-radioactive energy dissipation [33–36]. Building a shell around inorganic nanofluorophores to form a core–shell structure is a universal strategy to retain the brightness of nanofluorophores after phase transfer. The outer inert shell with a higher bandgap (energy difference between top of valence band and bottom of conduction band) would tightly wrap the emitting core and prevent it from interacting with water molecules. Besides water-induced quenching, another major factor leading to the quenching of inorganic nanofluorophores is the surfactant with high vibrational energy coating on the surface of nanoparticles [37]. To this end, surface coating and modification can circumvent the quenching effect by inserting hydrophobic alkyl chains between surfactant chains and prevent the surfactant chains from rotating freely.

Rare-earth nanoparticles (RENPs) adopt lanthanide (III) ions as its emitting center, whose fluorescence can be from either upconversion (UC) or down conversion (DC) emission, which differ by the direction of Stokes shift. DC-RENPs with normal Stokes shift and longer emission wavelength than excitation are considered desirable NIR-II imaging agents due to the sharp emission bands with many available emission wavelengths [21, 22]. An undoped hexagonal $NaYF_4$ layer with low phonon energy is commonly adopted to increase the distance between lanthanide ions and surface quenchers, thereby preventing the emitting core from interacting with water molecules to alleviate the quenching effect [38]. As a general rule, a thicker inert shell is usually required for DC particles than UC ones to achieve high QY based on experimental results (Fig. 5.2d) [20, 39]. By varying the thickness of the inert $NaYF_4$ shell of a NIR-II fluorescent nanocrystal comprising Er/Ce co-doped $NaYbF_4$, the QY of the RENP was optimized to 2.73% in an aqueous solution, representing the highest among all down conversion RENPs reported to date [20]. Taking advantage of the bright emission at ~1550 nm in the NIR-IIb

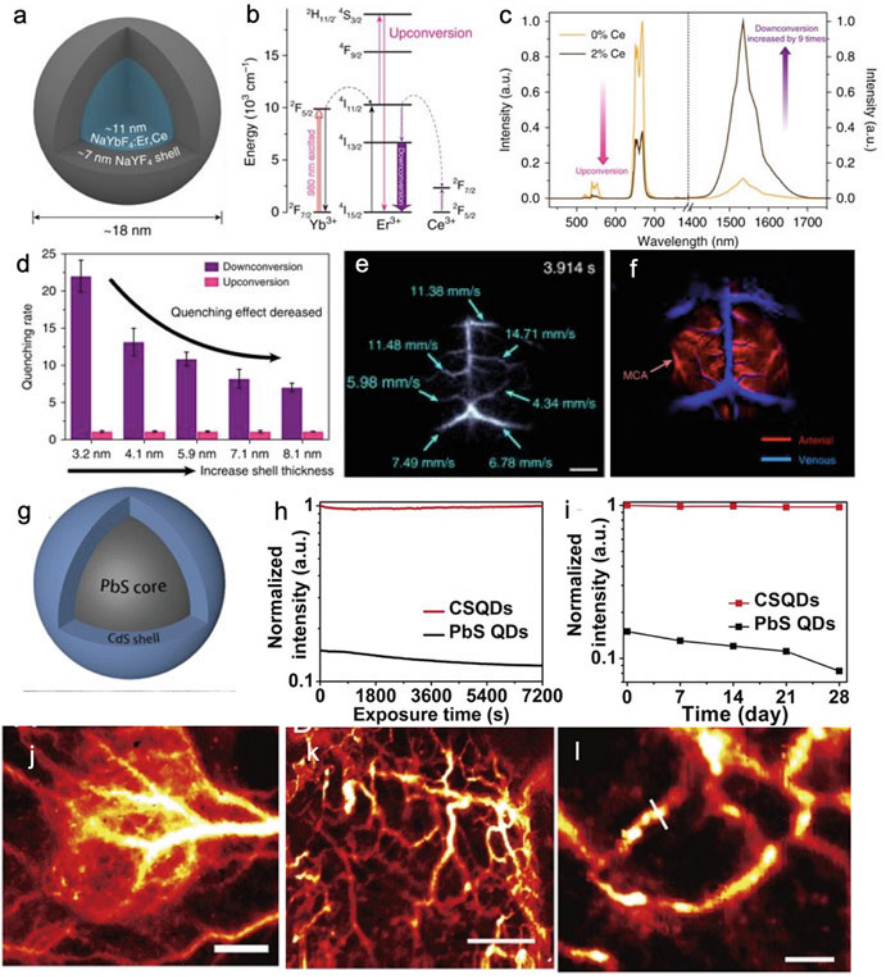

Fig. 5.2 DC RENP NIR-IIb imaging agent. (**a**) Schematic of a $NaYbF_4$:Er,Ce@$NaYF_4$ core–shell nanoparticle. (**b**) Simplified energy-level diagrams depicting the energy transfer between Yb^{3+}, Er^{3+}, and Ce^{3+} ions. (**c**) UC and DC luminescence spectra of the Er-RENPs with 0 and 2% Ce^{3+} doping. (**d**) Quenching rate of UC and DC emission as a function of shell thickness (from 3.2 to 8.1 nm). (**e**) NIR-IIb fluorescence image of a mouse brain showing the perfusion of RENPs into various cerebral vessels. (Ex: 980 nm, Em: >1500 nm, 20 ms exposure time). Blood-flow velocities are indicated for different vessels. (**f**) Cerebral vascular image in the NIR-IIb region with corresponding principal components showing arterial (red) and venous (blue) vessels [20]

window (1500–1700 nm), fast non-invasive imaging of mouse cerebral vasculatures was achieved with a short exposure time of 20 ms using the core/shell RENPs (Fig. 5.2e and f).

Besides the RENPs, QDs constitute another major class of inorganic nanofluorophores. Among QDs, lead sulfide (PbS) QDs is one of the most promising

imaging agents owing to its bright and tunable emission, which spans the entire NIR-II window (Fig. 5.3a) [17, 40–43]. However, the desirable optical properties of PbS QDs are subject to oxidation reactions on the surface defects, hindering their biological applications where oxygen is abundant. As an effective method to address this challenge, a shell layer of cadmium sulfide (CdS) was coated on the PbS core as a protection and passivation layer to both reduce surface defects and prevent degradations [44–46], thus retaining the high fluorescence QY of the PbS core after phase transfer to aqueous environment. Significantly, it has been demonstrated that CdS-coated PbS QDs (core/shell QDs or CSQDs) resulted in approximately 6–7× brighter fluorescence than that of bare PbS QDs in aqueous solution with greater photostability (Fig. 5.3b and c) [17]. The bright CSQDs allowed for fast, real-time imaging of blood flows with exposure time down to ~2 to 5 ms at an unprecedented frame rate of 60 fps, representing the fastest NIR-II imaging reported so far (Fig. 5.3d). Meanwhile, using the CSQDs as a bright fluorescence contrast agent in the NIR-IIb window, non-invasive in vivo confocal imaging clearly resolved 7.9 μm tumor vessels even at the depth of ~1.2 mm, successfully profiling the vasculature in a 3D fashion (Fig. 5.3e–g) (Table 5.1).

5.2 NIR-II Fluorophores with Long Emission Wavelengths

As mentioned above, an ideal window for fluorescence imaging calls for reduced scattering, minimum absorption, and negligible tissue autofluorescence. Imaging in the long end of NIR-II window (i.e., the NIR-IIb window within the range of 1500 to 1700 nm) offers a balance of photon scattering and water absorption. As the photon scattering scales as $\lambda^{-\alpha}$, where λ is the photon wavelength and α varies within 0.2–4 for different tissues, the scattering curve declines for all tissues as wavelength increases [52]. Photon scattering would cause the emitted fluorescence photons to deviate from original paths, not only attenuating the fluorescence signal from signal sources but also increasing the background noise. Imaging at longer wavelengths in the NIR-IIb window can overcome above problems by reducing the photon scattering and suppressing autofluorescence, affording higher resolution and facilitating deep tissue imaging [53, 54]. Nonetheless, there is a caveat to the statement that longer imaging wavelengths lead to better imaging performance: Water molecules start to have strong absorption peaks at increasing wavelengths. As shown in the spectra of water absorption and biological tissue extinction, the ~1600 nm region is located in a local minimum of the absorption/extinction spectra between two water absorption peaks at 1450 nm and > 1800 nm, which are attributed to the vibrational overtone and combination of –OH stretching and bending modes (Fig. 5.4a) [54]. Besides, photon extinction by skin and muscle is also relatively low in this wavelength range. As a result, imaging around ~1600 nm presents a minimum influence of water absorption and tissue extinction to minimize attenuation of fluorescence signal caused by water molecules in the aqueous biological environment.

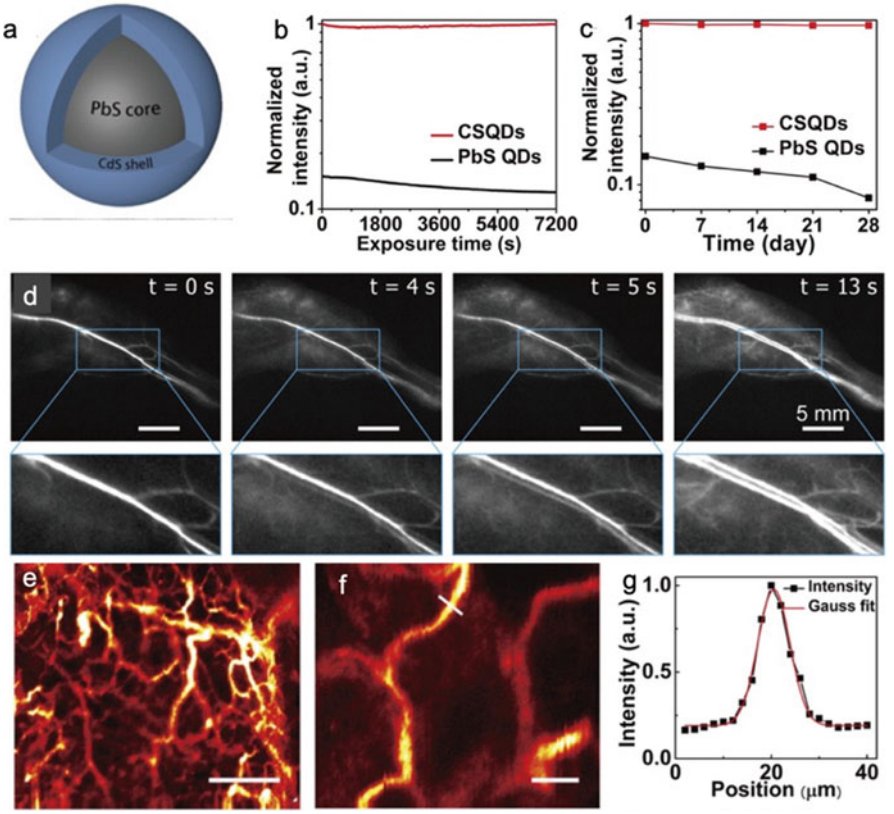

Fig. 5.3 Core–shell PbS/CdS QDs with high QY. (**a**) Schematic design of PbS/CdS CSQDs. (**b**) Photostability of PEGylated PbS QDs and PbS/CdS CSQDs in PBS under continuous 808-nm laser exposure for 2 h. (**c**) Long-term fluorescence stability of PEGylated PbS QDs and PbS/CdS CSQDs stored in PBS at 4 °C over the course of 4 weeks. (**d**) Real-time wide-field hind limb imaging in NIR-IIb window (Ex: 808 nm, Em: >1500 nm, 5 ms exposure time). $t = 0$ is defined as the time point when NIR-IIb signal started to show up in the femoral vein. (**e** and **f**) Confocal images of mouse hind limb vessels at a depth of ~270 μm after intravenous injection of PEGylated CSQDs, where a larger field of view of 2000 × 2000 μm (scale bar, 500 μm) and a smaller field of view of 300 μm × 300 μm (scale bar, 50 μm) are shown in (e) and (f), respectively. (**g**) Cross-sectional fluorescence intensity profile of the hind limb vessel marked in f with a FWHM of ~7.9 μm and a signal-to-background ratio of 6.3 [17]

To date, different NIR-IIb fluorophores with long emission wavelengths have been developed for in vivo imaging, including semiconducting single-walled carbon nanotubes [54], rare-earth down conversion nanocrystals [20], indium arsenide (InAs) quantum dots [50], PbS quantum dots [17, 43], etc. More fluorophores with high brightness that maximizes the efficiency of photon emission in this important spectral window are still being developed.

Table 5.1 Summary of NIR-II fluorophores with high QY in aqueous environment

Fluorophore	Peak emission wavelength	QY in water	Applications	Ref
IR-FGP	1050 nm	1.9%	Molecular imaging with antibody conjugation; 3D brain tissue confocal imaging	[47]
IR-FEP	1050 nm	2%	Ultrafast hind limb imaging (>25 fps); xenograft tumor imaging	[14]
IR-FTAP	1048 nm	5.3%	Hind limb vessel imaging	[15]
CH-4 T with protein complex	1050 nm in PBS; 1000 nm in FBS	~5% in FBS; ~11% after heated	Ultrafast vascular imaging (>50 fps); deep lymph nodes imaging (5–8 mm depth)	[30]
FD-1080 with protein complex	1080 nm	5.94%	Hind limb vasculature and brain vessel imaging; respiratory rate quantification	[48]
p-FE (IR-FE encapsulated in polymer matrix)	1010 nm	16%	Real-time blood flow tracking in mouse brain vessels; 3D brain tissue confocal imaging; two-color tumor imaging	[32]
TB1 encapsulated in polymer matrix	1000 nm	6.2%	Brain tumor imaging with c-RGD conjugated	[49]
Ag_2S QDs	1200 nm	15.5%	Xenograft tumor imaging	[19]
InAs-based core–shell–shell (CSS) QDs	1000–1400 nm (tunable by size and structure)	5–31%	Heartbeat and breathing rates quantification; 3D quantitative brain vasculature blood flow mapping	[50]
$NaYbF_4$:2%Er,2% Ce@$NaYF_4$	1550 nm	2.73%	Cerebral vascular imaging and blood-flow velocity quantification	[20]
PbS@CdS@SiO2@F-127 NPs	900–1700 nm	5.79%	Real-time brain vessels imaging	[51]
PdS/CdS CSQDs	1600 nm	22%	Ultrafast vasculature imaging (60 fps); 3D tumor vasculature confocal imaging	[17]

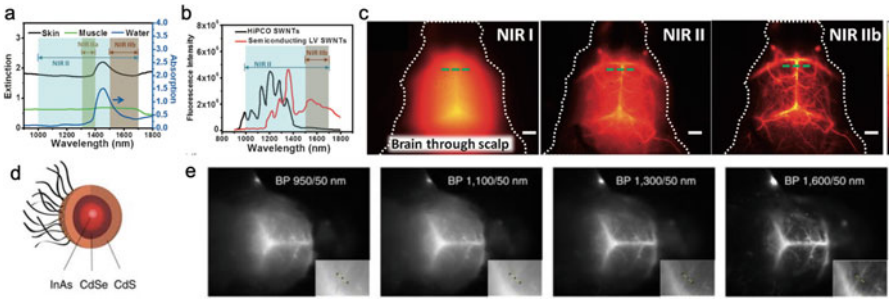

Fig. 5.4 Semiconducting LV SWCNT and InAs QDs emitting in NIR-IIb window. (**a**) Optical absorption spectrum of water and extinction spectra of mouse skin and muscle. (**b**) Fluorescence emission spectra of HiPCO and semiconducting LV SWCNTs under an 808 nm excitation. (**c**) Fluorescence imaging of mouse cerebral vasculature by LV SWCNTs without craniotomy in the NIR-I, NIR-II, and NIR-IIb windows. (**d**) Schematic structure of InAs/CdSe/CdS CSS QDs with surface modification. (**e**) Fluorescence imaging of mouse brain vasculature through intact skin and skull using a mixture of CSS QDs. The four images were collected using four different bandpass filters (50 nm spectral width) centered at 950, 1100, 1300, and 1600 nm, respectively [50, 54]

Successful in vivo fluorescence imaging in the NIR-IIb window was firstly demonstrated by applying semiconducting SWCNTs produced by laser vaporization (LV) [54]. The LV SWCNTs showed higher brightness in NIR-IIb window due to the smaller bandgaps and larger diameters than high-pressure CO conversion (HiPCO) SWCNTs (Fig. 5.4b). Brain imaging through scalp in NIR-I, NIR-II, and NIR-IIb windows reveals the highest signal-to-background ratio (SBR) achieved in the NIR-IIb window with longest wavelengths (Fig. 5.4c). In vivo vascular imaging with spatial resolution up to approximately 4 μm at ~3 mm depth, as well as single-vessel-resolved blood-flow speed mapping for multiple hind limb arterial vessels, was explored in the NIR-IIb window by using LV SWCNTs.

With size-tunable emission, broad absorption spectra, and relatively high QYs, QDs emerge as a promising fluorophore in the long end of the NIR window for better imaging quality with improved spatiotemporal resolution, increased penetration depths, and unprecedented sensitivity. InAs core–shell–shell (CSS) nanocrystals were demonstrated for non-invasive fluorescence imaging of mouse brain vasculature (Fig. 5.4d) [50]. Emission wavelength of the InAs CSS QDs relies on the size, which is dependent on the injection rate of the precursors during the synthesis. By systematic optimization of size distribution, different InAs CSS QDs with emission wavelengths spanning the entire sensitivity range of the InGaAs cameras (900–1600 nm) were obtained. For paralleled comparison, CSS QDs emitting at 950, 1110, 1300, and 1600 nm under 808 nm excitation were intravenously injected for vascular imaging of mouse brain, among which longer emission wavelength enhanced the imaging spatial resolution by significantly improving the SBR (Fig. 5.4e). Lead sulfide (PbS) QDs with strong and tunable emission have also been regarded as a promising candidate for biomedical imaging owing to narrow bandgap and large Bohr's radii. The size-dependent emission wavelength of PbS QDs affords

bright fluorescence in the NIR-IIb window for better imaging quality. With CdS shell protecting the PbS core from photochemical degradation as discussed above, PbS/CdS CSQDs showed an emission peak at 1650 nm under 808 nm excitation with superior photostability [17].

RENPs are capable of emitting fluorescence in the NIR-IIb window with large Stokes shift by its down conversion luminescence. Progress has been made by synthesizing different core–shell structured RENP fluorophores to achieve high spatial resolution and deep penetration for in vivo imaging in the NIR-II window. Among all the lanthanide elements that are used to construct RENPs, Er^{3+} is the most widely used emitting center that generates luminescence in the NIR-IIb window with a central emission wavelength at ~1500 nm, which results from electron transition from $^4I_{13/2}$ to $^4I_{15/2}$ energy levels with low energy photons released. Through experimental design, rare-earth nanofluorophores consisting of a $NaYF_4$ Yb:Ln doped core (Ln: Er, Ho, Tm, or Pr) surrounded by an undoped shell of $NaYF_4$ were synthesized and their emitting properties were systematically studied [55]. The emitting center and doped core elements can be manipulated to fine tune the emission wavelength. Er-doped nanofluorophore revealing emission at 1525 nm shows highest fluorescence intensity compared with other doped nanofluorophores. The nanofluorophore was successfully applied for real-time and multispectral disease-targeted imaging. More recently, a core–shell–shell structured RENP with Er^{3+} as the emitting center was also synthesized. Compared with early reported Nd-doped nanoparticles emitting at 1060 nm, Er-doped nanoparticles showed deeper penetration depth and higher SBR with improved imaging quality [22]. As described in above section, by introducing Er/Ce co-doped $NaYbF_4$ nanocrystal core with an inert $NaYF_4$ shell, a brighter DC-RENP was obtained (Fig. 5.2a) [20]. Ce-doping was believed to weaken the two-photon absorption process after energy transfer from absorption center Yb^{3+} to emitting center Er^{3+}. The energy spacing between $^4F_{5/2}$ and $^4F_{7/2}$ provides a small mismatch with the spacing between $^4I_{11/2}$ and $^4I_{13/2}$ of Er^{3+} to accelerate non-radiative relaxation from the Er^{3+} $^4I_{11/2}$ to $^4I_{13/2}$ level (Fig. 5.2b). As a result, the UC process was suppressed, and down conversion emission was boosted by approximately nine fold (Fig. 5.2c), making the Er/Ce co-doped $NaYbF_4$ nanoparticles a desirable NIR-IIb imaging agent.

5.3 Favorable Pharmacokinetics and Biocompatibility

A main concern of the existing NIR-II imaging fluorophores is related to their unfavorable pharmacokinetics and biocompatibility, hindering in vivo applications and in particular potential clinical translations [7]. To mitigate this concern, chemical components, chemical stability, and morphological features of nanofluorophores should be systematically evaluated and optimized to afford better pharmacokinetics and biocompatibility before in vivo applications. Systemically administered fluorescent agents are excreted via two major pathways: renal and biliary excretion pathways. Molecules with size smaller than the renal filtration cutoff of ~40 kDa,

which corresponds to a hydrodynamic diameter of ~5 nm, could be rapidly excreted by urine [56]. In contrast, fluorophores with sizes exceeding the renal cutoff are trapped within the reticuloendothelial system (RES, e.g., liver and spleen) and then excreted slowly through feces. Blood circulation half-life is an important metric to evaluate the excretion ability of systemically administered agents. Renal excretable fluorophores accompanied with a shorter blood circulation half-life are generally considered more biocompatible while longer circulating agents raised more safety concerns as the chance of getting trapped by the RES system increases as they circulate inside the body. Despite potential safety concerns, when it comes to functional in vivo imaging, fluorophores with prolonged blood half-life often result in higher accumulation in targeted regions such as cancerous tissue with precise localization. For example, particles with longer blood half-life exhibit higher tumor-to-normal tissue ratio owing to the enhanced permeability and retention (EPR) effect [57]. A high tumor-to-background signal ratio of intraoperative imaging facilitates precise imaging-guided tumor removal, beneficial for potential clinical translation of NIR-II imaging.

A number of studies have been conducted to alleviate safety concerns of NIR-II fluorophores and facilitate FDA approval to pave the way for clinical translation of NIR-II imaging. For NIR-II nanofluorophores, surface modification is a common approach to increase the biocompatibility. To this end, amphiphilic polymers are usually designed and applied to stabilize and solubilize nanofluorophores, which are often synthesized in organic solvents with hydrophobic surface [58, 59]. As a representative example, PbS/CdS CSQDs were surface-functionalized with oleylamine-branched polyacrylic acid (OPA) as an efficient coating layer. The van der Waals interaction between the hydrophobic polymer tails and alkyl chains on QD surface provides strong binding between the surface capping molecules and the QDs, while the subsequent PEGylation on the hydrophilic moiety endows the QDs fully dispersed in the aqueous environment. As a result, PEGylation extended the blood circulation half-life time as long as ~7 h, with a high tumor-to-normal tissue ratio up to ~32 achieved through EPR effect. The majority (~76%) of administered CSQDs were excreted through feces, whereas only 7% remained in seven major organs (liver, spleen, heart, lung, kidneys, stomach, gut) after injection, significantly reducing the potential toxicity [17]. For Er-doped RENPs, poly(maleic anhydride-alt-1-octadecene) (PMH) comprising an alkyl chain and an anhydride group was adopted to stabilize the nanoparticles. The anhydride groups can be hydrolyzed in alkaline environment for further PEGylation to improve the biocompatibility of the RENPs. After PEGylation and injection into mice, Er-doped RENPs were observed to mostly accumulate in the liver and spleen over a period of 48 h post-injection and slowly excreted via feces [20].

Recently, different surface functionalization strategies were employed for InAs-based core–shell (CS) and core–shell–shell (CSS) QDs for various applications [18]. Specifically, phospholipid micelles impart the QDs with long blood circulation by preventing them from phagocytosis by macrophages. QDs incorporated into lipoproteins enabled non-invasive imaging and direct quantification of organ metabolism processes in real time. Large composite particles with sufficient brightness allowed

for mapping three-dimensional blood flow in local tissue microenvironment by single particle tracking with intravital microscopy. The phospholipid coating mimics the lipid bilayer of cell membrane, thus preventing the QDs from being recognized by the immune system as foreign bodies and promoting QDs stability with mitigated adverse effect in vivo.

Inspired by the clinically approved NIR-I fluorophore ICG, developing NIR-II contrast agents with favorable excretion pharmacokinetics would facilitate FDA approval and clinical translation of NIR-II imaging. The first NIR-II fluorophore with pharmacokinetic profiles comparable to FDA-approved fluorophores is CH-1055-PEG (Fig. 5.5a) [16, 60]. PEGylation endows the fluorophore with good solubility and stability in the physiological environment. Owing to the highly conjugated π backbone, CH-1055-PEG exhibited a peak fluorescence emission at ~1055 nm. The small size (molecular weight of ~8.9 kDa, much smaller than the size cutoff for renal excretion, ~40 kDa) and excellent stability in the physiological environment make the CH-1055-PEG rapidly excreted through urine, with ~90% excretion through the renal system at 24 h post-injection (p.i.) (Fig. 5.5d). Molecular imaging of tumor cells was accomplished by conjugating CH1055 to a monoclonal antibody targeting epidermal-growth factor receptor (mAb EGFR).

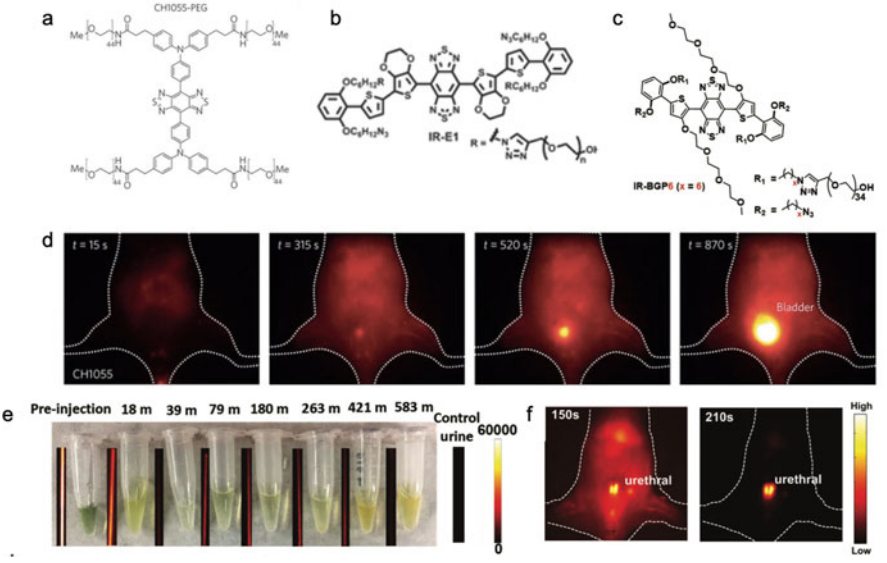

Fig. 5.5 Renal excretable NIR-II fluorophores. Chemical structures of (**a**) CH1055-PEG, (**b**) IR-E1, and (**c**) IR-BGP6. (**d**) Selected time points from video-rate NIR-II imaging of a mouse in the supine position after an intravenous injection of CH1055-PEG (Ex: 808 nm, Em: >1200 nm, 100 ms exposure time). High signal in bladder indicates renal excretion. (**e**) Collections of urine of mice injected with IR-BGP6 and their corresponding fluorescence images at different time points after injection. (**f**) High-resolution urethral imaging by CP-IRT (Ex: 808 nm, Em: >1200 nm, 200 ms exposure time) [16, 28, 62]

Moreover, by conjugating CH1055 to a follicle-stimulating hormone (FSH), in vivo live imaging of FSH receptors in gonads and bones in the NIR-II window was realized [60]. In the following work, a NIR-II fluorophore (IR-E1) with higher QY was demonstrated to possess fast renal excretion behavior, of which ~83% can be excreted within 24 h p.i. (Fig. 5.5b) [28]. Non-invasive NIR-II fluorescence imaging using IR-E1 enabled observation of cerebral hypoperfusion and neurovascular changes following traumatic brain injury (TBI) in mice. Recently, a NIR-II fluorophore named IR-BGP6 with an even higher QY of ~1.5%, fast renal excretion, and low tissue accumulation (~91% excreted in urine within the first 10 h p.i.) was reported (Fig. 5.5c, e) [61]. Molecular imaging of immune checkpoint was explored after covalent conjugation of IR-BGP6 to the programmed cell death ligand-1 monoclonal antibody (PD-L1 mAb).

Probes specific to cancer biomarkers are of growing interest for early diagnosis of cancer and targeted therapy. Antibody-conjugated NIR-II fluorophore complexes exhibit high binding affinity and selectivity towards tumor tissues, and thus are widely used for molecular imaging of tumor. However, the large size of antibody (~150 kDa) hampers the excretion of the fluorophore conjugate from the body, imposing potential toxicity in the long term. Compared to antibodies, peptides are much smaller in size and can also exhibit high and specific affinity towards corresponding biomarkers [63, 64], making them promising alternatives of antibodies for making fluorophore conjugates that target specific biomarkers. To this end, a molecular imaging agent comprising a CD133 targeting peptide CP and NIR-II fluorophore IRT was successfully developed recently [65]. The molecular imaging agent efficiently pinpointed the tumor and was excreted rapidly via the renal pathway, demonstrating the great potential for clinical translations. Furthermore, with this agent, non-invasive imaging of urethra of mice was successfully realized for the first time (Fig. 5.5f).

5.4 Outlook

Owing to the salient advantages for in vivo imaging as described above, more and more NIR-II fluorophores are being developed. With the development of chemical engineering and material science, the structure, components, and characteristics of NIR-II fluorophores can be precisely manipulated to fulfill the requirements towards various applications. In sum, NIR-II agents with high QYs, long emission wavelengths, and favorable pharmacokinetics are preferred for in vivo imaging to afford superior imaging quality, the ability of monitoring the dynamic physiological process, and good biocompatibility. Despite significant progress during the last decade, there are still many potential future directions in the field of NIR-II imaging.

1. Design and synthesis of NIR-II molecular fluorophores with high extinction coefficients.

Although QY is a key factor affecting the brightness of NIR-II fluorophores, when comparing the exact brightness of fluorophores, adsorption and extinction coefficients should also be taken into consideration. All small-molecule NIR-II fluorophores developed so far suffer from low extinction coefficients, which are usually one to two orders of magnitude smaller than those of conventional fluorophores with emission in the visible and NIR-I windows, thus significantly limiting the brightness of available NIR-II fluorophores. One possible approach to address this challenge is to introduce highly "absorbing" moiety with a high extinction coefficient, e.g., cyanine, into the molecular structure of NIR-II fluorophores without blue shift of emission wavelength. Simulation can be used to assist the molecular design of NIR-II fluorophores with high extinction coefficient.

2. Design and synthesis of renal-excreted NIR-II fluorophores with high brightness. The pharmacokinetic behavior of fluorophores is always a major factor for consideration when it comes to clinical applications. The trade-off between favorable pharmacokinetics and brightness of NIR-II fluorescence emission has been a long-standing challenge for clinical translation of NIR-II imaging. Specifically, a few renal-excreted NIR-II fluorophores were successfully developed with suboptimal fluorescence QYs (Table 5.2), resulting in limited imaging performance. Appropriate surface modification and encapsulation of bright small-molecule and nanoparticle fluorophores appear to be a straightforward method to maintain the stability and brightness of these fluorophores while ensuring their sizes below the cutoff of renal excretion.
3. Design and synthesis of NIR-II fluorophores compatible with NIR-II confocal imaging. Unlike two-dimensional (2D) wide-field imaging, confocal imaging collects signal from a small probed volume at the focus while rejecting all

Table 5.2 Summary of renal excretable NIR-II fluorophores

Fluorophore	Peak emission wavelength	Size (MW /diameter)	Application	Ref
CH-1055-PEG	1055 nm	8.9 kDa	Lymphatic vasculature and sentinel lymphatic mapping, targeted tumor imaging with anti-EGFR affibody conjugation	[16]
IR-E1	1071 nm	4.5 kDa 3.6 nm	Non-invasive brain imaging for cerebrovascular injury in TBI mouse model	[28]
IR-BGP6	1047 nm	3.5 nm	PD-L1 molecular imaging after conjugation with antibody	[61]
CP-IRT	1047 nm	5 nm	Molecular tumor imaging targeting a tumor stem cell biomarker CD133	[65]
SXH	1100 nm	<5.5 nm	Tumor imaging	[66]

out-of-focus signals, allowing for 3D imaging by raster-scanning the laser focal point in x–y–z directions. Therefore, 3D confocal imaging provides more structural information than 2D wide-field imaging for better understanding the spatial distribution of labeled structures and molecules of interest. However, a prerequisite for confocal imaging is the use of bright fluorophores in order to collect enough fluorescence photons at increased tissue depth within the safety limit of laser power density and reasonable scanning speed. For this reason, it was not until recently that 3D NIR-II imaging has been implemented under the confocal imaging mode. However, constrained by the brightness of fluorophores and detection efficiency of imaging instrumentations, the capability of deep 3D confocal imaging in the NIR-II window has not been fully exploited. To this end, besides the design of brighter NIR-II fluorophores as discussed above, future directions should also be focused on the optimization of the confocal setup and image acquisition, achieving new horizons of 3D volumetric NIR-II imaging in deep tissue of live organisms in synergy with the newly developed bright fluorophores.

References

1. Ntziachristos V et al (2005) Looking and listening to light: the evolution of whole-body photonic imaging. Nat Biotechnol 23(3):313
2. Guo Z et al (2014) Recent progress in the development of near-infrared fluorescent probes for bioimaging applications. Chem Soc Rev 43(1):16–29
3. Choi HS et al (2013) Targeted zwitterionic near-infrared fluorophores for improved optical imaging. Nat Biotechnol 31(2):148
4. Naumova AV et al (2014) Clinical imaging in regenerative medicine. Nat Biotechnol 32(8):804–818
5. Frangioni JV (2003) In vivo near-infrared fluorescence imaging. Curr Opin Chem Biol 7(5):626–634
6. Hof M et al (2005) Fluorescence spectroscopy in biology: Advanced methods and their applications to membranes. Springer, New York, p 305
7. Hong G, Antaris AL, Dai HJNBE (2017) Near-infrared fluorophores for biomedical imaging. Nat Biomed Eng 1(1):0010
8. Smith AM, Mancini MC, Nie S (2009) Bioimaging: second window for in vivo imaging. Nat Nanotechnol 4(11):710–711
9. Ding F et al (2018) Recent advances in near-infrared II fluorophores for multifunctional biomedical imaging. Chem Sci 9(19):4370–4380
10. Welsher K et al (2009) A route to brightly fluorescent carbon nanotubes for near-infrared imaging in mice. Nat Nanotechnol 4(11):773
11. Li C, Wang Q (2018) Challenges and opportunities for intravital near-infrared fluorescence imaging technology in the second transparency window. ACS Nano 12(10):9654–9659
12. Hong G et al (2012) Multifunctional in vivo vascular imaging using near-infrared II fluorescence. Nat Med 18(12):1841
13. Bushberg JT, Boone JM (2011) The essential physics of medical imaging. Lippincott Williams & Wilkins, Philadelphia
14. Yang Q et al (2017) Rational Design of Molecular Fluorophores for biological imaging in the NIR-II window. Adv Mater 29:12

15. Yang Q et al (2018) Donor engineering for NIR-II molecular fluorophores with enhanced fluorescent performance. J Am Chem Soc 140(5):1715–1724
16. Antaris AL et al (2016) A small-molecule dye for NIR-II imaging. Nat Mater 15(2):235–242
17. Zhang M et al (2018) Bright quantum dots emitting at approximately 1,600 nm in the NIR-IIb window for deep tissue fluorescence imaging. Proc Natl Acad Sci U S A 115(26):6590–6595
18. Bruns OT et al (2017) Next-generation in vivo optical imaging with short-wave infrared quantum dots. Nat Biomed Eng 1:0056
19. Hong G et al (2012) In vivo fluorescence imaging with Ag2S quantum dots in the second near-infrared region. Angew Chem Int Ed Engl 51(39):9818–9821
20. Zhong Y et al (2017) Boosting the down-shifting luminescence of rare-earth nanocrystals for biological imaging beyond 1500 nm. Nat Commun 8(1):737
21. Naczynski DJ et al (2013) Rare-earth-doped biological composites as in vivo shortwave infrared reporters. Nat Commun 4:2199
22. Wang R et al (2014) Epitaxial seeded growth of rare-earth nanocrystals with efficient 800 nm near-infrared to 1525 nm short-wavelength infrared downconversion photoluminescence for in vivo bioimaging. Angew Chem Int Ed Engl 53(45):12086–12090
23. Hong G et al (2014) Through-skull fluorescence imaging of the brain in a new near-infrared window. Nat Photonics 8(9):723–730
24. Friend R et al (1999) Electroluminescence in conjugated polymers. Nat 397(6715):121
25. Hong G et al (2014) Ultrafast fluorescence imaging in vivo with conjugated polymer fluorophores in the second near-infrared window. Nat Commun 5:4206
26. Qian G et al (2008) Band gap tunable, donor−acceptor−donor charge-transfer heteroquinoid-based chromophores: near infrared photoluminescence and electroluminescence. Chem Mater 20(19):6208–6216
27. Sun Y et al (2016) Novel benzo-bis (1, 2, 5-thiadiazole) fluorophores for in vivo NIR-II imaging of cancer. Chem Sci 7(9):6203–6207
28. Zhang XD et al (2016) Traumatic brain injury imaging in the second near-infrared window with a molecular Fluorophore. Adv Mater 28(32):6872–6879
29. Desmettre T, Devoisselle J, Mordon SJSoo (2000) Fluorescence properties and metabolic features of indocyanine green (ICG) as related to angiography. Surv Ophthalmol 45(1):15–27
30. Antaris AL et al (2017) A high quantum yield molecule-protein complex fluorophore for near-infrared II imaging. Nat Commun 8:15269
31. Siegel JJCCRAL (2007) Principles of fluorescence spectroscopy. Choice Curr Rev Acad Lib 44:1196–1196
32. Wan H et al (2018) A bright organic NIR-II nanofluorophore for three-dimensional imaging into biological tissues. Nat Commun 9(1):1171
33. Gapontsev VP et al (1981) Mechanism and parameters of the quenching of luminescence of rare-earth ions by hydroxyl impurity groups in laser phosphate glass. Sov J Quantum Electron 11(8):1101–1103
34. Su Q et al (2012) The effect of surface coating on energy migration-mediated upconversion. J Am Chem Soc 134(51):20849–20857
35. Zhang L, Hu HJJoP, Solids Co (2002) The effect of OH− on IR emission of Nd3+, Yb3+ and Er3+ doped tetraphosphate glasses. J Phys Chem Solids 63(4):575–579
36. Yan Y, Faber AJ, De Waal HJJoN-CS (1995) Luminescence quenching by OH groups in highly Er-doped phosphate glasses. J Non-Cryst Solids 181(3):283–290
37. Heer S et al (2004) Highly efficient multicolour upconversion emission in transparent colloids of lanthanide-doped NaYF4Nanocrystals. Adv Mater 16(23–24):2102–2105
38. Yi G-S, Chow G-MJCoM (2007) Water-soluble NaYF4: Yb, Er (tm)/NaYF4/polymer core/shell/shell nanoparticles with significant enhancement of upconversion fluorescence. Chem Mater 19(3):341–343
39. Zhang F et al (2012) Direct imaging the upconversion nanocrystal core/shell structure at the subnanometer level: shell thickness dependence in upconverting optical properties. Nano Lett 12(6):2852–2858

40. Hines MA, Scholes GDJAM (2003) Colloidal PbS nanocrystals with size-tunable near-infrared emission: observation of post-synthesis self-narrowing of the particle size distribution. Adv Mater 15(21):1844–1849
41. Weidman MC et al (2014) Monodisperse, air-stable PbS nanocrystals via precursor stoichiometry control. ACS Nano 8(6):6363–6371
42. Tang J et al (2011) Colloidal-quantum-dot photovoltaics using atomic-ligand passivation. Nat Mater 10(10):765
43. Ma Z et al (2018) Near-infrared IIb fluorescence imaging of vascular regeneration with dynamic tissue perfusion measurement and high spatial resolution. Adv Funct Mater 28(36):1803417
44. Jin L et al (2016) Engineering interfacial structure in "Giant" PbS/CdS quantum dots for photoelectrochemical solar energy conversion. Nano Energy 30:531–541
45. Neo DC et al (2014) Influence of shell thickness and surface passivation on PbS/CdS core/shell colloidal quantum dot solar cells. ACS Nano 26(13):4004–4013
46. Supran GJ et al (2015) High-performance shortwave-infrared light-emitting devices using core–shell (PbS–CdS) colloidal quantum dots. Adv Mater 27(8):1437–1442
47. Zhu S et al (2017) Molecular imaging of biological systems with a clickable dye in the broad 800- to 1,700-nm near-infrared window. Proc Natl Acad Sci U S A 114(5):962–967
48. Li B et al (2018) An efficient 1064 nm NIR-II excitation fluorescent molecular dye for deep-tissue high-resolution dynamic bioimaging. Angew Chem Int Ed Engl 57(25):7483–7487
49. Sheng Z et al (2018) Bright aggregation-induced-emission dots for targeted synergetic NIR-II fluorescence and NIR-I Photoacoustic imaging of Orthotopic brain tumors. Adv Mater 30:1800766
50. Franke D et al (2016) Continuous injection synthesis of indium arsenide quantum dots emissive in the short-wavelength infrared. Nat Commun 7:12749
51. Zebibula A et al (2018) Ultrastable and biocompatible NIR-II quantum dots for functional bioimaging. Int J Nanomed 28(9):1703451
52. Bashkatov A et al (2005) Optical properties of human skin, subcutaneous and mucous tissues in the wavelength range from 400 to 2000 nm. J Phys D Appl Phys 38(15):2543
53. Diao S et al (2015) Biological imaging without autofluorescence in the second near-infrared region. Nano Res 8(9):3027–3034
54. Diao S et al (2015) Fluorescence imaging in vivo at wavelengths beyond 1500 nm. Angew Chem Int Ed Engl 54(49):14758–14762
55. Naczynski D et al (2013) Rare-earth-doped biological composites as in vivo shortwave infrared reporters. Nat Commun 4:2199
56. Choi HS et al (2007) Renal clearance of quantum dots. Nat Biotechnol 25(10):1165
57. Maeda H et al (2000) Tumor vascular permeability and the EPR effect in macromolecular therapeutics: a review. J Control Release 65(1–2):271–284
58. Zhao H et al (2011) Effect of different types of surface ligands on the structure and optical property of water-soluble PbS quantum dots encapsulated by amphiphilic polymers. J Phys Chem C 115(5):1620–1626
59. Moroz P et al (2014) Infrared emitting PbS nanocrystal solids through matrix encapsulation. Chem Mater 26(14):4256–4264
60. Feng Y et al (2017) Live imaging of follicle stimulating hormone receptors in gonads and bones using near infrared II fluorophore. Chem Sci 8(5):3703–3711
61. Wan H et al (2018) Developing a bright NIR-II Fluorophore with fast renal excretion and its application in molecular imaging of immune checkpoint PD-L1. Adv Funct Mater
62. Wang W et al (2018) Molecular cancer imaging in the second near-infrared window using a renal-excreted NIR-II Fluorophore-peptide probe. Adv Mater 30(22):1800106
63. Saito T et al (2016) Two FOXP3+ CD4+ T cell subpopulations distinctly control the prognosis of colorectal cancers. Nat Med 22(6):679

64. Peng M et al (2016) Self-delivery of a peptide-based prodrug for tumor-targeting therapy. Nano Res 9(3):663–673
65. Wang W et al (2018) Molecular cancer imaging in the second near-infrared window using a renal-excreted NIR-II Fluorophore-peptide probe. Adv Mater 30(22):e1800106
66. Sun Y et al (2017) Novel bright-emission small-molecule NIR-II fluorophores for in vivo tumor imaging and image-guided surgery. Chem Sci 8(5):3489–3493

Chapter 6
Near Infrared Spectral Imaging of Carbon Nanotubes for Biomedicine

Prakrit V. Jena, Christian Cupo, and Daniel A. Heller

6.1 Introduction

Photoluminescent single-walled carbon nanotubes (SWCNTs) exhibit unique optical and structural properties that have motivated their development for applications including imaging and sensing, photothermal therapy, and drug delivery [1]. As optical probes for biosensing and imaging [2], the essential promise is a palette of >20 completely photostable fluorophores that function in the tissue-transparent [3, 4] near infrared (NIR) region of the spectrum [5]. Compared to other fluorescent probes [6, 7], SWCNTs are intrinsically multiplexed and capable of sensing/responding to their immediate environment. Building on over a decade of productive research [8] which has resulted in applications in live cells, plants, and small animals [9], recent developments (Fig. 6.1) have dramatically accelerated the process of engineering carbon nanotube optical reporters for biomedical applications [10].

In this chapter, we first introduce the fundamental structural and optical properties of single-walled carbon nanotubes (Sect. 6.2). We then identify the benefits resulting from the intrinsic NIR bandgap photoluminescence coupled with the unique linear nanomaterial structure (Sect. 6.3). Next (Sect. 6.4), we highlight the available instrumentation platforms that can be used to measure SWCNT photoluminescence in biological systems. We assess the utility of hyperspectral imaging (Sect. 6.5) to characterize photoluminescent carbon nanotubes with single-nanotube resolution. In the subsequent Sect. 6.6, spectral imaging in live cells is

P. V. Jena · C. Cupo
Memorial Sloan Kettering Cancer Center, New York, NY, USA

D. A. Heller (✉)
Memorial Sloan Kettering Cancer Center, New York, NY, USA

Weill Cornell Medicine, New York, NY, USA
e-mail: hellerd@mskcc.org

A. Benayas et al. (eds.), *Near Infrared-Emitting Nanoparticles for Biomedical Applications*, https://doi.org/10.1007/978-3-030-32036-2_6

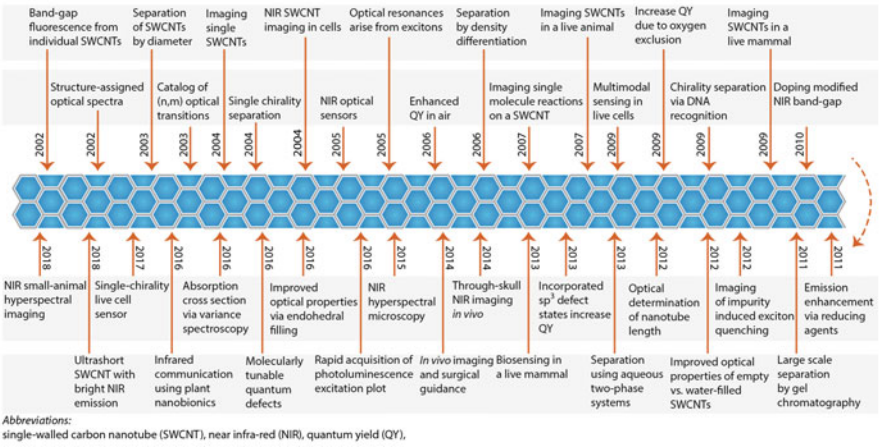

Fig. 6.1 A timeline highlighting the achievements across various aspects of carbon nanotube research, including developments in material processing, chemical functionalization, analytical methods, near infrared imaging, and engineered biomedical applications. Figure adapted with permission [10]

explored with an in-depth focus on the example of a sensor for lipid measurements in live cells. Following this, we assess spectral imaging for ex vivo and in vivo applications (Sect. 6.7). We end the chapter (Sect. 6.8) by identifying the challenges and potential ahead. For the sake of clarity, we shall use the term nanotube or SWCNTs interchangeably to refer to single-walled carbon nanotubes.

6.2 Optophysical Properties of Single-Walled Carbon Nanotubes

Single-walled carbon nanotubes are one-dimensional nanocarbons formed purely of sp^2-hybridized carbon atoms [11], and can be visualized as open-ended hollow cylinders formed by rolling a rectangular sheet of graphene (Fig. 6.2a). The angle at which sheet is rolled can be defined in terms of unit (chiral) vectors along the natural axis [12], and these (n, m) chiral indices [13] uniquely label each possible nanotube structure and describe their physical and optical properties (Fig. 6.2b). In addition, SWCNT structures exist as enantiomers of the form (n,m) and (m,n).

Carbon nanotubes are synthesized via a number of methods [16], and the resulting material is a combination of nanotube chiralities, metallic catalysts, and carbonaceous impurities. Efforts to synthesize single-nanotube chiralities are in progress [17], and have achieved the growth of short single-chirality nanotubes adhered to the reaction surface [18, 19]. As-produced SWCNTs are hydrophobic and exist as a dry soot. A variety of dispersion techniques have been developed

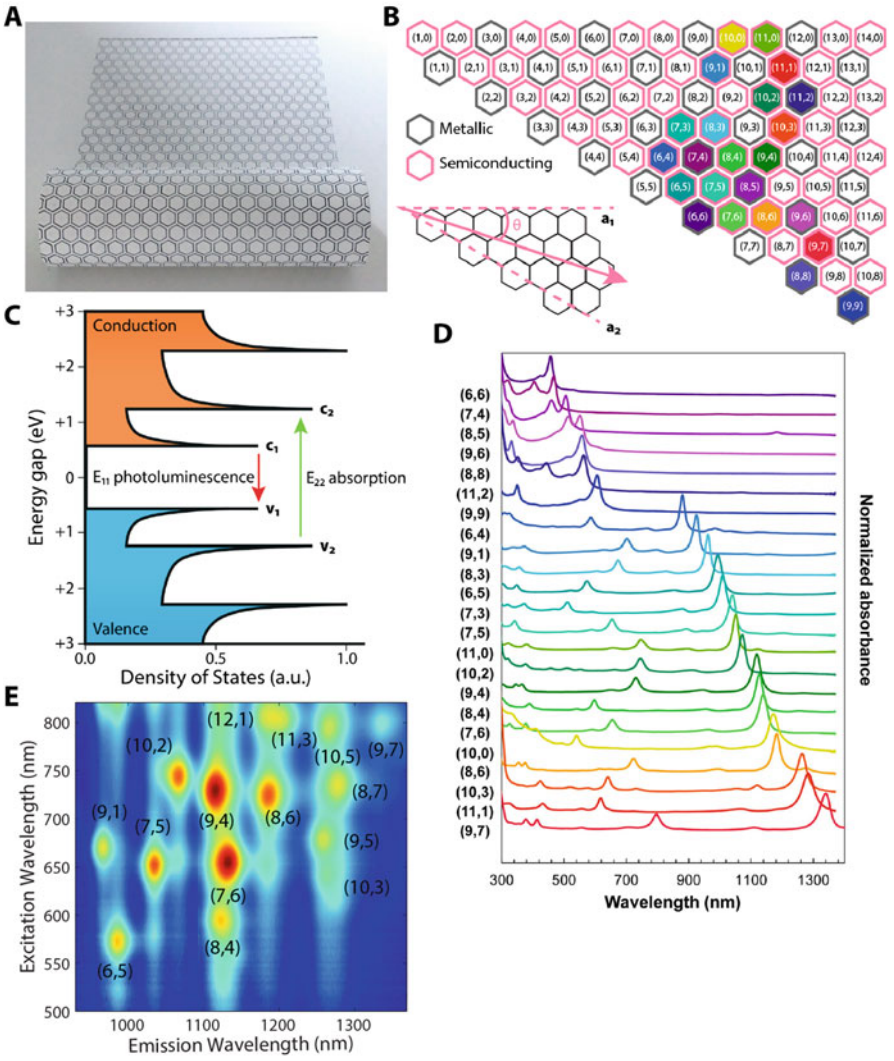

Fig. 6.2 Fundamental physical and optical properties of single-walled carbon nanotubes. (**a**) Graphical representation of a carbon nanotube, as a rolled sheet of graphene (hand-rendered, provided by Joseph Cohen). (**b**) The angle of rolling along the natural axes a_1 and a_2 determines the chirality (n,m) of the specific nanotube, and determines whether the chirality is metallic (gray) or semiconducting (pink). (**c**) The 1-D density of states of semiconducting nanotubes results in intrinsic near infrared bandgap photoluminescence, typically with E_{22} absorption resulting in E_{11} emission. (**d**) Absorption spectrum of isolated single-chirality nanotube samples, color-coded to the chirality map in panel B (reproduced with permission) [14]. (**e**) A 2D photoluminescence excitation–emission (PLE) plot of sodium deoxycholate-SWCNT in water is plotted as the square-root of intensity to visually amplify lower intensity regions, with emissive semiconducting nanotubes identified by their excitation and emission maxima [15]

to solubilize SWCNTs in organic solvents, or to impart water solubility via appropriate covalent and non-covalent functionalization [20]. Out of all the possible nanotube structures (Fig. 6.2b), theoretical calculations of the bandgap predicted approximately 1/3rd to be metallic (0 meV bandgap) and 2/3rd to be semiconducting (> 500 meV bandgap) [13] and experimental results have validated these predictions [21, 22].

6.2.1 Intrinsic Bandgap Photoluminescence

As a quasi-one-dimensional material, the density of states of semiconducting nanotubes is distinguished by sharp peaks known as van Hove singularities [23]. These optical resonances arise from excitons [24], and the resulting exciton dynamics following the absorption of a photon result in individual semiconducting nanotubes exhibiting bandgap fluorescence [25] in the NIR wavelength range [26]. As evident from the density of states schematic (Fig. 6.2c), photoexcitation at any of the absorption transitions (E_{11} or E_{22}) can result in the emission of a NIR photon via the E_{11} exciton-hole recombination pathway. The specific excitation and emission peaks for all semiconducting nanotube chiralities have been calculated [27] and are closely matched by experimental values [28].

6.2.2 Isolation of Single-Nanotube Chiralities

Separation techniques to isolate individual carbon nanotube chiralities [29] have achieved success in providing highly pure preparations of SWCNTs [30]. These include density ultracentrifugation [31], chromatography [32, 33], and aqueous two-phase extraction methods [34, 35]. Single-stranded DNA (ssDNA) emerged as a multifunctional and biocompatible polymer that enables nanotube separation following non-covalent functionalization, initially using chromatographic methods [36] and now via various aqueous two-phase extraction methodologies with purities above 95% [14, 37]. Furthermore, specific enantiomers of over 20 (n,m) species functionalized with ssDNA have been separated (Fig. 6.2d) [14]. Recently, surfactant-encapsulated presorted SWCNTs were re-wrapped to produce DNA-encapsulated SWCNTs at high yields [38]. As these various methods are further refined, the goal is the ability to independently control the functionalization on the SWCNT and to select a purified species/chirality.

6.2.3 Inherent Multiplicity of Nanotube Structures

Empirical functions mapping the inherent multiplicity of single-walled carbon nanotubes have been used to tabulate the optical transition values for over 100 nanotube chiralities [28], though in practice, the number of distinct chiralities physically present in a given sample depends on both the starting material and the solubilization method used. Optically characterizing photoluminescent carbon nanotube species is best achieved via a two-dimensional photoluminescence excitation–emission plot (PLE) as shown in Fig. 6.2e [15], where each isolated intensity maximum corresponds to a nanotube chirality. For the specific sodium deoxycholate (SDC)-suspended SWCNT sample shown, ~ 15 emitters in a ~ 500 nm emission range are distinctly visible. The broad excitation window (indicated by the elongated vertical lines emerging from each excitation–emission center) allows for off-resonance excitation of SWCNTs. Although different nanotube synthesis methods produce different population distributions, a large number of different species are present in most commercially available nanotube preparations.

6.2.4 Biocompatibility

The biocompatibility of SWCNTs has been the subject of intense studies [39–41], with conclusions indicating that the biosafety profile depends crucially on the specifications of the nanomaterial. The type of nanotube (single/double/multi-walled), the length distribution of the sample [42], the method and extent of functionalization (non-covalent vs covalent, chemical or polymer-based) [43], the purification steps performed, the stability of the final complex [44], the method of facilitating biological interactions [45, 46], the local concentration of the nanotube [47], and naturally the total cellular nanomaterial load [48] all alter the biocompatibility of the nanotube [49]. Optimized protocols for specific applications have led to nanotube constructs which were safely used in cells [50], plants, and animals [51, 52]. However, there are no broad guidelines that generally define a safety profile for carbon nanotube constructs.

We believe a practical disadvantage of SWCNTs arises from the large phase space covered by the nanotube molecular identity, i.e., multi-walled vs single-walled, short vs long, covalently or non-covalently functionalized, degree of biocompatibility, etc. are all referred to as “carbon nanotubes.” To the general research community, any results pertaining to one subset of carbon nanotubes are assumed to apply to the rest of the nanotube family. Standardizing the sensor to a well-defined molecular entity is not an optical issue per se, but can hinder the rate of SWCNT adoption for preclinical and clinical applications.

6.3 Photoluminescent SWCNTs as Imaging and Sensing Agents

The intrinsic bandgap near infrared photoluminescence confers an unusual combination of advantageous properties to carbon nanotubes. The one-dimensional structure is intrinsically sensitive to its environment, as each carbon atom is on the surface and directly interacts with the surrounding environment.

6.3.1 Structural Properties of Linear SWCNTs

The semi-rigid linear shape of the single-walled carbon nanotube results in diffusional and rotational movement that is distinct from the typical spherical nanoparticle. For example, when introduced to three-dimensional tumor spheroids, carbon nanotubes display anomalously fast diffusion within the spheroid when compared to spherical particles of comparable dimensions [53]. This anisotropic dimensionality (>100 nm on one axis, $\sim$ 1 nm on another) has been exploited to investigate the permeability of multicellular tumor spheroids [54] and to map the nanoscale organization within the extracellular space of a live mouse brain [55]. Similarly, multiple efforts to use the nanotube as a scaffold for drug delivery are also being developed, with unexpected pharmacological behavior observed in vitro [56] and in vivo [57, 58]. In addition, gene delivery applications in plants were recently demonstrated using nanotubes as delivery agents [59, 60].

6.3.2 Advantageous Optical Properties

For the purpose of biological applications, it is helpful to compare the photoluminescent properties of carbon nanotubes with their organic fluorophore analogs [61]. One immediate drawback we must note is the relatively low quantum yield of SWCNTs (ranging from 0.01% to 10%) [62, 63]. Fortuitously, multiple independent optical properties can be leveraged to compensate for the low brightness of SWCNT emission. As each SWCNT can be excited at multiple absorption peaks (E_{22} and E_{11}) [64, 65] but emits only at the E_{11} peak, the functional Stokes shift can be several hundred nanometers (Fig. 6.3a). This is convenient when designing optical platforms, as leaked excitation light does not spectrally overlap or interfere with the detection window.

Second, SWCNTs do not structurally degrade under standard conditions and thus maintain their intrinsic photoluminescence capabilities. Nanotube sensors embedded in a gel in vivo maintained their ability to photoluminescence over 300 days (Fig. 6.3b) [66]. While biofouling and other biological changes likely occurred on the nanotube surface, the graphitic structure remained undamaged

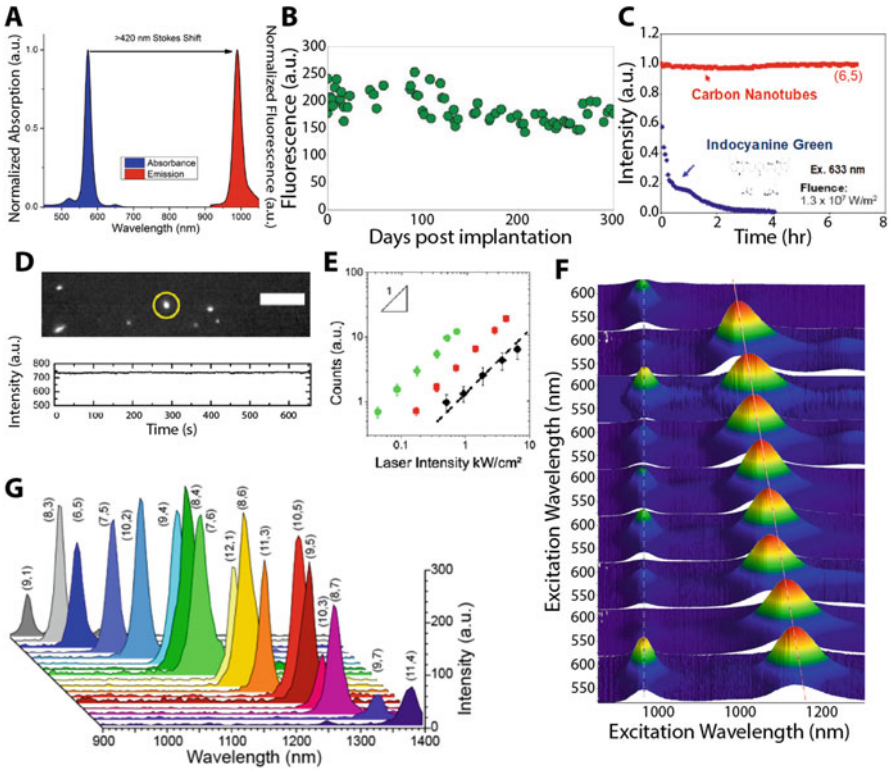

Fig. 6.3 Advantageous optical properties of SWCNTs. (**a**) A large effective Stokes shift following E_{22} excitation to achieve E_{11} emission, shown for the (6,5) chirality. (**b**) The intrinsic photoluminescence capability of SWCNTs is stable in biological systems over extended periods of time [66]. (**c**) Under high laser intensity, a nanotube solution does not photobleach [67]. (**d**) Emission from an isolated surface-adsorbed SWCNT is photostable under 6 kW/cm^2 of laser excitation [15]. (**e**) The emission intensity scales linearly with the absorbed photon count [65]. (**f**) Emission from a specific nanotube chirality can be molecularly tuned to a specific desired wavelength [68]. (**g**) The narrow emission linewidth of an SWCNT allows for over 17 chiralities to be directly imaged in a 500 nm window [15]

and preserved its sensing capability. Direct solution measurements that continually illuminate bulk samples in solution indicate that under high excitation power, nanotube photoluminescence emission remains stable while organic fluorophores photobleach (Fig. 6.3c) [67]. In a single-nanotube study, individual SWCNTs exposed to 6 kW/cm^2 laser excitation maintained steady photoluminescence emission (Fig. 6.3d) [15]. In comparison to the 20–50 mW lasers used for visible fluorescence studies using organic fluorophores, >1 W lasers are routinely used for nanotube imaging.

Third, the excited state lifetime of an exciton is very short (on the order of picoseconds, compared to nanoseconds for organic fluorophores) [26]. This results

in nanotube emission scaling linearly with laser intensity for direct excitation, upconversion [64], and off-resonance excitation (Fig. 6.3e) [65]. Combined, the short lifetime and photostability allow for the use of high-power laser excitation to compensate for the relative low quantum yield.

Further expanding the range of emitters is the recent advancement of introducing molecular defects [69] as organic color centers to tune the nanotube emission [70]. As seen in Fig. 6.3f, the emission peak of the (6,5) nanotube can be translated over 100 nm [68]. Additionally, when compared to other fluorophores, the SWCNT emission linewidth is narrow. As a result, 17 nanotube chiralities were simultaneously imaged in a 500 nm emission window, following excitation at a single wavelength (Fig. 6.3g) [15]. Without requiring spectral deconvolution techniques, methods exploiting this property could enable quantitative imaging in biological systems with unprecedented multiplicity.

6.3.3 Photoluminescence Modulation by Environment

A fundamental property of single-walled carbon nanotubes is the dependence of photoluminescence emission on the surrounding environment [2]. As each constituent carbon atom is on the nanotube surface and exposed to the environment, SWCNT emission is intrinsically sensitive to any perturbations on the nanotube surface [71]. This contrasts with solid nanoparticles where only a fraction of the constituent matter is on the nanoparticle surface. The current framework for signal transduction is based on an analyte–nanotube interaction either inducing (a) a change in the dielectric environment of the nanotube [72, 73], resulting in a change in emission wavelength (solvatochromism) [74, 75], (b) a charge transfer, which, depending on the relative redox potentials, can increase or decrease the intensity of emission, or (c) a combination of both dielectric and redox effects.

An early observation was that the emission spectrum can vary with the functionalization used to solubilize the nanotube, in addition to the solvent environment. Subsequent studies indicated that the SWCNT emission could be modulated by the interaction with various analytes, the contents of the inner nanotube volume, and other relevant characteristics of the environment. The first set of sensors worked in the solution phase [76] and were extended to surface-adsorbed single molecule applications [77–79]. In recent years, SWCNT optical sensors of small molecules, proteins, nucleic acids, lipids, and other classes of biomolecules that function in live cells, plants [80], and animals have been developed. Robust theoretical and experimental frameworks have been employed to develop sensors, using a variety of approaches including high-throughput screening [81] and thermodynamic models of surface interactions [82].

6.3.4 *Multimodal Functionalization of the Nanotube Structure*

The carbon nanotube structure can be functionalized to either modulate optical properties, or impart analyte sensing capabilities, or both. These functionalizations can be applied to three distinct regions of the carbon nanotube structure, i.e., the inner volume, the outer surface, and the two ends (Fig. 6.4a), and can be reversible and non-covalent or irreversible chemical modifications.

The internal volume of the nanotube can be filled or empty [83], and introducing different molecules (Fig. 6.4b) [84] within the endohedral volume [85] can enhance the photoluminescence quantum yield [86]. The general aim of these modifications is to improve and homogenize the optical properties of a population of SWCNT. Novel optical properties can be introduced via the generation of a new emission peak by stochastically placing chemically induced molecular defects (functioning as organic color centers) along the nanotube surface (Fig. 6.4c) [69], with the type and concentration of the defect determining the amplitude and wavelength of the defect emission peak [70].

For developing carbon nanotube optical reporters, the general approach is to create an interface on the nanotube surface that couples analyte detection with optical signal transduction. This interface can be a bifunctional polymer in a specific conformation on the nanotube surface, which both detects the analyte and modulates the nanotube optical response (Fig. 6.4d) [82]. Alternately, the polymer can have a distinct region for interacting with the analyte via, for example, hybridization (Fig. 6.4e) to a target nucleic acid [87]. In another application, the surface coverage of a stable nanotube-adsorbed polymer exposed the nanotube surface as an attractive

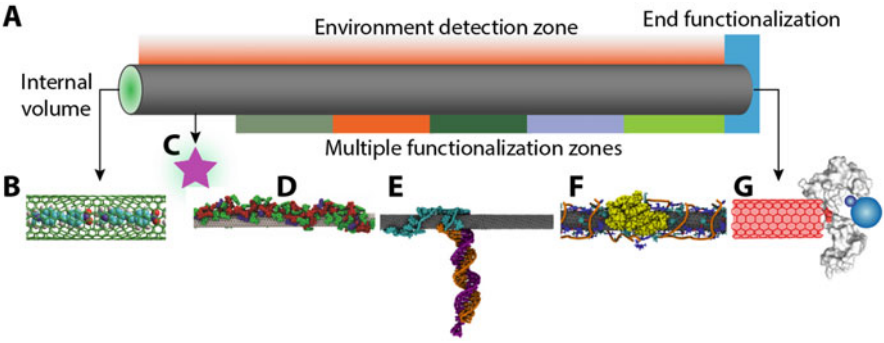

Fig. 6.4 Advantageous structural properties of SWCNTs. (**a**) Multiple independent molecular recognition elements can be engineered at various sites on the extended linear structure of the SWCNT. (**b**) Selectively controlling the internal volume can constrain the detection capabilities of the nanotube in changing the baseline intensity and emission wavelength [84]. (**c**) New emission peaks can be introduced via organic color centers [70]. (**d**) A highly specific polymer adsorbed to the nanotube surface can modulate the corona [82]. Perturbations of the environment due to, for example, (**e**) DNA hybridization [87] or (**f**) lipid binding along the nanotube length result in a change in the nanotube emission intensity or wavelength [88]. (**g**) The sensing moiety could be specifically located on the nanotube ends [89]

binding site for hydrophobic lipids (Fig. 6.4f) [88]. Specific chemical reactions to the nanotube ends [89] provide two additional binding sites that can be used in parallel (Fig. 6.4g).

6.3.5 Comparison to Other NIR Agents

Due to the optical advantages of bioimaging in the NIR window [90] of tissue-transparency [4], multiple classes of nanomaterials are being developed for biomedical applications [6, 91]. Concomitantly, organic fluorophores [92–94] and fluorescent proteins [95] have been engineered to emit at increasingly longer wavelengths, existing dyes are being tested for NIR-imaging applications [96] and new techniques for conjugating fluorophores to antibodies under development [97]. Depending on the applications, NIR agents including short-wave quantum dots and modified small-molecule dyes [98, 99] can have clear advantages and disadvantages [100]. In contrast to many of these imaging agents, the linear dimension of the SWCNT is potentially larger than the target of interest (though ultrashort SWCNTs are being developed) [101]. The major advantage of SWCNTs is the intrinsic multiplexed optical sensing ability, coupled with the novel biodistribution capability due to the small size and aspect ratio. Issues including potential toxicity (2.4) and nanomaterial non-uniformity (4.1) are discussed in other sections.

6.4 Instrumentation for Near Infrared Spectroscopy-Resolved Imaging

The extension of fluorescence-based optical imaging from the visible to the NIR wavelength range has accelerated with the availability of germanium and indium-gallium-arsenide (InGaAs) detectors, inexpensive NIR lasers and LEDs, and NIR-optimized optical components. These developments uniformly benefit the field of NIR imaging and general-purpose instruments are becoming readily available. In contrast to other spherical nanomaterials, SWCNTs have novel properties that require new imaging and analysis techniques.

6.4.1 New Imaging Tools

Three major challenges especially motivate the need for spectrally resolved imaging of single-walled carbon nanotubes. Firstly, the carbon nanotube aspect ratio of ~100–1000:1 is highly unusual and deviates significantly from the prototypical spherical material on which most analytical methods are based [11, 91]. For example, routine analytical techniques such as dynamic light scattering (DLS)

and zeta potential measurements base their results on the assumption that the source material is spherical [102]. In practice, only a limited number of techniques (including absorption, photoluminescence, and Raman spectroscopy [103, 104]) can be used to characterize the optical properties of an SWCNT sample.

Secondly, the physical characteristics—especially the length distribution—of an SWCNT sample is quite broad [105]. The majority of research applications use SWCNTs solubilized via sonication, which further complexifies the length distribution of the functionalized SWCNT material [106]. Though chromatographic methods to sort SWCNT samples exist, these are rarely used due to the loss of a significant fraction of the material [107]. As many of the optical properties [108] depend on parameters of the individual nanotube, including its length [109, 110], quality, defect density, how empty the inner volume is, and whether the ends are open or capped, analysis of an SWCNT sample requires characterizing each property of the heterogeneous nanomaterial as a distribution of linear rods [111, 112].

Thirdly, the chirality of the SWCNT is a highly critical parameter [113] that governs both optical (bandgap, excitation, and emission maximum) and physicochemical properties (such as stability of the functionalized nanomaterial [114], interactions with biomolecules, analyte sensing capability [115]). Resolving the property of interest as a function of chirality is highly advantageous and critical for fully understanding the engineered nanomaterial, for both fundamental research and biomedical applications.

In response to these challenges, researchers have developed novel analytical techniques to accurately interpret data acquired from linear SWCNTs. A majority of these techniques investigate properties of individual nanotubes to accurately characterize the distribution of parameters [116], including absorption cross sections [116–118], and mass-to-molarity conversion [119]. Optical techniques [103, 120] have the advantage of enabling measurements in solution [121], in vitro and in vivo. In the next section, we present the major optical imaging modalities that maximize both the data acquired and the range of biological systems where these techniques are used.

6.4.2 NIR Imaging of SWCNTs in Biological Systems

Imaging platforms developed for using SWCNT-based optical probes in complex biological systems have generally been motivated by the goal of observing either the intensity or the emission spectrum of specific nanotube chiralities. As carbon nanotubes exhibit solvatochromic (i.e., wavelength shifting) properties based on the local environment, spectral variations confer potentially useful information. Optical sensors based on this property have multiple technical advantages. For instance, as wavelength shift is an intensive quantity, it is independent of the concentration of the optical sensor. Additionally, using full spectra instead of intensity enables more sensitive signal separation from the background noise.

Multiple approaches to isolate the detected signal to a specific nanotube chirality have been successful. The ideal method would be performing the experiment with a single-chirality sample, as this would remove the actual source of any contaminating signal. A spectroscopic approach to optical gating used specific excitation wavelengths and limited observation to narrow optical windows which enabled the spectra of 12 nanotube chiralities to be acquired from live cells (Fig. 6.5a) [122]. In an innovative approach to imaging solvatochromic sensors in live cells, the emission intensity from a specific nanotube chirality was split at the peak wavelength using a dichroic mirror to obtain an intensity ratio that reflected the underlying wavelength shift (Fig. 6.5b) [123]. The one drawback to this split-emission imaging platform is the requirement of purchasing individual optical components for each chirality of interest. A probe-based portable spectroscopy instrument (Fig. 6.5c) was developed for acquiring data from SWCNTs known to localize at a specific organ within a mouse [124]. The advantage of a probe is the versatility of applications, where aiming the probe at SWCNT results in excitation and emission being detected from that specific region.

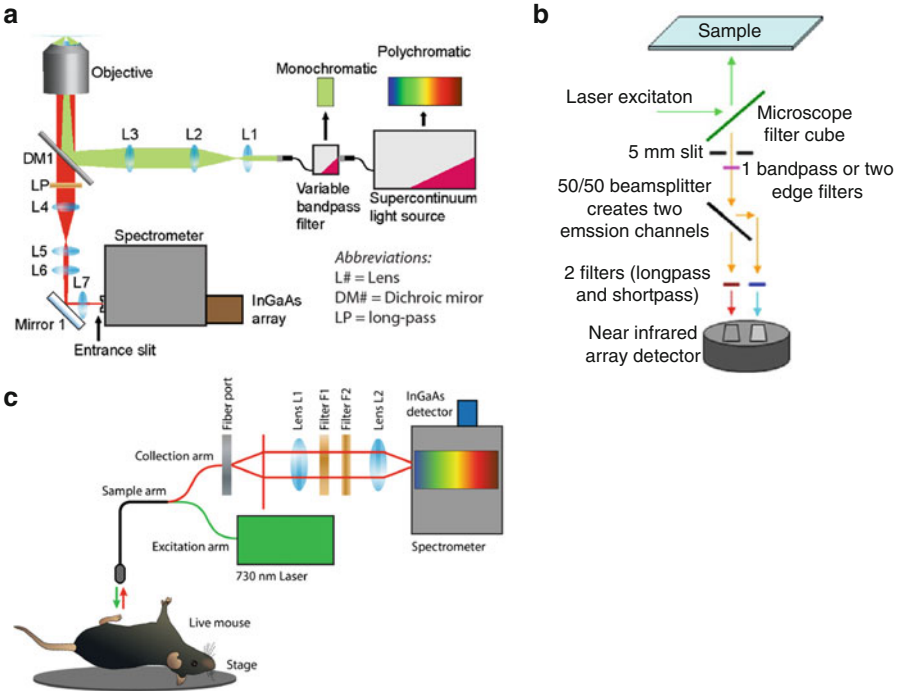

Fig. 6.5 Optical platforms for detecting solvatochromic changes in the nanotube emission in complex biological systems (**a**) High-magnification photoluminescence excitation–emission spectroscopy of nanotubes on a live cell [122]. (**b**) Separating the emission intensity above and below a specific wavelength to effectively detect an emission shift as a ratio of intensities [123]. (**c**) Acquisition of nanotube spectra from a live mouse using a fiber-optic probe system. Image kindly provided by LipidSense, Inc

6.5 Global NIR Hyperspectral Imaging

Spectral imaging is a family of optical techniques that combine spectroscopy with imaging [125]. Hyperspectral microscopy is a form of spectral imaging in which wavelength information is acquired for each pixel in a microscope field-of-view. Conceptually, hyperspectral data can be obtained either by sequentially acquiring the spectra from each pixel or row of pixels or by sequentially collecting the entire image at each wavelength band. Global hyperspectral imaging [126], a high-resolution optical technique used in astronomy and satellite-based remote sensing (Fig. 6.6a), was recently developed into a near infrared microscopy platform [15]. The core technology is a continuously tunable filter based on volume Bragg gratings (VBG) which is rotated with respect to the incoming full-spectrum image (Fig. 6.6b) to optically isolate each wavelength. The end result, referred to as a "hyperspectral cube," is a stack of monochromatic images corresponding to each wavelength band in the initial image (Fig. 6.6c). As a microscopy platform, hyperspectral imaging can be used for observing SWCNTs on a surface, in fixed tissues and in cells (Fig. 6.6d). Additionally, the VBG-based hyperspectral platform was recently applied for spectral imaging of carbon nanotube emission in a live mouse (Fig. 6.6e). Situated in the optical path between the emission and the detector, the VBG has also been integrated into existing NIR-imaging systems by multiple research groups.

6.5.1 Hyperspectral Imaging of SWCNTs in Biological Systems

The major advantage of NIR hyperspectral microscopy is the ability to collect an entire set of spectral parameters from material with single pixel resolution in complex biological systems, including live cells and small animals. In a model system of surfactant-encapsulated SWCNT adsorbed on a glass surface, hyperspectral data of an individual nanotube provides the photoluminescence intensity, center wavelength, and full-width at half-maximum for each pixel (Fig. 6.6d). Nanometrological measurements of spectral variations within a single nanotube, including direct observation of the emission spectrum from different regions of the same nanotube, on multiple nanotubes simultaneously, are relatively facile (Fig. 6.6e).

The set of single-wavelength images provided by hyperspectral imaging fundamentally requires a greater number of photons, and thus takes longer to experimentally acquire [15]. Additionally, approximately 50% of the emitted signal is reduced by the VBG. As each data cube is a stack of images in wavelength space, several images should be acquired in order to produce a single-wavelength image. If the sample is moving significantly during the data acquisition process, then wavelength artifacts can result if the speed of sample movement is significant compared to the rate at which the hyperspectral cube is acquired. Practically, this

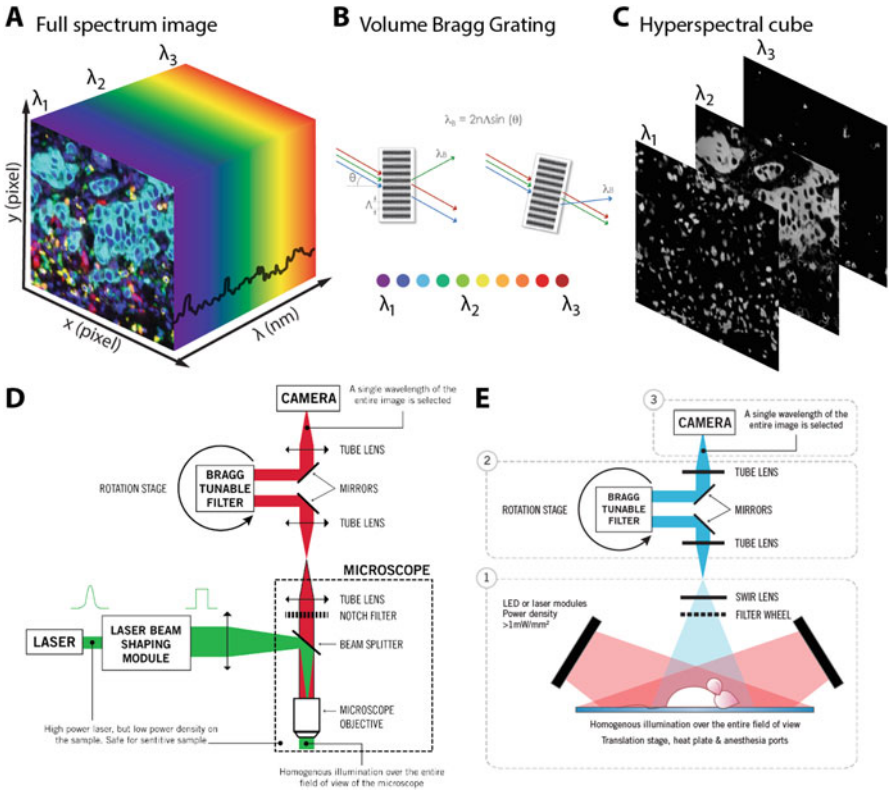

Fig. 6.6 Overview of hyperspectral microscopy with implementation (**a**) An experimentally acquired intensity image is fundamentally composed of photons at different wavelengths, and can be considered a set of images at each wavelength. (**b**) A volume Bragg grating (VBG) is an optical device that separates incident polychromatic light into its monochromatic components. (**c**) The result is a stack of monochromatic images corresponding to a single discrete wavelength, called the hyperspectral cube, and is a projection of the full-spectrum intensity image into wavelength space. (**d**) Individual SWCNTs on a glass surface observed at 150× magnification using a hyperspectral microscope, with single pixel intensity, wavelength, and full-width at half-maximum (FWHM) resolution, and (**e**) spectrum of the labeled pixels from (**d**). Optical platforms for global hyperspectral imaging: (**f**) Hyperspectral microscope schematic for imaging a sample compatible with a conventional inverted or upright fluorescence microscope. (**g**) A preclinical hyperspectral imager optimized for multiple band imaging of small animals in the NIR. Images in panels **a**, **b**, **c**, **f**, and **g** kindly provided by "Photon etc."

problem can be resolved by imaging at lower magnifications, which limits the range of pixels a nanotube can traverse. For highly optimized applications which focus on the wavelength-shift of a specific chirality of interest, hyperspectral imaging will generally be most efficient in terms of signal and acquisition time.

6.5.2 *Applications for Characterizing Individual Carbon Nanotubes*

The photoluminescence emission from an unsorted sample of SWCNTs consists of emission from multiple wavelength bands, corresponding to the emission spectrum from each individual carbon nanotube. In a model system of DNA-functionalized SWCNTs adsorbed on a glass surface, hyperspectral data of an individual nanotube provides the photoluminescence intensity, center wavelength, and full-width at half-maximum for each pixel present (Fig. 6.7a). Nanometrological measurements of spectral variations within a single nanotube, including direct observation of the emission spectrum from different regions of the same nanotube, are easy to perform (Fig. 6.7b).

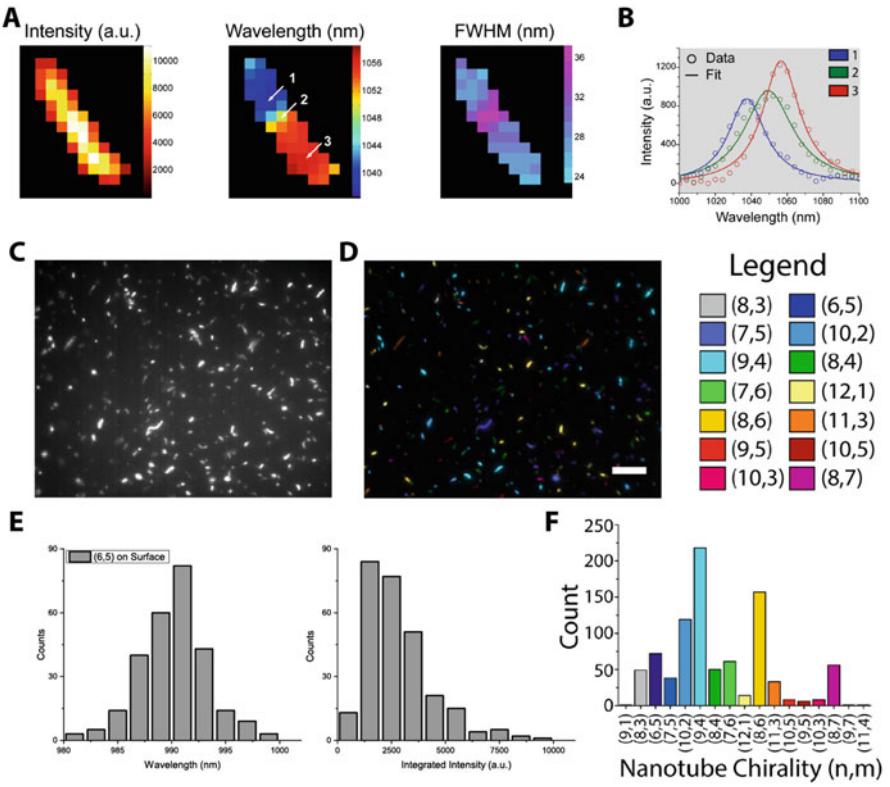

Fig. 6.7 Hyperspectral microscopy of individual SWCNTs on a surface. (**a**) Individual SWCNTs on a glass surface, observed at 150× magnification using a hyperspectral microscope, with single pixel intensity, wavelength, and full-width at half-maximum (FWHM) resolution, and (**b**) spectrum of the labeled pixels from (**a**). (**c**) Near infrared broadband intensity image of SWCNTs in a field-of-view [15]. (**d**) False-colored image where each SWCNT in (**c**) is mapped to a specific chirality (**e**) Wavelength and intensity distribution of single nanotubes of the specific (6,5) chirality. (**f**) The chirality distribution of the emissive nanotube population in the starting sample [15]

Single-nanotube analyses of all SWCNTs in a field of view allow the ensemble properties to be accurately characterized. As shown in the broadband intensity image of an SWCNT population adsorbed on a surface (Fig. 6.7c), the emission spectra acquired from each nanotube can be assigned a specific chirality (Fig. 6.7d). In this specific application, a k-means algorithm was used to assign each nanotube to one of 17 possible chiralities. Notably, k-means requires accurate knowledge of the wavelength range allotted to each chirality of interest—in novel chemical environments, the algorithm could be less accurate. Furthermore, the wavelength and intensity distribution (Fig. 6.7e) can be obtained for each chirality present in the starting sample (Fig. 6.7f). In the subsequent section, we present how such precise measurements can also be performed in significantly complex biological systems.

6.6 Spectral Imaging in Live Cells

Over the past 10 years, multiple applications of SWCNTs as imaging and sensing agents have been developed for use in live cells [9]. The ability to directly observe individual nanotubes over extended time scales has proven to be an advantage over other fluorescent probes. Though organic fluorophores perform well as imaging agents in cells, in order to function as sensors, they generally need to be coupled to a signal-transduction mechanism. A key advantage of nanotubes is their ability to play the dual role of analyte detection and signal transduction. This property has been exploited to develop carbon nanotube optical reporters for chemotherapeutic drugs [127], riboflavin [82], lysosomal lipids [88], and cell-surface potential [122], amongst others.

6.6.1 Applications in Live Cells

Generalized spectral imaging, i.e., the ability to acquire the spectra emitted by each emissive nanotube at each spatial location, provides two independent forms of information. Combined, the information obtained leads to: (a) knowledge of the spatial location of the nanotube which may allow the photoluminescence emission to report on some property of the immediate environment. For example, the shift in emission wavelength of a solvatochromic sensor for riboflavin, measured as an intensity ratio above and below a certain wavelength value, changes as the sensor interacts with the target analyte [82]. In this application, the riboflavin concentration gradient across a live cell was visually mapped as a function of time (Fig. 6.8a). A more in-depth example, focusing on lipid accumulation specifically within the endolysosomes, is discussed in Sect. 6.6.2. (b) Definitive knowledge of the environment-dependent spectra enables the spatial location of the nanotube to be determined. In the application shown (Fig. 6.8b), the nanotube was

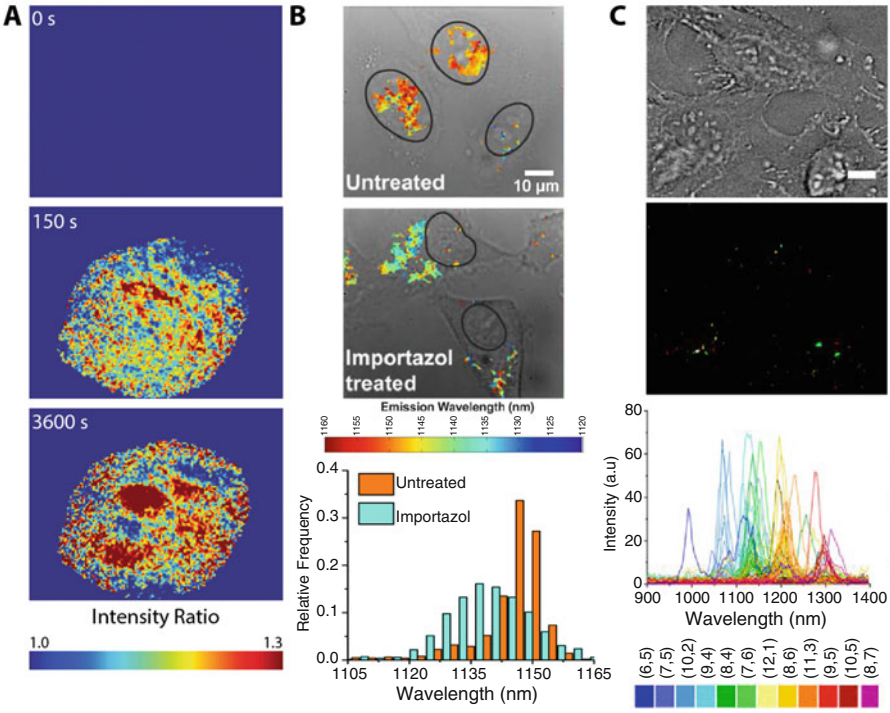

Fig. 6.8 Applications of NIR spectral imaging of carbon nanotubes in live cells. (**a**) Time course of intensity-ratio images of a riboflavin SWCNT sensor in cells, following the addition of riboflavin, where the ratio of intensity above and below a specific wavelength is used to image the shift of one nanotube chirality [82]. (**b**) Emission wavelength of a nanotube sensor that differs in the nucleus and the cytoplasm (figures adapted for use with permission) [128]. (**c**) False color image showing the emission of several nanotube chiralities in live mammalian cells, in addition to spectra from individual regions-of-interest [15]

engineered so that its emission would be at longer wavelengths in the highly charged nucleus [128]. By observing the emission of the sensor in live cells, the nanotube environment could definitely be determined as being nuclear or not, via the spectra alone.

The major advantage of hyperspectral imaging is the potential for scaling these capabilities to over a dozen optical sensors, by acquiring the spectra from every chirality present in each pixel. In the demonstration presented in Fig. 6.8c, a multi-chirality sample of surfactant-encapsulated SWCNTs was imaged within a mammalian cell using hyperspectral microscopy [15]. From the spectra, parameters of individual nanotubes such as center wavelength, FWHM, and intensity, in addition to population-level parameters, including the chirality distribution and relative fluorescence modulation, can be analyzed in live cells.

6.6.2 *Spectral Imaging of a Sensor for Endolysosomal Lipids*

We focus here on the use of hyperspectral imaging for a specific application, the development and application of a carbon nanotube optical reporter for lipids [88]. In this work, solution-phase spectroscopy was used to initially screen single-chirality:DNA-sequence combinations, followed by hyperspectral microscopy of single nanotubes adsorbed on a surface for in-depth characterization of the eventual hit. To experimentally observe the solvatochromic sensor in live cells, hyperspectral microscopy was leveraged to characterize the emission wavelength at different resolutions including within single pixels, across individual organelles within one cell, across different cells, and as a function of pharmacological perturbations, time and other biological factors.

The sensor was empirically validated in live cells by visually comparing and then quantifying the hyperspectral images. As shown in Fig. 6.9a, the overlays of peak center wavelength from each emissive pixel over a transmitted light

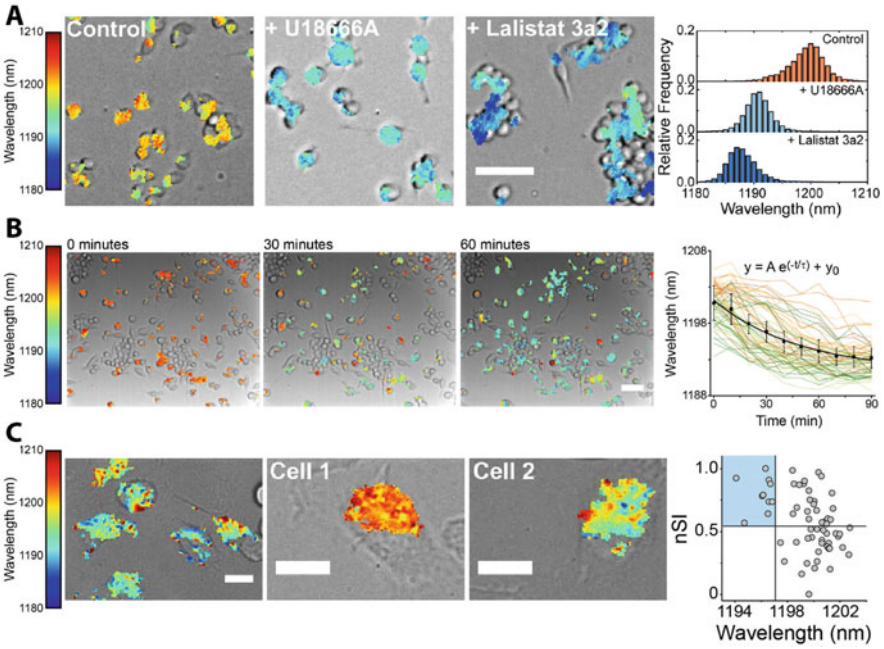

Fig. 6.9 Hyperspectral imaging of an endolysosomal lipid sensor in live cells. (**a**) Emission wavelength maps in live cells from control RAW macrophages, and cells treated with U18666A and Lalistat 3a2, which inhibit proteins involved with lysosomal lipid processing. Scale bar is 50 μm. (**b**) Time course of hyperspectral images from RAW macrophages following the addition of acetylated LDL and U18666A, with the single-cell kinetics of sensor emission. Scale bar is 50 μm. (**c**) High-resolution map of the lipid sensor in bone marrow-derived macrophages, focusing on two typical cells that are used to derive the normalized Simpson's index (nSI). Scale bar is 10 μm

image of the cells are blue-shifted in cells treated with U18666A and Lalistat, two drugs that induce lipid accumulation by blocking the function of specific lysosomal proteins required for lipid processing. These images are quantitative, as histograms describing this equilibrium lysosomal lipid content distribution can be directly compared across various conditions. To dynamically observe the kinetics of lipid accumulation, the mean emission wavelength of each cell was tracked as a function of time (Fig. 6.9b). Live cells are mobile, and the extent of movement depends on various factors including the type of cell, temperature, and nutrient environment of the cell. The movement of cells containing nanotubes during the data acquisition window can result in inaccurate boundary detection of each cell, a change in the number of pixels a cell covered, and defocusing errors due to the three-dimensional shape of the cells. These experimental artifacts compromise emission intensity measurements, whereas the emission wavelength obtained by fitting the data remains accurate.

High-resolution lipid maps were analyzed to quantify the endolysosomal lipids within individual cells. In the 100× magnification images (Fig. 6.9c), regions of different colors are visible within the same cell. For each cell (identified via the transmitted light image), tabulated reporter emission values for each pixel within the cell were used to calculate (1) the mean emission value for the cell, and (2) the normalized Simpson's index (nSI)—a metric modified from ecology, where it is used to describe the species diversity in an ecosystem. In this application, nSI reflected the degree of "color" variation within a cell, i.e., intracellular heterogeneity. Interestingly, a scatter plot of mean reporter value vs. the nSI for each cell helped identify cells in the top-left quadrant, where cells were both "blue-shifted" and showed high nSI. These cells with mostly lipid-filled lysosomes still contained lysosomes that remained relatively lipid-free. Identifying novel population subsets by this phenotype highlights the advantage of measuring wavelength in addition to intensity, and decouples local sensor concentration from the sensor readout.

6.7 Spectral Imaging in Vivo

Biomedical research in small animals, though technically more challenging and requiring significantly more resources than investigations in cells, is far more informative and predictive of human biology. From our perspective, a small animal presents three major challenges: (1) The ability of light to travel through tissue is severely limited, and this reduces both excitation power at the emitter and detection efficiency of the emitted signal; (2) As an animal has intrinsic movement (cardiac and respiratory motion) and complex interaction between various tissues with different wavelengths of light, accurately separating the signal from the noise is complex; (3) The number of fluorophores available, optical components, detectors, etc. are typically optimized for the visible wavelength range. Though NIR light is theoretically better suited for facile non-invasive small-animal imaging than visible light, only recently have multiple research fields focused on exploiting this imaging modality.

6.7.1 Technical Challenges to NIR In Vivo Imaging

NIR imaging of the available NIR optical emitters, including small molecules [92] and fluorescent proteins [93], nanoparticles including quantum dots, nanodiamonds, metal clusters, and SWCNTs, is generally performed using intensity alone. Background subtraction is performed on an image by thresholding all pixels above a certain intensity value. While the detected intensity value naturally depends on the concentration of SWCNTs, as noted in Sect. 6.4.1, multiple intrinsic factors affect the absolute emission intensity of an SWCNT. Depending on how close the excitation wavelength is to being on-resonance, the detected emission intensity from different SWCNT chiralities present in an unsorted sample can vary significantly.

We believe hyperspectral imaging in live animals significantly enhances the ability to discern emission from background noise. Experimentally, we observe that each source of background signal—for example, scattered light resulting from the excitation laser interacting with the skin of a mouse, or residual NIR autofluorescence in the liver—results in an emission profile. While the amplitude of this emission varies from animal-to-animal and tissue-to-tissue, the characteristic shape remains constant. This allows sophisticated background subtraction and signal processing algorithms that use the functional form of the background signal. A similar computational approach to spectral triangulation has been developed to localize SWCNT emitters in 3D [129, 130].

6.7.2 Spectral Imaging in Complex Biological Systems

In this section, we highlight applications of hyperspectral imaging of SWCNTs in fixed tissues and live animals, using the instrumentation introduced in Sect. 6.5. The first report established the capability of multiplexed imaging of SWCNTs in fixed tissues, before extending hyperspectral imaging to live zebrafish and live mice. Surfactant-functionalized nanotubes were subcutaneously injected under the skin of a hairless SK1 mouse, before the animal was sacrificed, and the excised tissue processed into slices. Using hyperspectral microscopy, NIR photoluminescence was observed from SWCNTs (Fig. 6.10a) and 8 chiralities could be identified in intact murine tissue by their characteristic emission peaks (Fig. 6.10b). Additionally, the presence of single peaks confirmed the nanotubes as being individually dispersed in vivo, and the lack of multiple peaks indicated that the SWCNTs were not being sequestered in a specific location, or aggregating within the mouse. Next, SWCNTs introduced to 3-day-old zebrafish embryos via cardinal vein injection were imaged after 30 minutes. Localized within the zebrafish vessel wall (Fig. 6.10c), individual SWCNT chiralities were identified by their emission spectra (Fig. 6.10d) and significantly, no nanotube aggregates (characterized by multiple emission peaks from one ROI) were observed in vivo.

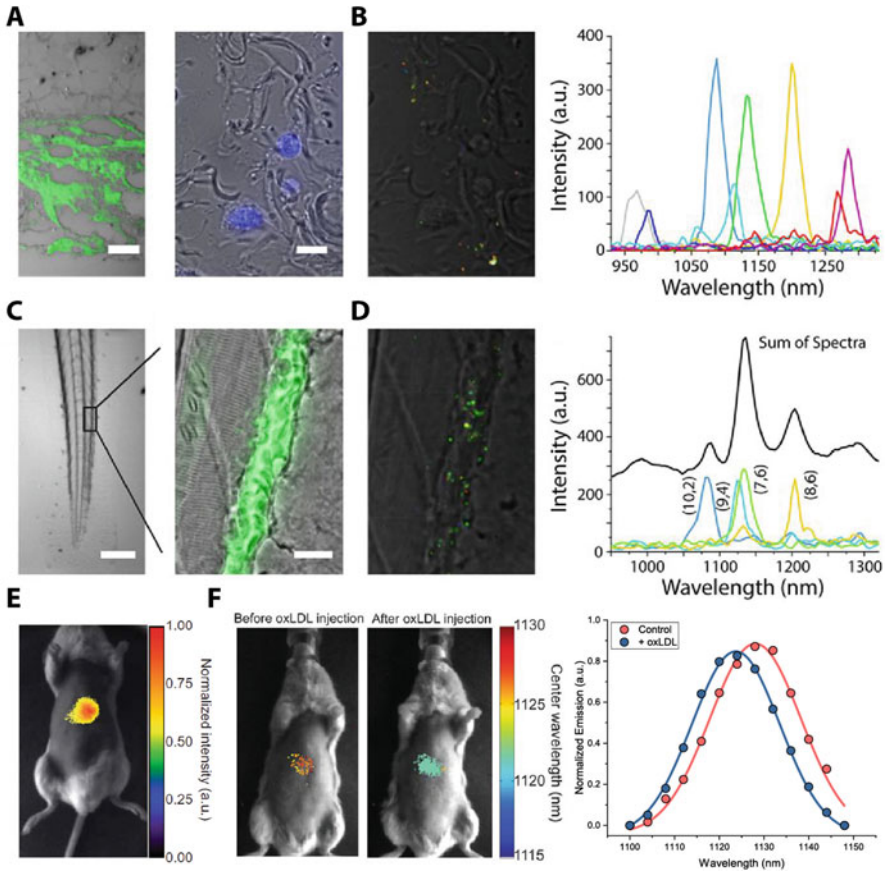

Fig. 6.10 Spectral imaging applications in vivo and ex vivo. (**a**) Multiplexed imaging of SWCNTs in fixed murine tissue, with NIR photoluminescence in green (scale bar is 50 μm) and the nuclei stained with DAPI in blue (scale bar is 50 μm). (**b**) Hyperspectral image with individual SWCNT false-colored and overlaid over tissue, along with the individual emission spectrum. (**c**) Emissive nanotubes localized in a live zebrafish tail fin (Scale bar is 200 μm) are colocalized with dextran (green, scale bar is 20 μm). (**d**) Hyperspectral image of distinct SWCNT chiralities within the zebrafish tail fin. (**e**) Photoluminescence emission intensity from a DNA-nanotube optical reporter overlaid over a live mouse. (**f**) Hyperspectral images false-colored by the emission peak of the lipid reporter, following the injection of oxidized-LDL, and the corresponding emission spectrum

6.7.3 Spectral Imaging of the Lipid Sensor in Live Animals

We focus on the development of a nanosensor for non-invasive optical detection of lipids accumulating in the lysosomes of the liver macrophages in a live mouse. As first introduced in Sect. 6.6.2, hyperspectral imaging was used to determine the localization of the sensor and test its functioning in live cells. In a live mouse, the injected nanosensor was imaged with the hyperspectral small-animal imager,

and found to localize specifically in the liver (Fig. 6.10e). The functionality was tested by observing the sensor wavelength following the injection of an analyte (oxidized LDL, a modified lipoprotein which accumulates in liver macrophages). Comparing the hyperspectral image indicated the sensor emission to have blue-shifted in response to lipid accumulation (Fig. 6.10f). Notably, the clear spectra obtained is a result of accurate baseline subtraction, where the background is modeled as a function in wavelength space, based on data acquired from multiple control animals.

6.8 Conclusion

We believe this is an exciting period for NIR imaging and sensing. As the field continues to mature, the transition of nanomaterials with exciting optical properties to well-understood and thoroughly characterized engineered biomedical tools provides a new set of challenges and opportunities. The use of carbon nanotubes for biomedical imaging and sensing applications has been built upon the progress made in nanotube processing and separation, the understanding of techniques to modulate their chemical and photophysical properties, and the development of new imaging and spectroscopic instrumentation. As with any novel nanomaterial, several challenges need to be simultaneously addressed for SWCNTs to reach their full potential.

6.8.1 The Challenges of Molecular Identity, Standardization, and Biocompatibility

Although promising due to their optical properties and recent advancements, the application of carbon nanotubes in biology and medicine still faces significant challenges. The relatively broad class of materials that are referred to as nanotubes but differ significantly in their material specifications (from synthesis to processing to functionalization) coupled with the dependence of both optical properties and biological interactions on these material specifications are challenging to synthesize into a cohesive framework for understanding SWCNTs. In particular, the biocompatibility of SWCNTs has been hard to define, with the complex interactions between the various engineered nanomaterials and biological test systems resulting in diverging findings from toxicity studies.

The starting material for producing single-walled carbon nanotubes, especially for bioimaging applications, is generally a carbon nanotube powder (Fig. 6.11a), obtained via a number of different production methods [131–133]. These materials differ in their starting SWCNT content, carbonaceous content, and metallic impurities, and therefore need to be processed differently in order to obtain a

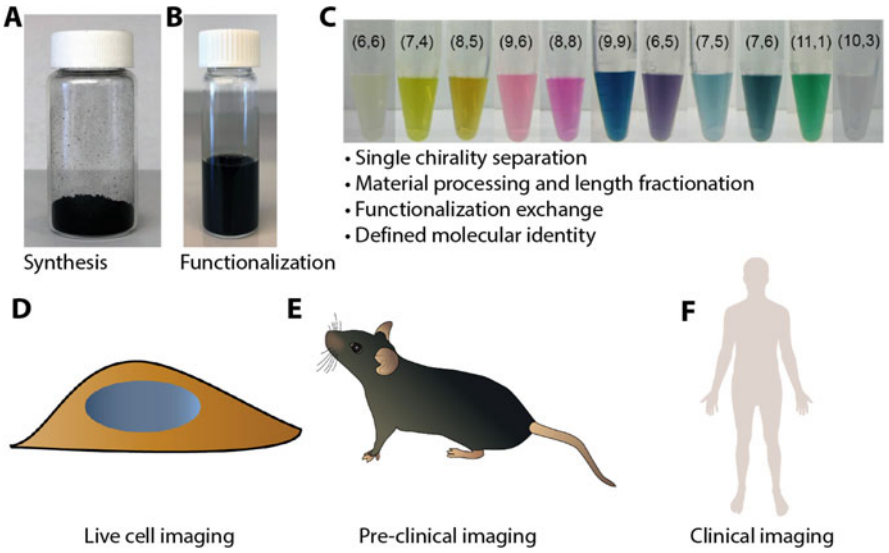

Fig. 6.11 Stages in the application of SWCNTs for biomedicine. (**a**) The starting nanomaterial is a dry soot. (**b**) Functionalization methods produce an aqueous SWCNT solution (image kindly provided by Daniel Tylawsky). (**c**) Isolated individual SWCNT chiralities in solution. (**d**) Techniques and procedures to enable nanotube interactions with live cells to be observed, quantified, and reported. (**e**) Preclinical research in small animals following the standards developed for translational biomedical research. (**f**) For carbon nanotubes to deliver on their potential for biomedicine, each of the preceding steps must be successfully executed with the clear goal of generating a robust and reliable development path leading to the first-in-human application of carbon nanotube spectral imaging

comparable end product. For biological applications, the end product is generally a water-soluble engineered nanomaterial with functionalization optimized for the particular application (Fig. 6.11b). Although new methods to synthesize nanotubes of a specific chirality are under development, separation techniques are currently the primary source of single-chirality nanotube preparations. A number of scalable techniques have emerged for isolating single-nanotube species (Fig. 6.11c), with some methods favoring yield and scalability while others optimize for sample purity. The resulting materials from these techniques have non-covalent functionalizations which can be easily exchanged to facilitate downstream applications. The specific processing path applied to each nanomaterial construct must be carefully defined and characterized, before exploring nanotube interactions with biological systems.

The interface of nanotechnology and biology is complex, and requires a new framework for experimental characterization and reporting [51]. Using a set of best practices, proposed for example, in the MIRIBEL (Minimum Information Reporting in the Bio-Nano Experimental Literature) framework, the experimental tools specifically developed for nanotube research would improve our understanding of nano-bio interactions. In live cells (Fig. 6.11d), labeling SWCNTs with visible fluorophores

will allow a large set of fluorescence imaging techniques (for example, localization in 3D, quantitative colocalization, or optically detecting dim or metallic nanotubes) routinely used in cell biology to supplement nanotube-specific analytical methods. In small animals (Fig. 6.11e), as the number of analytical techniques capable of in vivo and ex vivo characterization of SWCNTs is limited, the NIR-emission from photoluminescent nanotubes must be leveraged for understanding their adsorption, distribution, metabolism, and excretion (ADME). The initial findings from optical imaging can help guide subsequent studies using pharmacokinetic techniques. The in vivo compatible instruments introduced in Sects. 6.4 and 6.5 will be vital for this objective.

One consequence of the broad nanomaterial identity and lack of standardized analysis techniques is the unclear status of SWCNT biocompatibility. Results from experiments using multi-walled or single-walled carbon nanotubes, with different sizes and functionalizations, are often conflated. Similarly, the specific method of measuring SWCNT concentration can provide significantly different conclusions on the nanotube safety profile. A naive question of the form, "are nanotubes safe," cannot be answered. Instead, each version of the engineered nanomaterial needs to be carefully characterized and results reported in a standardized method that facilitates direct quantitative comparison with previous findings. Our suggestions above are guided by the overarching goal of employing carbon nanotube optical reporters for a broad range of basic research and biomedical applications in humans. Necessarily, the level of rigor required for the latter is significantly higher than expected for laboratory research.

6.8.2 Crossroad for Nanotubes: Tool for Basic Research and Translational Biomedicine

To maximize their utility as optical sensing agents, we propose the need of a library of well-characterized carbon nanotube complexes, with defined opto-physical properties and modular options for subsequent chemical functionalizations. For a researcher, designing a carbon nanotube optical reporter for a specific application would require answering the following questions: how can the analyte recognition element be conjugated to the nanotube, how can the nanotube be targeted to the organ, cell, or organelle of interest, and which nanotube (chirality, processing, functionalization) will maximize selectivity and sensitivity in the relevant chemical environment? Whether to report on fundamental biological processes, to accelerate drug-discovery efforts, as tools for non-invasive optical imaging of small animals in preclinical research, or potentially in humans, there are multiple unmet needs in the biomedicine pathway that could successfully be addressed using single-walled carbon nanotubes.

References

1. Hong G, Diao S, Antaris AL, Dai H (2015) Carbon nanomaterials for biological imaging and nanomedicinal therapy. Chem Rev 115:10816–10906
2. Pan J, Li F, Choi JH (2017) Single-walled carbon nanotubes as optical probes for bio-sensing and imaging. J Mater Chem B 5:6511–6522
3. Jacques SL (2013) Optical properties of biological tissues: a review. Phys Med Biol 58:R37–R61
4. Cheong WF, Prahl SA, Welch AJ (1990) A review of the optical properties of biological tissues. IEEE J Quantum Electron 26:2166–2185
5. Won N et al (2012) Imaging depths of near-infrared quantum dots in first and second optical windows. Mol Imaging 11:338–352
6. Hemmer E, Benayas A, Légaré F, Vetrone F (2016) Exploiting the biological windows: current perspectives on fluorescent bioprobes emitting above 1000 nm. Nanoscale Horiz 1:168–184
7. Hong G, Antaris AL, Dai H (2017) Near-infrared fluorophores for biomedical imaging. Nat Biomed Eng 1:0010
8. Li Y (2017) The quarter-century anniversary of carbon nanotube research. ACS Nano 11:1–2
9. Farrera C, Torres Andón F, Feliu N (2017) Carbon nanotubes as optical sensors in biomedicine. ACS Nano 11:10637–10643
10. Jena PV, Galassi TV, Roxbury D, Heller DA (2017) Review—progress toward applications of carbon nanotube photoluminescence. ECS J Solid State Sci Technol 6:M3075–M3077
11. Segawa Y, Ito H, Itami K (2016) Structurally uniform and atomically precise carbon nanostructures. Nat Rev Mater 1:15002
12. Dresselhaus MS, Dresselhaus G, Jorio A, Filho AGS, Saito R (2002) Raman spectroscopy on isolated single wall carbon nanotubes. Carbon 19
13. Bachilo SM (2002) Structure-assigned optical spectra of single-walled carbon nanotubes. Science 298:2361–2366
14. Ao G, Streit JK, Fagan JA, Zheng M (2016) Differentiating left- and right-handed carbon nanotubes by DNA. J Am Chem Soc 138:16677–16685
15. Roxbury D et al (2015) Hyperspectral microscopy of near-infrared fluorescence enables 17-chirality carbon nanotube imaging. Sci Rep 5:14167
16. Prasek J et al (2011) Methods for carbon nanotubes synthesis—review. J Mater Chem 21:15872
17. Liu B, Wu F, Gui H, Zheng M, Zhou C (2017) Chirality-controlled synthesis and applications of single-wall carbon nanotubes. ACS Nano 11:31–53
18. Sanchez-Valencia JR et al (2014) Controlled synthesis of single-chirality carbon nanotubes. Nature 512:61–64
19. Yang F et al (2014) Chirality-specific growth of single-walled carbon nanotubes on solid alloy catalysts. Nature 510:522–524
20. Huang YY, Terentjev EM (2012) Dispersion of carbon nanotubes: mixing, sonication, stabilization, and composite properties. Polymers 4:275–295
21. Naumov AV et al (2009) Quantifying the semiconducting fraction in single-walled carbon nanotube samples through comparative atomic force and photoluminescence microscopies. Nano Lett 9:3203–3208
22. Nogaj LJ et al (2015) Bright fraction of single-walled carbon nanotubes through correlated fluorescence and topography measurements. J Phys Chem Lett 6:2816–2821
23. O'Connell MJ (2002) Band gap fluorescence from individual single-walled carbon nanotubes. Science 297:593–596
24. Wang F (2005) The optical resonances in carbon nanotubes arise from excitons. Science 308:838–841
25. Ma Y-Z, Valkunas L, Bachilo SM, Fleming GR (2005) Exciton binding energy in semiconducting single-walled carbon nanotubes. J Phys Chem B 109:15671–15674

26. Amori AR, Hou Z, Krauss TD (2018) Excitons in single-walled carbon nanotubes and their dynamics. Annu Rev Phys Chem 69:81–99
27. Hagen A, Hertel T (2003) Quantitative analysis of optical spectra from individual single-wall carbon nanotubes. Nano Lett 3:383–388
28. Weisman RB, Bachilo SM (2003) Dependence of optical transition energies on structure for single-walled carbon nanotubes in aqueous suspension: an empirical Kataura plot. Nano Lett 3:1235–1238
29. Zheng M (2018) Structure-defined DNA-carbon nanotube hybrids and their applications. ECS Trans 85:511–517
30. Zheng M (2017) Sorting carbon nanotubes. Top Curr Chem 375:13
31. Green AA, Hersam MC (2011) Nearly single-chirality single-walled carbon nanotubes produced via orthogonal iterative density gradient ultracentrifugation. Adv Mater 23:2185–2190
32. Liu H, Nishide D, Tanaka T, Kataura H (2011) Large-scale single-chirality separation of single-wall carbon nanotubes by simple gel chromatography. Nat Commun 2:309
33. Yomogida Y et al (2016) Industrial-scale separation of high-purity single-chirality single-wall carbon nanotubes for biological imaging. Nat Commun 7:12056
34. Fagan JA et al (2014) Isolation of specific small-diameter single-wall carbon nanotube species via aqueous two-phase extraction. Adv Mater 26:2800–2804
35. Subbaiyan NK et al (2015) Bench-top aqueous two-phase extraction of isolated individual single-walled carbon nanotubes. Nano Res 8:1755–1769
36. Tu X, Manohar S, Jagota A, Zheng M (2009) DNA sequence motifs for structure-specific recognition and separation of carbon nanotubes. Nature 460:250–253
37. Ao G, Khripin CY, Zheng M (2014) DNA-controlled partition of carbon nanotubes in polymer aqueous two-phase systems. J Am Chem Soc 136:10383–10392
38. Streit JK, Fagan JA, Zheng M (2017) A low energy route to DNA-wrapped carbon nanotubes via replacement of bile salt surfactants. Anal Chem 89:10496–10503
39. Ong L-C, Chung FF-L, Tan Y-F, Leong C-O (2016) Toxicity of single-walled carbon nanotubes. Arch Toxicol 90:103–118
40. Ema M, Gamo M, Honda K (2016) A review of toxicity studies of single-walled carbon nanotubes in laboratory animals. Regul Toxicol Pharmacol 74:42–63
41. Pan H, Lin Y-J, Li M-W, Chuang H-N, Chou C-C (2011) Aquatic toxicity assessment of single-walled carbon nanotubes using zebrafish embryos. J Phys Conf Ser 304:012026
42. Jin S, Wijesekara P, Boyer PD, Dahl KN, Islam MF (2017) Length-dependent intracellular bundling of single-walled carbon nanotubes influences retention. J Mater Chem B 5:6657–6665
43. Wu L et al (2014) Tuning cell autophagy by diversifying carbon nanotube surface chemistry. ACS Nano 8:2087–2099
44. Elgrabli D et al (2015) Carbon nanotube degradation in macrophages: live nanoscale monitoring and understanding of biological pathway. ACS Nano 9:10113–10124
45. Andersen AJ et al (2013) Single-walled carbon nanotube surface control of complement recognition and activation. ACS Nano 7:1108–1119
46. Ge C et al (2011) Binding of blood proteins to carbon nanotubes reduces cytotoxicity. Proc Natl Acad Sci 108:16968–16973
47. Singh AV et al (2014) Carbon nanotube-induced loss of multicellular chirality on micropatterned substrate is mediated by oxidative stress. ACS Nano 8:2196–2205
48. Bussy C et al (2015) Microglia determine brain region-specific neurotoxic responses to chemically functionalized carbon nanotubes. ACS Nano 9:7815–7830
49. Gao Z, Varela JA, Groc L, Lounis B, Cognet L (2016) Toward the suppression of cellular toxicity from single-walled carbon nanotubes. Biomater Sci 4:230–244
50. Zhu W et al (2016) Nanomechanical mechanism for lipid bilayer damage induced by carbon nanotubes confined in intracellular vesicles. Proc Natl Acad Sci 113:12374–12379
51. Alidori S et al (2017) Carbon nanotubes exhibit fibrillar pharmacology in primates. PLoS One 12:e0183902

52. Wang X et al (2016) Toxicological profiling of highly purified metallic and semiconducting single-walled carbon nanotubes in the rodent lung and *E. coli*. ACS Nano 10:6008–6019
53. Wang Y, Bahng JH, Che Q, Han J, Kotov NA (2015) Anomalously fast diffusion of targeted carbon nanotubes in cellular spheroids. ACS Nano 9:8231–8238
54. Jena PV et al (2016) Photoluminescent carbon nanotubes interrogate the permeability of multicellular tumor spheroids. Carbon 97:99–109
55. Godin AG et al (2017) Single-nanotube tracking reveals the nanoscale organization of the extracellular space in the live brain. Nat Nanotechnol 12:238–243
56. Bhirde AA et al (2014) Targeted therapeutic nanotubes influence the viscoelasticity of cancer cells to overcome drug resistance. ACS Nano 8:4177–4189
57. Alidori S et al (2016) Deconvoluting hepatic processing of carbon nanotubes. Nat Commun 7:12343
58. Ruggiero A et al (2010) Paradoxical glomerular filtration of carbon nanotubes. Proc Natl Acad Sci 107:12369–12374
59. Demirer GS et al (2019) High aspect ratio nanomaterials enable delivery of functional genetic material without DNA integration in mature plants. Nat Nanotechnol
60. Kwak S-Y et al (2019) Chloroplast-selective gene delivery and expression in planta using chitosan-complexed single-walled carbon nanotube carriers. Nat Nanotechnol
61. Pansare VJ, Hejazi S, Faenza WJ, Prud'homme RK (2012) Review of long-wavelength optical and NIR imaging materials: contrast agents, fluorophores, and multifunctional nano carriers. Chem Mater 24:812–827
62. Ju S-Y, Kopcha WP, Papadimitrakopoulos F (2009) Brightly fluorescent single-walled carbon nanotubes via an oxygen-excluding surfactant organization. Science 323:1319–1323
63. Lefebvre J, Austing DG, Bond J, Finnie P (2006) Photoluminescence imaging of suspended single-walled carbon nanotubes. Nano Lett 6:1603–1608
64. Akizuki N, Aota S, Mouri S, Matsuda K, Miyauchi Y (2015) Efficient near-infrared up-conversion photoluminescence in carbon nanotubes. Nat Commun 6:8920
65. Danné N et al (2018) Comparative analysis of photoluminescence and upconversion emission from individual carbon nanotubes for bioimaging applications. ACS Photonics 5:359–364
66. Iverson NM et al (2013) In vivo biosensing via tissue-localizable near-infrared-fluorescent single-walled carbon nanotubes. Nat Nanotechnol 8:873–880
67. Boghossian AA et al (2011) Near-infrared fluorescent sensors based on single-walled carbon nanotubes for life sciences applications. ChemSusChem 4:848–863
68. Kwon H et al (2016) Molecularly tunable fluorescent quantum defects. J Am Chem Soc 138:6878–6885
69. Piao Y et al (2013) Brightening of carbon nanotube photoluminescence through the incorporation of sp3 defects. Nat Chem 5:840–845
70. Kim M et al (2018) Mapping structure-property relationships of organic color centers. Chem 4:2180–2191
71. Hirana Y, Tanaka Y, Niidome Y, Nakashima N (2010) Strong micro-dielectric environment effect on the band gaps of (n,m) single-walled carbon nanotubes. J Am Chem Soc 132:13072–13077
72. Larsen BA et al (2012) Effect of solvent polarity and electrophilicity on quantum yields and solvatochromic shifts of single-walled carbon nanotube photoluminescence. J Am Chem Soc 134:12485–12491
73. Walsh AG et al (2008) Scaling of exciton binding energy with external dielectric function in carbon nanotubes. Phys E Low-Dimens Syst Nanostruct 40:2375–2379
74. Choi JH, Strano MS (2007) Solvatochromism in single-walled carbon nanotubes. Appl Phys Lett 90:223114
75. Gao J, Gomulya W, Loi MA (2013) Effect of medium dielectric constant on the physical properties of single-walled carbon nanotubes. Chem Phys 413:35–38
76. Heller DA (2006) Optical detection of DNA conformational polymorphism on single-walled carbon nanotubes. Science 311:508–511

77. Ahn J-H et al (2011) Label-free, single protein detection on a near-infrared fluorescent single-walled carbon nanotube/protein microarray fabricated by cell-free synthesis. Nano Lett 11:2743–2752
78. Jin H et al (2010) Detection of single-molecule H2O2 signalling from epidermal growth factor receptor using fluorescent single-walled carbon nanotubes. Nat Nanotechnol 5:302–309
79. Landry MP et al (2017) Single-molecule detection of protein efflux from microorganisms using fluorescent single-walled carbon nanotube sensor arrays. Nat Nanotechnol 12:368–377
80. Wong MH et al (2017) Nitroaromatic detection and infrared communication from wild-type plants using plant nanobionics. Nat Mater 16:264–272
81. Kim J-H et al (2009) The rational design of nitric oxide selectivity in single-walled carbon nanotube near-infrared fluorescence sensors for biological detection. Nat Chem 1:473–481
82. Zhang J et al (2013) Molecular recognition using corona phase complexes made of synthetic polymers adsorbed on carbon nanotubes. Nat Nanotechnol 8:959–968
83. Cambré S et al (2012) Luminescence properties of individual empty and water-filled single-walled carbon nanotubes. ACS Nano 6:2649–2655
84. Cambré S et al (2015) Asymmetric dyes align inside carbon nanotubes to yield a large nonlinear optical response. Nat Nanotechnol 10:248–252
85. Campo J et al (2016) Enhancing single-wall carbon nanotube properties through controlled endohedral filling. Nanoscale Horiz 1:317–324
86. Almadori Y et al (2014) Chromophore ordering by confinement into carbon nanotubes. J Phys Chem C 118:19462–19468
87. Harvey JD et al (2017) A carbon nanotube reporter of microRNA hybridization events in vivo. Nat Biomed Eng 1:0041
88. Jena PV et al (2017) A carbon nanotube optical reporter maps endolysosomal lipid flux. ACS Nano 11:10689–10703
89. Yoshimura SH et al (2012) Site-specific attachment of a protein to a carbon nanotube end without loss of protein function. Bioconjug Chem 23:1488–1493
90. Diao S et al (2015) Biological imaging without autofluorescence in the second near-infrared region. Nano Res 8:3027–3034
91. Reineck P, Gibson BC (2017) Near-infrared fluorescent nanomaterials for bioimaging and sensing. Adv Opt Mater 5:1600446
92. Antaris AL et al (2016) A small-molecule dye for NIR-II imaging. Nat Mater 15:235–242
93. Antaris AL et al (2017) A high quantum yield molecule-protein complex fluorophore for near-infrared II imaging. Nat Commun 8:15269
94. Yang Q et al (2017) Rational design of molecular fluorophores for biological imaging in the NIR-II window. Adv Mater 29:1605497
95. Shcherbakova DM et al (2016) Bright monomeric near-infrared fluorescent proteins as tags and biosensors for multiscale imaging. Nat Commun 7:12405
96. Carr JA et al (2018) Shortwave infrared fluorescence imaging with the clinically approved near-infrared dye indocyanine green. Proc Natl Acad Sci 115:4465–4470
97. Zhu S et al (2017) Molecular imaging of biological systems with a clickable dye in the broad 800- to 1,700-nm near-infrared window. Proc Natl Acad Sci 114:962–967
98. Bruns OT et al (2017) Next-generation in vivo optical imaging with short-wave infrared quantum dots. Nat Biomed Eng 1:0056
99. Cassette E et al (2013) Design of new quantum dot materials for deep tissue infrared imaging. Adv Drug Deliv Rev 65:719–731
100. Dang X et al (2016) Layer-by-layer assembled fluorescent probes in the second near-infrared window for systemic delivery and detection of ovarian cancer. Proc Natl Acad Sci 113:5179–5184
101. Danné N et al (2018) Ultrashort carbon nanotubes that fluoresce brightly in the near-infrared. ACS Nano 12:6059–6065
102. Bhattacharjee S (2016) DLS and zeta potential – what they are and what they are not? J Control Release 235:337–351

103. Zhang D, Yang J, Li M, Li Y (2016) (n,m) Assignments of metallic single-walled carbon nanotubes by Raman spectroscopy: the importance of electronic Raman scattering. ACS Nano 10:10789–10797
104. Piao Y et al (2016) Intensity ratio of resonant Raman modes for (n,m) enriched semiconducting carbon nanotubes. ACS Nano 10:5252–5259
105. Cherukuri TK, Tsyboulski DA, Weisman RB (2012) Length- and defect-dependent fluorescence efficiencies of individual single-walled carbon nanotubes. ACS Nano 6:843–850
106. Mouri S, Miyauchi Y, Matsuda K (2012) Dispersion-process effects on the photoluminescence quantum yields of single-walled carbon nanotubes dispersed using aromatic polymers. J Phys Chem C 116:10282–10286
107. Khripin CY, Tu X, Howarter J, Fagan J, Zheng M (2012) Concentration measurement of length-fractionated colloidal single-wall carbon nanotubes. Anal Chem 84:8733–8739
108. Crochet J, Clemens M, Hertel T (2007) Quantum yield heterogeneities of aqueous single-wall carbon nanotube suspensions. J Am Chem Soc 129:8058–8059
109. Fagan JA et al (2007) Length-dependent optical effects in single-wall carbon nanotubes. J Am Chem Soc 129:10607–10612
110. Rajan A, Strano MS, Heller DA, Hertel T, Schulten K (2008) Length-dependent optical effects in single walled carbon nanotubes. J Phys Chem B 112:6211–6213
111. Naumov AV, Tsyboulski DA, Bachilo SM, Weisman RB (2013) Length-dependent optical properties of single-walled carbon nanotube samples. Chem Phys 422:255–263
112. Silvera Batista CA, Zheng M, Khripin CY, Tu X, Fagan JA (2014) Rod hydrodynamics and length distributions of single-wall carbon nanotubes using analytical ultracentrifugation. Langmuir 30:4895–4904
113. Zhao Q, Zhang J (2014) Characterizing the chiral index of a single-walled carbon nanotube. Small 10:4586–4605
114. Jena PV, Safaee MM, Heller DA, Roxbury D (2017) DNA–carbon nanotube complexation affinity and photoluminescence modulation are independent. ACS Appl Mater Interfaces 9:21397–21405
115. Lefebvre J (2016) Real time hyperspectroscopy for dynamical study of carbon nanotubes. ACS Nano 10:9602–9607
116. Sanchez SR, Bachilo SM, Kadria-Vili Y, Lin C-W, Weisman RB (2016) (n,m)-specific absorption cross sections of single-walled carbon nanotubes measured by variance spectroscopy. Nano Lett 16:6903–6909
117. Liu K et al (2014) Systematic determination of absolute absorption cross-section of individual carbon nanotubes. Proc Natl Acad Sci 111:7564–7569
118. Streit JK, Bachilo SM, Ghosh S, Lin C-W, Weisman RB (2014) Directly measured optical absorption cross sections for structure-selected single-walled carbon nanotubes. Nano Lett 14:1530–1536
119. Galassi TV, Jena PV, Roxbury D, Heller DA (2017) Single nanotube spectral imaging to determine molar concentrations of isolated carbon nanotube species. Anal Chem 89:1073–1077
120. Schöppler F, Rühl N, Hertel T (2013) Photoluminescence microscopy and spectroscopy of individualized and aggregated single-wall carbon nanotubes. Chem Phys 413:112–115
121. Naumov AV, Ghosh S, Tsyboulski DA, Bachilo SM, Weisman RB (2011) Analyzing absorption backgrounds in single-walled carbon nanotube spectra. ACS Nano 5:1639–1648
122. Roxbury D, Jena PV, Shamay Y, Horoszko CP, Heller DA (2016) Cell membrane proteins modulate the carbon nanotube optical Bandgap via surface charge accumulation. ACS Nano 10:499–506
123. Heller DA et al (2011) Peptide secondary structure modulates single-walled carbon nanotube fluorescence as a chaperone sensor for nitroaromatics. Proc Natl Acad Sci 108:8544–8549
124. Galassi TV et al (2018) An optical nanoreporter of endolysosomal lipid accumulation reveals enduring effects of diet on hepatic macrophages in vivo. Sci Transl Med 10:eaar2680
125. Lerner JM, Gat N, Wachman E (2010) Approaches to spectral imaging hardware. Curr Protoc Cytom 53:12.20.1–12.20.40

126. Adão T et al (2017) Hyperspectral imaging: a review on UAV-based sensors, data processing and applications for agriculture and forestry. Remote Sens 9:1110
127. Heller DA et al (2009) Multimodal optical sensing and analyte specificity using single-walled carbon nanotubes. Nat Nanotechnol 4:114–120
128. Budhathoki-Uprety J, Langenbacher RE, Jena PV, Roxbury D, Heller DA (2017) A carbon nanotube optical sensor reports nuclear entry via a noncanonical pathway. ACS Nano 11:3875–3882
129. Lin C-W et al (2017) In vivo optical detection and spectral triangulation of carbon nanotubes. ACS Appl Mater Interfaces 9:41680–41690
130. Streit JK, Bachilo SM, Weisman RB (2013) Chromatic aberration short-wave infrared spectroscopy: nanoparticle spectra without a spectrometer. Anal Chem 85:1337–1341
131. Bronikowski MJ, Willis PA, Colbert DT, Smith KA, Smalley RE (2001) Gas-phase production of carbon single-walled nanotubes from carbon monoxide via the HiPco process: a parametric study. J Vac Sci Technol Vac Surf Films 19:1800–1805
132. Godwin MA et al (2018) An efficient method to completely remove catalyst particles from HiPCO single walled carbon nanotubes. J Nano Res 53:64–75
133. Kitiyanan B, Alvarez WE, Harwell JH, Resasco DE (2000) Controlled production of single-wall carbon nanotubes by catalytic decomposition of CO on bimetallic Co–Mo catalysts. Chem Phys Lett 317:497–503

Chapter 7
Near Infrared-Emitting Carbon Nanomaterials for Biomedical Applications

Tayline V. de Medeiros and Rafik Naccache

7.1 Near Infrared-Emitting Carbon Nanomaterials

Carbon is one of the most abundant and versatile elements on earth, being found as diverse allotropes in nature. In each of its allotropic forms, carbon presents different types of chemical bonds, hybridization, and structural conformation. Therefore, unique physical and chemical properties such as mechanical strength, biocompatibility, electrical and thermal conductivity are observed. Carbon nanomaterials (CNs) combine the inherent properties of carbonaceous materials with the exceptional optical phenomena observed only in nanoscale, giving rise to a singular class of materials [1, 2].

The optical properties of the CNs are directly related to its size, shape, and structure. Electronic transitions can be observed from UV–Vis to near infrared region (NIR), due to the predominant sp^2 hybridization of carbon and the presence of π-bonds in these materials. The variation in size and the introduction of defects on the structure, such as sp^3-hybridized regions, create new electronic states that leads to photoluminescence (PL) phenomena. Some CNs emit in the blue or green region, others in the red-NIR region. NIR-emitting materials are especially suitable for biomedical applications due to their deep tissue penetration, reduced light scattering, and minimal autofluorescence typically associated with fluorescence from the background or the surrounding environment [3–5].

Among the wide variety of known NIR-emitting CNs, carbon nanotubes (CNTs), graphene dots (GDs), and carbon dots (CDs) have gained particular attention in the past decade (Fig. 7.1).

T. V. de Medeiros · R. Naccache (✉)
Department of Chemistry and Biochemistry and Centre for NanoScience Research, Concordia University, Montreal, QC, Canada
e-mail: taylinepaloma.demedeiros@mail.concordia.ca; rafik.naccache@concordia.ca

A. Benayas et al. (eds.), *Near Infrared-Emitting Nanoparticles for Biomedical Applications*, https://doi.org/10.1007/978-3-030-32036-2_7

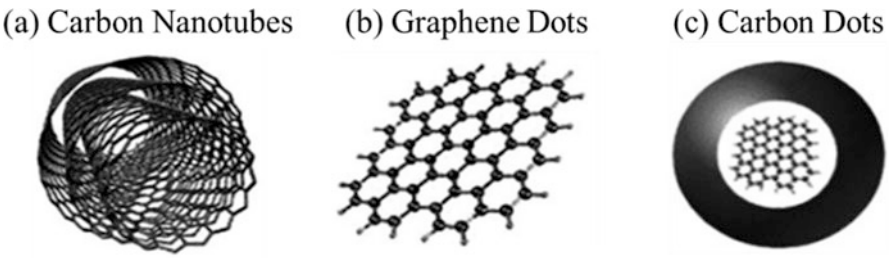

Fig. 7.1 CNs schematic representation, showing the structure of carbon nanotubes (**a**), graphene dots (**b**), and carbon dots (**c**) [6]. Image adapted from reference [6]. Copyright (2017) Royal Society of Chemistry reproduced with permission

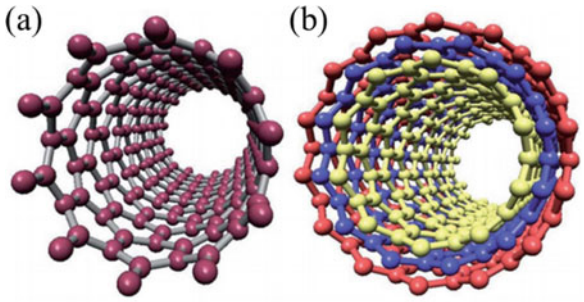

Fig. 7.2 Carbon nanotubes schematic representation, SWNTs (**a**) and MWNTs (**b**) [8]. Adapted from reference [8]. Copyright (2013) RSC publishing reproduced with permission

7.2 Carbon Nanomaterials

7.2.1 Carbon Nanotubes

Carbon nanotubes (CNTs) are essentially comprised of sp^2-hybridized carbon atom bonds, forming six membered rings in a cylindrical structure. According to the number of layers on the structure, CNTs can be classified as single-wall nanotubes (SWNTs) (Fig. 7.2a), when only one layer is present, or multiwall nanotubes (MWNTs) (Fig. 7.2b), when more than one layer is observed. Despite presenting a similar composition, the change in the number of layers on the nanotube structure is strictly related to the synthetic procedures and the properties of the material obtained [7].

Unlike the MWNTs, the synthesis of SWNTs requires a metallic catalyst, which typically leads to a poor purity and requires extensive purification processes. MWNTs present emission between the visible and the near infrared region (NIR), while SWNTs present a characteristic broad emission band in the NIR and show resistance to photobleaching [9]. Moreover, the characterization of SWNTs is usually more facile in comparison to its MWCNT counterpart. Lastly, SWNTs are considered to be more suitable for biological applications due to their reduced accumulation in biological systems when compared to MWNTs [7, 10].

The presence of the strong sp^2 bonds between the carbon atoms on the CNTs structure gives rise to an impressive tensile strength and elasticity for these materials. The aromatic structure and the electronic delocalization on CNTs also confer to their metallic or semiconducting properties, varying accordingly to the rolling up direction and diameter [11, 12]. Furthermore, CNTs present large surface area, electron delocalization, and excellent chemical stability enabling drug conjugation. However, biomedical applications require a complete purification, which is necessary to remove all metals and other carbon particles [13].

Optically, unlike the solid state, aqueous CNTs exhibit intense fluorescence, which is directly related to the nanotube diameter, chirality, and dielectric constant. In general, SWNTs with semiconductor characteristics exhibit fluorescence, while the metallic ones do not; metallic structure-induced quenching, just as in MWNTs, leads to low or no fluorescence from these materials [14]. The presence of NIR photoluminescence in semiconducting SWNTs is especially interesting for biomedical applications. Therefore, these materials can be used as imaging and sensing agents [6, 14].

7.2.2 Carbon Dots

Carbon dots (CDs) are quasi-spherical amorphous nanomaterials, with sizes below 10 nm in diameter, formed basically by sp^2-hybridized carbon with the coexistence of some sp^3-hybridized regions (Fig. 7.3). CDs are composed of carbon, hydrogen, nitrogen, and oxygen, and can be obtained from different precursors including organic molecules [15], such as citric acid [16, 17], to natural products and wastes [18], namely coffee grounds [19] and paper ashes [20]. This composition is directly related to precursors and synthetic route used. Functional groups such as carboxylic and amine moieties are normally present on the surface of these materials, imparting excellent water dispersibility. Studies reported to date have shown that CDs present

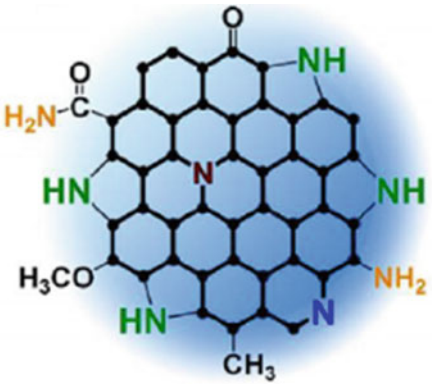

Fig. 7.3 Carbon dots schematic structure [26]. Adapted from reference [26]. Copyright (2017) Elsevier reproduced with permission

low chemical toxicity and good biocompatibility rendering them attractive for biological applications [21–25].

Regarding their optical properties, CDs present excitation-dependent photoluminescence. Therefore, with the increase of the wavelength, the emission will red-shift, being tunable from the UV range to the NIR [27, 28]. The fluorescence mechanisms remain unclear and still demand further investigation to elucidate the origins of their optical properties; however, the main processes apparently involved are related to quantum confinement effects, the presence of defects, as well as functional groups on the surface of the dot. For molecules smaller than the Bohr radius such as CDs, the bandgap energy can sometimes decrease with an increase of the particle size, thereby leading to a red-shift in their fluorescence (Fig. 7.4) [29–32].

The presence of both sp^2- and sp^3-hybridized carbon and other defects, as the oxygenated functional groups present on the surface of the CDs contribute to its multicolor excitation. These defects, created mostly by the oxidation of the surface, act as traps for the excitons, introducing surface states that give rise to surface-state-related fluorescence. The increase of the oxidation level of the surface increases the number of surface states, leading to a red-shift in the fluorescence (PL) spectra (Fig. 7.4b). The same effect is observed when different functional groups are present on the CDs' surface [29, 33–35].

In order to have a wavelength-independent emission and increase the quantum yield, it is possible to passivate the CDs' surface. The passivating agents, typically amino groups [36] and polymers [37], create a cap on the surface reducing the number of defects and the level of oxidation of the surface. Thereby, non-radiative multiple fluorescence pathways become unfavored, and the fluorescence becomes wavelength-independent [38, 39].

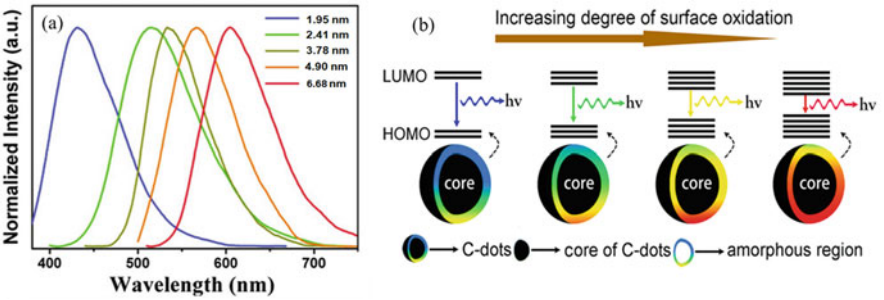

Fig. 7.4 Wavelength-dependent mechanisms of luminescence for CDs. Tunable luminescence according to the size (**a**) and surface oxidation level (**b**) [30, 33]. Adapted from references [30] and [33]. Copyright (2017) Wiley Online Library and (2016) ACS publications reproduced with permission

7.2.3 *Graphene Dots*

Graphene dots (GDs) are essentially composed of sp^2-hybridized carbon atoms, forming graphene nanostructures with a lateral dimension smaller than 100 nm and a thickness less than 10 layers [40–42]. Unlike CDs, GDs are crystalline, due to their regularly repeating structure containing minimal defects. The presence of functional groups on the surface, as the oxygenated group moieties on the edges of the layers, imparts excellent water solubility. Furthermore, the presence of these oxygenated functional groups gives rise to edge effects that play an important role in the optical properties of GDs [43, 44].

GDs present absorption in the UV region and emission ranging from the blue to NIR regions of the spectrum. Like CDs, the emission mechanisms for GDs remain unclear. However, as the edge effects and the quantum confinement are the most accepted, the photoluminescence mechanisms for the GDs are described as size/edge-dependent [45–47]. The graphene core, with the presence of the conjugated π bonds, is responsible for the intrinsic PL emission. Due to the small size of GDs, quantum confinement effects are observed and the emission is size-dependent (Fig. 7.5a) [48, 49].

The presence of oxygenated functional groups on GDs creates the surface states (as observed for CDs) that tune the emission accordingly to the level of the oxidation and the localization of the functional groups (Fig. 7.5b). Mahasin et al. showed that the presence of –COOH and –OH groups causes a red-shift in their PL emission. However, this effect is more drastic when the oxygenated groups are on the basal plane, instead of the edges of the GDs, because of the disruption of the conjugation of the π bonds [44, 49].

The quantum yield and the PL intensity of GDs can be improved by modification of the edges by non-trapping sites, as well as introduction of electron-rich groups on the surface to improve the π conjugation and passivation of the surface to avoid non-radiative pathways [50].

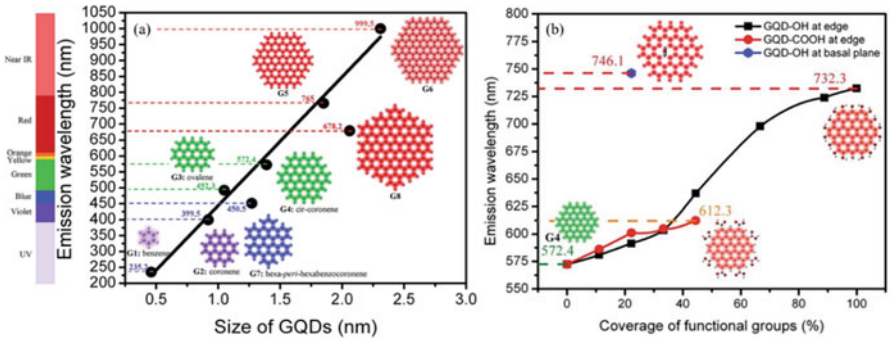

Fig. 7.5 Effects of quantum size confinement (**a**) and presence of edge-oxygenated groups (**b**) on the PL mechanisms of GQDs [49]. Adapted from reference [49]. Copyright (2014) Royal Society of Chemistry reproduced with permission

7.3 Synthesis of Carbon Nanomaterials

Several methods have already been reported for the synthesis of CNs. According to the synthesis strategy, they can be classified as top-down or bottom-up. In top-down methods, the CNs are formed by breaking down carbonaceous materials to achieve a desired nanomaterial. Such methods include arc-discharge, laser ablation, and chemical-assisted cleavage. This approach proves useful in maintaining similar physico-chemical properties to the parent structure, but usually leads to a wide particle size distribution and can be of high cost. In contrast, in bottom-up methodologies, CNs are formed by assembling precursors through synthesis approaches such as chemical vapor deposition (CVD) [51], pyrolysis [52], microwave [53–55], and solvothermal [56] assisted reactions. These methods provide greater control over the CN's properties; however, it often leads to competing side products and impurities due to the complexity of the reaction mechanism(s). Moreover, in some instances, the use of metallic catalysts requires additional purification steps [57, 58].

7.3.1 Top-Down Synthesis of Nanomaterials

7.3.1.1 Using Arc-Discharge and Laser Ablation for the Synthesis of Carbon Nanomaterials

The electric-arc-discharge is the oldest method for the synthesis of CNs [59]. The process occurs inside a chamber supplied with inert gas (Fig. 7.6). Electric current is produced upon application of a voltage between two electrodes. This electric

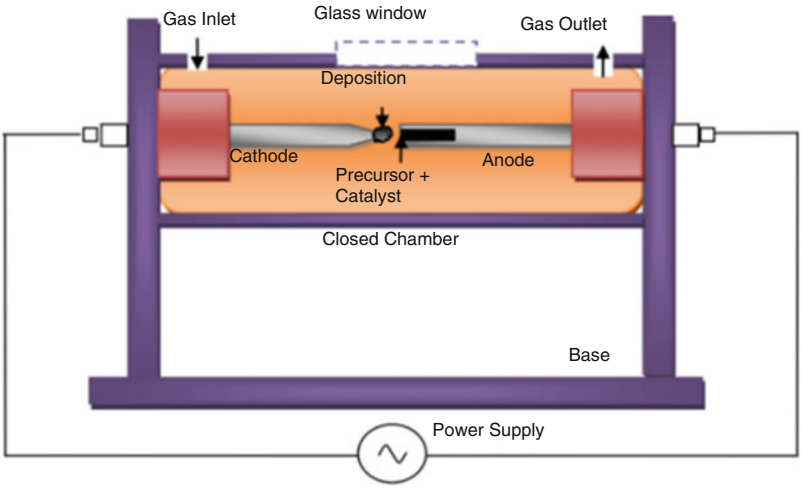

Fig. 7.6 Arc-discharge setup for CNs production [62]. From reference [62]. Copyright (2014) Elsevier reproduced with permission

current leads to resistive heating and the achievement of high temperatures (2000–3000 °C) allowing the conversion of the gases inside the chamber into plasma. These temperatures are also responsible for the vaporization of carbon sources that convert into ions due to the thermal flux of the plasma and aggregates to form viscous carbon clusters [60, 61].

In contact with the cathode (that possesses lower temperatures than the anode), the carbon clusters suffer a phase change, turning into liquid carbon. This temperature gradient and the quenching effects of the atmosphere solidifiers promote crystallization of the liquid carbon, forming structures that grow on the cathode [62, 63]. Like the arc-discharge, laser ablation uses heat (in this case, from the pulsed laser) to vaporize the carbon source. The carbon nanomaterials grow on the cooler part of the reactor (Fig. 7.7).

Synthesis of Carbon Nanotubes by Arc-Discharge, Laser Ablation, and Optical Properties

CNTs were initially synthesized via top-down methods using high temperatures, as laser ablation [65] and arc-discharge [62]. As mentioned above, only the SWNTs present emission in the NIR region of the electromagnetic spectrum. Therefore, the synthetic routes presented here will focus on the obtention of SWNTs.

Regardless of the synthetic procedure, CNTs are always formed with impurities including amorphous carbon, fullerenes, metals (from the metallic catalysts), among others. The types and quantities of impurities present are directly related to the synthesis [7, 64, 66, 67]. Table 7.1 summarizes the general properties of the arc-discharge and laser ablation synthetic routes for obtention of CNTs and their

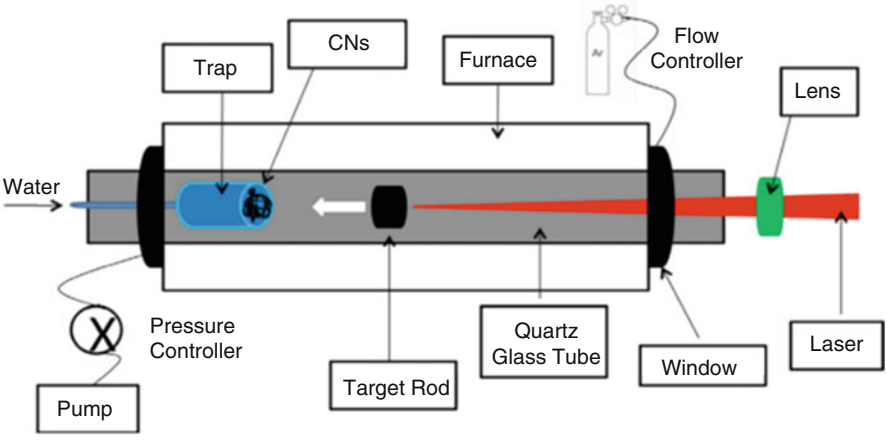

Fig. 7.7 Laser ablation setup for CNs production [64]. Adapted from reference [64]. Copyright (1995) Elsevier reproduced with permission

Table 7.1 Comparison between CNTs top-down synthetic routes: arc-discharge and laser ablation [68]

	Arc-discharge	Laser ablation
Description	Evaporation of carbon source due to the arc-discharge; deposition of CNTs on electrode	Evaporation of carbon source due to the pulsed laser; deposition of CNTs on receiver
Temperature	> 3000 °C	> 3000 °C
Pressure	50–7600 Torr, generally under vacuum	200–750 Torr, generally under vacuum
Advantages	Good quality nanotubes	SWNTs with good quality
Disadvantages	High temperatures required, production of high quantities of impurities, poor size control	High temperatures required, expensive apparatus

Adapted from reference [67]

Table 7.2 Effect of different growth parameters on CNT synthesis using arc-discharge and laser ablation [62, 75]

Parameter	Effect on size of nanotube
Temperature	Increase in temperature leads to more crystalline structures and smaller diameters. The temperature required to form SWNTs is higher than to MWNTs
Atmosphere	Diameters of SWNTs change as the inert gas is varied; the use of hydrogen combined with noble gas leads to a greater purity and higher control of diameter size
Pressure	SWNT diameter is independent of pressure in pure He environment
Catalyst	Smaller diameters and higher purity are achieved when Ni and Co (for laser ablation) and Ni and Fe-based (for arc-discharge) catalysts are used

respective outcomes [68]. Generally, the laser ablation approach forms SWNTs with narrow size distribution, higher yields and purity when compared to the arc-discharge method [69].

Despite the many attempts to propose the mechanism of CNT formation by arc-discharge and laser ablation, the exact growth mechanism still remains unclear [66–70]. However, growth conditions as temperature, pressure, and catalyst are strictly related to the structure of the formed CNTs. Table 7.2 summarizes how the variation of the growth parameters affects the CNT size.

Arc-discharge and laser ablation methodologies produce CNTs with higher quality and yield than other known synthetic routes. However, both present disadvantages due to the presence of high amount of side products and impurities, the need for expensive equipment, and high temperatures required for synthesis [7, 64].

SWNTs possess strong absorbances in the NIR region. The semiconductor SWNTs have direct electronic transitions, with bandgap of the order of 1 eV, presenting PL in the NIR region (800–2000 nm) [76]. The absorption and fluorescence energies of SWNTs are associated with the nanotube diameter and chirality, due to the strong effect of Coulomb interactions [77]. The PL mechanism is related to generation and recombination of excitons where the SWCNT is photoexcited,

Table 7.3 Comparison between CDs top-down synthetic routes: arc-discharge and laser ablation [21, 34, 88, 89]

	Arc-discharge	Laser ablation
Description	Phase change of carbon material assisted by arc-discharge	Phase change of carbon material assisted by laser source
Size control	Poor	High
Size distribution	Small	Small
Advantages	Small particles size	Control of morphology and size
Disadvantages	Requires purification, low yield	Low quantum yield, high costs

creating the electron–hole pairs in the form of excitons that are annihilated when the photons' emissions occur [78]. The presence of defects on the surface of the tube generates non-radiative relaxation pathways, leading to quenching [79]. However, chemical modifications of the nanotube surface can modulate the optical properties by creating surface states. The controlled insertion of defects including covalent doping [80], introduction of functional groups [79], as well as sp^3-hybridized carbon in the sp^2 lattice [81] can lead to a red-shift of the emission.

The arc-discharge method generates CNTs with good quality, but a mixture of MWCNT and SWCNT is formed with higher contents of impurities. In contrast, the laser ablation method produces SWNTs with good quality and narrow size distribution. Thereby, the PL properties of the CNTs produced by laser ablation are typically more substantial.

Synthesis of Carbon Dots by Arc-Discharge, Laser Ablation, and Optical Properties

Xu et al. reported the accidental discovery of the CD structures during the purification of SWNTs obtained from arc-discharge [82]. Since then, many approaches have been developed to synthesize CDs including laser ablation [37, 83], oxidation [84, 85], ultrasonic treatment [86], thermal decomposition [87], solvothermal [28], and microwave [53] assisted reactions. Table 7.3 summarizes the general properties of the arc-discharge and laser ablation synthetic routes for obtention of CDs and their respective outcomes.

The main challenge associated with CD production is the aggregation of the particles during the carbonization process, as well as achieving good uniformity and control of the size and surface properties. CDs can be synthesized by arc-discharge using the same procedure to obtain SWNTs [82]. However, as a side product, the yield obtained during arc-discharge synthesis of CDs is low, requiring extensive purification [90]. For this reason, arc-discharge was not established as a major top-down methodology to synthesize CDs.

Laser ablation has been widely used as synthetic route to produce CDs, mostly due to its high control of morphology and size. In this method, the CDs are formed by the laser ablation of solid carbon targets, such as graphite, or dispersions of the

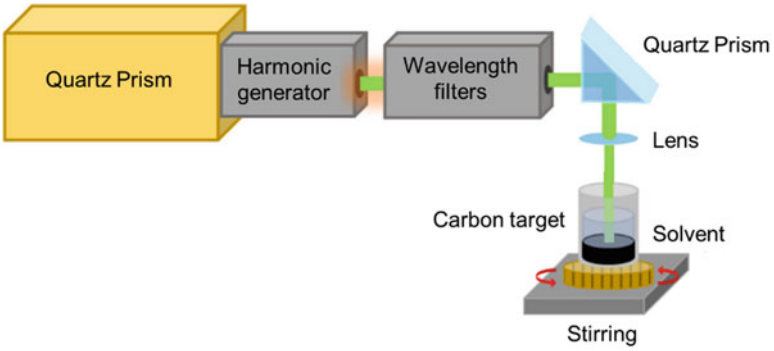

Fig. 7.8 Laser ablation setup for CDs production using liquid targets [94]. Adapted from reference [94]. Copyright (2018) Elsevier reproduced with permission

carbon source(s). The use of liquid targets (Fig. 7.8) allows the application of laser ablation for the suspension of microparticles or powders that would otherwise be inefficient using conventional procedures [91–93].

The heat generated by the laser source promotes the formation of bubbles inside the liquid that due to the space confinement expands to a maximum radius. When the laser pulse is switched off, the bubbles start to shrink due to the external pressure of the surrounding liquid, creating a region with a lower temperature in which the nucleation phenomenon occurs. Due to the formation of bubbles with different sizes, the CDs are formed with large size distribution [89, 93]. The choice of the dispersion media is extremely important as the solvent must be capable of stabilizing the CDs and also be physico-chemically stable during the synthesis. The laser intensity is also an important parameter. Reyes et al. reported that the use of a short-wavelength UV laser leads to a formation of CD structures, while a longer wavelength laser results in the formation of agglomerates. Therefore, it is possible to modulate the size of the obtained CDs according to the laser wavelength used [92, 96].

In general, CDs synthesized by arc-discharge methods present reduced size and considerable amount of oxygen resulting in a multicolor PL emission with extremely low quantum yield [97] in contrast to CDs obtained by laser ablation of graphite targets in inert atmosphere, which are non-fluorescent. However, with surface passivation or functionalization a bright blue-to-red emission may be observed and quantum yields in the range of 20% have already been reported [36, 90, 92]. Passivation and surface functionalization can be used to control the size aiming to produce bigger molecules as well as tune the PL emission up to the NIR region [99, 100].

Synthesis of Graphene Dots by Laser Ablation and Optical Properties

Top-down approaches to synthesize GDs are based on the defected-mediated cleavage of bulk graphene structures as graphene sheets, graphene oxide (GO), carbon nanotubes, among others [101]. In these methods, the oxygen moieties act as reactive sites, allowing the fragmentation of the bulk structures into smaller structures. Russo et al. reported the obtention of GDs using the laser ablation of GO. The density of defects on the structure appears to be directly related to the ablation time [102]. The mechanisms of formation of GDs remain unclear; however, some studies have been carried out in this field to address this topic. Lin et al. proposed that the reaction starts with the photochemical desorption of the oxygen groups, followed by reduction of these groups by the hydrogen formed during water dissociation. With continuous laser irradiation, high local pressure and temperatures are generated, leading to straining in the bonds that fragment to form the GDs [103].

Laser ablation is an environmentally sustainable approach, with high reproducibility. However, the synthesized nanomaterials present a low quantum yield. For this reason, top-down approaches as chemical ablation and electrochemical exfoliation have attracted some focus [104]. The chemical oxidation approach consists in treating the bulk graphene structures with an oxidative reagent, as strong acids [105] or oxidants [106]. This method produces GDs with higher levels of oxidation, imparting them with interesting PL properties, including NIR emission. However, the synthesized molecules can present different levels of oxidation, and the removal of the oxidant agent requires extensive purification process [104].

7.3.2 Bottom-Up Synthesis of Carbon Nanomaterials

7.3.2.1 Carbon Vapor Deposition Reactions

Bottom-up methodologies recently gained attention as it requires lower temperatures and provides stricter control over the CNTs shape, size, density, orientation, and purity.

Chemical vapor deposition is the reaction on vapor phase that leads to a deposition of a solid in a heated surface. In the case of CNs, the CVD process occurs with the decomposition of hydrocarbon precursors into carbon and hydrogen catalyzed by transition metals, namely nickel, cobalt, and iron. The volatile product is then deposited on a substrate [51, 107]. CVD reactions occur inside a quartz reactor placed in a tubular furnace (Fig. 7.9). The catalyst is placed at the beginning of the tube called preheating zone, where the decomposition will occur and CNs will be formed in the reaction zone. An inert atmosphere (e.g., argon) must be used before the start of the reaction to ensure that the system is free of oxygen. A carrier gas, such as H_2, is also required to carry the vapors through the tube [64, 108].

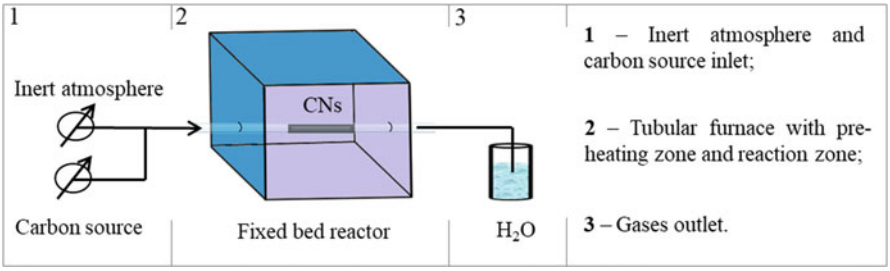

Fig. 7.9 CVD setup for CNs production

Synthesis of Carbon Nanotubes by Chemical Vapor Deposition (CVD)

The synthesis and several modifications of this system have been reported in the literature including the use of fixed [109, 110] or fluidized beds [111, 112], floating catalysts [113], or combination of these methods [114, 115]. It is possible to modify the reactor design to tailor the properties of the desired product. Some studies regarding the synthesis of carbon dots [116] and graphene dots [117, 118] by CVD methods were already reported. However, due to the complexity of parameters present in these procedures and the difficulty to control the size, physical and optical properties of the synthesized materials, the CVD methodology is not among the most widely used methods for obtaining these materials. For this reason, these methods will not be shown here.

Nonetheless, for CNTs the CVD method presents many advantages and is among the most used. CNTs, through CVD, can be carried out using different carbon sources as methane, carbon monoxide, benzene, and ethanol, among others. In general, the formation of SWNTs or MWNTs is governed by the size of the catalyst and the temperature of the reaction. Small metallic catalyst particles (5–25 nm) and lower temperatures (300–600 °C) produce SWNTs, while large particles (25–100 nm) and high temperatures (600–1000 °C) produce MWNTs [110, 119].

While high yields and good chirality control can be obtained for CNTs produced by CVD, the particles present more defects than the ones synthesized by arc-discharge and laser ablation. As discussed before, the PL properties of CNTs are directly related to the chirality, diameter, and the presence of defects. Therefore, the PL emission in the NIR region of the nanomaterials synthesized by CVD can be tuned accordingly to the synthetic parameters. Besides that, the smaller graphitization level present on these materials due to the defects creates the defect-induced emission states [79].

7.3.2.2 Solvothermal and Microwave Assisted Reactions

Microwave assisted reactions occur through the interaction of the materials with electromagnetic radiation. This interaction is determined by the material properties

as the kinetic energy from the rotation of molecules is converted into heat. The major advantage in using microwave methods is related to the fast heating rates that decrease the reaction times [120, 121], while the main disadvantage is related to limitation of solvents that can be used, due to their ability to effectively absorb microwave radiation, as well as pressure buildup inside the vessel usually limited to 300 psi. Solvothermal methods consist of using a reactor that can achieve moderately high temperatures (∼ 250 °C) and elevated pressures (200–3000 psi) to obtain the desired products. In this case, solvents with low boiling points can be used without major limitations and large-scale reactions can be performed. However, a uniform heating must occur to obtain good results and to avoid large particle size distributions.

Both approaches can be used as top-down and bottom-up methods. Bulk structures can be converted to NPs, as in the synthesis of GDs; carbon precursors can also be used to produce nanomaterials, as in the case of CNTs and CDs. Many studies were already reported regarding the synthesis of these NPs using microwave and solvothermal assisted reactions. However, for CNTs this approach does not present advantages when compared to well-established ones, as CVD.

Synthesis of Carbon Dots by Microwave and Solvothermal Assisted Reactions

Microwave irradiation of carbon precursors has been recently investigated as a synthetic route to obtain CDs. This method presents several advantages, namely low cost, short time reactions, and small size distributions. However, due to the pressure limitations, only small volumes and certain solvents can be used. The photoluminescence properties of the CDs synthesized by microwave reactions are directly related to the precursor used, as well as the solvent. The presence of heteroatoms (e.g., N and S) and the physico-chemical characteristics of the surface, as mentioned above, play a major role in dictating the optical properties and the fluorescence mechanisms [15, 122, 123]. Solvothermal assisted reactions to produce CDs consist of a single-step that uses high temperatures and pressures leading to decomposition of the carbon source and consequent formation of the dot's structure. This method requires a simple apparatus and as the pressure is not a limiting factor, high conversion efficiency is typically observed. However, the inhomogeneous heating can lead to a large size distribution. When compared to microwave assisted reactions, the solvothermal synthesis presents longer reaction times usually on the order of 4–24 h [28, 34]. Table 7.4 presents a comparison between the microwave and solvothermal assisted reactions and its outcomes.

The CDs synthesized by both methods can present NIR emission, in the 650–800 nm range (according to the precursors used, and as a consequence, the surface functionalization or passivation). Pan et al. reported NIR emissive CDs produced by thermal decomposition of glutathione in formamide assisted by microwave. The presence of functional groups (C=O, C=N, and C=S) on the surface of the CDs generated surface molecular states, tuning the emission to the NIR range (650–780 nm) [124].

Table 7.4 Comparison between CDs bottom-up synthetic routes: solvothermal and microwave assisted reactions [21, 34, 88]

	Microwave assisted reaction	Solvothermal assisted reaction
Description	Microwave assisted decomposition of a carbon precursor dispersed in a solvent	Decomposition of carbon precursor under high pressure and temperature
Size control	Poor	Poor
Size distribution	Small	Small
Advantages	Short reaction times, uniform heating distribution	High quantum efficiency, low cost
Disadvantages	Pressure limitations reduce the possibilities of solvents and volumes used	Inhomogeneous heating, long reaction times

Lan et al. obtained NIR CDs by solvothermal treatment of polythiophene and diphenyl diselenide. These CDs presented many nitrogen-containing groups, with emission centered at 710 nm related to surface states [99]. Li et al. investigated how the presence of functional groups on the surface of CDs could tune the emission to NIR. The CDs synthesized in this work were functionalized by polymers and molecules rich in sulfoxide and carbonyl moieties, leading to discrete energy levels that were responsible for the NIR emission [125].

Synthesis of Graphene Dots by Microwave and Solvothermal Assisted Reactions

Microwave assisted reactions have proved to be fast and efficient to synthesize GDs. The thermal cutting of bulk carbonaceous structures as graphene, GO, and SWNTs into GDs can be performed using different reaction media. The resultant product presents higher yields and smaller size distribution when compared to other methodologies. Another advantage related to this method is the simultaneous cleavage and reduction of the bulk structures without the need of using reductant agents [126, 127].

Solvothermal GDs synthesis have been vastly studied. As on the microwave procedure, different reaction media can be used, namely water, oxidizing acidic and basic solutions. The increase in the temperature leads to smaller size nanomaterials. Tetsuka et al. reported the synthesis of amino-functionalized GDs, with specific edges and tunable PL showing that it is possible to control the surface and functionalization accordingly to the reaction conditions and precursors. The presence of the $–NH_2$ on the edges of the aromatic layers changes the delocalization of electrons on the structure; the interaction of the delocalized π orbitals and the molecular orbital on the $–NH_2$ group leads to a decrease on the bandgap. The more amino groups present, the more the PL emission is tuned [128].

As previously discussed, the PL is directly related to the size, edges, and level of functionalization of the surface. Most of GDs synthesized by microwave and solvothermal assisted reactions present blue to green emission, and a QY in the range of 15–30% [126]. However, surface modification and passivation can tune the emission of the previously synthesized GDs to the NIR, up to 900 nm, as already demonstrated in previous reports [129, 130].

7.4 Biomedical Applications

Many particles have been studied for biomedical applications, from metal clusters to proteins, these materials present fluorescent emission imparting them with suitable properties as biomedical probes. Figure 7.10 presents the emission range for the most common molecules applied on biomedical applications [3].

Organic dyes and fluorescent proteins figure as the most studied bioprobes, mostly due to their lower cost and vast availability. Metal clusters and CNs also present emission in the NIR range, being promising as bioimaging and biosensors probes.

Due to the NIR optical properties of the CNs, these materials are especially suitable for in vivo applications where the use of NIR presents many advantages. Many reports have been published regarding the use of CNs for bioimaging, as drug carriers, biosensors, among others [6, 131, 132]. However, aspects as

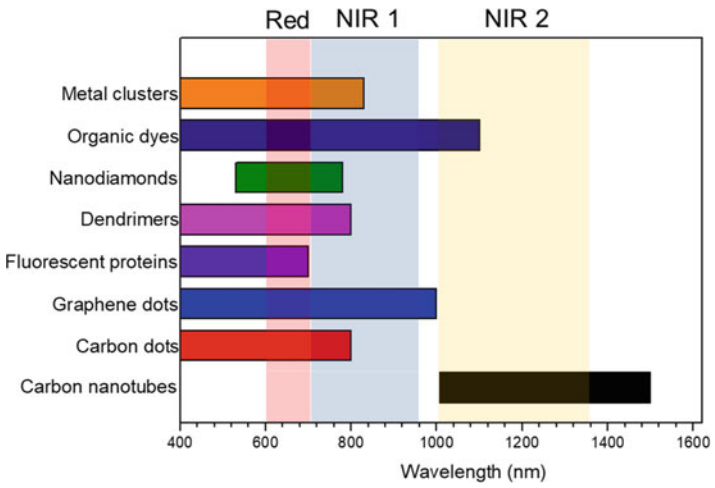

Fig. 7.10 Fluorescence emission range for selected materials studied on biomedical applications [3]. Adapted from reference [3]. Copyright (2017) Wiley Online Library, reproduced with permission

Table 7.5 Comparison between optical and toxicity properties presented on biomedical probes

Material	Quantum yield	Molar absorption coefficient	Photostability	Toxicity and biocompatibility
Metal clusters [133]	2–65%	10^4–10^5	Medium	Presents in general low toxicity and good biocompatibility
Organic dyes [134]	5–25%	10^4–10^5	Low	Very low to high according to the dye
Nanodiamonds [135]	80–99%	10^6	Very high	Presents in general low toxicity and good biocompatibility
Dendrimers [136]	55–80%	10^4	Low	Poor biocompatibility
Fluorescent proteins [137]	22–90%	10^4	Medium	Presents in general low toxicity and good biocompatibility
Graphene dots [105]	0.5–30%	10^5	High	Available studies suggest low toxicity and good biocompatibility
Carbon dots [3]	2–80%	10^4–10^5	High	Available studies suggest low toxicity and good biocompatibility
Carbon nanotubes [76]	1–7%	10^7	High	Moderated toxicity related to the precursors and metals used in synthesis

toxicity, photostability, and biocompatibility must be considered. Table 7.5 presents a comparison between these properties of several molecules and CNs.

The quantum yield is an important aspect when studying photoluminescent materials, as is related to the photon emission efficiency. It is possible to observe that some particles, such as fluorescent proteins, present high quantum yield unlike others, namely CNTs. Nevertheless, their applicability as probes is related to the fluorescent brightness that is essential to produce a good contrast on the microscopy image. This brightness is dictated by not only the quantum yield but also the molar absorption coefficient.

Some properties such as biocompatibility and toxicity must also be taken into consideration when materials are applied as bioprobes. According to the available reports, CNs present good biocompatibility and low toxicity, unlike some organic dyes.

Most of the molecules present some drawbacks such as the solvent-dependent PL presented by organic dyes, due to the solvatochromism effect; low photostability of the dendrimers; high costs of nanodiamonds. For these reasons, CNs have gained much attention as nanoprobes. The sections below present some of the most outstanding biomedical applications of NIR-emitting SWNTs, CDs, and GDs.

7.4.1 NIR Bioimaging

Fluorescence bioimaging is an important resource in diagnostic medicine. This tool uses NIR excitation wavelengths to glean information regarding the state of cells and biological tissues with the main advantage being the use of non-hazardous radiation for imaging. SWNTs, CDs, and GDs are promising candidates for NIR bioimaging probes due to their fluorescent properties.

SWNTs present high chemical and photostability, low toxicity, absence of photobleaching and quenching effects [6]. Weisman et al. were the first to report cell imaging through fluorescence of SWNTs (Fig. 7.11); they prepared nanotubes that were ingested by microphage cells, and subsequently imaged using NIR fluorescence microscopy without presenting toxic effects [138]. This work was a landmark on the interaction between nanomaterials and cells.

Subsequently, many studies regarding the use of SWNTs for bioimaging were performed [77]. Liang et al. reported the use of SWCTs for imaging and photothermal treatment of primary tumors and cancer cells in a mice brain. This method presented many advantages such as deep penetration depths (>2.0 mm) and high resolution all the while not being as invasive as a craniotomy. The obtained images also allowed the obtention of the dynamic cardiovascular activity of the mice, which was especially promising to follow biological process for molecular in situ analysis [139].

Walsher et al. performed an anatomical imaging of mice using SWNTs coated with PEGylated phospholipid (DSPE-mPEG) with increased biocompatibility. The sample containing the SWNTs was administered intravenously, and the pathway

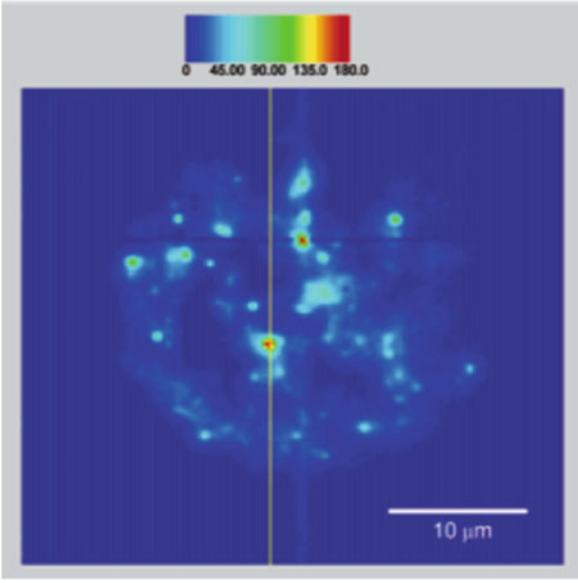

Fig. 7.11 Fluorescence image of a macrophage-like cell incubated with SWNTs [138]. Adapted from reference [138]. Copyright (2004) ACS publications reproduced with permission

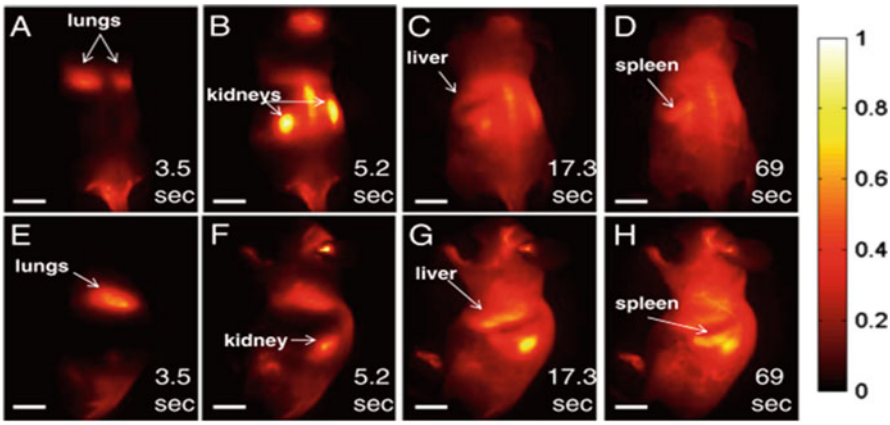

Fig. 7.12 Video-rating imaging of SWNTs coated with DSPE-mPEG inside a live mouse. On **A** and **E** frames (3.5 s after the injection) the lungs are dominant, showing the flow of oxygen-poor blood rich in SWNTs to the lungs. **B** and **F** frames (after 5.2 s) show the flow of the SWNTs through the highly vascularized kidney. **C** and **G** frames show that the liver becomes apparent after 17.3 s, whereas **D** and **H** frames show that the spleen becomes apparent after 69 s [140]. Adapted from reference [140]. Copyright (2011) Proceedings of the National Academy of Sciences reproduced with permission

through the body was followed by video image monitoring of the NIR emission (Fig. 7.12) [140].

After the injection (3.5 s), the poorly oxygenated blood containing the SWNTs flows to the lungs to be oxygenated before being redistributed to the body (Fig. 7.12, frames A and E). The next organ reached by the SWNTs are the kidneys (Fig. 7.12, frames B and F), followed by the liver (Fig. 7.12, frames C and G), and finally the spleen (Fig. 7.12, frames D and H). Further studies showed no accumulation or retention of the SWNTs in organs and tissues, providing an efficient dynamic contrast imaging method [140].

Kataura et al. reported the imaging of brown fat in mice through fluorescence of SWNTs. Structural modifications of the CNTs with a polymer (2-methacryloyloxyethyl phosphorylcholine-co-n-butyl methacrylate; PMB) allowed the targeting of endothelial cells, as the polymer has similar surface properties of plasma membranes and serum lipoproteins. Imaging using SWNTs-PMB allowed for the successful identification of the density of the tissues in which it accumulates, and as a consequence, the heat production capacity of each tissue [141].

Many studies regarding the use of CDs and GDs for bioimaging have been reported. These materials have been used for in vitro and in vivo analysis, presenting low toxicity and good biocompatibility [142]. Tao et al. reported the in vivo bioimaging of mice using CDs obtained from CNTs and graphene. Different images were obtained by varying the excitation wavelength included in the NIR. The biodistribution of the CDs was also studied over time, and no signs of toxicity were observed [25]. Pan et al. performed a two-photon fluorescence imaging of

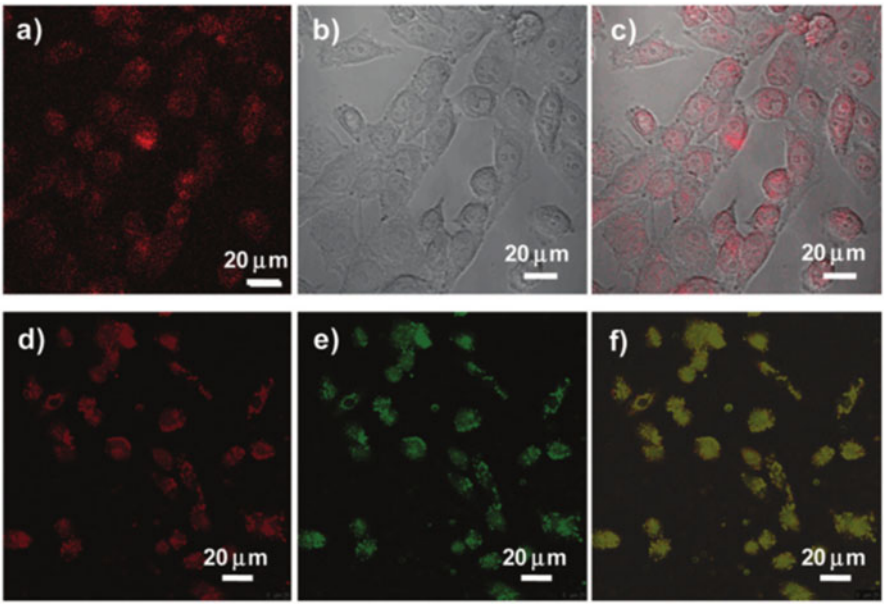

Fig. 7.13 Two-photon fluorescence of human breast cancer cells using CDs obtained from glutathione and formamide; (**a**–**c**) images obtained under excitation of 850 nm; (**d**–**e**) obtained under excitation of 488 nm; (**d**) image obtained in the range of 550–750 nm; (**e**) image obtained in the range of 493–540 nm; (**f**) overlay image of (**d**) and (**e**) [124]. Adapted from reference [124]. Copyright (2016) Royal Society of Chemistry reproduced with permission

human breast cancer cells, using CDs obtained by the thermal decomposition of glutathione in formamide (Fig. 7.13). The material presented an excitation-independent mechanism; however, the pH directly affected the PL of the CDs. The presence of amino-functionalization on the surface of the CDs also imparted them with the capability for conjugation with drugs, acting as drug carriers [124].

Nurunnabi et al. used GDs obtained from the exfoliation process of carbon fibers to perform whole-body NIR bioimaging of organs and tissues of mice (Fig. 7.14). The fluorescence signal appeared more intense in the liver and kidneys, indicating a larger accumulation in these organs. However, the biotoxicity tests revealed no significant toxicity from the GDs [143].

Zu et al. reported the use of GDs, synthesized by the solvothermal reduction of GO, as probes for bioimaging of osteosarcoma cancer cells (MG-63 cells). The nanoprobes showed a lower cytotoxicity and the addition of 400 μg of GDs to the culture media (10^4 cells) did not significantly affect the cell activity (Fig. 7.15a). Confocal fluorescence microscopy was performed in order to analyze the uptake of the GDs by cells and for bioimaging. The observed green area in Fig. 7.15c indicates the translocation of the GDs inside the cell's membrane under 405 nm excitation. The excitation-dependent emission of the GDs can be observed in Fig. 7.15d, under 488 nm, the emission turns yellow [144].

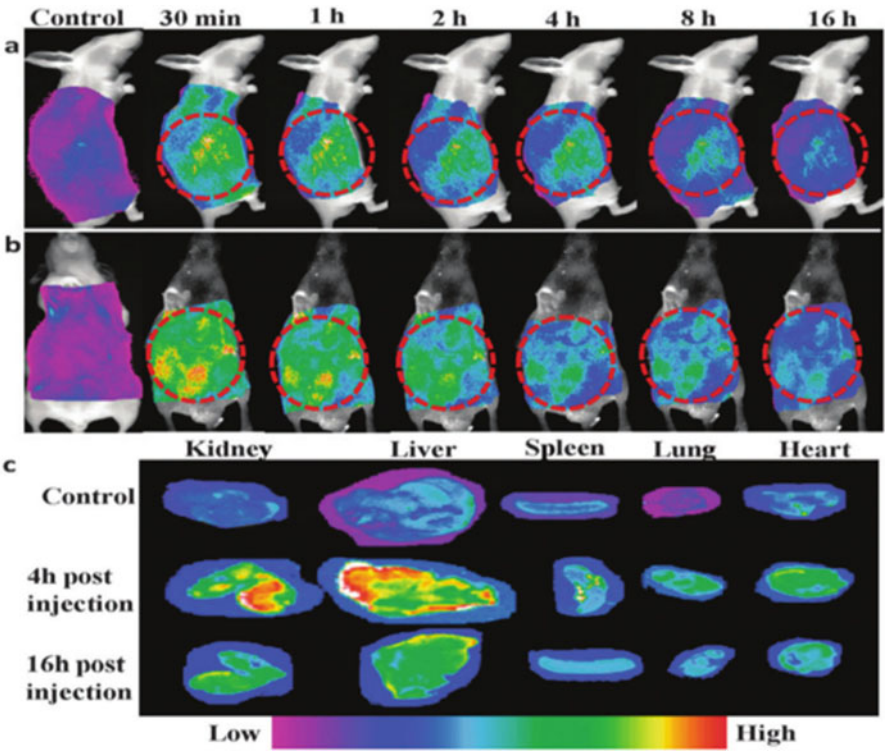

Fig. 7.14 NIR bioimaging of whole-body mice using GDs obtained from the exfoliation of carbon fibers. (**a**) Side and (**b**) front-view images of the mice. It is possible to see a decrease of fluorescence intensity over time of injection of the GDs. (**c**) Biodistribution and accumulation of GDs in the organs [143]. From reference [143]. Copyright (2013) Royal Society of Chemistry reproduced with permission

7.4.2 Biosensors

SWNTs, CDs, and GDs have also been investigated as biosensors. The conjugation with biomolecules (as DNA and proteins), cations, and metals results in the quenching of the fluorescence of the system. Kim et al. reported the use of a conjugated system containing SWNTs and luciferin enzymes that present a bioluminescent selective response to ATP. When ATP reacts with the enzyme in the presence of Mg^{2+}, NIR fluorescence of the SWNT is quenched (Fig. 7.16) [145].

The complex formed by the nanoprobe and the ATP presented a very strong fluorescence, distinct from the NIR SWNTs. The system was also very selective, being inert to molecules such as ADP, AMP, CTP, and GTP.

Li et al. proposed GD nanoprobes for glucose sensing in aqueous media. The synthesized GDs presented a cationic substituent on the surface boronic acid-substituted bipyridinium salt (BBV) with the pristine units acting as a fluorescing

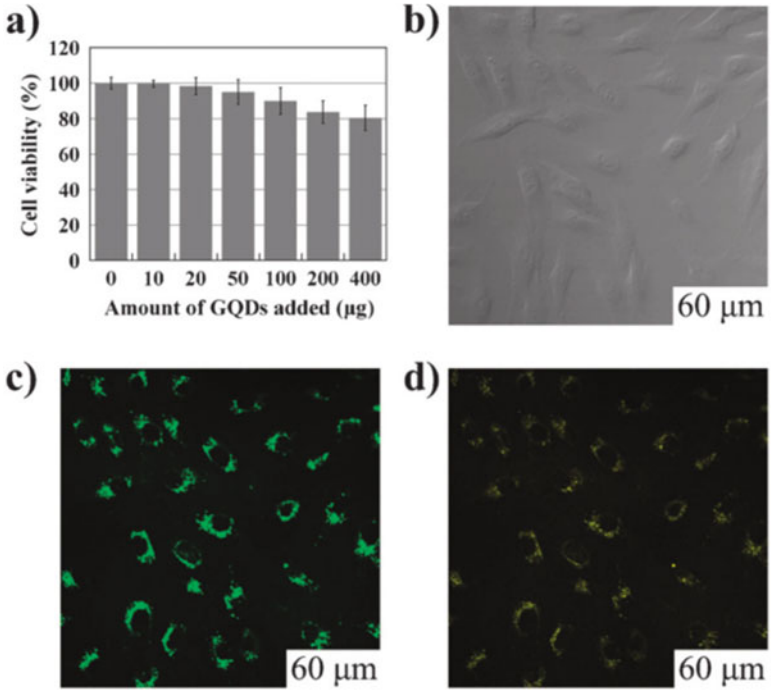

Fig. 7.15 Effect of the cell viability after injection of GDs on MG-63 cells (**a**). Washed cells on bright field (**b**), and under excitation of 405 nm (**c**) and 488 nm (**d**) [144]. From reference [144]. Copyright (2011) Royal Society of Chemistry reproduced with permission

system, while the BBV acted as a quencher and a glucose receptor simultaneously. The interaction of the GDs and the BBV forms a complex with quenched fluorescence that is recovered when the glucose molecule was added to the system. This was attributed to the formation of tetrahedral anionic glucoboronate esters (Fig. 7.17) [146].

Many biosensors geared towards the detection of nucleic acids, proteins, and cations were already successfully reported for these materials. It was observed that the surface functionalization of the CNs has a major impact on the interaction with the target molecule [6].

7.5 Challenges and Perspectives

Carbon nanomaterials have been extensively studied due to their inherent physical and chemical attributes. They present many versatile properties including good stability, biocompatibility, and mechanical strength. However, their unique fluorescence properties have gained attention due to the possibility of integration in

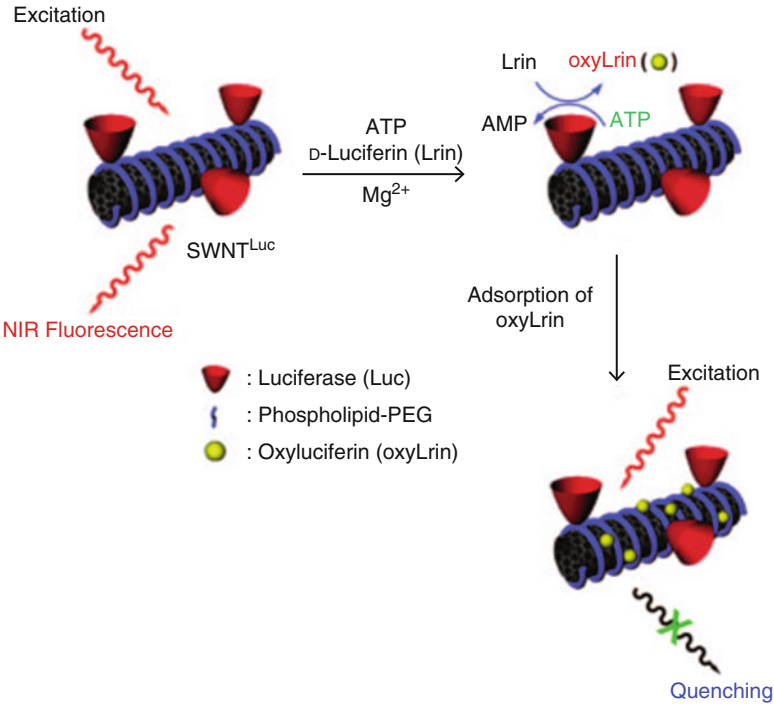

Fig. 7.16 Illustrative scheme of the biosensing application of SWNTs-luciferase nanoprobe for the detection of ATP molecules [145]. From reference [145], Copyright (2010) Wiley Online Library reproduced with permission

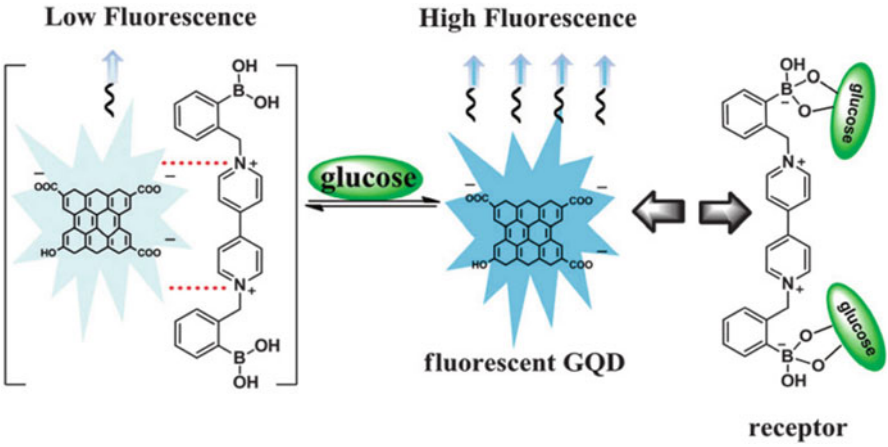

Fig. 7.17 GDs modified with BBV used as a nanoprobe for glucose sensing mechanism [146]. From reference [146]. Copyright (2013) Royal Society of Chemistry reproduced with permission

biomedical applications. SWNTs, CDs, and GDs present NIR emission that is especially suitable due to its deeper tissue penetration and reduced background scattering.

Many studies have been reported regarding the synthesis and the applications of these materials, and they showed to be extremely promising. They can be used in bioimaging, providing a non-invasive means to characterize cells and tissues, and to also investigate biological process in situ. The NIR-emitting materials can also be applied as nanoprobes for sensing purposes. Indeed, many biomolecules, metals, and cations can be identified and complexed by the CNs. Many other applications including drug delivery and photo-thermometry have also been studied, presenting promising results [147].

However, further studies regarding the toxicity and bioaccumulation are still required. The mechanisms of interaction between cells, tissues, and CNs are not clear yet. It is already known that some nanomaterials can cause toxic effects such as inflammation, oxidative stress, and genotoxicity [148]. These processes are extremely important and an intimate understanding will result in fundamental knowledge that will further our understanding of the materials, their interactions, and how materials design can reconcile them.

Perhaps on a more fundamental note, the mechanisms of fluorescence, the role of the surface, and the interaction between the NPs and biomolecules remain a hotly debated topic. It is already known that the presence of functional groups on the surface of the nanomaterials can tune the emission. Nonetheless, it is crucial to further our understanding of how it occurs and the mechanisms of tunability.

Carbon nanomaterials hold an immense potential and a bright future that we believe will change the entire biomedical landscape and will result in the development of novel diagnostic and imaging tools for the most challenging problems in nanomedicine.

References

1. Hirsch A (2010) The era of carbon allotropes. Nat Mater 9:868–871
2. Georgakilas V, Perman JA, Tucek J, Zboril R (2015) Broad family of carbon nanoallotropes: classification, chemistry, and applications of fullerenes, carbon dots, nanotubes, graphene, nanodiamonds, and combined superstructures. Chem Rev 115:4744–4822
3. Reineck P, Gibson BC (2017) Near-infrared fluorescent nanomaterials for bioimaging and sensing. Adv Opt Mater 5
4. Kozák O et al (2016) Photoluminescent carbon nanostructures. Chem Mater 28:4085–4128
5. Feng L-L et al (2017) Near infrared graphene quantum dots-based two-photon nanoprobe for direct bioimaging of endogenous ascorbic acid in living cells. Anal Chem 89:4077–4084
6. Liu H, Zhang L, Yan M, Yu J (2017) Carbon nanostructures in biology and medicine. J Mater Chem B 5:6437–6450
7. Sajid MI et al (2016) Carbon nanotubes from synthesis to in vivo biomedical applications. Int J Pharm 501:278–299
8. Akbari E et al (2014) An analytical model and ANN simulation for carbon nanotube based ammonium gas sensors. RSC Adv 4:36896–36904

9. Wang F, Dukovic G, Brus LE, Heinz TF (2004) Time-resolved fluorescence of carbon nanotubes and its implication for radiative lifetimes. Phys Rev Lett 92:177401
10. Farrera C, Torres Andón F, Feliu N (2017) Carbon nanotubes as optical sensors in biomedicine. ACS Nano 11:10637–10643
11. Ruoff RS, Lorents DC (1995) Mechanical and thermal properties of carbon nanotubes. Carbon N Y 33:925–930
12. Wildöer JWG, Venema LC, Rinzler AG, Smalley RE, Dekker C (1998) Electronic structure of atomically resolved carbon nanotubes. Nature 391:59–62
13. Monaco AM, Giugliano M (2014) Carbon-based smart nanomaterials in biomedicine and neuroengineering. Beilstein J Nanotechnol 5:1849–1863
14. Yang W et al (2010) Carbon nanomaterials in biosensors: should you use nanotubes or graphene. Angew Chemie – Int Ed 49:2114–2138
15. Chandra S et al (2012) Tuning of photoluminescence on different surface functionalized carbon quantum dots. RSC Adv 2:3602
16. Dhenadhayalan N, Lin K-C, Suresh R, Ramamurthy P (2016) Unravelling the multiple emissive states in citric-acid-derived carbon dots. J Phys Chem C 120:1252–1261
17. Dong Y et al (2012) Blue luminescent graphene quantum dots and graphene oxide prepared by tuning the carbonization degree of citric acid. Carbon N Y 50:4738–4743
18. Sharma V, Tiwari P, Mobin SM (2017) Sustainable carbon-dots: recent advances in green carbon dots for sensing and bioimaging. J Mater Chem B 5:8904–8924
19. Hsu PC, Shih ZY, Lee CH, Chang HT (2012) Synthesis and analytical applications of photoluminescent carbon nanodots. Green Chem 14:917–920
20. Wei J et al (2013) Simple one-step synthesis of water-soluble fluorescent carbon dots derived from paper ash. RSC Adv 3:13119
21. Lim SY, Shen W, Gao Z (2014) Carbon quantum dots and their applications. Chem Soc Rev 44:362–381
22. Baker SN, Baker GA (2010) Luminescent carbon nanodots: emergent nanolights. Angew Chemie Int Ed 49:6726–6744
23. Demchenko AP, Dekaliuk MO (2013) Novel fluorescent carbonic nanomaterials for sensing and imaging. Methods Appl Fluoresc 1:042001
24. Emam AN, Loutfy SA, Mostafa AA, Awad H, Mohamed MB (2017) Cyto-toxicity, biocompatibility and cellular response of carbon dots–plasmonic based nano-hybrids for bioimaging. RSC Adv 7:23502–23514
25. Yang S-T et al (2009) Carbon dots for optical imaging in vivo. J Am Chem Soc 131:11308–11309
26. Hu R, Li L, Jin WJ (2017) Controlling speciation of nitrogen in nitrogen-doped carbon dots by ferric ion catalysis for enhancing fluorescence. Carbon N Y 111:133–141
27. Chen Y et al (2018) Concentration-induced multi-colored emissions in carbon dots: origination from triple fluorescent centers. Nanoscale 10:6734–6743
28. Guo L et al (2016) Tunable multicolor carbon dots prepared from well-defined polythiophene derivatives and their emission mechanism. Nanoscale 8:729–734
29. Gan Z, Xu H, Hao Y (2016) Mechanism for excitation-dependent photoluminescence from graphene quantum dots and other graphene oxide derivates: consensus, debates and challenges. Nanoscale 8:7794–7807
30. Yuan F et al (2017) Bright multicolor bandgap fluorescent carbon quantum dots for electroluminescent light-emitting diodes. Adv Mater 29
31. Li H et al (2010) Water-soluble fluorescent carbon quantum dots and photocatalyst design. Angew Chemie – Int Ed 49:4430–4434
32. Yuan F et al (2016) Shining carbon dots: synthesis and biomedical and optoelectronic applications. Nano Today 11:565–586
33. Ding H, Yu S-B, Wei J-S, Xiong H-M (2016) Full-color light-emitting carbon dots with a surface-state-controlled luminescence mechanism. ACS Nano 10:484–491
34. Wang Y, Hu A (2014) Carbon quantum dots: synthesis, properties and applications. J Mater Chem C 2:6921

35. Bao L, Liu C, Zhang Z-L, Pang D-W (2015) Photoluminescence-tunable carbon nanodots: surface-state energy-gap tuning. Adv Mater 27:1663–1667
36. Li X, Zhang S, Kulinich SA, Liu Y, Zeng H (2015) Engineering surface states of carbon dots to achieve controllable luminescence for solid-luminescent composites and sensitive Be2+ detection. Sci Rep 4:4976
37. Sun YP et al (2006) Quantum-sized carbon dots for bright and colorful photoluminescence. J Am Chem Soc 128:7756–7757
38. Dimos K (2016) Carbon quantum dots: surface passivation and functionalization. Curr Org Chem 20:682–695
39. Sachdev A, Matai I, Gopinath P (2014) Implications of surface passivation on physicochemical and bioimaging properties of carbon dots. RSC Adv 4:20915–20921
40. Li L et al (2013) Focusing on luminescent graphene quantum dots: current status and future perspectives. Nanoscale 5:4015
41. Zhou X et al (2012) Photo-Fenton reaction of graphene oxide: a new strategy to prepare Graphene quantum dots for DNA cleavage. ACS Nano 6:6592–6599
42. Sun H, Wu L, Wei W, Qu X (2013) Recent advances in graphene quantum dots for sensing. Mater Today 16:433–442
43. Rajender G, Giri PK (2016) Formation mechanism of graphene quantum dots and their edge state conversion probed by photoluminescence and Raman spectroscopy. J Mater Chem C 4:10852–10865
44. Wang Z, Zeng H, Sun L (2015) Graphene quantum dots: versatile photoluminescence for energy, biomedical, and environmental applications. J Mater Chem C 3:1157–1165
45. Journal AI, Kittiratanawasin L, Hannongbua S (2016) The effect of edges and shapes on band gap energy in graphene quantum dots. Integr Ferroelectr 175:211–219
46. Choi S-H (2017) Unique properties of graphene quantum dots and their applications in photonic/electronic devices. J Phys D Appl Phys 50:103002
47. Zhang R et al (2015) Size and refinement edge-shape effects of graphene quantum dots on UV – visible absorption. J Alloys Compd 623:186–191
48. Eda G et al (2010) Blue photoluminescence from chemically derived graphene oxide. Adv Mater 22:505–509
49. Sk MA, Ananthanarayanan A, Huang L, Lim KH, Chen P (2014) Revealing the tunable photoluminescence properties of graphene quantum dots. J Mater Chem C 2:6954–6960
50. Zhu S et al (2017) Nano today photoluminescence mechanism in graphene quantum dots: quantum confinement effect and surface / edge state. Nano Today 13:10–14
51. Pang J et al (2016) CVD growth of 1D and 2D sp2 carbon nanomaterials. J Mater Sci 51:640–667
52. Zahid MU, Pervaiz E, Hussain A, Shahzad MI, Niazi MBK (2018) Synthesis of carbon nanomaterials from different pyrolysis techniques: a review. Mater Res Express 5:052002
53. Zhu H et al (2009) Microwave synthesis of fluorescent carbon nanoparticles with electrochemiluminescence properties. Chem Commun 7:5118
54. Ohta K et al (2014) Synthesis of carbon nanotubes by microwave heating: influence of diameter of catalytic Ni nanoparticles on diameter of CNTs. J Mater Chem A 2:2773–2780
55. Shi K, Yan J, Lester E, Wu T (2014) Catalyst-free synthesis of multiwalled carbon nanotubes via microwave-induced processing of biomass. Ind Eng Chem Res 53:15012–15019
56. Kokorina AA, Prikhozhdenko ES, Sukhorukov GB, Sapelkin AV, Goryacheva IY (2017) Luminescent carbon nanoparticles: synthesis, methods of investigation, applications. Russ Chem Rev 86
57. Hou P, Liu C, Cheng H (2008) Purification of carbon nanotubes. Carbon N Y 46:2003–2025
58. Chiang IW, Brinson BE, Smalley RE, Margrave JL, Hauge RH (2001) Purification and characterization of single-wall carbon nanotubes. J Phys Chem B 105:1157–1161
59. Iijima S (1991) Helical microtubules of graphitic carbon. Nature 354:56–58
60. Rafique MMA, Iqbal J (2011) Production of carbon nanotubes by different routes – a review. J Encapsulation Adsorpt Sci 1:29–34

61. Joselevich E, Dai H, Liu J, Hata K, Windle AH (2008) Carbon nanotube synthesis and organization. Organization 164:101–164
62. Arora N, Sharma NN (2014) Arc discharge synthesis of carbon nanotubes: comprehensive review. Diam Relat Mater 50:135–150
63. Huang Z, Ling Z, Guangming H, Rongsheng S (1998) Synthesis of various forms of carbon nanotubes by AC arc discharge. Carbon N Y 36:259–261
64. Mubarak NM, Abdullah EC, Jayakumar NS, Sahu JN (2014) An overview on methods for the production of carbon nanotubes. J Ind Eng Chem 20:1186–1197
65. Guo T, Nikolaev P, Thess A, Colbert DT, Smalley RE (1995) Catalytic growth of single-walled nanotubes by laser vaporization. Chem Phys Lett 243:49–54
66. Kruusenberg I et al (2011) Effect of purification of carbon nanotubes on their electrocatalytic properties for oxygen reduction in acid solution. Carbon N Y 49:4031–4039
67. Prasek J et al (2011) Methods for carbon nanotubes synthesis – review. J Mater Chem 21:15872–15884
68. See CH, Harris AT (2007) A review of carbon nanotube synthesis via fluidized-bed chemical vapor deposition. Ind Eng Chem Res 46:997–1012
69. Szabó A et al (2010) Synthesis methods of carbon nanotubes and related materials. Materials (Basel) 3:3092–3140
70. Zhou D, Chow L (2003) Complex structure of carbon nanotubes and their implications for formation mechanism. J Appl Phys 93:9972–9976
71. Ugarte D (1994) High-temperature behaviour of “fullerene black”. Carbon N Y 32:1245–1248
72. Gamaly EG, Ebbesen TW (1995) Mechanism of carbon nanotube formation in the arc discharge. Phys Rev B 52:2083–2089
73. Scott CD, Arepalli S, Nikolaev P, Smalley RE (2001) Growth mechanisms for single-wall carbon nanotubes in a laser-ablation process. Appl Phys A 580:573–580
74. Gorbunov AA, Graff A, Jost O, Pompe W (2001) Mechanism of carbon nanotube synthesis by laser ablation. In: Libenson, M. N., pp 212–217
75. Das R, Shahnavaz Z, Ali ME, Islam MM, Abd Hamid SB (2016) Can we optimize arc discharge and laser ablation for well-controlled carbon nanotube synthesis? Nanoscale Res Lett 11:510
76. Akizuki N, Aota S, Mouri S, Matsuda K, Miyauchi Y (2015) Efficient near-infrared up-conversion photoluminescence in carbon nanotubes. Nat Commun 6:1–6
77. Jena PV, Galassi TV, Roxbury D, Heller DA (2017) Progress toward applications of carbon nanotube photoluminescence. ECS J Solid State Sci Technol 6:M3075–M3077
78. Wang F (2011) The optical resonances in carbon. Science 80:838–841
79. Chiu CF, Saidi WA, Kagan VE, Star A (2017) Defect-induced near-infrared photoluminescence of single-walled carbon nanotubes treated with polyunsaturated fatty acids. J Am Chem Soc 139:4859–4865
80. Ghosh S, Bachilo SM, Simonette RA, Beckingham KM, Weisman RB (2010) Oxygen doping modifies near-infrared band gaps in fluorescent single-walled carbon nanotubes. Science 330:1656–1660
81. Piao Y et al (2013) Brightening of carbon nanotube photoluminescence through the incorporation of sp3 defects. Nat Chem 5:840–845
82. Xu X et al (2004) Electrophoretic analysis and purification of fluorescent single-walled carbon nanotube fragments. J Am Chem Soc 126:12736–12737
83. Yang ST et al (2009) Carbon dots as nontoxic and high-performance fluorescence imaging agents. J Phys Chem C 113:18110–18114
84. Qiao ZA et al (2010) Commercially activated carbon as the source for producing multicolor photoluminescent carbon dots by chemical oxidation. Chem Commun 46:8812–8814
85. Lu J et al (2009) One-pot synthesis of fluorescent carbon graphene by the exfoliation of graphite in ionic liquids. ACS Nano 3:2367–2375
86. Li H et al (2012) Carbon quantum dots/Cu2O composites with protruding nanostructures and their highly efficient (near) infrared photocatalytic behavior. J Mater Chem 22:17470–17475

87. Ma CB et al (2015) A general solid-state synthesis of chemically-doped fluorescent graphene quantum dots for bioimaging and optoelectronic applications. Nanoscale 7:10162–10169
88. Wang R, Lu K-Q, Tang Z-R, Xu Y-J (2017) Recent progress in carbon quantum dots: synthesis, properties and applications in photocatalysis. J Mater Chem A 5:3717–3734
89. Bottini M et al (2006) Isolation and characterization of fluorescent nanoparticles from pristine and oxidized electric arc-produced single-walled carbon nanotubes. J Phys Chem B 110:831–836
90. Zuo P, Lu X, Sun Z, Guo Y, He H (2016) A review on syntheses, properties, characterization and bioanalytical applications of fluorescent carbon dots. Microchim Acta 183:519–542
91. Castro HPS et al (2016) Synthesis and characterisation of fluorescent carbon Nanodots produced in ionic liquids by laser ablation. Chem – A Eur J 22:138–143
92. Reyes D et al (2016) Laser ablated carbon nanodots for light emission. Nanoscale Res Lett 11:424
93. Nguyen V, Yan L, Si J (2016) Synthesis of broad photoluminescence carbon nanodots by femtosecond laser ablation in liquid. In: 2016 IEEE 16th international conference on nanotechnology (IEEE-NANO) 901–903, IEEE
94. Calabro RL, Yang D, Kim DY (2018) Journal of colloid and Interface science liquid-phase laser ablation synthesis of graphene quantum dots from carbon nano-onions: comparison with chemical oxidation. J Colloid Interface Sci 527:132–140
95. Li H, Kang Z, Liu Y, Lee S (2012) Carbon nanodots: synthesis, properties and applications. J Mater Chem 22:24230
96. Suda Y (2002) Preparation of carbon nanoparticles by plasma-assisted pulsed laser deposition method—size and binding energy dependence on ambient gas pressure and plasma condition. Thin Solid Films 415:15–20
97. Wang Y, Zhu Y, Yu S, Jiang C (2017) Fluorescent carbon dots: rational synthesis, tunable optical properties and analytical applications. RSC Adv 7:40973–40989
98. Hu S et al (2009) One-step synthesis of fluorescent carbon nanoparticles by laser irradiation. J Mater Chem 19:484–488
99. Lan M et al (2017) Two-photon-excited near-infrared emissive carbon dots as multifunctional agents for fluorescence imaging and photothermal therapy. Nano Res 10:3113–3123
100. Li H et al (2013) Near-infrared light controlled photocatalytic activity of carbon quantum dots for highly selective oxidation reaction. Nanoscale 5:3289
101. Iannazzo D, Ziccarelli I, Pistone A (2017) Graphene quantum dots: multifunctional nanoplatforms for anticancer therapy. J Mater Chem B 5:6471–6489
102. Russo P et al (2016) Single-step synthesis of graphene quantum dots by femtosecond laser ablation of graphene oxide dispersions. Nanoscale 8:8863–8877
103. Lin TN et al (2015) Laser-ablation production of graphene oxide nanostructures: from ribbons to quantum dots. Nanoscale 7:2708–2715
104. Zhou S, Xu H, Gan W, Yuan Q (2016) Graphene quantum dots: recent progress in preparation and fluorescence sensing applications. RSC Adv 6:110775–110788
105. Sun Y et al (2013) Large scale preparation of graphene quantum dots from graphite with tunable fluorescence properties. Phys Chem Chem Phys 15:9907
106. Zheng XT, Ananthanarayanan A, Luo KQ, Chen P (2015) Glowing graphene quantum dots and carbon dots: properties, syntheses, and biological applications. Small 11:1620–1636
107. Su M, Zheng B, Liu J (2000) A scalable CVD method for the synthesis of single-walled carbon nanotubes with high catalyst productivity. Chem Phys Lett 322:321–326
108. Mubarak NM, Yusof F, Alkhatib MF (2011) The production of carbon nanotubes using two-stage chemical vapor deposition and their potential use in protein purification. Chem Eng J 168:461–469
109. Zhao N, He C, Jiang Z, Li J, Li Y (2006) Fabrication and growth mechanism of carbon nanotubes by catalytic chemical vapor deposition. Mater Lett 60:159–163
110. Koziol K, Boskovic BO, Yahya N (2010) Synthesis of carbon nanostructures by CVD method. Carbon 77:23–49

111. Corrias M et al (2003) Carbon nanotubes produced by fluidized bed catalytic CVD: first approach of the process. Chem Eng Sci 58:4475–4482
112. Li YL et al (2004) Synthesis of single-walled carbon nanotubes by a fluidized-bed method. Chem Phys Lett 384:98–102
113. Hiraoka T, Bandow S, Shinohara H, Iijima S (2006) Control on the diameter of single-walled carbon nanotubes by changing the pressure in floating catalyst CVD. Carbon N Y 44:1853–1859
114. Tay B, Sheeja D, Lau S, Guo J (2003) Study of surface energy of tetrahedral amorphous carbon films modified in various gas plasma. Diam Relat Mater 12:2072–2076
115. Lin CH, Lee SH, Hsu CM, Kuo CT (2004) Comparisons on properties and growth mechanisms of carbon nanotubes fabricated by high-pressure and low-pressure plasma-enhanced chemical vapor deposition. Diam Relat Mater 13:2147–2151
116. Yan L et al (2016) Synthesis of carbon quantum dots by chemical vapor deposition approach for use in polymer solar cell as the electrode buffer layer. Carbon N Y 109:598–607
117. Kumar S, Aziz ST, Girshevitz O, Nessim GD (2018) One-step synthesis of N-doped Graphene quantum dots from chitosan as a sole precursor using chemical vapor deposition. J Phys Chem C 122:2343–2349
118. Fan L et al (2013) Direct synthesis of graphene quantum dots by chemical vapor deposition. Part Part Syst Charact 30:764–769
119. Kukovitsky EF, L'vov SG, Sainov N a, Shustov V a, Chernozatonskii LA (2002) Correlation between metal catalyst particle size and carbon nanotube growth. Chem Phys Lett 355:497–503
120. Schwenke AM, Hoeppener S, Schubert US (2015) Synthesis and modification of carbon nanomaterials utilizing microwave heating. Adv Mater 27:4113–4141
121. Nüchter M, Müller U, Ondruschka B, Tied A, Lautenschläger W (2003) Microwave-assisted chemical reactions. Chem Eng Technol 26:1207–1216
122. López C et al (2015) Microwave-assisted synthesis of carbon dots and its potential as analysis of four heterocyclic aromatic amines. Talanta 132:845–850
123. Liu Y et al (2014) One-step microwave-assisted polyol synthesis of green luminescent carbon dots as optical nanoprobes. Carbon N Y 68:258–264
124. Pan L, Sun S, Zhang L, Jiang K, Lin H (2016) Near-infrared emissive carbon dots for two-photon fluorescence bioimaging. Nanoscale 8:17350–17356
125. Li D et al (2018) Near-infrared excitation/emission and multiphoton-induced fluorescence of carbon dots. Adv Mater 30:1–8
126. Li K et al (2017) Technical synthesis and biomedical applications of graphene quantum dots. J Mater Chem B 5:4811–4826
127. Lin L et al (2014) Luminescent graphene quantum dots as new fluorescent materials for environmental and biological applications. TrAC – Trends Anal Chem 54:83–102
128. Tetsuka H et al (2012) Optically tunable amino-functionalized graphene quantum dots. Adv Mater 24:5333–5338
129. Bacon M, Bradley SJ, Nann T (2014) Graphene quantum dots. Part Part Syst Charact 31:415–428
130. Shen J, Zhu Y, Yang X, Li C (2012) Graphene quantum dots: emergent nanolights for bioimaging, sensors, catalysis and photovoltaic devices. Chem Commun 48:3686
131. Zhao P et al (2018) Near infrared quantum dots in biomedical applications: current status and future perspective. Wiley Interdiscip Rev Nanomed Nanobiotechnol 10:e1483
132. Li X, Zhang S, Kulinich SA, Liu Y, Zeng H (2015) Engineering surface states of carbon dots to achieve controllable luminescence for solid-luminescent composites and sensitive Be2+ detection. Sci Rep 4:4976
133. Zhang L, Wang E (2014) Metal nanoclusters: new fluorescent probes for sensors and bioimaging. Nano Today 9:132–157
134. Resch-Genger U, Grabolle M, Cavaliere-Jaricot S, Nitschke R, Nann T (2008) Quantum dots versus organic dyes as fluorescent labels. Nat Methods 5:763–775

135. Say JM et al (2011) Luminescent nanodiamonds for biomedical applications. Biophys Rev 3:171–184
136. Chen M, Yin M (2014) Design and development of fluorescent nanostructures for bioimaging. Prog Polym Sci 39:365–395
137. Wall KP, Dillon R, Knowles MK (2015) Fluorescence quantum yield measurements of fluorescent proteins: a laboratory experiment for a biochemistry or molecular biophysics laboratory course. Biochem Mol Biol Educ 43:52–59
138. Cherukuri P, Bachilo SM, Litovsky SH, Weisman RB (2004) Near-infrared fluorescence microscopy of single-walled carbon nanotubes in phagocytic cells. J Am Chem Soc 126:15638–15639
139. Hong G et al (2014) Through-skull fluorescence imaging of the brain in a new near-infrared window. Nat Photonics 8:723–730
140. Welsher K, Sherlock SP, Dai H (2011) Deep-tissue anatomical imaging of mice using carbon nanotube fluorophores in the second near-infrared window. Proc Natl Acad Sci 108:8943–8948
141. Yudasaka M et al (2017) Near-infrared photoluminescent carbon nanotubes for imaging of brown fat. Sci Rep 7:44760
142. Song Y, Zhu S, Yang B (2014) Bioimaging based on fluorescent carbon dots. RSC Adv 4:27184
143. Nurunnabi M, Khatun Z, Reeck GR, Lee DY, Lee Y (2013) Near infra-red photoluminescent graphene nanoparticles greatly expand their use in noninvasive biomedical imaging. Chem Commun 49:5079
144. Zhu S et al (2011) Strongly green-photoluminescent graphene quantum dots for bioimaging applications. Chem Commun 47:6858
145. Kim J-H et al (2010) A luciferase/single-walled carbon nanotube conjugate for near-infrared fluorescent detection of cellular ATP. Angew Chemie Int Ed 49:1456–1459
146. Li YH, Zhang L, Huang J, Liang RP, Qiu JD (2013) Fluorescent graphene quantum dots with a boronic acid appended bipyridinium salt to sense monosaccharides in aqueous solution. Chem Commun 49:5180–5182
147. Bardhan NM (2017) 30 years of advances in functionalization of carbon nanomaterials for biomedical applications: a practical review. J Mater Res 32:107–127
148. Malik MA, Wani MY, Hashim MA, Nabi F (2011) Nanotoxicity: dimensional and morphological concerns. Adv Phys Chem 2011:15

Chapter 8
NIR-Persistent Luminescence Nanoparticles for Bioimaging, Principle and Perspectives

Bruno Viana, Cyrille Richard, Victor Castaing, Estelle Glais, Morgane Pellerin, Jianhua Liu, and Corinne Chanéac

8.1 Introduction

Since the discovery of $SrAl_2O_4:Eu^{2+},Dy^{3+}$ long-persistent luminescence (PersL) by Matsuzawa et al. more than 20 years ago [1], many persistent phosphors have been developed and studied. In the past decade, visible persistent phosphors based on sulfides, aluminates, gallates, and silicates hosts doped with various active ions have been developed [2, 3]. Several compounds with sufficiently strong and long-lasting (>10 h) persistent luminescence properties in the green and blue ranges have already been commercialized and widely used in various applications, such as security and emergency route signs, dials, and displays. More recently, persistent

B. Viana (✉) · V. Castaing
Chimie ParisTech, PSL University, CNRS UMR 8247, Institut de Recherche de Chimie Paris, Paris, France
e-mail: bruno.viana@chimieparistech.psl.eu

C. Richard · J. Liu
Unité de Technologies Chimiques et Biologiques pour la Santé, Paris, France

CNRS UMR 8258, INSERM U1267, Paris, France

Université Paris Descartes, Sorbonne Paris Cité, Faculté des Sciences Pharmaceutiques et Biologiques, Paris, France

E. Glais · M. Pellerin
Chimie ParisTech, PSL University, CNRS UMR 8247, Institut de Recherche de Chimie Paris, Paris, France

Sorbonne Université, CNRS, Collège de France, Laboratoire de Chimie de la Matière Condensée de Paris, Paris, France

C. Chanéac
Sorbonne Université, CNRS, Collège de France, Laboratoire de Chimie de la Matière Condensée de Paris, Paris, France

A. Benayas et al. (eds.), *Near Infrared-Emitting Nanoparticles for Biomedical Applications*, https://doi.org/10.1007/978-3-030-32036-2_8

phosphors in the deep red emission range at nanometric scale have been proposed for in vivo bioimaging [4–9]. Optical imaging is highly complementary to other imaging methods, such as X-rays or magnetic resonance imaging, in particular due to its potential for data acquisition at high speeds. It allows the visualization of dynamic biological processes, events related to physiology, and disease progression [10]. For that purpose, luminescent probes enable the study of biological processes in great details [11]. Among these probes, semiconductor quantum dots (QDs) exhibiting fluorescence optical properties have emerged as a class of nanoparticles for bioimaging and diagnostics. The possibility to detect and diagnose cancer or other human diseases at earlier stages than with current imaging methods caused a drastic increase of interest in nano-imaging technology. A non-invasive very cheap imaging technique, which is comfortable, portable, highly sensitive, and that allows real-time imaging is still to be developed. The field of biomedical optics has matured rapidly during the last 10 years, and is expected to continue its maturation in the next years. It provides a rapid, immediate (real-time dynamics), and cheap method for diagnosis. However, in spite of these great advantages, biomedical optics is limited because photons are scattered and absorbed by the tissues and this limits the spatial resolution. The penetration depth of photons inside a tissue depends strongly on the type of tissue [12], but most importantly, it depends on the wavelength (λ) of the photons used. Scattering drastically decreases when λ increases in the so-called tissue transparency window [13] (see in Fig. 8.1 that mainly the red and near infrared photons can go through living tissues). In vivo imaging of exogenous fluorescent probes that target diseased tissues has also shown promising results in clinical settings, such as the early detection of breast cancer, the outlining of tumor margins during surgery and endoscopic diagnosis of cancer micrometastasis. However, the method is limited by tissue attenuation (scattering and absorption of the excitation or the emission light) and by tissue autofluorescence [14]. To minimize tissue attenuation effects, researchers have been concentrated on deep red and near infrared (NIR) fluorophores that are excited and emit in the spectral window between wavelengths of 650–950 nm. However, tissue autofluorescence still produces a substantial background signal in this spectral range that severely limits the quality of images, especially when very low concentrations of the fluorescent probe accumulate at the target site and there is recent works to move toward NIR/SWIR ranges [15–18].

Persistent luminescence phosphors are materials able to store optical energy and release it gradually by photon emission. This particular property is linked to the presence of trapping levels located in the forbidden gap of the material (see Fig. 8.1) [2, 19, 20]. Optical excitation of these materials leads to photoluminescence (PL) but can also induce charge trapping [21]. The trapped charges (electrons, holes) can then slowly be released following thermal stimulation, leading to their recombination at emitting centers followed by light emission for a long time (typically from minutes to hours [1, 22, 23]) after stopping the irradiation. For persistent luminescence, the trap depth, that is the energetic difference between the trap and the conduction band, should be smaller than 1 eV to enable charging and discharging at the body temperature [2].

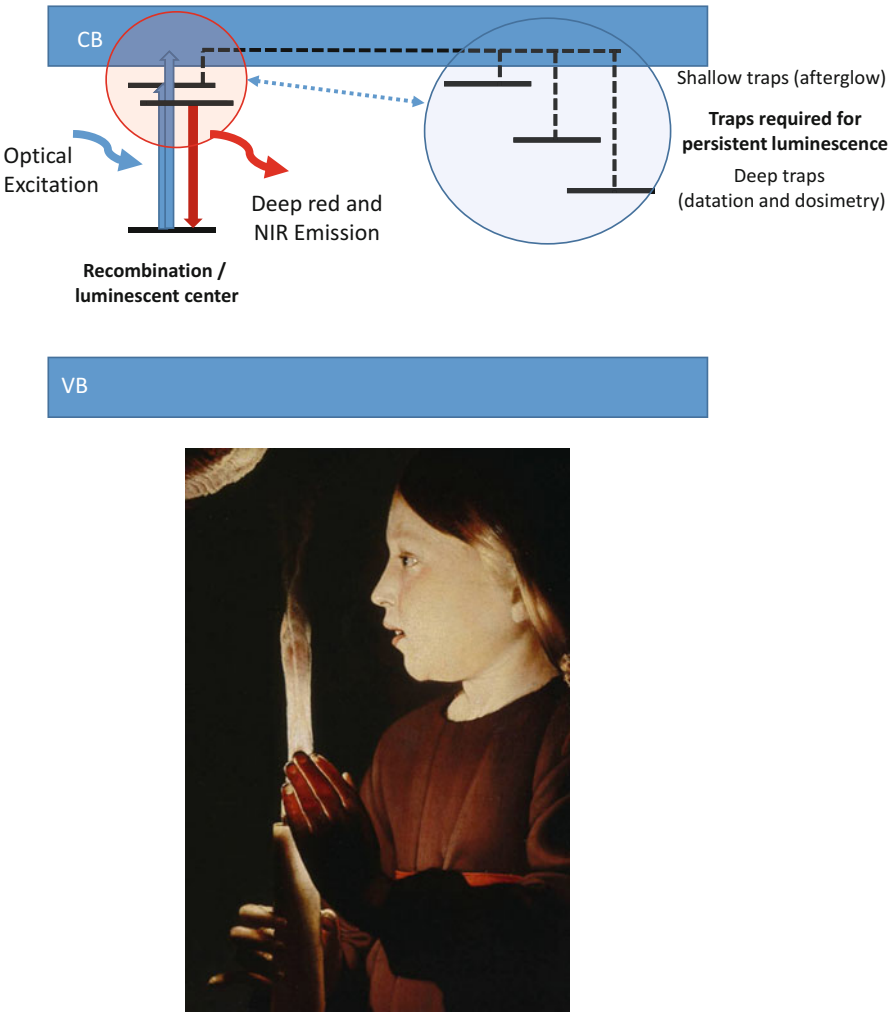

Fig. 8.1 **Top**: Schematic of the energy levels and traps involved in the persistent luminescence mechanisms (Reprinted with permission from ref. [5]). **Bottom**: Partial transparency of living tissues in deep red range (see light through the young girl's left hand and Fig. 8.11c), extracted from Saint Joseph charpentier, G. de La Tour, 1643, Musée du Louvre, Paris, France

It appeared that metal transition cations such as Mn^{2+} or Cr^{3+}, or rare-earth elements are good dopants for in vivo optical bioimaging based on persistent luminescence in the deep red/NIR range [4, 24], but other compounds listed below have recently demonstrated a lot of interest. Please notice that $ZnGa_2O_4:Cr^{3+}$ (ZGO) is one of the most interesting long-lasting phosphor in the gallate family. It shows deep red emission centered at 696 nm originating from the ^2E to $^4A_2$ transition of Cr^{3+} ions [25]. A focus on this compound and its main characteristics are presented in the following parts of the chapter.

Persistent luminescence phenomenon, whereby luminescent materials keep emitting light after the excitation stopped, has intrigued people since several centuries. As this property occurs in inorganic materials when the excitation has been stopped, this is sometimes compared to the bioluminescence mechanism observed in some animals (such as fireflies and jellyfishes). Other fluorescent probes in the NIR range also reported in this book are the semiconductor quantum dots (QDs) or upconversion nanoparticles (UCNPs).

8.2 Main Characteristics of the Persistent Luminescence Materials

Long-persistent luminescence is controlled by the slow liberation of trapped charge carriers at body temperature by a simple thermal de-excitation process. The luminescence can last for several minutes to hours after removal of the excitation source (typically several minutes of ultraviolet light) [1, 69]. In persistent luminescence materials, energy can be stored by traps/defects that are charged under irradiation. Emergency signage that can be used in case of electricity failure is one of the main applications of these persistent phosphors, but others applications were proposed such as watch dials, when radioactive elements were fully forbidden more than 20 years ago, decorative objects and toys and more recently for bioimaging as described in this chapter.

For the materials concerned with the persistent luminescence properties, there is in the literature plenty of compounds tested with various successes. Rare-earth and transition metal cations have been widely used as dopant for persistent luminescence materials in last years. More than 200 combinations of host materials and activator ions have been depicted. The reader could see reviews and book chapters on the topic [2, 3]. For bioimaging and in vivo application, as seen in Table 8.1, the past 5 years have witnessed several major advances to establish deep red/near infrared-emitting persistent luminescence nanomaterials as a novel approach for real time used in vivo in small animal.

The main requirements that the materials must fulfill for this application are the following: (1) compounds prepared as nanoparticles (PLNPs with size <100 nm) and even ultrasmall nanoparticles (<10 nm), (2) intensive emission extending in the deep red toward the near infrared range in the first or second windows corresponding to the tissue transparency [16], (3) efficient functionalization, (4) colloidal or chemical stability, and (5) persistent emission over hours. These points are the reasons why applications using deep red emitting persistent phosphors for bio-applications were barely investigated in the first step of the development of the persistent phosphors and the investigation started in 2007 after our pioneer paper [29]. Several materials were further developed for imaging applications (see Table 8.1 and review papers such as [70]). Notice that at first all the researches were focused in the BW1 range (high transmission range of the living tissue, see

Table 8.1 Main nanoparticles used with metal transition (MT) cations and rare-earth (RE) cations for red/near infrared emission and applications in bioimaging. Emission ranges are indicated in the NIR BW1: (deep red and <1000 nm); BW2: (1000–1500 nm), and BW3: (>1500 nm)

Hosts	Dopants	Comments and applications in bioimaging *(BW1 or see below)*	Year and Refs
Gd_2O_2S	Eu^{3+},Mg^{2+},Ti^{4+}	NPs regular shape, bimodality optical/MRI	[26] (2015)
$Ca_3(PO_4)_2$/HAP	Mn^{2+},Tb^{3+},Dy^{3+}	Fully biocompatible, NPs and in vivo imaging	[26] (2015)
$Ca_2Si_5N_8$	Eu^{2+},Tm^{3+}	Bioimaging applications	[8] (2012)
$SrAl_2O_4$	Eu^{2+},Dy^{3+}	NPs, functionalization, bioimaging applications, (*green emission*)	[27, 28] (2014, 2018)
$Ca_{0.2}Zn_{0.9}Mg_{0.9}Si_2O_6$	Mn^{2+},Eu^{2+},Dy^{3+}	NPs, functionalization, pioneer work for bioimaging: cancer cells imaging, cell targeting	[29–31] (2007, 2011, 2012)
$Ca_{1.86}Mg_{0.14}ZnSi_2O_7$	Eu^{2+},Dy^{3+}	FRET and various biosensing applications	[32] (2018)
$CaMgSi_2O_6$	Mn^{2+},Eu^{2+},Pr^{3+}	NPs, functionalization, bioimaging	[33] (2011)
$MAlO_3$ (M=La, Gd)	Mn^{4+}/Ge^{4+}	Bioimaging in pork tissue	[34] (2016)
$GdAlO_3$	Mn^{4+},Ge^{4+}@Au	Trimodality imaging	[34] (2016)
	Sm^{3+},Cr^{3+}	Optical and magnetic dual mode imaging	[35] (2018)
$ZnGa_2O_4$	Cr^{3+}	NPs, functionalization, bioimaging (cancer cells imaging), cell targeting, cytotoxicity, visible light stimulation NIR photostimulation, X-rays activation	[7] (2014) (2014) [36, 37] (2017), (2018)
		Oral administration and breast cancer imaging	[38] (2018)
		Toxicology analysis	[39] (2017)
		Protobiotic analysis	[40] (2017)
$ZnGa_2O_4$ in hollow cavity	Cr^{3+}	Photodynamic therapies	[41] (2018)
$ZnGa_2O_4$	Cr^{3+},Gd^{3+}	NPs, functionalization, bimodality optical/NMR imaging	[42] (2015)
$ZnGa_2O_4/SiO_2$	Cr^{3+}	NPs, core–shell structure, drug delivery	[43] (2014)
$ZnGa_2O_4/Fe_2O_3$	Cr^{3+}	NPs, core-shell, magnetic properties	[44] (2018)
ZGOCS@MSNs@Gd_2O_3	Cr^{3+}	Cell labeling and magnetic vectorization, Multimodal nanoprobes	[45] (2017)
$Zn_{1.1}Ga_{1.8}Ge_{0.1}O_4/SiO_2$	Cr^{3+},Eu^{3+}	NPs, core–shell structure, drug delivery	[46] (2015)
$ZnGa_2O_4$	Cr^{3+},Yb^{3+}	NPs exctarcted from glass-ceramics	[146] (2019)

(continued)

Table 8.1 (continued)

Hosts	Dopants	Comments and applications in bioimaging *(BW1 or see below)*	Year and Refs
$Zn_3Ga_2Ge_2O_{10}$	Cr^{3+}	Imaging of pork tissue, photostimulation, cytotoxicity	[47] (2014)
$Zn_{1.1}Ga_{1.8}Ge_{0.1}O_4@SiO_2$	Cr^{3+}	Bioimaging and drug delivery	[48] (2018)
$Zn_{1.25}Ga_{1.5}Ge_{0.25}O_4$	Cr^{3+},Yb^{3+},Er^{3+}	Metastasis tracking and chemo-photodynamic therapy	[49] (2018)
$Zn_{1.1}Ga_{1.8}Ge_{0.1}O_4$	Cr^{3+}	Nanothermometry	[50] (2017)
$Zn_3Ga_2Sn_1O_{10}$	Cr^{3+}	Imaging of goldfish	[51] (2014)
$Zn_{2.94}Ga_{1.96}Ge_2O_{10}$	Cr^{3+},Pr^{3+}	NPs, functionalization	[52] (2013)
$Zn_3Ga_2Ge_2O_{10}$	Cr^{3+}	Recognition of breast cancer cells	[53] (2015)
$Zn_3Ga_2GeO_8$	Cr^{3+},Yb^{3+},Er^{3+}	Upconversion	[54] (2014)
$LiGa_5O_8$	Cr^{3+}/PEG-OCH_3	NPs, functionalization, bioimaging, visible light stimulation, photostimulation	[55, 56] (2013, 2014)
$Ca_3Ga_2Ge_3O_{12}$	Cr^{3+},Yb^{3+},Tm^{3+}	NIR stimulation, upconversion	[57] (2014)
	Pr^{3+},Yb^{3+}	In vivo imaging	[58] (2017)
$mSiO_2@Gd_3Ga_5O_{12}$	Cr^{3+},Nd^{3+}	Multimodal imaging and cancer therapy	[59] (2018)
Sr_2SnO_4	Nd^{3+}	Finger image (*BW2*)	[60] (2014)
$SiO_2/CaMgSi_2O_6$	Eu^{2+},Pr^{3+},	Bioimaging, intraperitoneal injection	[61] (2014)
YAGG (garnet)	Mn^{2+},Er^{3+},Cr^{3+}	Photostimulation imaging of pork tissue (*BW2*) Imaging in the second biological window	[14] (2018)
$NaYF_4+SrAl_2O_4$	Yb^{3+},Tm^{3+},Eu^{2+},Dy^{3+}	Upconversion and photodynamic therapy	[62] (2018)
$Sr_2MgSi_2O_7$	$Eu^{2+/3+}$,Dy^{3+}	Photodynamic activation	[63] (2016)
		Visualization of abdominal inflammation	[64] (2018)
$La_3Ga_5GeO_{14}$ @SiO_2@Van	Cr^{3+},Zn^{2+}	Bioimaging-guided in vivo and drug delivery	[65] (2018)
$CaTiO_3$	Pr^{3+},Yb^{3+},Tm^{3+}	Upconverting and guided photothermal therapy	[66] (2017)
$ZnSn_2O_4$	Cr^{3+},Eu^{3+}	Cellular and deep-tissue imaging	[67] (2017)
$Sr_3Sn_2O_7$	Nd^{3+}	Second window imaging (*BW2*)	[68] (2017)

Notice that the emission range is BW 1 for most of the nanomaterials except when indicated

also Figs. 8.1 and 8.11) where the Si detector also reaches its maximal sensitivity. More recently researchers extend the range to the second and third biological windows (BW) even if the results are still very preliminary in that 1000–1350 nm spectral range (BW2) [15–18] and above 1500 nm (BW3) as presented in the following parts of the chapter. In the development of the new phosphors with long-persistent luminescence for bio-applications, one should keep in mind that various synthesis strategies are used for small-size preparation of PLNPs with good crystallinity but also with the optimum of defects at the origin of the persistent luminescence. Hydrothermal, solvothermal, sol–gel, and coprecipitation methods have been widely used. In addition, effective surface functionalization strategies along with the biocompatibility issues required attention to make them useful for in vivo bioimaging.

8.3 Persistent Luminescence Mechanisms

The physics behind the phenomenon is however not that simple and intensive researches have been carried out during the last past years. For the trapping processes, which is the primary and very important step in the persistent luminescence mechanism, two kinds of strategies are envisioned:

(1) *Intrinsic defects and optimization of the traps by composition variation and thermal annealing*. Intrinsic defects have been well identified in lots of materials [19, 71]. In garnet hosts, antisite defects for instance are very likely, they shorten some Y–O bonds and create shallow electron traps close to the conduction band. Antisite defects in the vicinity of Cr^{3+} ions have been proposed to be involved in the persistent luminescence mechanism of the zinc-gallate spinel host [25, 72]. One should also notice that thermal annealing under reducing atmosphere is often used to create or enhance intrinsic traps such as oxygen vacancies, which correspond to electron traps that can be responsible for the persistent luminescence [73].

(2) *Traps optimization by co-doping*. Co-doping is the second strategy that has been intensively tested to enhance the persistent luminescence. Co-doping with one or two lanthanides cations is most of the time used to enhance the property. For instance, Dy^{3+} was used as electrons trap in the first mix enstatite/diopside silicate for the proof of concept of the in vivo bioimaging application with PLNPs [29]. Moreover it appeared that Pr^{3+} was indeed better when only the diopside bandgap was considered [33]. The variation of traps depth strongly depends on the host/dopant couple and corresponds to a so-called bandgap engineering as introduced in previous works [74, 75], with the prediction of the energy level diagram [76, 77]. Such bandgap engineering was proposed in various hosts used for persistent luminescence but was also tested with success in others *photonic applications* such as scintillation and lighting. It is then currently possible to vary the position of the conduction band and

the traps depth by varying the composition playing with cationic and anionic substitutions, or a careful choice of the doping cation for an optimal couple composition/dopant.

To go in deeper understanding, knowledge of the energy formation of defects, defects stability, and defects energy position are required, through band structure and defects calculations [78]. The persistent luminescence mechanism has been characterized by lots of different spectroscopies including optical (absorption, emission, excitation, decay profiles), electron paramagnetic resonance (EPR) [79], and X-ray spectroscopies [80] to give insights to the mechanism, thermoluminescence [33], and photoconductivity [81, 82] to estimate the traps depth [19, 83]. In the case of electron traps and hole traps [84, 85], the stored charges can be released by various processes as expressed in the following parts such as thermal [86], optical [87], or other physical stimulations [88], resulting in stimulated emissions from the active recombination centers.

8.4 Focus on One Developed Materials $ZnGa_2O_4$:Cr Nanoparticles for Persistent Luminescence Applications in the BW1 Range

If metal transition-doped $ZnGa_2O_4$ nanoparticles can be obtained by different techniques, our activity recently focused on the hydrothermal synthesis assisted by microwave heating in order to obtain ultrasmall nanoparticles with persistent luminescence properties. To avoid sintering and keep the nanometric size during the following thermal treatment, the nanoparticles are embedded in a silica layer using a sol–gel chemistry way. A mixture of TEOS:EtOH 1:4 is added to a basic solution of nanoparticles. Using such a method, nanoparticles can be doped by various transition metal cations and even rare-earth cations for persistent emission in the near infrared. Focused on the BW1 where the sensitivity of the Si detector is maximum, we choose the trivalent Cr^{3+} for deep red/NIR emission. The obtained $ZnGa_2O_4$:Cr^{3+},Bi^{3+}@SiO_2 nanoparticles are then calcined in air during 2 h at 1000 °C to improve crystallinity. The nanoparticles are monodispersed with a sub-10 nm size [89].

To better characterize the persistent luminescence properties of the $ZnGa_2O_4$:Cr^{3+} nanocrystals, we also recently proposed with colleagues from Orleans, France to prepare these nanocrystals embedded in a glass phase in the so-called ZGO nano glass-ceramics. The TEM pictures of both the nano-objects are presented in Fig. 8.2. The nanoparticles embedded in glassy matrix present an average diameter about 16 nm, while after hydrothermal synthesis assisted by microwave, nanoparticles smaller than 10 nm in diameter can be obtained (see Fig. 8.2). The nanoparticles are spherical and well dispersed. In both cases, after crystallization at 900 °C and thermal treatment at 1000 °C, respectively, the obtained nano-objects are well crystallized in the pure ordered spinel phase and present persistent luminescence properties. NPs can be further extracted from these glass-ceramics.

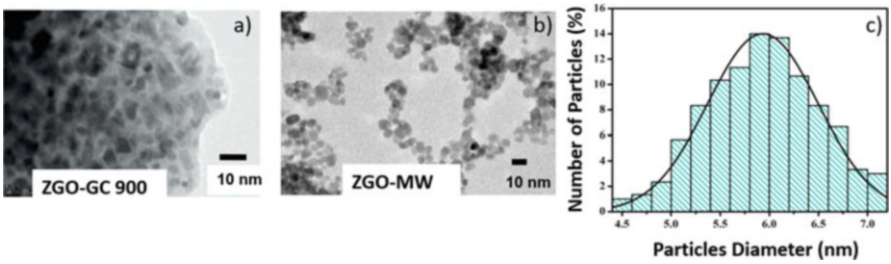

Fig. 8.2 TEM pictures of (**a**) $ZnGa_2O_4:Cr^{3+}$ (ZGO) nanoparticles embedded in glass matrix (crystallization temperature = 900 °C), (**b**) ZGO nanoparticles after hydrothermal synthesis assisted by microwave heating, (**c**) associated distribution diagram of the ZGO nanoparticles after hydrothermal synthesis assisted by microwave heating without coating, adapted from [89, 90]

Cr^{3+}-doped ZGO nanoparticles photoluminescence and persistent luminescence spectra are presented in Fig. 8.3-a. Several contributions of the chromium emission are well identified: the R line corresponding to the zero phonon line, Stokes and anti-Stokes phonon side bands (S-PSB and AS-PSB, respectively). The N2 line is attributed to the Cr^{3+} emission in antisite defect vicinity [25]. The persistent luminescent emission spectrum is mostly dominated by the N2 line, indicating that these cations, spatially closed to electron traps are partly responsible of the persistent luminescence phenomenon (see following parts). Figure 8.3-b shows the persistent luminescence decay after 2 min of UV irradiation of $ZGO:Cr^{3+}$ nanoparticles. Even with these ultrasmall nanoparticles, it is possible to detect the signal more than 2 hours after switching off the UV lamp.

As experimentally determined as well as calculated [92, 93], in such nanomaterials, antisites defects around the Cr^{3+} cations are needed to get persistent luminescence properties. Nuclear magnetic resonance (NMR) and EPR spectroscopies can give some insights on the local disorder of the structure, especially on the Ga^{3+} and Cr^{3+} site symmetry in the crystals, respectively, while thermoluminescence gives insights on the persistent luminescence capability [90]. In the particular case of $ZnGa_2O_4:Cr^{3+}$ and derivatives, EPR is a technique of choice to learn about Cr^{3+} environments. Indeed, there is a splitting of the $^4A_2$ chromium level into two degenerated states (one $m_s = \pm 3/2$ and one $m_s = \pm ½$) due to the crystal field distortion and the spin–orbit coupling. An application of a magnetic field can raise the degeneracy of these levels. Depending on the Cr^{3+} vicinity, the splitting of these levels may be different leading to various EPR signals. Several EPR studies have been performed on $ZnGa_2O_4:Cr^{3+}$, resulting in a better understanding of the local material structure and the possibility to distinguish several Cr^{3+} environments using simulations. First, the simulations on powder phosphors have shown that five different Cr^{3+}surroundings may exist in $ZnGa_2O_4:Cr^{3+}$ material [92]. The results also strengthened the assumption about the role of antisite defects on persistent luminescence properties. Indeed, it has been demonstrated that the charge trapping in $ZnGa_2O_4:Cr^{3+}$ may be related to two antisite defects in the Cr^{3+} neighborhood

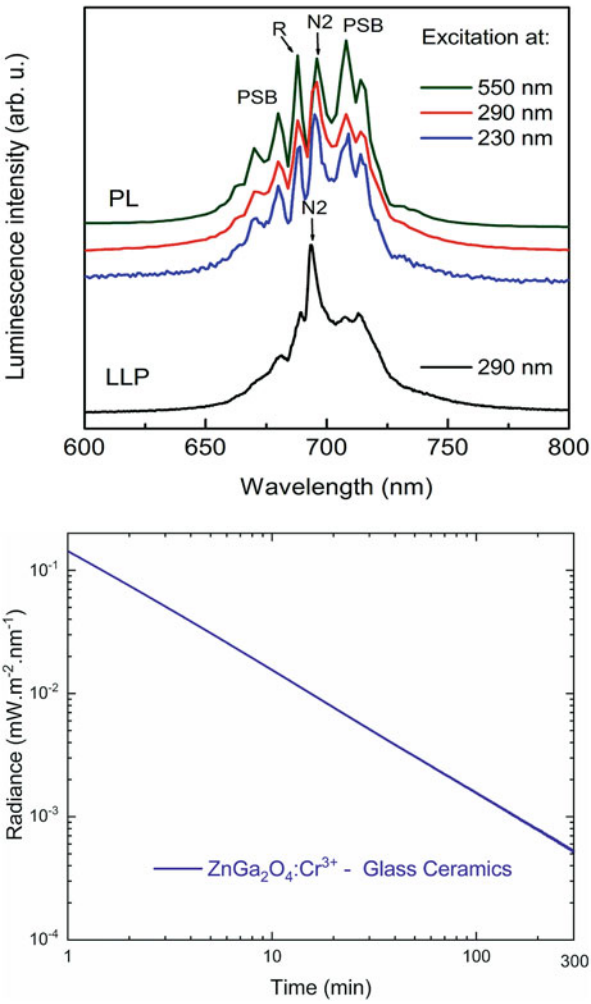

Fig. 8.3 **Top**: (PL) Emission spectra of photoluminescence and (LLP) persistent luminescence at room temperature. Reprinted with permission from ref. [21]. **Bottom**: Persistent luminescence decay of $ZnGa_2O_4:Cr^{3+}$ nanoparticles (within more than 2 h). Adapted from [91]

(Cr-γ, Cr-δ, Cr-ε). We recently demonstrated that simulations using these five kinds of Cr^{3+} also perfectly fit our nanocrystals [90] (see Fig. 8.4). An important EPR result in this system is the possible quantification of chromium environment. This quantification enables to estimate the dependence on synthesis parameters. For instance, in the case of glass-ceramics, one can notice a global increase of undistorted Cr^{3+} environment when T_{cryst} increases revealing a better symmetry around Cr^{3+} in agreement with the improvement of crystalline quality (Table 8.2).

Thermoluminescence (TL) or thermally stimulated luminescence (TSL) is the most common technique used to demystify the traps number and their depths. This is a required characterization technique prior to persistent luminescence NPs development. At first, in the thermoluminescence experiments, traps must be

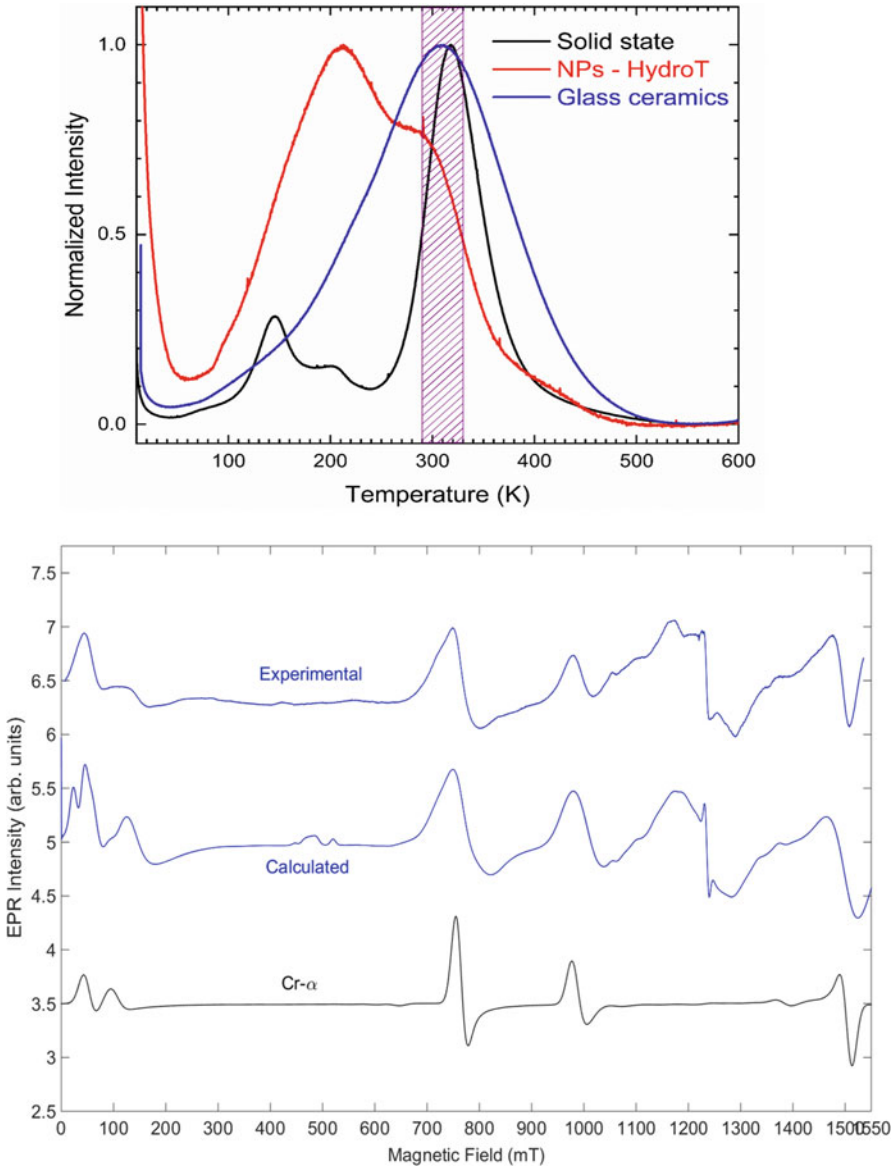

Fig. 8.4 **Top**: Thermoluminescence glow curves with different sizes and shapes. **Bottom**: Simulation and experimental EPR spectra for the ZGO:Cr. Adapted from [90]

filled by optical (from X-rays to NIR photons) or others stimulations. Notice that mechanoluminescence [94] is also recently an important field of investigation. As mentioned above, in a second step, thermal energy or other excitation processes can release these traps. During the TL experiments, the sample is linearly heated,

Table 8.2 EPR parameters and Cr^{3+} surrounding. Adapted from [90]

	Cr_α	Cr_β	$Cr_\gamma + Cr_\delta + Cr_\varepsilon$	Φ
ZGO-GC 900 °C	5.4 %	59.9 %	24.5 %	10.2 %
ZGO-GC 1000 °C	18.2 %	52.4 %	21.5 %	7.9 %

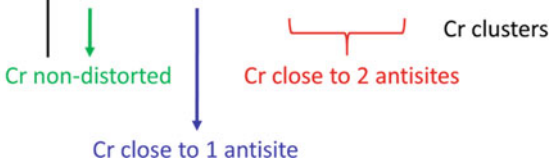

from 10 K to 600 K in our facility. When the thermal energy brought by the heater is sufficient, i.e., in the order of the energy difference between a recombination center and the traps, charges start to be detrapped. After being released, charges can either be trapped again in the same or other traps in the vicinity or recombine on the emitting centers. In this latest process, thermoluminescence occurs and can be recorded. The result of the experiment, as presented in Fig. 8.4, shows luminescent intensity as a function of the temperature. The number and position of the glow curve peaks give insights on the trap depths and distributions. Regarding the glow curve shape, several equations can correlate the trap depth to the peak temperature [95]. In case of broader bands, which appears to be often the case for PLNPs, a simple estimation can be made using [96]:

$$E = \frac{T_m}{500}$$

where E is the trap depth and T_m is the temperature of the peak maximum. For the persistent luminescence properties, the release should occur at room temperature, and in case of in vivo applications it has to be close to the living tissues temperature. This means that materials should present thermoluminescence peaks centered at ca. 310 K to be suitable for this application. Another option is to design materials with several trap depths, traps corresponding to room temperature and deeper traps that cannot be thermally emptied at room temperature. In that case, a possible in vivo reactivation of the persistent luminescence via trap redistribution using optical stimulation (using for instance NIR light [97]) can be envisioned.

The thermoluminescence results for $ZnGa_2O_4:Cr^{3+}$ are displayed in Fig. 8.4 for several particle sizes and various shapes. The bulk material shows a relatively sharp thermoluminescence peak, labeled as the main peak, centered at 318 K, making it suitable for in vivo imaging based on persistent luminescence. It also shows two shallow traps, weaker in intensity around 145 and 200 K. Going from bulk material elaborated via solid-state method to nanoparticles elaborated by hydrothermal synthesis assisted by microwave heating, the thermoluminescence

glow curve becomes quite different. Indeed, the corresponding profile presents a broad signal that seems to be composed of two major contributions, one around 210 K and one around 300 K.

The first one can be related to the shallow traps whereas the second can be related to the previous main peak. As the surface over volume ratio increases when the size is reduced, surface defects may have a major contribution in case of nanoparticles. With that in mind, it has been assumed that the shallow traps can be related to surface defects. The thermoluminescence glow curve of $ZnGa_2O_4:Cr^{3+}$ glass-ceramics elaborated at 900 °C, reported in the same figure (see Fig. 8.4), presents a broad main peak centered at ca. 310 K. Two shallow traps can be observed at lower temperatures. In the glass-ceramics samples, the surface over volume ratio is very high because of the nanoscale of the crystals. Still, the surface defects quantity may be very low comparing to nanoparticles elaborated via microwave assisted hydrothermal method as the nanocrystals are in that case embedded in a glassy matrix. Thermoluminescence is therefore a good tool to investigate the local order and thus the crystal quality.

8.5 Biocompatibility

To be used in vivo, the nanoprobes should have the lowest toxicity. The main matrices presented above (see Table 8.1) are either NPs incorporated into silica (it can also be mesoporous silica as seen below) or oxide-based NPs. Biocompatibility was investigated by several groups (see for instance [98]). No pathological abnormality could be observed in both gross and microscopic histological examinations of various tissues including heart, liver, spleen, lung, and kidney up to 1 month after vein injection into mice, suggesting that the mesoporous silica PLNPs had not caused significant tissue toxicity and inflammation.

It was confirmed that neither gross nor histopathological abnormalities could be observed in the major organs [99]. Furthermore, at a high vein-injection dose of 50 mg kg^{-1} per day, the acute toxicity of PLNPs at longer times was almost negligible compared to the blank control according to the monitoring of the body-weight change, the visible and/or palpable dermal infection, the presence of ascites, the grooming or the impaired mobility. At an extremely high dose of 1200 mg kg^{-1}, no mouse survived after intraperitoneal or intravenous injection of MCM-41-type or SBA-15-type mesoporous silica nanoparticles (MSNs); however, the subcutaneous injection did not cause death at an equally high administration dose and doses of up to 200 mg kg^{-1}, which was high enough for drug loading and delivery owing to their high drug loading capacities, both by intraperitoneal and intravenous injection [100].

Concerning persistent luminescence nanoparticles themselves, two articles have been recently published concerning biocompatibility and toxicity assays in vivo on the ZGO:Cr PLPNs. The first one was reported in 2017 by Ramirez-Garcia et al. In this study, mice were injected with a single intravenous administration of

either hydroxylated or PEGylated persistent luminescence nanoparticles at different concentrations, from 1 to 8 mg per mice and a set of standard tests were carried out 1 day, 1 month and even 6 months after the administration [39]. High concentrations of hydroxylated nanoparticles generate structural alterations at histology level, endoplasmic reticulum damage and oxidative stress in liver, as well as rising in white blood cells counts. A mechanism involving the endoplasmic reticulum damage could be responsible for the observed injuries in case of ZGO-OH. On the contrary, no toxicological effects related to PEGylated nanoprobes treatment were noted during the in vivo experiments, denoting the protective effect of PEG functionalization and thereby, their potential as biocompatible in vivo diagnostic probes. In 2018, Zhang and coworkers [101] reported a 60 days in vivo study of ZGO derivatives ($Zn_{1.1}Ga_{1.8}Sn_{0.1}O_4:Cr^{3+}$) compound. In this work, healthy Balb/c mice were intravenously injected with ZGO derivative at a dose of 10 mg/kg. ZGO pre-irradiated with a 254 nm UV lamp was also set as one of the factors to evaluate the possible effect of NIR-persistent luminescence of ZGO in vivo. No signs of apparent weakness, spontaneous animal death, and significant body weight gain or loss were observed within 60 days. It was found that all of the parameters were in the normal reference range. In the hematological analysis, various serum biochemical parameters were measured with particular attention paid to liver and kidney function. Indicators of kidney function, including creatinine and urea nitrogen, were also within normal ranges and were similar to these of control mice. These results show no obvious injury to the liver and kidney with ZGO exposure in mice, even at long exposure times. Based on long-term in vivo biodistribution studies, the major organs from mice were sliced for hematoxylin and eosin staining and histological examination to determine whether or not ZGO exposure caused tissue damage, inflammation, or lesions. The structures of the organs hardly exhibited any difference from the control group. No apparent histopathological abnormalities or lesions were found in any of the experimental groups. All of these data suggested that no significant toxicity was induced by ZGO injection, even up to 60 days.

8.6 Excitation Capabilities and Long-Term In Vivo Imaging

Though intended for diagnosis applications in living animals, persistent luminescence nanoparticles suffer from severe limitations. First, as the release of photons is thermally activated, long-time accumulations of the signal (from seconds to minutes) are required during recording and materials with intensive persistent luminescence on one side and low noise detector on the other side should be used. The second point concerns the excitation mechanisms of the PLNPs but recent improvements have been made as described in this part of the chapter. Indeed the first generation of PLNPs has to be excited ex vivo by UV light prior to systemic administration preventing long-term imaging in living animal. Depending on the nanoparticles characteristics, slow accumulation of stealth nanocarriers within malignant stroma by the enhanced permeability and retention effect usually

requires from 2 to 24 h [102]. This was far too long in relation to the emission from persistent luminescence nanoparticles, which hardly exceeds 1 h in vivo.

To overcome this major restriction, developments of new materials and of new modalities have been undertaken. First, efforts to optimized compositions and enhanced optical characteristics have been made. In that sense, compounds based on gallate and gallo-germanate spinels have attracted large attention, due to their bright deep persistent luminescence when doped with trivalent chromium (Cr^{3+}) after UV excitation in comparison with the previously used silicate nanoprobes. Then one strategy is to play with the tunable wavelengths in the biological window. Various emission ranges are indicated in the NIR in three main ranges: BW1: deep red and <1000 nm; BW2: 1000–1500 nm, and BW3: >1500 nm. Furthermore one important point is to excite the persistent luminescence material at the lowest energy in the biological window (BW1 or BW2) and if possible, long time after the injection. The new modality has been proposed in different ways as seen in Fig. 8.5.

Figure 8.5 summarizes the various approaches that can be followed for long-term in vivo imaging with persistent luminescent nanoparticles. A suspension of PLNPs in a biological buffer can be pre-activated ex situ, then injected into the animal and placed under a photon-counting system to detect the emitted persistent luminescence signal (see step 1, Fig. 8.5). PLNPs can be activated or reactivated in situ (after the injection) through animal tissues (step 2, Fig. 8.5). This breakthrough for in vivo optical imaging allows the most simple and convenient recovery of the persistent luminescence signal, whenever required. The efficiency is lower than for the persistent luminescence under UV excitation (step 1) but is indeed sufficient to be detected and to localize the probe in vivo. Furthermore, for some inorganic persistent luminescent NPs, when deeper traps are observed in the thermoluminescence spectra such as in garnet and spinels hosts, deep red persistent emission can be stimulated by near infrared light, as the traps can be depopulated by low-energy light stimulation in the so-called photostimulated persistent luminescence (PSPL) [87, 103]. The photostimulation capability of several materials is widely reported [104–106] and researchers have focused their attention on the Cr^{3+}-doped samples. The photostimulation technique has been used over the years for UV dosimetry, as well as for dating geological and archeological materials [107]. One can adjust the depth of the traps responsible for the persistent luminescence and therefore control carefully the composition. In that case, the release of the traps and thus the emission could be *started at the convenience of the user* using a red/near infrared LED for instance, which will be in the best transparency range. The first preliminary carried out tests have shown the originality and feasibility of this new modality [97]. The excitation energy for charge detrapping may vary from red to NIR lamps, LED or laser sources. The photostimulation or excitation by low-energy light can also be carried out by additional step, corresponding to wavelength conversion [54, 57, 97], or possible charge through second-order effects under high excitation power [90, 108].

However, in vivo tracking is still hindered by its limited penetration in tissue even in the near infrared. An alternative way is to use NIR or X-ray as excitation source for imaging techniques. Indeed compared to the traditional excitation

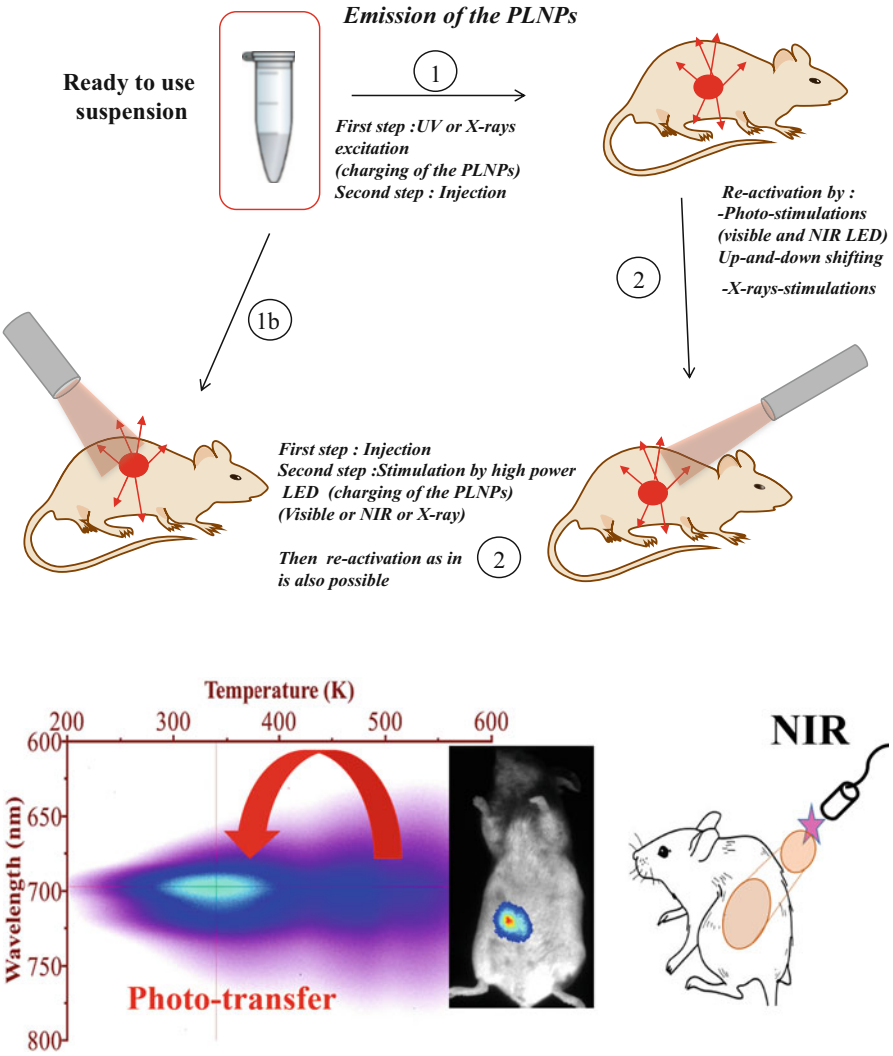

Fig. 8.5 **Top**: Different strategies to perform in vivo optical imaging with persistent luminescence nanoparticles (PLNPs). Reprinted with permission from ref. [6]. (1) Excitation of a suspension of nanoparticles followed by tail vein injection and optical imaging using a photon-counting camera. (2) Once the in vivo persistent luminescence signal has completely disappeared, some PLNPs can give further persistent luminescence signal either by photo- or X-rays stimulations. (1b) Some PLNPs can be excited without preliminary excitation (with lower efficiency) in the animal body using visible, near infrared (for upconversion) or X-rays photons, **Bottom**: Traps could be emptied by a near infrared source (energy $\sim$ 1 eV) showing the crucial role of charge-storage to deep traps and photo-transfer to shallow traps leading to persistent luminescence. This demonstrated the photostimulation capability at convenient time. Within this experiment, one observed long-lasting phosphorescence under 977 nm light excitation, (adapted from [97]), making in vivo excitation of the spinels probes envisioned and possible long-term imaging applications

source, X-ray possesses competitive advantages of weaker scattering and deeper penetration depth in tissues, as well as simplified image reconstruction for optical tomography. Developing X-ray rechargeable persistent luminescence nanoplatform, by combining the advantages of X-ray excitation and NIR-persistent emission in the second biological window, will enable to localize tumors and achieve treatment simultaneously [109]. This opens the door for achieving deeper tissue and higher sensitivity optical bioimaging with better spatial resolution. An example of such modality with ZGO:Cr PLNPs is presented in the following parts of the chapter.

8.7 Strategies Developed to Perform Long-Time Imaging

The pioneer work using persistent luminescence nanoparticles (PLNPs) for optical in vivo bioimaging was reported in 2007 by Scherman and coworkers [29]. As discussed in the previous section, to be used in vivo, the probe should have a nanometric scale and should emit light in one of the biological windows (>650 nm). In their work, the authors prepared a silicate doped with Eu^{2+}, Dy^{3+}, and Mn^{2+} and in vivo imaging without any background was performed for 30 min to 1 h without any in vivo excitation, allowing in vivo imaging without autofluorescence. Then after these pioneer works, lots of bio-applications and various modalities have been presented as seen in Table 8.1, and some of them are detailed in the following parts of the chapter. To overcome this major restriction and to allow longer time imaging, in 2014 Maldiney et al. changed the matrix and used zinc gallium oxide doped with Cr^{3+} [7]. As can be seen in Fig. 8.6, contrary to the first silicate-type generation,

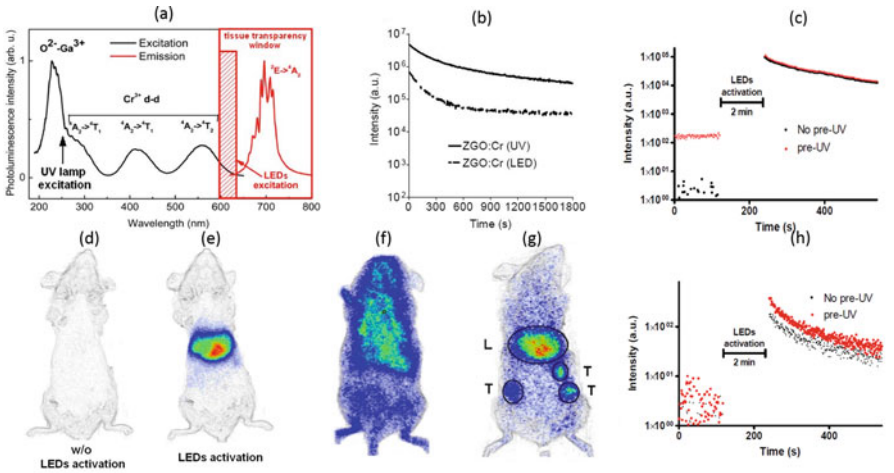

Fig. 8.6 In vivo imaging using in situ excitable PLNPs. (**a–c**) Optical properties of powder after either UV or visible excitation. (**d–h**) In vivo excitation of unfunctionalized PLNPs (**e**) or stealth ZGO in healthy (**f**) on tumor-bearing mice (**g**). Adapted from [7] and reprinted with permission from ref. [5]

this material has several excitation peaks, among them one being at the limit of the tissue transparency window (Fig. 8.6a) which can also sensitize the persistence luminescence. On nanosized $ZnGa_2O_4$:Cr, they observed a persistent luminescence decay signal after both UV and activation with visible orange/red light-emitting diodes (LEDs) (Fig. 8.6b). A suspension of this material dispersed into 5% glucose was injected into mice, and for the first time the authors have shown that the probe could be activated in vivo with orange/red light-emitting diodes. The authors have also shown that UV pre-excitation before LED reactivation is favorable but not necessary (Fig. 8.6c and h). In such conditions, there was no more time limit and the probe could be detected in vivo whenever wanted through a simple excitation with the LEDs (Fig. 8.6e–g).

It is of great importance to develop deep red/NIR PLNPs with rechargeable nature in vivo by a deep tissue penetrating source (see Fig. 8.1, old painting showing only red light through living tissues). Recent years have witnessed the rapid development of utilizing innovative excitation sources for imaging techniques [110]. For instance X-ray photon energies are able to stimulate luminescent centers in phosphors and then generate light. Furthermore, compared with the traditional excitation sources (UV/visible/NIR), X-rays possess competitive advantages of weaker scattering and deeper penetration depth in tissues and simplified image reconstruction for optical tomography [111]. As a proof of concept, Xue et al. selected $ZnGa_2O_4:Cr^{3+}$ PLNPs as models for X-ray-activated NIR-persistent emission [37]. In vivo NIR-persistent luminescence bioimaging based on these X-PLNPs was demonstrated (see Fig. 8.7). More importantly, these X-PLNPs were also repeatedly charged by X-rays at a deep location up to 20 mm. These results revealed that X-rays could act as a new excitation source for persistent renewable bioimaging with a deep penetration depth based on NIR PLNPs.

8.8 Multimodal Imaging

Multimodal imaging has drawn much attention in biomedical applications because it provides more accurate, complete, and reliable information on diagnosis [113]. Each imaging modality has its own advantages and disadvantages regarding sensitivity, spatial/temporal resolution, and penetration depth. The NIR optical imaging possesses the advantage of high sensitivity but presents limited spatial resolution. In contrast, MRI provides excellent spatial resolution and unlimited depth penetration but remains at an inherently low sensitivity [114]. The combination of NIR emitting PLNPs and MRI contrast agent into one single nanoplatform would offer attractive synergistic advantages in biomedical imaging with high sensitivity, good spatial resolution, high signal over noise ratio, and no ionizing radiation.

Several strategies have been reported using for instance gadolinium to perform bimodal imaging PLNPs. In 2014, Yan and coworkers reported the surface functionalization of $Zn_{1.1}Ga_{1.8}Ge_{0.1}O_4$ with DTPA–Gd complexes to get bimodal imaging agents, able to be detected both by optical imaging and as a positive T_1 MRI

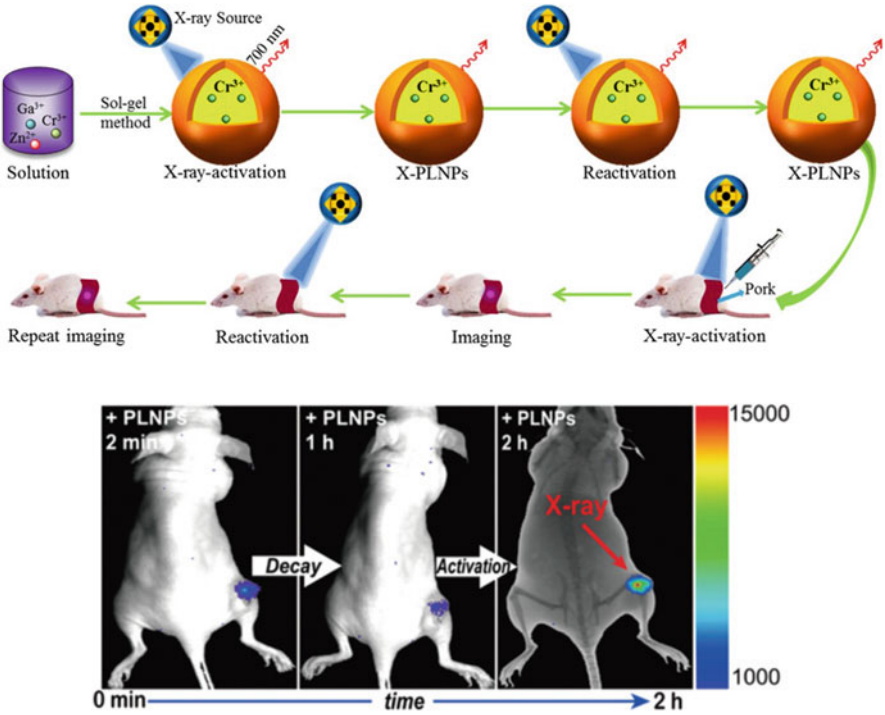

Fig. 8.7 **Top**: Principle of in vivo imaging using X-ray excitation and applications in vivo. Reprinted with permission from ref. [37] and L. Song et al. **Bottom**: Repeatable deep-tissue activation of persistent luminescence nanoparticles by soft X-ray for high sensitivity long-term in vivo bioimaging Nanoscale 2017, 9, 2718] [37, 112]

contrast agent [115]. In 2015, Maldiney et al. reported another method to prepare PLNPs-based bimodal imaging agents. In their strategy, instead of using the surface of the PLNPs to link DTPA–Gd complexes, the authors co-doped their NPs by incorporating various amount of Gd^{3+} ions at the beginning of the synthesis, by substituting Ga^{3+} ions [42]. In such conditions, a negative contrast was obtained, with a r_2 value close to 60 mM^{-1} s^{-1}. In 2017, Zou et al. used a third strategy to prepare bimodal imaging agents. In their work, a novel core–shell structure multimodal imaging probe was prepared, based on the coverage of mesoporous silica nanoparticles (MSNs) loaded with $ZnGa_2O_4$:Cr^{3+}, Sn^{4+} (ZGOCS@MSNs) by a Gd_2O_3 shell (~1.5 nm) [45]. Compared with previously reported Gd^{3+}-based NIR-persistent luminescence multimodal nanoprobes, the as-prepared nanoparticles enable available surface, no persistent intensity loss, and only a slight size increase.

Instead of gadolinium, ultrasmall iron oxide nanoparticles (also called USPIO) are used in clinic as negative (T_2) MRI contrast agents. In 2015, Teston et al. reported the first synthesis of mesoporous nanohybrids (MPNHs) composed of a combination of PLNPs and USPIOs embedded into a mesoporous silica structure to

get a bimodal imaging agent [116]. In addition of its bimodal imaging property, the authors showed that this nanoplatform could be attracted by a magnet. They used this property to label and attract cells in vivo [44].

8.9 Theranostics Nanoprobes

During the past 10 years, it has been shown that diagnosis and therapy could be combined within a single multifunctional nanomaterial, known as theranostic nanoparticles [5, 117]. The ideal theranostic nanomaterial should possess several advantages [118]: (1) the ability for highly selective accumulation in the diseased tissue, (2) the capability of delivering an effective therapeutic action selectively, and (3) safety concerns. The material should undergo biodegradation into non-toxic byproducts. Such nanomaterials are one of the keys for detection and treatment of early-stage cancer in the twenty-first century [119]. Theranostic nanoparticles are still in the very early translational stages, with nearly all efforts devoted to preclinical studies and no clinical trials to date. In this section, we highlight the recent use of PLNPs for the development of new theranostic nanoprobes.

Typically, mesoporous silica ($m\mathrm{SiO_2}$) can be used as a promising drug carrier because of its stable mesoporous structure, high specific surface area, and good biocompatibility [120]. Using mesoporous silica alone as a drug carrier appears impossible to effectively locate a target site (i.e., tumor) and monitor in real time due to the lack of detectable signals. In 2014, Maldiney et al. introduced a multifunctional nanoplatform based on persistent luminescence nanoparticles for both in vivo optical imaging and drug delivery [43]. Taking advantage of the well-known biocompatibility of mesoporous silica and non-toxic ZGO, the authors modeled a novel core–shell structure on the basis of a hybrid chromium-doped zinc gallate/mesoporous silica architecture specifically designed to allow both highly sensitive optical detection through living tissues and concomitant drug delivery. With doxorubicin as a drug model, the authors demonstrated that these mesoporous persistent luminescence nanophosphors can be successfully loaded with an anticancer agent, and subsequently initiate its progressive release in a pH-sensitive manner. The use of such doxorubicin-loaded theranostic agent is finally shown to induce acute cytotoxicity toward U87MG cells in vitro, preserved persistent luminescence properties, and allowed both sensitive and non-invasive localization of the carrier in vivo.

In 2016, Zhang and coworkers developed another core–shell NPs composed of $\mathrm{Gd_2O_3}$, ZGO, and $\mathrm{mSiO_2}$ [121]. This multimodal nanoprobe could be detected both by MRI and optical imaging and was used to monitor its biodistribution in healthy and tumor-bearing mice after loading with doxorubicin (see Fig. 8.8).

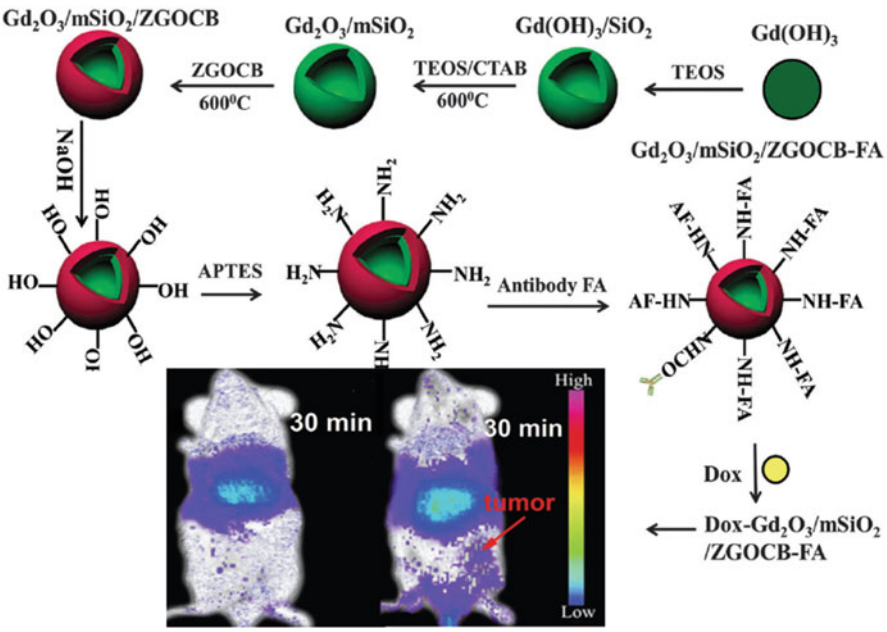

Fig. 8.8 Synthesis procedure of mesoporous ZGO, loading with Dox and in vivo application. Reprinted with permission from ref. [121]

8.10 Photodynamic Therapy with PLNPs

A few photosensitizers (PSs), such as porfimer sodium, have been approved by the US Food and Drug Administration (FDA) to treat certain cancers. However, most of the available PSs for photodynamic therapy (PDT) can only be activated under the UV/visible light (<700 nm) with low tissue penetration. New strategies in order to use such molecules in better conditions are under investigation.

PDT is a relatively new modality for cancer treatment [122]. PDT consists of three essential components: light, oxygen, and a photosensitizer [123]. Photosensitizers, often pharmacologically inactive without illumination, can be activated by light of a specific wavelength. This activation is followed by transfer of energy to nearby oxygen molecules to generate cytotoxic reactive oxygen species (ROS), and most importantly singlet oxygen ($^1O_2$). PDT is a relatively less invasive treatment modality, inducing low systematic toxicity and causing little intrinsic or acquired resistance. One primary downside of PDT, however, is its inability to treat tumors located deep under the skin due to the short penetration depth of light in tissues [124]. This problem can be partially alleviated by advanced light-delivering technologies that allow for illumination of certain internal cavities, such as the bladder, prostate, lung, and esophagus. Nevertheless, it is considered as challenging or impossible for conventional PDT to treat tumors of large volumes or multiple *loci*.

High X-ray dose (>5.0 Gy) is needed for efficient cancer therapy, and this dose was comparable or even higher than the fraction dose used in clinical radiotherapy [125]. Many researches have shown that high-dose X-rays irradiation inevitably causes damages to normal tissues [126].

In this regard, reducing X-ray dose is a major concern for deep-tissue PDT practical applications. Persistent luminescence nanoparticles (PLNPs) are promising luminescent materials that can store excitation energy and then slowly release the trapped charge carriers to emit persistent luminescence without continuous excitation. PLNPs alone have limited impact on cancer cells development [127]. In 2015, a novel X-ray inducible photodynamic therapy (X-PDT) approach was reported that allows PDT to be regulated by X-rays [112]. Upon X-ray irradiation, the integrated nanosystem, which corresponds to a core of a nanoscintillator $SrAl_2O_4:Eu^{2+}$ (SAO) and a mesoporous silica coating loaded with photosensitizers (MW540), converts X-ray photons to visible photons to activate the photosensitizers and cause efficient tumor shrinkage (see Fig. 8.9).

In 2018, Yang and coworkers have shown that Zn (II) phthalocyanine tetrasulfonic acid (ZnPcS4) can be covalently linked to ZGO in order to fabricate PDT nanoplatform (ZGO:Cr/W–ZnPcS4). After the X-ray irradiation has been removed, the persistent luminescence continuously excites the coupled PS, resulting in significantly reduced X-ray dosage (≈0.18 Gy), minimizing the side effects of PDT treatment [36].

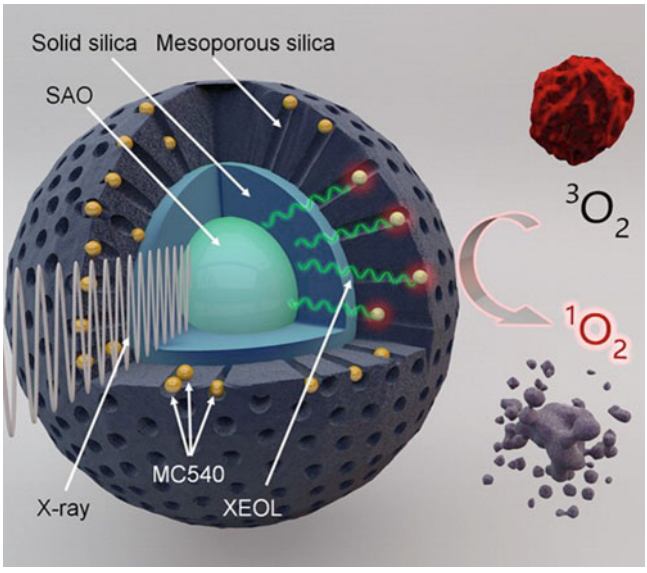

Fig. 8.9 Schematic of PLNPs loaded with PDT agent (MW540). Reprinted with permission from ref. [112]

8.11 Photothermal Therapy with PLNPs

Among all the cancer treatments, near infrared (NIR 700–1000 nm) laser-induced photothermal therapy (PTT) is a non-invasive mode that can generate heat at the tumor site [128]. Compared with conventional therapies, it has attracted much interest in tumor therapy as a minimally invasive and noninjurious therapeutic program as well as large penetration into bio-tissues. Photothermal therapy agents are capable of converting light energy into heat inducing a rise in the local temperature beyond 42 °C and killing consequently cancer cells. As an FDA-approved drug, indocyanine green (ICG) is attractive for localized hyperthermia by absorbing near infrared light (around 800 nm) even in deep tissue to generate heat. To further enhance the fluorescence stability and enhanced permeation and retention effect (EPR) of ICG in vivo, a variety of nanocarriers has been developed. Therefore, the ICG-loading nanoparticle is a brand-new photothermal therapy agent which could be diffusely used in clinic for photothermal therapy. Nevertheless, the traditional ICG-loading nanoparticles cannot be tracked when they circulate in the body; therefore, it is out of the question to ensure an accurate irradiation with additional near infrared (700–1000 nm) laser. Optical imaging-guided therapy has received great attention recently and become a fine choice of loading the ICG and tracking it for PTT [66] (Fig. 8.10).

In 2017, Chang and coworkers used ZGO NPs and ICG co-loaded into mesoporous silica nanoparticles (ICG@mZGO nanoparticles) for imaging-guided PTT [129]. The ICG@mZGO nanoparticles consisted of two parts: (1) Mesoporous $SiO_2/ZnGa_2O_4:Cr^{3+}$ (mZGO) near infrared PLNPs were used as near infrared-emitting probe to track NPs in vivo after excited by light. They found that mesoporous silica nanoparticles could be a fine template to synthesize ZGO phosphors in situ with good morphology and expected size. Mesoporous silica nanoparticles could also load and protect ICG, which had the ability to avoid particle aggregation effectively during the transportation. (2) Indocyanine green (ICG), a kind of tricarbocyanine dye, which substantially absorbed the near infrared light (NIR) and in result returned a photothermal response.

In a different approach, upconverting PLNPs and photo-absorbing agents ICG co-loaded into $mSiO_2$ (UCPLNPs and ICG co-loaded $mSiO_2$) nanoparticles were developed for upconverting and persistent luminescent imaging-guided PTT [66]. The UCPLNPs and ICG co-loaded $mSiO_2$ nanoparticles include three parts: (1) the upconverting PLNPs, doped with Pr^{3+}, Er^{3+}, and Tm^{3+} chosen for upconverting and persistent luminescent imaging. These NPs could be excited by NIR light and emit upconverting luminescence, which can be used for in vivo imaging when the persistent luminescence signal became weak; (2) the ICG (indocyanine green), a water-soluble anionic tricarbocyanine dye, which is the only NIR agent approved by FDA and which has been widely used clinically for PTT; (3) the mesoporous silica nanoparticles working as a three-dimensional hard template for loading and protecting both upconverting PLNPs and ICG [66].

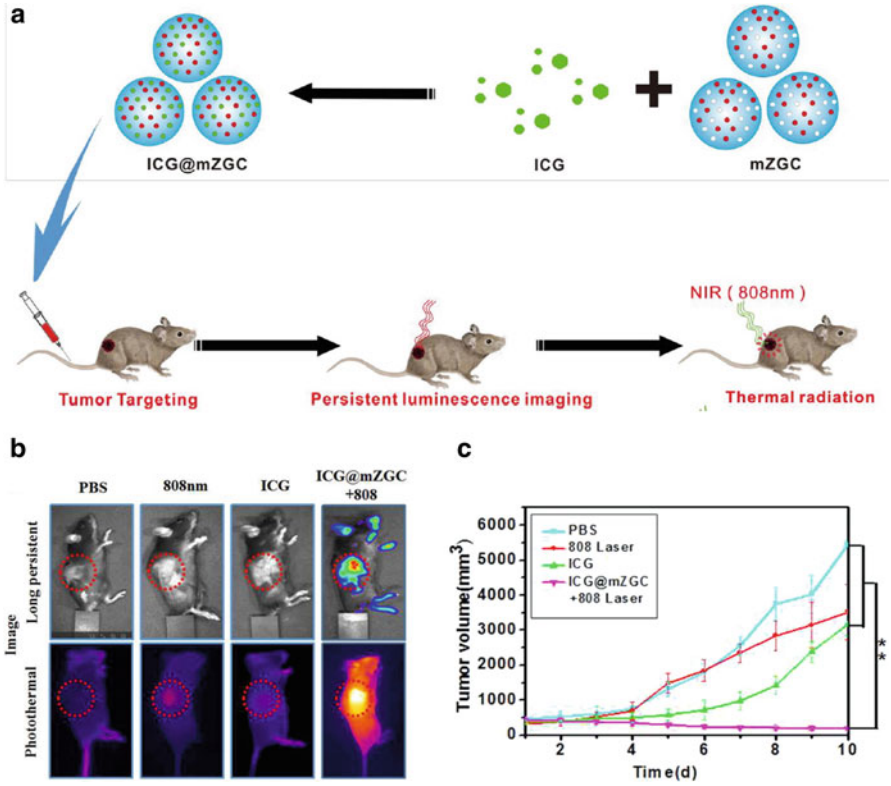

Fig. 8.10 PTT induced by using ICG loaded in PLNPs. (**a**) Schematic, (**b**) in vivo results, and (**c**) effects to reduce tumor volume. Reprinted with permission from ref. [129]

8.12 Perspectives of the NIR-Persistent Luminescence Nanoparticles for Bioimaging

One of the main challenges is to move the persistent emission wavelength from the first to the second and third biological windows (see Fig. 8.11c). Indeed in the NIR, three main ranges are relevant: BW1: deep red and <1000 nm; BW2: 1000–1500 nm, and BW3: >1500 nm, but mainly the BW1 has been investigated at the present time. Different approaches are currently explored: (1) Traps can be coupled to various rare-earth cations (Yb^{3+}, Nd^{3+}, Er^{3+}, Ho^{3+}, Tm^{3+}, or even Pr^{3+}) well known in the case of NIR lasers (see Fig. 8.11b) [16]. (2) Down shifting can also be obtained by coupling different rare-earth cations or transition metal (TM) and rare-earth cations. The so-called traps redistribution by energy transfer can downshift the persistent emission wavelengths (see Fig. 8.11a). Such downconversion processes were proposed recently for garnet and perovskite hosts coupling metal transition cation (Cr^{3+}) with rare-earth cations to promote by

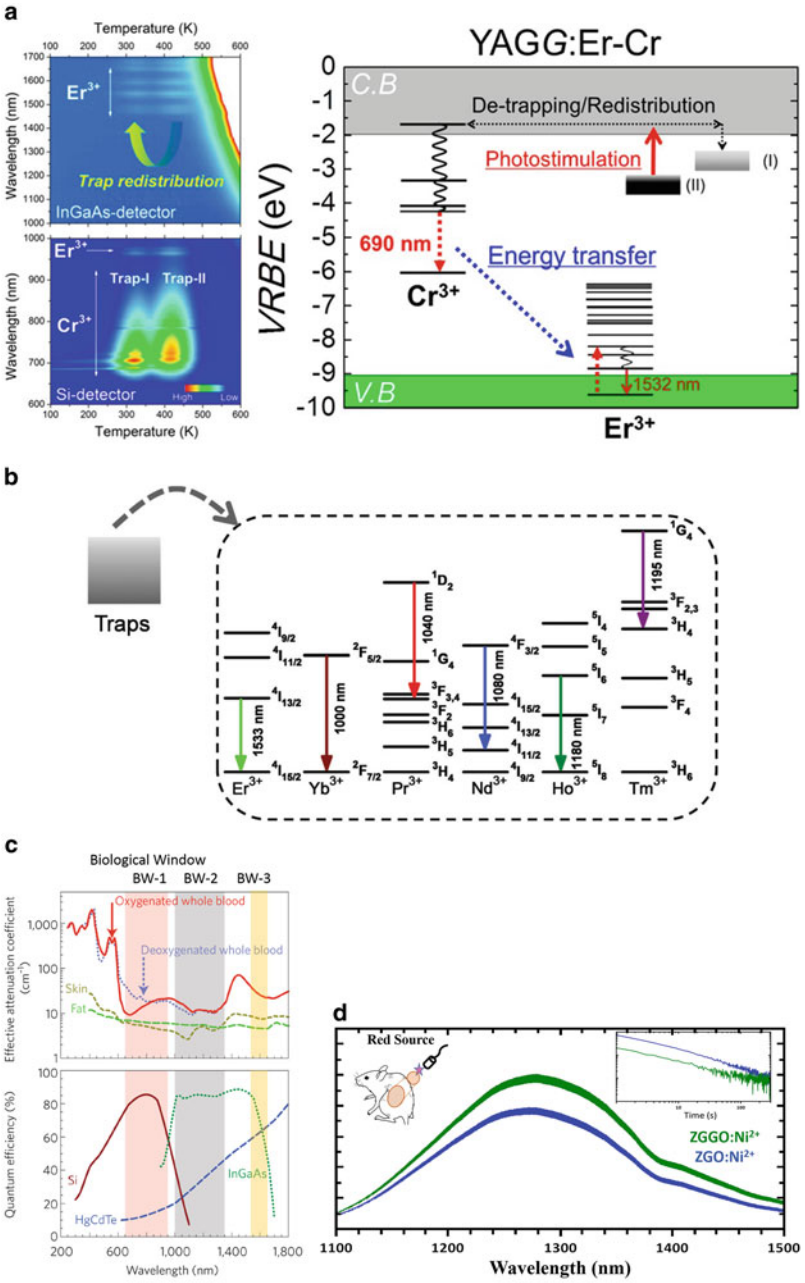

Fig. 8.11 (**a**) Trap redistribution and persistent energy transfer in metal transition (Cr) and rare earth-doped garnet. Reprinted with permission from ref. [15]. (**b**) Trivalent rare-earth cations as efficient emitters for short-wave infrared persistent luminescence. Reprinted with permission from ref. [16]. (**c**) Optical window in biological tissues. Adapted from [17]. **Top**: attenuation coefficient (log) as a function of the wavelength. **Bottom**: sensitivity of different cameras (silicon (Si) cameras, indium gallium arsenide (InGaAs) or mercury cadmium telluride (HgCdTe)) and (**d**) optical features and persistent luminescence of $ZnGa_2O_4$:Ni and $Zn(GeGa)_2O_4$:Ni. Decay profiles and scheme of excitation. Adapted from [18]

Table 8.3 Characteristics of the NIR and deep red sensors (From princetoninstrument.com web site)

	1.5 micron NIR camera	Visible camera
Material type	InGaAs	Si/CMOS
Pixel size	About 15 μm	About 4 μm
Quantum efficiency Readout noise Dark current	75–80% About 30 e^- 100 ke^-/pixels/s	75–80% About 1 e^- <0.5 e^-/pixels/s

persistent energy transfer the persistent luminescence in the deep red (from Cr^{3+}), but also in the second or third biological windows (results were obtained with Yb^{3+}, Nd^{3+}, Er^{3+}, Ho^{3+} ions) [15, 130, 131]. (3) Transition metal cations such as Ni^{2+} or Co^{2+} were also recently investigated [18, 132] (see Fig. 8.11d) to cover the second biological window and these TM cations have also large potential. Indeed, recently, Qiu and coworkers reported a strategy for tuning the emission bandwidth and intensity in persistent luminescence phosphors by synthetizing Ni^{2+}-doped $Zn_{1+y}Sn_yGa_{2-x-2y}O_4$ phosphors, with an emission band peaking from 1270 to 1430 nm in the second near infrared (NIR) window [133]. Ueda [134] and Tanabe [135] and our groups also reported compositions able to be used in the second transparency window [18].

Secondly, moving to the second and third near infrared transparency windows (1000–1700 nm) allows further reducing of scattering, absorption, and tissue autofluorescence effects. Moreover, if the quantum efficiency values, for Si, InGaAs (and HgCdTe) can be comparable, the acquisition time is also to be taken into account. For a CCD camera the dark current is of the order a few electron/pixel/hour and is about 100 ke/pixel/s for InGaAs. The readout noise has also to be taken into account (see values in Table 8.3). By the end, the signal is one to two orders of magnitude smaller for InGaAs detector (and HgCdTe) in the NIR range with respect to the Si detector in BW1. Imaging platforms then require the use of powerful and cooled cameras.

Then the balance between benefits NIR and drawbacks for these two aspects related to the second and third biological windows remains to be explored. In a decade, persistent luminescence has emerged as a useful property for the development of new optical imaging nanoprobes. Thanks to this property of long-lasting luminescence, imaging in the first transparency window (BW1) with high target to background ratio has been reported by several research groups (more than 40 research groups all over the world and more than 250 papers published in the last 10 years). Beyond their uses for imaging and therapy, new applications have emerged. We can cite for instance their use for the development of nanothermometers. For this purpose, the idea is to use the luminescence emitted by nanoprobes to detect temperature variations at the nanoscale [50, 136–138].

8.13 Conclusions

Very recent and promising works on persistent luminescence nanoparticles concern the development of biocompatible nanoprobes for multimodal imaging, theranostics and drug delivery, photodynamic and photothermal therapies, nanothermometry and hyperthermia. These PLNPs were even recently proposed as a guide during surgery operation for accurate delineation of hepatocellular carcinoma [139].

One of the next challenge will be: Can these PLNPs be used at wavelengths longer than 1000 nm? Indeed, optical imaging in the second near infrared region (1.0–1.5 μm) has recently attracted significant attention owing to some advantages: If the ballistic light (without diffusion) and the so-called "snake" light with limited diffusion remain about the same, the diffuse light – where the information is lost – can be limited moving in that NIR range. Photons in the BW2 region can provide high spatial resolution at deep tissue penetration depths owing to the reduced scattering of long-wavelength photons [140–142]. Furthermore, imaging in the second near infrared region addresses several challenges simultaneously: minimal autofluorescence – of biological tissue leading to increased sensitivity and significantly reduced light attenuation from scattering and from absorption by the blood and other structures – enables imaging with high spatiotemporal resolution and penetration depth [143]. Consequently, large organisms such as a whole mouse may be rendered translucent when imaged in this area [144]. The image reconstruction is also a very important work as was done for instance in the acousto-optic images [145].

Nevertheless there is still several others challenges for the scientific community, such as the synthesis of long circulating "stealth" nanomaterials, the functionalization with targeting agents prerequisite for PLNPs later use. Others important requirements are to keep a high intensity at the nanoscale, and to well control the surface properties in order to stabilize the PLNPs in different biological media. Then, with the nano-objects, imagination will be the only limit to the use and applications of these fascinating nanoparticles.

Acknowledgments This work was supported by the French National Research Agency (ANR Natlurim and ANR PEPSI 14-CE08-0016-01), by a grant from the Pres Sorbonne Paris-Cité (ODICEO project), by CNRS, by Biospace Lab, by the PRC Japan JSPS/French Bilateral grant (PRC1248) and by PHC Procore (33122PA), the cluster of excellence MATISSE (ANR-11-IDEX-0004-02) and by DGA (Direction Générale de L'Armement, France). The authors acknowledge their collaborators: Q. le Masne de Chermont, T. Maldiney, E. Teston, G. Ramirez-Garcia, T. Lécuyer, J. Seguin, D. Scherman, D. Gourier, A. Bessière, L. Binet, M. Allix, S. Sharma, S. Tanabe, F. Gazeau and L. Laumonier. Imagin Plateform LIOPA is also acknowledged.

References

1. Matsuzawa T, Aoki Y, Takeuchi N, Murayama Y (1996) New long phosphorescent phosphor with high brightness, SrAl2O4:Eu^{2+},Dy^{3+}. J Electrochem Soc 143(8):2670–2673
2. Van den Eeckhout K, Smet PF, Poelman D (2010) Persistent luminescence in Eu^{2+}-doped compounds: a review. Materials 3(4):2536–2566; Van den Eeckhout K, Poelman D, Smet PF (2013) Persistent luminescence in non-Eu^{2+}-doped compounds: a review. Materials 6(7):2789–2818
3. Phosphors P, Smet PF, Van den Eeckhout K, De Clercq OQ, Poelman D (2015) Handbook on the physics and chemistry of rare earths, Vol. 48. Chapter:274
4. Viana B, Sharma SK, Gourier D, Maldiney T, Teston E, Scherman D, Richard C (2016) Long term in vivo imaging with Cr^{3+} doped spinel nanoparticles exhibiting persistent luminescence. J Lumin 170:879–887
5. Lécuyer T, Teston E, Ramirez-Garcia G, Maldiney T, Viana B, Seguin J, Mignet N, Scherman D, Richard C (2016) Chemically engineered persistent luminescence nanoprobes for bioimaging. Theranostics 6(13):2488–2524
6. Jaque D, Richard C, Viana B, Soga K, Liu XG, Sole JG (2016) Inorganic nanoparticles for optical bioimaging. Adv Opt Photon 8(1):1–103
7. Maldiney T, Bessiere A, Seguin J, Teston E, Sharma SK, Viana B, Bos AJJ, Dorenbos P, Bessodes M, Gourier D, Scherman D, Richard C (2014) The in vivo activation of persistent nanophosphors for optical imaging of vascularization, tumours and grafted cells. Nat Mater 13(4):418–426
8. Maldiney T, Sraiki G, Viana B, Gourier D, Richard C, Scherman D, Bessodes M, Van den Eeckhout K, Poelman D, Smet PF (2012) In vivo optical imaging with rare earth doped Ca2Si5N8 persistent luminescence nanoparticles. Opt Mater Express 2(3):261–268
9. Liu J, Lécuyer T, Seguin J, Mignet N, Scherman D, Viana V, Richard C (2019) Imaging and therapeutic applications of persistent luminescence nanomaterials. Adv Drug Deliv Rev 138:193–210
10. Hillman EMC, Amoozegar CB, Wang T, McCaslin AFH, Bouchard MB, Mansfield J, Levenson RM (2011) In vivo optical imaging and dynamic contrast methods for biomedical research. Philos Trans Royal Soc A Math Phys Eng Sci 369(1955):4620–4643
11. de Jong M, Essers J, van Weerden WM (2014) Imaging preclinical tumour models: improving translational power. Nat Rev Cancer 14(7):481–493
12. Huang Y-Y, Hamblin M, Chen AC-H (2009) Low-level laser therapy: an emerging clinical paradigm. SPIE Newsroom
13. Matcher SJ, Cope M, Delpy DT (1997) In vivo measurements of the wavelength dependence of tissue scattering coefficients between 760 and 900 nm measured with time-resolved spectroscopy. Appl Optics 36:386–396
14. Yukawa H, Watanabe M, Kaji N, Baba Y (2015) Influence of autofluorescence derived from living body on in vivo fluorescence imaging using quantum dots. Cell Medicine 7:75–82
15. Xu J, Murata D, Ueda J, Viana B, Tanabe S (2018) Toward rechargeable persistent luminescence for the first and third biological windows via persistent energy transfer and electron trap redistribution. Inorg Chem 57(9):5194–5203
16. Liang Y, Liu F, Chen Y, Wang X, Sun K, Pan Z (2017) Extending the applications for lanthanide ions: efficient emitters in short-wave infrared persistent luminescence. J Mater Chem C 5(26):6488–6492
17. Smith AM, Mancini MC, Nie S (2009) Bioimaging, second window for in vivo imaging. Nat Nanotechnol 4(11):710–711
18. Pellerin M, Castaing V, Gourier D, Chanéac C, Viana B (2018) Persistent luminescence of transition metal (Co, Ni...)-doped $ZnGa_2O_4$ phosphors for applications in the near-infrared range, SPIE OPTO, SPIE, p 8
19. Holsa J, Aitasalo T, Jungner H, Lastusaari M, Niittykoski J, Spano G (2004) Role of defect states in persistent luminescence materials. J Alloys Compd 374(1–2):56–59

20. Holsa J, Laamanen T, Lastusaari M, Malkamaki M, Novak P (2009) Persistent luminescence – Quo vadis? J Lumin 129(12):1606–1609
21. Bessière A, Sharma SK, Basavaraju N, Priolkar KR, Binet L, Viana B, Bos AJ, Maldiney T, Richard C, Scherman D (2014) Storage of visible light for long-lasting phosphorescence in chromium-doped zinc gallate. Chem Mater 26(3):1365–1373
22. Aitasalo T, Deren P, Holsa J, Jungner H, Krupa JC, Lastusaari M, Legendziewicz J, Niittykoski J, Strek W (2003) Persistent luminescence phenomena in materials doped with rare earth ions. J Solid State Chem 171(1–2):114–122
23. Dorenbos P (2005) Mechanism of persistent luminescence in $Eu2^{2+}$ and Dy^{3+} codoped aluminate and silicate compounds. J Electrochem Soc 152(7):H107–H110
24. Sharma SK, Gourier D, Viana B, Maldiney T, Teston E, Scherman D, Richard C (2014) Persistent luminescence of AB(2)O(4):Cr^{3+} (A = Zn, Mg, B = Ga, Al) spinels: new biomarkers for in vivo imaging. Opt Mater 36(11):1901–1906
25. Bessiere A, Jacquart S, Priolkar K, Lecointre A, Viana B, Gourier D (2011) $ZnGa_2O_4$:Cr^{3+}: a new red long-lasting phosphor with high brightness. Opt Express 19(11):10131–10137
26. Rosticher C, Chanéac C, Viana B, Fortin MA, Lagueux J, Faucher L (2015) Red persistent luminescence and magnetic properties of nanomaterials for multimodal imaging. SPIE, Oxide-based Materials and Devices VI, OE108
27. Sun M, Li Z-J, Liu C-L, Fu H-X, Shen J-S, Zhang H-W (2014) Persistent luminescent nanoparticles for super-long time in vivo and in situ imaging with repeatable excitation. J Lumin 145:838–842
28. Zeng P, Wei XT, Yin M, Chen YH (2018) Investigation of the long afterglow mechanism in SrAl2O4:$Eu2^{+}$/$Dy3^{+}$ by optically stimulated luminescence and thermoluminescence. J Lumin 199:400–406
29. de Chermont Q l M, Chaneac C, Seguin J, Pelle F, Maitrejean S, Jolivet J-P, Gourier D, Bessodes M, Scherman D (2007) Nanoprobes with near-infrared persistent luminescence for in vivo imaging. Proc Natl Acad Sci U S A 104(22):9266–9271
30. Maldiney T, Richard C, Seguin J, Wattier N, Bessodes M, Scherman D (2011) Effect of core diameter, surface coating, and PEG chain length on the biodistribution of persistent luminescence nanoparticles in mice. ACS Nano 5(2):854–862
31. Maldiney T, Kaikkonen MU, Seguin J, de Chermont Q l M, Bessodes M, Airenne KJ, Yla-Herttuala S, Scherman D, Richard C (2012) In vitro targeting of avidin-expressing glioma cells with biotinylated persistent luminescence nanoparticles. Bioconjug Chem 23(3):472–478
32. Sun SK, Wang HF, Yan XP (2018) Engineering persistent luminescence nanoparticles for biological applications: from biosensing/bioimaging to theranostics. Acc Chem Res 51(5):1131–1143
33. Maldiney T, Lecointre A, Viana B, Bessiere A, Bessodes M, Gourier D, Richard C, Scherman D (2011) Controlling electron trap depth to enhance optical properties of persistent luminescence nanoparticles for in vivo imaging. J Am Chem Soc 133(30):11810–11815
34. Liu JM, Liu YY, Zhang DD, Fang GZ, Wang S (2016) Synthesis of $GdAlO_3$:Mn^{4+},Ge^{4+}@Au core-shell nanoprobes with plasmon-enhanced near-infrared persistent luminescence for in vivo trimodality bioimaging. ACS Appl Mater Interfaces 8(44):29939–29949
35. Li JL, Wang CC, Shi JP, Li PH, Yu ZF, Zhang HW (2018) Porous $GdAlO_3$: Cr^{3+}, Sm^{3+} drug carrier for real-time long afterglow and magnetic resonance dual-mode imaging. J Lumin 199:363–371
36. Song L, Li PP, Yang W, Lin XH, Liang H, Chen XF, Liu G, Li J, Yang HH (2018) Low-dose X-ray activation of W(VI)-doped persistent luminescence nanoparticles for deep-tissue photodynamic therapy. Adv Funct Mater 28(18)
37. Xue ZL, Li XL, Li YB, Jiang MY, Liu HR, Zeng SJ, Hao JH (2017) X-ray-activated near-infrared persistent luminescent probe for deep-tissue and renewable in vivo bioimaging. ACS Appl Mater Interfaces 9(27):22132–22142

38. Liu HH, Ren F, Zhang H, Han YB, Qin HZ, Zeng JF, Wang Y, Sun Q, Li Z, Gao MY (2018) Oral administration of highly bright Cr^{3+} doped $ZnGa_2O_4$ nanocrystals for &ITin vivo &ITtargeted imaging of orthotopic breast cancer. J Mater Chem B 6(10):1508–1518
39. Ramirez-Garcia G, Gutierrez-Granados S, Gallegos-Corona MA, Palma-Tirado L, d'Orlye F, Varenne A, Mignet N, Richard C, Martinez-Alfaro M (2017) Long-term toxicological effects of persistent luminescence nanoparticles after intravenous injection in mice. Int J Pharm 532(2):686–695
40. Liu YY, Liu JM, Zhang DD, Ge K, Wang PH, Liu HL, Fang GZ, Wang S (2017) Persistent luminescence Nanophosphor involved near-infrared optical bioimaging for investigation of foodborne probiotics biodistribution in vivo: a proof-of-concept study. J Agric Food Chem 65(37):8229–8240
41. Wang J, Li JL, Yu JN, Zhang HW, Zhang BB (2018) Large hollow cavity luminous nanoparticles with near-infrared persistent luminescence and tunable sizes for tumor afterglow imaging and chemo-/photodynamic therapies. ACS Nano 12(5):4246–4258
42. Maldiney T, Doan B-T, Alloyeau D, Bessodes M, Scherman D, Richard C (2015) Gadolinium-doped persistent Nanophosphors as versatile tool for multimodal in vivo imaging. Adv Funct Mater 25(2):331–338
43. Maldiney T, Ballet B, Bessodes M, Scherman D, Richard C (2014) Mesoporous persistent nanophosphors for in vivo optical bioimaging and drug-delivery. Nanoscale 6(22):13970–13976
44. Teston E, Maldiney T, Marangon I, Volatron J, Lalatonne Y, Motte L, Boisson-Vidal C, Autret G, Clement O, Scherman D, Gazeau F, Richard C (2018) Nanohybrids with magnetic and persistent luminescence properties for cell labeling, tracking, in vivo real-time imaging, and magnetic vectorization. Small 14(16)
45. Zou R, Gong SM, Shi JP, Jiao J, Wong KL, Zhang HW, Wang J, Su Q (2017) Magnetic-NIR persistent luminescent dual-modal ZGOCS@MSNs@Gd_2O_3 core-shell nanoprobes for in vivo imaging. Chem Mater 29(9):3938–3946
46. Shi J, Sun X, Li J, Man H, Shen J, Yu Y, Zhang H (2015) Multifunctional near infrared-emitting long-persistence luminescent nanoprobes for drug delivery and targeted tumor imaging. Biomaterials 37:260–270
47. Li Y, Zhou S, Dong G, Peng M, Wondraczek L, Qiu J (2014) Anti-stokes fluorescent probe with incoherent excitation. Sci Rep 4:4059
48. Liu JM, Zhang DD, Fang GZ, Wang S (2018) Erythrocyte membrane bioinspired near-infrared persistent luminescence nanocarriers for in vivo long-circulating bioimaging and drug delivery. Biomaterials 165:39–47
49. Li YJ, Yang CX, Yan XP (2018) Biomimetic persistent luminescent Nanoplatform for autofluorescence-free metastasis tracking and chemophotodynamic therapy. Anal Chem 90(6):4188–4195
50. Yang J, Liu YX, Zhao YY, Gong Z, Zhang M, Yan DT, Zhu HC, Liu CG, Xu CS, Zhang H (2017) Ratiometric afterglow Nanothermometer for simultaneous in situ bioimaging and local tissue temperature sensing. Chem Mater 29(19):8119–8131
51. Li Y, Zhou S, Li Y, Sharafudeen K, Ma Z, Dong G, Peng M, Qiu J (2014) Long persistent and photo-stimulated luminescence in Cr^{3+}-doped Zn-Ga-Sn-O phosphors for deep and reproducible tissue imaging. J Mater Chem C 2(15):2657–2663
52. Abdukayum A, Chen J-T, Zhao Q, Yan X-P (2013) Functional near infrared-emitting Cr^{3+}/Pr^{3+} co-doped zinc gallogermanate persistent luminescent nanoparticles with superlong afterglow for in vivo targeted bioimaging. J Am Chem Soc 135(38):14125–14133
53. Li J, Shi J, Shen J, Man H, Wang M, Zhang H (2015) Specific recognition of breast cancer cells in vitro using near infrared-emitting long-persistence luminescent $Zn_3Ga_2Ge_2O_{10}$:Cr^{3+} nanoprobes. Nanomicro Lett 7(2):138–145
54. Liu F, Liang Y, Pan Z (2014) Detection of up-converted persistent luminescence in the near infrared emitted by the $Zn_3Ga_2GeO_8$: Cr3(+), Yb^{3+}, Er^{3+} phosphor. *Phys Rev Lett 113*(17):177401

55. Fu X, Liu C, Shi J, Man H, Xu J, Zhang H (2014) Long persistent near infrared luminescence nanoprobes LiGa5O8:Cr^{3+}-PEG-OCH_3 for in vivo imaging. Opt Mater 36(11):1792–1797
56. Liu F, Yan W, Chuang Y-J, Zhen Z, Xie J, Pan Z (2013) Photostimulated near-infrared persistent luminescence as a new optical read-out from Cr^{3+}-doped $LiGa_5O_8$. Sci Rep 3:1554
57. Chen D, Chen Y, Lu H, Ji Z (2014) A bifunctional Cr/Yb/Tm:$Ca_3Ga_2Ge_3O_{12}$ phosphor with near-infrared long-lasting phosphorescence and upconversion luminescence. Inorg Chem 53(16):8638–8645
58. Dai WB, Lei YF, Zhou J, Xu M, Chu LL, Li L, Zhao P, Zhang ZH (2017) Near-infrared quantum-cutting and long-persistent phosphor $Ca_3Ga_2Ge_3O_{12}$: Pr^{3+}, Yb^{3+} for application in in vivo bioimaging and dye-sensitized solar cells. J Alloys Compd 726:230–239
59. Shi JP, Sun X, Zheng SH, Li JL, Fu XY, Zhang HW (2018) A new near-infrared persistent luminescence nanoparticle as a multifunctional nanoplatform for multimodal imaging and cancer therapy. Biomaterials 152:15–23
60. Kamimura S, Xu C-N, Yamada H, Terasaki N, Fujihala M (2014) Long-persistent luminescence in the near-infrared from Nd^{3+}-doped $Sr^{3+}SnO_4$ for in vivo optical imaging. Jpn J Appl Phys 53(9):092403
61. Li Z, Shi J, Zhang H, Sun M (2014) Highly controllable synthesis of near-infrared persistent luminescence SiO_2/$CaMgSi_2O_6$ composite nanospheres for imaging in vivo. Opt Express 22(9):10509–10518
62. Hu LD, Wang PY, Zhao MY, Liu L, Zhou L, Li BH, Albaqami FH, El-Toni AM, Li XM, Xie Y, Sun XF, Zhang F (2018) Near-infrared rechargeable "optical battery" implant for irradiation-free photodynamic therapy. Biomaterials 163:154–162
63. Homayoni H, Ma L, Zhang JY, Sahi SK, Rashidi LH, Bui B, Chen W (2016) Synthesis and conjugation of $Sr_2MgSi_2O_7$:Eu^{2+}, Dy^{3+} water soluble afterglow nanoparticles for photodynamic activation. Photodiagnosis Photodyn Ther 16:90–99
64. Yu ZZ, Liu B, Pan W, Zhang TT, Tong LL, Li N, Tang B (2018) A simple approach for glutathione functionalized persistent luminescence nanoparticles as versatile platforms for multiple in vivo applications. Chem Commun 54(28):3504–3507
65. Zhan DD, Liu JM, Song N, Liu YY, Dang M, Fang GZ, Wang S (2018) Fabrication of mesoporous $La_3Ga_5GeO_{14}$:Cr^{3+},Zn^{2+} persistent luminescence nanocarriers with super-long afterglow for bioimaging-guided in vivo drug delivery to the gut. J Mater Chem B 6(10):1479–1488
66. Zhao PQ, Ji W, Zhou SY, Qiu LH, Li LF, Qian ZZ, Liu XM, Zhang HL, Cao XC (2017) Upconverting and persistent luminescent nanocarriers for accurately imaging-guided photothermal therapy. Korean J Couns Psychother 79:191–198
67. Li JL, Shi JP, Wang CC, Li PH, Yu ZF, Zhang HW (2017) Five-nanometer $ZnSn_2O_4$: Cr, Eu ultra-small nanoparticles as new near infrared-emitting persistent luminescent nanoprobes for cellular and deep tissue imaging at 800 nm. Nanoscale 9(25):8631–8638
68. Kamimura S, Xu CN, Yamada H, Marriott G, Hyodo K, Ohno T (2017) Near-infrared luminescence from double-perovskite $Sr_3Sn_2O_7$:Nd^{3+}: a new class of probe for in vivo imaging in the second optical window of biological tissue. J Cerma Soc Jpn 125(7):591–595
69. Brito HF, Holsa J, Laamanen T, Lastusaari M, Malkamaki M, Rodrigues LCV (2012) Persistent luminescence mechanisms: human imagination at work. Opt Mater Exp 2(4):371–381
70. Singh SK (2014) Red and near infrared persistent luminescence nano-probes for bioimaging and targeting applications. RSC Adv 4(102):58674–58698
71. Stanek CR, Jiang C, Yadav SK, McClellan KJ, Uberuaga BP, Andersson DA, Nikl M (2013) The effect of Ga-doping on the defect chemistry of $RE_3Al_5O_{12}$ garnets. Phys Status Solidi B Basic Solid State Phys 250(2):244–248
72. Zhuang Y, Ueda J, Tanabe S, Dorenbos P (2014) Band-gap variation and a self-redox effect induced by compositional deviation in ZnxGa$_2$O^{3+}x:Cr^{3+} persistent phosphors. J Mater Chem C 2(28):5502–5509

73. Blahuta S, Bessiere A, Viana B, Ouspenski V, Mattmann E, Lejay J, Gourier D (2011) Defects identification and effects of annealing on $Lu_2(1\text{-}x)Y_2xSiO_5$ (LYSO) single crystals for scintillation application. Materials 4(7):1224–1237
74. Ueda J, Kuroishi K, Tanabe S (2014) Development of blue excitable persistent phosphor of Ce^{3+}-doped garnet ceramics by bandgap engineering and metal sensitization. Oxide-Based Mater Devices V 8987
75. Katayama Y, Kayumi T, Ueda J, Tanabe S (2018) Enhanced persistent red luminescence in Mn^{2+}-doped (Mg,Zn)GeO_3 by electron trap and conduction band engineering. Opt Mater 79:147–151
76. Dorenbos P (2013) Lanthanide 4f-electron binding energies and the nephelauxetic effect in wide band gap compounds. J Lumin 136:122–129
77. Dorenbos P (2013) Electronic structure and optical properties of the lanthanide activated RE3(Al1-xGax)(5)O-12 (RE=Gd, Y, Lu) garnet compounds. J Lumin 134:310–318
78. Kunkel N, Sontakke AD, Kohaut S, Viana B, Dorenbos P (2016) Thermally stimulated luminescence and first-principle study of defect configurations in the perovskite-type hydrides $LiMH_3:Eu^{2+}$ (M = Sr, Ba) and the corresponding deuterides. J Phys Chem C 120(51):29414–29422
79. Sharma SK, Bessiere A, Basavaraju N, Priolkar KR, Binet L, Viana B, Gourier D (2014) Interplay between chromium content and lattice disorder on persistent luminescence of $ZnGa_2O_4$:Cr-3 for in vivo imaging. J Lumin 155:251–256
80. Korthout K, Van den Eeckhout K, Botterman J, Nikitenko S, Poelman D, Smet PF (2011) Luminescence and x-ray absorption measurements of persistent SrAl2O4:Eu,Dy powders: evidence for valence state changes. Phys Rev B 84(8):085140
81. Ueda J, Tanabe S, Nakanishi T (2011) Analysis of Ce3+ luminescence quenching in solid solutions between $Y_3Al_5O_{12}$ and $Y_3Ga_5O_{12}$ by temperature dependence of photoconductivity measurement. J Appl Phys 110(5):53102–531026
82. Lecointre A, Bessiere A, Bos AJJ, Dorenbos P, Viana B, Jacquart S (2011) Designing a red persistent luminescence phosphor: the example of $YPO_4:Pr^{3+}$,Ln(3+) (Ln = Nd, Er, Ho, Dy). J Phys Chem C 115(10):4217–4227
83. Casillas-Trujillo L, Andersson DA, Dorado B, Nikl M, Sickafus KE, McClellan KJ, Stanek CR (2014) Intrinsic defects, nonstoichiometry, and aliovalent doping of A(2+)B(4)+O-3 perovskite scintillators. Phys Status Solidi B Basic Solid State Phys 251(11):2279–2286
84. Bessiere A, Lecointre A, Benhamou RA, Suard E, Wallez G, Viana B (2013) How to induce red persistent luminescence in biocompatible Ca-3(PO4)(2). J Mater Chem C 1(6):1252–1259
85. Bos AJJ, Dorenbos P, Bessiere A, Viana B (2008) Lanthanide energy levels in YPO4. Radiat Meas 43(2–6):222–226
86. Van den Eeckhout K, Bos AJJ, Poelman D, Smet PF (2013) Revealing trap depth distributions in persistent phosphors. Phys Rev B 87(4):11
87. Chuang Y-J, Zhen Z, Zhang F, Liu F, Mishra JP, Tang W, Chen H, Huang X, Wang L, Chen X, Xie J, Pan Z (2014) Photostimulable near-infrared persistent luminescent nanoprobes for ultrasensitive and longitudinal deep-tissue bio-imaging. Theranostics 4(11):1112–1122
88. Botterman J, Van den Eeckhout K, De Baere I, Poelman D, Smet PF (2012) Mechanoluminescence in BaSi2O2N2:Eu. Acta Mater 60(15):5494–5500
89. Glais E, Pellerin M, Alloyeau D, Touati N, Viana B, Chanéac C (2018) Luminescence properties of $ZnGa_2O_4:Cr^{3+}$,Bi3$^+$ nanophosphors for thermometry applications. RSC Adv 8:41767–41774
90. Castaing V, Sontakke AD, Fernández-Carrión AJ, Touati N, Binet L, Allix M, Gourier D, Viana B (2017) Persistent luminescence of $ZnGa_2O_4:Cr^{3+}$ transparent glass ceramics: effects of excitation wavelength and excitation power. Eur J Inorg Chem 2017(44):5114–5120
91. Castaing V, Pellerin M, Sontakke A, Carrión AF, Chaneac C, Allix M, Gourier D, Viana B Persistent luminescence in $ZnGa_2O_4$: Cr^{3+} transparent glass-ceramics. Proc. of SPIE Vol, 2017; pp 101050R-1

92. Gourier D, Bessière A, Sharma SK, Binet L, Viana B, Basavaraju N, Priolkar KR (2014) Origin of the visible light induced persistent luminescence of Cr 3+-doped zinc gallate. J Phys Chem Solid 75(7):826–837
93. De Vos A, Lejaeghere K, Vanpoucke DEP, Joos JJ, Smet PF, Hemelsoet K (2016) First-principles study of antisite defect configurations in $ZnGa_2O_4$:Cr persistent phosphors. Inorg Chem 55(5):2402–2412
94. Feng A, Smet PF (2018) A review of mechanoluminescence in inorganic solids: compounds, mechanisms, models and applications. Materials 11(4):484
95. Bos AJJ (2017) Thermoluminescence as a research tool to investigate luminescence mechanisms. Materials 10(12):1357
96. Randall JT, Wilkins MHF (1945) Proc R Soc A Math Phys Eng Sci 184(999):365–389
97. Sharma SK, Gourier D, Teston E, Scherman D, Richard C, Viana B (2017) Persistent luminescence induced by near infra-red photostimulation in chromium-doped zinc gallate for in vivo optical imaging. Opt Mater 63:51–58
98. He Q, Zhang Z, Gao F, Li Y, Shi J (2011) In vivo biodistribution and urinary excretion of mesoporous silica nanoparticles: effects of particle size and PEGylation. Small 7(2):271–280
99. Lu J, Liong M, Li Z, Zink JI, Tamanoi F (2010) Biocompatibility, biodistribution, and drug-delivery efficiency of mesoporous silica nanoparticles for cancer therapy in animals. Small 6(16):1794–1805
100. Hudson SP, Padera RF, Langer R, Kohane DS (2008) The biocompatibility of mesoporous silicates. Biomaterials 29(30):4045–4055
101. Sun X, Shi J, Fu X, Yang Y, Zhang H (2018) Long-term in vivo biodistribution and toxicity study of functionalized near-infrared persistent luminescence nanoparticle. Sci Rep [Online] 8:10595. PubMed
102. Duncan R, Sat YN (1998) Tumour targeting by enhanced permeability and retention (EPR) effect. Ann Oncol 9:39–39
103. Katayama Y, Viana B, Gourier D, Xu J, Tanabe S (2016) Photostimulation induced persistent luminescence in Y 3 Al 2 Ga 3 O 12: Cr 3+. Opt Mater Express 6(4):1405–1413
104. Burbano DCR, Rodriguez EM, Dorenbos P, Bettinelli M, Capobianco JA (2014) The near-IR photo-stimulated luminescence of $CaS:Eu^{2+}/Dy^{3+}$ nanophosphors. J Mater Chem C 2(2):228–231
105. Zhuang Y, Ueda J, Tanabe S (2012) Photochromism and white long-lasting persistent luminescence in Bi^{3+}-doped $ZnGa_2O_4$ ceramics. Opt Mater Express 2(10):1378–1383
106. Zhuang Y, Ueda J, Tanabe S (2013) Tunable trap depth in Zn(Ga1-xAlx)(2)O-4:Cr,Bi red persistent phosphors: considerations of high-temperature persistent luminescence and photostimulated persistent luminescence. J Mater Chem C 1(47):7849–7855
107. Bowman SGE, Chen R (1979) Super-linear filling of traps in crystals due to competition during irradiation. J Lumin 18–19:345–348
108. Chen Y, Liu F, Liang Y, Wang X, Bi J, Wang X, Pan Z (2018) A new up-conversion charging concept for effectively charging persistent phosphors using low-energy visible-light laser diodes. J Mater Chem C 6(30):8003–8010
109. Liang S, Pei-Pei L, Wen Y, Xia-Hui L, Hong L, Xiao-Feng C, Gang L, Juan L, Huang-Hao Y (2018) Low-dose X-ray activation of W(VI)-doped persistent luminescence nanoparticles for deep-tissue photodynamic therapy. Adv Funct Mater 28(18):1707496
110. Naczynski DJ, Sun C, Tuerkcan S, Jenkins C, Koh AL, Ikeda D, Pratx G, Xing L (2015) X-ray-induced shortwave infrared biomedical imaging using rareearth nanoprobes. Nano Lett 15(1):96–102
111. Chen H, Moore T, Qi B, Colvin DC, Jelen EK, Hitchcock DA, He J, Mefford OT, Gore JC, Alexis F, Anker JN (2013) Monitoring pH-triggered drug release from radioluminescent nanocapsules with X-ray excited optical luminescence. ACS Nano 7(2):1178–1187
112. Chen H, Wang GD, Chuang Y-J, Zhen Z, Chen X, Biddinger P, Hao Z, Liu F, Shen B, Pan Z, Xie J (2015) Nanoscintillator-mediated X-ray inducible photodynamic therapy for in vivo cancer treatment. Nano Lett 15(4):2249–2256

113. Lee D-E, Koo H, Sun I-C, Ryu JH, Kim K, Kwon IC (2012) Multifunctional nanoparticles for multimodal imaging and theragnosis. Chem Soc Rev 41(7):2656–2672
114. Reddy LH, Arias JL, Nicolas J, Couvreur P (2012) Magnetic nanoparticles: design and characterization, toxicity and biocompatibility, pharmaceutical and biomedical applications. *Chem Rev* 112(11):5818–5878
115. Abdukayum A, Yang C-X, Zhao Q, Chen J-T, Dong L-X, Yan X-P (2014) Gadolinium complexes functionalized persistent luminescent nanoparticles as a multimodal probe for near-infrared luminescence and magnetic resonance imaging in vivo. Anal Chem 86(9):4096–4101
116. Teston E, Lalatonne Y, Elgrabli D, Autret G, Motte L, Gazeau F, Scherman D, Clement O, Richard C, Maldiney T (2015) Design, properties, and in vivo behavior of superparamagnetic persistent luminescence nanohybrids. Small 11(22):2696–2704
117. Tassa C, Shaw SY, Weissleder R (2011) Dextran-coated iron oxide nanoparticles: a versatile platform for targeted molecular imaging, molecular diagnostics, and therapy. Acc Chem Res 44(10):842–852
118. Fan Z, Fu PP, Yu H, Ray PC (2014) Theranostic nanomedicine for cancer detection and treatment. J Food Drug Anal 22(1):3–17
119. Zhang Y, Chan HF, Leong KW (2013) Advanced materials and processing for drug delivery: the past and the future. Adv Drug Deliv Rev 65(1):104–120
120. Asefa T, Tao Z (2012) Biocompatibility of mesoporous silica nanoparticles. Chem Res Toxicol 25(11):2265–2284
121. Dai WB, Lei YF, Ye S, Song EH, Chen Z, Zhang QY (2016) Mesoporous nanoparticles Gd2O3@mSiO(2)/$ZnGa_2O_4$:Cr^{3+},Bi^{3+} as multifunctional probes for bioimaging. J Mater Chem B *4*(10):1842–1852
122. Lim C-K, Heo J, Shin S, Jeong K, Seo YH, Jang W-D, Park CR, Park SY, Kim S, Kwon IC (2013) Nanophotosensitizers toward advanced photodynamic therapy of cancer. Cancer Lett 334(2):176–187
123. Lovell JF, Liu TWB, Chen J, Zheng G (2010) Activatable photosensitizers for imaging and therapy. Chem Rev 110(5):2839–2857
124. Wang C, Cheng L, Liu Z (2013) Upconversion nanoparticles for photodynamic therapy and other cancer therapeutics. Theranostics 3(5):317–330
125. Oh SB, Park HR, Jang YJ, Choi SY, Son TG, Lee J (2013) Baicalein attenuates impaired hippocampal neurogenesis and the neurocognitive deficits induced by gamma-ray radiation. Br J Pharmacol 168(2):421–431
126. Rothkamm K, Lobrich M (2003) Evidence for a lack of DNA double-strand break repair in human cells exposed to very low x-ray doses. Proc Natl Acad Sci U S A 100(9):5057–5062
127. Ramirez-Garcia G, Martinez-Alfaro M, d'Orlye F, Bedioui F, Mignet N, Varenne A, Gutierez-Granados S, Richard C (2017) Photo-stimulation of persistent luminescence nanoparticles enhances cancer cells death. Int J Pharm 532(2):696–703
128. Shanmugam V, Selvakumar S, Yeh C-S (2014) Near-infrared light-responsive nanomaterials in cancer therapeutics. Chem Soc Rev 43(17):6254–6287
129. Chen H, Zheng B, Liang C, Zhao L, Zhang Y, Pan H, Ji W, Gong X, Wang H, Chang J (2017) Near-infrared persistent luminescence phosphors $ZnGa_2O_4$:Cr^{3+} as an accurately tracker to photothermal therapy in vivo for visual treatment. Mater Sci Eng C Mater Biol Appl 79:372–381
130. Xu J, Murata D, Katayama Y, Ueda J, Tanabe S (2017) Cr^{3+}/Er^{3+} co-doped $LaAlO_3$ perovskite phosphor: a near-infrared persistent luminescence probe covering the first and third biological windows. J Mater Chem B 5(31):6385–6393
131. Castaing V, Sontakke AD, Xu J, Fernández-Carrión AJ, Allix M, Tanabe S, Viana, B (2018) Persistent luminescence in both first and second biological windows in $ZnGa_2O_4$:Cr^{3+},Yb^{3+} glass ceramics. SPIE OPTO, SPIE: 2018; p 7
132. Feng L, Yanjie L, Yafei C, Zhengwei P (2016) Divalent nickel-activated gallate-based persistent phosphors in the short-wave infrared. Adv Opt Mater 4(4):562–566

133. Nie J, Li Y, Liu S, Chen Q, Xu Q, Qiu J (2017) Tunable long persistent luminescence in the second near-infrared window via crystal field control. Sci Rep 7:12392
134. Xu J, Tanabe S, Sontakke AD, Ueda J (2015) Near-infrared multi-wavelengths long persistent luminescence of Nd^{3+} ion through persistent energy transfer in Ce^{3+}, Cr^{3+} co-doped Y3Al2Ga3O12 for the first and second bio-imaging windows. Appl Phys Lett 107(8):081903
135. Xu J, Murata D, Ueda J, Tanabe S (2016) Near-infrared long persistent luminescence of Er^{3+} in garnet for the third bio-imaging window. J Mater Chem C 4(47):11096–11103
136. Brites CDS, Lima PP, Silva NJO, Millan A, Amaral VS, Palacio F, Carlos LD (2012) Thermometry at the nanoscale. Nanoscale 4(16):4799–4829
137. Jaque D, Vetrone F (2012) Luminescence nanothermometry. Nanoscale 4(15):4301–4326
138. Martin Rodriguez E, Lopez-Pena G, Montes E, Lifante G, Garcia Sole J, Jaque D, Armando Diaz-Torres L, Salas P (2017) Persistent luminescence nanothermometers. Appl Phys Lett 111(8):081901
139. Ai T, Shang W, Yan H, Zeng C, Wang K, Gao Y, Guan T, Fang C, Tian J (2018) Near infrared-emitting persistent luminescent nanoparticles for hepatocellular carcinoma imaging and luminescence-guided surgery. Biomaterials 167:216–225
140. Welsher K, Sherlock SP, Dai H (2011) Deep-tissue anatomical imaging of mice using carbon nanotube fluorophores in the second near-infrared window. Proc Natl Acad Sci U S A 108(22):8943–8948
141. Bruns OT, Bischof TS, Harris DK, Franke D, Shi Y, Riedemann L, Bartelt A, Jaworski FB, Carr JA, Rowlands CJ, Wilson MWB, Chen O, Wei H, Hwang GW, Montana DM, Coropceanu I, Achorn OB, Kloepper J, Heeren J, So PTC, Fukumura D, Jensen KF, Jain RK, Bawendi MG (2017) Next-generation in vivo optical imaging with short-wave infrared quantum dots. Nat Biomed Eng 1(4):0056
142. He S, Song J, Qu J, Cheng Z (2018) Crucial breakthrough of second near-infrared biological window fluorophores: design and synthesis toward multimodal imaging and theranostics. Chem Soc Rev 47(12):4258–4278
143. Hemmer E, Benayas A, Legare F, Vetrone F (2016) Exploiting the biological windows: current perspectives on fluorescent bioprobes emitting above 1000 nm. Nanoscale Horiz 1(3):168–184
144. Hong G, Diao S, Chang J, Antaris AL, Chen C, Zhang B, Zhao S, Atochin DN, Huang PL, Andreasson KI, Kuo CJ, Dai H (2014) Through-skull fluorescence imaging of the brain in a new near-infrared window. Nat Photonics 8(9):723–730
145. Boccara C (2009) Reflects of Phys 13:10–13
146. Castaing V, Sontakke AD, Xu J, Fernández-Carrión AJ, Genevois C, Tanabe S, Allix M, Viana B (2019) Persistent energy transfer in ZGO: Cr^{3+}, Yb^{3+}: a new strategy to design nano glass-ceramics featuring deep red and near infrared persistent luminescence. Phys Chem Chem Phys 21(35):19458–19468

Chapter 9
Near Infrared-Emitting Bioprobes for Low-Autofluorescence Imaging Techniques

Dirk H. Ortgies and Emma Martín Rodríguez

9.1 Introduction

> And after eight days again his disciples were within, and Thomas with them: then came Jesus, the doors being shut, and stood in the midst, and said, Peace be unto you. Then saith he to Thomas, reach hither thy finger, and behold my hands; and reach hither thy hand, and thrust it into my side: and be not faithless, but believing. And Thomas answered and said unto him, My Lord and my God. Jesus saith unto him, Thomas, because thou hast seen me, thou hast believed: blessed are they that have not seen, and yet have believed. (John 20:26–29, King James Bible)

Human beings are visual animals. This is reflected in our daily dependence on the sense of vision to orient ourselves and in the evolutionary development of vision into our strongest sense with the most direct responses by our central nervous system, for example if we see a quick movement or a change in the visual environment. This is also reflected in our tendency towards drastic visual media and phrases like "a picture says more than 1000 words" or the biblical episode of the "Doubting Thomas" (vide supra). Therefore, the history of medicine and human biology goes hand in hand with the visual study of diseases, symptoms, tissues, and organs. The visual approach towards biomedicine received a strong boost with the development

D. H. Ortgies
Nanobiology Group, Instituto Ramón y Cajal de Investigación Sanitaria, IRYCIS, Madrid, Spain

Fluorescence Imaging Group, Departamento de Física de Materiales – Facultad de Ciencias, Universidad Autónoma de Madrid, Madrid, Spain
e-mail: dirk.ortgies@uam.es

E. Martín Rodríguez (✉)
Nanobiology Group, Instituto Ramón y Cajal de Investigación Sanitaria, IRYCIS, Madrid, Spain

Fluorescence Imaging Group, Departamento de Física Aplicada – Facultad de Ciencias, Universidad Autónoma de Madrid, Madrid, Spain
e-mail: emma.martin@uam.es

A. Benayas et al. (eds.), *Near Infrared-Emitting Nanoparticles for Biomedical Applications*, https://doi.org/10.1007/978-3-030-32036-2_9

of optical and fluorescence microscopy, and people saw themselves ever closer to looking into the human body. But even though optical imaging at a cellular level became standard, it is still far away on a human scale. Modern medicine is dominated by analytical and clinical chemistry techniques, giving us an idea of what happens inside the body but for the seeing is believing approach we rely on non-optical imaging techniques. They mostly require expensive instrumentation, based on computed tomography and spectroscopy techniques, where visualization is only possible after various signal transformations and algorithms. The resulting images are often not very intuitive and require the trained eyes of specialists to see the differences in, e.g. X-Ray, magnetic resonance, or ultrasound diagnostics. Hence, why is it still not possible to just look into the body? Basically, our eyes see in the therefore so-called visible part of the electromagnetic spectrum (400–680 nm) but we are also intransparent in this area. This intransparency is due to the absorption and scattering of light in this region by some of the principal components of most mammalian tissues (fat, skin and blood, especially hemo- and oxyhemoglobin) and has been described in various references on the topic (see Fig. 9.1 for a very illustrative representation of the topic by Hong et al.) [1]. This figure also demonstrates the alternative to relying on visible light for imaging or why it has become popular to investigate the neighbouring region of the electromagnetic spectrum, the near infrared (NIR). Depending on the definition this zone roughly comprises the wavelength from 700 to 2000 nm. Originally, infrared radiation had found its application in thermal imaging or temperature measurements as well as night-vision and military applications but in 2002, Weissleder et al. defined the biological windows in the near infrared (NIR-I and NIR-II) [2]. NIR-I and NIR-II are zones between 680 and 980 nm and 1000 to 1450 nm where, as is visible in Fig. 9.1, absorption and scattering are low. The absorption of water (the principal ingredient of any living being) is also reduced and its main absorptions define the separation between NIR-I (absorption at 980 nm), and NIR-IIa and NIR-IIb (1460 nm). Therefore, NIR light can penetrate biological tissues up to a few centimetres in these windows employing current excitation sources and more importantly, because due to advances in semiconductor techniques, infrared detectors and cameras also became more readily available. Therefore, research interest into optical imaging techniques was rekindled and NIR-based imaging probes and contrast agents started to be investigated, making it possible again to dream of inexpensive and easy optical whole-body imaging.

Interestingly, the signal-to-noise ratio due to autofluorescence especially in the NIR-I region became a new challenge, confronting investigators who tried to broaden infrared fluorescence imaging techniques. Autofluorescence stems from endogenous small (hemes, protoporphyrins, chlrophyll, aromatic rings, NADP/H) and large molecules (e.g. peptides, lipofuscin, melanin, and collagen). In the visible region various molecular probes and organic dyes with huge emission intensities and brightness are readily available for cellular imaging, often overcoming signal-to-noise issues and known autofluorescence in cellular microscopy, where no large

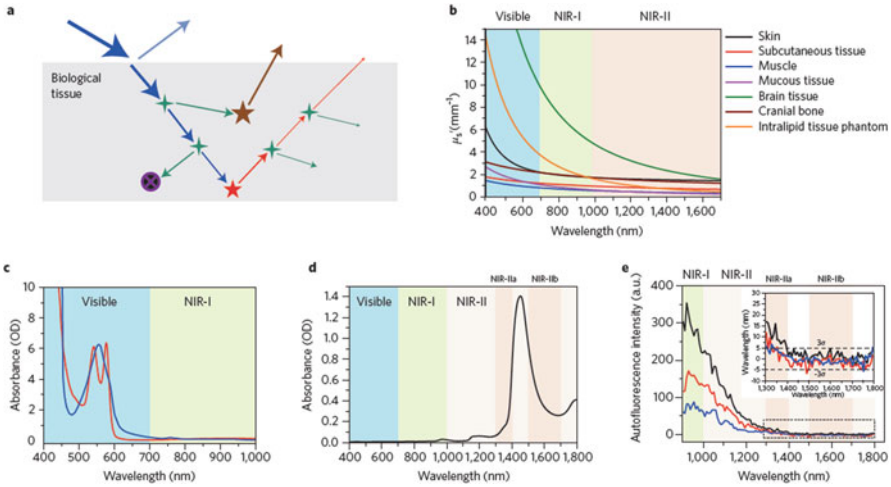

Fig. 9.1 (**a**) Light–tissue interactions resulting from impinging excitation light (blue). Interface reflection (cyan), scattering (green), absorption (black circle with purple cross) and autofluorescence (brown) all contribute to the loss of signal (fluorescence, red) and the gain of noise. (**b**) Reduced scattering coefficients of different biological tissues and of intralipid scattering tissue phantom as a function of wavelength in the 400–1700 nm region, which covers the visible, NIR-I and NIR-II windows (blue, green and red shaded regions, respectively). They all show reduced scattering at longer wavelengths. (**c**) Absorption spectra of oxyhaemoglobin (red) and deoxyhaemoglobin (blue) through a 1-mm long path in human blood. (**d**) Absorption spectrum of water through a 1-mm long path. *OD* optical density. (**e**) Autofluorescence spectra of ex vivo mouse liver (black), spleen (red) and heart tissue (blue) under 808 nm excitation light, showing the absence of autofluorescence in the >1500 nm NIR-II window. Inset: Autofluorescence spectra at high wavelengths. The dashed lines denote the values at three standard deviations from the baseline. Figure from [1] Reprinted by permission from Springer Nature: Nature, Nature Biomedical Engineering 2017, 1, 0010 (Near infrared fluorophores for biomedical imaging, Hong et al.), © 2017

penetration depths are required of the excitation light. Additionally, the endogenous autofluorescence, especially in the case of nicotinamide adenine dinucleotide phosphate (NADP) and its reduced form (NADPH), both involved heavily in the energy metabolism of cells, were adapted into a spectroscopy technique that does not require external fluorescent dyes but relies on the ratio of the autofluorescence signals to visualize metabolically active regions of the cells. Nevertheless, overcoming autofluorescence is more difficult in animal in vivo imaging and became a challenge in the NIR as is explained in the following sections.

In this chapter we present a review of the different strategies that have been used until now to eliminate the contribution of autofluorescence in biomedical imaging. We have classified them in two big blocks: approaches based on filtering the autofluorescence from the image (spectral filtering and time-domain filtering) and approaches based on avoiding the excitation of the molecules causing autofluorescence (by using fluorophores that do not require in situ excitation with light).

9.2 Autofluorescence Filtering Strategies

9.2.1 Spectral Filtering of the Autofluorescence: NIR-II-Emitting Nanoparticles

The first, and most extensively employed, strategy to avoid the presence of autofluorescence is spectral filtering (i.e. use of optical filters to collect only the signals emitted at wavelengths longer than 1200 nm). Hence, in order to apply this approach, the use of fluorophores that present emissions in this range is necessary. Although it is possible to develop organic dyes with emissions in this region, nanoparticles (NPs) present important advantages, as NIR-emitting organic dyes are mostly hydrophobic, instable and reactive due to the nature of the chromophore (extended conjugated double bonds/aromatic system). Therefore, they often also require long, complex synthetic routes and present easily a non-negligible cytotoxicity. In comparison, NPs with emissions in the NIR-II or above are readily synthesized, stable and, through surface functionalization, transferable into aqueous media.

As this method is the easiest to implement from all the methods that are going to be described herein (a large number of works presenting nanostructures with emissions in the NIR-II above 1200 nm and in the NIR-IIb), we are going to classify them depending on the material used for the preparation of the nanoparticle.

9.2.1.1 Carbon Nanotubes

Carbon nanotubes (CNTs), or more precisely single-walled CNTs (SWCNTs), were in fact the initiators of the field of NIR-II in vivo imaging. They are semiconductor materials and their NIR-II emissions are due to transitions between their bandgaps [3]. Despite their promising spectral properties, their use had previously been hampered because SWCNTs are highly hydrophobic, which made them incompatible with biological applications. In 2009, Welsher et al. were able to prepare biocompatible SWCNTs and obtain whole-body images of mice by using excitation light in the NIR-I and recording the emissions in the NIR-II [4]. The biocompatibility was achieved by coating the SWCNTs with phospholipid–polyethylene glycol, following a ligand exchange procedure. The use of the NIR-II window allowed the acquisition of deep-tissue images, and the visualization of the vasculature of a tumour located under the skin (Fig. 9.2).

Since this first demonstration, SWCNTs have been used as fluorescent contrast agents in a large number of experiments, including imaging of mice organs [5, 6], tumour targeting [7–11], and dynamic visualization of the vascular system [12–15]. All these works are based on the use of small-diameter SWCNTs, which present an improvement in terms of image contrast and tissue penetration but still work in a region where autofluorescence contributions can be detected. Even better results in terms of image contrast and penetration depth can be achieved

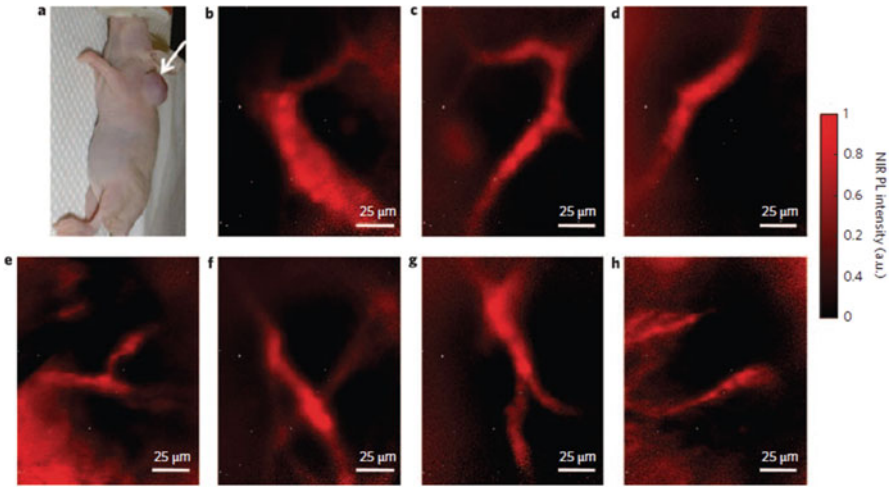

Fig. 9.2 (**a**) Optical image of LS174T tumour-bearing mouse used for intravital microscopy. (**b**–**h**) High-magnification NIR photoluminescence images taken within 90 min of injection of a high concentration (~170 mg L^{-1}, 300 μL) of exchange SWNTs. Tumour vessels can be resolved to a few micrometres, approaching the diffraction limit. Exposure times for all images were 1 s. Figure from [4] Reprinted by permission from Springer Nature: Nature, Nature Nanotechnology 2009, 4, 773–780 (A route to brightly fluorescent carbon nanotubes for near infrared imaging in mice, Welsher et al.), © 2017

by using large-diameter SWCNTs with emissions in the 1500–1700 nm range, where autofluorescence is undetectable [16]. This improvement was empirically demonstrated in 2015 by Diao et al., in a work where they obtained highly detailed in vivo images of the vessels in the brain and in the hind limb of living mice [17] and more recently by Wan et al. to highlight tumour location [18].

The main handicap of SWCNTs for in vivo imaging is their low fluorescence quantum yield (~0.5%), but these pioneering results encouraged the development of other luminescent probes with absorption and emission bands in these advantageous spectral ranges.

9.2.1.2 Quantum Dots and Semiconducting Nanoparticles

Inorganic semiconductor nanoparticles, mostly quantum dots (QDs), are very popular for bioimaging applications due to their small size and bright emissions whose wavelength can be adjusted by the appropriate selection of crystal composition and size. In order to obtain biological images in the NIR-II region, metal chalcogenide nanocrystals (mainly Ag_2S and PbS) have been widely employed obtaining very good results. In particular, Ag_2S presents the important advantage of no highly toxic metals in its composition, which facilitates their biocompatibility [19]. In addition, Ag_2S nanocrystals show a very bright fluorescence around 1200 nm, with a quantum

yield of ~15% [20] that has been used to obtain high-contrast images of different systems: subcutaneous injections [21], tumours (showing an excellent targeting efficiency, even for passive targeting) [22–27], vascular vessels in angiogenesis [28], lymphatic vessels, real-time tracking of proteins [29], and mesenchymal cells [30, 31]. Ag_2Se nanocrystals exhibit similar properties and a slightly longer wavelength; however, this material has not been so extensively studied [32, 33].

Worse perspectives for clinical translation have PbS nanocrystals due to the presence of lead; however, their good spectroscopic characteristics (extremely high quantum yield and long emission wavelength) have given place to a large number of in vivo applications after proper functionalization of the surface [34–36]. As directly encapsulated PbS nanocrystals show easy surface luminescence quenching, they are currently employed as part of a core/shell structure in which a PbS core is shielded by a CdS shell; the size of the core allows the tuning of the emission in the 1100–1300 nm range [37, 38]. To avoid leakage of Cd from the shell, a third protective layer is usually added (e.g. SiO_2, ZnS). In vivo applications that can be found in the literature include imaging of the gastrointestinal track and vascular vessels [39], subcutaneous injections [40], lymph nodes, cerebral blood vessels, breast tumours, phagocytic cells in mice [41, 42], and biodistribution studies [34, 43].

9.2.1.3 Rare Earth-Doped Nanoparticles

Rare earth-doped nanoparticles consist in inorganic nanomaterials (usually fluorides or oxides) that present fluorescent emissions due to doping with rare-earth trivalent ions (usually lanthanide ions). They have become popular in the last decade for biomedical applications thanks to their ability to emit visible light under excitation with NIR light, a process known as upconversion. However, several rare-earth ions present emissions in the NIR-II after being excited with light in the NIR-I. Compared with other luminescent nanomaterials, rare earths have the advantage of showing very sharp emission bands whose spectral position is not affected by the environment, which makes them ideally suited for multicolour imaging. As a drawback, they present a low absorption cross section, and therefore co-doping with several ions is very common, one acting as sensitizer (to enhance the absorption of the excitation radiation) and the other(s) acting as activators (light emitters). It was also observed that interactions of the ions located close to the surface of the nanoparticle with solvent molecules can quench the luminescence of the ions; to avoid this effect the preparation of a protective shell that shields the ions in the core from the environment is a typical strategy. This shell (or shells) can be limited to a protective function or include other dopant ions that enhance the luminescence performance of the core or/and provide new colours in order to have a multicolour luminescent probe [44]. The ions that have been proposed as activators because they present strong emissions in the region of NIR-II are neodymium, erbium, thulium, holmium and praseodymium. Several works can be found based on the use of Nd for imaging; however, they are based on the 1060 nm wavelength emission, which lies in a region where the contribution of the autofluorescence is

still strong [45–52]; Nevertheless, Nd is a valid candidate for autofluorescence-free imaging as it presents another band at 1300 nm. Despite this, it has been less employed due to its weaker intensity [53]. The NIR-II emission bands of the other mentioned ions (erbium, thulium, holmium and praseodymium) appear in the regions where the autofluorescence contribution has decreased and were employed to obtain high-contrast in vivo images of organs and tumours in living mice after proper functionalization or encapsulation to ensure good dispersibility in aqueous media [54–60].

9.2.1.4 Polymeric Nanoparticles

Polymeric nanoparticles are usually composed by a NIR-II-emitting dye loaded in a polymeric nanomaterial or micelle. They are designed to overcome the drawbacks that present inorganic materials and NIR dyes: inorganic nanomaterials have compositions that are difficult to translate to clinical applications whereas low-molecular-weight NIR dyes show a composition that is often highly biocompatible but they are poorly soluble in water, and thus cannot be expected to circulate in the blood stream. Therefore, the decoration or encapsulation with amphiphilic polymers solves this problem. In addition, small molecules present an excellent clearance from the organism; thus, no toxicity effect from long-term accumulation has to be expected; this feature can be preserved by controlling the size of the polymeric nanomaterial.

NIR-II-emitting dyes have been known for a long time, as they have been used as dye lasers. In fact, the first work reporting NIR-II imaging with polymer nanoparticles used the well-known IR-1061 laser dye encapsulated in a poly(acrylic acid) nanoparticle. Stability in aqueous solutions was achieved by functionalizing the particle with polyethylene glycol (PEG), and dynamic organ registration and femoral vasculature imaging of living mice was possible [61]. Organic dyes present a very broad emission band and high quantum yield. Therefore, although the emission of the dye used in this work peaked below 1200 nm wavelength, the authors were able to filter the emissions below 1300 nm and observed the increase in the image contrast due to the elimination of the autofluorescence (Fig. 9.3). The same dye was also used with good results for the detection of ovarian cancer [62].

Another approach was employed with pDA, a dye normally used in solar cells, consisting in the synthesis of a series of conjugated copolymers with an intrinsic fluorescence of 1050–1350 nm through donor–acceptor (D–A) alternating copolymerization [63]. The authors applied the nanostructure to ultrafast blood flow tracking by taking advantage of the high luminescence quantum yield of the dye that allowed the use of short integration times for the acquisition of the images.

The disadvantages of the encapsulation techniques are the possibility of leaking of the hydrophobic dyes into the blood stream and the difficulty to obtain monodisperse nanoparticles with a small size that permits fast renal clearance. For this reason, the research on NIR-II-emitting dyes is directed towards techniques to improve the hydrophilicity of the molecules by covalent conjugation of a water-

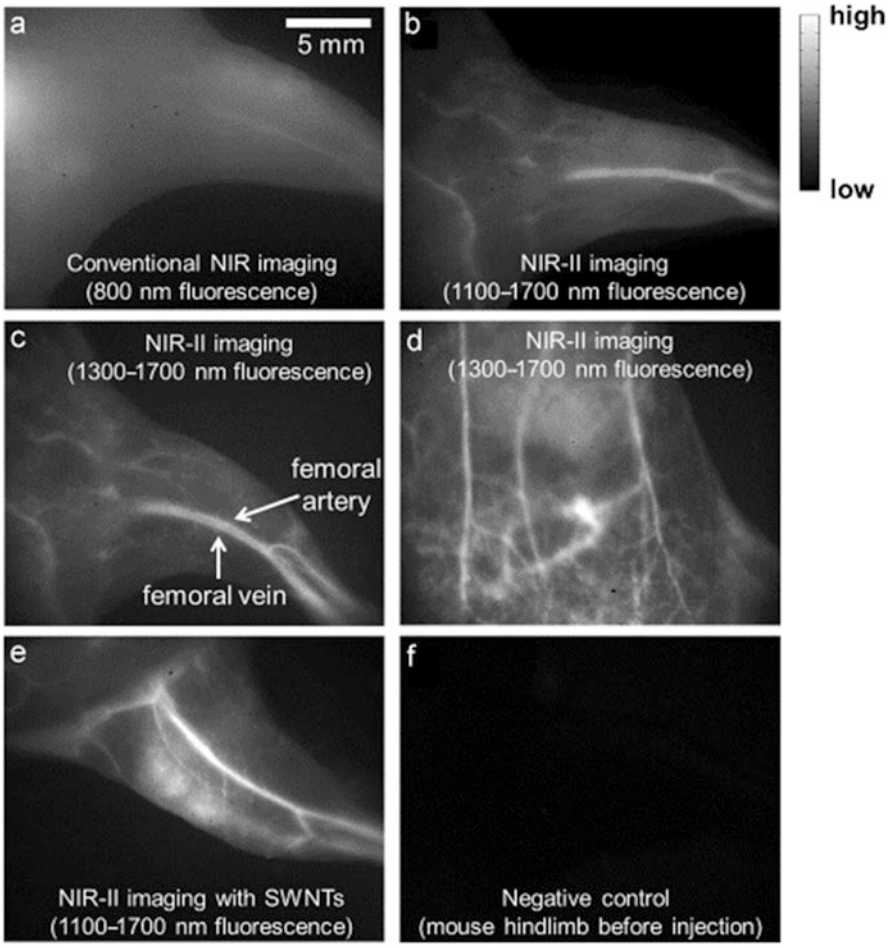

Fig. 9.3 In vivo NIR imaging of the hindlimb and abdomen of nude mice with fluorophores circulating in the blood streams after intravenous injection. (**a**) Image of a mouse hindlimb taken in the NIR window at ca. 800 nm after IRDye 800 injection. (**b**, **c**) Images recorded after injection of IR-PEG nanoparticles under 808 nm laser excitation in the 1.1–1.7 μm and 1.3–1.7 μm NIR-II regions, respectively. (**d**) An NIR-II fluorescence image of the abdomen taken in the 1.3–1.7 μm NIR-II region under 980 nm laser excitation after injection of IR-PEG nanoparticles. (**e**) Image of a mouse hindlimb taken in the 1.1–1.7 μm NIR-II region after injection of single-walled carbon nanotubes under 808 nm laser excitation. (**f**) Image of a mouse hindlimb taken in the 1.1–1.7 μm NIR-II region without injection of any fluorophores, thus showing minimal autofluorescence. Figure from [61] Figure with permission from Tao et al., Biological Imaging Using Nanoparticles of Small Organic Molecules with Fluorescence Emission at Wavelengths Longer than 1000 nm, Angewandte Chemie International Edition 2013, 52, 13,002–13,006, John Wiley and Sons, Copyright © 2013, John Wiley and Sons

solubilizing moiety directly to the fluorophore. This strategy was used by Antaris et al. who were able to show in real time the fast renal clearance characteristic of this type of molecules [64]. The good results obtained by the careful choice of the small molecules' structure made the encapsulation approach superfluous.

9.2.2 Time-Domain Filtering of Autofluorescence: Time-Gating Techniques

Time-gating techniques for autofluorescence removal are based on the use of fluorophores that present fluorescence lifetimes orders of magnitude longer (μs to ms) than the lifetimes of the molecules causing the autofluorescence (usually in the range of ns). The sample is illuminated with pulsed light and the acquisition of the image is initiated a time after the end of the pulse when the autofluorescence signal has already decayed but the signal coming from the fluorophore is still strong. The potential sensitivity improvement obtained with time-gating is especially helpful when a low dose of the imaging probe is required, as the signal-to-noise ratio increases very quickly with the delay time even if the long-lifetime fluorophore is present at a concentration a million-fold lower than the fluorophores causing the autofluorescence. For instance, the contrast ratio at 50 ns post-excitation can be larger than 10^{25} [65]. In addition, these techniques can be used for autofluorescence removal even with visible emitting fluorophores. Yet, optimal results for in vivo imaging are achieved in the NIR by taking advantage of the autofluorescence removal and the reduced scattering suffered by NIR light that allows to obtain high-resolution images of deeper tissues. However, it is not easy to obtain biocompatible NIR fluorophores with fluorescence lifetimes significantly greater than 1–10 ns, due to the quantum mechanical selection rules associated with organic molecules or direct gap semiconductors [66].

One example of this technique that can be found in the literature is the work of Gu and co-workers, which was based on the use of porous silicon nanoparticles [65]. Although silicon is a semiconductor material, it does not share the important drawbacks that many of the semiconductors used for the preparation of luminescent semiconductor nanoparticles or QDs present (e.g. CdS or CdSe). In particular, silicon nanoparticles were demonstrated to be biodegradable and to have low toxicity [67]. Regarding their luminescence properties, the most important difference between silicon and the other materials in use comes from the fact that silicon is an indirect gap semiconductor. This makes the lifetime of the excited state much longer than the typical lifetimes of QDs, displaying values from hundreds of nanoseconds to several microseconds. This property was used by the authors to obtain high-resolution in vivo images of human ovarian cancer tumours after injecting polyethylene-glycol-coated porous silicon nanoparticles (PEG-LPSiNPs) in a live mouse [65]. With a commercial system and nanocrystals having emissions in the NIR-I and a lifetime between 5–13 μs they completely removed the

autofluorescence component of the tissue obtaining a 20-fold increase in contrast. A couple of years later they improved their results by designing a system adapted to the lifetime values of their SiNPs, and obtained high-resolution images of a brain tumour by active targeting with iRGD functionalized PSiNPs [68]. However, the application in vivo is still limited by the excitation wavelength of the nanocrystals that belongs to the UV-blue region of the electromagnetic spectrum, preventing deep-tissue imaging.

Lanthanide-based nanomaterials are especially interesting for time-gating due to their very long fluorescence lifetimes. Their emission stems from forbidden 4f-4f transitions, which results in very slow emission rates (i.e. long lifetimes from microseconds to milliseconds). For this reason, lanthanides have been traditionally used for high sensitivity detection, in particular for immunoassays, but usually as part of molecular complexes [69, 70]. These compounds had to be excited in the UV part of the spectrum, and therefore, are used for in vitro assays but are not appropriate for in vivo imaging. However, the inception of nanochemistry made the development of lanthanide-doped materials possible, whose absorption bands are located in the biological windows and can be applied for in vivo imaging.

The first example on the use of rare earth-doped nanoparticles for autofluorescence-free in vivo imaging was published by Zheng et al. They employed a homemade set-up that consisted in a 980 nm pulsed laser diode synchronized with a chopper wheel situated in front of an NIR detection camera, so the camera started receiving signal a few microseconds after the laser pulse had finished [71]. Through the subcutaneous injection of $NaLuF_4$ nanoparticles co-doped with Tm^{3+} and Yb^{3+} they obtained autofluorescence-free images of living mice by detecting the 800 nm upconversion emission of Tm after excitation with 980 nm. They demonstrated not only the increase in contrast achieved thanks to the time-gated detection but also that the pulsed excitation reduced the heating produced in the animals due to the use of 980 nm excitation wavelength.

A proof-of-concept paper on the use of time-gating imaging for autofluorescence removal in the NIR-II was presented by del Rosal et al. employing long-lifetime $NaGdF_4$:Nd^{3+} nanoparticles [72]. However, large nanoparticles with a size of 600–800 nm were required to achieve the long-lifetime values (around 200 μs), which is too large for many biomedical applications. Nevertheless, employing these particles, the authors obtained time-gated optical imaging of living mice at 1050 nm, showing a remarkable improvement in the contrast of fluorescence images due to the removal of autofluorescence, and thereby paved the way for the design of nanoparticles for time-gated imaging in NIR-II (Fig. 9.4).

The duration of the luminescence lifetime of rare earth-doped nanoparticles can be selected through appropriate relative concentrations of the dopants; two examples varying concentrations in neodymium and ytterbium co-doped nanoparticles are presented in the work of Tan et al. [73]. Although many examples of nanoparticles co-doped with ytterbium can be found in the literature, they could cause overheating in biological samples due to the presence of a water absorption overlapping the excitation band of ytterbium, and therefore, ytterbium-based materials are considered not optimal for in vivo imaging [74]. Still, when talking about autofluorescence

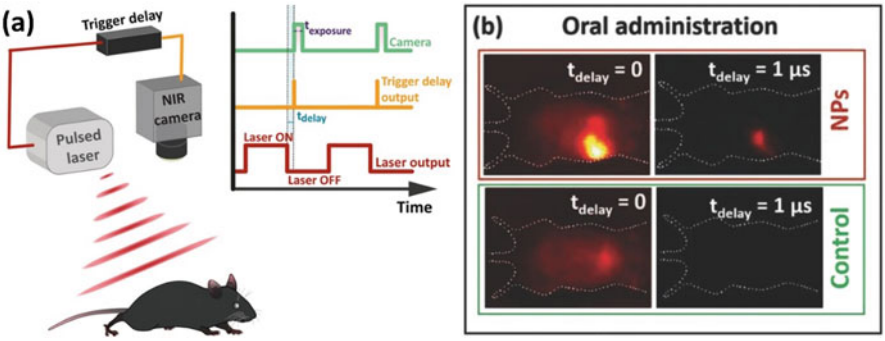

Fig. 9.4 (**a**) Schematic representation of the experimental set-up used to collect autofluorescence-free NIR images. The trigger output of an 808 nm pulsed laser diode is connected to an electronic circuit used as "Trigger delay", which produces an output pulse after a certain delay time (which can be adjusted between 1 and 200 μs) after the laser pulse has ended. The output signal of this delay circuit is used as a trigger for the NIR camera, whose exposure time is set so that the image recording has finished well before the start of the next laser pulse. (**b**) Infrared images obtained for two C57BL/6 mice, one of which was orally administered 200 μL of an aqueous dispersion of NPs, while the other acts as a control. Images are shown for zero delay, where a clear autofluorescence signal is observed for both mice, and for a 1 μs delay, where fluorescence is only present in the mouse with NPs. Figure with permission from del Rosal et al., Overcoming Autofluorescence: Long-Lifetime Infrared Nanoparticles for Time-Gated In Vivo Imaging, Advanced Materials 28, 10,188–10,193, John Wiley and Sons, © 2013, John Wiley and Sons, Reference [72]

elimination, ytterbium presents the advantage of a very long emission lifetime, close to 1 ms, which may be exploited provided that the excitation can be changed from 980 nm to a different, more biologically compatible wavelength. This is usually done by co-doping the material with neodymium, which can be excited at 800 nm and can transfer the energy to ytterbium. In the previously commented work, two strategies were used: the first one was to incorporate thulium (Tm^{3+}) dopants in Yb^{3+}/Nd^{3+} co-doped $NaGdF_4$ NPs (~13 nm), while the second one is to utilize a core/shell structure to produce enhanced and long-lifetime emissions from $NaYF_4:Yb^{3+}$, $Nd^{3+}@CaF_2$ core/shell NPs (~9 nm). For the first case, it was observed that it was possible to obtain NPs with a lifetime larger than 1 ms [73]. In the second case, the optimization of doping concentrations of both Nd^{3+} and Yb^{3+} ions in the $NaYF_4$ core, which enabled enhancing the absorption of excitation light at 800 nm, increased the luminescence intensity at 1000 nm by about 45 times and the lifetime from about 50 to 830 μs [73]. The possibility of using these probes for high penetration, autofluorescence-free in vivo NIR time-gated imaging was experimentally demonstrated through the performance of two different in vivo experiments in murine models: real-time tracking of gastrointestinal absorption of orally administered NPs and transcranial autofluorescence-free imaging of intracerebrally injected NPs. Bioimaging of the brain is a good example of a situation where the concentration of the fluorophores has to be limited to avoid toxic effects and therefore, the contrast achieved by time-gating imaging is crucial.

In general, the time-gated experiments presented until now are essentially steady-state intensity measurements, in which the intensity is measured over a period of time following pulsed excitation. However, time-gating techniques are interesting because they are compatible with time-resolved measurements, which contain more information than is available from the steady-state data. By employing the appropriate instrumentation, it is possible not only to eliminate the autofluorescence component of the image, but also to measure the fluorescence lifetime of the fluorophore. This is important because the value of the lifetime is independent from the concentration of the fluorophore; when doing imaging experiments the local concentrations of the fluorophores are unknown and can change during the measurement due to washout or photobleaching, which makes it very difficult to obtain quantitative results purely based on the local intensity values. The existence of fluorophores that display changes in the lifetime because of an interaction with the environment (such as pH, temperature or presence of certain analytes), allows the development of lifetime-sensing techniques. Other processes, such as fluorescence resonance energy transfer (FRET), reveal the interactions between molecules by changes in the value of the lifetime of the probe or in the shape of the decay curve. Current technologies allow the acquisition of lifetime images (images where the contrast is given by the value of the lifetime) and they are extensively used in fluorescence-lifetime imaging microscopy (FLIM), but the same concept can be applied to 3D imaging by working with fluorophores with long-lifetime NIR emissions. A first step in this direction was presented by Ortgies and co-workers who employed fluoride nanoparticles co-doped with neodymium and ytterbium [75]. They were able to use multiplexed images to compare the biodistribution of nanoparticles that had been administered to mice via two different pathways (oral and intravenous) because the nanoparticles employed for each pathway had different luminescence lifetimes. In particular, they employed $NaY_{0.9-x}Yb_{0.1}Nd_xF_4@CaF_2$ core/shell NPs with Nd^{3+} concentrations $x = 0.1$, 0.2, 0.3, 0.5, 0.8, and 0.9, which resulted in lifetimes for the 980 nm emission band of Yb^{3+} in the range 1.4–0.2 ms. The mouse under study received 200 μL of an aqueous dispersion of NPs with a Nd^{3+} content of $x = 0.3$ ($\tau = 0.7$ ms) through oral administration and an intravenous injection of 100 μL of a PBS dispersion of NPs with a Nd^{3+} content of $x = 0.2$ ($\tau = 1.3$ ms). The intensity-based image showed the accumulation of both types of nanoparticles in the abdominal zone, making the analysis of the results in vivo very difficult (Fig. 9.5 bottom (a)). However, the acquisition of multiple images at different delay times as shown in the top figure enabled the conversion of the intensity-weighted image to a lifetime-weighted image where the different distributions of the nanoparticles can be clearly observed (stomach for oral and liver for intravenous). This work provided a first approach for the design of in vivo lifetime-based multiplexed studies. It demonstrated also an additional advantage of working with long-lifetime nanoparticles: they allow using later detection than regular lifetime imaging. Typical lifetime imaging implies working with temporally overlapping fluorophores, and the correct interpretation of the images requires the

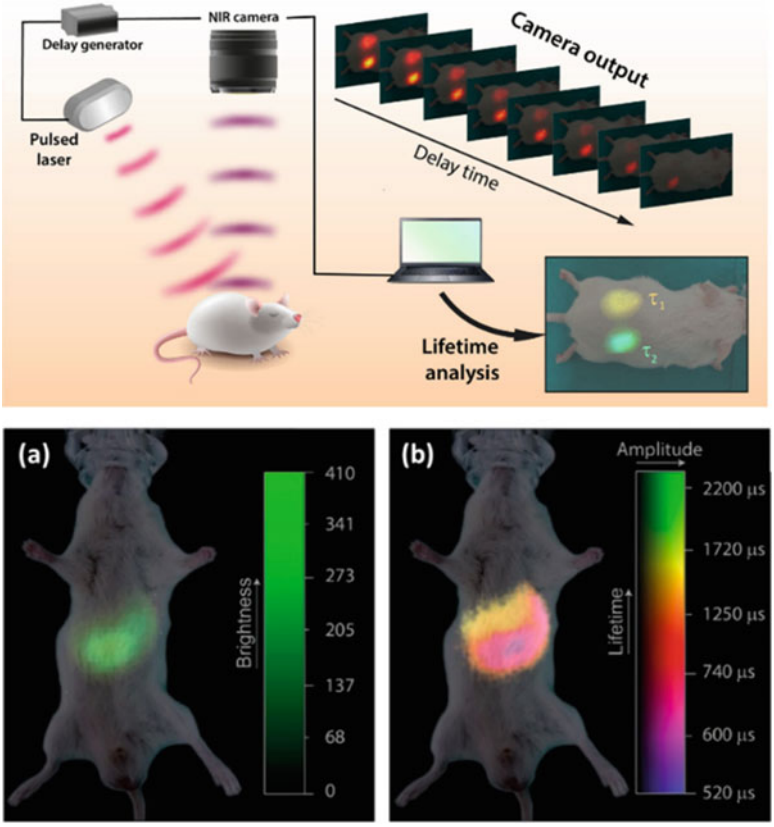

Fig. 9.5 (Top) Schematic diagram of the experimental set-up used for the acquisition of in vivo lifetime images: Image acquisition is synchronized with the excitation pulse. Analysis of fluorescence images acquired with different time delays in respect to the laser pulse leads to lifetime images that allows in vivo multiplexing in the time domain. The fluorescence images obtained for different time delays as well as the lifetime image included as an example correspond to real measurements performed on a mouse with two subcutaneous injections of $NaYF_4$:Yb,Nd @CaF_2 NPs with neodymium contents of $x = 0.3$ and $x = 0.5$ with fluorescence lifetimes of $\tau_1 = 0.7$ ms and $\tau_2 = 0.4$ ms, respectively. (Bottom) (**a**) Intensity-based infrared image of a mouse after oral and intravenous injection of $NaY_{0.9-x}Yb_{0.1}Nd_xF_4$@$CaF_2$ NPs with a Nd^{3+} content of $x = 0.3$ and 0.2, respectively. (**b**) Lifetime-based image of same mouse as in (a). The different location of the two types of NPs is evidenced. Reprinted with permission from (Ortgies DH et al. (2018) Lifetime-Encoded Infrared-Emitting Nanoparticles for In Vivo Multiplexed Imaging ACS Nano 12:4362–4368). Copyright (2018) American Chemical Society

unmixing of the signals by using model fitting (e.g. multiexponential fits). The possibility of employing time gates where the contribution of autofluorescence has completely disappeared eliminates the risk of getting false results due to potential errors in model assumptions. The same idea was used by Fan et al. with the 1500 nm emission of Er^{3+} to identify tumour subtypes in living mice [76].

9.3 Excitation-Free Approaches

Another possibility to avoid the excitation of the molecules responsible for autofluorescence consists in using fluorophores that do not require in-body excitation. Different mechanisms make this possible, for example the use of materials showing afterglow (i.e. showing fluorescent emission a long time after the excitation source has been removed), or materials that do not require light as excitation source (e.g. bioluminescent or chemiluminescent materials). Some examples of these strategies will be discussed in the next section.

9.3.1 Long-Persistent-Luminescence Nanoparticles

Long-persistent-luminescence materials are materials that have the capacity of emitting light a long time after the excitation source has been removed [77]. This is possible thanks to the presence of defects in the material that can trap electrons and release them slowly. The use of these materials allows the acquisition of autofluorescence-free images because in situ excitation is not needed: it is possible to excite the materials outside of the body and inject them in the excited state into the body. Traditionally these materials have been prepared for solid-state applications in the visible; however, over the last years some attempts of moving the emissions of the persistence towards wavelengths of biological interest have been made.

9.3.1.1 Persistent Luminescence with Inorganic Nanoparticles

Persistent luminescent materials (usually known as long-persistence phosphors, LPPs) have been known and applied for a long time (almost a thousand years according to Chinese legends) and have been commercially exploited for the last 100 years mainly for solid-state applications such as safety signals, dials, displays and decoration. There are many well-known combinations of host materials and dopants (usually Eu^{2+} as emitter ions and Dy^{3+} or Sm^{3+} as enhancer of the persistence) that show persistence times of hours or even days. However, the emission bands of those materials are located in the blue and green regions of the electromagnetic spectrum, which has traditionally hampered their biological applications. The attempts to move the persistent emissions towards the red or even the NIR are relatively recent and have proven to be difficult, as this red shift was usually accompanied by a remarkable shortening of the afterglow time. Several different strategies were employed in order to obtain NIR-emitting long LPPs: (1) the use of new rare-earth and transition metal ions with emission in the NIR as activators (e.g. Nd^{3+}, Bi^{2+}, Yb^{3+}, Mn^{2+}, Mn^{4+} and Cr^{3+}); (2) modulating the crystal field in order to red-shift the emissions of already known LPPs; (3) using

visible LPPs co-doped with NIR-luminescent ions in order to induce energy transfer to excite the NIR emissions of the latter.

In 2007, le Masne de Chermont demonstrated the possibility of in vivo bioimaging with LPPs whose emission belonged to the NIR-I spectral region by varying the activator ions [78]. They synthesized $Ca_{0.2}Zn_{0.9}Mg_{0.9}Si_2O_6$ particles doped with Eu^{2+}, Dy^{3+} and Mn^{2+} that presented afterglow at 700 nm for more than 1 h after irradiation with UV light for 5 min. The reduced size of the particles (50–100 nm, much smaller than typical LPPs) allowed the acquisition of in vivo images of living mice after intramuscular injection of the particles at different depths. They also studied the biodistribution of a solution of the LPPs injected through the tail vein, although the size of the particles resulted in accumulation in the lungs, which was attributed to the accumulation of particles in the small capillaries of these organs, and in liver and spleen uptake. The work of Pan and co-workers [79] on the use of Cr^{3+}-activated gallates provided LPPs with long afterglow emission in the 650–1000 nm region, presenting excellent properties for in vivo imaging, initiating a great number of studies using Cr^{3+}-doped materials for bioimaging. One example was the work of Li and co-workers, on the imaging of goldfish with times as long as 2 h after injection, and demonstrating the possibility of reactivating the afterglow by using incoherent NIR light [80]. In the same year, Maldiney et al. reported on the in vivo imaging and vascularization visualization of mice by using $ZnGa_{1.995}Cr_{0.005}O_4$, a material that showed persistence in the NIR and whose afterglow could be reactivated in vivo by using red light [81]. Ai et al. used the same Cr^{3+}-based LPP ($ZnGa_2O_4Cr_{0.004}$) for biodistribution studies, tumour targeting and guided surgery of Hepatocellular Carcinoma [82] and Sun and co-workers for evaluation of long-term effects and biodistribution of these materials [83]. Chen et al. used a nanoplatform based on LPP and CuS nanoparticles for imaging and photothermal imaging [84]. Wang et al. developed an aptamer-guided $Zn_{1+x}Ga_{2-2x}Ge_xO_4$:Cr, $0 \leq x \leq 0.5$ bioprobe and demonstrated an excellent tumour-specific accumulation [85]. Especially interesting is the recent work of Wang et al. who prepared hollow nanostructured LPPs and used them for in vivo imaging, drug delivery and photodynamic therapy [86]. Other activators for afterglow in the NIR windows have been proposed but their application in vivo remains unexplored; they include Mn^{4+} and Bi^{2+} [87], Nd^{3+} [88] or Yb^{3+} [89]. In addition to the introduction of new activators, some works have reported on the control of the crystal field as a way to shift the emissions of already exploited activators towards the NIR. This is the case of the work of Li et al. who synthesized $Zn_{(2-x)}Al_{2x}Sn_{(1-x)}O_4$:Cr and were able to control the position of the Cr^{3+} emission band between 720 and 800 nm [90], or the work of Nie et al. who prepared Ni^{2+}-doped $Zn_{1+y}Sn_yGa_{2-x-2y}O_4$ phosphors and tuned the emission band from 1270 to 1430 nm [91].

The third strategy to obtain long persistence times in the NIR is based on systems that present an efficient energy transfer from activator ions with long persistence in the visible to luminescent ions with emission in the NIR, phenomenon that has been named as persistence energy transfer (PET). PET has been demonstrated for example from Eu^{2+} to Nd^{3+}, obtaining long-persistence emissions at 890 and 1060 nm wavelength [92] and Er^{3+}, obtaining long persistence in the emission

at 1500 nm wavelength [93]. Other ions employed as donors were Ce^{3+} in combination with Nd^{3+} to obtain persistent emissions longer than 10 h in the NIR-I and NIR-II regions of the spectrum [94].

Traditionally this type of phosphors is synthesized forming irregular microstructures due to the post-synthesis high-temperature annealing treatments that need to be performed to activate the persistence of the material. In consequence, many studies have been focused on synthetic procedures to obtain more biocompatible sizes and morphologies (e.g. [95]) or in the surface modification of the already existing materials in order to extend their applications in the biomedical field; many examples can be found for instance in the review paper by Sun et al. [96].

9.3.1.2 Persistent Luminescence with Organic Molecules

Recently, it has become feasible to shift the luminescence of organic semiconductors into the infrared and turn them into emitters of persistent luminescence. Most often, the applied term is afterglow, indicating a persistent emission after illumination. The design of completely organic nanomaterials brings often an increased biocompatibility and reduced toxicity with it due to the lack of heavy metals that are normally responsible for fluorescence in inorganic nanomaterials, especially quantum dots. Furthermore, organic polymers are readily modified and functionalized to achieve specific functionalities suited to the application. In the context of autofluorescence-free imaging this means that semiconducting polymer nanoparticles (SPNs) have been developed for afterglow imaging, demonstrating excellent signal-to-noise ratios and a more pronounced shift into the infrared.

In 2015, the group of Rao published a work with a similar SPN + IR dye combination they had previously used for bioluminescence imaging (see below) [97]. The SPNs allowed excitation with blue light (465 nm), and the electrons were trapped in defects of the SPN. Upon temperature increase, the electrons were released leading to persistent emission of the polymer and subsequent highly desired energy transfer to the included IR dye IR 775. The authors applied the particles towards in vivo biodistribution studies in mice and were able to follow the emission for minutes as distributed into the different organs. Re-excitation was also possible, showing a distribution of SPNs throughout the whole animal after 24 h [97].

Recently, this concept was taken up by one of the authors and continued to further demonstrate the advantages of SPN by studying in detail the underlying mechanism for their afterglow luminescence. They achieved a 127-fold better signal-to-noise-ratio than typical NIR-II fluorescence contrast agents. Qingqing Miao et al. started out systematically investigating seven fluorescent semiconducting polymers as principal ingredient for afterglow nanoparticles and determined that only phenylenevinylene (PPV)-based SPNs demonstrated afterglow. The best results were obtained with poly[2-methoxy-5-(2-ethylhexyloxy)-1,4-phenylenevinylene] (MEHPPV) that showed the strongest afterglow emission centred around 600–650 nm when excited at 465 nm. Next, they demonstrated that the vinyl bonds in the

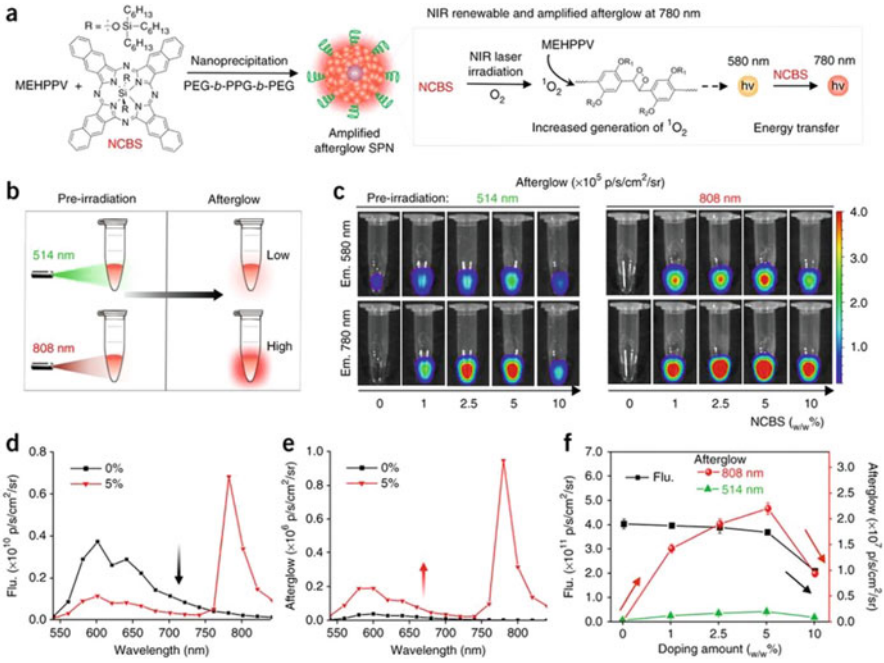

Fig. 9.6 (**a**) Schematic illustration of the proposed mechanism. (**b**) Schematic illustration of SPN-NCBS pre-irradiated by an 808 nm laser for afterglow enhancement versus a 514 nm laser. (**c**) Afterglow luminescence images of 12.5 μg/mL SPN-NCBS (based on the mass of MEHPPV) pre-irradiated at 514 (left) or 808 nm (right). The nanoparticle solutions were pre-irradiated by 808 or 514 nm laser (1 W/cm^2) for 1 min, and then the afterglow images were acquired under bioluminescence mode with an acquisition time of 30 s after removal of the laser source. (**d**, **e**) Fluorescence (**d**) and NIR-induced afterglow luminescence spectra (e) of SPN-MEHPPV and SPN-NCBS5 in 1× PBS buffer (pH = 7.4). (**f**) Quantification of the absolute fluorescence and afterglow luminescence intensities of SPN-MEHPPV at different doping amounts of NCBS. The error bars represent the s.d. (n = 3). Figure from reference [98] Reprinted by permission from Springer Nature: Nature Biotechnology 2017, 35, 1102–1110 (Molecular afterglow imaging with bright, biodegradable polymer nanoparticles, Miao et al.), © 2017 Springer Nature

polymer backbone are key for the afterglow luminescence. Irradiation leads to their oxidation with $^1O_2$ and breaking of the polymer into aldehyde and acid fragments under light emission (Fig. 9.6). This reaction is also temperature dependent, and therefore, the SPNs can also be employed for nanothermometry [99], which was demonstrated by the authors in a more recent work. In order to be truly applicable for in vivo imaging the afterglow emission should possibly be in the infrared and not the red. Therefore, an infrared-excitable $^1O_2$ sensitizer was added to the composition of the SPNs, allowing to shift the pre-irradiation. But more importantly, in addition to the excitation at 808 nm, 2,3-naphthalocyanine bis(trihexylsilyloxide) (NCBS) added also an emission in the NIR-I to the SPNs at 780 nm, making the afterglow particles true NIR contrast agent. The particles demonstrated to have excellent tissue penetration properties and proved themselves well in in vivo imaging [98].

Recently, they further improved the formulation of the SPNs into a self-assembling nanoparticle by turning to an amphiphilic polymer [100]. The main disadvantage of the above described MEHPPV SPNs was the need for co-precipitation with a block copolymer (PEG-*b*-PPG-*b*-PEG) forming micelles to achieve water dispersibility due to the hydrophobicity of the SP. Therefore, they set out to add PEG chains onto the PPV polymer backbone. This was achieved through the modification of the side-chains of the polymer and addition of PEG on these side-chains through click chemistry. The authors demonstrated that copolymerisation of the MEHPPV monomer with PEG-modified PPV monomer in a ratio of 8 to 1 led to the best so far obtained results through self-assembly precipitation in PBS. Doping with 2% of the $^1O_2$ sensitizer NCBS achieved a further shift into the infrared (emission at 780 nm) and the so-obtained nanoparticles SPPVN were revealed to all out surpass the previously employed MEHPPV. The particles had a smaller hydrodynamic diameter (24 vs 34 nm), showed better energy transfer (FRET efficiency 51 vs 24%), and most importantly even brighter afterglow luminescence (1.3-fold). The authors reasoned that due to the smaller size and higher PEG loading on the NPs surface, the higher accumulation in tumours could be explained, and tumours as small as 1 mm^3 and peritoneal metastatic tumours that are invisible to the eye could be imaged with the afterglow (Fig. 9.7). This afterglow nanoplatform presented by the group of Pu will be an interesting alternative to other autofluorescence-free imaging techniques, allowing irradiation pre-injection/application and combining this with excellent biodegradability, which is part of the luminescence mechanism and enable deep-tissue imaging without simultaneous irradiation [100].

9.3.2 Bioluminescence

Bioluminescence imaging is a technique based on the interaction between a light-emitting molecule (generally luciferin) that can be oxidized in the presence of a biocatalyst (usually an enzyme, sometimes the presence of other cofactors is needed) to an excited state that decays by emitting visible radiation. The absence of excitatory light leads to lower background and hence higher sensitivity. Bioluminescence imaging experiments are commonly based on the use of oxyluciferin, a metabolic product of the firefly luciferin, which after adenylation by firefly luciferase, followed by a reaction with molecular oxygen emits green light (ca. 560 nm) [101]. Targeting bioimaging applications, several studies have been performed to shift these bioluminescent emissions to the NIR-I window (650–950 nm), including some successful demonstrations of autofluorescence-free in vivo imaging [102–111].

In 2006, So et al. proposed a novel strategy to obtain luminescent markers for autofluorescence-free in vivo imaging [112]. They employed luciferases as bioluminescence imaging agent combining the luminescent enzymes with quantum dots to achieve an energy transfer and emission at a different wavelength than that of the enzyme based on the characteristics of the employed QDs [112]. In analogy to

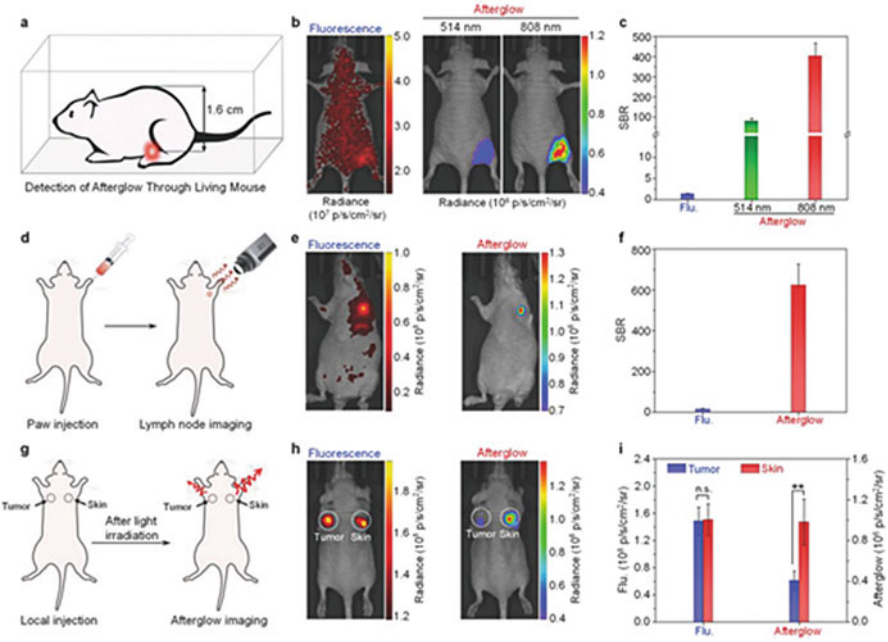

Fig. 9.7 In vivo tissue-penetration study and lymph node imaging. (**a**) Schematic illustration of fluorescence and afterglow imaging through a living mouse. SPPVN solution was placed under the mouse with the depth of 1.6 cm. (**b**) Fluorescence and afterglow luminescence images of SPPVN solution through a living mouse. The fluorescence image was acquired at 780 nm with excitation at 710 nm. Before the collection of afterglow luminescence images, SPPVN solution (130 μg mL^{-1}, 50 μL) was pre-irradiated at 514 or 808 nm (1 W cm^{-2}) for 1 min. (**c**) Signal-to-background ratios (SBRs) of fluorescence and afterglow luminescence imaging in (**b**). (**d**) Schematic illustration of lymph node imaging. (**e**) Fluorescence and afterglow luminescence images of a lymph node in the living mouse at 60 min after intradermal injection of SPPVN (450 μg mL^{-1}, 50 μL) into the forepaw of mouse. Afterglow luminescence images were acquired for 30 s after laser irradiation at 808 nm (0.3 W cm^{-2}) for 1 min. (**f**) SBRs of fluorescence and afterglow luminescence imaging of lymph node in (**e**). (**g**) Schematic illustration of hypoxia and normoxia imaging in a living mouse. SPPVN was purged with nitrogen to remove oxygen before injection. (**h**) Fluorescence and afterglow luminescence images of tumour and skin after local injection of SPPVN (130 μg mL^{-1}, 50 μL). (**i**) Fluorescence and afterglow intensities of tumour and skin after local injection of SPPVN (130 μg mL^{-1}, 50 μL). Error bars represent standard deviations of three separate measurements ($n = 3$). n.s.: not significant, $**$statistically significant difference ($p < 0.01$, $n = 3$). Figure with permission from reference [100] Xie et al., Self-Assembled Semiconducting Polymer Nanoparticles for Ultrasensitive Near Infrared Afterglow Imaging of Metastatic Tumors, Advanced Materials 30, 1,801,331, John Wiley and Sons, © 2018, John Wiley and Sons

the well-known Förster or Fluorescence Resonance Energy Transfer (FRET), this concept had been named Bioluminescence Resonance Energy Transfer (BRET). The structures, as they did not need an external excitation source, were named self-illuminating QDs. In this particular work, the authors used a derivative of *R. reniformis* luciferase as the energy donor and CdSe/ZnS core–shell quantum dots

(with emission at 650 nm) as the acceptor and demonstrated that BRET emission could be imaged in cells and small animals with a greatly enhanced sensitivity. In addition, they showed that the system was compatible with bioluminescence and fluorescence imaging, and with in vivo multiplexed bioluminescence imaging of multiple targets thanks to their distinct BRET emission spectra. This approach has continued to be used in order to obtain images of different systems with high sensitivity: interactions between intracellular proteins [113], lymph node mapping [114, 115], apoptotic cells [116], growth factors [117], and mammalian reproductive cells [118].

A very interesting combination of bioluminescence with autofluorescence-free imaging was also presented by the group of Rao already in 2012 [119]. L. Xiong et al. combined both of these energy transfer concept, FRET and BRET, in single polymer (PS-PEG-COOH) nanoparticles that contained poly(2-methoxy-5-((2-ethylhexyl)oxy)-*p*-phenylenevinylene) (MEH-PPV) forming SPNs for a FRET transfer to the also included dye NIR 775 and were functionalized on the surface with Luciferase8 (an eight-mutation variant of *R. reniformis* luciferase) for BRET to the MEH-PPV [119]. This combination resulted in self-luminescing NPs in the presence of the substrate coelenterazine for the enzyme and was after further functionalization with a targeting-peptide employed in successful lymph node and tumour imaging in vivo in mice. The authors demonstrated the effectiveness of the BRET-FRET that resulted in improved penetration depths over free luciferase or combinations with QDs due to the emission in the NIR-I and showed a good signal-to-noise ratio overcoming autofluorescence [119]. The same approach was used in a study by Kuchimaru et al. who developed an injectable BRET-based imaging probe, which achieved highly specific and fast detection of intra-tumoral activity of the hipoxia-inducible factor in various cancer models, without having the drawback of inefficient membrane transduction that present nanoparticle-based probes [120].

9.3.3 Chemiluminescence

Chemiluminescence (or chemoluminescence) is the emission of light as the result of a chemical reaction. The subclass of biochemical/enzymatic reactions producing luminescence is generally known as bioluminescence and discussed above. As no light excitation is required, background signal arising from autofluorescence does not exist, and high sensitivity and signal-to-noise ratios can be achieved. However, chemiluminescence presents several drawbacks for its application for in vivo imaging: the light produced by the reaction presents in most cases a weak intensity, short emission durations, and short emission wavelengths. Therefore, it has been used in a similar way to BRET to achieve the excitation of NIR-emitting nanomaterials in order to obtain deep-tissue in vivo images. In this case, the process is named chemiluminescence resonant energy transfer (CRET). The first demonstration of CRET was done in 2006 by Wang et al. based on the co-injection of luminol and horseradish peroxidase-functionalized QDs as energy acceptor [121].

Luminol attached to the QDs and generated light through the luminol/hydrogen peroxide chemiluminescent reaction, and this light was transferred to the QDs whose emission (in this case in the green and red parts of the spectrum) could be observed [121]. To afford CRET imaging in vivo, the chemiluminescent reaction of luminol with hypochlorous acid (metabolite of the enzyme myeloperoxidase) was used by Zhang et al. In this manner, a highly sensitive detection of myeloperoxidase activity in vivo, which is upregulated in immune deficiency, coronary artery disease and inflammation, was possible in deep tissues [122].

Another type of nanomaterials that has been more widely used for CRET in vivo are conjugated polymer-based polymer dots (Pdots). Pdots were prepared for in vivo imaging by joining chemiluminescent substrates inside them. These substrates react with the molecule, which is intended to be imaged, generating radiation that excites the luminescent component of the Pdot. This approach was used by Lee et al. in 2007 to detect the presence of hydrogen peroxide during an inflammatory response in living mice [123], and more recently for the detection of reactive oxygen species (ROS) and reactive nitrogen species (RNS) [124–126] or the presence of H_2S in colorectal cancer [127]. The other employed possibility consists in the conjugation of chemiluminescent catalysts onto the surface of Pdots. This approach achieves ultrahigh sensitivity and long chemiluminescence duration (when compared to direct chemiluminescence) and it is widely used in clinical diagnosis such as immunoassay. This strategy was employed in vivo for ROS detection and for excitation-free photodynamic therapy [128, 129].

Although the chemiluminescence approach for autofluorescence-free imaging has made great progress, the challenge to develop new probes with strong intensity and long emission duration in a wavelength compatible with deep-tissue bioimaging remains.

9.4 Multiphoton Excitation in the NIR-II

The last reported strategy to avoid the contribution of autofluorescence in bioimaging involves the use of multiphoton excitation with a wavelength longer than 1200 nm and the detection of the shorter wavelength emissions. In this manner the molecules responsible for the autofluorescence are not excited and thus, they do not reduce the contrast of the image. This approach was recently employed by Li et al.: they demonstrated that it is possible to excite carbon nanodots with a 1400 nm femtosecond laser and they consequently observed the NIR-I emission of the dots (700 nm) in the stomach of a mouse [130].

A similar idea but operating only in the NIR-II window was shown with a new type of Er^{3+}-sensitized upconversion nanoparticles, which presented both excitation (1530 nm) and emission (1180 nm) located in the NIR-II window for in vivo biosensing of inflammation [131].

9.5 Conclusions and Perspectives

We hope that we were able to illustrate the advantages for bioimaging when being able to work without having to worry about autofluorescence. Taking away these autogenous signals of the animals under study drastically improves the signal-to-noise ratio and applicability of optical imaging, thereby presenting a paradigm for in vivo deep-tissue or whole-body imaging. Although the use of these techniques and NIR-II contrast agents/sensors is still at an early stage, it is easy to see their potential and how, over the next years, they will be developed into maturity and will find their way into the clinic. The latter point mostly depends on the reproducibility of the synthesis and fabrication of the nanomaterials as well as their toxicity and long-term biocompatibility. Nevertheless, this is not limited to the field of NIR-II imaging but a general drawback that nanoparticle applications have suffered so far and will therefore in our opinion be addressed in the near future by the whole nanotechnology community. Even though this has not yet been achieved, the here presented advances in the application and for in vivo imaging give hope that once clinically safe nanomaterials are obtained, the autofluorescence-free imaging techniques to employ them in real life are ready.

As was described above, the removal of autofluorescence is possible by employing a large variety of materials but also through a number of different experimental approaches, all having different advantages and drawbacks. This makes the task of establishing a criterion to select the optimal method for autofluorescence-free in vivo imaging difficult. One quantity that is very often used for the comparison of different fluorophores is the fluorescence quantum yield (QY). The QY is the ratio of the number of emitted photons relative to the number of absorbed photons; the larger the QY, the brighter is the emission of the material. However, the reality is that obtaining absolute values for the QY is very challenging, and therefore, very different QY values can be found for the same material [132]. Another drawback of a comparison based on the QY is that it does not take into account the absorption cross section of the materials. This is especially problematic when comparing rare earth-doped NPs, which present very large QY values but have a very low absorption cross section. In consequence, higher energy densities are needed for the excitation of this type of particles. For other materials the standard definition of QY is difficult to apply due to their luminescence mechanism. For example, in the case of persistent fluorescence materials QYs larger than 100% are obtained. In the case of bio- and chemiluminescence the QY yield is defined in terms of photons emitted in relation to the number of fluorescent molecules present in the medium. Nevertheless, in order to have a first approximation of a comparison for the materials discussed in this chapter, we have summarized the values of the QYs of different types of compounds (see Table 9.1). The table exemplifies the high dispersion of QYs even for the same type of material, which can be attributed to the aggregation state of the particles, the defects that are generated during the preparation, the coating of the surface, etc. In principle, materials with high QY are always desired, but in the bioimaging context, a material with low QY but an emission in the NIR-II

Table 9.1 Fluorescence quantum yields of different materials covered in this chapter

Material		Quantum yield	References
Single-walled carbon nanotubes (SWCNTs)	Aggregated	<0.05%	[133, 134, 3, 135]
	Individual	1%	[136]
		3%	[137]
		7%	[138]
		8%	[139]
		18%	[140]
		20%	[141]
		15–40%	[142]
Ag_2S nanocrystals		1%	[143, 144]
		1–2%	[145]
		4–5%	[27]
		6–15.5%	[20]
PbS nanocrystals		5–30%	[146]
		5%	[147]
Nd-doped NPs	$GdF_3:Nd^{3+}$	1%	[148]
	$LiLuF_4$:10%Nd Nd@Lu NPs	15% 32%	[149]
	$LaF_3:Nd^{3+}$	20–80%	[150]
	$NaGdF_4:Nd^{3+}/NaGdF_4$	40%	[151]
Dyes	IR-1061	1.8%	[61]
	pDA-PEG	1.7%	[63]
	CH1055-PEG	0.3%	[64]
Porous silicon NPs		>32%	[152]
		23%	[153, 154]
Firefly bioluminescence		41%	[155]
		61%	[156]
Chemiluminescence		1.23%	[157]

can be a better fluorescent marker than a material with a higher QY but a shorter emission wavelength. In fact, the beauty of some of the approaches herein presented is that, once the autofluorescence is removed, it is possible to employ fluorophores with a not-so-high QY but other interesting features (e.g. NIR-II-emitting small molecules).

In terms of comparing the herein presented approaches and not so much the materials, the most readily available, inexpensive, and facile one is NIR-II imaging above 1200 nm with the silver- or carbon-based nanoprobes and simple optical filters. This technique can basically be applied with any available IR-camera and a long-pass filter and no complicated optical set-up or knowledge is required. Therefore, we are expecting to see a strong rise in the studies and applications of especially Ag_2S nanodots but also other NIR-II contrast agents.

Among the other presented techniques, BRET- and CRET-based approaches will find some application but in general are limited due to the complexity of the materials as well as the targets. Nonetheless, the latter is also the advantage of this interesting approach because if a suitable target substrate for BRET or CRET (a biomarker, hormone, clinical analyte, etc.) is identified, no excitation via any kind of irradiation source is required, and on top of avoiding autofluorescence, selectivity is gained. This is to some extent also the case for the persistent luminescence approaches where, although still necessary, the light source employed for excitation can be separated locally from the patient/objects of study and therefore irradiation powers can be adjusted more freely. This will also come in handy for multisite treatments or parallel treatments, and therefore, this technique will find its place in biomedicine.

Last but definitely not least and although one of the so far least developed techniques, time-gating clearly has a great future ahead, even though a pulsed laser, whose triggering signal to the IR-camera needs to be delayable, is required and a slightly more complex engineering and doping strategy for the nanosensors is necessary. This stems from the fact that the time-gating approach and lifetime-based nanoparticles are especially well suited for more complex imaging modalities like hyperspectral imaging and multiplexing. Additionally, the lifetime itself can be influenced by its surroundings and therefore act as a multifunctional sensor, e.g. for nanothermometry. This potential of time-gated imaging for multimodality and multifunctionality, barely touched in the examples that have been published so far, makes it in our opinion the most promising technique for autofluorescence-free bioimaging, especially when combined with the NIR-II approach and long-lifetime nanoprobes which can emit above 1200 nm.

References

1. Hong G, Antaris AL, Dai H (2017) Near-infrared fluorophores for biomedical imaging. Nat Biomed Eng 1:0010
2. Weissleder R (2001) A clearer vision for in vivo imaging. Nat Biotechnol 19:316–317
3. O'Connell MJ et al (2002) Band gap fluorescence from individual single-walled carbon nanotubes. Science 297:593–596
4. Welsher K, Liu Z, Sherlock SP, Robinson JT, Chen Z, Daranciang D, Dai H (2009) A route to brightly fluorescent carbon nanotubes for near-infrared imaging in mice. Nat Nanotechnol 4:773
5. Diao S et al (2012) Chirality enriched (12,1) and (11,3) single-walled carbon nanotubes for biological imaging. J Am Chem Soc 134:16971–16974
6. Welsher K, Sherlock SP, Dai H (2011) Deep-tissue anatomical imaging of mice using carbon nanotube fluorophores in the second near-infrared window. Proc Natl Acad Sci USA 108:8943–8948
7. Antaris AL, Robinson JT, Yaghi OK, Hong G, Diao S, Luong R, Dai H (2013) Ultra-low doses of chirality sorted (6,5) carbon nanotubes for simultaneous tumor imaging and photothermal therapy. ACS Nano 7:3644–3652

8. Ghosh D, Bagley AF, Na YJ, Birrer MJ, Bhatia SN, Belcher AM (2014) Deep, noninvasive imaging and surgical guidance of submillimeter tumors using targeted M13-stabilized single-walled carbon nanotubes. Proc Natl Acad Sci 111:13948–13953
9. Robinson JT, Hong G, Liang Y, Zhang B, Yaghi OK, Dai H (2012) In vivo fluorescence imaging in the second near-infrared window with long circulating carbon nanotubes capable of ultrahigh tumor uptake. J Am Chem Soc 134:10664–10669
10. Robinson JT, Welsher K, Tabakman SM, Sherlock SP, Wang H, Luong R, Dai H (2010) High performance in vivo near-IR (>1 μm) imaging and photothermal cancer therapy with carbon nanotubes. Nano Res 3:779–793
11. Yi H, Ghosh D, Ham M-H, Qi J, Barone PW, Strano MS, Belcher AM (2012) M13 phage-functionalized single-walled carbon nanotubes as nanoprobes for second near-infrared window fluorescence imaging of targeted tumors. Nano Lett 12:1176–1183
12. Hong G et al (2014) Near-infrared II fluorescence for imaging Hindlimb vessel regeneration with dynamic tissue perfusion measurement. Circ Cardiovasc Imaging 7:517–525
13. Hong G et al (2012) Multifunctional in vivo vascular imaging using near-infrared II fluorescence. Nat Med 18:1841–1846
14. Hong GS et al (2014) Through-skull fluorescence imaging of the brain in a new near-infrared window. Nat Photonics 8:723–730
15. Yomogida Y, Tanaka T, Zhang M, Yudasaka M, Wei X, Kataura H (2016) Industrial-scale separation of high-purity single-chirality single-wall carbon nanotubes for biological imaging. Nat Commun 7:12056
16. Diao S, Hong G, Antaris AL, Blackburn JL, Cheng K, Cheng Z, Dai H (2015) Biological imaging without autofluorescence in the second near-infrared region. Nano Res 8:3027–3034
17. Diao S et al (2015) Fluorescence imaging in vivo at wavelengths beyond 1500 nm. Angew Chem Int Ed 54:14758–14762
18. Wan H et al (2018) A bright organic NIR-II nanofluorophore for three-dimensional imaging into biological tissues. Nat Commun 9:1171
19. Zhang Y et al (2013) Biodistribution, pharmacokinetics and toxicology of Ag_2S near-infrared quantum dots in mice. Biomaterials 34:3639–3646
20. Zhang Y, Hong G, Zhang Y, Chen G, Li F, Dai H, Wang Q (2012) Ag_2S quantum dot: a bright and biocompatible fluorescent nanoprobe in the second near-infrared window. ACS Nano 6:3695–3702
21. Jiang P, Zhu C-N, Zhang Z-L, Tian Z-Q, Pang D-W (2012) Water-soluble Ag_2S quantum dots for near-infrared fluorescence imaging in vivo. Biomaterials 33:5130–5135
22. Chen J et al (2016) Facile synthesis of β-lactoglobulin capped Ag_2S quantum dots for in vivo imaging in the second near-infrared biological window. J Mater Chem B 4:6271–6278
23. Ding C, Zhang C, Yin X, Cao X, Cai M, Xian Y (2018) Near-infrared fluorescent Ag_2S nanodot-based signal amplification for efficient detection of circulating tumor cells. Anal Chem 90:6702–6709
24. Hong G, Robinson JT, Zhang Y, Diao S, Antaris AL, Wang Q, Dai H (2012) Vivo fluorescence imaging with Ag_2S quantum dots in the second near-infrared region. Angew Chem Int Ed 51:9818–9821
25. Hu F, Li C, Zhang Y, Wang M, Wu D, Wang Q (2015) Real-time in vivo visualization of tumor therapy by a near-infrared-II Ag_2S quantum dot-based theranostic nanoplatform. Nano Res 8:1637–1647
26. Li C et al (2015) Preoperative detection and intraoperative visualization of brain tumors for more precise surgery: a new dual-modality MRI and NIR nanoprobe. Small 11:4517–4525
27. Zhao D-H, Yang J, Xia R-X, Yao M-H, Jin R-M, Zhao Y-D, Liu B (2018) High quantum yield Ag_2S quantum dot@polypeptide-engineered hybrid nanogels for targeted second near-infrared fluorescence/photoacoustic imaging and photothermal therapy. Chem Commun 54:527–530
28. Li C et al (2014) In vivo real-time visualization of tissue blood flow and angiogenesis using Ag_2S quantum dots in the NIR-II window. Biomaterials 35:393–400

29. Li C, Li F, Zhang Y, Zhang W, Zhang X-E, Wang Q (2015) Real-time monitoring surface chemistry-dependent in vivo behaviors of protein nanocages via encapsulating an NIR-II Ag_2S quantum dot. ACS Nano 9:12255–12263
30. Chen G et al (2015) In vivo real-time visualization of mesenchymal stem cells tropism for cutaneous regeneration using NIR-II fluorescence imaging. Biomaterials 53:265–273
31. Chen G, Tian F, Zhang Y, Zhang Y, Li C, Wang Q (2014) Tracking of transplanted human mesenchymal stem cells in living mice using near-infrared Ag_2S quantum dots. Adv Funct Mater 24:2481–2488
32. Dong B, Li C, Chen G, Zhang Y, Zhang Y, Deng M, Wang Q (2013) Facile synthesis of highly photoluminescent Ag_2Se quantum dots as a new fluorescent probe in the second near-infrared window for in vivo imaging. Chem Mater 25:2503–2509
33. Ma J-J et al (2018) Gd-DTPA-coupled Ag_2Se quantum dots for dual-modality magnetic resonance imaging and fluorescence imaging in the second near-infrared window. Nanoscale 10:10699–10704
34. Kong Y et al (2016) Highly fluorescent ribonuclease-A-encapsulated Lead sulfide quantum dots for ultrasensitive fluorescence in vivo imaging in the second near-infrared window. Chem Mater 28:3041–3050
35. Nakane Y, Tsukasaki Y, Sakata T, Yasuda H, Jin T (2013) Aqueous synthesis of glutathione-coated PbS quantum dots with tunable emission for non-invasive fluorescence imaging in the second near-infrared biological window (1000–1400 nm). Chem Commun 49:7584–7586
36. Sasaki A, Tsukasaki Y, Komatsuzaki A, Sakata T, Yasuda H, Jin T (2015) Recombinant protein (EGFP-protein G)-coated PbS quantum dots for in vitro and in vivo dual fluorescence (visible and second-NIR) imaging of breast tumors. Nanoscale 7:5115–5119
37. Tsukasaki Y, Komatsuzaki A, Mori Y, Ma Q, Yoshioka Y, Jin T (2014) A short-wavelength infrared emitting multimodal probe for non-invasive visualization of phagocyte cell migration in living mice. Chem Commun 50:14356–14359
38. Tsukasaki Y et al (2014) Synthesis and optical properties of emission-tunable PbS/CdS core–shell quantum dots for in vivo fluorescence imaging in the second near-infrared window. RSC Adv 4:41164–41171
39. Zebibula A et al (2018) Ultrastable and biocompatible NIR-II quantum dots for functional bioimaging. Adv Funct Mater 28:1703451
40. Benayas A et al (2015) PbS/CdS/ZnS quantum dots: a multifunctional platform for in vivo near-infrared low-dose fluorescence imaging. Adv Funct Mater 25:6650–6659
41. Imamura Y, Yamada S, Tsuboi S, Nakane Y, Tsukasaki Y, Komatsuzaki A, Jin T (2016) Near-infrared emitting PbS quantum dots for in vivo fluorescence imaging of the thrombotic state in septic mouse brain. Molecules 21:1080
42. Jin T, Imamura Y (2016) Applications of highly bright PbS quantum dots to non-invasive near-infrared fluorescence imaging in the second optical window. ECS J Solid State Sci Technol 5:R3138–R3145
43. Chen J et al (2016) Direct water-phase synthesis of lead sulfide quantum dots encapsulated by β-lactoglobulin for in vivo second near infrared window imaging with reduced toxicity. Chem Commun 52:4025–4028
44. Labrador-Páez L et al (2018) Core–shell rare-earth-doped nanostructures in biomedicine. Nanoscale 10:12935–12956
45. Dai Y et al (2017) Mussel-inspired polydopamine-coated lanthanide nanoparticles for NIR-II/CT dual imaging and photothermal therapy. ACS Appl Mater Interfaces 9:26674–26683
46. del Rosal B et al (2016) Neodymium-based stoichiometric ultrasmall nanoparticles for multifunctional deep-tissue photothermal therapy. Adv Opt Mater 4:782–789
47. Ren F et al (2018) Ultra-small nanocluster mediated synthesis of Nd^{3+}-doped core-shell nanocrystals with emission in the second near-infrared window for multimodal imaging of tumor vasculature. Biomaterials 175:30–43
48. Rocha U et al (2014) Neodymium-doped LaF3 nanoparticles for fluorescence bioimaging in the second biological window. Small 10:1141–1154

49. Villa I et al (2015) 1.3 μm emitting $SrF_2:Nd^{3+}$ nanoparticles for high contrast in vivo imaging in the second biological window. Nano Res 8:649–665
50. Wang P et al (2018) NIR-II nanoprobes in-vivo assembly to improve image-guided surgery for metastatic ovarian cancer. Nat Commun 9:2898
51. Wang X, Hu H, Zhang H, Li C, An B, Dai J (2018) Single ultrasmall Mn^{2+}-doped $NaNdF_4$ nanocrystals as multimodal nanoprobes for magnetic resonance and second near-infrared fluorescence imaging. Nano Res 11:1069–1081
52. Yang D, Cao C, Feng W, Huang C, Li F (2018) Synthesis of $NaYF_4:Nd@NaLuF_4@SiO_2@PS$ colloids for fluorescence imaging in the second biological window. J Rare Earths 36:113–118
53. Yang Q, Li X, Xue Z, Li Y, Jiang M, Zeng S (2018) Short-wave near-infrared emissive $GdPO_4:Nd^{3+}$ theranostic probe for in vivo bioimaging beyond 1300 nm. RSC Adv 8:12832–12840
54. Deng Z, Li X, Xue Z, Jiang M, Li Y, Zeng S, Liu H (2018) A high performance Sc-based nanoprobe for through-skull fluorescence imaging of brain vessels beyond 1500 nm. Nanoscale 10:9393–9400
55. Kamimura M, Kanayama N, Tokuzen K, Soga K, Nagasaki Y (2011) Near-infrared (1550 nm) in vivo bioimaging based on rare-earth doped ceramic nanophosphors modified with PEG-b-poly(4-vinylbenzylphosphonate). Nanoscale 3:3705–3713
56. Kamimura M, Matsumoto T, Suyari S, Umezawa M, Soga K (2017) Ratiometric near-infrared fluorescence nanothermometry in the OTN-NIR (NIR II/III) biological window based on rare-earth doped β-NaYF4 nanoparticles. J Mater Chem B 5:1917–1925
57. Lei X et al (2018) Intense near-infrared-II luminescence from $NaCeF_4$:Er/Yb nanoprobes for in vitro bioassay and in vivo bioimaging. Chem Sci 9:4682–4688
58. Naczynski DJ et al (2013) Rare-earth-doped biological composites as in vivo shortwave infrared reporters. Nat Commun 4:2199
59. Shao W, Chen G, Kuzmin A, Kutscher HL, Pliss A, Ohulchanskyy TY, Prasad PN (2016) Tunable narrow band emissions from dye-sensitized core/shell/shell nanocrystals in the second near-infrared biological window. J Am Chem Soc 138:16192–16195
60. Tao Z et al (2017) Early tumor detection afforded by in vivo imaging of near-infrared II fluorescence. Biomaterials 134:202–215
61. Tao Z et al (2013) Biological imaging using nanoparticles of small organic molecules with fluorescence emission at wavelengths longer than 1000 nm. Angew Chem Int Ed 52:13002–13006
62. Dang X, Gu L, Qi J, Correa S, Zhang G, Belcher AM, Hammond PT (2016) Layer-by-layer assembled fluorescent probes in the second near-infrared window for systemic delivery and detection of ovarian cancer. Proc Natl Acad Sci 113:5179–5184
63. Hong G et al (2014) Ultrafast fluorescence imaging in vivo with conjugated polymer fluorophores in the second near-infrared window. Nat Commun 5:4206
64. Antaris AL et al (2016) A small-molecule dye for NIR-II imaging. Nat Mater 15:235–242
65. Gu L et al (2013) In vivo time-gated fluorescence imaging with biodegradable luminescent porous silicon nanoparticles. Nat Commun 4:2326
66. Berezin MY, Achilefu S (2010) Fluorescence lifetime measurements and biological imaging. Chem Rev 110:2641–2684
67. Park J-H, Gu L, von Maltzahn G, Ruoslahti E, Bhatia SN, Sailor MJ (2009) Biodegradable luminescent porous silicon nanoparticles for in vivo applications. Nat Mater 8:331–336
68. Joo J, Liu X, Kotamraju VR, Ruoslahti E, Nam Y, Sailor MJ (2015) Gated luminescence imaging of silicon nanoparticles. ACS Nano 9:6233–6241
69. Wei C, Ma L, Wei H, Liu Z, Bian Z, Huang C (2018) Advances in luminescent lanthanide complexes and applications. Science China Technol Sci 61(9):1265–1285
70. Zhang KY, Yu Q, Wei H, Liu S, Zhao Q, Huang W (2018) Long-lived emissive probes for time-resolved photoluminescence bioimaging and biosensing. Chem Rev 118:1770–1839
71. Zheng X et al (2016) High-contrast visualization of upconversion luminescence in mice using time-gating approach. Anal Chem 88:3449–3454

72. del Rosal B, Ortgies DH, Fernández N, Sanz-Rodríguez F, Jaque D, Rodríguez EM (2016) Overcoming autofluorescence: long-lifetime infrared nanoparticles for time-gated in vivo imaging. Adv Mater 28:10188–10193
73. Tan M et al (2018) Rare-earth-doped fluoride nanoparticles with engineered long luminescence lifetime for time-gated in vivo optical imaging in the second biological window. Nanoscale 10(37)
74. Chen G, Qiu H, Prasad PN, Chen X (2014) Upconversion nanoparticles: design, nanochemistry, and applications in theranostics. Chem Rev 114:5161–5214
75. Ortgies DH et al (2018) Lifetime-encoded infrared-emitting nanoparticles for in vivo multiplexed imaging. ACS Nano 12:4362–4368
76. Fan Y et al (2018) Lifetime-engineered NIR-II nanoparticles unlock multiplexed in vivo imaging. Nat Nanotechnol 13(10):941–946
77. Li Y, Gecevicius M, Qiu J (2016) Long persistent phosphors—from fundamentals to applications. Chem Soc Rev 45:2090–2136
78. le Masne de Chermont Q et al (2007) Nanoprobes with near-infrared persistent luminescence for in vivo imaging. Proc Natl Acad Sci 104:9266–9271
79. Pan Z, Lu Y-Y, Liu F (2011) Sunlight-activated long-persistent luminescence in the near-infrared from Cr^{3+}-doped zinc gallogermanates. Nat Mater 11:58
80. Li Y et al (2014) Long persistent and photo-stimulated luminescence in Cr^{3+}-doped Zn–Ga–Sn–O phosphors for deep and reproducible tissue imaging. J Mater Chem C 2:2657–2663
81. Maldiney T et al (2014) The in vivo activation of persistent nanophosphors for optical imaging of vascularization, tumours and grafted cells. Nat Mater 13:418–426
82. Ai T et al (2018) Near infrared-emitting persistent luminescent nanoparticles for hepatocellular carcinoma imaging and luminescence-guided surgery. Biomaterials 167:216–225
83. Sun X, Shi J, Fu X, Yang Y, Zhang H (2018) Long-term in vivo biodistribution and toxicity study of functionalized near-infrared persistent luminescence nanoparticles. Sci Rep 8:10595
84. Chen L-J, Sun S-K, Wang Y, Yang C-X, Wu S-Q, Yan X-P (2016) Activatable multifunctional persistent luminescence nanoparticle/copper sulfide Nanoprobe for in vivo luminescence imaging-guided photothermal therapy. ACS Appl Mater Interfaces 8:32667–32674
85. Wang J et al (2017) Autofluorescence-free targeted tumor imaging based on luminous nanoparticles with composition-dependent size and persistent luminescence. ACS Nano 11:8010–8017
86. Wang J, Li J, Yu J, Zhang H, Zhang B (2018) Large hollow cavity luminous nanoparticles with near-infrared persistent luminescence and tunable sizes for tumor afterglow imaging and chemo-/photodynamic therapies. ACS Nano 12:4246–4258
87. Li Y et al (2014) A strategy for developing near infrared long-persistent phosphors: taking $MAlO_3$:Mn^{4+},Ge^{4+} (M = La, Gd) as an example. J Mater Chem C 2:2019–2027
88. Kamimura S, Xu C-N, Yamada H, Terasaki N, Fujihala M (2014) Long-persistent luminescence in the near-infrared from Nd^{3+}-doped Sr_2SnO_4 for in vivo optical imaging. Jpn J Appl Phys 53:092403
89. Caratto V et al (2014) NIR persistent luminescence of lanthanide ion-doped rare-earth oxycarbonates: the effect of dopants. ACS Appl Mater Interfaces 6:17346–17351
90. Li Y et al (2015) Tailoring of the trap distribution and crystal field in Cr3+-doped non-gallate phosphors with near-infrared long-persistence phosphorescence. NPG Asia Mater 7:e180
91. Nie J, Li Y, Liu S, Chen Q, Xu Q, Qiu J (2017) Tunable long persistent luminescence in the second near-infrared window via crystal field control. Sci Rep 7:12392
92. Teng Y, Zhou J, Ma Z, Smedskjaer MM, Qiu J (2011) Persistent near infrared phosphorescence from rare earth ions co-doped strontium aluminate phosphors. J Electrochem Soc 158:K17–K19
93. Yu N, Liu F, Li X, Pan Z (2009) Near infrared long-persistent phosphorescence in $SrAl_2O_4$:Eu^{2+},Dy^{3+},Er^{3+} phosphors based on persistent energy transfer. Appl Phys Lett 95:231110
94. Xu J, Tanabe S, Sontakke AD, Ueda J (2015) Near-infrared multi-wavelengths long persistent luminescence of Nd^{3+} ion through persistent energy transfer in Ce^{3+}, Cr^{3+} co-doped $Y_3Al_2Ga_3O_{12}$ for the first and second bio-imaging windows. Appl Phys Lett 107:081903

95. Zhan-Jun L, Hong-Wu Z, Meng S, Jiang-Shan S, Hai-Xia F (2012) A facile and effective method to prepare long-persistent phosphorescent nanospheres and its potential application for in vivo imaging. J Mater Chem 22:24713–24720
96. Sun S-K, Wang H-F, Yan X-P (2018) Engineering persistent luminescence nanoparticles for biological applications: from biosensing/bioimaging to Theranostics. Acc Chem Res 51:1131–1143
97. Palner M, Pu K, Shao S, Rao J (2015) Semiconducting polymer nanoparticles with persistent near-infrared luminescence for in vivo optical imaging. Angew Chem Int Ed 54:11477–11480
98. Miao Q et al (2017) Molecular afterglow imaging with bright, biodegradable polymer nanoparticles. Nat Biotechnol 35:1102
99. Zhen X, Xie C, Pu K (2018) Temperature-correlated afterglow of a semiconducting polymer nanococktail for imaging-guided photothermal therapy. Angew Chem Int Ed 57:3938–3942
100. Xie C, Zhen X, Miao Q, Lyu Y, Pu K (2018) Self-assembled semiconducting polymer nanoparticles for ultrasensitive near-infrared afterglow imaging of metastatic tumors. Adv Mater 30:1801331
101. Viviani VR (2002) The origin, diversity, and structure function relationships of insect luciferases cellular and molecular. CMLS Cell Mol Life Sci 59:1833–1850
102. Iwano S et al (2013) Development of simple firefly luciferin analogs emitting blue, green, red, and near-infrared biological window light. Tetrahedron 69:3847–3856
103. Jathoul AP, Grounds H, Anderson JC, Pule MA (2014) A dual-color far-red to near-infrared firefly luciferin analogue designed for multiparametric bioluminescence imaging. Angew Chem Int Ed 53:13059–13063
104. Kitada N et al (2018) Toward bioluminescence in the near-infrared region: tuning the emission wavelength of firefly luciferin analogues by allyl substitution. Tetrahedron Lett 59:1087–1090
105. Kiyama M et al (2018) Quantum yield improvement of red-light-emitting firefly luciferin analogues for in vivo bioluminescence imaging. Tetrahedron 74:652–660
106. Kojima R et al (2015) Development of a sensitive bioluminogenic probe for imaging highly reactive oxygen species in living rats. Angew Chem Int Ed 54:14768–14771
107. Kojima R, Takakura H, Ozawa T, Tada Y, Nagano T, Urano Y (2013) Rational design and development of near-infrared-emitting firefly luciferins available in vivo. Angew Chem Int Ed 52:1175–1179
108. Miura C et al (2013) Synthesis and luminescence properties of biphenyl-type firefly luciferin analogs with a new, near-infrared light-emitting bioluminophore. Tetrahedron 69:9726–9734
109. Mofford DM, Reddy GR, Miller SC (2014) Aminoluciferins extend firefly luciferase bioluminescence into the near-infrared and can be preferred substrates over d-luciferin. J Am Chem Soc 136:13277–13282
110. Rumyantsev KA, Turoverov KK, Verkhusha VV (2016) Near-infrared bioluminescent proteins for two-color multimodal imaging. Sci Rep 6:36588
111. Wu W et al (2017) cybLuc: an effective aminoluciferin derivative for deep bioluminescence imaging. Anal Chem 89:4808–4816
112. So M-K, Xu C, Loening AM, Gambhir SS, Rao J (2006) Self-illuminating quantum dot conjugates for in vivo imaging. Nat Biotechnol 24:339
113. Quiñones GA, Miller SC, Bhattacharyya S, Sobek D, Stephan J-P (2012) Ultrasensitive detection of cellular protein interactions using bioluminescence resonance energy transfer quantum dot-based nanoprobes. J Cell Biochem 113:2397–2405
114. Kamkaew A, Sun H, England CG, Cheng L, Liu Z, Cai W (2016) Quantum dot–NanoLuc bioluminescence resonance energy transfer enables tumor imaging and lymph node mapping in vivo. Chem Commun 52:6997–7000
115. Wu Q, Chu M (2012) Self-illuminating quantum dots for highly sensitive in vivo real-time luminescent mapping of sentinel lymph nodes. Int J Nanomedicine 7:3433–3443
116. Tsuboi S, Jin T (2017) Bioluminescence resonance energy transfer (BRET)-coupled Annexin V-functionalized quantum dots for near-infrared optical detection of apoptotic cells. Chembiochem 18:2231–2235

117. Tsuboi S, Jin T (2018) Recombinant protein (luciferase-IgG binding domain) conjugated quantum dots for BRET-coupled near-infrared imaging of epidermal growth factor receptors. Bioconjug Chem 29:1466–1474
118. Feugang JM, Youngblood RC, Greene JM, Willard ST, Ryan PL (2015) Self-illuminating quantum dots for non-invasive bioluminescence imaging of mammalian gametes. J Nanobiotechnol 13:38
119. Xiong L, Shuhendler AJ, Rao J (2012) Self-luminescing BRET-FRET near-infrared dots for in vivo lymph-node mapping and tumour imaging. Nat Commun 3:1193
120. Kuchimaru T, Suka T, Hirota K, Kadonosono T, Kizaka-Kondoh S (2016) A novel injectable BRET-based in vivo imaging probe for detecting the activity of hypoxia-inducible factor regulated by the ubiquitin-proteasome system. Sci Rep 6:34311
121. Huang X, Li L, Qian H, Dong C, Ren J (2006) A resonance energy transfer between chemiluminescent donors and luminescent quantum-dots as acceptors (CRET). Angew Chem Int Ed 45:5140–5143
122. Zhang N, Francis KP, Prakash A, Ansaldi D (2013) Enhanced detection of myeloperoxidase activity in deep tissues through luminescent excitation of near-infrared nanoparticles. Nat Med 19:500
123. Lee D et al (2007) In vivo imaging of hydrogen peroxide with chemiluminescent nanoparticles. Nat Mater 6:765
124. Li P, Liu L, Xiao H, Zhang W, Wang L, Tang B (2016) A new polymer Nanoprobe based on chemiluminescence resonance energy transfer for ultrasensitive imaging of intrinsic superoxide anion in mice. J Am Chem Soc 138:2893–2896
125. Shuhendler AJ, Pu K, Cui L, Uetrecht JP, Rao J (2014) Real-time imaging of oxidative and nitrosative stress in the liver of live animals for drug-toxicity testing. Nat Biotechnol 32:373
126. Zhen X, Zhang C, Xie C, Miao Q, Lim KL, Pu K (2016) Intraparticle energy level alignment of semiconducting polymer nanoparticles to amplify chemiluminescence for ultrasensitive in vivo imaging of reactive oxygen species. ACS Nano 10:6400–6409
127. Xu G et al (2018) Imaging of colorectal cancers using activatable nanoprobes with second near-infrared window emission. Angew Chem Int Ed 57:3626–3630
128. Cai L, Deng L, Huang X, Ren J (2018) Catalytic chemiluminescence polymer dots for ultrasensitive in vivo imaging of intrinsic reactive oxygen species in mice. Anal Chem 90:6929–6935
129. Zhang Y et al (2014) Small molecule-initiated light-activated semiconducting polymer dots: an integrated nanoplatform for targeted photodynamic therapy and imaging of cancer cells. Anal Chem 86:3092–3099
130. Li D et al (2018) Near-infrared excitation/emission and multiphoton-induced fluorescence of carbon dots. Adv Mater 30:1705913
131. Liu L, Wang S, Zhao B, Pei P, Fan Y, Li X, Zhang F (2018) Er^{3+} sensitized 1530 nm to 1180 nm second near-infrared window upconversion nanocrystals for in vivo biosensing. Angew Chem Int Ed 57:7518–7522
132. Fery-Forgues S, Lavabre D (1999) Are fluorescence quantum yields so tricky to measure? a demonstration using familiar stationery products. J Chem Educ 76:1260
133. Huang L, Pedrosa HN, Krauss TD (2004) Ultrafast ground-state recovery of single-walled carbon nanotubes. Phys Rev Lett 93:017403
134. Jones M, Engtrakul C, Metzger WK, Ellingson RJ, Nozik AJ, Heben MJ, Rumbles G (2005) Analysis of photoluminescence from solubilized single-walled carbon nanotubes. Phys Rev B 71:115426
135. Wang F, Dukovic G, Brus LE, Heinz TF (2004) Time-resolved fluorescence of carbon nanotubes and its implication for radiative lifetimes. Phys Rev Lett 92:177401
136. Crochet J, Clemens M, Hertel T (2007) Quantum yield heterogeneities of aqueous single-wall carbon nanotube suspensions. J Am Chem Soc 129:8058–8059
137. Carlson LJ, Maccagnano SE, Zheng M, Silcox J, Krauss TD (2007) Fluorescence efficiency of individual carbon nanotubes. Nano Lett 7:3698–3703

138. Lefebvre J, Austing DG, Bond J, Finnie P (2006) Photoluminescence imaging of suspended single-walled carbon nanotubes. Nano Lett 6:1603–1608
139. Tsyboulski DA, Rocha J-DR, Bachilo SM, Cognet L, Weisman RB (2007) Structure-dependent fluorescence efficiencies of individual single-walled carbon nanotubes. Nano Lett 7:3080–3085
140. Miyauchi Y, Iwamura M, Mouri S, Kawazoe T, Ohtsu M, Matsuda K (2013) Brightening of excitons in carbon nanotubes on dimensionality modification. Nat Photonics 7:715
141. Ju S-Y, Kopcha WP, Papadimitrakopoulos F (2009) Brightly fluorescent single-walled carbon nanotubes via an oxygen-excluding surfactant organization. Science 323:1319–1323
142. Hou Z, Krauss TD (2017) Photoluminescence brightening of isolated single-walled carbon nanotubes. J Phys Chem Lett 8:4954–4959
143. Gao J, Wu C, Deng D, Wu P, Cai C (2016) Direct synthesis of water-soluble Aptamer-Ag2S quantum dots at ambient temperature for specific imaging and photothermal therapy of cancer. Adv Healthc Mater 5:2437–2449
144. Yang T et al (2017) Size-dependent Ag2S Nanodots for second near-infrared fluorescence/photoacoustics imaging and simultaneous photothermal therapy. ACS Nano 11:1848–1857
145. Wang Y, Yan X-P (2013) Fabrication of vascular endothelial growth factor antibody bioconjugated ultrasmall near-infrared fluorescent Ag2S quantum dots for targeted cancer imaging in vivo. Chem Commun 49:3324–3326
146. Deng D et al (2012) Forming highly fluorescent near-infrared emitting PbS quantum dots in water using glutathione as surface-modifying molecule. J Colloid Interface Sci 367:234–240
147. Freyria FS et al (2017) Near-infrared quantum dot emission enhanced by stabilized self-assembled J-aggregate antennas. Nano Lett 17:7665–7674
148. Pokhrel M, Mimun LC, Yust B, Kumar GA, Dhanale A, Tang L, Sardar DK (2014) Stokes emission in GdF_3:Nd^{3+}nanoparticles for bioimaging probes. Nanoscale 6:1667–1674
149. Qin Q-S et al (2017) Ultralow-power near-infrared excited neodymium-doped nanoparticles for long-term in vivo bioimaging. Nanoscale 9:4660–4664
150. Rocha U et al (2013) Subtissue thermal sensing based on neodymium-doped LaF3 nanoparticles. ACS Nano 7:1188–1199
151. Chen G et al (2012) Core/shell NaGdF4:Nd3+/NaGdF4 nanocrystals with efficient near-infrared to near-infrared downconversion photoluminescence for bioimaging applications. ACS Nano 6:2969–2977
152. Joo J et al (2016) Enhanced quantum yield of photoluminescent porous silicon prepared by supercritical drying. Appl Phys Lett 108:153111
153. Gelloz B, Kojima A, Koshida N (2005) Highly efficient and stable luminescence of nanocrystalline porous silicon treated by high-pressure water vapor annealing. Appl Phys Lett 87:031107
154. Joo J, Cruz JF, Vijayakumar S, Grondek J, Sailor MJ (2014) Photoluminescent porous Si/SiO2 core/shell nanoparticles prepared by borate oxidation. Adv Funct Mater 24:5688–5694
155. Ando Y et al (2007) Firefly bioluminescence quantum yield and colour change by pH-sensitive green emission. Nat Photonics 2:44
156. Niwa K et al (2010) Quantum yields and kinetics of the firefly bioluminescence reaction of beetle luciferases. Photochem Photobiol 86:1046–1049
157. Ando Y et al (2007) Development of a quantitative bio/chemiluminescence spectrometer determining quantum yields: re-examination of the aqueous luminol chemiluminescence standard. Photochem Photobiol 83:1205–1210

Chapter 10
Polymer-Functionalized NIR-Emitting Nanoparticles: Applications in Cancer Theranostics and Treatment of Bacterial Infections

Neelkanth M. Bardhan and Angela M. Belcher

Abbreviations

2D/3D	Two-dimensional/three-dimensional
5-ALA	5-aminolevulinic acid
BSA	Bovine serum albumin
CRISPR-Cas9	Clustered regularly interspaced short palindromic repeats—CRISPR-associated endonuclease protein 9
CTC	Circulating tumor cell
DBCO-NHS	Dibenzocyclooctyne-*N*-hydroxysuccinimide
DMD	Duchenne muscular dystrophy
DNA	Deoxyribonucleic acid
DPPC	1,2-dipalmitoyl-*sn*-glycero-3-phosphatidylcholine
DSPE-mPEG	1,2-distearoyl-*sn*-glycero-3-phosphoethanolamine-*N*-[methoxy(polyethylene glycol)]

N. M. Bardhan
The David H. Koch Institute for Integrative Cancer Research, Massachusetts Institute of Technology, Cambridge, MA, USA

Department of Materials Science and Engineering, Massachusetts Institute of Technology, Cambridge, MA, USA
e-mail: bardhan@mit.edu

A. M. Belcher (✉)
The David H. Koch Institute for Integrative Cancer Research, Massachusetts Institute of Technology, Cambridge, MA, USA

Department of Materials Science and Engineering, Massachusetts Institute of Technology, Cambridge, MA, USA

Department of Biological Engineering, Massachusetts Institute of Technology, Cambridge, MA, USA
e-mail: belcher@mit.edu

A. Benayas et al. (eds.), *Near Infrared-Emitting Nanoparticles for Biomedical Applications*, https://doi.org/10.1007/978-3-030-32036-2_10

EDC-NHS	Ethyl(dimethylaminopropyl) carbodiimide-*N*-hydroxysuccinimide
EPR	Enhanced permeability and retention
FDA	United States Food and Drug Administration
FITC	Fluorescein isothiocyanate
GNR	Graphene nanoribbon
GO	Graphene oxide
GQD	Graphene quantum dot
HA	Hyaluronic acid
ICG	Indocyanine green
LSPR	Localized surface plasmon resonance
mPEG2000-DSPE	*N*-(carbonyl-methoxy polyethylene glycol 2000)-1,2-distearoyl-*sn*-glycero-3 phosphoethanolamine
MB	Methylene blue
MHC	Major histocompatibility complex
MRI	Magnetic resonance imaging
NIR	Near infrared
NIR-I/NIR-II	First-window near infrared (700–900 nm)/second-window near infrared (1000–1700 nm)
NO	Nitric oxide
NP	Nanoparticle
PAA	Polyacrylic acid or polyallyl amine (depending on the context)
PDT	Photodynamic therapy
PEG	Poly(ethylene glycol)
PEI	Polyethylene imine
PET	Positron emission tomography
PL	Phospholipid
PLL	Poly L-lysine
PPI	Polypropylene imine
PS	Polystyrene
PSMA	Prostate-specific membrane antigen
PTT	Photothermal therapy
PVA	Polyvinyl alcohol
QD	Quantum dot
RES	Reticulo-endothelial system (also known as the mononuclear phagocyte system)
RGD	Arginine-glycine-aspartic (Arg-Gly-Asp) sequence of amino acid residues
rGO	Reduced graphene oxide
RNA	Ribonucleic acid
ROS	Reactive oxygen species
SDF-1α	Stromal cell-derived factor 1alpha, a chemokine protein encoded by the CXCL 12 gene in humans
SPARC	Secreted protein, acidic and rich in cysteine
ssDNA/dsDNA	Single-stranded/double-stranded DNA

SWNT	Single-walled carbon nanotube
TNF-α	Tumor necrosis factor alpha, a cytokine involved in systemic inflammation
UCNP/DCNP	Upconversion nanoparticle/downconversion nanoparticle

10.1 Introduction: Why Use Polymer Functionalization of Nanoparticles?

The properties of nanoparticles, including their surface charge, hydrodynamic diameter (or size), and the presence of targeting functional groups all affect their interactions with cells and in vivo environments in important ways [1, 2]. Therefore, having fine-grained control over the nanoparticle surface is essential, in order to determine their fate in the biological environment for imaging and therapeutic applications.

Among the main arguments in favor of using polymeric functionalization of nanoparticles for biomedical applications [3, 4] are the following: (a) To provide targeting capability: This enables the nanoparticles to selectively recognize and bind to specific membrane receptors or antigens on the target cells (such as cancer cells or bacterial pathogens of interest). Alternatively, it allows the nanoparticles to interact with the host through specific interaction mechanisms (such as adsorption or endocytosis leading to cellular internalization), which helps decrease the non-specific background and improve the signal-to-noise in imaging applications; especially for the detection of deep-tissue cancers and infectious diseases. (b) To improve biocompatibility, increase circulation and residence time [5], and tailor the clearance mechanism: Non-specific interactions of the nanoparticles, such as with the extracellular matrix, as well as with components of the serum and the host's immune system (when administered intravenously) can strongly hinder the efficient delivery of the nanoparticles to the disease site of interest. Adsorption or opsonization of the plasma proteins can lead to recognition by the phagocytic cells of the immune system and lead to rapid clearance via the RES pathway [6]. To avoid this fate, coating nanoparticles with appropriate polymers can offer them a "stealth" functionality to increase residence time, and improve the chances of on-target trafficking. An added benefit of this approach is the potential to create nanoparticles which leverage the enhanced permeability and retention (EPR) effect [7], even without the presence of active targeting. Additionally, it has been reported [8] that polymeric nanomaterials (and certain micellar structures, such as filomicelles) can be used to scavenge cancer cell debris and other metabolic by-products from the circulation. (c) To enhance the functionality of the fluorophore: There are strategies available to enhance the fluorescence emission of an emitter, such as an organic dye molecule, using a nanoparticle with a large scattering cross section placed proximally to the emitter, with a plasmon resonance frequency tuned to the emission frequency of the fluorophore [9]. Such strategies can significantly aid in contrast

enhancement [10] and lead to higher sensitivity of detection or lower threshold of detection, both of which are important for early diagnosis of diseases such as metastatic cancers. It is no coincidence that most of the nanoparticles commercially available [11], in clinical-use or under-investigation for clinical translation use some sort of polymer-based approach [12]: through coating of a polyethylene glycol (PEG) layer on top of liposomes (PEGylated "stealth" liposomes), as polymeric micelles, or micellar nanoparticles of layers of polymers encapsulating a payload of interest (such as small-molecule drugs, biologics, vaccines, or imaging agents).

For a detailed overview of the considerations in designing coating materials for the functionalization of nanoparticles, the reader is referred to a comprehensive review by Nam et al. [13].

10.2 Types of NIR-Emitting Nanoparticles

As outlined in Fig. 10.1, the 5 main classes of long-wavelength (>900 nm) NIR-emitting nanomaterials [20], which are of strong interest for clinical translation to human patients, are as follows: (a) Organic dyes and other small-molecule probes; (b) Inorganic quantum dots; (c) Gold nanoparticles; (d) Carbon dots, carbon nanotubes, graphene and their derivatives; and (e) Upconversion or downconversion nanoparticles.

In the following sections, we shall delve into the applications of polymer functionalization of each of these classes of nanoparticles, in considerable detail.

Fig. 10.1 (continued) Wang et al. [17], ©2010 The Royal Society of Chemistry. Schematic of the phenomena occurring at the interface between lanthanide-doped UCNPs, and the biological environment. Reprinted (adapted) with permission from Gnach et al. [18], ©2014 The Royal Society of Chemistry. Bottom panel: The upconversion emission color can be fine-tuned from the visible to the NIR, using a single host ($NaYF_4$) doped with rare-earth ions such as Yb^{3+}, Tm^{3+}, or Er^{3+}. Reprinted (adapted) with permission from Wang and Liu [19], ©2008 American Chemical Society. (**Lower left:**) Molecular structure of the FDA-approved NIR dye, indocyanine green (ICG), rendered using ChemSpider. Example of a microscope image of endothelial cells stained with multiple fluorescent dyes. Credit: user: de:Benutzer:Jan R/Wikimedia Commons/Public Domain. Inset: A range of emission spectra of commonly available small-molecule organic dyes, with emission mostly in the visible range (under 750 nm). Image courtesy of Olympus Corporation. Reprinted (adapted) with permission. (**Top left:**) Schematic of a PbS quantum dot, with complete passivation by oleic acid, oleylamine, and hydroxyl ligands (size $\approx$ 5 nm). Credit: user: Zherebetskyy/Wikimedia Commons/CC BY-SA 3.0. Color photograph of vials of QDs with vivid colors, ranging from violet to deep red. Credit: user: Antipoff/Wikimedia Commons/CC BY-SA 3.0. Inset: Fluorescence spectra of CdTe quantum dots of various sizes. Different sized QDs emit at different wavelengths due to the quantum confinement effect. Credit: user: Antipoff/Wikimedia Commons/CC BY-SA 4.0

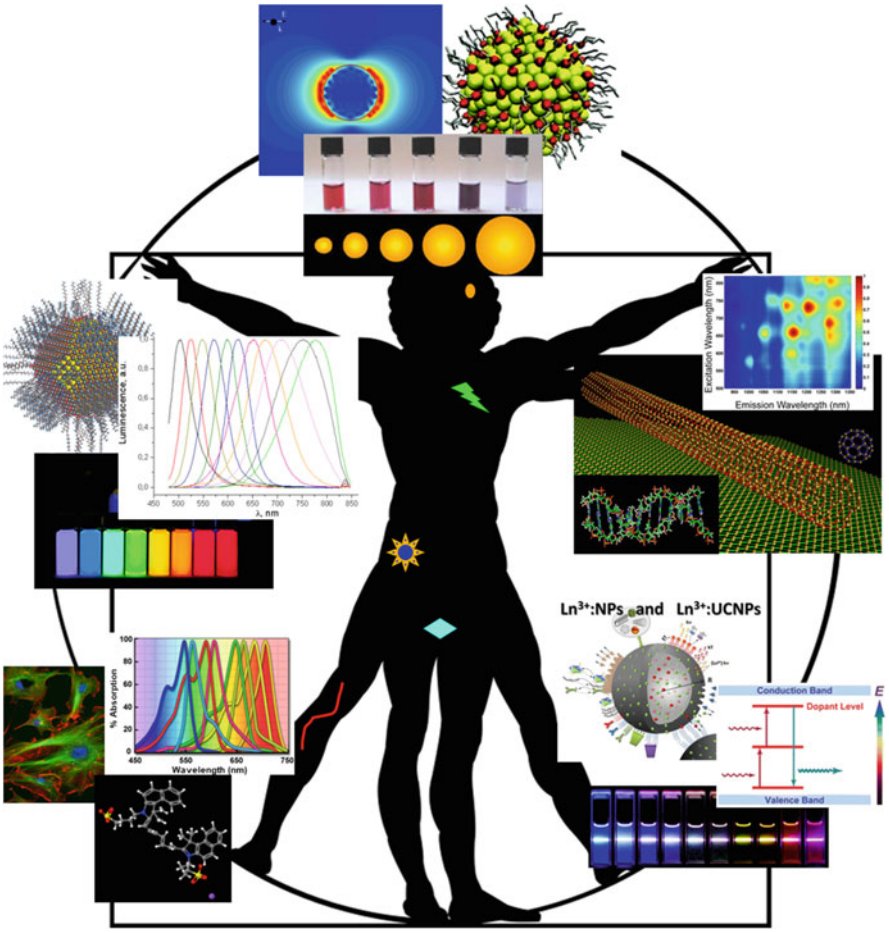

Fig. 10.1 Overview of the **5** classes of NIR-emitting nanomaterials for human theranostics. (clockwise, from top) (**Top:**) Simulation showing the electric field intensity enhancement around a 60 nm Au nanosphere in water, with a localized surface plasmon resonance peak of 532 nm, using the discrete dipole approximation calculation. Reprinted (adapted) with permission from Juluri, B.K. Simulated structure of thiol-protected nanocluster of Au atoms. Reprinted (adapted) with permission from Mariscal et al. [14], with permission of the PCCP Owner Societies, ©2010 The Royal Society of Chemistry. The bottom image shows the different colors of colloidal gold solutions, due to different sizes of the Au nanoparticles in the vials (increasing from left-to-right). As particle size increases, the surface plasmon resonance peak shifts to a longer wavelength, with the blue light being reflected more. Credit: Alexander Kondinski/CC BY-SA 4.0. (**Upper right:**) Schematic of a graphene sheet, a (6, 5) SWNT, and a C_{60} bucky ball, rendered using VESTA [15]. The gold spheres represent C atoms. Schematic of a double-stranded DNA molecule used as a biopolymer, to functionalize SWNTs and graphene. Credit: user: Zephyris/Wikimedia Commons/CC BY-SA 3.0. Inset: Photoluminescence (excitation-emission) map of SWNTs wrapped with a mix of polycarbodiimide polymers, showing strong NIR-II emission over 1000 nm. Reprinted (adapted) with permission from Budhathoki-Uprety et al. [16], ©2014 American Chemical Society. (**Lower right:**) Energy-band diagram, showing the multi-photon energy transfer process (one of several energy transfer mechanisms) happening in UCNPs. Reprinted with permission from

10.2.1 Organic Dyes and Small-Molecule Probes

While most of the other classes of NIR-II-emitting nanomaterials (inorganic quantum dots, carbon nanotubes, up/downconversion nanoparticles) are based on inorganic molecules, the development of long-wavelength emission organic dyes has generated a great source of excitement in the last few years. This is because NIR-II dyes with similar function and biocompatibility compared to visible-wavelength dyes already approved by the US Food and Drug Administration (FDA), or in investigational use in the clinic [21] (such as indocyanine green, ICG; methylene blue, MB; 5-aminolevulinic acid, 5-ALA; fluorescein sodium folate, folate-FITC; IRDye 800CW conjugate or IRDye 700DX conjugate) would pave the way for rapid transition from basic research to clinical application. For a review of the current clinical applications of near infrared fluorescent probes used in image-guided cancer surgery, the reader is referred to Vahrmeijer et al. [22] and van Driel et al. [23].

Among the various organic dyes, it is worth taking a closer look at indocyanine green (ICG), which fluoresces at ~800 nm, and is the only NIR contrast agent (to date) approved by the FDA. Consequently, imaging systems leveraging the fluorescence of ICG have been used in a number of clinical trials in cancer management. One of the most well-studied uses is for the purpose of mapping sentinel lymph nodes (Fig. 10.2a–f) in breast cancer [29–36] (National Clinical Trials NCT02279108, NCT01468649, and NCT01856452 in the USA, the European Union Clinical Trials Register EudraCT #2009-016743-18, and Netherlands Trial Register NTR2084, to name a few). Recent meta-analyses [37, 38] have suggested that the use of ICG fluorescence has valid diagnostic performance for the detection of sentinel lymph nodes and is potentially a better approach towards staging compared to the use of radioisotopes. In addition to breast cancer, there have been numerous small clinical trials for sentinel lymph node mapping by ICG fluorescence, in patients with melanoma [39], head-and-neck cancer [40], lung cancer [41, 42], colorectal cancer [43, 44], prostate cancer [45], as well as for tumor imaging in ovarian cancer [46, 47], hepatocellular carcinoma [48, 49] and liver metastases [50], and other applications such as imaging of vascular features in the body. Most recently, there has been great excitement in the field of molecular imaging, due to the discovery of short-wave infrared (>1000 nm) fluorescence emission of ICG (Fig. 10.2k–n). Work done by Bawendi, M.G. and co-workers has shown tremendous promise for direct clinical application of ICG for near infrared imaging. In a report by Carr et al. [25], it was shown that ICG-PEG2000 phospholipids (ICG conjugated to 1,2-dioleoyl-*sn*-glycero-3-phosphoethanolamine-*N*-[methoxy(polyethylene glycol)-2000]) can be used to perform intravital microscopy, noninvasive real-time imaging of blood and lymph vessels, imaging of the hepatobiliary clearance pathway, and targeted in vivo imaging, with 808 nm excitation, and long-pass emission over 1300 nm. In parallel, Annapragada, A. and co-workers have also developed ICG nanoparticles for NIR-II fluorescence imaging. In early reports, Starosolski et al. compared the contrast-to-noise ratio (CNR) of NIR-I:NIR-II for ICG (free form in PBS), and found ~2× enhancement in the NIR-II in in vivo imaging [51], which was significantly higher than that of a commercially

available dye, IR-E1050. More recently, using a liposomal formulation of ICG (liposomes consisting of DPPC, cholesterol, and mPEG-2000-DSPE in the molar ratio 87:10:3), Bhavane et al. demonstrated superior in vivo imaging in deep vascular structures (≥4 mm) in the hindlimb and cranium of mice, due to the improved vascular retention of these liposomes [52]. However, these liposomes exhibited much faster clearance (∼ few hours) from the circulation compared to PEGylated liposomes (∼18–24 h), which could potentially be attributed to in vivo leakage of the ICG from the liposomes. More work, therefore, remains to be done to design well-encapsulated, actively targeted, polymer-functionalized nanoparticles for the improved circulation and efficient delivery of NIR-II dyes for fluorescence imaging applications. For a good overview of the polymer-conjugated uses of ICG for biomedical applications, the review by Han et al. [53] is worth a perusal.

Towards the goal of developing a new class of small-molecule organic fluorophores, a great body of work has been produced by Dai, H. and co-workers. In early work, Tao et al. developed a polymer nanoparticle (polyacrylic acid, PAA)-encapsulated dye [54], using the organic dye IR-1061, further coated with DSPE−mPEG (5 kDa), with emission longer than 1000 nm. This approach resulted in a stable aqueous suspension of the organic dye and was used for mouse hindlimb and abdominal imaging with low autofluorescence. Subsequently, Hong et al. have used an approach based on co-polymerization of an electron-donating and electron-withdrawing monomer, to create a brightly fluorescent copolymer, poly(benzo[1,2-b:3,4-b']difuran-*alt*-fluorothieno-[3,4-b]thiophene), termed "pDA," with long-wavelength emission [55] at ∼1050 nm, and a large Stokes' shift of ∼400 nm, with a reasonably high quantum yield of ∼1.7%. Functionalized with PEG, they utilized this molecule for hindlimb blood flow imaging, as well as for dynamic fluorescence imaging at 25 frames/s, for cardiac cycle measurements. More recently, Antaris et al. have reported the synthesis [24] of an organic small molecule (Fig. 10.2g) of size 970 Da, termed CH1055, utilizing a donor–acceptor–donor electronic structure, which showed better performance than ICG in imaging mouse vasculature and sentinel lymph node mapping. Further, they were able to demonstrate high tumor uptake (Fig. 10.2i, j) of PEG-coated CH1055 dye in a brain tumor mouse model (Fig. 10.2h), at depths of 4 mm, and this molecule was also shown to have favorable clearance characteristics (with ∼90% renal excretion within 24 h). Subsequently, the same group of authors have reported a strategy to improve upon the low quantum yield of CH1055-PEG (∼0.3%), by changing the functional groups from carboxylic to sulfonic acid [56]. This change resulted in a derivative NIR-II dye, termed CH-4T, which forms supramolecular assemblies with plasma proteins to cause an enhancement in the fluorescent intensity. An advantage of this approach is the high quantum yield, reported to be ∼5% in serum, and the ability to boost the quantum yield as high as ∼11% by heating to 70 °C for 10 min. By complexing the dye with protein prior to injection, they were able to show ultra-fast imaging, at 50 frames/second, with great temporal resolution of cardiac cycles. This approach also showed promise for deep-tissue lymph-node imaging at depths of ∼5–8 mm. Most recently, the same group of researchers has shown three-dimensional imaging into biological tissues using an NIR-II organic

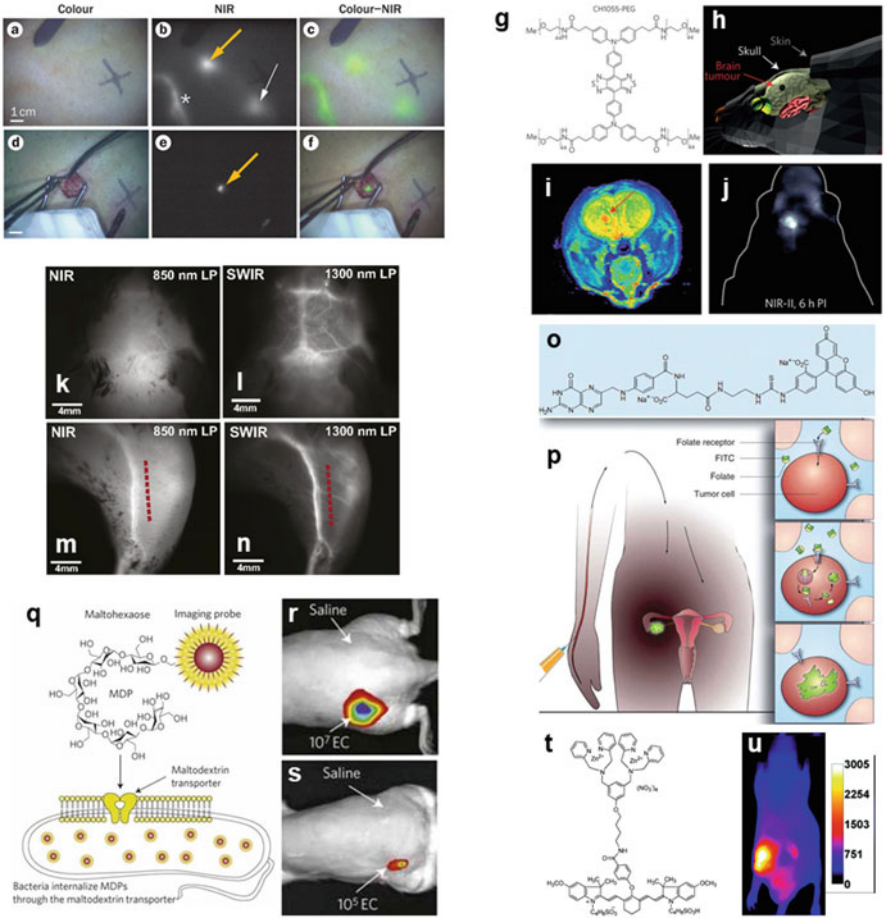

Fig. 10.2 A representative sample of the preclinical and clinical applications of fluorescent organic dyes. (**a–f**) Sentinel lymph node mapping in a melanoma patient using ICG at 800 nm, as shown in the (**a, d**) color photos, (**b, e**) NIR fluorescence images, and (**c, f**) merged images. The arrows in (**b**) and (**e**) point to the identified lymph node. The NIR images allow for surgical resection of the lymph node using the mini-FLARE system. Reprinted (adapted) with permission from Vahrmeijer et al. [22], ©2013 Nature Publishing Group. (**g–i**) Schematic of the (**g**) structure of the newly synthesized NIR-II fluorescent CH1055-PEG dye molecule, and (**h**) the location of an orthotopic glioblastoma brain tumor located under the scalp and skull in a mouse. (**i**) The sagittal view of T2-weighted MRI image (false color), and the corresponding (**j**) high-magnification NIR-II fluorescence image showing tumor detection through skull at a depth of ~4 mm, non-invasively, at 6 h post-intravenous injection. Reprinted (adapted) with permission from Antaris et al. [24], ©2016 Nature Publishing Group. (**k–n**) Recent discovery of the NIR-II fluorescence emission of ICG (>1300 nm), showing higher image contrast compared to ICG emission in the NIR-I wavelength range. Image of mouse brain vasculature post-intravenous injection of ICG-phospholipids, in (**k**) NIR-I, using 850 nm long-pass filter, and (**l**) NIR-II, using 1300 nm long-pass filter, showing greatly improved vessel contrast. Similarly, (**m**) shows only large hindlimb vessels, while (**n**) shows resolution of smaller vessels in NIR-II. Reprinted (adapted) with permission from Carr et al. [25], ©2018 National Academy of Sciences.

dye. In a study [57] by Wan et al., the newly synthesized molecule, termed "p-FE" (comprised of a hydrophobic NIR-II-emitting organic dye, FE, encapsulated in the core of an amphiphilic polymer, poly(styrene-co-chloromethyl styrene)-graft-poly(ethylene glycol), or PS-*g*-PEG) was shown to be a highly promising imaging agent for 3D fluorescence microscopy of blood vessels in the mouse brain, at depths of ~1.3 mm, with spatial resolution of ~5–7 μm. These dyes can also be combined with other NIR-II fluorophores, such as single-walled carbon nanotubes, to achieve multiplexed NIR-II imaging of tumors and blood vessels.

The use of small-molecule organic dyes for the detection of bacterial infections has been well-investigated. In the early days, work done by Piwnica-Worms, D., Smith, B.D., and co-workers has made use of a newly synthesized molecule comprising a carbocyanine fluorophore (near infrared emitting) attached to an affinity group containing two zinc(II) dipicolylamine (Zn-DPA) units [58] (Fig. 10.2t), for imaging bacterial infections in living mice. Using this approach, Leevy et al. have reported [28] noninvasive whole-body imaging of mice, which allowed them to detect *Staphylococcus aureus* infections in a mouse leg infection model (Fig. 10.2u), with a minimum threshold of 5×10^7 cfus of bacteria, with a signal-to-background ratio of 3.9 ± 0.5 compared to the uninfected tissue. In a subsequent study, Ning et al. [27] have developed a maltodextrin-based probe, which takes advantage of the maltodextrin transport pathway of bacterial cells (but not mammalian cells), to internalize an NIR dye, IR786 into the bacterial cell (Fig. 10.2q) for imaging purposes. Based on this technique, they were able to detect infection of *E. coli*, *P. aeruginosa*, *B. subtilis*, and *S. aureus* strains in a mouse model of intramuscular (thigh) infection (Fig. 10.2r), and distinguish between infections and inflammation. A benefit of this approach is that the authors reported a very low threshold of 10^5 cfus of *E. coli*, showing very high sensitivity of detection (Fig. 10.2s) compared to previously reported studies in the literature. In more recent work, Bardhan, N.M. and co-workers have leveraged the M13 bacteriophage, loaded with an NIR dye (Alexa

Fig. 10.2 (continued) (**o, p**) Another example of the clinical application of small-molecule dyes. (**o**) The compound folate-FITC (fluorescein isothiocyanate, with an emission of ~520 nm) used to target epithelial ovarian cancer, and (**p**) schematic showing the mechanism of targeting towards FR-α, followed by binding, internalization, and delivery of folate-FITC into the cytoplasm, which is then used for fluorescence image-guided surgery in human ovarian cancer patients. This allowed for real-time image-guided resection of tumors as small as ~1 mm. Reprinted (adapted) with permission from van Dam et al. [26], ©2011 Nature Publishing Group. (**q–s**) A small-molecule fluorescence imaging probe, designed to take advantage of the maltodextrin transport pathway in bacteria. (**q**) Structure of the NIR-fluorescent dye (such as IR786) linked to a maltose sugar, for internalization into bacterial cells. (**r**) Detection of an infection of 10^7 cfus of *E. coli*, in a rat model of infection, and (**s**) down to 10^5 cfus in vivo, showing very high sensitivity of detection. Reprinted (adapted) with permission from Ning et al. [27], ©2011 Nature Publishing Group. (**t, u**) Use of a (t) Zn(II) coordination complex molecule with dipicolylamine ligands to target the anionic cell surface of bacterial cells, and (u) NIR fluorescence images, showing the detection of an intramuscular infection of 5×10^7 cfus of *S. aureus* in mice, at 21 h post-intravenous injection of the DPA-Zn(II) probe, at 830 nm emission. Reprinted (adapted) with permission from Leevy et al. [28], ©2008 American Chemical Society

Fluor 750), and conjugated with an anti-bacterial antibody, for targeted imaging [59] of intramuscular *S. aureus* and *E. coli* infections. For an overview of the state-of-the-art optical imaging techniques available for the study and treatment of infectious diseases, the reader is referred to the review by Krafft [60] and the book chapter by Archer et al. [61].

For an in-depth perspective into the recent advances in the development of small-molecule probes for bioimaging, tumor detection, and guided surgery applications, the reader is referred to the excellent review by Haque et al. [62].

10.2.2 Inorganic Quantum Dots

Semiconductor nanocrystals, also known as quantum dots (QDs), are a class of fluorophores which are of considerable interest in biological diagnostics, because compared to conventional dye-based fluorophores, they have a narrow, tunable, symmetric emission spectrum (simply by controlling the size of the QDs), and are stable to photochemical bleaching. In some of the earliest work involving QDs, work done by the groups of Alivisatos, A.P., Nie, S., and others was used for cell labeling. For example, Bruchez et al. showed single-excitation, dual-emission labeling of mouse fibroblasts [63] using silica-coated CdSe (core)−ZnS/CdS (shell) near-IR emitting nanocrystals. Subsequently, Chan, W.C.W. and Nie, S. have shown ultra-sensitive detection (at the level of a single QD), using receptor-mediated endocytosis of CdSe QDs coated with transferrin (an iron-transporter protein) into HeLa cells [64], which was ∼20× brighter and ∼100× more stable against photobleaching, as compared to rhodamine, a common dye. In follow-up work, Wu et al. showed [65] simultaneous labeling of anti-Her2 antibody-coated QDs on the breast cancer receptor Her2 in live cells, as well as the staining of actin and microtubule fibers in the cytoplasm of mouse fibroblasts, and nuclear antigens inside the nucleus, which made it possible to image 2 cellular targets using a single excitation wavelength. In one of the first reported applications of the use of QDs in in vivo targeting applications, Åkerman et al. showed [66] the use of homing peptides (GFE, F3, or LyP-1, Fig. 10.3e) to target intravenously injected

Fig. 10.3 (continued) of synthesis techniques, functionalizations, and imaging modalities being developed using next-generation QDs, using varied architectures such as core–shell–shell, and coated with different functionalization molecules. Reprinted (adapted) with permission from Bruns et al. [70], ©2017 Nature Publishing Group. (**l**) Schematic showing the mechanism of generation of reactive oxygen species using CdTe QDs, which can be used to enhance the efficacy of antibiotics to treat multi-drug-resistant bacterial infection strains at normally ineffective low doses. Credit: Courtney et al. [71] CC BY-NC 4.0. (**m, n**) An overview of the (**m**) general structure of QDs investigated in the literature, showing the numerous core/shell materials, as well as the various conjugations strategies using inorganic coatings (such as silica), polymers (PEG, polyols, lipids, amphiphiles), and biomolecules such as DNA, RNA, or proteins. (**n**) One of the dependencies of the toxicity (as measured by the IC_{50} of the QDs) to the type of surface functionalization, as well as the size of the QD. Reprinted (adapted) with permission from Oh et al. [72], ©2016 Nature Publishing Group

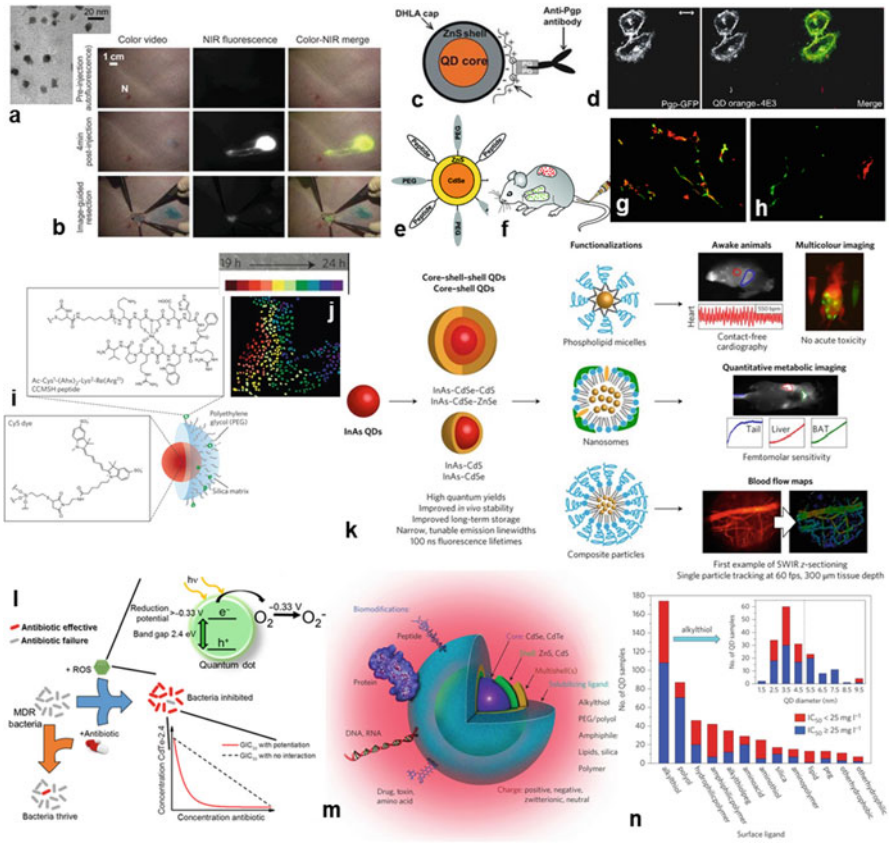

Fig. 10.3 Applications and safety considerations of NIR-emitting quantum dots. (**a, b**) Sentinel lymph node mapping achieved using NIR-II-emitting QDs. (**a**) Transmission electron micrograph (TEM) image of water-dispersible CdTe/CdSe core/shell QDs, which were coated with phosphine to make them soluble in aqueous buffer, and (**b**) image of the surgical field of a pig injected with 400 pmol of the QD suspension, intradermally injected in the groin. Image-guided resection of the lymph node can be performed using the fluorescence of the QDs. Reprinted (adapted) with permission from Kim et al. [67], ©2004 Nature Publishing Group. (**c, d**) Structure of the anti-Pgp antibody-conjugated core–shell QD, with orange emission. (**d**) The merged fluorescence and brightfield images are taken to show specificity of the antibody-labeled QDs to the cells expressing Pgp-EGFP, showing the potential for long-term tracking using these QDs. Reprinted (adapted) with permission from Jaiswal et al. [68], ©2003 Nature Publishing Group. (**e–h**) Structure of the (**e**) CdSe/ZnS core/shell QDs, co-coupled with a peptide for targeting, and with PEG-5000 for colloidal stability. (**f**) Intravenous injection was used, showing (**g**) targeting of the F3 QDs (red) to blood vessels in tumor tissue (green), and (**h**) accumulation of LyP-1 QDs (red) in tumor tissue, but not co-localized with blood vessels (green). Reprinted (adapted) with permission from Åkerman et al. [66], ©2002 National Academy of Sciences. (**i, j**) Schematic of the PEG-coated, NIR-fluorescent silica NPs, known as "Cornell dots" or "C dots," with a size ∼6 nm, which are the only QDs known to be under early-stage clinical trial. The colormap in (**j**) shows a time-lapse analysis of cells undergoing ferroptosis under amino-acid starved conditions, from left-to-right (green indicates cell death). Reprinted (adapted) with permission from Kim et al. [69], ©2016 Nature Publishing Group. (**k**) An overview of the different types

QDs to specific vascular sites in living mice (Fig. 10.3g, h), with an additional coating of polyethylene glycol (PEG) to maintain solubility in aqueous media and minimize non-specific binding. While they reported excellent specificity of homing to the vascular site of the tumors, they observed less accumulation of the QDs in the tumor tissue compared to peptides labeled with fluorescein (a green dye), possibly due to the large size of the former impeding tissue penetration. Work done by Jaiswal et al. showed [68] two approaches of using QDs to label live cells (endocytosis and membrane-impermeable labeling of the biotinylated cell surface using avidin-coated QDs, Fig. 10.3c), and tracked them for 12 days using multi-color imaging (Fig. 10.3d), which did not affect normal cell growth/development and had no adverse effects on cellular signaling. Work done by Liu et al. showed cysteine-coated CdSe/ZnCdS core/shell QDs can be used for in vivo targeted imaging, with rapid renal clearance [73] which helps improve the signal-to-noise ratio in target tissues. In an innovative approach, Valencia et al. used a single-step assembly process [74], enabled by rapid mixing in a microfluidic channel, to create self-assembled lipid-polymer (PLGA, lecithin, and DSPE-PEG) and lipid-QD nanoparticles, which can be used for imaging or drug delivery applications. In a recent study, Lee et al. have reported a class of stable, water-soluble QDs, with a number of conjugation handles [75], for labeling and tracking single molecules on the cell surface. QDs have also been studied extensively for therapeutic applications, such as their potential for photodynamic therapy (PDT). For example, work done by Samia et al. has shown the interaction between CdSe QDs coupled to a silicon phthalocyanine photosensitizer, Pc4, through the Förster resonance energy transfer (FRET) mechanism and can be used to increase the yield of the single-oxygen species [76] which is useful for cytotoxic cell death in targeted tumors. For a review of the applications of QDs for photosensitization in PDT, the reader is referred to Yaghini et al. [77]. A large body of work demonstrating the use of QDs for in vivo imaging applications was done by the groups of Bawendi, M.G. and Frangioni, J.V. In early reports, Kim et al. showed the use of NIR-I QDs (Fig. 10.3a), emitting at 840–860 nm, for sentinel lymph node mapping [67], in a large animal (pig), which allowed them to image at 1 cm depth at low irradiation of 5 mW/cm^2; which can potentially be applied for visual guidance during cancer surgery (Fig. 10.3b). In an interesting demonstration of multifunctional QDs, Bagalkot et al. have reported the functionalization of CdSe/ZnS core/shell QDs with the A10 RNA aptamer against prostate-specific membrane antigen (PSMA), followed by intercalation of doxorubicin (an anti-cancer drug), which resulted in a simultaneous imaging and therapeutic agent [78] against prostate cancer cells. Work done by Jaque, D. and co-workers has used low-dose QDs both for in vivo fluorescence imaging and for "nanothermometry" applications. Based on a PbS/CdS/ZnS core–shell design (with the emission wavelength tuned by the size of the PbS core, and the toxicity concerns mitigated by the ZnS shell), Benayas et al. reported [79] the use of these QDs as a high-resolution thermal sensing platform, with extremely low doses (~0.04 mg/ml) for in vivo imaging, at good depth of penetration (~1.5 cm for 1270 nm emitting QDs). In some recent work, Bruns et al. have reported the synthesis of a class of short-wave infrared QDs based on indium arsenide (Fig. 10.3k), which allowed for

high-resolution multi-color imaging of several organs in real time in unrestrained mice [70], as well as detailed 3D imaging of the mouse brain. For a deep dive into the prospects of application of QDs for tumor imaging, the reader is referred to the review articles by Rhyner et al. [80], Walling et al. [81], and Liu et al. [82].

Among the more well-studied NIR-II-emitting quantum dots, the work done by Wang, Q., Dai, H., and co-workers, towards the development of Ag_2S, Ag_2Se and similar Group II-VI QDs deserves special mention. In early reports, Shen et al. developed a one-pot synthesis of Ag_2S-ZnS hetero-nanostructures, in a "matchstick" assembly conformation [83], which showed dual photoluminescence in the UV-visible (2 peaks, at ∼380 nm and ∼450 nm) and NIR-II (∼1155 nm). Subsequently, Zhang et al. used a ligand-exchange technique to substitute the dodecanethiol-coated Ag_2S with dihydrolipoic acid, and further functionalized with 6-arm PEG via EDC/NHS coupling, for added stability [84]. In vitro, incubated with certain cell lines, it was shown that with this functionalization chemistry, the incubated Ag_2S QDs caused minimal toxicity effects—in terms of cell proliferation, apoptosis and necrosis, DNA damage, or the generation of reactive oxygen species. Based on this approach, using these 6-arm PEG-coated biocompatible Ag_2S QDs, Hong et al. demonstrated fluorescence imaging in vivo [85], with a bright NIR-II emission around ∼1200 nm, and a long circulation half-life of ∼4 h. In a long-term (2-month) study of the in vivo toxicology of these PEG-functionalized Ag_2S QDs in mice, Zhang et al. showed [86] that upon intravenous injection, the nanoparticles accumulate mainly in the RES organs, namely, in the liver and spleen, and are gradually cleared from the system by fecal excretion. At the two tested dosage levels of 15 and 30 mg/kg, no toxicity was reported to be observed via blood biochemistry, hematology analyses, and histological examinations, which suggests that these QDs have promise as an NIR-II imaging agent in vivo. It is worth noting here, however, that the genotoxicity and reproductive toxicity effects of chronic systemic exposure to these QDs were not investigated, and remain a cause for concern. More recently, there has been a great body of work on using these QDs for real-time tracking of transplanted stem cells, blood flow, tumor angiogenesis, as well as for combination therapies. For example, Chen et al. were able to dynamically monitor and track [87] human mesenchymal stem cells in the lung and liver over a long time (∼30 days), with high spatiotemporal resolution (∼30 μm, ∼100 ms) using NIR-II imaging, by labeling the cells with few (∼1000) Ag_2S QDs. In another application, Li et al. used these long-circulating Ag_2S QDs for ultra-high resolution (∼40 μm) imaging, which enabled them to observe [88] angiogenesis from a tiny tumor (∼2–3 mm diameter) in vivo. Following up on this work, Wu et al. designed dual-modality probes [89], comprised of indocyanine green conjugated to PEGylated Ag_2S QDs. While the QDs were used for NIR-II fluorescence imaging, the ICG was used for real-time monitoring of atherosclerotic plaque in the aorta, using contrast-enhanced photoacoustic imaging. Recently, Hao et al. reported a "programmable" combination chemotherapy-immunotherapy for breast cancer treatment [90], guided by dual-color NIR-II fluorescence imaging. In a two-step process, they first used Ag_2Se QDs (NIR-II emission at ∼1350 nm) to deliver doxorubicin (an anti-cancer drug) and SDF-1α to the tumor, and second

used natural killer (NK-92) cells pre-labeled with Ag_2S QDs (NIR-II emission at ~1050 nm) functionalized with the Tat peptide, for adoptive immunotherapy, in a mouse model of breast cancer. This dual-modality approach using NIR-II imaging allowed the researchers to monitor the delivery of each step in real-time in vivo, and enabled them to optimize the dosing regimen for maximum efficacy of tumor inhibition. Based on these numerous reports, it gives us reason to be cautiously optimistic that among the various types of quantum dots, these NIR-II nanoparticles, based on Ag_2S or Ag_2Se, functionalized with a coating layer such as multi-arm PEG, can offer a good combination of properties desirable for in vivo biomedical applications, including high NIR-II fluorescence retention, long half-life in circulation, and low chronic toxicity observed in mice; however, toxicology studies in large mammals, and eventually in humans, are yet to be performed. For a deep dive into the methods of synthesis and biomedical applications in imaging, sensing, and drug delivery using NIR QDs, the reader is referred, respectively, to the recent reviews by Sadovnikov and Gusev [91], and by Zhao et al. [92].

In recent years, QDs have fallen out of favor with researchers, as potential high-contrast fluorophores for in vivo optical imaging applications, due to concerns about their toxicity [93]. Till date, there has been only one reported investigative clinical study [94] of the clinical translation of NIR-emitting QDs: namely, the PEG-coated NIR-fluorescent silica particles, known as "Cornell dots" or "C dots." In more recent work, Kim et al. [69] have shown that the C dots (Fig. 10.3i), surface functionalized with a 14-mer peptide analog (alpha-melanocyte stimulating hormone, or α-MSH), in combination with amino acid starvation, can be used to induce programmed ferroptosis (loading iron into cells, Fig. 10.3j), and high-dose particle delivery can inhibit tumor growth, in a xenograft mouse model of human melanoma. As noticed by the researchers, however, the silica nanoparticles themselves have some ability to induce ferroptosis, and more work needs to be done to establish the safety of these nanoparticles. The concerns about the toxicity effects of QDs in cells and tissues, both in vitro and in vivo, are not particularly new; a review by Hardman, R. in 2005 first looked at these issues in some detail [95], and found that the absorption, distribution, metabolism, excretion, and toxicity of quantum dots depend on many factors: size, surface charge, concentration used, the bio-activity of the outer coating layers (capping material, as well as other functional groups), and their stability in terms of mechanical, oxidative and photolytic activity. Since then, much has been written and debated about the systemic toxicity profiles. A study by Choi et al. showed that a coating layer of zwitterionic or neutral charge prevents adsorption of serum proteins on to the QDs, resulting in a hydrodynamic diameter <5.5 nm, which is favorable for the rapid and efficient clearance through the renal pathway [96] to urinary excretion. Over the years, work done by Chan, W.C.W. and co-workers has tried to delve into the nuances of quantum-dot toxicity, through various in vitro and in vivo studies. In Sprague-Dawley rats dosed with up to 60 nmol of QDs over a period of 4 weeks, Hauck et al. did not observe [97] renal damage or other signs of toxicity. In follow-up work, however, Tsoi et al. tried to probe into the discrepancy between the reported toxicity of QDs to cell culture, versus the apparent lack of toxicity to animals [98], and hypothesized that these differences

could be attributed to the differences in the availability of QD concentrations in vivo, upon systemic dosing, compared to the constant dosing conditions in cell culture. In a review article by Bottrill, M. and Green, M., the authors surmised [99] that there are 2 sources of toxicity caused by QDs: (a) Metals such as Cd, Se, which form the basis for the quantum dots such as CdSe, PbS, PbSe, etc. These can be controlled by minimizing the leakage of these ions, by encapsulating the QDs with a protective polymer shell. (b) The production of reactive oxygen species, or other free radicals, by the QDs. This is harder to control, due to the resonance energy transfer occurring between the QDs and molecular oxygen. For a good review on the subject of quantum dot toxicity, encompassing subjects from the cellular level to non-human primates, the reader is referred to an excellent review by Yong et al. [100]. A novel approach to understanding the toxicity of Cd-containing QDs was recently reported [72] by Oh et al., who used a random forest regression model with a prediction accuracy R^2 ~0.68 for cell viability, and R^2 ~0.77 for IC_{50}, across a sample of over 300 publications involving QD studies (Fig. 10.3n). The main attributes of polymer functionalization agents which were significant in having an impact on QD-induced toxicity were found to be diameter, surface ligand, shell, and surface modification (Fig. 10.3m). While this work pertains mainly to a specific type of core/shell architecture of CdSe/CdTe and ZnS/CdS shells, the analytical exercise, nevertheless, is instructive, and can be applied in designing other forms of QDs, to minimize toxicity and improve their biodistribution, pharmacokinetics, and biocompatibility for medical applications. More such analyses are necessary to draw definitive conclusions about the validity of toxicity concerns, in order to ascertain their true potential for clinical translation.

While the toxicity profiles of QDs make them less desirable for in vivo diagnostic or therapeutic applications (at least until there is definitive evidence about the safety of these nanoparticles), the same attributes can be put to good use for the detection and treatment of bacterial infections. For example, Hahn et al. have shown the ability to detect *E. coli* serotype O157:H7 at single-cell resolution [101] using a fluorescent assay based on QDs, which offers a sensitivity at least 2 orders-of-magnitude better than using a conventional organic dye. Edgar et al. have used an approach based on using phage biology to target specific strains of bacteria. By combining in vivo biotinylation of host-specific bacteriophage with the conjugation of streptavidin-coated QDs, they were able to demonstrate [102] the detection of as few as ~10 bacterial cells per ml, with a signal-to-background ratio of ~1000 in 1 h. In the past couple of years, there has been great excitement generated over the prospects of targeting and killing multi-drug-resistant "superbugs" using quantum-dot technology, based on the work done by Nagpal, P., Chatterjee, A., and co-workers. For example, Courtney et al. have shown that photo-excited QDs can be used to kill a wide range of multi-drug-resistant bacteria [103], such as methicillin-resistant *Staphylococcus aureus* (MRSA), carbapenem-resistant *E. coli*, and other strains. Importantly, the visible/NIR light-absorbing QDs could be tailored through size-dependent quantum confinement to specifically kill bacterial cells, while leaving mammalian cells intact, in a co-culture of *E. coli* with HEK 293T cells. In subsequent work, the same group of authors have shown that ROS

superoxide generation can help improve the potency of antibiotics against a wide range of gram-negative bacteria with high multi-drug resistance, resulting in a minimal inhibitory concentration (MIC) ~1000× lower than the clinical sensitivity level for the antibiotic alone [71], at depths up to 1–2 cm below skin. Similarly, Jian et al. have reported the use of carbon quantum dots synthesized from spermidine, as an effective antibacterial treatment [104] against *E. coli*, *S. aureus*, *P. aeruginosa*, and others, with a MIC ~2500× lower than that of the polyamine (Spermidine) alone, and can be used as an effective treatment for corneal infections due to its in vivo ocular biocompatibility.

10.2.3 Au Nanoparticles

Among the class of metal nanoparticles, we devote a special section to the discussion of gold nanoparticles, owing to the intense interest in these materials since the ancient times; and their unique combination of properties which render them suitable for use as multifunctional anti-cancer agents. Due to the bright, vivid colors shown by Au NPs of varying sizes with <300 Au atoms [105], they have been used in historical objects—especially for creating stained glass, such as the Lycurgus Cup from Roman Empire around the fourth century A.D. More recently, Au nanoparticles have been studied extensively [106] for their potential as contrast agents for tumor imaging, drug delivery agents, and for the enhancement of the efficacy of photothermal therapy for cancer treatment, through a phenomenon known as plasmon resonance [107], which we shall discuss below. This is aided by the fact that the Au nanoparticle surface is one of the most stable, and easiest to functionalize, in terms of modifications desirable for molecular conjugation. In this regard, it is worth noting the work done by Zheng and co-workers [108], in designing functionalized, luminescent Au nanoparticles with different sizes, photoluminescent characteristics, and efficient clearance properties for bioimaging applications. In early work, Zhou et al. demonstrated [109] that glutathione-coated, 2 nm Au nanoparticles (GS-AuNPs) showed ~10–100× better renal clearance, compared to AuNPs coated with other polymers such as bis(*p*-sulfonatophenyl)phenylphosphine or cysteine. Subsequently, Zhou et al. synthesized glutathione-coated [^{198}Au]AuNPs, as a dual-modality radiotracer and NIR-emitting fluorescent probe [110], with rapid renal clearance kinetics. Using the enhanced permeability and retention (EPR) effect, Liu et al. compared [111] the tumor uptake and retention of GS-AuNPs to a small-molecule dye (IRDye 800CW), and observed that they were retained for much longer in the tumor, while being cleared faster from normal healthy tissue, compared to other small-molecule organic dyes, which provides a desirable characteristic for tumor-imaging applications. More recently, Peng et al. have used [112] these renal-clearable, GS-AuNPs for passively targeted imaging of orthotopic murine gliomas. Ultrasmall, 3 nm-sized GS-AuNPs were able to utilize the vascular leakage of gliomas to enter the tumor interstitium, and were retained in the brain tumors for a long time, used for invasive in vivo NIR-I imaging at

830 nm, while being efficiently cleared from the rest of the system with little non-specific accumulation. Interestingly, in a side-by-side comparison of two different approaches to functionalization of Au NPs using either polyethylene glycol (PEG, a polymer) or glutathione (GSH, a zwitterionic tripeptide), Liu et al. concluded [113] that both methods of functionalization resulted in NPs with almost identical photo-physical properties and core size. PEGylation, however, results in ∼3× more efficient tumor uptake compared to GS-AuNPs, while the latter exhibit much more rapid tumor uptake and clearance times. For a good understanding of the tumor targeting mechanisms (via the EPR effect) and the impact of the size, shape, and surface chemistry of the NPs on their clearance through the RES system, the reader is referred to the review article by Yu and Zheng [7].

Localized surface plasmon resonance (LSPR) occurs when light drives the oscillation of the free electron cloud in metal nanoparticles. Consequently, the confinement of the electromagnetic field can result in the generation of intense thermal energy upon excitation with an external field (electro-optical excitation), due to relaxation mechanisms via electron–electron scattering and electron–phonon coupling. These effects also account for the strong scattering and absorption of light at certain wavelengths, which depends upon the geometry and molecular architecture of the NPs. Depending upon the type of nanoparticle response [114], they have been suitably adapted to achieve utility towards molecular sensing, imaging, and spectroscopy (optical output), delivery of payload or cell death through hyperthermia (thermal output), and molecular capturing, trapping, and manipulation for sensing (mechanical output), using plasmon-nanoparticle interactions. To achieve deeper penetration into soft tissue, it is beneficial to tune the plasmonic peaks of the Au NPs to red-shift from the visible to NIR-II, by engineering [115] their shape (nanorods, nanoshells, and nanocages, to name a few) and their structure (solid or hollow core/shell). A significant body of work has been done in this area by the groups of West, J.L., Halas, N.M., Xia, Y., and co-workers. For example, Tam et al. have reported the fluorescence enhancement of indocyanine green (ICG) by ∼50×, using a plasmon resonance of Au nanoshell [9] tuned to the 850 nm emission of the dye. Subsequently, using human serum albumin as a spacer layer between Au nanoshells and an organic dye (Fig. 10.4f), IR800, Bardhan et al. reported the enhancement of the quantum yield [10] of the dye from ∼7% in the free dye to ∼86% in the plasmonic structure (Fig. 10.4g). Several groups have used biocompatible, non-toxic Au NPs for tumor targeting, detection, and treatment. For example, Qian et al. have reported the use of thiol-polyethylene glycol (PEG−SH) coated Au nanoparticles as multi-modal imaging probes [120] (Fig. 10.4o), for targeted tumor imaging in mice (Fig. 10.4p), as well as for spectroscopic detection (Fig. 10.4q) through surface-enhanced Raman scattering (SERS). For a good overview of the physics of plasmonic enhancement of Au nanoparticles, and their applications, the reader is referred to a recent review article by Amendola et al. [123].

Gold nanoparticles, such as nanorods, gold/silica core/shell structures, nanocages, or nanospheres, have also been extensively studied for NIR photothermal therapy (PTT) applications [124, 125] in vivo, often in conjunction

with NIR fluorescence imaging, typically with a laser irradiation at 808 nm. In this field, pioneering work has been done by the groups of El-Sayed, M., West, J.L., Xia, Y., and others. In most of these studies, it was demonstrated that the localized temperature achieved in the tumor was over ~55 °C after PTT for ~1–10 min. [117, 126–130], resulting in significant tumor growth inhibition (Fig. 10.4h), or complete remission of the tumor, resulting in tumor-free survival of the majority of the animals over the duration of the study (Fig. 10.4i). Other groups have also explored the possibility of using NIR irradiation on Au nanoparticles for drug delivery applications. In one example, von Maltzahn et al. have reported [118] the development of 2-component Au nanoparticle systems (Signaling and Receiving, Fig. 10.4j) that "communicate" with each other through endogenous biological pathways (Fig. 10.4k). Using this signal amplification scheme, they were able to demonstrate ~40× enhancement in the tumor accumulation, and consequent reduction in tumor volume, compared to conventional ligand-mediated targeting strategies (Fig. 10.4l). In another embodiment, Timko et al. reported [131] the use of hollow Au nanoshells for triggered sustained release of insulin in rats, through an implantable device, activated by 808 nm irradiation. Most recently, there has been a great deal of excitement in the field of in vivo gene editing, using the CRISPR-Cas9 system. In this arena, work done by Doudna, J.A., Murthy, N., and co-workers has pioneered the use of Au nanoparticles as delivery vehicles for intracellular delivery of payloads such as ribonucleoproteins, using a "CRISPR-Gold" construct (Fig. 10.4 r, t). In one application, Lee et al. used the CRISPR-Gold to deliver the Cas9 and donor DNA, endocytosed through an endosomal disruptive polymer, poly(*N*-(*N*-(2-aminoethyl)-2-aminoethyl) aspartamide), and used [121] it to achieve homology-directed repair (Fig. 10.4s), for the correction of point mutations, deletions, and other defects present in disorders such as Duchenne muscular dystrophy (DMD), with minimal off-target effects. Subsequently, Lee et al. modified [122] the CRISPR-Gold construct to deliver Cas9 and edit Cpf1 genes in the brain, through an intracranial injection (Fig. 10.4u). Through this approach,

Fig. 10.4 (continued) using ChemSpider. Auranofin, an anti-rheumatic clinically approved drug, also finds uses in treatment of bacterial infections, amebiasis, and HIV. (**n**) Survival efficacy of auranofin treatment in a mouse model of MRSA (methicillin-resistant *Staphylococcus aureus*) infection. Reprinted (adapted) with permission from Harbut et al. [119], ©2015 National Academy of Sciences. (**o–q**) Surface-enhanced Raman scattering (SERS) tags (**o**) attached onto Au nanoparticles, and the colloid stabilized with thiolated PEG coating. (**p**) A 20 mW NIR laser focused on the site of tumor, with (**q**) the output of the EGFR-targeted SERS tag showing the tumor signal compared to the liver. Reprinted (adapted) with permission from Qian et al. [120], ©2008 Nature Publishing Group. (**r, s**) Schematic of the (**r**) CRISPR-Gold construct, and (**s**) the mechanism of release of Cas9 and donor DNA into the cytoplasm after endocytosis into the cell. Reprinted (adapted) with permission from Lee et al. [121], ©2017 Nature Publishing Group. (**t–v**) Another variant of the CRISPR-Gold system, used for (**u**) delivery of Cas9 or Cpf1 into the mouse brain, to control neuronal protein expression. (**v**) An example of higher expression of the tdTomato vector in cells with the STOP codon deleted using CRISPR-Gold targeted delivery. Reprinted (adapted) with permission from Lee et al. [122], ©2018 Nature Publishing Group

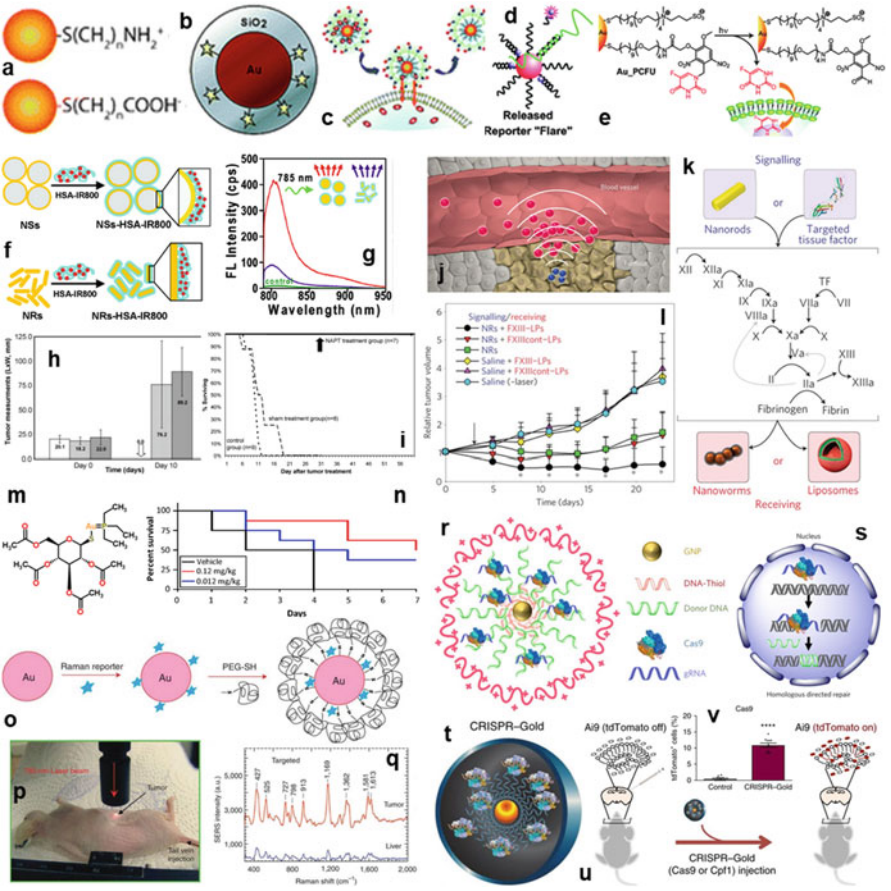

Fig. 10.4 A representative sample of the preclinical and clinical applications of Au nanoparticles. (**a–e**) Some of the strategies available for conjugation of gold nanoparticles to other functional molecules: (**a**) electrostatic adsorption, (**b**) silane encapsulation, (**c**) hydrophobic entrapment, (**d**) oligonucleotide hybridization, and (**e**) photo-cleavable linkage. Reprinted (adapted) with permission from Dreaden et al. [116], ©2012 Royal Society of Chemistry. (**f, g**) Shown are the (**f**) schematics of the gold nanoshells (NSs) and gold nanorods (NRs) used for conjugating human serum albumin, with an NIR-fluorescent dye (IR800), resulting in (**g**) fluorescence enhancement of ~40× and ~9× compared to the control. Reprinted (adapted) with permission from Bardhan et al. [10], ©2009 American Chemical Society. (**h, i**) Tumor sizes, prior to treatment (Day 0) and after nanoshell-assisted PTT (Day 10). Complete tumor necrosis and survival of the treated group was seen in (**i**), compared to the control or sham treatment groups. Reprinted (adapted) with permission from O'Neal et al. [117], ©2004 Elsevier Publishing Group. (**j–l**) Schematic of the nanoparticle "communication" for amplified targeting in tumors, with the (**j**) tumor-targeted signaling nanoparticles broadcasting the location to receiving nanoparticles in circulation, and (**k**) the molecular signaling pathway between the signaling (Au nanorods or targeted tissue factor) and receiving components (Au nanoworms or liposomes). (l) The decrease in tumor volumes post-NIR irradiation (at 0.75 W/cm^2 for 20 min. at 810 nm), with the strongest effect seen for Au nanorods in combination with FXIII-LPs. Reprinted (adapted) with permission from von Maltzahn et al. [118], ©2011 Nature Publishing Group. (**m, n**) Structure of the auranofin molecule, rendered

they were able to show gene editing (Fig. 10.4v) in multiple cell types including neurons, astrocytes, and microglia, and were shown to have therapeutic efficacy in mice for treating a form of autism spectrum disorder with a single-gene mutation. For a comprehensive review on the subject of using Au nanoparticles in biomedicine (Fig. 10.4a–e), the reader is referred to the article by Dreaden et al. [116].

Considering the fact that Chinese and Arabic physicians have been using colloidal gold preparations in their medical formulations since the ancient times (as far back as 2500 B.C.) [132], it is apropos that we look at some of the clinical trials seeking to establish the efficacy of using Au nanoparticle formulations in modern medicine. In recent times, there have been reports of the use of compound formulations of gold salts (such as gold sodium thiomalate, gold sodium thiosulfate, and colloidal gold sulfide), first introduced by the French physician Jacques Forestier for the treatment of rheumatoid arthritis in the 1920s [133]. Since then, there have been a few products on the market: gold sodium thiomalate (trade name "Myocrisin" or "Myochrysine"), auranofin (trade name "Ridaura," Fig. 10.4m), and aurothioglucose (trade name "Solganal"), which have been prescribed mainly for their immunosuppressive effects for the management of rheumatoid arthritis. Moreover, there has been some promise shown by the use of these formulations in anti-retroviral therapy (for HIV) [134], in the treatment of amebiasis (infection by species such as *Entamoeba histolytica*, with auranofin showing $\sim 10\times$ the potency of treatment [135] compared to the clinically used amebicidal, metronidazole) and in the treatment of bacterial infections [119] such as methicillin-resistant *Staphylococcus aureus* (Fig. 10.4n) and *Mycobacterium tuberculosis*. However, these formulations of gold salts often lead to side effects such as skin rash and diarrhea in patients being treated for rheumatoid arthritis. Following up on Forestier's approach, Abraham, G.E. and Himmel, P.B. reported the results of a private, open trial ($N = 10$) patients, in which they administered colloidal formulation of Au nanoparticles ($\sim$20 nm) at a concentration of 30 or 60 mg/day, via oral dosing. In rheumatoid arthritis patients who showed no improvement with Myochrysine or Ridaura, they reported significant decrease in the tenderness and swelling of joints, with marked improvement after 24 weeks of colloidal gold therapy. Importantly, there was no evidence of toxicity in any of the patients. Although the results of this small-scale clinical trial using Au nanoparticles were largely positive both in terms of safety and efficacy, it is worth noting here that the trial was not registered with, approved or administered by the US Food and Drug Administration, and it is uncertain whether scientific "best practices" were followed in this trial. In another example of the successful clinical use of Au nanoparticles, a nanotherapy platform "Aurimune" by Cytimmune Sciences, Inc. (Rockville, Maryland, USA) has been tested in patients with advanced-stage solid tumors who were no longer responsive to conventional chemotherapy. The first product, CYT-6091, comprised of 27 nm colloidal Au NPs, with a thiolated PEG coating, to which recombinant human tumor necrosis factor alpha (rhTNF-α) is bound. Compared to the toxicity effects observed in direct delivery, CYT-6091 enabled the delivery of $3\times$ the amount of rhTNF-α, with nanoparticle accumulation observed in tumor biopsies but not in surrounding healthy tissue [136], in small

interventional trials ($N = 30$ in NCT00356980, $N = 108$ in NCT00436410). The same company is working on another combination therapeutic, CYT021000, which is intended to simultaneously deliver a small-molecule drug (paclitaxel, or "Taxol"), a biologic (rhTNF-α) carried by the same Au nanoparticle platform, which is still in the preclinical stage. In another approach, Nanospectra Biosciences, Inc. has developed a technology known as "AuroLase Therapy" aims to use selective thermal ablation (photothermal therapy, or PTT) using Au nanoshells. In this technique, silica-coated gold nanoshells termed "AuroShells" are injected intravenously into the patient's blood stream (at 2 concentrations: 4.5 or 7.5 ml/kg of NPs, at an optical density of O.D. 100), and upon passive accumulation into the solid tumor, are heated with an NIR laser (at 3 levels of power intensity: 3.5, 4.5, or 5 W) for PTT. Two non-randomized clinical trials (NCT00848042 for head-and-neck cancers, and NCT01679470 for primary or metastatic lung cancers) were initiated by Nanospectra, of which the latter was terminated for unknown reasons, and trial results are awaited to be disclosed for the former, with the study having been completed a few years ago. Finally, it is worth mentioning the NANOM-FIM randomized open blinded end-point clinical trial ($N = 180$, NCT01270139) for the treatment of coronary atherosclerosis through atheroregression, which consisted of 3 study arms ($N = 60$ each), of which the first two utilized Au NPs, and the third was a control arm. The first two groups consisted of core/shell silica/Au NP (through a bioengineered on-artery patch), or core/shell silica/AuNP iron-bearing particle (with targeted microbubbles and stem cells using a magnetic navigation system), while the control group was simply stent implantation [137]. In the first two groups, NPs were activated by an NIR laser for plasmonic PTT, after targeting to the site of plaque deposit. The result of the study was that plasmonic resonance PTT using the silica/Au NPs showed significant regression of total atheroma volume, with significantly lower risk of death ($\sim$91.7% survival) compared to the other 2 groups ($\sim$81.7% and $\sim$80% survival, respectively). Given the hype and hope surrounding the promise of nanotechnology in revolutionizing medical imaging and therapeutics, it is indeed a bit sobering to review the limited number of clinical trials which have gone on to successful completion, in spite of gold nanoparticles being one of the earliest and most well-studied formulations.

10.2.4 Carbon Dots, Carbon Nanotubes, Graphene and their Derivatives

In the field of NIR-emitting nanomaterials, low-dimensional forms of carbon such as carbon dots, fullerenes, single-walled carbon nanotubes (SWNTs), and graphene and their derivatives have generated great excitement in the past few decades. These materials offer strong potential for biomedical applications, because of their unique optical properties, large surface area, the chemical and mechanical properties which allow for various approaches to functionalization, and the physical

dimensions of these nanoparticles—which are comparable to those of biomolecules such as DNA or proteins. For a deep dive into the numerous strategies available for the functionalization of carbon nanomaterials, the reader is referred to a review by Bardhan [138]. For a comprehensive review of the strategies used for the development of CNT-based materials for immunotherapy applications, the review article by Fadel and Fahmy [139] is highly insightful.

Among the choice of polymers available, poly(ethylene glycol), PEG, and its derivatives have long been used as a preferred polymer for the functionalization of nanomaterials, for targeted optical imaging [140] as well as for intracellular drug delivery [141] applications. Work done by Dai and co-workers [142] has produced a great body of literature on the methods and applications for the use of polymer-stabilized single-walled carbon nanotubes as NIR-II fluorophores for imaging applications. In one approach, phospholipid-polyethylene glycol (PL-PEG) is used as a surface-coating agent for SWNTs. Being an amphiphilic molecule, the hydrophobic phospholipid chain sticks to the nanotube sidewall, while the hydrophilic PEG end forms the outward-facing layer, resulting in a strong supramolecular complex in water. The terminal end groups such as $-NH_2$ or $-COOH$ at the end of the PEG chain allow for additional functionality, by adding targeting agents, drug molecules or other application-specific moieties. Based on a surfactant-exchange method (Fig. 10.5b), Welsher et al. have used a PL-PEG polymer (1,2-distearoyl-*sn*-glycero-3-phosphoethanolamine-*N*-[methoxy(polyethylene glycol)], ~5 kDa mol. wt.). At a low injected dose of ~170 μg/ml, they demonstrated high-resolution intravital microscopy [144] of the tumor vasculature beneath the skin, in a mouse model. In subsequent work, they have used an image-processing technique called Principal Component Analysis to track the whole-body circulation (Fig. 10.5c) of PL-PEG-coated SWNTs injected into the tail vein of mice [145]. Leveraging the benefits of NIR-II imaging using SWNTs, they were able to clearly distinguish organ-level anatomical features, by deciphering the pharmacokinetics and distribution of the injected SWNTs. In another approach, using SWNTs dispersed using poly(maleic anhydride-*alt*-1-octadecene)-methoxy-PEG, C18−PMH−mPEG (Fig. 10.5a), Robinson et al. have shown ultra-high passive tumor uptake [152], ~30% injected dose/gm, using the enhanced permeability and retention (EPR) effect, in a xenograft mouse model of breast cancer. Based on a similar functionalization approach, Hong et al. have used DSPE−mPEG functionalized SWNTs to visualize the vasculature in a mouse model of peripheral arterial disease [146], with high spatiotemporal resolution (~30 μm, <200 ms per frame), at 1–3 mm depth in the hindlimb (Fig. 10.5d). Beyond the realm of non-invasive imaging applications, there have been some developments in the use of PEGylated SWNTs for monitoring of therapy and for drug delivery applications. For example, Hong et al. have shown deep-brain imaging, at depths >2 mm in the mouse brain, through the skull with sub-10 μm resolution, using a technique called NIR-II fluorescence angiography [153]. By observing the perfusion of injected SWNTs in the cerebral vessels in real time (Fig. 10.5e), they were able to monitor arterial occlusion in a mouse model of cerebral stroke. PEGylated nanotubes have also been used for drug delivery and photodynamic therapy applications, in conjunction with near infrared imaging.

Using chirality-purified (6, 5) SWNTs, Antaris et al. have reported simultaneous tumor imaging and photothermal therapy [154] with SWNTs. Taking advantage of the molecular structure of the nanotube wall, Liu et al. have shown ultra-high loading capacity [155] of an anti-cancer agent, doxorubicin, by π-stacking on to PEG-coated SWNTs, with pH-triggered release characteristics. This approach can also work well for the delivery of water-insoluble drugs such as paclitaxel, as Liu et al. have shown $\sim$10$\times$ tumor uptake of PTX in a murine breast cancer model [156] by delivering it through PEG-coated SWNTs with a cleavable ester linkage. The reader is referred to a comprehensive article on the use of PL-PEG conjugation methods for SWNTs, by Liu et al. [157]. At this point, it is also worth pointing out the study [158] of the effects of administration of SWNTs in mice, by Schipper et al. Although this was a pilot study with a small sample size, the results seem to indicate that systemic (intravenous) administration of high doses of PEG-functionalized SWNTs did not lead to acute or chronic toxicity, despite the persistence of these nanomaterials within the macrophages of the liver and spleen for several months.

A unique "bio-polymer" approach to the functionalization of carbon nanomaterials has been demonstrated by Belcher, A.M. and co-workers, using the development of M13 bacteriophage as a multifunctional platform for actively targeted delivery of aqueous-dispersed SWNTs. Single-walled carbon nanotubes are $\sim$0.5–1 μm in length and $\sim$1 nm in diameter. M13 is a long, cylindrical, non-lytic bacteriophage, with a size of $\sim$880 nm in length and $\sim$6 nm in diameter. The main advantage of this approach is the availability of 5 capsid proteins (p3, p5, p7, p8, and p9) of the virus, which can be genetically engineered to display peptides with specific functionality, such as targeting ligands against tumor cells or bacterial pathogens, conjugation centers for drug molecules, or binding sites for fluorophores for imaging applications. Given the similarity in the length dimension of M13 and SWNTs, Dang et al. have shown [159] that SWNTs can be longitudinally functionalized along the major coat protein, p8, of the M13 virus, through a multivalent π-π interaction. This M13-SWNT complex is water-dispersible, and maintains a high fluorescence in serum and other physiological media, which makes it suitable for in vivo imaging and diagnostic applications. For example, Yi et al. have used this M13-functionalized SWNT, with a targeting moiety against the prostate-specific membrane antigen (PSMA), for demonstrating targeted imaging [148] in a xenograft mouse model of PSMA-positive prostate cancer (Fig. 10.5i, j). In an ovarian cancer disease model, Ghosh et al. have modified the p3 protein of the M13 virus to express a peptide against SPARC (SPARC-binding peptide or SBP), a secreted matricellular protein which is overexpressed in highly aggressive subtypes of ovarian cancer. With this SBP-M13-SWNT probe, they were able to show the detection of millimeter-scale tumors in the pre-surgical planning step (Fig. 10.5k), in a mouse model of orthotopic human ovarian cancer [149]; which leads to hope for "optimal debulking" (Fig. 10.5l) in ovarian cancer patients upon clinical translation of this technology. This approach can also be useful for the detection and monitoring of deep-tissue bacterial infections. In one embodiment, work done by Bardhan and co-workers [147] has shown that this M13-SWNT complex can be used to image bacterial infections (Fig. 10.5f, g) at an order-of-magnitude lower dosage, compared to

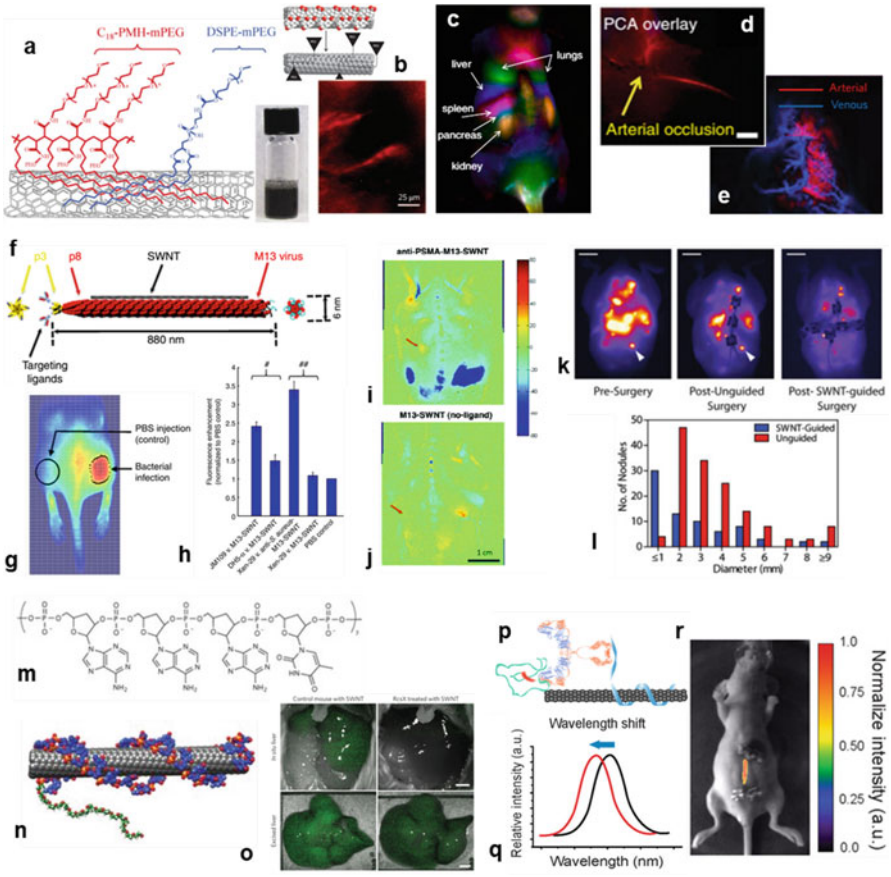

Fig. 10.5 Three approaches to polymer functionalization of SWNTs. (**a**) Mixed (50%-50%) C_{18}−PMH−mPEG and DSPE−mPEG surfactants used to functionalize SWNTs, with the vial showing stable aqueous dispersion. Reprinted (adapted) with permission from Robinson et al. [143], ©Tsinghua University Press and Springer-Verlag Berlin Heidelberg 2010. (**b**) An example of the surfactant-exchange process, used to displace cholate molecules (red dots) with PL-PEG (black triangles). This has been used for intravital microscopy in mice, with the tumor blood vessel resolution ∼ microns. Reprinted (adapted) with permission from Welsher et al. [144], ©2009 Nature Publishing Group. (**c**) Principal Component Analysis (PCA) used as a spatiotemporal analysis technique to identify various organs, through the biodistribution of NIR-II fluorescent PEG-functionalized SWNTs injected through the tail vein, similar to those in (**a**). Reprinted (adapted) with permission from Welsher et al. [145], ©2011 National Academy of Sciences. (**d, e**) Mouse hindlimb vasculature, in a model of (**d**) hindlimb ischemia and (**e**) cerebral artery occlusion (stroke), imaged using SWNTs similar to (**a**). Reprinted (adapted) with permissions from Hong et al. [146] and Hong et al. [55], ©2012 and 2014 Nature Publishing Group, respectively. (**f**) Schematic of the M13-functionalized SWNT, used for targeted imaging of deep-tissue bacterial infections (**g, h**) and cancer imaging (**i–l**). The probe is targeted using either antibodies conjugated to the p3 minor coat protein, or through target peptides expressed on the surface of the virus. (**g**) An example of fluorescent imaging of an intramuscular bacterial infection of *E. coli* in a mouse using M13-SWNT, and (**h**) plot showing the relative fluorescence enhancement in a model of deep-tissue endocarditis infection of *S. aureus* in mice. Reprinted (adapted) with permission from

other small-molecule organic dyes used in the literature. In a mouse model of *Staphylococcus aureus* endocarditis (infection of the heart valves), this targeted imaging approach using M13-SWNT showed a ~5.7× enhancement in the signal intensity compared to background (Fig. 10.5h), which is a significant milestone towards the development of non-invasive, early detection techniques for managing the spread of antibiotic-resistant infectious diseases. Likewise, other groups in the literature have also utilized the anti-microbial properties of polymer-functionalized SWNTs on both gram-positive and gram-negative strains, including a number of clinically relevant pathogens such as *Salmonella typhimurium*, *Bacillus subtilis*, *Staphylococcus aureus*, *Staphylococcus epidermidis*, and *Escherichia coli*. These methods work through mechanical disruption of bacterial biofilms, or through oxidative stress (i.e., generation of radical species) caused by the nanotube [160–162], or even as a sensitizer for photothermal therapy [163] of infections.

The use of single-stranded DNA (ssDNA) as a functionalization agent for carbon nanotubes has been explored by several groups. The aromatic bases of the ssDNA interact through π-π interaction with the SWNT, with the helical DNA structure extending along the length of the nanotube wall. Acting as an amphiphilic polymer, the nitrogenous bases of the DNA bind to the hydrophobic SWNT wall, with the hydrophilic phosphate and sugar moieties facing outward, making the SWNT water-dispersible. In the first realization of this approach, Zheng et al. modeled and achieved helical wrapping [164] of ssDNA on the surface of SWNTs. Further, they showed that DNA-wrapping can be used to separate and purify fractions of SWNTs with different chirality, based on their electronic structure, using chromatographic techniques. This method offers fine-grained control to select and separate [165, 166] the length [167] and chirality [168] of SWNTs based on

Fig. 10.5 (continued) Bardhan et al. [147], ©2014 Nature Publishing Group. (**i, j**) Use of the M13-SWNT probe for imaging of xenograft prostate cancer in a mouse, with (**i**) or without (**j**) targeting, using the anti-PSMA antibody. The red arrow indicates the location of the tumor. Reprinted (adapted) with permission from Yi et al. [148], ©2012 American Chemical Society. (**k, l**) Use of the M13-SWNT probe for pre-surgical planning for optimal cytoreductive surgery, in an orthotopic mouse model of human ovarian cancer. (**k**) Shows the fewer residual tumors left after using SWNT-guided surgical planning, while the plot in (**l**) shows the increased number of sub-millimeter sized tumor nodules removed with SWNT-guidance (blue bars) relative to unguided surgery (red bars). Reprinted (adapted) with permission from Ghosh et al. [149], ©2014 National Academy of Sciences. (**m–o**) DNA-functionalized SWNTs for sensing nitric oxide (NO). (**m**) Structure of the ds$(AAAT)_7$ oligonucleotide, with selectivity to NO, and (**n**) schematic of the DNA-wrapped SWNT. (**o**) Fluorescence quenching can be used to detect NO as an inflammation sensor, in the liver of a mouse without inflammation (left column), and with inflammation (right column). Reprinted (adapted) with permission from Iverson et al. [150], ©2013 Nature Publishing Group. (**p–r**) An implantable optical nanosensor constructed of an antibody-targeted DNA-wrapped SWNT, for the detection of an ovarian cancer biomarker. (**p**) Schematic of the Ab-DNA-SWNT complex, conjugated to the HE4 biomarker (cyan), and (**q**) the wavelength shift used for the optical detection. (**r**) An example of an animal with the implanted sensor, showing the optical signal detected noninvasively. Credit: Williams et al. [151] CC BY-NC 4.0

the DNA sequence used and has subsequently been developed to individually sort all the major species of single-chirality SWNTs from a heterogeneous mixture, using a randomized, high-diversity DNA library [169]. In another example of the use of DNA-functionalized SWNTs, Strano, M.S. and colleagues have used this approach to create a gas sensor for the detection of nitric oxide (NO), by designing an optical sensor based on the fluorescence perturbation of SWNTs [150]. Iverson et al. were able to design a double-stranded DNA oligonucleotide, $ds(AAAT)_7$ for wrapping the SWNTs (Fig. 10.5m, n), which allows for selective detection of NO (Fig. 10.5o) generated through intracellular signaling pathways [170]. Even after additional functionalization with alginate- or PEG-hydrogel, these DNA-wrapped SWNT nanosensors show remarkable sensitivity to biomolecules such as NO (useful in the detection of inflammation) or riboflavin [171]. In another unique application, Giraldo et al. have showcased a "nanobionics" approach to augmented photosynthesis [172], which increases the photosynthetic activity of plant leaves by $\sim 3\times$ through the delivery of $ss(AT)_{15}$ DNA-coated SWNT nanocomposites infiltrated into the chloroplasts. Reverting back to biomedical applications of DNA-functionalized carbon nanotubes, recent work done by Heller, D.A. and co-workers has focused on the use of SWNTs as optical sensors. In a report by Williams et al. [151], a nanosensor comprised of an antibody with an ssDNA conjugated to a SWNT (Ab-DNA-SWCNT, Fig. 10.5p) was used to target and detect human epididymis protein 4 (HE4), one of the two FDA-approved serum biomarkers for human ovarian cancer. Based on a design of a PVDF membrane-based implantable device, the researchers were able to measure tumor-associated levels of HE4 in mouse models of ovarian cancer (Fig. 10.5r), by measuring a blue shift (~ 2 nm) in the SWNT emission (Fig. 10.5q).

Graphene and its derivatives (graphene oxide, GO, or reduced graphene oxide, rGO) have generated tremendous interest for biomedical applications [173], including sensing, imaging, and drug delivery. However, it is important to functionalize them, since pristine graphene is hydrophobic in nature, and the functionalization can be used to selectively add properties of interest. In this regard, polymer functionalization of graphene has proven to be quite versatile. In one approach, the technique of "DNA Origami" has been used to assemble nanostructures into unique geometries on the graphene surface. For example, Liu et al. have reported [174] a method to pattern gold nanoparticles into 2D arrays on the surface of GO and rGO decorated with DNA, and this metal-carbon hybrid nanostructure retains the optical absorbance properties of the constituent nanomaterials. Several groups of researchers have used GO as a platform for rapid detection of biomolecules, such as a single-bacterium resolution device (Fig. 10.6d) by Mohanty and Berry [176], or DNA detection (Fig. 10.6e) by complementary sequence binding resulting in quenching of the fluorescence emission, by Lu et al. [183]. Conventional polymers, such as polyethylene glycol (PEG), have also been extensively used for the functionalization of graphene and its derivatives, for cellular imaging and drug delivery applications. For example, Robinson et al. used [175] nano-rGO, non-covalently functionalized with PEG, together with an Arg-Gly-Asp (RGD) motif (Fig. 10.6a) for targeting cells for photoablation (Fig. 10.6b, c). Work done

by Nagrath, S. and co-workers has focused on the use of GO functionalized with PL-PEG-NH_2 for the capture of circulating tumor cells. In one report, Yoon et al. have described [181] the use of EpCAM antibody-conjugated functionalized GO (Fig. 10.6o) to capture CTCs with a yield of ~73% from whole blood. Further, they have also shown a method [184] to achieve thermally triggered release of the captured CTCs, using functionalized GO as the capture agent, embedded in a matrix of a thermoresponsive polymer, which yields viable and intact CTCs for downstream processing applications. In yet another application of nano-scale GO, several groups have utilized this material for fluorescence imaging. For example, Zhang et al. have reported [185] the synthesis of water-soluble graphene quantum dots, with high quantum yield ~14%, without the need for polymeric surfactants or other stabilizers. Compared to non-functionalized conventional inorganic QDs, these bare GQDs were shown to be remarkably less toxic, and could be used in vitro for labeling of different types of cells. In an alternative approach, Pan et al. have devised [186] a way to chemically "cut" graphene sheets into GQDs, with strong green fluorescence, which could then be used for confocal microscopy imaging of HeLa cells. Work done by Nahain et al. has used [187] functionalized rGO, conjugated with hyaluronic acid (HA) as the targeting molecule, spiropyran as the fluorescent agent, and doxorubicin as an anti-cancer drug, for combined in vivo imaging and drug delivery to cancer cells expressing CD44 as the target receptor. In another strategy combining GO with Au NPs and organic dye fluorophores, Zhang et al. reported [188] the development of GO-AuNP-FITC hybrids, which can be used as a bimodal imaging agent for fluorescence and Raman imaging in cancer cells. In yet another combination approach, Ji et al. synthesized [189] a composite nanoprobe, by co-deposition of a glycoprobe and an anti-cancer drug, camptothecin, on the surface of GO. It was hypothesized that this composite showed higher efficacy of treatment towards liver cancer cells due to the clustering effect of the GO, resulting in multi-valent receptor binding of the glyco-ligand. Another promising application of graphene-based nanomaterials is for photoacoustic imaging, in which non-ionizing laser irradiation is used to generate wideband ultrasonic emission, which can be detected as an imaging signal. In one instance, Patel et al. have reported [190] the synthesis of strong NIR-absorbing graphene nanosheets using a one-pot nitronium oxidation reaction, which generate non-radiative acoustic waves upon 700 or 800 nm excitation, which can potentially be used for biological imaging applications. In another case, Lalwani et al. have studied [191] single-walled and multi-walled graphene nanoribbons (GNRs) as NIR contrast agents for photoacoustic/thermoacoustic tomography. Most recently, Toumia et al. reported [192] a novel imaging approach based on ethylene diamine-functionalized polyvinyl alcohol (PVA) microbubbles decorated with graphene nanosheets. This was used for in vivo real-time photoacoustic imaging in mice with a very low dose ($<1\ \mu g$ of graphene), in the NIR range of 680 to 850 nm.

Work done by Chen, G-Y. and co-workers has relied on the functionalization of GO with PEG or other peptides, after annealing "pre-treatment" to improve the distribution of the oxygen functional groups in GO. Previously, it was shown [193] by Grossman, J.C., Belcher, A.M., and co-workers that it is possible to structurally

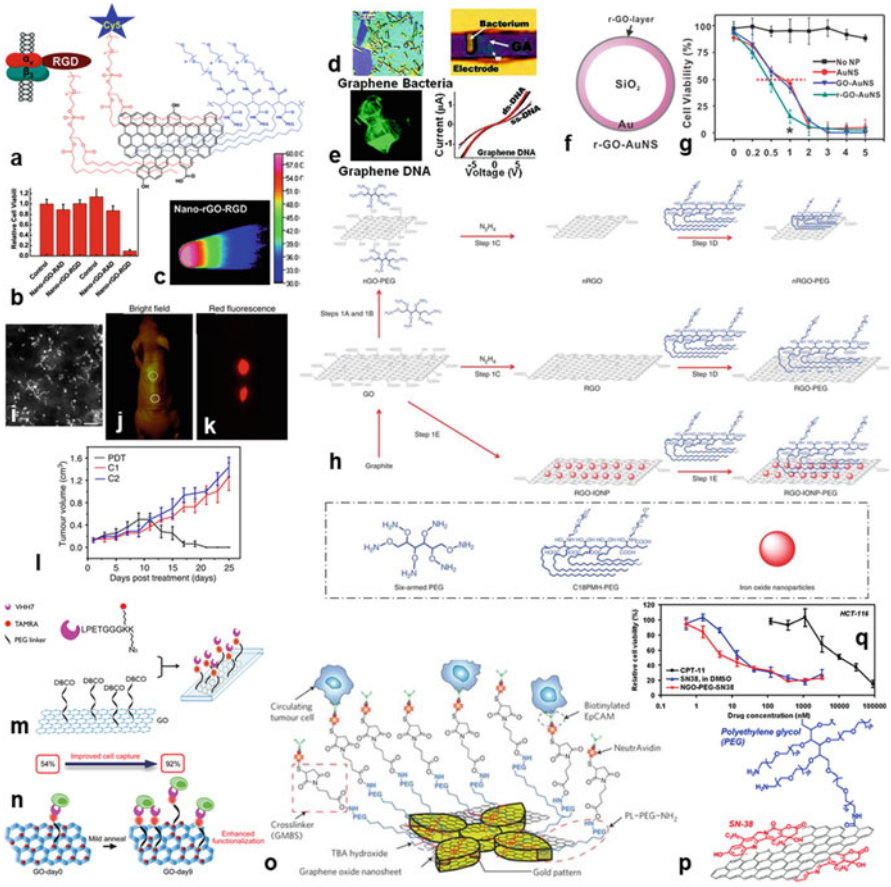

Fig. 10.6 A small sampling of the beauty of the diversity of applications of polymer-functionalized graphene and its derivatives. (**a–c**) Photothermal therapy in cancer, using functionalized nano graphene oxide. (**a**) Structure of the nano-rGO, conjugated with PEG for stability in biological suspensions, targeting using Arg-Gly-Asp (RGD) peptide, and Cy5 dye for fluorescence imaging. (**b**) Plot of cell viability at 24 h post-NIR irradiation, showing maximum effect for the nano-rGO-RGD case, and (**c**) thermal image of a vial of U87MG cells treated with nano-rGO-RGD, after 8 min. of 808 nm irradiation at 15.3 W/cm^2. Reprinted (adapted) with permission from Robinson et al. [175], ©2011 American Chemical Society. (**d, e**) Graphene-based biosensors. (**d**) A graphene-amine based p-type device which has single bacterial-cell resolution, measured by changes in conductivity, and (**e**) a DNA transistor, which measures the hybridization/de-hybridization of ssDNA on GO, by changes in conductivity. Reprinted (adapted) with permission from Mohanty and Berry [176], ©2008 American Chemical Society. (**f, g**) Improved photothermal therapy, by using plasmonic-enhanced rGO. (**f**) Schematic of the structure of Au nanoshells on SiO_2 coated with a layer of rGO, and (**g**) plot of the cell viability of human umbilical vein endothelial cells after NIR PTT at 808 nm for 30s, 2 min. or 5 min., using 808 nm at 3 W/cm^2, showing the effect of plasmonic enhancement of the rGO-Au-NS on the cell viability. Reprinted (adapted) with permission from Lim et al. [177], ©2013 American Chemical Society. (**h**) Steps for the synthesis and functionalization of graphene and its various derivatives: including GO, rGO, nano-rGO, as well as their PEG derivatives, and additional functionalization such as loading iron oxide nanoparticles. Reprinted (adapted) with permission from Yang et al. [178], ©2013

engineer a scalable phase transformation in graphene oxide by a mild thermal annealing treatment, resulting in a redistribution of the oxygen functional groups on the 2D graphene surface, without loss of oxygen content. Based on this idea, upon conjugating diamine-terminated PEG ($NH_2-(PEG)_n-NH_2$) to the surface of *pre-treated* GO, the terminal amines of the PEG chains can then be used to react with DBCO-NHS ester, to activate it for a "click" coupling reaction. This has been used by Bardhan et al. [180] to conjugate VHH7 nanobodies (single-chain fragments of conventional antibodies, which are specific to murine Class-II MHC^+ cells) to the DBCO handle (Fig. 10.6m), for highly efficient, very specific cell capture of white blood cell populations (Fig. 10.6n) from small volumes ($\sim 30\,\mu$l) of murine whole blood, under ambient conditions, with a relatively inexpensive cell-capture device. Subsequently, Cheng et al. have reported [194] the use of thermally annealed GO, with blue-shifted fluorescence, as an agent for cellular imaging and drug delivery, without the need for additional labeling or fluorescent markers. In another interesting application by Yang et al. [195], the annealed GO was coated with osteogenic growth peptide, and was shown to have improved adhesion of human mesenchymal stem cells, resulting in enhanced osteogenic differentiation compared to as-synthesized GO. For a great overview of the numerous approaches to the functionalization of graphene and its derivatives with biocompatible polymers such as PEG, the reader is referred to the protocol (Fig. 10.6h) by Yang et al. [178]. For a deep dive into the methods available for chemical modification of graphene in synthetic biology, the reader is referred to the review article by Servant et al. [196].

Fig. 10.6 (continued) Nature Publishing Group. (**i–l**) Graphene quantum dots (GQDs) used for photodynamic therapy. (**i**) TEM image of GQDs, with the scale bar 20 nm. (**j, k**) Bright field and red fluorescence image, after subcutaneous injection of the GQDs. (**l**) Inhibition of the growth of tumor volume in a murine xenograft model of subcutaneous breast cancer, with PDT using GQDs, by singlet-oxygen generation. White light was used, with a power density of 80 mW/cm^2. C1 refers to GQDs only, C2 refers to light irradiation only. Reprinted (adapted) with permission from Ge et al. [179], CC BY-NC-ND 4.0. (**m, n**) Improved cell capture on a GO-based device, using a mild thermal annealing treatment. (**m**) Functionalization scheme to attach nanobodies on to the GO thin films, using $NH_2-PEG-NH_2$ linkers, functionalized with dibenzocyclooctyne, and used to attach the nanobody via an azidelinker through the LPETGGG motif, in a sortase-catalyzed "click" reaction. (**n**) Thermal annealing at 80 °C for 9 days results in almost doubling of the efficiency of cell capture, from ~54% to ~92%. Reprinted (adapted) with permission from Bardhan et al. [180], ©2017 American Chemical Society. (**o**) Graphene oxide used for highly sensitive capture of circulating tumor cells. Shown is the schematic of the surface of the microfluidic chip, which consists of a gold pattern, on which GO nanosheets are adsorbed, followed by a PL-PEG$-NH_2$ linker, which is then bound to the GMBS crosslinker for attaching biotinylated EpCAM antibodies for capturing CTCs in blood, from human patient samples. Reprinted (adapted) with permission from Yoon et al. [181], ©2013 Nature Publishing Group. (**p, q**) Nano-scale GO with PEG functionalization used for improved delivery of water-insoluble anti-cancer drugs. (**p**) Shown here is SN38, a pro-drug used for the treatment of colon cancer, loaded onto nano GO-PEG. (**q**) Plot of the relative cell viability, showing ~1000× potency of the GO-PEG-SN38, compared to CPT-11, an FDA-approved camptothecin analog. Reprinted (adapted) with permission from Liu et al. [182], ©2008 American Chemical Society

In the realm of drug delivery and photothermal (PTT)/photodynamic (PDT) therapy [197], numerous research studies have utilized GO/rGO grafted with polymer chains (such as polyethylene glycol (PEG), poly L-lysine (PLL), polystyrene (PS), polyvinyl alcohol (PVA), polyallylamine (PAA), and polyethylene imine (PEI), to name a few), containing other useful reactive functional groups such as amines, hydroxyls or carboxyl groups. Work done by Dai, H., Liu, Z., and co-workers has used this method to great advantage. For example, nano-scale graphene oxide, with PEGylation functionalization, has been reported [182] by Liu et al. as a delivery agent for loading and delivering the water-insoluble anti-cancer drug, SN38, through π-π stacking (Fig. 10.6p), which was found to be $\sim$1000$\times$ more potent (Fig. 10.6q) than the equivalent clinically approved formulation of camptothecin. Subsequently, Yang et al. have shown [198] highly efficient passive EPR targeting in xenograft tumors in mice, using pristine graphene. Using this approach for near infrared photothermal therapy, they showed an improvement in the survival from $\sim$16 days in the control group, to $>$40 days in the treated group. In further development [199], Zhang et al. used a combination of chemotherapy (using the drug doxorubicin) and photothermal therapy in an in vivo mouse model, using PEGylated GO, to achieve higher therapeutic effect. Likewise, Tian et al. have reported [200] PDT-enhanced PTT, delivered by nano-GO, by loading a photosensitizer molecule (Chlorine6) on to PEGylated GO. In more recent work, Feng et al. have used [201] dual-functionalized nano-scale GO, wrapped with PEG and PEI, to effectuate photothermal-enhanced delivery of siRNA, by increasing the permeability of the target cell membrane using low-power NIR irradiation. Similarly, Lim et al. have developed [177] NIR-activated plasmonic nanomaterials, comprising Au nanoshells or nanorods coated with rGO (Fig. 10.6f), for improving the efficacy of photothermal therapy (Fig. 10.6g) by reducing the dosage or the exposure time. In an alternative approach, PLL has been used as a polymer functionalization agent by several groups of researchers, which is useful for numerous applications involving biosensing, electrochemical sensing, promoting cell adhesion, and drug delivery. For instance, Hu et al. have conjugated [202] quantum dots on PLL-coated rGO, for fluorescence bioimaging in cells targeted through the folate receptor, and for performing in situ, monitored PTT. In another promising technique, Akhavan, O. and Ghaderi, E. have developed [203] a nanomesh of rGO, which is functionalized by PEG, and uses RGD as the targeting peptide, which has excellent absorbance in the NIR 808 nm wavelength range. At very low concentrations ($\sim$1–10 μg/ml), at low NIR laser power (0.1 W/cm^2 for 7 min.) for in vivo PTT, they were able to achieve 100% tumor elimination in a mouse model of human glioblastoma, resulting in remarkable survival $>$100 days post-treatment, compared to $<$38 days in the control group. Likewise, Wang et al. developed [204] a multifunctional platform, consisting of mesoporous Si-coated graphene nanosheets, conjugated with a targeting peptide, and loaded with doxorubicin, for PTT-assisted drug delivery in a murine model of glioma; the concentration- and laser power-dependence of the targeted graphene approach was asserted to be superior to that of PTT using SWNTs. Similarly, Sahu et al. have used [205] GO as a delivery vehicle for the delivery of an FDA-approved dye, methylene

blue (MB), for combined PDT/PTT. The nanoGO-mediated delivery was shown to have strong in vivo effect, combining the pH-responsive release (in the acidic tumor microenvironment) of MB, with the enhanced PDT/PTT effect, resulting in completed tumor ablation. In another interesting application, Li et al. have used [206] the high NIR absorbance of GO, to show PTT in Alzheimer's disease. Using a complex of GO with an amyloid-β staining dye, the authors showed that this strategy can be used to cross the blood–brain barrier, and effectively dissociate amyloid deposits in the cerebrospinal fluid of mice. In yet another combination therapy strategy [207], Shi et al. have coupled GO with magnetic iron oxide nanoparticles, as well as plasmonic Au nanoparticles, followed by PEG coating and targeting with the folate receptor, to show dual-mode X-ray and magnetic resonance imaging, as well as PTT-mediated tumor ablation in subcutaneous breast-cancer xenografts in mice. Similarly, Yang et al. have formulated [208] a nanocomposite of rGO and iron oxide nanoparticles, noncovalently functionalized with PEG, for triple mode (fluorescence, photoacoustic, and MR) imaging in vivo, targeted using the EPR effect. This formulation was shown to have ultra-efficient tumor ablation capability in subcutaneous breast cancer tumors in mice, at low NIR power density of 0.5 W/cm^2. In an alternative synthesis technique, Sheng et al. created [209] bovine serum albumin (BSA)-functionalized nano rGO, which could then be used as an in vivo NIR contrast agent for combined photoacoustic imaging and PTT, in mice with breast cancer tumors. In yet another combination approach, Moon et al. have reported [210] the synthesis of Au nanorods coated with rGO, with increased NIR absorption at 750 nm, which results in enhancement of the photothermal effect and an $\sim$4$\times$ amplification of the acoustic wave signal for highly sensitive photoacoustic imaging compared to ordinary rGO or Au NPs, in subcutaneously injected mice. As an alternative to using Au NPs or iron oxide NPs, Taratula et al. have used [211] a phthalocyanine dye as a photosensitizer for generating reactive oxygen species, encapsulated into a generation-IV polypropyleneimine (PPI) dendrimer, and loaded onto nano-scale rGO. Using this construct, they showed intracellular ROS generation by NIR light activation, and were also able to show strong targeting of the NIR PDT/PTT effect in xenograft tumors in mice. Several groups have also reported the development of graphene quantum dots (GQDs) as agents for imaging and photodynamic therapy. For example, Ge et al. reported [179] GQDs (Fig. 10.6i) with a quantum yield of $\sim$1.3 for singlet-oxygen generation. Based on these NIR-absorbing GQDs (Fig. 10.6j, k), with good biocompatibility and aqueous-dispersion capability, they showed complete inhibition (Fig. 10.6l) of breast cancer tumors in a xenograft mouse model, with performance superior to that of conventional photosensitizers such as porphyrins or phthalocyanine dyes. Recently, Thakur et al. have reported [212] a "green" synthesis approach to prepare NIR-responsive GQDs from waste tree leaves, which can be used as dual imaging and 808 nm PDT /PTT probes for tracking cancer cell death. In a variation of this approach, Guo et al. have developed a method to target and deliver nitric oxide (NO) to the mitochondria of cancer cells, with controlled release triggered by NIR activation. By using ruthenium nitrosyl-functionalized, N-doped GQDs, they demonstrated [213] NO-mediated cancer therapy in vivo, by NIR irradiation using 808 nm at 1 W/cm^2.

In a similar approach, Zhang et al. reported [214] the use of Ru(II)-PEG complex-modified nano rGO, as a combined PDT/PTT agent. Using this nanohybrid, the researchers showed lysosome-targeted phosphorescent imaging, as well as Ru-PEG mediated ROS generation, for significant tumor ablation in subcutaneous tumors in mice. In addition to NIR optical imaging, these techniques have also been suitably modified and adapted for radio-imaging applications. As an example, Hong et al. have developed [215] ^{64}Cu-labeled, TRC105 antibody-targeted, PEGylated nano GO, for in vivo positron emission tomography (PET) imaging of subcutaneous tumors in mice, targeted through the tumor vasculature using antibodies against CD105 expression.

10.2.5 Upconversion or Downconversion Nanoparticles

Up- or down-conversion nanoparticles (UCNPs/DCNPs) are generally comprised of an inorganic host crystal, with lanthanide dopant ions embedded in the host lattice. Typical host materials commonly used in biological studies are as follows: Y_2O_3, Y_2O_2S, LaF_3, $NaYF_4$, and $NaGdF_4$, to name a few, with high quantum yields being obtained from the lanthanide metal ions Er^{3+}, Tm^{3+}, and Ho^{3+} under relatively low excitation power densities, which make them suitable for biomedical imaging applications; especially in the NIR wavelengths over 1000 nm [216]. For a good discussion on the choice of available host–guest materials for upconversion, the reader is referred to the review by Wang et al. [17].

Some of the earliest work in the field of upconverting photoluminescent nanomaterials for biomedical applications was done by the group of Weissleder, R. and co-workers. In one example, Hilderbrand et al. reported a surface modification of Y_2O_3 upconverting nanoparticles, with polymers such as polyacrylic acid (PAA), polyethylene glycol (PEG), and NIR carbocyanine dyes, to create a multiplexed fluorophore, which was used for optical imaging [217] of the blood vessels in a mouse ear following tail-vein injection. Around the same time, Vinegoni et al. reported the first case of autofluorescence-free transillumination imaging [218] of mice using similar biocompatible upconverting nanoparticles (coated with PAA, followed by a second coating of 2 kDa mPEG-NH_2 polymer for aqueous stability), compared to imaging with Cy5.5 dye, and demonstrated the two-photon nature of the emission process in UCNPs. Work done by the group of Zhang and colleagues [219] was the first to report the synthesis of very bright core/shell-structured pure hexagonal-phase $NaYF_4$ nanoparticles, co-doped with Yb and Er/Tm as the sensitizers, and coated with a silica shell. In the following years, several groups have developed in vivo applications for the use of these NIR-emitting nanomaterials. For example, Zhan et al. have shown super-high contrast in vivo targeted imaging [220] using 915 nm laser excitation of DSPE-mPEG (5 kDa) encapsulated UCNPs, which is supposed to offer the same benefits of NIR-to-NIR upconversion without the strong heating effects (due to water absorption) caused by excitation using 980 nm laser irradiation. Further, Naczynski et al. have reported increased tumor

accumulation and retention of human serum albumin-coated rare earth-doped nanoparticles [221], for localized NIR signal amplification and multiplexed real-time imaging in an in vivo model of melanoma. Work done by the group of Han, G. and co-workers has focused on the use of UCNPs for deep-tissue imaging and photodynamic therapy. Till date, the deepest reported depth of optical imaging was by Chen et al. [222], using core–shell (α-$NaYbF_4$:Tm^{3+})/CaF_2 nanoparticles, with highly efficient quantum yields ~0.6%, which resulted in UCNP imaging through ~3.2 cm of pork tissue, as well as in exceptionally high-contrast small-animal whole-body imaging (with a signal-to-noise ratio of ~310). In a subsequent report by Punjabi et al., they used UCNPs with a high quantum yield (~3.2%, which is ~15× higher than the then-known core/shell β-phase UCNPs) conjugated to amino-levulinic acid [223], a clinically approved prodrug for photodynamic therapy, using a hydrazone linkage, and showed better performance under NIR-II irradiation in reducing subcutaneous tumors in in vivo mouse models even under 12 mm of pork tissue. Meanwhile, work done by Belcher, A.M. and co-workers has revealed the true benefits of the use of up/downconversion nanoparticles as image contrast agents, in a head-to-head comparison with the other classes of NIR-II-emitting fluorophores (organic dyes, inorganic quantum dots, or carbon nanotubes, Fig. 10.7f–i). In a recent report by Dang et al., layer-by-layer polymer-coated biocompatible UCNPs (Fig. 10.7c) showed optimal performance [225] (in terms of biodistribution, pharmacokinetics, and toxicity profiles, Fig. 10.7d, e) in an application as a diagnostic in vivo imaging probe for high-grade serous ovarian cancer. Based on these insights, Tao et al. have subsequently reported [226] enhanced sensitivity, improved spatial contrast, and increased depths of tissue penetration to facilitate early tumor detection (Fig. 10.7l) using NIR-II imaging, in a mouse model of intraperitoneal ovarian cancer (Fig. 10.7j), using rare-earth UCNPs (Fig. 10.7k). Another novel embodiment of the biomedical applications of UCNPs is their use for "nanothermometry,"pioneered by Jaque, D. and co-workers, which is based on the concept of temperature-sensitive fluorescence of these rare earth-doped nanoparticles. In early reports, Vetrone et al. showed the first successful use of $NaYF_4$:Er^{3+},Yb^{3+} nanoparticles for measuring temperature gradients in cells [230] with uptake of these nanoparticles, by measuring the relative changes in the ratio of the $^2H_{11/2} \rightarrow {}^4I_{15/2}$ and $^2S_{3/2} \rightarrow {}^4I_{15/2}$ emissions of the Er^{3+} ion, which could be potentially useful for monitoring hyperthermia-assisted cell death in cancer treatment. In a similar approach [231], Dong et al. used two-photon excitation of UCNPs as biocompatible probes for cellular imaging of HeLa cells, at penetration depth of ~2 mm, as well as for temperature sensing by measuring the ratio of the fluorescence intensities (I_{538}/I_{522} for the CaF_2:Er^{3+},Yb^{3+}, and I_{790}/I_{800} for the CaF_2:Tm^{3+},Yb^{3+} UCNPs, respectively). In another novel combination approach, Huang et al. have reported [232] the design of multifunctional nanoparticles based on a liposomal formulation, with $NaGdF_4$:Er^{3+},Yb^{3+} UCNPs and doxorubicin co-encapsulated. The energy transfer between the UCNP-Dox donor-acceptor pair results in quenching of the green upconversion fluorescence emission of the UCNPs, which can then be used to monitor drug release over time (through observation of the recovery of the green intensity). Other studies have also attempted to use

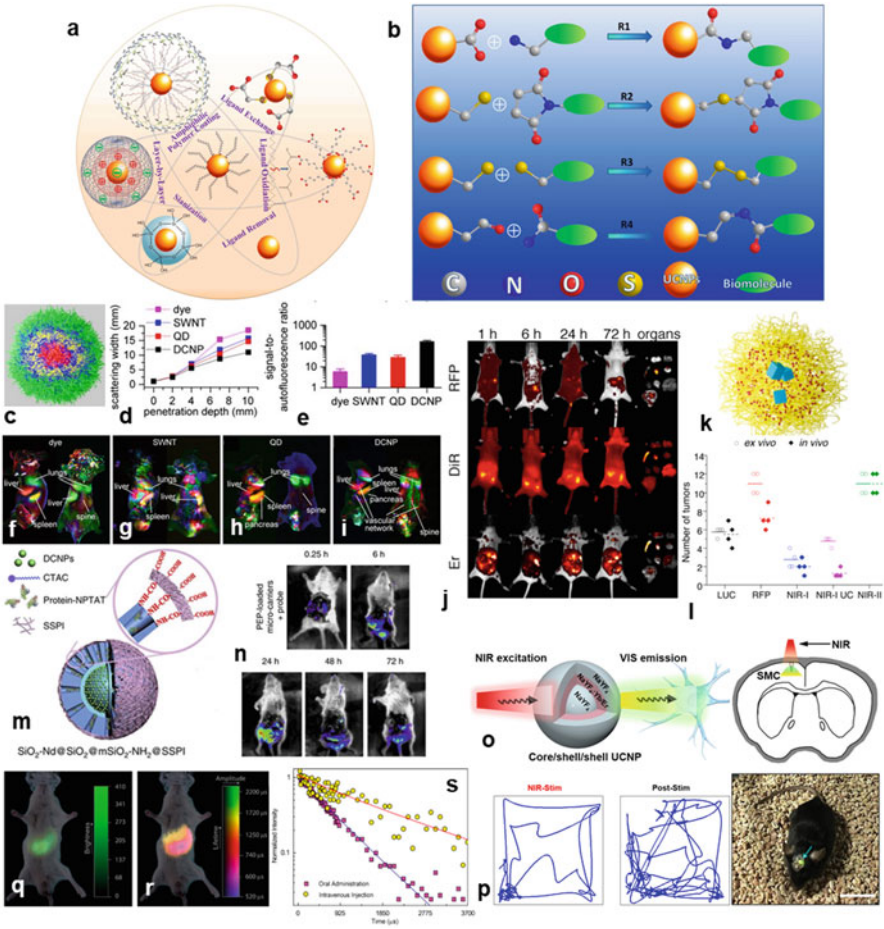

Fig. 10.7 A representative sample of the diverse applications of polymer-functionalized DCNPs/UCNPs. (**a, b**) Schematic of the (**a**) general strategies (layer-by-layer assembly, coating of amphiphilic polymer, ligand exchange, ligand oxidation, ligand removal, or silanization) used for surface functionalization of UCNPs/DCNPs, and (**b**) common conjugation chemistries for coupling UCNPs to select biomolecules. The reactions are as follows. R1 (EDC coupling): carboxylic acid + primary amine → amide bond; R2: thiol group + maleimide bond → thio-ether bond; R3: disulfide linkage between 2 thiol groups; R4: aldehyde group + amine group → imine bond. Reprinted (adapted) with permission from Chen et al. [224], ©2014 American Chemical Society. (**c–i**) A comparative study of four of the most common NIR-II-emitting fluorescent nanoparticles, *viz*. organic dyes, SWNTs, QDs, and UCNPs. (**c**) Layer-by-layer polymer-wrapped nanoparticle, with the NIR-II core (red), dextran sulfate (yellow), poly(L-arginine), PLA (blue), and hyaluronic acid, HA (green). (**d, e**) Among the various types of NPs, the UCNPs/DCNPs show the best characteristics, in terms of the lowest scattering width at all depths of penetration, and the highest signal-to-autofluorescence ratio. (**f–i**) Results of Principal Component Analysis (PCA) performed on the whole-body images of mice, in the first 5 min. post-tail-vein injection of the 4 types of NPs. For each composite image, the red, green, and blue channels correspond to the combined positive and negative areas of the 2nd, 3rd, and 4th principal components, respectively. Note the sharper anatomical features, as well as additional organs (pancreas, vascular network of the skin, and

UCNPs for monitoring drug release in vivo. In one notable study, Wang et al. reported [227] the synthesis of a mesoporous core/shell microcarrier (Fig. 10.3m), SiO_2-Nd@SiO_2@mSiO_2-NH_2@SSPI (succinylated soy protein isolate polymer), containing DCNPs for NIR-II imaging of orally delivered protein drugs in the GI tract (Fig. 10.7n). This construct allowed them to track the nanoparticles, as well as monitor the drug release semi-quantitatively, by using dual excitation sources at 730 nm and 808 nm. Most recently, Ortgies et al. have demonstrated [229] a method to synthesize $NaYF_4$:Yb,Nd@CaF_2 UCNPs with tunable lifetimes (~0.1–1.5 ms, Fig. 10.7s), which is medium-independent, which can be used for multiplexed in vivo imaging (Fig. 10.7q, r). For a review of the advances in in vivo luminescence nanothermometry, the reader is guided to the article by del Rosal et al. [233]. It is worth noting here that a number of groups have also looked at dual-modality imaging, using targeted UCNPs NIR-II fluorescence imaging combined with magnetic resonance imaging [234, 235], or as a contrast agent for X-ray CT [236]. A great summary of the various available strategies for surface functionalization of UCNPs/DCNPs (Fig. 10.7a), as well as the methods for conjugation of biomolecules of interest to these imaging contrast agents (Fig. 10.7b) is provided in the review by Chen et al. [224]. For a discussion on the toxicity aspects of upconversion nanomaterials, the reader is referred to the review article by Gnach et al. [18].

Fig. 10.7 (continued) spine) identified through PCA of the DCNPs. Reprinted (adapted) with permission from Dang et al. [225], ©2016 National Academy of Sciences. (**j–l**) Early tumor detection in a mouse model of human ovarian cancer, using NIR-II imaging of lanthanide NPs. (**j**) Images taken at various time points (1 h, 6 h, 24 h, and 72 h) post-NP injection, for the red fluorescent protein, NIR-I dye (DiR) and the NIR-II-emitting Er-doped DCNP, with (**k**) showing the schematic of the core–shell NPs, with the PEO-b-PCL diblock copolymer (yellow), the organic dye DiR (red), and the Er-doped DCNPs (blue). (l) Plot showing the number of tumors detected, at 2 weeks post-tumor cell implantation. The solid markers indicate in vivo tumors detected, while the hollow markers are for ex vivo excised tumors. The highest number of tumors was identified using the NIR-II fluorescence of the DCNPs. Reprinted (adapted) with permission from Tao et al. [226], ©2017 Elsevier. (**m, n**) NIR-II imaging used to monitor drug release in vivo, in the GI tract. (**m**) The NIR-II fluorescent microcarrier used, and (**n**) in vivo bioimaging used to assess release and delivery of a peptide drug, over 72 h after oral administration. Reprinted (adapted) with permission from Wang et al. [227], CC BY 4.0. (**o, p**) Wireless optogenetic inhibition in the mouse brain, using core–shell–shell UCNPs. (**o**) Schematic of the $NaYF_4$@$NaYF_4$:Yb/Er@$NaYF_4$ core–shell–shell structure, used for converting NIR-II irradiation into visible light for inhibiting activity of neurons expressing an opsin protein, eNpHR. (**p**) Color photograph of the implant in the cortex of a freely mobile mouse brain, used for NIR-activated optogenetic inhibition. The locomotion figures of the animal show dramatic changes (reduction) when the NIR-II illumination is turned ON, and returns to normal after the stimulation is turned OFF. Reprinted (adapted) with permission from Lin et al. [228], ©2018 American Chemical Society. (**q–s**) Multiplexed in vivo imaging, using $NaYF_4$:Yb,Nd@CaF_2 core/shell NIR-II-emitting NPs, with tunable luminescence lifetimes. Two modes of imaging are used: (**q**) Intensity-based imaging and (**r**) Lifetime-based imaging. (**s**) Decay curves of the fluorescence signal, obtained at two different locations, after oral or intravenous administration to an animal. Reprinted (adapted) with permission from Ortgies et al. [229], ©2018 American Chemical Society

Most recently, there has been great excitement in the field of deep-brain stimulation using near infrared nanoparticles for optogenetic studies. Work done by Deisseroth, K., Anikeeva, P., and co-workers has led to the development of methods for depolarizing the plasma membrane of a neural cell, by the use of upconversion lanthanide-doped nanoparticles [237] placed in proximity to the neural cell (which has been engineered to express light-responsive opsin proteins on the plasma membrane). A recent report by Lin et al. showed [228] wireless optical transduction for optogenetic inhibition of neuronal activity (Fig. 10.7p) in the rat brain, by matching the upconversion emission peak of Yb^{3+}-doped UCNPs with the excitation spectrum of halorhodopsin (Fig. 10.7o), a commonly used inhibitory protein. In the first reported use of non-invasive optogenetic manipulation, Chen et al. reported the use of trans-cranial NIR UCNP-mediated release of dopamine [238], from genetically tagged neurons, among other effects, and were also successful in utilizing NIR stimulation to achieve non-invasive synchronization of neuronal activity, as well as behavioral modification in an awake animal.

10.3 Discussion and Future Prospects

With the progress in the areas of near infrared imaging for biomedical applications, where does the field go from here? Three areas of research are worth highlighting:

- Enhancing polymer functionalization for achieving multi-component systems: While NIR contrast agents are an important component of biomedical imaging for screening, diagnosis, therapy planning, treatment, and real-time monitoring of patient response, the focus is increasingly shifting towards combination strategies utilizing a single vehicle (such as a polymer-coated nanoparticle) for simultaneous delivery of an imaging agent and/or multiple therapeutic agents [239] (such as small-molecule drugs, protein therapeutics, or gene editing toolkits). Towards this goal, achieving new orthogonal polymer chemistries, with additional handles such as pH-, temperature-, or time-controlled behavior mechanisms is highly beneficial, and the reader is referred to a review by Blasco et al. [240].
- Machine learning approaches: An upcoming area of research where there is potential for tremendous progress is the use of computational techniques [241] and/or physical modeling to predict the properties of polymeric materials [242] for their intended or desired application in the field of biomedical imaging, in the areas of (a) finding new image contrast agents [243, 244] for biomedical imaging applications, with long-wavelength, high quantum yield emission in the near infrared, (b) performing in silico optimization of the polymer architecture to optimize the loading conditions, and (c) evaluating the release characteristics [245, 246] of the payload (image contrast agent, drug, or some combination thereof), as well as the cellular uptake and cytotoxicity of the nanoparticle carrier on the target cell [247].

- Applicability to clinical translation: Arguably the most important factor for the real-world success of NIR-emitting nanomaterials is their translation from the research lab into the clinic, and this is where polymer functionalization can play a critical role [248–252]. Nanoparticle-based imaging and diagnostic solutions offer the promise of higher specificity, selectivity, and efficacy, at lower doses of treatment compared to conventional therapies; however, they must overcome several hurdles [253]: safety concerns and a strict regulatory framework before they reach the clinic. Given these challenges, it is imperative that researchers take into consideration the path to clinical translation at the earliest stages while designing and developing new polymer-functionalized nanomaterials for NIR imaging applications, in order to graduate from a purely academic exercise to a truly useful bio-nanotechnology with real-world clinical impact.

Acknowledgements N.M.B. acknowledges support of the Mazumdar-Shaw International Oncology Postdoctoral Fellowship, and the Misrock Postdoctoral Fellowship. N.M.B. and A.M.B. gratefully acknowledge the Koch Institute Frontier Research Program. Portions of the authors' own research presented in this chapter were supported in part by funding from a Cancer Center Support (core) Grant #P30-CA14051 from the National Cancer Institute, National Cancer Institute Center for Cancer Nanotechnology Excellence (Grant #5-U54-CA151884-03), the Bridge Project (a partnership between the Koch Institute for Integrative Cancer Research at MIT, and the Dana-Farber/Harvard Cancer Center (DF/HCC)), and the US Army Research Office Institute of Collaborative Biotechnologies through Grant #W017251-022. A.M.B. would like to gratefully acknowledge support of the Marble Center for Cancer Nanomedicine.

Author Contributions Statement
N.M.B. and A.M.B. jointly outlined the chapter, discussed the sections, co-wrote the chapter manuscript and made revisions to the content.

Additional Information
Competing Financial Interest(s) disclosure: The authors declare no competing financial interests.

References

1. Jiang W, Kim BYS, Rutka JT, Chan WCW (2008) Nanoparticle-mediated cellular response is size-dependent. Nat Nanotechnol 3:145–150
2. Davis ME (2012) Fighting cancer with nanoparticle medicines–The nanoscale matters. MRS Bull 37:828–835
3. Heidel JD, Davis ME (2011) Clinical developments in nanotechnology for cancer therapy. Pharm Res 28:187–199
4. Ediriwickrema A, Saltzman WM (2015) Nanotherapy for cancer: targeting and multifunctionality in the future of cancer therapies. ACS Biomater Sci Eng 1:64–78
5. Bertrand N et al. (2017) Mechanistic understanding of *in vivo* protein corona formation on polymeric nanoparticles and impact on pharmacokinetics. Nat Commun 8:777
6. Longmire M, Choyke PL, Kobayashi H (2008) Clearance properties of nano-sized particles and molecules as imaging agents: considerations and caveats. Nanomedicine 3:703–717
7. Yu M, Zheng J (2015) Clearance pathways and tumor targeting of imaging nanoparticles. ACS Nano 9:6655–6674
8. Schroeder A et al. (2012) Treating metastatic cancer with nanotechnology. Nat Rev Cancer 12:39–50

9. Tam F, Goodrich GP, Johnson BR, Halas NJ (2007) Plasmonic enhancement of molecular fluorescence. Nano Lett 7:496–501
10. Bardhan R, Grady NK, Cole JR, Joshi A, Halas NJ (2009) Fluorescence enhancement by Au nanostructures: Nanoshells and nanorods. ACS Nano 3:744–752
11. Peer D et al. (2007) Nanocarriers as an emerging platform for cancer therapy. Nat Nanotechnol 2:751–760
12. Anselmo AC, Mitragotri S (2016) Nanoparticles in the clinic. Bioeng Transl Med 1:10–29
13. Nam J et al. (2013) Surface engineering of inorganic nanoparticles for imaging and therapy. Adv Drug Deliv Rev 65:622–648
14. Mariscal MM, Olmos-Asar JA, Gutierrez-Wing C, Mayoral A, Yacaman MJ (2010) On the atomic structure of thiol-protected gold nanoparticles: a combined experimental and theoretical study. Phys Chem Chem Phys 12:11785–11790
15. Momma K, Izumi, F (2011) VESTA 3 for three-dimensional visualization of crystal, volumetric and morphology data. J Appl Crystallogr 44:1272–1276
16. Budhathoki-Uprety J , Jena PV, Roxbury D , Heller DA (2014) Helical polycarbodiimide cloaking of carbon nanotubes enables inter-nanotube exciton energy transfer modulation. J Am Chem Soc 136:15545–15550
17. Wang F, Banerjee D, Liu Y, Chen X, Liu X (2010) Upconversion nanoparticles in biological labeling, imaging, and therapy. Analyst 135:1839–1854
18. Gnach A, Lipinski T, Bednarkiewicz A, Rybka J, Capobianco JA (2015) Upconverting nanoparticles: assessing the toxicity. Chem Soc Rev 44:1561–1584
19. Wang F, Liu X (2008) Upconversion multicolor fine-tuning: Visible to near-infrared emission from lanthanide-doped $NaYF_4$ nanoparticles. J Am Chem Soc 130:5642–5643
20. Hemmer E, Benayas A, Légaré F, Vetrone F (2016) Exploiting the biological windows: current perspectives on fluorescent bioprobes emitting above 1000 nm. Nanoscale Horiz. 1:168–184
21. Nagaya T, Nakamura YA, Choyke PL, Kobayashi H (2017) Fluorescence-guided surgery. Front Oncol 7
22. Vahrmeijer AL, Hutteman M, van der Vorst JR, van de Velde CJH, Frangioni JV (2013) Image-guided cancer surgery using near-infrared fluorescence. Nat Rev Clin Oncol 10:507–518
23. van Driel PBAA, Keereweer S, Snoeks TJA, Löwik CWGM (2014) Fluorescence-guided surgery: a promising approach for future oncologic surgery. In: Brahme A (ed) Comprehensive biomedical physics. Elsevier, Oxford, pp 301–333
24. Antaris AL et al. (2016) A small-molecule dye for NIR-II imaging. Nat Mater 15:235–242
25. Carr JA et al. (2018) Shortwave infrared fluorescence imaging with the clinically approved near-infrared dye Indocyanine Green. In: Proceedings of the National Academy of Sciences of the USA, pp 201718917
26. van Dam GM et al. (2011) Intraoperative tumor-specific fluorescence imaging in ovarian cancer by folate receptor-α targeting: first in-human results. Nat Med 17:1315–1319
27. Ning X et al. (2011) Maltodextrin-based imaging probes detect bacteria *in vivo* with high sensitivity and specificity. Nat Mater 10:602–607
28. Leevy WM et al. (2008) Noninvasive optical imaging of *Staphylococcus aureus* bacterial infection in living mice using a Bis-Dipicolylamine-Zinc(II) affinity group conjugated to a near-infrared fluorophore. Bioconjug Chem 19:686–692
29. Hojo T, Nagao T, Kikuyama M, Akashi S, Kinoshita T (2010) Evaluation of sentinel node biopsy by combined fluorescent and dye method and lymph flow for breast cancer. Breast 19:210–213
30. Wishart G, Loh SW, Jones L, Benson J (2012) A feasibility study (ICG-10) of indocyanine green (ICG) fluorescence mapping for sentinel lymph node detection in early breast cancer. Eur J Surg Oncol (EJSO) 38:651–656
31. Vorst JRvd et al. (2012) Randomized comparison of near-infrared fluorescence imaging using indocyanine green and 99^{m} Technetium with or without patent blue for the sentinel lymph node procedure in breast cancer patients. Ann Surg Oncol 19:4104–4111

32. Schaafsma BE et al. (2013) Clinical trial of combined radio- and fluorescence-guided sentinel lymph node biopsy in breast cancer. Br J Surg 100:1037–1044
33. Verbeek FPR et al. (2014) Near-infrared fluorescence sentinel lymph node mapping in breast cancer: a multicenter experience. Breast Cancer Res Treat 143:333–342
34. Jung SY et al. (2014) Comparison of sentinel lymph node biopsy guided by the multimodal method of Indocyanine Green fluorescence, radioisotope, and blue dye versus the radioisotope method in breast cancer: a randomized controlled trial. Ann Surg Oncol 21:1254–1259
35. Samorani D et al. (2015) The use of indocyanine green to detect sentinel nodes in breast cancer: A prospective study. Eur J Surg Oncol (EJSO) 41:64–70
36. Sugie T et al. (2016) Evaluation of the clinical utility of the ICG fluorescence method compared with the radioisotope method for sentinel lymph node biopsy in breast cancer. Ann Surg Oncol 23:44–50
37. Zhang X et al. (2016) Diagnostic performance of indocyanine green-guided sentinel lymph node biopsy in breast cancer: A meta-analysis. PLoS One 11:e0155597
38. Sugie T, Ikeda T, Kawaguchi A, Shimizu A, Toi M (2017) Sentinel lymph node biopsy using indocyanine green fluorescence in early-stage breast cancer: a meta-analysis. Int J Clin Oncol 22:11–17
39. Vorst J Rvd et al. (2012) Dose optimization for near-infrared fluorescence sentinel lymph node mapping in patients with melanoma. Br J Dermatol 168:93–98
40. Bredell MG (2010) Sentinel lymph node mapping by indocyanin green fluorescence imaging in oropharyngeal cancer-preliminary experience. Head Neck Oncol 2:31
41. Yamashita S-i et al. (2012) Sentinel node navigation surgery by thoracoscopic fluorescence imaging system and molecular examination in non-small cell lung cancer. Ann Surg Oncol 19:728–733
42. Moroga T et al. (2012) Thoracoscopic segmentectomy with intraoperative evaluation of sentinel nodes for Stage I non-small cell lung cancer. Ann Thorac Cardiovasc Surg 18:89–94
43. Kusano M et al. (2008) Sentinel node mapping guided by Indocyanine Green fluorescence imaging: A new method for sentinel node navigation surgery in gastrointestinal cancer. Dig Surg 25:103–108
44. Hirche C et al. (2013) An experimental study to evaluate the Fluobeam 800 imaging system for fluorescence-guided lymphatic imaging and sentinel node biopsy. Surg Innov 20:516–523
45. Jeschke S et al. (2012) Visualisation of the lymph node pathway in real time by laparoscopic radioisotope- and fluorescence-guided sentinel lymph node dissection in prostate cancer staging. Urology 80:1080–1087
46. Kosaka N, Mitsunaga M, Longmire MR, Choyke PL, Kobayashi H (2011) Near infrared fluorescence-guided real-time endoscopic detection of peritoneal ovarian cancer nodules using intravenously injected indocyanine green. Int J Cancer 129:1671–1677
47. Tummers QRJG et al. (2015) The value of intraoperative near-infrared fluorescence imaging based on enhanced permeability and retention of Indocyanine Green: feasibility and false-positives in ovarian cancer. PLoS One 10:e0129766
48. Ishizawa T et al. (2009) Real-time identification of liver cancers by using indocyanine green fluorescent imaging. Cancer 115:2491–2504
49. Gotoh K et al. (2009) A novel image-guided surgery of hepatocellular carcinoma by indocyanine green fluorescence imaging navigation. J Surg Oncol 100:75–79
50. Peloso A et al. (2013) Combined use of intraoperative ultrasound and Indocyanine Green fluorescence imaging to detect liver metastases from colorectal cancer. HPB15:928–934
51. Starosolski Z et al. (2017) Indocyanine green fluorescence in second near-infrared (NIR-II) window. PLoS One 12:e0187563
52. Bhavane R, Starosolski Z, Stupin I, Ghaghada KB, Annapragada A (2018) NIR-II fluorescence imaging using indocyanine green nanoparticles. Sci Rep 8:14455
53. Han Y-H, Kankala RK, Wang S-B, Chen A-Z (2018) Leveraging engineering of Indocyanine Green-encapsulated polymeric nanocomposites for biomedical applications. Nanomaterials 8:360

54. Tao Z et al. (2013) Biological imaging using nanoparticles of small organic molecules with fluorescence emission at wavelengths longer than 1000 nm. Angew Chem Int Ed 52:13002–13006
55. Hong G et al. (2014) Ultrafast fluorescence imaging *in vivo* with conjugated polymer fluorophores in the second near-infrared window. Nat Commun 5:4206
56. Antaris AL et al. (2017) A high quantum yield molecule-protein complex fluorophore for near-infrared II imaging. Nat Commun 8:15269
57. Wan H et al. (2018) A bright organic NIR-II nanofluorophore for three-dimensional imaging into biological tissues. Nat Commun 9:1171
58. Leevy WM et al. (2006) Optical imaging of bacterial infection in living mice using a fluorescent near-infrared molecular probe. J Am Chem Soc 128:16476–16477
59. Bardhan NM, Ghosh D, Belcher AM (2014) M13 Virus based detection of bacterial infections in living hosts. J Biophotonics 7:617–623
60. Krafft C (2016) Modern trends in biophotonics for clinical diagnosis and therapy to solve unmet clinical needs. J Biophotonics 9: 1362–1375
61. Archer NK, Francis KP, Miller LS (2017) Optical imaging. Springer International Publishing, Cham, pp 43–76
62. Haque A, Faizi MSH, Rather JA, Khan MS (2017) Next generation NIR fluorophores for tumor imaging and fluorescence-guided surgery: a review. Bioorg Med Chem 25:2017–2034
63. Bruchez M, Moronne M, Gin P, Weiss S, Alivisatos AP (1998) Semiconductor nanocrystals as fluorescent biological labels. Science 281:2013–2016
64. Chan WCW, Nie S (1998) Quantum dot bioconjugates for ultrasensitive nonisotopic detection. Science 281: 2016–2018
65. Wu X et al. (2003) Immunofluorescent labeling of cancer marker Her2 and other cellular targets with semiconductor quantum dots. Nat Biotechnol 21:41–46
66. Åkerman ME, Chan WCW, Laakkonen P, Bhatia SN, Ruoslahti E (2002) Nanocrystal targeting *in vivo*. Proc Natl Acad Sci USA 99: 12617–12621
67. Kim S et al. (2004) Near-infrared fluorescent type II quantum dots for sentinel lymph node mapping. Nat Biotechnol 22: 93–97
68. Jaiswal JK, Mattoussi H, Mauro JM, Simon SM (2003) Long-term multiple color imaging of live cells using quantum dot bioconjugates. Nat Biotechnol 21:47–51
69. Kim SE et al. (2016) Ultrasmall nanoparticles induce ferroptosis in nutrient-deprived cancer cells and suppress tumour growth. Nat Nanotechnol 11:977–985
70. Bruns OT et al. (2017) Next-generation *in vivo* optical imaging with short-wave infrared quantum dots. Nat Biomed Eng 1:0056
71. Courtney CM et al. (2017) Potentiating antibiotics in drug-resistant clinical isolates via stimuli-activated superoxide generation. Sci Adv 3:e1701776
72. Oh E et al. (2016) Meta-analysis of cellular toxicity for cadmium-containing quantum dots. Nat Nanotechnol 11:479–486
73. Liu W et al. (2007) Compact cysteine-coated CdSe(ZnCdS) quantum dots for *in vivo* applications. J Am Chem Soc 129: 14530–14531
74. Valencia PM et al. (2010) Single-step assembly of homogenous lipid–polymeric and lipid–quantum dot nanoparticles enabled by microfluidic rapid mixing. ACS Nano 4: 1671–1679
75. Lee J, Feng X, Chen O, Bawendi MG, Huang J (2018) Stable, small, specific, low-valency quantum dots for single-molecule imaging. Nanoscale 10:4406–4414
76. Samia ACS, Chen X, Burda C (2003) Semiconductor quantum dots for photodynamic therapy. J Am Chem Soc 125:15736–15737
77. Yaghini E, Seifalian AM, MacRobert AJ (2009) Quantum dots and their potential biomedical applications in photosensitization for photodynamic therapy. Nanomedicine 4:353–363
78. Bagalkot V et al. (2007) Quantum dot–aptamer conjugates for synchronous cancer imaging, therapy, and sensing of drug delivery based on bi-fluorescence resonance energy transfer. Nano Letters 7: 3065–3070
79. Benayas A et al. (2015) PbS/CdS/ZnS quantum dots: a multifunctional platform for *in vivo* near-infrared low-dose fluorescence imaging. Adv Funct Mater 25:6650–6659

80. Rhyner MN et al. (2006) Quantum dots and multifunctional nanoparticles: new contrast agents for tumor imaging. Nanomedicine 1: 209–217
81. Walling MA, Novak JA, Shepard JRE (2009) Quantum dots for live cell and *in vivo* imaging. Int J Mol Sci 10:441–491
82. Liu L, Miao Q, Liang G (2013) Quantum dots as multifunctional materials for tumor imaging and therapy. Materials 6:483–499
83. Shen S, Zhang Y, Peng L, Du Y, Wang Q (2011) Matchstick-shaped Ag_2S–ZnS heteronanostructures preserving both UV/blue and near-infrared photoluminescence. Angew Chem Int Ed 50:7115–7118
84. Zhang Y et al. (2012) Ag_2S quantum dot: A bright and biocompatible fluorescent nanoprobe in the second near-infrared window. ACS Nano 6:3695–3702
85. Hong G et al. (2012) *In vivo* fluorescence imaging with Ag_2S quantum dots in the second near-infrared region. Angew Chem Int Ed 51:9818–9821
86. Zhang Y et al. (2013) Biodistribution, pharmacokinetics and toxicology of Ag_2S near-infrared quantum dots in mice. Biomaterials 34:3639–3646
87. Chen G et al. (2013) Tracking of transplanted human mesenchymal stem cells in living mice using near-infrared Ag_2S quantum dots. Adv Funct Mater 24:2481–2488
88. Li C et al. (2014) *In vivo* real-time visualization of tissue blood flow and angiogenesis using Ag_2S quantum dots in the NIR-II window. Biomaterials 35:393–400
89. Wu C, Zhang Y, Li Z, Li C, Wang Q (2016) A novel photoacoustic nanoprobe of ICG@PEG–Ag_2S for atherosclerosis targeting and imaging *in vivo*. Nanoscale 8:12531–12539
90. Hao X et al. (2018) Programmable chemotherapy and immunotherapy against breast cancer guided by multiplexed fluorescence imaging in the second near-infrared window. Adv Mater 0:1804437
91. Sadovnikov IS, Gusev IA (2017) Recent progress in nanostructured silver sulfide: from synthesis and nonstoichiometry to properties. J Mater Chem A 5:17676–17704
92. Zhao P et al. (2018) Near infrared quantum dots in biomedical applications: current status and future perspective. Wiley Interdiscip Rev Nanomed Nanobiotechnol 10:e1483
93. Ganguly P, Breen A, Pillai SC (2018) Toxicity of nanomaterials: exposure, pathways, assessment, and recent advances. ACS Biomater Sci Eng 4:2237–2275
94. Phillips E et al. (2014) Clinical translation of an ultrasmall inorganic optical-PET imaging nanoparticle probe. Sci Transl Med 6:260ra149–260ra149
95. Hardman R (2006) A toxicologic review of quantum dots: Toxicity depends on physicochemical and environmental factors. Environ Health Perspect 114:165–172
96. Choi HS et al. (2007) Renal clearance of quantum dots. Nat Biotechnol 25:1165–1170
97. Hauck TS, Anderson RE, Fischer HC, Newbigging S, Chan WCW (2009) *In vivo* quantum-dot toxicity assessment. Small 6:138–144
98. Tsoi KM, Dai Q, Alman BA, Chan WCW (2013) Are quantum dots toxic? Exploring the discrepancy between cell culture and animal studies. Acc Chem Res 46:662–671
99. Bottrill M, Green M (2011) Some aspects of quantum dot toxicity. Chem Commun 47:7039–7050
100. Yong K-T et al. (2013) Nanotoxicity assessment of quantum dots : from cellular to primate studies. Chem Soc Rev 42:1236–1250
101. Hahn MA, Tabb JS, Krauss TD (2005) Detection of single bacterial pathogens with semiconductor quantum dots. Anal Chem 77:861–4869
102. Edgar R et al. (2006) High-sensitivity bacterial detection using biotin-tagged phage and quantum-dot nanocomplexes. Proc Natl Acad Sci USA 103:4841–4845
103. Courtney CM et al. (2016) Photoexcited quantum dots for killing multidrug-resistant bacteria. Nat Mater 15:529–534
104. Jian H-J et al. (2017) Super-cationic carbon quantum dots synthesized from spermidine as an eye drop formulation for topical treatment of bacterial keratitis. ACS Nano 11:6703–6716
105. Sardar R, Funston AM, Mulvaney P, Murray RW (2009) Gold nanoparticles: past, present, and future. Langmuir 25:13840–13851

106. Lim Z-ZJ, Li J-EJ, Ng C-T, Yung L-YL, Bay, B.-H. (2011) Gold nanoparticles in cancer therapy. Acta Pharmacol Sin 32:983–990
107. Hu M et al. (2006) Gold nanostructures: engineering their plasmonic properties for biomedical applications. Chem Soc Rev 35:1084–1094
108. Zheng J, Zhou C, Yu M, Liu J (2012) Different sized luminescent gold nanoparticles. Nanoscale 4:4073–4083
109. Zhou C, Long M, Qin Y, Sun X, Zheng J (2011) Luminescent gold nanoparticles with efficient renal clearance. Angew Chem Int Ed 50:3168–3172
110. Zhou C et al. (2012) Near-infrared emitting radioactive gold nanoparticles with molecular pharmacokinetics. Angew Chem Int Ed 51:10118–10122
111. Liu J et al. (2013) Passive tumor targeting of renal-clearable luminescent gold nanoparticles: Long tumor retention and fast normal tissue clearance. J Am Chem Soc 135:4978–4981
112. Peng C et al. (2017) Targeting orthotopic gliomas with renal-clearable luminescent gold nanoparticles. Nano Research 10:1366–1376
113. Liu J et al. (2013) PEGylation and zwitterionization: Pros and cons in the renal clearance and tumor targeting of near-IR-emitting gold nanoparticles. Angew Chem Int Ed 52:12572–12576
114. Zheng YB, Kiraly B, Weiss PS, Huang TJ (2012) Molecular plasmonics for biology and nanomedicine. Nanomedicine 7:751–770
115. West JL, Halas NJ (2003) Engineered nanomaterials for biophotonics applications: Improving sensing, imaging, and therapeutics. Annu Rev Biomed Eng 5:285–292
116. Dreaden EC, Alkilany AM, Huang X, Murphy CJ, El-Sayed MA (2012) The golden age: gold nanoparticles for biomedicine. Chem Soc Rev 41:2740–2779
117. O'Neal DP, Hirsch LR, Halas NJ, Payne JD, West JL (2004) Photo-thermal tumor ablation in mice using near infrared-absorbing nanoparticles. Cancer Lett 209:171–176
118. Maltzahn Gv et al. (2011) Nanoparticles that communicate *in vivo* to amplify tumour targeting. Nat Mater 10:545–552
119. Harbut MB et al. (2015) Auranofin exerts broad-spectrum bactericidal activities by targeting thiol-redox homeostasis. Proc Natl Acad Sci USA 112:4453–4458
120. Qian X et al. (2008) *In vivo* tumor targeting and spectroscopic detection with surface-enhanced Raman nanoparticle tags. Nat Biotechnol 26:83–90
121. Lee K et al. (2017) Nanoparticle delivery of Cas9 ribonucleoprotein and donor DNA *in vivo* induces homology-directed DNA repair. Nat Biomed Eng 1:889–901
122. Lee B et al. (2018) Nanoparticle delivery of CRISPR into the brain rescues a mouse model of fragile X syndrome from exaggerated repetitive behaviours. Nat Biomed Eng 2:497–507
123. Amendola V, Pilot R, Frasconi M, Maragò OM, Iatì MA (2017) Surface plasmon resonance in gold nanoparticles: a review. J Phys Condens Matter 29:203002
124. Hirsch LR et al. (2003) Nanoshell-mediated near-infrared thermal therapy of tumors under magnetic resonance guidance. Proc Natl Acad Sci USA 100:13549–13554
125. Jain PK, Huang X, El-Sayed IH, El-Sayed MA (2008) Noble metals on the nanoscale: Optical and photothermal properties and some applications in imaging, sensing, biology, and medicine. Acc Chem Res 41:1578–1586
126. Gobin AM et al. (2007) Near-infrared resonant nanoshells for combined optical imaging and photothermal cancer therapy. Nano Lett 7:1929–1934
127. Schwartz JA et al. (2009) Feasibility study of particle-assisted laser ablation of brain tumors in orthotopic canine model. Cancer Res 69:1659–1667
128. Chen J et al. (2010) Gold nanocages as photothermal transducers for cancer treatment. Small 6:811–817
129. Choi WI et al. (2011) Tumor regression *in vivo* by photothermal therapy based on gold-nanorod-loaded, functional nanocarriers. ACS Nano 5:1995–2003
130. Jang B, Park J-Y, Tung C-H, Kim I-H, Choi Y (2011) Gold nanorod–photosensitizer complex for near-infrared fluorescence imaging and photodynamic/photothermal therapy *in vivo*. ACS Nano 5:1086–1094
131. Timko BP et al. (2014) Near-infrared–actuated devices for remotely controlled drug delivery. Proc Natl Acad Sci USA 111:1349–1354

132. Huaizhi Z, Yuantao N (2001) China's ancient gold drugs. Gold Bull 34:24–29
133. Forestier J (1934) Rheumatoid arthritis and its treatment by gold salts. Lancet 224:646–648
134. Lewis MG et al. (2011) Gold drug auranofin restricts the viral reservoir in the monkey AIDS model and induces containment of viral load following ART suspension. AIDS 25:1347
135. Debnath A et al. (2012) A high-throughput drug screen for *Entamoeba histolytica* identifies a new lead and target. Nat Med 18:956–960
136. Libutti SK et al. (2010) Phase I and pharmacokinetic studies of CYT-6091, a novel PEGylated colloidal gold-rhTNF nanomedicine. Clin Cancer Res 16:6139–6149
137. Kharlamov AN et al. (2015) Silica–gold nanoparticles for atheroprotective management of plaques: results of the NANOM-FIM trial. Nanoscale 7:8003–8015
138. Bardhan NM (2017) 30 years of advances in functionalization of carbon nanomaterials for biomedical applications: a practical review. J Mater Res 32:107–127
139. Fadel TR, Fahmy TM (2014) Immunotherapy applications of carbon nanotubes: From design to safe applications. Trends Biotechnol 32:198–209
140. Dubertret B et al. (2002) *In vivo* imaging of quantum dots encapsulated in phospholipid micelles. Science 298:1759–1762
141. Cheng J et al. (2007) Formulation of functionalized PLGA–PEG nanoparticles for *in vivo* targeted drug delivery. Biomaterials 28:869–876
142. Hong G, Antaris AL, Dai H (2017) Near-infrared fluorophores for biomedical imaging. Nat Biomed Eng 1:0010
143. Robinson JT et al. (2010) High performance *in vivo* near-IR (>1 μm) imaging and photothermal cancer therapy with carbon nanotubes. Nano Res 3:779–793
144. Welsher K et al. (2009) A route to brightly fluorescent carbon nanotubes for near-infrared imaging in mice. Nat Nanotechnol 4:773–780
145. Welsher K, Sherlock SP, Dai H (2011) Deep-tissue anatomical imaging of mice using carbon nanotube fluorophores in the second near-infrared window. Proc Natl Acad Sci USA 108:8943–8948
146. Hong G et al. (2012) Multifunctional *in vivo* vascular imaging using near-infrared II fluorescence. Nat Med 18:1841–1846
147. Bardhan NM, Ghosh D, Belcher AM (2014) Carbon nanotubes as *in vivo* bacterial probes. Nat Commun 5:4918
148. Yi H et al. (2012) M13 Phage-functionalized single-walled carbon nanotubes as nanoprobes for second near-infrared window fluorescence imaging of targeted tumors. Nano Lett 12:1176–1183
149. Ghosh D et al. (2014) Deep, noninvasive imaging and surgical guidance of submillimeter tumors using targeted M13-stabilized single-walled carbon nanotubes. Proc Natl Acad Sci USA 111:13948–13953
150. Iverson NM et al. (2013) *In vivo* biosensing via tissue-localizable near-infrared-fluorescent single-walled carbon nanotubes. Nat Nanotechnol 8:873–880
151. Williams RM et al. (2018) Noninvasive ovarian cancer biomarker detection via an optical nanosensor implant. Sci Adv 4:eaaq1090
152. Robinson JT et al. (2012) *In vivo* fluorescence imaging in the second near-infrared window with long circulating carbon nanotubes capable of ultrahigh tumor uptake. J Am Chem Soc 134:10664–10669
153. Hong G et al. (2014) Through-skull fluorescence imaging of the brain in a new near-infrared window. Nat Photonics 8:723–730
154. Antaris AL et al. (2013) Ultra-low doses of chirality sorted (6,5) carbon nanotubes for simultaneous tumor imaging and photothermal therapy. ACS Nano 7:3644–3652
155. Liu Z, Sun X, Nakayama-Ratchford N, Dai H (2007) Supramolecular chemistry on water-soluble carbon nanotubes for drug loading and delivery. ACS Nano 1:50–56
156. Liu Z et al. (2008) Drug delivery with carbon nanotubes for *in vivo* cancer treatment. Cancer Res 68:6652–6660
157. Liu Z, Tabakman SM, Chen Z, Dai H (2009) Preparation of carbon nanotube bioconjugates for biomedical applications. Nat Protoc 4:1372–1381

158. Schipper ML et al. (2008) A pilot toxicology study of single-walled carbon nanotubes in a small sample of mice. Nat Nanotechnol 3:216–221
159. Dang X et al. (2011) Virus-templated self-assembled single-walled carbon nanotubes for highly efficient electron collection in photovoltaic devices. Nat Nanotechnol 6:377–384
160. Arias LR, Yang L (2009) Inactivation of bacterial pathogens by carbon nanotubes in suspensions. Langmuir 25:3003–3012
161. Rodrigues DF, Elimelech M (2010) Toxic effects of single-walled carbon nanotubes in the development of *E. coli* biofilm. Environ Sci Technol 44:4583–4589
162. Aslan S et al. (2010) Antimicrobial biomaterials based on carbon nanotubes dispersed in poly(lactic-*co*-glycolic acid). Nanoscale 2:1789–1794
163. Kim J-W, Shashkov EV, Galanzha EI, Kotagiri N, Zharov VP (2007) Photothermal antimicrobial nanotherapy and nanodiagnostics with self-assembling carbon nanotube clusters. Lasers Surg Med 39:622–634
164. Zheng M et al. (2003) DNA-assisted dispersion and separation of carbon nanotubes. Nat Mater 2:338–342
165. Zheng M (2003) et al. Structure-based carbon nanotube sorting by sequence-dependent DNA assembly. Science 302:1545 –1548
166. Strano MS et al. (2004) Understanding the nature of the DNA-assisted separation of single-walled carbon nanotubes using fluorescence and Raman spectroscopy. Nano Lett 4:543–550
167. Huang X, Mclean RS, Zheng M (2005) High-resolution length sorting and purification of DNA-wrapped carbon nanotubes by size-exclusion chromatography. Anal Chem 77:6225–6228
168. Zheng M, Semke ED (2007) Enrichment of single chirality carbon nanotubes. J Am Chem Soc 129:6084–6085
169. Tu X, Manohar S, Jagota A, Zheng M (2009) DNA sequence motifs for structure-specific recognition and separation of carbon nanotubes. Nature 460:250–253
170. Ulissi ZW et al. (2014) Spatiotemporal intracellular nitric oxide signaling captured using internalized, near-infrared fluorescent carbon nanotube nanosensors. Nano Lett 14:4887–4894
171. Iverson NM et al. (2016) Quantitative tissue spectroscopy of near infrared fluorescent nanosensor implants. J Biomed Nanotechnol 12:1035–1047
172. Giraldo JP et al. (2014) Plant nanobionics approach to augment photosynthesis and biochemical sensing. Nat Mater 13:400–408
173. Ghosal K, Sarkar K (2018) Biomedical applications of graphene nanomaterials and beyond. ACS Biomater Sci Eng
174. Liu J, Li Y, Li Y, Li J, Deng Z (2010) Noncovalent DNA decorations of graphene oxide and reduced graphene oxide toward water-soluble metal–carbon hybrid nanostructures via self-assembly. J Mater Chem 20:900–906
175. Robinson JT et al. (2011) Ultrasmall reduced graphene oxide with high near-infrared absorbance for photothermal therapy. J Am Chem Soc 133:6825–6831
176. Mohanty N, Berry V (2008) Graphene-based single-bacterium resolution biodevice and DNA transistor: Interfacing graphene derivatives with nanoscale and microscale biocomponents. Nano Lett 8:4469–4476
177. Lim D-K et al. (2013) Enhanced photothermal effect of plasmonic nanoparticles coated with reduced graphene oxide. Nano Lett 13:4075–4079
178. Yang K, Feng L, Hong H, Cai W, Liu Z (2013) Preparation and functionalization of graphene nanocomposites for biomedical applications. Nat Protoc 8:2392–2403
179. Ge J et al. (2014) A graphene quantum dot photodynamic therapy agent with high singlet oxygen generation. Nat Commun 5:4596
180. Bardhan NM et al. (2017) Enhanced cell capture on functionalized graphene oxide nanosheets through oxygen clustering. ACS Nano 11:1548–1558
181. Yoon HJ et al. (2013) Sensitive capture of circulating tumour cells by functionalized graphene oxide nanosheets. Nat Nanotechnol 8:735–741
182. Liu Z, Robinson JT, Sun X, Dai H (2008) PEGylated nanographene oxide for delivery of water-insoluble cancer drugs. J Am Chem Soc 130:10876–10877

183. Lu C-H, Yang H-H, Zhu C-L, Chen X, Chen G-N (2009) A graphene platform for sensing biomolecules. Angew Chem Int Ed 48:4785–4787
184. Yoon HJ et al. (2016) Tunable thermal-sensitive polymer–graphene oxide composite for efficient capture and release of viable circulating tumor cells. Adv Mater 28:4891–4897
185. Zhang M et al. (2012) Facile synthesis of water-soluble, highly fluorescent graphene quantum dots as a robust biological label for stem cells. J Mater Chem 22:7461–7467
186. Pan D et al. (2012) Cutting sp^2 clusters in graphene sheets into colloidal graphene quantum dots with strong green fluorescence. J Mater Chem 22:3314–3318
187. Nahain A-A, Lee J-E, Jeong JH, Park SY (2013) Photoresponsive fluorescent reduced graphene oxide by spiropyran conjugated hyaluronic acid for *in vivo* imaging and target delivery. Biomacromolecules 14:4082–4090
188. Zhang Z et al. (2015) Graphene oxide as a multifunctional platform for Raman and fluoresence imaging of cells. Small 11:3000–3005
189. Ji D.K. et al. (2015) Receptor-targeting fluorescence imaging and theranostics using a graphene oxide based supramolecular glycocomposite. J Mater Chem B 3:9182–9185
190. Patel MA et al. (2013) Direct production of graphene nanosheets for near infrared photoacoustic imaging. ACS Nano 7:8147–8157
191. Lalwani G, Cai X, Nie L, Wang LV, Sitharaman B (2013) Graphene-based contrast agents for photoacoustic and thermoacoustic tomography. Photoacoustics 1:62–67
192. Toumia Y et al. (2016) Graphene meets microbubbles: a superior contrast agent for photoacoustic imaging. ACS Appl Mater Interfaces 8:16465–16475
193. Kumar PV et al. (2014) Scalable enhancement of graphene oxide properties by thermally driven phase transformation. Nat Chem 6:151–158
194. Cheng S-J et al. (2018) Simultaneous drug delivery and cellular imaging using graphene oxide. Biomater Sci 6:813–819
195. Yang J-W et al. (2018) Enhanced osteogenic differentiation of stem cells on phase-engineered graphene oxide. ACS Appl Mater Interfaces 10:12497–12503
196. Servant A, Bianco A, Prato M, Kostarelos K (2014) Graphene for multi-functional synthetic biology: the last 'zeitgeist' in nanomedicine. Bioorg Med Chem Lett 24:1638–1649
197. Jaque D et al. (2014) Nanoparticles for photothermal therapies. Nanoscale 6:9494–9530
198. Yang K et al. (2010) Graphene in mice: Ultrahigh *in vivo* tumor uptake and efficient photothermal therapy. Nano Lett 10:3318–3323
199. Zhang W et al. (2011) Synergistic effect of chemo-photothermal therapy using PEGylated graphene oxide. Biomaterials 32:8555–8561
200. Tian B, Wang C, Zhang S, Feng L, Liu Z (2011) Photothermally enhanced photodynamic therapy delivered by nano-graphene oxide. ACS Nano 5:7000–7009
201. Feng L et al. (2013) Polyethylene glycol and polyethyleneimine dual-functionalized nano-graphene oxide for photothermally enhanced gene delivery. Small 9:1989–1997
202. Hu S-H, Chen Y-W, Hung W-T, Chen I-W, Chen S-Y (2012) Quantum-dot-tagged reduced graphene oxide nanocomposites for bright fluorescence bioimaging and photothermal therapy monitored *in situ*. Adv Mater 24:1748–1754
203. Akhavan O, Ghaderi E (2013) Graphene nanomesh promises extremely efficient *in vivo* photothermal therapy. Small 9:3593–3601
204. Wang Y et al. (2013) Multifunctional mesoporous silica-coated graphene nanosheet used for chemo-photothermal synergistic targeted therapy of glioma. J Am Chem Soc 135:4799–4804
205. Sahu A, Choi WI, Lee JH, Tae G (2013) Graphene oxide mediated delivery of methylene blue for combined photodynamic and photothermal therapy. Biomaterials 34:6239–6248
206. Li M, Yang X, Ren J, Qu K, Qu X (2012) Using graphene oxide high near-infrared absorbance for photothermal treatment of Alzheimer's disease. Adv Mater 24:1722–1728
207. Shi X et al. (2013) Graphene-based magnetic plasmonic nanocomposite for dual bioimaging and photothermal therapy. Biomaterials 34:4786–4793
208. Yang K et al. (2012) Multimodal imaging guided photothermal therapy using functionalized graphene nanosheets anchored with magnetic nanoparticles. Adv Mater 24:1868–1872

209. Sheng Z et al. (2013) Protein-assisted fabrication of nano-reduced graphene oxide for combined *in vivo* photoacoustic imaging and photothermal therapy. Biomaterials 34:5236–5243
210. Moon H et al. (2015) Amplified photoacoustic performance and enhanced photothermal stability of reduced graphene oxide coated gold nanorods for sensitive photoacoustic imaging. ACS Nano 9:2711–2719
211. Taratula O et al. (2015) Phthalocyanine-loaded graphene nanoplatform for imaging-guided combinatorial phototherapy. Int J Nanomedicine 2015:2347–2362
212. Thakur M, Kumar Kumawat M, Srivastava R (2017) Multifunctional graphene quantum dots for combined photothermal and photodynamic therapy coupled with cancer cell tracking applications. RSC Adv 7:5251–5261
213. Guo M et al. (2017) Ruthenium nitrosyl functionalized graphene quantum dots as an efficient nanoplatform for NIR-light-controlled and mitochondria-targeted delivery of nitric oxide combined with photothermal therapy. Chem. Commun. 53:3253–3256
214. Zhang D-Y et al. (2017) Graphene oxide decorated with Ru(II)—Polyethylene Glycol complex for lysosome-targeted imaging and photodynamic/photothermal therapy. ACS Appl Mater Interfaces 9:6761–6771
215. Hong H et al. (2012) *In vivo* targeting and imaging of tumor vasculature with radiolabeled, antibody-conjugated nanographene. ACS Nano 6:2361–2370
216. Hemmer E et al. (2013) Upconverting and NIR emitting rare earth based nanostructures for NIR-bioimaging. Nanoscale 5:11339–11361
217. Hilderbrand SA, Shao F, Salthouse C, Mahmood U, Weissleder R (2009) Upconverting luminescent nanomaterials: application to *in vivo* bioimaging. Chem Commun 28:4188–4190
218. Vinegoni C et al. (2009) Transillumination fluorescence imaging in mice using biocompatible upconverting nanoparticles. Opt Lett 34:2566–2568
219. Li Z, Zhang Y, Jiang S (2008) Multicolor core/shell-structured upconversion fluorescent nanoparticles. Adv Mater 20:4765–4769
220. Zhan Q et al. (2011) Using 915 nm laser excited $Tm^{3+}/Er^{3+}/Ho^{3+}$-doped $NaYbF_4$ upconversion nanoparticles for *in vitro* and deeper *in vivo* bioimaging without overheating irradiation. ACS Nano 5:3744–3757
221. Naczynski DJ et al. (2013) Rare-earth-doped biological composites as *in vivo* shortwave infrared reporters. Nat Commun 4:2199
222. Chen G et al. (2012) (α-$NaYbF_4$:Tm^{3+})/CaF_2 core/shell nanoparticles with efficient near-infrared to near-infrared upconversion for high-contrast deep tissue bioimaging. ACS Nano 6:8280–8287
223. Punjabi A et al. (2014) Amplifying the red-emission of upconverting nanoparticles for biocompatible clinically used prodrug-induced photodynamic therapy. ACS Nano 8:10621–10630
224. Chen G, Qiu H, Prasad PN, Chen X (2014) Upconversion nanoparticles: Design, nanochemistry, and applications in theranostics. Chem Rev 114:5161–5214
225. Dang X et al. (2016) Layer-by-layer assembled fluorescent probes in the second near-infrared window for systemic delivery and detection of ovarian cancer. Proc Natl Acad Sci USA 113:5179–5184
226. Tao Z et al. (2017) Early tumor detection afforded by *in vivo* imaging of near-infrared II fluorescence. Biomaterials 134:202–215
227. Wang R, Zhou L, Wang W, Li X, Zhang F (2017) *In vivo* gastrointestinal drug-release monitoring through second near-infrared window fluorescent bioimaging with orally delivered microcarriers. Nat Commun 8:14702
228. Lin X et al. (2018) Core–shell–shell upconversion nanoparticles with enhanced emission for wireless optogenetic inhibition. Nano Lett 18:948–956
229. Ortgies DH et al. (2018) Lifetime-encoded infrared-emitting nanoparticles for *in vivo* multiplexed imaging. ACS Nano 12:4362–4368
230. Vetrone F et al. (2010) Temperature sensing using fluorescent nanothermometers. ACS Nano 4:3254–3258

231. Dong N-N et al. (2011) NIR-to-NIR two-photon excited $CaF_2:Tm^{3+},Yb^{3+}$ nanoparticles: Multifunctional nanoprobes for highly penetrating fluorescence bio-imaging. ACS Nano 5:8665–8671
232. Huang Y, Hemmer E, Rosei F, Vetrone F (2016) Multifunctional liposome nanocarriers combining upconverting nanoparticles and anticancer drugs. J. Phys. Chem. B 120:4992–5001
233. Blanca dR, Erving X, Ueslen R, Daniel J (2017) *In vivo* luminescence nanothermometry: from materials to applications. Adv Opt Mater 5:1600508
234. Jin J et al. (2013) Upconversion nanoparticles conjugated with Gd^{3+}-DOTA and RGD for targeted dual-modality imaging of brain tumor xenografts. Adv Healthc Mater 2:1501–1512
235. Ni D et al. (2014) Dual-targeting upconversion nanoprobes across the blood–brain barrier for magnetic resonance/fluorescence imaging of intracranial glioblastoma. ACS Nano 8:1231–1242
236. Liu Z et al. (2012) Long-circulating Er^{3+}-doped Yb_2O_3 up-conversion nanoparticle as an *in vivo* X-Ray CT imaging contrast agent. Biomaterials 33:6748–6757
237. Anikeeva P, Deisseroth K (2012) Upconversion of light for use in optogenetic methods. In: International classification A61M37/00; cooperative classification B82Y5/00, A61N5/06, A61K41/0038; European classification A61K41/00P, B82Y5/00
238. Chen S et al. (2018) Near-infrared deep brain stimulation via upconversion nanoparticle-mediated optogenetics. Science 359:679–684
239. Liao L et al. (2014) A convergent synthetic platform for single-nanoparticle combination cancer therapy: Ratiometric loading and controlled release of Cisplatin, Doxorubicin, and Camptothecin. J Am Chem Soc 136:5896–5899
240. Blasco E, Sims MB, Goldmann AS, Sumerlin BS, Barner-Kowollik C (2017) 50th anniversary perspective: polymer functionalization. Macromolecules 50:5215–5252
241. Steinhauser MO, Hiermaier S (2009) A review of computational methods in materials science: examples from shock-wave and polymer physics. Int J Mol Sci 10:5135–5216
242. Audus DJ, de Pablo JJ (2017) Polymer informatics: opportunities and challenges. ACS Macro Lett 6:1078–1082
243. Mannodi-Kanakkithodi A, Pilania G, Huan TD, Lookman T, Ramprasad R (2016) Machine Learning strategy for accelerated design of polymer dielectrics. Sci Rep 6:20952
244. Jørgensen PB et al. (2018) Machine learning-based screening of complex molecules for polymer solar cells. J Chem Phys 148:241735
245. Husseini GA, Mjalli FS, Pitt WG, Abdel-Jabbar NM (2009) Using artificial neural networks and model predictive control to optimize acoustically assisted doxorubicin release from polymeric micelles. Technol Cancer Res Treat 8:479–488
246. Zawbaa HM, Szlęk J, Grosan C, Jachowicz R, Mendyk A (2016) Computational intelligence modeling of the macromolecules release from PLGA microspheres—Focus on feature selection. PLoS One 11:e0157610
247. Jones DE, Ghandehari H, Facelli JC (2016) A review of the applications of data mining and machine learning for the prediction of biomedical properties of nanoparticles. Comput Methods Prog Biomed 132:93–103
248. Gref R et al. (1994) Biodegradable long-circulating polymeric nanospheres. Science 263:1600–1603
249. Gref R et al. (1995) The controlled intravenous delivery of drugs using PEG-coated sterically stabilized nanospheres. Adv Drug Deliv Rev 16:215–233
250. Uhrich KE, Cannizzaro SM, Langer RS, Shakesheff KM (1999) Polymeric systems for controlled drug release. Chem Rev 99:3181–3198
251. Langer R, Tirrell DA (2004) Designing materials for biology and medicine. Nature 428:487–492
252. Peppas NA, Hilt JZ, Khademhosseini A, Langer R (2006) Hydrogels in Biology and Medicine: From molecular principles to Bionanotechnology. Adv Mater 18:1345–1360
253. Alvarez MM et al. (2017) Emerging trends in micro- and nanoscale technologies in medicine: From basic discoveries to translation. ACS Nano 11:5195–5214

Chapter 11
Near Infrared Ag_2S Quantum Dots: Synthesis, Functionalization, and In Vivo Stem Cell Tracking Applications

Guangcun Chen, Yejun Zhang, Chunyan Li, and Qiangbin Wang

Abbreviations

Ald	Alendronate
CT	Computed tomography
DHLA	Dihydrolipoic acid
EDC	Ethyl(dimethylaminopropyl) carbodiimide
FA	Folate
FBS	Fetal bovine serum
GSH	Reduced glutathione
HNSs	Heteronanostructures
HRTEM	High-resolution transmission electron microscopy
HuNu	Anti-human nuclear antigen antibody
ICG	Indocyanine green
2MPA	2-mercaptopropionic acid
MSCs	Mesenchymal stem cells
MTT	3-(4,5-dimethylthiazol-2-yl)-2,5-diphenyltetrazolium bromide
NHS	N-hydroxysuccinimide
NIRFI	Near infrared fluorescence imaging
NIR-II	The second near infrared window
NPs	Nanoparticles
OA	Oleic acid
ODA	Octadecylamine
ODE	1-octadecane

G. Chen · Y. Zhang · C. Li · Q. Wang (✉)
CAS Key Laboratory of Nano-Bio Interface, Division of Nanobiomedicine and i-Lab, CAS Center for Excellence in Brain Science, Suzhou Institute of Nano-Tech and Nano-Bionics, Chinese Academy of Sciences, Suzhou, China
e-mail: qbwang2008@sinano.ac.cn

A. Benayas et al. (eds.), *Near Infrared-Emitting Nanoparticles for Biomedical Applications*, https://doi.org/10.1007/978-3-030-32036-2_11

PA	Photoacoustic
PBS	Phosphate-buffered saline
PEG	Poly(ethylene glycol)
PEI	Polyethylene imine
PET	Positron emission tomography
QDs	Quantum dots
QDSSCs	Quantum dot-sensitized solar cells
QY	Quantum yield
RES	Reticuloendothelial system
RfLuc	Red-emitting firefly luciferase
RGD	Cyclic arginine-glycine-aspartic acid peptide
RNase A	Ribonuclease-A
ROS	Reactive oxygen species
SDF-1α	Stromal cell-derived factor-1α
TEM	Transmission electron microscopy
TNAs	Titanium dioxide nanotube arrays
UCNPs	Upconversion nanoparticles
XANES	X-ray absorption near-edge structure

11.1 Introduction

With the revolutionary development of near infrared (NIR, 700–1700 nm) fluorescence nanoprobes, NIR fluorescence imaging (NIRFI) has become one of the most powerful tools in biomedical imaging research [1–3]. Among these nanoprobes, NIR fluorescent semiconductor quantum dots (QDs) have attracted considerable attentions in biomedical imaging for their good optical and chemical stability, large effective stokes shifts, tunable emission, and being capable of imaging multiple targets [2–5]. In particular, NIR-II-emitting (1000–1700 nm) QDs developed in recent years have significantly improved the tissue penetration depth, sensitivity, temporal and spatial resolution of QD-based in vivo fluorescence imaging because of the reduced absorption and scattering of NIR-II light in tissues [2–4, 6].

At present, a class of NIR-II emission QDs have been developed and applied in biomedical research, such as the group IV-VI NIR QDs (PbS, PbSe) [7, 8], group II-VI QDs (HgS, HgTe) [9, 10], group I-VI NIR QDs (Ag_2S, Ag_2Se, Ag_2Te) [11–17], group III-V NIR QDs (InAs, InP) [18, 19], group IV QDs (Si nanoparticles) [20, 21], and so forth (Table 11.1). These NIR-II emission QDs have a narrow bandgap typically less than 1.1 eV. And because of the confinement of electron movement in the nanocrystals called "quantum confinement effect," these semiconductor nanocrystals can exhibit strong and tunable fluorescence emission in the NIR-II window. Thus, they have been widely applied in various biomedical studies, including stem cell labeling and tracking, tumor diagnosis and therapy, imaging-guided tumor surgery, blood flow imaging, lymphatic system imaging, biosensing, and so forth. Consequently, numerous synthesis routes have also been developed to

Table 11.1 Properties, synthesis routes, and biomedical applications of typical NIR QDs emitting in the NIR-II window

Group	QDs	Emission (nm)	Size (nm)	QYs (%)	Synthesis routes	Biomedical applications	Ref.
Group IV-VI QDs	PbS	950–1400, 800–1050	4.45 ± 0.27, 4	20.3, 3.6	Water-phase synthesis or biomineralization	In vivo imaging in mice, bioluminescence resonance energy transfer imaging	[7, 22]
	PbSe	1238–1516, 1000–1850	7–12, 3–8	80	Organic phase synthesis and silica coating	Cell cytotoxicity study	[8, 23]
Group II-VI QDs	HgS	680–800	3.8 ± 0.2	4–5	Biomineralization	Metal-ion sensing	[9]
	HgTe	1300–5000	14.5	/	Two-step injection method	/	[10]
Group I-VI QDs	Ag_2S	975–1175, 1200	2.4–7, 5.4	15.5	Single-source precursor method	Stem cell tracking, tumor diagnosis, imaging-guided tumor surgery blood flow imaging, lymphatic system imaging, etc.	[13, 15, 16]
	Ag_2Se	1300, 700–820	2.3, 1.5–2.4	13.2	Solvothermal method	In vivo imaging of blood vessel, tracking of cell-derived microvesicles, etc.	[11, 17]
	Ag_2Te	995–1068, 930–1084	3.8–4.7	13.1–15.2, 20	One-pot aqueous synthesis, silica shell coating, etc.	Targeted imaging of tumor cells, etc.	[14, 24]
Group III-V QDs	InAs/CdSe/ZnSe	800–1600	1.9–6.3	40	Organic phase synthesis	/	[18]
	Cu:InP/ZnSe	630–1100	1.8–4	35–40	Epitaxial growth of a ZnSe diffusion barrier for the dopants	/	[19]
Group IV QDs	Si NPs	700–900	10, 126	10.2	Electrochemical etching of single-crystal silicon wafers, etc.	Imaging of tumor in live animals, cancer therapy	[20, 21]

prepare different types of NIR-II QDs. For a detailed overview of the NIR QDs, the reader is referred to a comprehensive review by Zhao and colleagues [3].

Among the existing NIR-II emission QDs, Ag_2S QDs have attracted a lot of attention from researchers because of their high potential in energy conversion, biomedical applications, and so forth. In the early research on Ag_2S QDs, narrow bandgap Ag_2S QDs were mainly developed for solar cell or photocatalysts study [4, 25, 26]. Due to their narrow bandgap energy, Ag_2S QDs can be utilized as the main light absorber and sensitizer in solar cells. For example, Hwang and colleagues developed an FTO/ZnO/CdS/Ag_2S electrode for quantum dot-sensitized solar cells (QDSSCs) with an improved short-circuit current (27.6 mA/cm^2) and an acceptable power conversion efficiency (2.4%) [25]. In addition, Ag_2S QD is also a promising material for photocatalysts. Li and colleagues prepared Ag_2S nanoparticles (NPs)-sensitized titanium dioxide nanotube arrays (Ag/TNAs) for photocatalysts [26]. Due to the sensitizing of narrow bandgap Ag_2S, the synthesized Ag/TNAs nanocomposites have a high capacity for absorbing visible light and a high photocatalytic efficiency of H_2 generation.

In 2010, Du et al. discovered Ag_2S quantum dots with high photoluminescence properties [12], which opened up the possibility of application of Ag_2S QDs in biomedical imaging. Nowadays, Ag_2S QDs have remained the most widely used QDs in biomedical imaging research among the existing NIR-II emission QDs [3, 4]. Because of the ultra-low solubility product constant ($K_{sp} = 6.3 \times 10^{-50}$) and absence of toxic heavy metals (Cd, Pb, As, and Hg), Ag_2S QDs have shown high biocompatibility in biological systems [15, 27–29]. In addition, Ag_2S QDs also possess several advantages, including tunable NIR-II emission, high quantum yield, and high photostability, thus have been successfully used in numerous biomedical imaging, including tumor diagnosis, anti-tumor drug evaluation, imaging-guided tumor surgery, in vivo stem cell tracking, and so forth [6, 30–33]. In particular, Ag_2S QD-based stem cell tracking methods with both high spatial and temporal resolution have been successfully developed and applied in a series of stem cell therapy models, which have not only improved our understanding of fundamental mechanisms of stem cell therapy but also offered a great opportunity for imaging-guided stem cell therapy [27, 30, 34]. In this chapter, methods for synthesizing photoluminescent Ag_2S QDs, surface functionalization strategies for preparing functional Ag_2S QDs, applications of Ag_2S QDs in stem cell-based regeneration medicine, and future prospects of Ag_2S QD-based research are systematically introduced and discussed.

11.2 Synthesis of Ag_2S QDs

The first synthesis of Ag_2S semiconductor colloidal NPs was reported by Brelle and colleagues in 1999 [35]. Then, a series of works were conducted to synthesize Ag_2S NPs by using different methods (Table 11.2). For instance, Liu and colleagues synthesized Ag_2S QDs with a mean diameter of 5.9 nm in water-in-supercritical

Table 11.2 Representative synthetic methods for preparing Ag_2S QDs

Synthesis method	Precursors	Solution	Temperature (°C)	Emission (nm)	Size (nm)	QYs (%)	Ref.
Organic synthesis method	$(C_2H_5)_2NCS_2Ag$	1-Dodecanethiol, cyclohexane, ethanol	130–160, 210	975–1175, 1200	2.4–7, 5.4	5.8, 15.5	[15, 16]
	Ag(OA), AgAc, S powder, hexamethyldisilathiane	Toluene	50, 80, 110	690–1227	1.5–4.6	0.15	[36]
	$AgNO_3$, 3-MPA	Ethylene glycol	145	510–1221	1.5, 6.3,	2.1	[37]
Aqueous phase synthesis	$AgNO_3$, Na_2S	Water	90	780–950	2.3–3.1	7–39	[38]
	$AgNO_3$, Sulfer-$N_2H_4{\cdot}H_2O$ complex	Water	95	687–1096	2.6–3.7	14.2–16.4	[39]
	Na_2S, $AgNO_3$, MPEG-SH, and CH_3COOH	Water	90	775–930	1.7–2.5	2–65	[40]
Cation-exchange synthesis	CdS QDs, $AgNO_3$	Water	Room temp.	905–1090	3.5	2.3	[41]
Biomimetic synthesis	$AgNO_3$, Na_2S	HepG2 cells	Room temp.	945	5.45	1.56	[42]
Photoinduced synthesis	Silver NPs, H_2S, aromatic thiol 4-tert-butylbenzenethiol	Toluene	10	820	2	/	[43]

CO_2 reverse microemulsion [44]. However, most of the synthesized Ag_2S NPs were used in solar cells or photocatalysts while the emission properties of Ag_2S NPs were not reported. In 2010, Du et al. firstly synthesized Ag_2S QDs with NIR emission at 1058 nm by using a single-source precursor method [12]. After that, a series of methods were developed to synthesize photoluminescent Ag_2S QDs, including organic phase synthesis, aqueous phase synthesis, cation-exchange synthesis, biomimetic synthesis, etc. (Table 11.2) [12, 38, 41–43]. In addition, methods for regulating the emission wavelength of Ag_2S QDs and synthesizing multifunctional Ag_2S QDs have also been developed [16, 32, 45].

11.2.1 Methods for Synthesizing Photoluminescent Ag_2S QDs

Nowadays, organic phase synthesis is the most widely used method for preparing photoluminescence Ag_2S QDs. Taking the first photoluminescent Ag_2S QDs for an example, the Ag_2S QDs were synthesized by a single-source precursor method in organic phase [12]. In this study, Ag(DDTC) $[(C_2H_5)_2NCS_2Ag]$ was used as a single-source precursor to prepare photoluminescent Ag_2S QDs in a mixture of oleic acid (OA), octadecylamine (ODA), and 1-octadecane (ODE) (Fig. 11.1a). The Ag(DDTC) contained both the silver metal and sulfur element, which can decompose under a certain temperature in organic solution to yield Ag_2S QDs. The as-synthesized Ag_2S QDs were single crystalline with a size distribution of 10.2 ± 0.4 nm (Fig. 11.1b). And the monoclinic Ag_2S QDs have an interplane distance in the lattice fringes of ~0.28 nm, which corresponds to that of the (112) facets in Ag_2S (Fig. 11.1c). With its narrow bulk bandgap of 0.9–1.1 eV, the Ag_2S QDs exhibited bright NIR emission at 1058 nm with a full-width at half-maximum of 21 nm (Fig. 11.1d and e). In addition to the single-source precursor method, a number of organic synthesis methods with modified routes also have been developed and proved to be effective strategies for the controlled preparation of high-quality Ag_2S QDs. For example, Jiang et al. developed a two-step organic method for synthesizing emission-tunable NIR Ag_2S QDs [36]. Moreover, aqueous phase synthesis, cation-exchange synthesis, biomimetic synthesis, and photoinduced synthesis methods also have been developed for preparing Ag_2S QDs (Table 11.2) [38, 41–43]. With the unique NIR emission properties, the as-obtained Ag_2S QDs may have great potential for biomedical imaging with high biocompatibility. For a detailed overview of the synthesis of Ag_2S QDs, the reader is referred to two comprehensive reviews by Gui and colleagues and Cui and colleagues [4, 46].

11.2.2 Emission Wavelength Regulation of Ag_2S QDs

As a typical direct bandgap semiconductor nanocrystalline, the emission wavelength of Ag_2S QDs can be regulated by the size of QDs because of the quantum

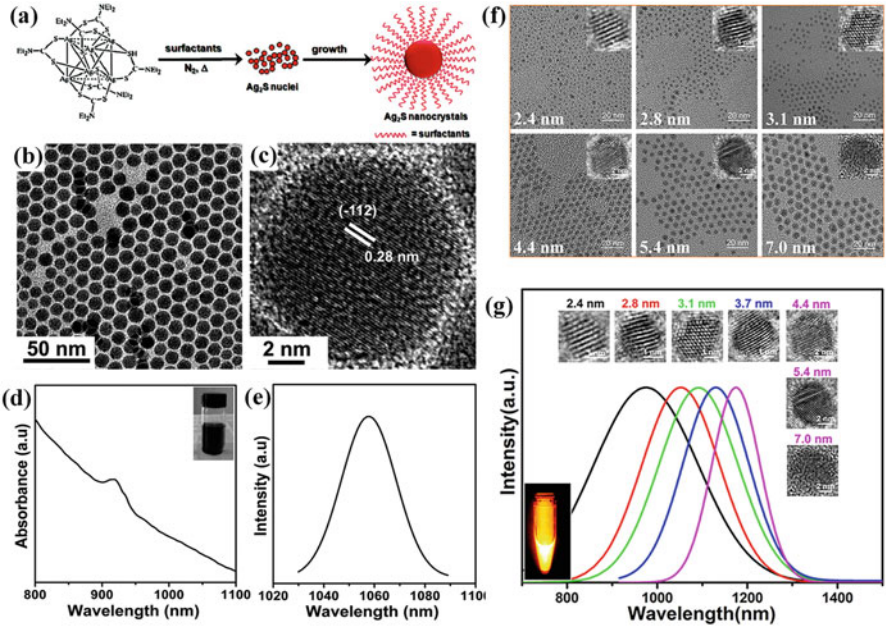

Fig. 11.1 Synthesis of Ag_2S QDs by a single-source precursor method. (**a**) Scheme illustrates the strategy for preparation of Ag_2S QDs from a single-source precursor of Ag(DDTC). (**b**) The transmission electron microscopy (TEM) image of as-synthesized Ag_2S QDs. (**c**) The high-resolution transmission electron microscopy (HRTEM) image of as-synthesized Ag_2S QDs. (**d**) NIR absorption spectrum of as-synthesized Ag_2S QDs. (**e**) NIR fluorescence emission spectrum of as-synthesized Ag_2S QDs. Reproduced with permission. [12] Copyright 2010, American Chemical Society. (**f**) Synthesis of Ag_2S QDs with different particle sizes from 2.4 to 7 nm. (**g**) Photoluminescence emission spectra of Ag_2S QDs with different particle sizes. Reproduced with permission. [16] Copyright 2014, American Chemical Society

confinement effect. For example, Jiang and colleagues found that the emission of Ag_2S QDs can be tuned from 690 to 1227 nm by increasing the size of Ag_2S [36]. Yang and colleagues synthesized a series of Ag_2S QDs with emission tunable from 1050 to 1294 nm by increasing the size of the Ag_2S QDs from 1.6 to 6.8 nm [47]. And more recently, Zhang and colleagues synthesized a number of high-quality Ag_2S QDs with tunable size from 2.4 to 7 nm by using the single-source precursor method [16]. Therefore, the emission wavelength of Ag_2S QDs can be precisely tuned from 975 to 1175 nm. In this study, thermal decomposition of Ag(DDTC) was used to produce the size-controlled nanocrystals. By controlling the reaction temperature from 130 to 230 °C and the reaction time from 1 to 60 min during the growth of Ag_2S nanocrystals under N_2 atmosphere, a series of Ag_2S QDs with a size of 2.4 nm, 2.8 nm, 3.1 nm, 3.7 nm, 4.4 nm, 5.4 nm, and 7 nm were obtained (Fig. 11.1f and g). Furthermore, Bohr radius, an important parameter to describe the smallest possible radius of an electron orbiting the nucleus in an atom of Ag_2S QDs, was experimentally determined to be 2.2 nm, which is consistent with the theoretical

result. These studies offered a fundamental understanding of the confinement effect of Ag_2S QDs and laid a solid ground for preparing Ag_2S QDs with tunable emission in the second near infrared window. Moreover, Ag_2S QDs with different emission wavelengths can be further used for simultaneously imaging multiple targets, which are urgently needed in numerous biomedical studies.

11.2.3 Synthesis of Multifunctional Ag_2S QDs

In order to meet the needs of complex biomedical imaging, a number of multifunctional Ag_2S QDs also have been developed using different synthesis strategies. By using a facile one-pot method, Shen et al. synthesized matchstick-shaped Ag_2S-ZnS heteronanostructures (HNSs) through thermal co-decomposing of single-source precursors Ag(DDTC) and $Zn(DDTC)_2$ in oleylamine/1-dodecanethiol [48]. The as-obtained Ag_2S-ZnS HNSs exhibited both NIR and UV/blue photoluminescence emissions due to the strong NIR emission of Ag_2S at 1155 nm and UV/blue emission of ZnS at approximately 380 and 450 nm. In another study of Shen and colleagues, the authors doped Mn in Ag_2S-ZnS HNSs by using a facile one-pot synthetic approach [49]. And the Mn-doped Ag_2S-ZnS HNSs showed multicolor emissions of blue, orange, and near infrared (Fig. 11.2a–d). With the multicolor emission property, the synthesized Ag_2S-ZnS HNSs may be potentially used in numerous biomedical studies, such as simultaneous bioimaging and optoelectronic devices.

On the other hand, multifunctional Ag_2S QDs have also been developed by integrating different contrast agents into Ag_2S QDs. For example, Wu et al. synthesized indocyanine green@polyethylene glycol-Ag_2S (ICG@PEG-Ag_2S) nanoprobes by assembling DT-Ag_2S QDs, amphipathic C18/PEG polymer molecules, and ICG [45]. The obtained ICG@PEG-Ag_2S can serve as a molecular probe for dual-modal NIRFI/photoacoustic (PA) imaging because Ag_2S QD is an ideal probe for NIRFI and ICG can serve as a contrast agent for PA imaging. Yang and colleagues synthesized Ag_2S nanodots through carefully controlled growth of Ag_2S in hollow human serum albumin nanocages. And the Ag_2S nanodots can serve as a theranostic agent for NIR-II fluorescence/PA multimodal imaging and simultaneous photothermal therapy (Fig. 11.2e and f) [50]. In another study, Li et al. conjugated a T1 MR imaging agent (Gd-DOTA) to the surface of Ag_2S QDs [32]. In this way, the synthesized Gd-Ag_2S nanoprobe can be used for in vivo T1-weighted MR/NIRFI dual-modal imaging. In a more recent study, Li and colleagues synthesized hybrid nanoparticle pyramids with Ag_2S QDs, Au-Cu_9S_5 NPs, and upconversion NPs (UCNPs) by smart pyramids self-assembly [51]. The as-synthesized multifunctional NPs can be used for NIR-II luminescence imaging, upconversion luminescence imaging, X-ray computed tomography (CT) imaging, and PA imaging in vivo. Moreover, the multifunctional NPs can also serve as an agent for tumor photothermal therapy. With the unique ability to provide multiple imaging information,

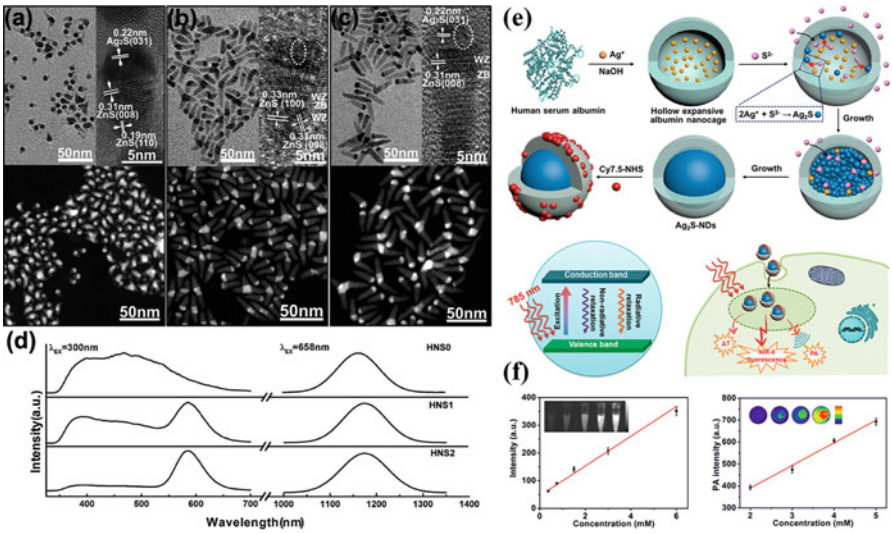

Fig. 11.2 Synthesis and applications of multifunctional Ag_2S QDs. (**a**–**c**) TEM, HRTEM, and STEM images of Mn-doped Ag_2S-ZnS HNSs named HNS0 (**a**), HNS1 (**b**), and HNS2 (**c**). (**d**) Normalized photoluminescence spectra of Mn-doped Ag_2S-ZnS HNSs. Reproduced with permission. [49] Copyright 2012, American Chemical Society. (**e**) Schematic illustration of Ag_2S nanodots synthesized through controlled growth of Ag_2S in hollow human serum albumin nanocages for in vivo dual model (NIR-II fluorescence/PA) imaging and photothermal therapy. (**f**) NIR-II fluorescence mapping and PA mapping of Ag_2S-NDs at various concentrations. Reproduced with permission. [50] Copyright 2017, American Chemical Society

these Ag_2S QD-based multimodal probes will provide numerous opportunities for potential applications in biomedical imaging researches, including stem cell tracking.

11.3 Surface Functionalization of Ag_2S QDs

The water solubility of QDs is a prerequisite for their biomedical applications. For the hydrophobic Ag_2S QDs prepared in organic phase, hydrophobic Ag_2S QDs should be converted into hydrophilic QDs by engineering their surface coating prior to their biomedical applications. Nowadays, numerous strategies have been developed to prepare hydrophilic Ag_2S QDs and improve their stability in biological systems [4, 6, 52]. In addition, the surface of Ag_2S QDs can be further functionalized with target or functional molecules for target imaging or specific biomedical studies [15, 27, 53, 54]. The large specific surface area and abundant reaction sites in QDs make them easier to surface functionalization, which also provides great potential for their applications in biomedical imaging researches.

11.3.1 Preparing Water Soluble and Stable Ag_2S QDs

Nowadays, a series of hydrophilic ligands have been developed to prepare hydrophilic Ag_2S QDs, such as dihydrolipoic acid (DHLA), 2-mercaptopropionic acid (2MPA), reduced glutathione (GSH), and so forth [6, 38, 52]. These ligands always contain one or more thiols so that they can bind well to the surface of Ag_2S QDs because of the high binding affinity between the bulk Ag_2S and the thiol. At present, ligand exchange and direct aqueous phase synthesis strategies are the most widely used methods to coat these ligands on the surface of Ag_2S QDs [6, 38, 52]. After surface coating, the water solubility, stability as well as the biocompatibility of Ag_2S QDs in biological systems can be distinctly increased. For example, Hong et al. converted hydrophobic Ag_2S QDs into hydrophilic QDs using the surfactant DHLA. Then, amine-functionalized six-armed PEG was conjugated to the DHLA-Ag_2S QDs by ethyl(dimethylaminopropyl) carbodiimide/N-hydroxysuccinimide (EDC/NHS) method to further improve the solubility and stability of Ag_2S QDs (Fig. 11.3) [6]. The as-prepared PEG-DHLA-Ag_2S QDs exhibited stable NIR-II emission at 1200 nm and showed highly soluble and stable under various aqueous and buffer conditions, including phosphate buffered saline (PBS), fetal bovine serum (FBS), and cell culture media (RPMI 1640) [6, 55]. With such high stability, the circulating half-life of PEG-Ag_2S QDs in the blood could reach 4.37 ± 0.75 h. In addition, in vitro and in vivo toxicity studies showed the hydrophilic Ag_2S QDs were highly biocompatible for biomedical studies [15, 29], suggesting the surface coating strategy by using the ligands of DHLA and PEG is an ideal method to prepare highly water soluble, stable, and biocompatible Ag_2S QDs. And the development of PEG-Ag_2S QDs lays a solid foundation for further biomedical applications of Ag_2S QDs.

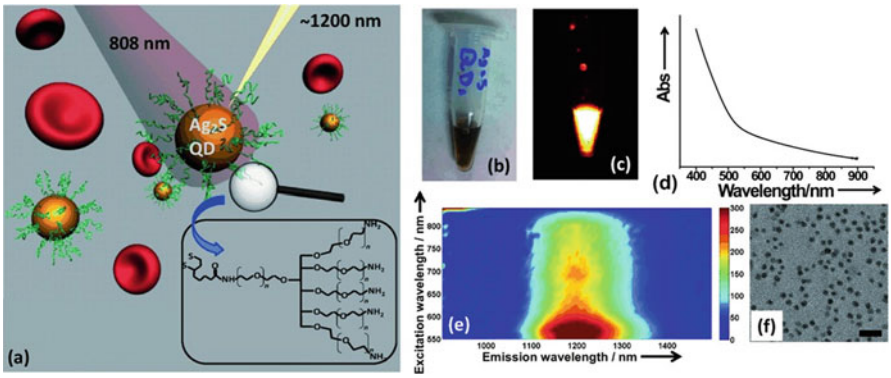

Fig. 11.3 Hydrophilic Ag_2S QDs with DHLA and PEG coating. (**a**) A scheme showing the hydrophilic PEG-Ag_2S QDs that emit at 1200 nm. (**b**) A white-light optical image of the PEG-Ag_2S QDs in PBS. (**c**) The photoluminescence image of the PEG-Ag_2S QDs solution under 808 nm excitation. (**d**) The absorption spectrum of the PEG-Ag_2S QD solution. (**e**) The photoluminescence versus excitation spectrum of the PEG-Ag_2S QD solution. (**f**) The TEM image of PEG-Ag_2S QDs. Scale bar = 20 nm. Reproduced with permission. [6] Copyright 2012, Wiley

11.3.2 Surface Functionalization and Biomedical Applications of Ag_2S QDs

Benefiting from the large specific surface area and abundant reaction sites in Ag_2S QDs, the surface of Ag_2S QDs can be further functionalized with target or functional molecules for cell labeling, tumor targeting and detection, biosensing, and other specific biomedical studies (Table 11.3). For example, Chen et al. synthesized Ribonuclease-A (RNase A) conjugated Ag_2S QDs via biomimetic route [60]. The RNase A-Ag_2S QDs showed highly stable and biocompatible properties and had potential applications for molecular imaging. Wang et al. conjugated anti-VEGF to the surface of the BSA-stabilized Ag_2S QDs. The as-synthesized anti-VEGF-Ag_2S QDs can be used for targeting VEGF-positive U87-MG tumors [61]. Zhang et al. conjugated cetuximab (Erbitux) protein and cyclic arginine-glycine-aspartic acid (RGD) peptides to the carboxyl groups on Ag_2S QD surfaces through the EDC/NHS method. Thus, the Erbitux-Ag_2S QDs or RGD-Ag_2S QDs can be used to specifically label EGFR-positive MDA-MB-468 cell line or $R_v\beta_3$-positive U87 MG cell line, respectively [15]. In a more recent study, a cell-penetrating peptide (Tat peptide) was conjugated to the surface of PEG-Ag_2S QDs through covalent bonding using the crosslinking reagent Sulfo-SMCC (Fig. 11.4a) [27]. The as-prepared

Table 11.3 Surface functionalization and biomedical applications of Ag_2S QDs

Surface functionalization	Biomedical applications	Ref.
Conjugated with Tat peptide	Labeling and tracking of transplanted stem cell	[27, 30]
Conjugated with RGD peptide	Labeling of U87-MG cells, 4T1 cells and MCF-7 cells, detecting glioma, breast cancer, etc.	[15, 33, 56, 57, 58, 59]
Conjugated with Erbitux	Target labeling of MDA-MB 468 cells	[15]
Coated with Ribonuclease-A	Decrease toxicity on HEK293T cells	[60]
Conjugated with anti-VEGF	Targeting VEGF-positive U87 MG tumors	[61]
Conjugated with alendronate	Bone targeting and bone tumor therapy	[62]
Conjugated with aptamer	Targeting MCF-7 cells or circulating tumor cells, and serve as an imaging agent for cancer diagnosis	[61, 63]
Conjugated with FA	Targeting FA-receptor overexpressed HeLa cells	[40, 64, 65]
Coated with Chitosan	In vivo imaging and light-triggered nitric oxide release	[66]
Coated with simian virus 40 protein nanocages and PEG	In vivo tracking of virus protein nanocages	[67]
Coated with PEG and Dox	Serve as a theranostic nanoplatform for tumor	[68]
Conjugated with PEI	Sensitive and selective detection of heparin and heparinase I	[69]
Coated with thioglycolic acid	Selective detection of Zn^{2+} and Cd^{2+}	[70]

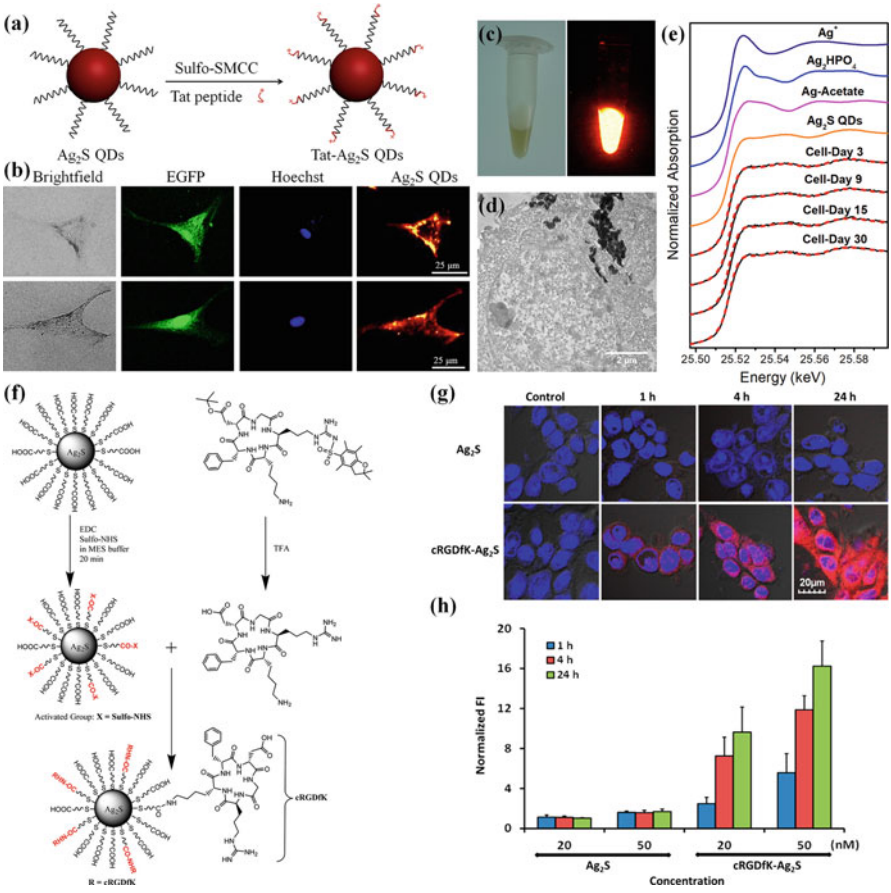

Fig. 11.4 Biomolecule functionalized Ag_2S QDs for cell or tissue targeting. (**a**) Schematic illustration of preparing the Tat-Ag_2S QDs for stem cell labeling. (**b**) Fluorescence images of MSCs labeled by Tat-Ag_2S QDs. Red hot: Ag_2S QDs. Green: EGFP. Blue: Hoechst. Reproduced with permission. [34] Copyright 2018, Wiley. (**c**) A white-light and photoluminescence image of the Ag_2S QDs-labeled MSCs solution. (**d**) Represent TEM images of Ag_2S QDs-labeled MSCs, black indicate the Ag_2S QD aggregations in cells. (**e**) Ag XANES spectra of the Ag_2S QD-labeled MSCs. The black solid lines show the spectra of Ag_2S QD-labeled MSCs. The red broken lines show the fit with data sets of the reference compounds. Reproduced with permission. [27] Copyright 2014, Wiley. (**f**) Schematic illustration of preparing the cRGDfK-Ag_2S QDs. (**g**) Internalization of cRGDfK-Ag_2S QDs in 4T1 cells. Red color indicates the fluorescence of cRGDfK-Ag_2S QDs. (**h**) Quantitative analysis of the fluorescence intensity in images of (**g**). Reproduced with permission. [58] Copyright 2015, American Chemical Society

Tat-Ag_2S QDs could effectively label mesenchymal stem cells (MSCs) without affecting the viability and stemness of MSCs. After penetrating into the cell, Ag_2S QDs were found predominantly located in the cytoplasm of cells (Fig. 11.4b–d). More importantly, the ultra-low solubility product constant ($K_{sp} = 6.3 \times 10^{-50}$) of

Ag_2S QDs ensures that Ag_2S QDs will not degrade within cells. The synchrotron radiation-based X-ray absorption near-edge structure (XANES) spectrum study further confirmed that Ag_2S QDs were extremely stable in MSCs without detectable degradation up to 30 days (Fig. 11.4e).

In addition to cell labeling and tracking, numerous surface functionalization strategies have also been developed for targeting and detecting different tumors in vivo. For example, Ag_2S QDs were conjugated with cyclic RGD peptides and had been extensively used for targeting glioma and breast cancer (Fig. 11.4f–h) [15, 33, 56–59]. In another example, Ag_2S QDs were conjugated with folate (FA) and showed enhanced targeting ability to FA-receptor overexpressed cervical tumor (HeLa) [40, 64, 65]. After being modified with targeting aptamers, Ag_2S QDs were successfully applied in targeting MCF-7 cells or circulating tumor cells and served as an imaging agent for cancer diagnosis [61, 63]. In a more recent study, Li and colleagues conjugated Ag_2S QDs with bone targeting alendronate (Ald). Then, the Ald-Ag_2S QDs were successfully applied for bone tumor treatment [62].

Surface functionalization strategies also enable Ag_2S QDs to be used in other biomedical fields such as biosensing [69–72]. For example, Ag_2S QDs were conjugated with polyethylene imine (PEI) and applied in sensitive and selective detection of heparin and heparinase I [69]. In another example, Ag_2S QDs were coated with thioglycolic acid and then can be used for selective detection of Zn^{2+} and Cd^{2+}. In addition, Ag_2S QDs have also been developed for photoelectrochemical detection of glucose and cancer cells [72].

11.4 Biocompatibility of Ag_2S QDs

The high biocompatibility of QDs is another prerequisite for their biomedical applications and further clinical transformation. Thus, numerous studies have been performed to study the biocompatibility of Ag_2S QDs in vitro and in vivo.

11.4.1 In Vitro Toxicity Study of Ag_2S QDs

The in vitro toxicity of Ag_2S QDs has been extensively studied in numerous cell lines, such as mouse fibroblast L929 cells, U87-MG cells, HEK293T cells, and stem cells. The ultra-low solubility product constant ($K_{sp} = 6.3 \times 10^{-50}$) of Ag_2S QDs ensures the minimal degradation of Ag_2S QDs within cells. In the study of Chen and colleagues, it has been found that Ag_2S QDs were extremely stable in cells without detectable degradation up to 30 days by using the synchrotron radiation-based XANES method [27]. The high chemical stability of Ag_2S QDs also ensures the high compatibility of Ag_2S QDs in biological systems. In an in vitro cytotoxicity testing, Zhang and colleagues exposed fibroblast L929 cells to Ag_2S QDs at five different concentrations (6.25, 12.5, 25, 50, and 100 μg/mL) for 72 h and found

that Ag_2S QDs did not inhibit cell proliferation, induce reactive oxygen species (ROS), trigger apoptosis and necrosis, or cause DNA damage in L929 cells [15]. In another study, Chen and colleagues also found Ag_2S QDs are highly biocompatible to HEK293T cells [60]. By using the fish cell lines (RTG-2), Munari and colleagues found CdS QDs exhibited a concentration-dependent genotoxicity in the sub-toxic range (0.01–1 μg/ml) while Ag_2S showed neither genotoxic nor cytotoxic effects [28].

In addition to normal cell lines, the potential cytotoxicity of Ag_2S QDs on stem cells has also been explored. As shown in Fig. 11.5a–h, hMSCs were treated with Tat-Ag_2S QDs at different concentrations (0, 6.25, 12.5, 25, and 50 μg/mL) for 24 h. It was found that Tat-Ag_2S QDs could effectively label MSCs without causing of ROS production, apoptosis/necrosis, and DNA damage in hMSCs (Fig. 11.5b–e) [27]. Moreover, Ag_2S QDs did not affect the proliferation, tropism capability, adipogenic and osteogenic differentiation, stemness gene (Nanog, Rex-1, Oct4, and Sox2) expression of hMSCs and their therapeutic abilities for liver and wound regeneration [27, 30]. The cell-penetrating peptide functionalization in combination with the high stability and high biocompatibility nature of Ag_2S QDs, the as-synthesized Tat-Ag_2S QDs may have great application prospects in labeling and in vivo tracking of stem cells. The high biocompatibility of Ag_2S QDs in biological systems laid a solid foundation for biomedical applications of Ag_2S QDs.

11.4.2 In Vivo Toxicity of Ag_2S QDs

The detailed studies of in vivo toxicity of Ag_2S QDs have also been performed in mice (Fig. 11.5i–k). In the study performed by Zhang and colleagues [29], PEGylated-Ag_2S QDs at a dose of 15 and 30 mg/kg were injected into mice and the biodistribution, pharmacokinetics, and toxicology of Ag_2S in mice were systematically studied. It was found that the injected PEGylated-Ag_2S QDs have no adverse effect on the body weight of mice during the 2-month experiment. Moreover, hematological toxicity assay and blood biochemistry analysis also demonstrated Ag_2S QDs do not cause appreciable toxicity at our tested doses (15 and 30 mg/kg) (Fig. 11.5k). Histological examinations of the liver, spleen, and kidney showed no obvious lesions or signs of hydropic damage were caused by Ag_2S QDs (Fig. 11.5j).

The biodistribution assay of Ag_2S QDs showed that the PEGylated-Ag_2S QDs were widely distributed in different organs and tissues and mainly accumulated in the reticuloendothelial system (RES) including liver and spleen after injection (Fig. 11.5i). And then, most of the PEGylated-Ag_2S QDs in mice were cleared out from the body at 60 days after injection, and a small amount of Ag_2S remained in liver, spleen, skin, bone, and intestine. It was also found that the injected Ag_2S QDs could be gradually cleared out mainly by fecal excretion. Similarly, Cheng and colleagues synthesized Ag_2S/chlorin e6 (Ce6)/DOX@DSPE-mPEG2000-folate (ACD-FA) and explored the in vivo toxicity of the ACD-FA in mice [64]. By injecting 1 mg of

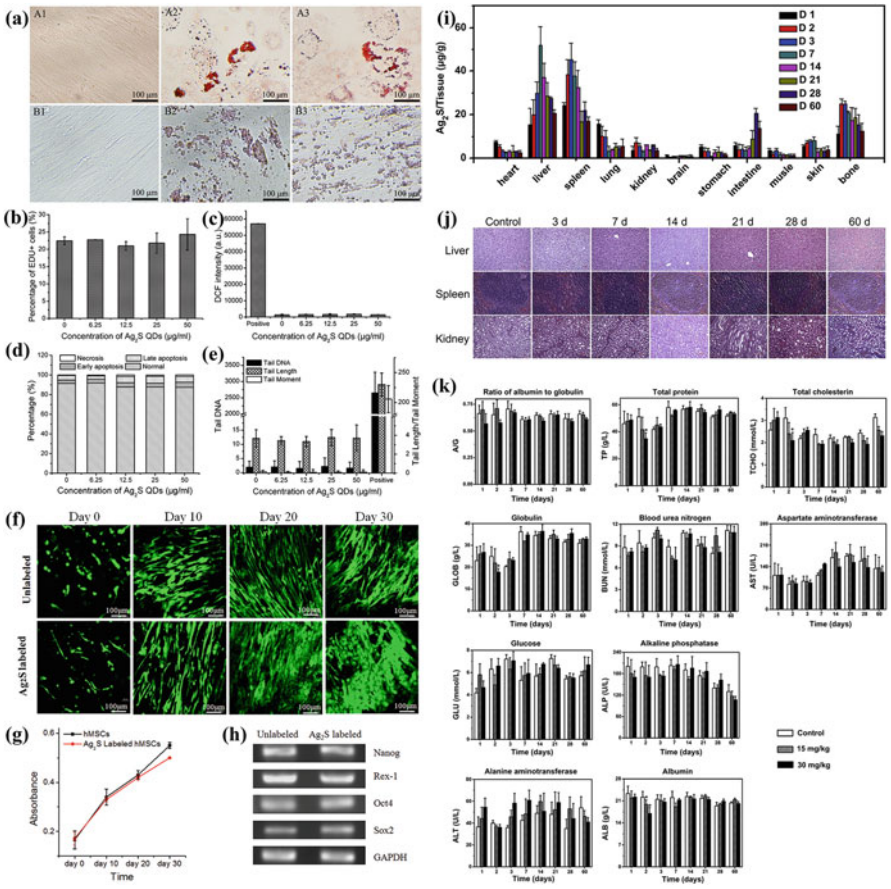

Fig. 11.5 In vitro and in vivo toxicity of Ag_2S QDs. (**a**) Effects of Ag_2S QDs on adipogenic (A1-A3) and osteogenic (B1-B3) differentiation of hMSCs. (**b**) Effects of Ag_2S QDs on cell proliferation. (**c**) ROS generation assay. (**d**) Apoptosis and necrosis assay. (**e**) DNA damage assay. Reproduced with permission. [27] Copyright 2014, Wiley. (**f**–**g**) Proliferation assessment of hMSCs and Ag_2S QDs-labeled hMSCs cultured in collagen scaffolds by calcein-AM staining (**f**) and 3-(4,5-dimethylthiazol-2-yl)-2,5-diphenyltetrazolium bromide (MTT) assay (**g**). (**h**) Stemness gene expression assay of hMSCs and Ag_2S QDs-labeled hMSCs. Reproduced with permission. [30] Copyright 2015, Elsevier. (**i**) Long-term biodistribution of PEGylated-Ag_2S QDs in Balb/c mice injected at a dosage of 15 mg/kg body weight. (**j**) H&E stained images of liver, spleen, and kidney collected from the control untreated mice and PEGylated-Ag_2S QDs (30 mg/kg) injected mice. (**k**) Blood biochemistry assay of Balb/c mice treated with PEGylated-Ag_2S QDs at the dose of 15 and 30 mg/kg. Reproduced with permission. [29] Copyright 2013, Elsevier

ACD-FA into BALB/c mice, the researchers found that the ACD-FA was nontoxic to normal mouse organs and was almost completely cleared out from the body 15 days after injection. Thus, the ACD-FA may serve as a safe agent for effective tumor therapy.

11.5 In Vivo Stem Cell Tracking Applications of Ag_2S QDs

Stem cell-based regenerative medicine has shown great potential for treating numerous incurable diseases [73–76]. Tracking and understanding the biodistribution, viability, and regenerative capabilities of transplanted stem cells in vivo is vital for improving the therapeutic efficacy and safety of stem cell-based therapy [77]. Thus, numerous NIR fluorescent nanoprobes have been developed for in vivo tracking of the transplanted stem cells [78–80]. Benefiting from the reduced photon absorbance, scattering, and autofluorescence in tissues, fluorescence imaging in the NIR-II region possesses several advantages for in vivo imaging, including high tissue penetration depth and excellent spatial and temporal resolution [1, 81]. By using NIR-II emission Ag_2S QDs, a high tissue penetration depth of better than 1.2 cm, a spatial resolution of approximately 25 μm, and a temporal resolution of approximately 30 ms have been achieved in in vivo fluorescence imaging [55]. In combination with its high stability and biocompatibility, Ag_2S QDs have shown as one of the excellent fluorescence probes for labeling and tracking of transplanted stem cells [27, 30, 34]. Thus, the real-time translocation, accurate distribution, and fate of transplanted stem cells in mouse models of liver and cutaneous regeneration have been explored by using the Ag_2S QD-based NIRFI [27, 30, 34]. The imaging findings are not only crucial for understanding the fundamental behaviors of transplanted stem cells but also help to improve the safety and therapeutic efficiency of stem cell therapy.

11.5.1 Tracking Transplanted Stem Cells for Liver Therapy

MSCs have shown great potential in treating of numerous liver diseases [74, 75]. However, the migration behaviors and engraftment efficiency of transplanted MSCs in living animal model are not fully understood partly due to the absence of in vivo imaging strategies with excellent sensitivity, high spatial and temporal resolution. By using the highly biocompatible and chemically stable Ag_2S QDs, for the first time, the whole-body translocation of MSCs in mice can be directly observed with both desirable sensitivity, and high temporal and spatial resolution [27].

First, the in vivo detecting sensitivity of stem cells can be distinctly improved by using the NIR-II-emitting Ag_2S QDs because of the high quantum yield of Ag_2S QDs (~15.5%) and the minimal autofluorescence of tissues in the NIR-II region [6, 12]. Thus, as few as 1000 of subcutaneously transplanted cells could be detected by using Ag_2S QD-based NIRFI. This detection sensitivity is much better than the imaging strategy using CdSe@ZnS 655 QDs, which only a detection limit of 50,000 subcutaneously transplanted cells was achieved [82].

Second, with the excellent properties of high temporal resolution, Ag_2S QD-based NIRFI can be applied in real-time monitoring of transplanted stem cells [34]. In the mouse model of acute liver failure, the whole-body translocation of

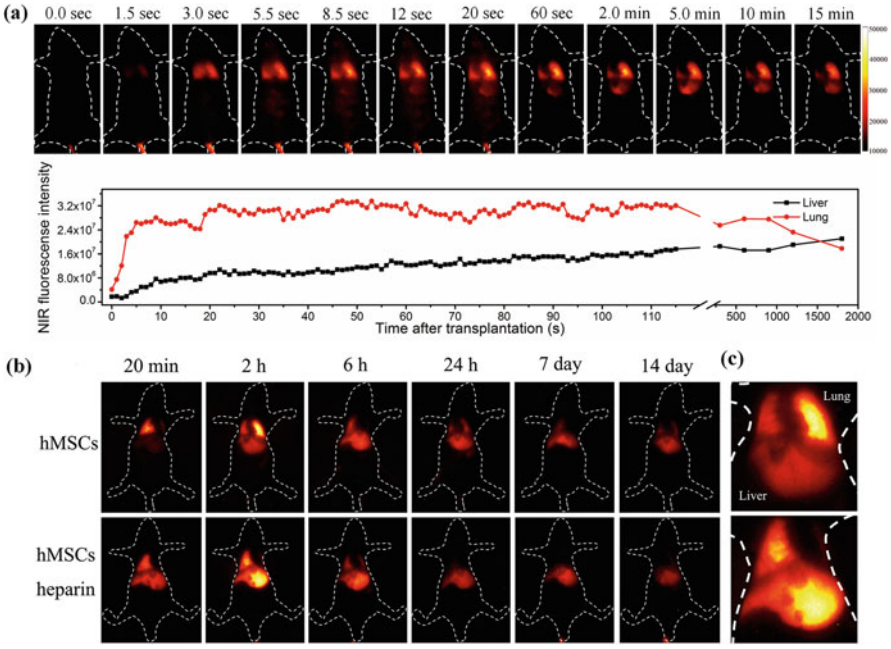

Fig. 11.6 Tracking of the transplanted MSCs in the mouse model of acute liver failure using NIR-II emission Ag_2S QDs. (**a**) In vivo real-time imaging of intravenously injected MSCs with a temporal resolution of 100 ms. Reproduced with permission. [34] Copyright 2018, Wiley. (**b**) Long-term tracking of intravenously transplanted MSCs with or without heparin in mice up to 14 days. (**c**) Higher magnification photoluminescence image of mice after 2 h of MSC transplantation in (**b**). Reproduced with permission. [27] Copyright 2014, Wiley

intravenously injected MSCs was observed with a temporal resolution of 100 ms. After intravenous injection, MSCs were firstly accumulated in the lung, maximized within 10 s, sustained for 2 min, and then gradually decreased and transferred to the liver (Fig. 11.6a). Furthermore, the amount of stem cells accumulated in the lung or liver can be semi-quantified by measuring the intensity of NIR-II fluorescence. The real-time monitoring of stem cell translocation is of great importance for the development of high-efficiency stem cell transplantation strategies aimed at improving the therapeutic potential of stem cell therapy.

Third, benefiting from the high spatial resolution of NIRFI, the accurate distribution of transplanted MSCs in the lung and liver of mice can be clearly observed, revealing that the heparin can accelerate the migration of MSCs from the lung to the liver (Fig. 11.6b and c) [27]. Moreover, Ag_2S QDs can also be used for long-term stem cell tracking due to the excellent chemical stability and photostability of Ag_2S QDs. For example, the NIR fluorescence of 1000 Ag_2S-labeled MSCs could be detected and no significant decrease was observed for up to 30 days after subcutaneous transplantation. Thus, the long-term distribution and translocation of

transplanted MSCs in the lung and liver of mice could be monitored up to 14 days, showing a part of transplanted MSCs retained in the liver and contribute to the liver regeneration (Fig. 11.6b).

11.5.2 Tracking Stem Cells for Cutaneous Regeneration

Mesenchymal stem cells (MSCs) have numerous therapeutic potentials for improving cutaneous wound regeneration in clinical practice [83]. However, the homing behavior of transplanted MSCs to the wound and the accurate distribution of transplanted stem cells in the wound microenvironment are still poorly understood. By using the Ag_2S QD-based NIRFI, the homing behavior of intravenously transplanted MSCs to the wound with and without stromal cell-derived factor-1α (SDF-1α) was directly visualized due to the desirable sensitivity and spatial resolution of the Ag_2S QD-based NIRFI (Fig. 11.7). It was found that the intravenously transplanted MSCs were slowly recruited at the wound and predominantly accumulated around the edge of the wound without SDF-1α. For the wound treated with the SDF-1α, much more MSCs were recruited at the wound within a much shorter time and thus enhanced the neovascularization, the re-epithelialization, and accelerated the wound healing.

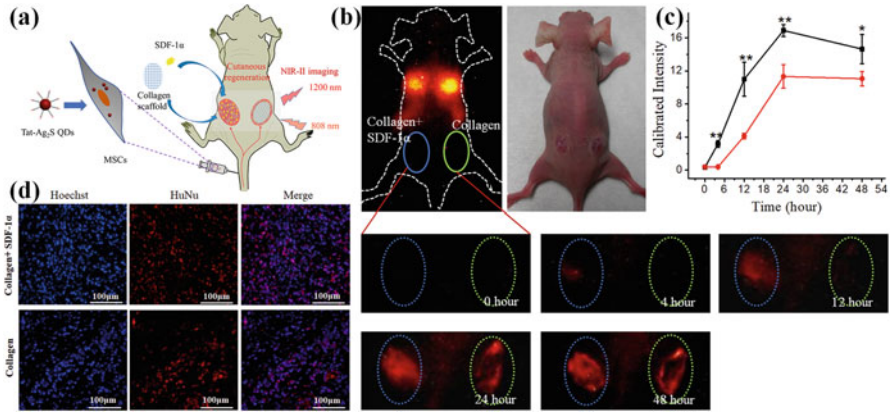

Fig. 11.7 Tracking of Ag_2S QD-labeled MSCs in the mouse model of cutaneous wound regeneration. (**a**) Schematic illustration of MSCs tracking in the mouse model of cutaneous wound regeneration. (**b**) In vivo NIRFI of mice at 0, 4, 12, 24, and 48 h after intravenous transplantation of Ag_2S QD-labeled MSCs. (**c**) Fluorescence quantifying the accumulation of intravenously transplanted MSCs in the wound with or without SDF-1α treatment ($n = 3$). $_{*}p < 0.05$, $_{**}p < 0.01$. (**d**) Immunofluorescence stain of the transplanted scaffolds with anti-human nuclear antigen antibody (HuNu). Blue: Hoechst. Red: HuNu. Reproduced with permission. [30] Copyright 2015, Elsevier

11.5.3 *Tracking the Fate of Stem Cells by Ag_2S QD-Based Multimodal Imaging*

Single modality imaging methods always have their inherent limitations thus are not possible to fully resolve the behaviors of the transplanted stem cells. Multimodal imaging strategies have shown great potential to overcome the above-mentioned limitations by combining the advantages of multiple imaging modalities. For Ag_2S QD-based imaging, numerous multimodal imaging technologies have been developed and applied in a series of biomedical imaging researches, such as the dual-modal NIRFI/PA imaging [45], the dual-modal T1-weighted MRI/NIRFI imaging [32], and the dual-modal BLI/NIRFI imaging [34]. Among these multimodal imaging strategies, the dual-modal BLI/NIRFI imaging have been successfully developed and applied in monitoring the fate of transplanted stem cells [34].

In this study, a dual-labeling strategy by using the exogenous Ag_2S QDs and endogenous red-emitting firefly luciferase (RfLuc) reporter gene were developed to label MSCs (Fig. 11.8). Thus, a dual-modal BLI/NIRFI imaging strategy was

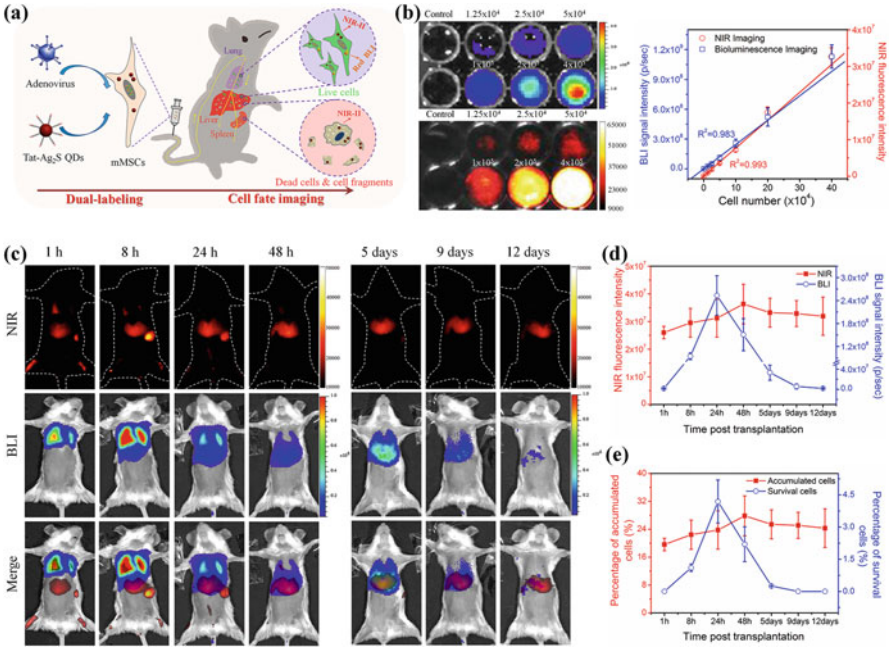

Fig. 11.8 A BLI/NIRFI dual-modal imaging strategy for tracking the fate of transplanted MSCs. (**a**) Schematic illustration of the BLI/NIRFI dual-modal imaging strategy. (**b**) In vitro BLI and NIRFI of MSCs dual-labeled by exogenous Tat-Ag_2S QDs and endogenous RfLuc. Rainbow: BLI. Red hot: NIRFI. (**c**) In vivo tracking the translocation and survival of intravenously injected MSCs in mice with acute liver failure by the BLI/NIRFI multimodal imaging method. (**d**–**e**) Quantifying the signal intensities of BLI and NIRFI in liver of mice. Reproduced with permission. [34] Copyright 2018, Wiley

successfully applied to monitor the fate of transplanted MSCs in a mouse model of acute liver failure (Fig. 11.8a and b). In this system, BLI of red-emitting RfLuc was used to specifically identify the living stem cells in vivo because only live cells can express RfLuc. And the NIR-II fluorescence of Ag_2S quantum dots was used to monitor the translocation of all transplanted MSCs in vivo with both high spatial and temporal resolution. By co-registering NIRFI signals with BLI signals in mice, the NIRFI signals combined with BLI signals can be used to indicate the living cells and the sole NIRFI signals can be used to indicate the dead cell components, thus allowing differentiating living cells from dead cell components in situ and in vivo reporting the fate of the transplanted stem cells (Fig. 11.8c–e). More interestingly, it was also clearly revealed that the time-dependent therapeutic effects on the acute liver failure after transplantation of MSCs coincided with the amount of live MSCs accumulated in the liver. Utilizing the cell fate monitoring capability of the dual-label system, the dual-modal imaging strategy will have great application prospects in a broad range of biomedical and stem cell researches, such as imaging-guided cell therapy, and so on.

11.6 Future Prospects

As a novel NIR-II emission nanoprobe, Ag_2S QDs possess a series of advantages including high compatibility, excellent chemical stability and photostability, and high quantum yield. Nowadays, numerous synthesis methods, surface functionalization strategies, and biomedical imaging applications of Ag_2S QDs have been successfully developed. In particular, the development of Tat-Ag_2S QD and its application to in vivo track transplanted stem cells in different stem cell therapy models have greatly enhanced the sensitivity, tissue penetration depth, spatiotemporal resolution of fluorescence imaging-based stem cell tracking method, and improved our understanding of the biodistribution, fate, and regenerative capabilities of transplanted stem cells. At present, the potential of utilizing Ag_2S QDs for in vivo stem cell tracking has only just performed in several stem cell therapy models [27, 30, 34]. To further improve the utility of Ag_2S QDs in stem cell-based regeneration studies and other biomedical studies, it is still necessary to further improve the Ag_2S QD-based fluorescence imaging in various aspects.

First, several molecular imaging nanoprobes have been tested in clinical trials, such as the ^{124}I-labeled cRGDY silica nanomolecular particle for positron emission tomography (PET) imaging of malignant brain tumor (Clinical Trials Registry, NCT 01266096) and fluorescent cRGDY PEG-Cy5.5 C dots for lymph node mapping (Clinical Trials Registry, NCT 02106598). Although Ag_2S QDs have been widely used in small animal model-based biomedical studies, clinical trials by using Ag_2S QDs have not been achieved yet. Unlike the well-studied silica dots, the safety of the inorganic semiconductor Ag_2S QDs, including the potential toxicity and the clearance of injected QDs, are not fully understood in preclinical studies. More studies involving the toxicity of Ag_2S QDs in large animal-based preclinical

studies are urgently needed before they are applied in clinical trials. Moreover, issues including the particle size, morphology features, surface functionalization of Ag_2S QDs should be carefully considered and studied to further improve the biocompatibility and pharmacokinetics of Ag_2S QDs in future preclinical and clinical studies.

Second, the quantum yield (QY) of Ag_2S QDs should be further improved to meet the needs of highly sensitive imaging in biomedical research and their further clinical applications. To date, the QY of NIR-II Ag_2S QDs is generally below 20%, which is still much lower than that of visible or NIR-I QDs [4, 5]. A series of parameters including the structure, composition, size, and surface coatings are all involved in the QY of QDs [4]. Thus, new synthesis methods and surface functionalization methods are needed to further improve the QY of Ag_2S QDs. And the high QY Ag_2S QDs may have great potentials in numerous biomedical applications, such as single cell detection, long-term cell tracking, and even single molecule detection. Moreover, the high fluorescence QY can distinctly reduce the dosage of Ag_2S QDs administrated in vivo and help to avoid the potential toxicity caused by a high dosage QDs in the future clinical utility.

Third, multimodal imaging has shown great potential to imaging multiple molecule events in biomedical research that cannot be resolved by a sole imaging method. However, Ag_2S QD-based multimodal imaging strategies are still quite limited. Thus, more multifunctional Ag_2S QDs and Ag_2S QD-based multimodal imaging strategies may be needed to further improve the applications of Ag_2S QDs in biomedical studies. In particular, multimodal imaging strategies that can simultaneously monitor the distribution, viability, and multiple differentiation behaviors of transplanted stem cells are urgently needed. Such multiple behaviors of stem cells after transplantation are crucial for fully understanding the regenerative mechanisms of transplanted stem cells and further improving the stem cell therapy. On the other hand, how exogenous and endogenous stem cells as well as other types of host cells participate in the therapeutic process is another critical issue that involved in the therapeutic efficiency of the stem cell therapy, which is not well understood. With the excellent nature of fluorescence imaging for multichannel imaging, it offers a high possibility for simultaneously tracking multiple functions of stem cells or multiple types of cells by using Ag_2S QDs with different emission wavelength [16]. In addition, further development of multimodal BLI/NIRFI imaging methods to integrate more imaging channels between the broad spectral regions of 400 to 1700 nm may also have great opportunities to simultaneously monitor multiple functions of stem cells.

Finally, benefiting from deep tissue penetration depth, NIR-II fluorescence can penetrate deep into tissues and may be used to regulate the in vivo behavior of stem cells. For example, UCNP-mediated optogenetics has been successfully applied to stimulate deep brains with high tissue penetrating NIR-II fluorescence [84]. Therefore, the development of Ag_2S QD-based stem cell regulation strategies by utilizing the advantages of NIR-II fluorescence may offer great opportunities for regulating the therapeutic behavior of stem cells in vivo and improving stem cell-based regenerative therapy.

Acknowledgements This work was supported by the National Key Research and Development Program (2016YFA0101503, 2017YFA0205503), the Strategic Priority Research Program (Grant No. XDB32030200) and Youth Innovation Promotion Association Program from Chinese Academy of Sciences (CAS), the National Natural Science Foundation of China (Grant No. 21778070, 21671198, 21425103, 21501192), the National Natural Science Foundation of Jiangsu Province (Grant BK20170066, BE2016682).

Author Contributions Statement
G.C.C., Y.J.Z., C.Y.L., and Q.B.W. outlined the chapter, co-wrote the chapter manuscript, and made revisions to the content.

Competing Financial Interest(s) Disclosure
The authors declare no competing financial interests.

References

1. Hong GS, Antaris AL, Dai HJ (2017) Near-infrared fluorophores for biomedical imaging. Nat Biomed Eng 1(1):0010
2. Kim D, Lee N, Park YI, Hyeon T (2017) Recent advances in inorganic nanoparticle-based NIR luminescence imaging: semiconductor nanoparticles and lanthanide nanoparticles. Bioconjug Chem 28(1):115–123
3. Zhao P, Xu Q, Tao J, Jin Z, Pan Y, Yu C, Yu Z (2018) Near infrared quantum dots in biomedical applications: current status and future perspective. Wiley Interdiscip Rev Nanomed Nanobiotechnol 10(3):e1483
4. Gui RJ, Jin H, Wang ZH, Tan LJ (2015) Recent advances in synthetic methods and applications of colloidal silver chalcogenide quantum dots. Coordin Chem Rev 296:91–124
5. van Veggel FCJM (2014) Near-infrared quantum dots and their delicate synthesis, challenging characterization, and exciting potential applications. Chem Mater 26(1):111–122
6. Hong G, Robinson JT, Zhang Y, Diao S, Antaris AL, Wang Q, Dai H (2012) In vivo fluorescence imaging with Ag_2S quantum dots in the second near-infrared region. Angew Chem Int Ed Engl 51(39):9818–9821
7. Chen J, Kong YF, Wang W, Fang HW, Wo Y, Zhou DJ, Wu ZY, Li YX, Chen SY (2016) Direct water-phase synthesis of lead sulfide quantum dots encapsulated by beta-lactoglobulin for in vivo second near infrared window imaging with reduced toxicity. Chem Commun 52(21):4025–4028
8. Tan TT, Selvan ST, Zhao L, Gao SJ, Ying JY (2007) Size control, shape evolution, and silica coating of near-infrared-emitting PbSe quantum dots. Chem Mater 19(13):3112–3117
9. Goswami N, Giri A, Kar S, Bootharaju MS, John R, Xavier PL, Pradeep T, Pal SK (2012) Protein-directed synthesis of NIR-emitting, tunable HgS quantum dots and their applications in metal-ion sensing. Small 8(20):3175–3184
10. Keuleyan S, Lhuillier E, Guyot-Sionnest P (2011) Synthesis of colloidal HgTe quantum dots for narrow Mid-IR emission and detection. J Am Chem Soc 133(41):16422–16424
11. Dong B, Li C, Chen G, Zhang Y, Zhang Y, Deng M, Wang Q (2013) Facile synthesis of highly photoluminescent Ag_2Se quantum dots as a new fluorescent probe in the second near-infrared window for in vivo imaging. Chem Mater 25(12):2503–2509
12. Du YP, Xu B, Fu T, Cai M, Li F, Zhang Y, Wang QB (2010) Near-infrared photoluminescent Ag_2S quantum dots from a single source precursor. J Am Chem Soc 132(5):1470–1471
13. Lu CH, Chen GH, Yu B, Cong HL (2018) Recent advances of low biological toxicity Ag_2S QDs for biomedical application. Adv Eng Mater 20(6):1700940
14. Yang M, Gui RJ, Jin H, Wang ZH, Zhang FF, Xia JF, Bi S, Xia YZ (2015) Ag_2Te quantum dots with compact surface coatings of multivalent polymers: ambient one-pot aqueous synthesis and the second near-infrared bioimaging. Colloid Surface B 126:115–120

15. Zhang Y, Hong G, Zhang Y, Chen G, Li F, Dai H, Wang Q (2012) Ag_2S quantum dot: a bright and biocompatible fluorescent nanoprobe in the second near-infrared window. ACS Nano 6(5):3695–3702
16. Zhang Y, Liu Y, Li C, Chen X, Wang Q (2014) Controlled synthesis of Ag_2S quantum dots and experimental determination of the exciton bohr radius. J Phys Chem C 118(9):4918–4923
17. Zhao JY, Chen G, Gu YP, Cui R, Zhang ZL, Yu ZL, Tang B, Zhao YF, Pang DW (2016) Ultrasmall magnetically engineered Ag_2Se quantum dots for instant efficient labeling and whole-body high-resolution multimodal real-time tracking of cell-derived microvesicles. J Am Chem Soc 138(6):1893–1903
18. Aharoni A, Mokari T, Popov I, Banin U (2006) Synthesis of InAs/CdSe/ZnSe core/shell1/shell2 structures with bright and stable near-infrared fluorescence. J Am Chem Soc 128(1):257–264
19. Xie RG, Peng XG (2009) Synthesis of Cu-doped InP nanocrystals (d-dots) with ZnSe diffusion barrier as efficient and color-tunable NIR emitters. J Am Chem Soc 131(30):10645–10651
20. Kim SE, Zhang L, Ma K, Riegman M, Chen F, Ingold I, Conrad M, Turker MZ, Gao MH, Jiang XJ, Monette S, Pauliah M, Gonen M, Zanzonico P, Quinn T, Wiesner U, Bradbury MS, Overholtzer M (2016) Ultrasmall nanoparticles induce ferroptosis in nutrient-deprived cancer cells and suppress tumour growth. Nat Nanotechnol 11(11):977–985
21. Park JH, Gu L, von Maltzahn G, Ruoslahti E, Bhatia SN, Sailor MJ (2009) Biodegradable luminescent porous silicon nanoparticles for in vivo applications. Nat Mater 8(4):331–336
22. Ma N, Marshall AF, Rao JH (2010) Near-infrared light emitting luciferase via biomineralization. J Am Chem Soc 132(20):6884–6885
23. Du H, Chen CL, Krishnan R, Krauss TD, Harbold JM, Wise FW, Thomas MG, Silcox J (2002) Optical properties of colloidal PbSe nanocrystals. Nano Lett 2(11):1321–1324
24. Jin H, Gui RJ, Sun J, Wang YF (2016) Glycerol-regulated facile synthesis and targeted cell imaging of highly luminescent Ag_2Te quantum dots with tunable near-infrared emission. Colloid Surface B 143:118–123
25. Hwang I, Seol M, Kim H, Yong K (2013) Improvement of photocurrent generation of Ag_2S sensitized solar cell through co-sensitization with CdS. Appl Phys Lett 103(2):023902
26. Liu X, Liu Z, Lu J, Wu X, Chu W (2014) Silver sulfide nanoparticles sensitized titanium dioxide nanotube arrays synthesized by in situ sulfurization for photocatalytic hydrogen production. J Colloid Interface Sci 413:17–23
27. Chen G, Tian F, Zhang Y, Zhang Y, Li C, Wang Q (2014) Tracking of transplanted human mesenchymal stem cells in living mice using near-infrared Ag_2S quantum dots. Adv Funct Mater 24(17):2481–2488
28. Munari M, Sturve J, Frenzilli G, Sanders MB, Brunelli A, Marcomini A, Nigro M, Lyons BP (2014) Genotoxic effects of CdS quantum dots and Ag_2S nanoparticles in fish cell lines (RTG-2). Mutat Res-Gen Tox En 775:89–93
29. Zhang Y, Hong G, He W, Zhou K, Yang K, Li F, Chen G, Liu Z, Dai H, Wang Q (2013) Biodistribution, pharmacokinetics and toxicology of Ag_2S near-infrared quantum dots in mice. Biomaterials 34(14):3639–3646
30. Chen G, Tian F, Li C, Zhang Y, Weng Z, Zhang Y, Peng R, Wang Q (2015) In vivo real-time visualization of mesenchymal stem cells tropism for cutaneous regeneration using NIR-II fluorescence imaging. Biomaterials 53:265–273
31. Hu F, Zhang Y, Chen G, Li C, Wang Q (2015) Double-walled Au nanocage/SiO_2 nanorattles: integrating SERS imaging, drug delivery and photothermal therapy. Small 11(8):985–993
32. Li C, Cao L, Zhang Y, Yi P, Wang M, Tan B, Deng Z, Wu D, Wang Q (2015) Preoperative detection and intraoperative visualization of brain tumors for more precise surgery: a new dual-modality MRI and NIR nanoprobe. Small 11(35):4517–4525
33. Song C, Zhang Y, Li C, Chen G, Kang X, Wang Q (2016) Enhanced nanodrug delivery to solid tumors based on a tumor vasculature-targeted strategy. Adv Funct Mater 26(23):4192–4200
34. Chen G, Lin S, Huang D, Zhang Y, Li C, Wang M, Wang Q (2018) Revealing the fate of transplanted stem cells in vivo with a novel optical imaging strategy. Small 14(3):1702679

35. Brelle MC, Zhang JZ, Nguyen L, Mehra RK (1999) Synthesis and ultrafast study of cysteine- and glutathione-capped Ag_2S semiconductor colloidal nanoparticles. J Phys Chem A 103(49):10194–10201
36. Jiang P, Tian ZQ, Zhu CN, Zhang ZL, Pang DW (2012) Emission-tunable near-infrared Ag_2S quantum dots. Chem Mater 24(1):3–5
37. Jiang P, Zhu CN, Zhang ZL, Tian ZQ, Pang DW (2012) Water-soluble Ag_2S quantum dots for near-infrared fluorescence imaging in vivo. Biomaterials 33(20):5130–5135
38. Hocaoglu I, Cizmeciyan MN, Erdem R, Ozen C, Kurt A, Sennaroglu A, Acar HY (2012) Development of highly luminescent and cytocompatible near-IR-emitting aqueous Ag_2S quantum dots. J Mater Chem 22(29):14674–14681
39. Gui RJ, Wan AJ, Liu XF, Yuan W, Jin H (2014) Water-soluble multidentate polymers compactly coating Ag_2S quantum dots with minimized hydrodynamic size and bright emission tunable from red to second near-infrared region. Nanoscale 6(10):5467–5473
40. Asik D, Yagci MB, Duman FD, Acar HY (2016) One step emission tunable synthesis of PEG coated Ag_2S NIR quantum dots and the development of receptor targeted drug delivery vehicles thereof. J Mater Chem B 4(11):1941–1950
41. Gui RJ, Sun J, Liu DX, Wang YF, Jin H (2014) A facile cation exchange-based aqueous synthesis of highly stable and biocompatible Ag_2S quantum dots emitting in the second near-infrared biological window. Dalton T 43(44):16690–16697
42. Tan LJ, Wan AJ, Li HL (2014) Synthesis of near-infrared quantum dots in cultured cancer cells. ACS Appl Mater Inter 6(1):18–23
43. Cao YT, Geng W, Shi R, Shang L, Waterhouse GIN, Liu LM, Wu LZ, Tung CH, Yin YD, Zhang TR (2016) Thiolate-mediated photoinduced synthesis of ultrafine Ag_2S quantum dots from silver nanoparticles. Angew Chem Int Ed Engl 55(48):14952–14957
44. Liu JC, Raveendran P, Shervani Z, Ikushima Y (2004) Synthesis of Ag_2S quantum dots in water-in-CO_2 microemulsions. Chem Commun 22:2582–2583
45. Wu C, Zhang Y, Li Z, Li C, Wang Q (2016) A novel photoacoustic nanoprobe of ICG@PEG-Ag_2S for atherosclerosis targeting and imaging in vivo. Nanoscale 8(25):12531–12539
46. Cui C, Li X, Liu J, Hou Y, Zhao Y, Zhong G (2015) Synthesis and functions of Ag_2S nanostructures. Nanoscale Res Lett 10(1):431
47. Yang HY, Zhao YW, Zhang ZY, Xiong HM, Yu SN (2013) One-pot synthesis of water-dispersible Ag_2S quantum dots with bright fluorescent emission in the second near-infrared window. Nanotechnology 24(5):055706
48. Shen S, Zhang Y, Peng L, Du Y, Wang Q (2011) Matchstick-shaped Ag_2S-ZnS heteronanostructures preserving both UV/blue and near-infrared photoluminescence. Angew Chem Int Ed Engl 50(31):7115–7118
49. Shen SL, Zhang YJ, Liu YS, Peng L, Chen XY, Wang QB (2012) Manganese-doped Ag_2S-ZnS heteronanostructures. Chem Mater 24(12):2407–2413
50. Yang T, Tang YA, Liu L, Lv XY, Wang QL, Ke HT, Deng YB, Yang H, Yang XL, Liu G, Zhao YL, Chen HB (2017) Size-dependent Ag_2S nanodots for second near-infrared fluorescence/photoacoustics imaging and simultaneous photothermal therapy. ACS Nano 11(2):1848–1857
51. Li S, Xu L, Sun M, Wu X, Liu L, Kuang H, Xu C (2017) Hybrid nanoparticle pyramids for intracellular dual microRNAs biosensing and bioimaging. Adv Mater 29(19):1606086
52. Tan LJ, Wan AJ, Li HL (2013) Conjugating S-nitrosothiols with glutathiose stabilized silver sulfide quantum dots for controlled nitric oxide release and near-infrared fluorescence imaging. ACS Appl Mater Inter 5(21):11163–11171
53. Duman FD, Erkisa M, Khodadust R, Ari F, Ulukaya E, Acar HY (2017) Folic acid-conjugated cationic Ag_2S quantum dots for optical imaging and selective doxorubicin delivery to HeLa cells. Nanomedicine 12(19):2319–2333
54. Jin H, Gui RJ, Gong J, Huang WX (2017) Aptamer and 5-fluorouracil dual-loading Ag_2S quantum dots used as a sensitive label-free probe for near-infrared photoluminescence turn-on detection of CA125 antigen. Biosens Bioelectron 92:378–384

55. Li CY, Zhang YJ, Wang M, Zhang Y, Chen GC, Li L, Wu DM, Wang QB (2014) In vivo real-time visualization of tissue blood flow and angiogenesis using Ag_2S quantum dots in the NIR-II window. Biomaterials 35(1):393–400
56. Tang R, Xu B, Shen D, Sudlow G, Achilefu S (2018) Ultrasmall visible-to-near-infrared emitting silver-sulfide quantum dots for cancer detection and imaging. Proc of SPIE 10508:105080G
57. Zhao DH, Yang J, Xia RX, Yao MH, Jin RM, Zhao YD, Liu B (2018) High quantum yield Ag_2S quantum dot@polypeptide-engineered hybrid nanogels for targeted second near-infrared fluorescence/photoacoustic imaging and photothermal therapy. Chem Commun 54(5):527–530
58. Tang R, Xue J, Xu B, Shen D, Sudlow GP, Achilefu S (2015) Tunable ultrasmall visible-to-extended near-infrared emitting silver sulfide quantum dots for integrin-targeted cancer imaging. ACS Nano 9(1):220–230
59. Chen H, Li B, Zhang M, Sun K, Wang Y, Peng K, Ao M, Guo Y, Gu Y (2014) Characterization of tumor-targeting Ag_2S quantum dots for cancer imaging and therapy in vivo. Nanoscale 6(21):12580–12590
60. Chen J, Zhang T, Feng L, Zhang M, Zhang X, Su H, Cui D (2013) Synthesis of Ribonuclease-A conjugated Ag_2S quantum dots clusters via biomimetic route. Mater Lett 96:224–227
61. Wang Y, Yan XP (2013) Fabrication of vascular endothelial growth factor antibody bioconjugated ultrasmall near-infrared fluorescent Ag_2S quantum dots for targeted cancer imaging in vivo. Chem Commun 49(32):3324–3326
62. Li C, Zhang Y, Chen G, Hu F, Zhao K, Wang Q (2017) Engineered multifunctional nanomedicine for simultaneous stereotactic chemotherapy and inhibited osteolysis in an orthotopic model of bone metastasis. Adv Mater 29(13):1605754
63. Ding C, Zhang C, Yin X, Cao X, Cai M, Xian Y (2018) Near-infrared fluorescent Ag_2S nanodot-based signal amplification for efficient detection of circulating tumor cells. Anal Chem 90(11):6702–6709
64. Cheng K, Yang XQ, Zhang XS, Chen J, An J, Song YY, Li C, Xuan Y, Zhang RY, Yang CH, Song XL, Zhao YD, Liu B (2018) High-security nanocluster for switching photodynamic combining photothermal and acid-induced drug compliance therapy guided by multimodal active-targeting imaging. Adv Funct Mater 28(36):1803118
65. Zhang XS, Xuan Y, Yang XQ, Cheng K, Zhang RY, Li C, Tan F, Cao YC, Song XL, An J, Hou XL, Zhao YD (2018) A multifunctional targeting probe with dual-mode imaging and photothermal therapy used in vivo. J Nanobiotechnol 16(1):42
66. Tan LJ, Wan A, Li HL (2013) Ag_2S quantum dots conjugated chitosan nanospheres toward light-triggered nitric oxide release and near-infrared fluorescence imaging. Langmuir 29(48):15032–15042
67. Li C, Li F, Zhang Y, Zhang W, Zhang XE, Wang Q (2015) Real-time monitoring surface chemistry-dependent in vivo behaviors of protein nanocages via encapsulating an NIR-II Ag_2S quantum dot. ACS Nano 9(12):12255–12263
68. Hu F, Li CY, Zhang YJ, Wang M, Wu DM, Wang QB (2015) Real-time in vivo visualization of tumor therapy by a near-infrared-II Ag_2S quantum dot-based theranostic nanoplatform. Nano Res 8(5):1637–1647
69. Yan D, He Y, Ge YL, Song GW (2017) Fluorescence "turn on-off" detection of heparin and heparinase I based on the near-infrared emission polyethyleneimine capped Ag_2S quantum dots. Sensor Actuat B-Chem 240:863–869
70. Wu Q, Zhou M, Shi J, Li Q, Yang M, Zhang Z (2017) Synthesis of water-soluble Ag_2S quantum dots with fluorescence in the second near-infrared window for turn-on detection of Zn(II) and Cd(II). Anal Chem 89(12):6616–6623
71. Theodorou IG, Jawad ZAR, Qin H, Aboagye EO, Porter AE, Ryan MP, Xie F (2016) Significant metal enhanced fluorescence of Ag_2S quantum dots in the second near-infrared window. Nanoscale 8(26):12869–12873
72. Zhang X, Liu M, Liu H, Zhang S (2014) Low-toxic Ag_2S quantum dots for photoelectrochemical detection glucose and cancer cells. Biosens Bioelectron 56:307–312

73. Granero-Molto F, Weis JA, Miga MI, Landis B, Myers TJ, O'Rear L, Longobardi L, Jansen ED, Mortlock DP, Spagnoli A (2009) Regenerative effects of transplanted mesenchymal stem cells in fracture healing. Stem Cells 27(8):1887–1898
74. Houlihan DD, Newsome PN (2008) Critical review of clinical trials of bone marrow stem cells in liver disease. Gastroenterology 135(2):438–450
75. Kuo TK, Hung SP, Chuang CH, Chen CT, Shih YRV, Fang SCY, Yang VW, Lee OK (2008) Stem cell therapy for liver disease: parameters governing the success of using bone marrow mesenchymal stem cells. Gastroenterology 134(7):2111–2121
76. Robinton DA, Daley GQ (2012) The promise of induced pluripotent stem cells in research and therapy. Nature 481(7381):295–305
77. Nguyen PK, Riegler J, Wu JC (2014) Stem cell imaging: from bench to bedside. Cell Stem Cell 14(4):431–444
78. Chen G, Zhang Y, Li C, Huang D, Wang Q, Wang Q (2018) Recent advances in tracking the transplanted stem cells using near-infrared fluorescent nanoprobes: turning from the first to the second near-infrared window. Adv Healthc Mater 7(20):1800497
79. Kircher MF, Gambhir SS, Grimm J (2011) Noninvasive cell-tracking methods. Nat Rev Clin Oncol 8(11):677–688
80. Yukawa H, Baba Y (2017) In vivo fluorescence imaging and the diagnosis of stem cells using quantum dots for regenerative medicine. Anal Chem 89(5):2671–2681
81. Smith AM, Mancini MC, Nie S (2009) Bioimaging: second window for in vivo imaging. Nat Nanotechnol 4(11):710–711
82. Yukawa H, Kagami Y, Watanabe M, Oishi K, Miyamoto Y, Okamoto Y, Tokeshi M, Kaji N, Noguchi H, Ono K, Sawada M, Baba Y, Hamajima N, Hayashi S (2010) Quantum dots labeling using octa-arginine peptides for imaging of adipose tissue-derived stem cells. Biomaterials 31(14):4094–4103
83. Maxson S, Lopez EA, Yoo D, Danilkovitch-Miagkova A, Leroux MA (2012) Concise review: role of mesenchymal stem cells in wound repair. Stem Cells Transl Med 1(2):142–149
84. Chen S, Weitemier AZ, Zeng X, He L, Wang X, Tao Y, Huang AJY, Hashimotodani Y, Kano M, Iwasaki H, Parajuli LK, Okabe S, Teh DBL, All AH, Tsutsui-Kimura I, Tanaka KF, Liu X, McHugh TJ (2018) Near-infrared deep brain stimulation via upconversion nanoparticle-mediated optogenetics. Science 359(6376):679–684

Chapter 12
Non-plasmonic NIR-Activated Photothermal Agents for Photothermal Therapy

L. Marciniak, K. Kniec, K. Elzbieciak, and A. Bednarkiewicz

12.1 Introduction

Current advancements of nanotechnology enable to solve medical problems, which up to very recent times were difficult to face. Photothermal therapy (PTT) called hyperthermia is one of the examples, where instead of a whole-body hyperthermia, localized and targeted heat treatment of cancer cells becomes possible. Moreover, numerous evidences have been demonstrated, where combined therapies, PTT + photodynamic therapy (PDT) [1, 2], PTT+ drug delivery demonstrated synergistic effects [3, 4]. Although some attempts to PTT have been made on humans, most efficient and most suitable materials are continuously sought because such PTT agents (PTTA) must exhibit well-defined and stringent properties, such as high efficiency of light-to-heat conversion at low photoexcitation doses and at small concentrations. Moreover, the PTTA must be biocompatible (both in terms of lack of self-toxicity and tendency for spontaneous aggregation), made easily biofunctionalized, show limited retention but long blood circulation time and efficient clearance. Additionally, PTTA shall be photoexcited preferably in NIR spectral region, where deepest light penetration into tissues, owing to smallest absorption and scattering, occurs. Finally, PTTA shall also enable to feedback control the local temperature deposition, either by inherent limits of material (saturation of absorption) or through volumetric temperature mapping and adjustments of photoexcitation intensity. On top of that, the temperature readout and mapping, made optically, shall be stable over treatment time, reliable (highly accurate ~0.1 °C and reproducible) and independent from experimental conditions or calibration, as well as technically feasible to make subcutaneous readouts and mapping. One shall therefore understand the suitability

L. Marciniak (✉) · K. Kniec · K. Elzbieciak · A. Bednarkiewicz (✉)
Institute of Low Temperature and Structure Research, Polish Academy of Sciences, Wroclaw, Poland
e-mail: l.marciniak@intibs.pl; a.bednarkiewicz@intibs.pl

A. Benayas et al. (eds.), *Near Infrared-Emitting Nanoparticles for Biomedical Applications*, https://doi.org/10.1007/978-3-030-32036-2_12

of different PTT nanomaterials, both plasmonic and non-plasmonic, has to be validated.

The aim of this chapter is to highlight the recent progress, constrained to last 5 years, in the field of non-plasmonic photothermal agents activated in NIR spectral range. Carbon-based materials, i.e., graphene and its derivatives dominate in number of studies, but significant achievements have been made also with rare earth-doped nanoparticles, polymeric, silicon or iron-based photothermal agents. Different mechanisms of light-to-heat conversion exist, whose fundamental common point is cascaded conversion of energy of photons to phonons, followed by energy dissipation to local environment. In the case of non-plasmonic nanoheaters, the ubiquitous mechanism responsible for light-to-heat conversion is non-radiative relaxation processes, which, through energy transfer from excited electronic levels to phonons or its overtones (i.e., multi-phonon) is dissipated to nearest neighborhood of the NPs. Even large energy gaps (~10,000 cm^{-1} in lanthanides, such as Yb^{3+}) can be efficiently quenched by the overtones of O–H vibrations (~3400 cm^{-1}), C–O (1091 cm^{-1}), –COOH (1640 cm^{-1}), $–CH_2$ (1400, 2850 cm^{-1}), –CH (1219, 3020 cm^{-1}) or other ones, which is evidenced by radical emission quantum yield decrease by 2–3 orders of magnitude in nanoparticles as compared to bulk (or not passivated NPs) counterparts. In TiO_2, for example, the energy gap between valence and conduction band becomes more shallow, facilitating non-radiative depopulation. In lanthanides, beside quenching by surface ligands or NPs solvents, one may also intentionally increase the probability of multiphonon non-radiative transitions, by involving energy exchange between respective energy levels of the lanthanides in the process of cross-relaxation. The most well-known example of such intentional light-to-heat conversion are Nd^{3+} ions [5, 6], where the resonant cross-relaxation ($^4F_{3/2}$; $^4I_{9/2}$) followed by a sequence of processes ($^4I_{15/2}$; $^4I_{15/2}$) → ($^4I_{13/2}$; $^4I_{13/2}$) + Q → ($^4I_{11/2}$; $^4I_{11/2}$) + Q → ($^4I_{9/2}$; $^4I_{9/2}$) + Q, generate heat with high quantum efficiency ($\eta_{h\upsilon \to Q}$~70%).

Studying different photothermal agents, a reliable method to compare their properties are required. The most common method is studying the kinetics of heating after switching on the photoexcitation as well as the kinetics of the cooling after switching it off (Fig. 12.1c). Following Roper's method [7], the photothermal conversion efficiency η can be calculated using the following equation:

$$\eta = \frac{hA \cdot (T_{MAX} - T_0) - Q_0}{I \cdot \left(1 - 10^{-OD}\right)} \tag{12.1}$$

where η, A, $T_{MAX} - T_0$, Q_0, I, and OD correspond to the heat transfer efficiency, heat transfer surface area, increase of temperature due to light-to-heat conversion, heat dissipation of the container and solvent (measured alone for cuvette filled with the solvent), incident laser power and optical density of the nanocrystals at excitation wavelength, respectively. The $OD = \varepsilon_\lambda Lc$, where the subsequent symbols are wavelength-dependent molar absorptivity, path length, and molar concentration. The $T_{MAX} - T_0$ is relative temperature increase, which may be measured either with a thermocouple placed in the colloidal solution of NPs or with a thermovision

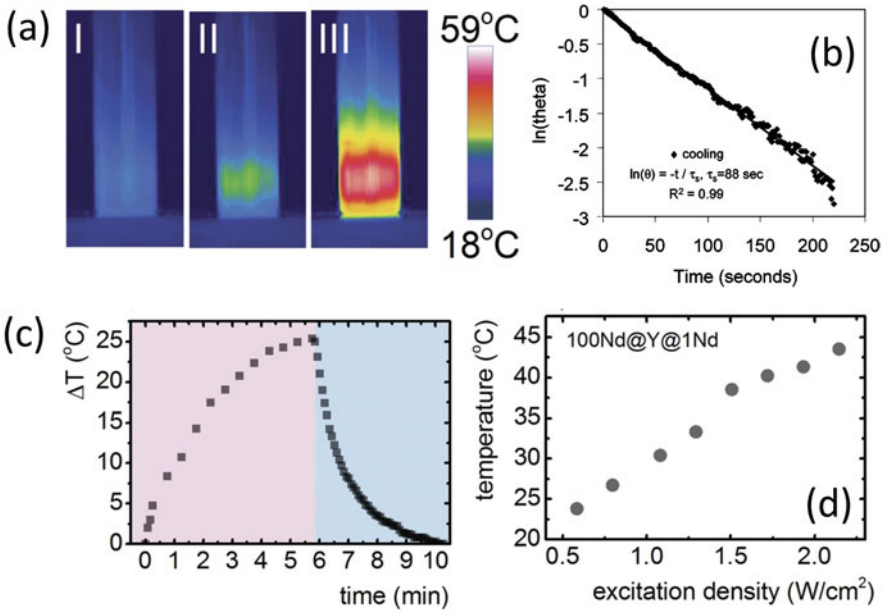

Fig. 12.1 Determination of light-to-heat conversion efficiency. (**a**) Temperature images of 1 cm cuvette filled with (I) pure chloroform and illuminated with a collimated laser beam @808 nm, (II) Y@1Nd core–shell nanoparticles in solvent, and (III) 100Nd@Y@1Nd core–shell–shell nanoparticles in solvent under $\lambda_{exc} = 808$ nm (2.0 W/cm^2) after 330 s of enlightenment; (**b**) representative cooling of the solution of NPs and fitting with Eq. (12.2), (**c**) heating (red part) and cooling down (blue part) rates of the 100Nd@Y@1Nd NP solution under 2 W/cm^2 at 808 nm; (**d**) and the saturation temperature T_{MAX} obtained in 100Nd@Y@1Nd nanoparticles colloidal solution studied as a function of excitation density ($\lambda_{exc} = 808$ nm) line

camera (Fig. 12.1a). Originally, such a sample cell was placed in vacuum chamber to eliminate convective heat transfer from the surface of the cell to the ambient air, which was motivated by the fact, the equation is valid when the thermal equilibrium within the system is achieved much faster than the energy exchange with the surroundings. In many studies, however, the vacuum chamber was disregarded and thermovision camera was used to record the temperature of the surface of the cuvette filled in with colloidal nanoparticles.

By defining a driving force temperature Θ determined with Eq. (12.2) for cooling part of the temperature kinetic curve [7],

$$\Theta = \frac{T_{AMB} - T}{T_{AMB} - T_{MAX}} = e^{-t/\tau_S} \tag{12.2}$$

one gets the only unknown hA value in Eq. (12.1). By evaluation of the decay of temperature T over time t after switching off the laser photoexcitation versus ambient (T_{AMB}) and saturation (T_{MAX}) temperatures under illumination (Fig. 12.1b), one

may determine time constant τ_S, which, coming from the model developed by Roper et al., equals to

$$\tau_S = \left[\sum_i m_i C_{p,i}\right] / hA \tag{12.3}$$

where m_i, $C_{p,i}$ mass and heat capacity of the system (i.e., solvent and container), respectively.

Originally, this method has been developed for gold nanoparticles, but recently it was adopted for numerous other types of light-to-heat converting nanoparticles. These relationships predict a linear relationship between the temperature increase proportionally to the concentration of NPs, absorbance value, and applied laser power.

Many different materials have been proposed to convert one type of energy (e.g., light, modulated magnetic field) into heat. Such approach enables not only to deposit heat in target subjects in remote way but also in highly confined manner. At the moment, most of bio-related hyperthermic studies demonstrate the suitability of HT treatment by injecting the HT agents into tumors, the ultimate goal of HT technology is to equip such nano-micro heaters with bio-specific recognition elements (e.g., antibodies), that will enable to accumulate such heaters in well-defined cellular and tissue structures. Finding appropriate HT agents require versatile characterization of their heat-generation capability and biosafety, and as will be demonstrated below, different materials cannot be easily compared to select most promising candidates. This difficulty comes from not uniform approach to quantification of heat generation, and often disregarding HT agents concentration or activation light dose. If the HT treatment is meant to be used in vivo, this information must be provided for factual judgment. Below, a state of the art and comparison of various non-plasmonic materials are presented.

12.2 Graphene and Its Derivatives

Carbon-based nanomaterials attracted particular attention in the photothermal therapy, which can be confirmed by numerous articles and reviews on this material [8–15]. These carbon-based nanomaterials various forms and morphologies, such as graphene and its derivatives, carbon quantum nanodots, carbon nanotubes, and other compounds, as described in the following sub-chapters.

Graphene, and graphene-based nanomaterials, such as graphene oxide (GO), reduced graphene oxide (rGO), and GO nanocomposites have unique chemical and physical properties—they are lightweight and show large specific area. Moreover, because of high absorption cross section of light from Vis to near

infrared (NIR) spectral range and high light-to-heat conversion efficiency, they exhibit high suitability for thermal ablation of cancer cells [10, 16, 17]. As it was already evidenced, light doses of <300 mW/cm^2 of NIR photoexcitation [18] enables to overcome >43 °C level, leading to hyperthermia of surrounding cells and tissues [19–22]. Moreover, as was recently shown, employing the graphene nanomaterials as a PTT agent enables to reduce the side effects of the treatment [16]. Despite all advantages of graphene-based nanomaterials their important drawback is related to the potential toxicity, in particular, the pure dispersion of graphene-based nanomaterials, which refers mainly to graphene oxide (GO) and reduced graphene oxide (rGO). Additionally, this kind of nanomaterials reveal low stability in aqueous solutions [20], therefore, additional surface modification via covalent or non-covalent modifications is required to assure biocompatibility and water dispersibility [8, 17]. It is worth noting that surface modification of graphene-based nanomaterials is feasible owing to π-electron-rich surface, which enables to form non-covalent π–π stack with different molecules to improve their multifunction capabilities [22]. Non-covalent modification may be also achieved by electrostatic attraction and van der Waals forces, whereas the covalent binding is obtained via chemical reactions [17]. Besides higher functionality and solubility, the non-covalent PEGylation of rGO may provide additional benefits, such as sixfold enhancement of NIR absorption in comparison to the GO counterpart, which was comparable to gold-based nanomaterials [23]. Below we present the overview of the very recent results concerning the in vitro and in vivo hyperthermia treatment by the use of graphene and its derivatives (Fig. 12.2).

12.2.1 Graphene

Graphene is a two-dimensional honeycomb-like carbon nanomaterial, which consists of sp^2-hybridized carbon atoms, with polyaromatic surface structure, which attracted great attention in many fields of application due to its extraordinary optoelectronic and thermal properties [19, 21, 23]. Because of its high absorbance both in the first (650–900 nm) and the second biological window (1000–1350 nm) as well as high probability of non-radiative energy depopulation it may be used as NIR light-to-heat converter [21]. As it was shown, tetrasulfonic acid tetrasodium salt copper phthalocyanine attached to the graphene via a non-covalent π–π interaction made it suitable as PTT reagent [22]. Such complex exhibited high water solubility, high light-to-heat conversion efficiency upon 650 nm photoexcitation which enabled over 35 °C temperature increase for 3 W/cm^2 excitation density, and thus enabled to reduce the HeLa cancer cells viability after 5 min of irradiation down to 29% for 15 μg/mL GR-TsCuPc concentration.

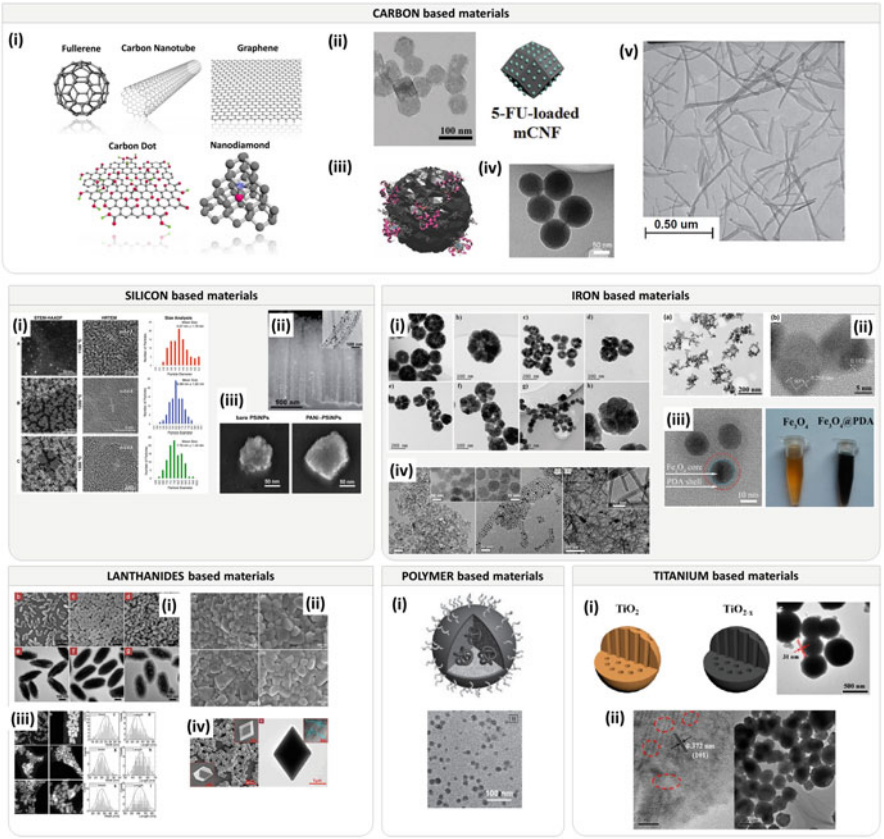

Fig. 12.2 Typical morphologies of the obtained light-to-heat nanoconverters **CARBON** (**i**) Carbon nanomaterials for biological imaging and nanomedicinal therapy, (**ii**) A designed synthesis of multifunctional carbon nanoframes for simultaneous imaging and synergistic chemo-photothermal cancer therapy, (**iii**) visualization of C-dot [28], (**iv**) TEM image of CNSs with diameters ranging from 30 to 100 nm [29], (**v**) TEM image of CNx-MWNT [30]. **SILICON** [24] (**i**) STEM-HAADF images, HRTEM images, and corresponding histogram of NC sizes for Si–NCs formed via thermal processing of HSQ for 1 h at (A) 1100, (B) 1200, and (C) 1300 °C [25], (**ii**) SEM and TEM (inset) images of the prepared AuNPs@SiNWs [26] (**iii**) SEM and TEM images of polyaniline/PSiNPs nanocomposites [27] **IRON** (**i**) TEM images of a series of Fe–NFs with a tunable diameter range (a and b) 200–250 nm, (c and d) 100–150 nm, (e and f) 75–125 nm, and (g and h) 70–80 nm [31], (**ii**) TEM and HR-TEM images of NIR optically active iron oxide cluster-structured nanoparticles (Fe_3O_4 CNPs) [32], (**iii**) TEM image of the Fe_3O_4@PDA NCs obtained by self-polymerization of DA on the surface of Fe_3O_4 NPs photo shows the color change between Fe_3O_4 NPs and Fe_3O4@PDA NCs [33] 2014, (**iv**) high-resolution transmission electron microscope (HRTEM) images of spherical, hexagonal, and wire-like Fe_3O_4 nanoparticles [34], and (**v**) highly crystallized iron oxide nanoparticles (HCIONPs) [35]. **LANTHANIDES** (**i**) typical SEM (up) and TEM (bottom) images of (b, e) precursors, (c, f) P@Si and (d, g) $Nd^{3+}/Yb^{3+}/Er^{3+}$GdOF@Si microcrystals [36], (**ii**) FE-SEM images of the (a) $Na_{0.5}Gd_{0.5}MoO_4$:$0.01Er^{3+}/0.03Yb^{3+}$, (b) $Na_{0.5}Gd_{0.5}MoO_4$:$0.01Er^{3+}/0.07Yb^{3+}$, (c) $Na_{0.5}Gd_{0.5}MoO_4$:$0.01Er^{3+}/0.11Yb^{3+}$, and (d) $Na_{0.5}Gd_{0.5}MoO_4$:$0.01Er^{3+}/0.20Yb^{3+}$ phosphors

12.2.1.1 Graphene Oxide

GO is a two-dimensional oxidized form of the graphene, which reveals a number of advantages in respect to the rGO nanomaterials. Due to the fact that its structure contains hydroxide and carboxyl groups, the GO is considered to be less toxic than rGO. Moreover, the presence of hydrophilic groups on the GO surface simplifies its functionalization [10]. On the other hand, NIR absorption of GO is depleted in respect to the rGO, which impose further surface modification [49]. Wang et al. proved that by creating the indocyanine green dye (ICG)–GO complex via π–π interactions between the two species, the 808 absorption cross section was 20 times enhanced in respect to the pure GO counterpart [49]. Furthermore, the cancer-targeting activity of such complex may be increased by further modification with the aid of folic acid (FA), which made the complex to become completely nontoxic and biocompatible. After 10 min of NIR irradiation (1 W/cm^2), the solution of nano-ICG-GO-FA (20 μg/mL) reached the temperature of about 60 °C. The in vivo studies of ICG-GO-FA on the HeLa cancer cells under 2 W/cm^2 NIR irradiation have shown successful ablation of tumor cells via photothermal therapy [49]. Kalluru et al. showed that folate-coated GO may be used as a bimodal agent for photodynamic and photothermal destruction of tumors [18]. It was shown that temperature of B16F0 melanoma tumor-bearing mice cells with GO-PEG-folate (8 mg/kg) upon 808 for 8 min and 980 nm for 10 min laser irradiation (250 mW/cm^2) was elevated by ΔT of 8.8 and 1.8 °C, respectively [18]. After 14 days of the treatment using 980 nm irradiation, the tumor cells were effectively damaged and a new skin began to develop, while for 808 nm irradiation slight increase of tumor volume was found. Anyway, this increase of tumor size was one order of magnitude lower in respect to the control.

Hu et al. have presented the quantum dot (QD)–rGO hybrid structure as a nanosized heater [50]. Namely, CdSe/ZnS quantum dots were attached to the FA covalently modified GO, which efficiently generated heat (increase of temperature to 67 °C) after 5 min irradiation with 808 nm excitation (2 W/cm^2). On the other hand, it was proved that surface modification with Pluronic F127 coating (nontoxic block copolymer) improved meaningfully the stability of the colloid. The obtained systems (nanoGO, 10 μg/ml) enabled to increase temperature from 28.5 °C to 45.5 °C after 3 min of 808 nm irradiation [19]. The in vivo treatment of living mice (10 mg/kg) enabled thermal ablation of HeLa cells after 2 min of irradiation (2 W/cm^2). Another interesting example of heat generation in GO-based

Fig. 12.2 (continued) [37], (**iii**) representative STEM-HAADF images and size distribution histograms for core 100Nd (a–d), core@shell—100Nd @ 1Nd (e–h) and core @shell @shell—100Nd @ Y @ 1Nd (i–l) nanocrystals [38], (**iv**) SEM (b) and TEM (c) of YF_3: 0.5%Tm^{3+}, 10%Yb^{3+} sample [39]. **POLYMER** (**i**) Schematic illustration of PFTTQ NP synthesis and FE-TEM image of PFTTQ NPs [40]. **TITANIUM** (**i**) schematic illustration of TiO_2 and black-TiO_{2-x} nanoparticles and TEM image of DOX@TiO_{2-x}@PDA-Cy5.5 [41] and (**ii**) TEM image of Ti_8O_{15} nanoparticles [42]

nanomaterial was demonstrated by Tao et al., who synthesized dual-polymer-functionalized GO (GGI) using polyethylene glycol (PEG) and polyetylenimine (PEI) as surface ligands [51]. The use of 10 μg/mL amount of GGI during the 5 min NIR radiation (808 nm, 2 W/cm^2) in the RAW264.7 cell solution caused efficient local heating. Furthermore, these nanomaterials were applied to the living mice, which suffered from the CT26, being a murine colon carcinoma. The solution of GGI was injected into back of the mouse (180 μg/kg) and exposed the 808 nm excitation (2 W/cm^2) over 5 min and the tumors were observed for 12 days. Provided treatment led to a ~50% growth inhibition of tumor, with no signs of damage to other organs like heart, spleen, liver, lung, and kidney [51]. Wang et al. proposed multifunctional GO-based system that combined optical and magnetic properties into single GO–IONP–PEG composite (IONP stands for iron oxide nanoparticle) for hyperthermia treatment [52]. The in vitro studies on human pancreatic carcinoma cells (BXPC-3) revealed that for 20 μg/mL and 40 μg/mL concentration of GO–IONP–PEG after 5 min of 2 W/cm^2 irradiation, the ablation of 32.45% and 56.56% of cells was observed, respectively. The enhancement of the excitation density up to 3 W/cm^2 caused further increase of the ablation efficiency leading to the 46.23% and 81.26% of killed cells, respectively. Moreover, low cytotoxicity of GO–IONP–PEG confirmed its applicative potential for in vivo studies [52].

Another modification of GO by fluorination was proposed by Romero-Aburto et al., who presented that after 1 min of 800 nm irradiation of 1.6 W/cm^2 excitation density of fluorinated graphene oxide (FGO), the glioma cancer cells (GI-1) cell culture temperature raised up by 37.3 °C to 62.3 °C [53]. Such fast local heat generation shall prevent the overheating and damaging of the neighboring healthy cells. In 2013, the heat generated by nanosized GO (NGO) via NIR irradiation was used for the first time as a transdermal pathway of treatment of melanoma skin cancer (B16F1), which is considered as a very hazardous skin cancer and the main cause of skin cancer-related mortality [54]. Before the in vitro and in vivo treatment, the NGO was coated with hyaluronic acid (HA). The 808 nm light (2 W/cm^2) led to the heat generation of NGO–HA (1 mg/mL) increasing the temperature up to 50 °C after 10 min of irradiation causing complete in vivo ablation of skin cancer cells. The black wound remaining after heat treatment was recovered to the normal skin in 1 month [54].

12.2.1.2 Reduced Graphene Oxide

Another example of graphene-based nanomaterial used for heat generation is reduced graphene oxide (rGO). Sheng et al. presented that bovine serum albumin-assisted rGO may be used for both photoacoustic imaging and photothermal therapy [23]. After 5 min of 808 nm irradiation (0.6 W/cm^2) of the 0.11 mg/mL BSA–rGO, local temperature of 55 °C was reached. The in vivo hyperthermia treatment on MCF-7 (breast cancer) in living mice confirmed that after 2 h of irradiation the temperature rise by 16 °C leads to the ablation of cancer cells [23]. The surface of rGO can be also modified by hyaluronic acid (HA) and conjugated with

poly(ethylene glycol)-g-poly(dimethylaminoethyl methacrylate) (PEG-g-PDMA, PgP) [20]. When it comes to the in vitro experiment, the 1 mg/ml of PgP/HA–rGO nanomaterials generated $\Delta T = 50$ °C higher temperature after 5 min (2 W/cm^2) in respect to the HA–GO counterpart. The in vivo study carried out on MDAMB tumor-bearing mice revealed the reduction of tumor volume size from 225 mm^3 to 55 mm^3 10 days after 5 min of NIR irradiation. Twenty days after treatment, total recovery from malignancy was observed [20]. It is also worth noting that rGO has been also demonstrated as a photothermal agent for effective killing of bacteria [55]. In order to achieve antibacterial effect, the rGO was integrated with magnetic NPs (MRGO) and glutaraldehyde (GA). This functionalization provides rapid bacteria aggregation and capturing when applying an external magnetic field. MRGO–GA at the concentration of 80 ppm and exposed to 808 light (1.5 W/cm^2) within 10 min, heated up the biological environment to 50 °C and killed 100% of *Escherichia coli* bacteria.

12.2.2 Carbon Quantum Nanodots (C-Dots, CQDs)

Carbon quantum nanodots (CQDs) are zero-dimensional carbon-based nanomaterials, consisting of amorphous or nanocrystalline cores, which can be a potential nontoxic alternative for semiconductors-based quantum dots [28]. C-dots are characterized by broad absorption, good photostability, two photon excitation in the near infrared (NIR) region, large Stokes shift, heat-generation capacity, and low costs of the synthesis [43, 56]. Moreover, CQDs exhibit many unique properties like high water solubility and surface modification flexibility [57]. Usually, small organic molecules, polymers, and compounds with non-carbon elements, like S, P, N, B are used for this purpose [28]. Furthermore, they are generally nontoxic and biocompatible, confirmed by in vivo *studies* on mice and zebrafish [28]. Plenty of mobile π-electrons in C-dots lead to strong electron–electron scattering and weak electron–phonon interactions [56]. In this case, most of the absorbed light is eventually converted into heat via several non-radiative relaxation pathways [56]. Furthermore, CQDs exhibit lower in vivo cytotoxicity than GO-based materials and functionalized CQDs show higher stability in biological environment and superior water solubility than GO sheets [58]. In 2015, polythiophene phenylpropionic acid (PPA)-conjugated C-dots were proposed as a promising agent for photothermal therapy [57]. After 10 min of exposure of 200 μg/mL PAA-based CQDs with 671 nm irradiation (2 W/cm^2), the temperature of the HeLa cancer cells was heated up by 26.6 °C, leading to 100% of their mortality with a photothermal conversion efficiency of ~38.5%. Additionally, based on in vivo treatment on HeLa tumor-bearing mice using PPA-based C-dots the temperature raised up to 50.4 °C after 2 W/cm^2 of 671 nm laser irradiation, leading to significant decrease of tumor growth. Moreover, after 16 days, the mice recovered completely [57]. Another proposed C-dots-based conjugate is prepared from cyanine dye [2-((E)-2-((E)-2-chloro-

3((E)-2-(1-(2-hydroxyethyl)-3,3-dimethylindolin-2-ylidene)ethylidene)cyclohex-1en-1-yl)vinyl)-1-(2-hydroxyethyl)-3,3-dimethyl-3H-indol-1-ium iodide, CyOH] and poly(ethylene glycol) (PEG800), which exhibit favorable hydrophilicity and excellent photostability (CyCD) [59]. CyCD shows numerous advantages such as excellent photostability, favorable hydrophilicity and satisfactory photothermal conversion efficiency of 38.5% [59]. In vitro study on the tumor cells treatment via heat generation by CyCD was conducted on the CT26 cells under 808 nm (2 W/cm^2) in 5 min, using 2 μg/mL of C-dots. After treatment almost all cancer cells were dead.

The influence of the heat generated by CyCD on tumor cell ablation was investigated in CT26 tumor-bearing BALB/c mice. After 1 h post injection of CyCD and 5 min of 808 nm laser irradiation (1–1.5 W/cm^2) the tumor reached a temperature of 45 °C. Furthermore, this treatment was conducted four times with 2-day intervals. The results confirmed 91% of tumor inhibitory rate [59]. Similarly, another type of C-dots was obtained by polythiophene benzoic acid (PBA) as carbon source and has shown satisfactory efficacy of light-to-heat conversion equal to 36.2% [60]. These C-dots were exposed to 635 nm (2 W/cm^2) irradiation for 10 min at different concentrations, from 20 μg/mL to 200 μg/mL, and can heat up the solution even by 30 °C for 200 μg/mL C-dots.

Another approach to implement C-dots to hyperthermia was the use of N-doped CNDs (N-CNDs), exhibiting biodegradability, excellent photostability, and strong optical NIR-absorbance [61]. The N-CNDs were obtained by carbonizing organic acids with a controllable nitrogen sources. The influence of heat generated by N-CNDs on the tumor cell viability was conducted on the HepG2 hepatic cells. After 10 min of 808 nm NIR irradiation of the 10 mg/mL N-CNDs (2 W/cm^2), the viability of HepG2 cells decreased by about 60%. Moreover, this treatment has shown the absence of tumor recurrence. It is widely known that surface modification of C-dots can improve the NIR-absorbance due to their high absorption cross section in this spectral range. Based on this concept, a novel supra-(carbon nanodots) were presented in 2016, which revealed broad absorption band (470–1000 nm) with the maximum at 700 nm [43]. This supra-(carbon nanodots) consist of surface charge-confined CNDs and the strong absorption in UV–NIR region can be related to the interparticle electron transitions between the trap-state energy levels on the surface. Moreover, the strong visible–NIR absorption in supra-CNDs can be achieved via assembly of CDNs in high concentration. This feature provided very efficient heat generation, which was estimated at 50% level. Exposing 100 ppm C-dots to 732 nm laser irradiation (2 W/cm^2) for 10 min, made the temperature of the solution to rise to 55.5 °C.

Li et al. explained the mechanism of heat generation in supra-C-dots in terms of non-radiative deactivation of the NIR-induced electrons on the d level, being 0.44 eV below the LUMO level, by recombination with the holes on the level, localized 0.31 eV above the HOMO level. Another C-dot-based photothermal agent presented by Li et al.—dopamine carbon nanodots (DA CNDs)—reveals the efficiency of heat generation ~35% [62]. The study on heat generation by this nanomaterial upon 808 nm NIR light (1.5 W/cm^2) after 5 min was conducted by

the use of different DA CNDs concentration in respect to the HeLa cells. It was shown that after irradiation time for 50 μg/mL of Da CNDs only 13% of tumor cells remained alive.

Recently, a new type of C-dots have been proposed, namely CDs co-doped with oxygen and nitrogen atoms CDs (N–O–CDs), having strong absorbance in the NIR region, high photostability, and biocompatibility [58]. N–O–CDs were obtained from 1,3,6-trinitropyrene (TNP) and N-containing polymer of branched polyethylenimine (BPEI). What distinguishes this material from the other C-dots mentioned here as a photothermal agent, is the fact that N–O–CDs show a satisfactory light-to-heat conversion (38.3%) using a low laser power density of 808 nm irradiation, namely 0.8 W/cm^2. It was presented that 200 μg/mL of N–O–CDs within 5 min can efficiently generate the heat and increase the temperature of the solution up to 55.4 °C. In the course of in vitro experiments, the HeLa cancer cells were exposed to 808 nm irradiation (0.8 W/cm^2) for 5 min at various N–O–CDs concentration. Then, the HeLa cells were incubated for 24 h or 48 h. The lowest value of cancer cells viability, namely 13% was obtained for 200 μg/mL, which confirmed the excellent photothermal properties of N–O–CDs. The in vivo study on the tumor-bearing mice were conducted in the same condition for 200 μg/mL of N–O–CDs. The tumor temperature rapidly increased from 35.8 to 57.4 °C and enabled ablation of 100% HeLa cells.

12.2.3 Carbon Nanotubes (CNT)

Carbon nanotubes belong to fullerene structural family and have cylindrical structures of one-dimensional hollow tubular bides, where each carbon atom is covalently connected with three other carbon atoms (Fig. 12.3). CNT exhibit numerous advantages, i.e., high heat conversion due to large NIR absorption coefficient (6.2×10^6 M^{-1} cm^{-1}), large surface area, easy functionalization, mechanical flexibility, resistance to the changes of temperature, small size, and unique mechanical properties [8, 10, 16, 47, 63–65]. The surface modification of hydrophobic CNT is required in terms of biological application and is possible due to the π–π stacking interactions [53]. All these features make the CNT a good candidates for hyperthermia treatment [8, 63]. Recently both single- and multi-walled carbon nanotubes have drawn the attention as remote heat generators [47].

12.2.3.1 Single-Walled Nanotubes (SWNCTs)

SWNCTs possess high surface area, which is due to the fact that all atoms are exposed on the surface [48, 66]. This feature enables non-covalent modification of their surface via aromatic hydrocarbon and another organic compounds, i.e., PEG leading to enhancement of their solubility in water [48, 66]. SWNTs exhibit an excellent biocompatibility and fast and efficient distribution via bloodstream

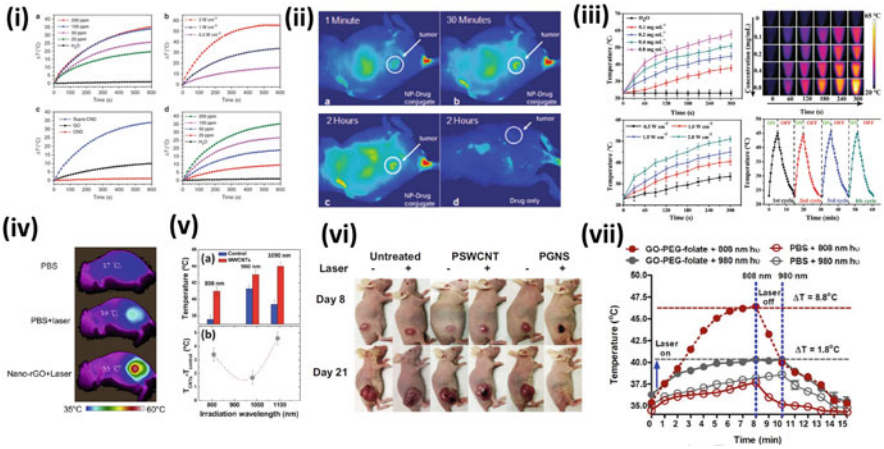

Fig. 12.3 (**i**) Photothermal profile of supra-CNDs. Temperature elevations of (a) supra-CND aqueous dispersions with different concentrations under 732 nm laser irradiation (1 W/cm^2) compared with pure water, (b) supra-CND aqueous dispersions (100 ppm) under 732 nm irradiation with increasing laser power densities, (c) supra-CND, GO, and CND aqueous dispersions (100 ppm) under 732 nm laser irradiation (1 W/cm^2), and (d) supra-CND aqueous dispersions with different concentrations under 808 nm laser irradiation (1 W/cm^2) compared with pure water. All experiments were conducted at room temperature [43]. (**ii**) Fluorescence images of a tumor-bearing mouse after being injected with PEG-GNP-Pc4 conjugates in normal saline, (a) 1 min, (b) 30 min, and (c) 120 min after intravenous tail injection. (d) Mouse injected with Pc4 alone [44]. (**iii**) (a) The temperature curves of mCNFs at different concentrations in aqueous solution under NIR laser irradiation (808 nm, 1.5 W/cm^2). (b) Photothermal images of mCNF solutions at different concentrations and pure water exposed to the 808 nm laser (1.5 W/cm^2) recorded at different time intervals (0, 60, 120, 180, 240, and 300 s). (c) NIR-induced temperature increase at various laser power densities in aqueous solution (808 nm, 0.2 mg mL1). (d) Cyclic photothermal stability tests of mCNFs [45]. (**iv**) Infrared thermographic maps of mice in different conditions [46]. (**v**) (a) Maximum temperature as obtained in the absence (control) and presence of the MWCNT injection when irradiated with three different laser wavelengths: 808 nm, 980 nm, and 1090 nm. Laser intensity was in all the cases 1 W/cm^2 and temperature values refer to the steady-state values. (b) Laser-induced temperature increment caused by the injected MWCNTs (with respect to control) for the three irradiation wavelengths used in this work. Dots are experimental data and the dashed line is a guide for the eyes [47]. (**vi**) Laser-induced photothermal anticancer effects of the PSWCNT and PGNS. SCC7-bearing mice were intravenously treated with PSWCNT or PGNS by administering a single injection on day 6. After 24 h, the tumor tissues were irradiated with an 808 nm laser at a power density of 1.2 W/cm^2 for 3 min. Starting on the following day (day 8), the appearances of the tumor sites were observed until day 21 [48]. (**vii**) Temperature rise profiles as a function of irradiation time for conditions in in vivo experiments on mice using graphene oxide [18]

[47]. As it was shown by Han et al., the thio-aptamer-conjugated carbon nanotubes (SWNTs–PEG–TA) reveal efficient light-to-heat conversion in in vivo experiments on breast tumor-bearing mice upon 5 min of 808 nm (1 W/cm^2) irradiation. The tumor temperature reached 63.1 °C, leading to cancer ablation 30 days after the treatment [66]. SWNTs were also functionalized by copolymer poloxamer 407 (PSWNTs), a hydrophilic nonionic surfactant [48]. The 10 μg/mL of PSWNTs generated heat in 5 min under 808 nm laser beam, which led to the increase of the solution temperature up to 48 ± 1.8 °C. Mori et al. proposed poly N-isopropylacrylamide and PEG copolymer with SWNTs (SWNT/PNIPAM–PEG) as a highly biocompatible and stable under biological condition heater platform, which led to the temperature increase upon 5 min of NIR excitation (4 W/cm^2) up to 45 °C [65]. Another interesting heating nanoplatform used for cancer ablation involves SWNTs and QDs like CdSe and ZnSe [67]. The biocompatibility of QD@CNT was achieved with folic acid (FA) functionalization. Temperature rise by 67 °C was reached in vitro after 3 min of 800 nm (1.75 W/cm^2) irradiation of 1 mg/mL of FA–QD@CNT as well as 50°–60 °C temperature rise was obtained in vivo on breast tumor (MCF7) after 4 min of irradiation. Another approach to provide the complete biocompatibility and dispersibility in water was obtained by modifying SWNTs with Lys-Phe-Lys-Ala $(KFKA)_7$ peptide [63]. As it was shown the SWNTs-$(KFKA)_7$ can convert the 808 nm light (1.2 W/cm^2) into the heat increasing the temperature of the surrounding by 20 °C within 5 min, leading to the damage of 55.8% of cultured colon 26 (colon cancer) and 86.7% of HepG2 (liver cancer) cells in vitro.

12.2.3.2 Multi-Walled Carbon Nanotubes

Multi-Walled Carbon Nanotubes (MWCNTs) display meaningfully larger surface in respect to the SWCNTs, offering more accessible electrons per nanotube. As a result, their absorption cross section for NIR irradiation is approximately 3 times higher compared to SWCNTs [47].

Maestro et al. proved that the solution of MWCNTs exposed to 808 nm, 980 nm, and 1090 nm light (1.4 W/cm^2) led to the rise of the temperature of the surrounding from 20 °C to 39 °C, 39.6 °C, and 39.5 °C, respectively [47]. In vivo studies carried out on living mice demonstrated that the maximum of tissue temperature (44 °C) was obtained for MWCNTs excited with 1090 nm (1 W/cm^2), whereas the lowest temperature enhancement, up to 41 °C, was in case of 808 nm light (1 W/cm^2). The observed difference was explained in terms of higher absorption cross section of tissues itself for 1090 nm in respect to the 808 nm.

The high light-to-heat conversion efficiency is important to reduce the amount of NIR excitation to avoid the risk of skin damage [68]. The MWCNTs–PEG show a strong capacity of converting 808 nm light into heat, because the NIR irradiation for 4 min raised the temperature by 32.7 °C, using the MWCNTs concentration of 100 μg/ml, whereas in the in vitro study, with the same amount of MWCNTs after 1 min irradiation (5 W/cm^2) caused the decrease of the viability of the breast

cancer cells (MCF-7 and MDA-231) up to 74.3%. After 1 min of laser excitation in vivo, the temperature on the surface of the cancer cell increased rapidly up to 73.4 ± 11.98 °C and to 47.3 ± 1.63 °C for the 10 μg and 1 μg of MWCNTs, respectively [68].

12.2.4 Mesoporous Carbon Nanoframes

Mesoporous carbon nanoframes (mCNFs) were proposed in 2018 as a new photothermal agent, which even in its small concentration (0.2 mg/mL) enable to raise the temperature of water solution to 42 °C under 5 min of 808 nm (1.5 W/cm^2) irradiation and even 58 °C for higher—i.e., 2 W/cm^2 excitation density [45]. The in vitro studies with the use of 50 μg/mL of mCNFs on the HeLa cells indicated reduction of the cell viability after 5 min of 808 nm irradiation.

12.2.5 Carbonaceous Nanospheres

Glucose-derived carbonaceous nanospheres (CNSs) were proposed in 2016 as a novel carbon-based photothermal agents [29], which demonstrated light-to-heat conversion efficiency equal 35.1% owing to large π-conjugated aromatic structure in the carbonized core. The capacity to heat generation by these nanomaterials was investigated in water solution, with the use of various material concentration exposed to 808 nm laser irradiation (2 W/cm^2) for 10 min. After 10 min of 808 nm irradiation (6 W/cm^2) of 0.16 mg/mL, less than 15% of cancer cells remained alive.

12.2.6 Single-Walled Carbon Nanohorns

Single-walled carbon nanohorns (SWNHs) modified with C_{18}PMH–PEG (poly(maleic anhydride-alt-1-octadecene-poly(ethylene glycol)) are another photothermal agents, characterized by biocompatibility and high stability [69]. The SWNHs/C_{18}PMH–PEG exhibited no acute toxicity. The 0.1 mg/mL concentration of SWNHs/C_{18}PMH–PEG after 5 min of 808 nm irradiation (0.4 W/cm^2) raised the temperature of the 4T1 tumor-bearing mice up to 55 °C, leading to the effective tumor ablation [69].

12.3 Rare Earth-Doped Photothermal Agents

In recent years, interest in nanoparticles doped with lanthanides has increased significantly (Fig. 12.4 (i)–(x)) [12, 70–75]. They are the main subject of research and find applications in the fields of bioimaging, biosensing, hyperthermia treatment,

photothermal ablation therapy (PTA), or in vitro and in vivo intracellular temperature sensing. Lanthanides owe their unique spectroscopic properties to the electronic configuration, thanks to which they usually present a rich energy level scheme, multicolor, photostable, narrow-band absorption, and emission. The light-to-heat conversion in this kind of materials is generated through non-radiative depopulation of excited electronic states. Neodymium (Nd^{3+}) is one of the most frequently used lanthanide ions in this kind of application [70]. In the case of this ion, heat is generated via concentration quenching mechanism $\{^4F_{3/2}, {}^4I_{9/2}\} \leftrightarrow \{^4I_{15/2}, {}^4I_{15/2}\}$ through cross-relaxation transitions as well as through a series of non-radiative multiphonon depopulation steps of higher laying excited states. Therefore, high dopant concentration is expected to facilitate the enhancement of the absorption cross section as well as light-induced heat generation. Interestingly, light-to-heat generation can be accompanied by simultaneous thermometric capabilities in NIR spectral region, which is a great advantage over other PTT agents [5]. In the case of up-converting nanoparticles, the quantum yield of luminescence turns out to be very small, what confirms that most of the absorbed energy is converted into heat. It must be mentioned that apart from many favorable features of Ln:NPs, heat generation process is limited by relatively low absorption cross section in lanthanide ions [12, 70]. Marciniak et al. [5] and Rocha et al. [76] demonstrated that $NaYF_4$ or LaF_3 nanoparticles activated with large concentrations (up to 100 or 25%) of Nd^{3+} ions can simultaneously operate as biologically compatible efficient nanoheaters and fluorescent nanothermometers (Fig. 12.4 (vii)). Ex vivo experiments based on local injection of aqueous solutions of LaF_3:Nd^{3+} nanoparticles into chicken breast tissues irradiated 808 nm excitation revealed that for 3.7 W/cm^2 of 808 nm irradiation the temperature of surface of chicken breast can be elevated by 20 °C and of the injecting point even by 30 °C. Interestingly, the core (multi)shell $NaNdF_4$@$NaYF_4$@$NaYF_4$:1%Nd^{3+} multifunctional single nanocrystallite-based platform may combine optimized and enhanced fluorescence intensity, reasonable temperature sensing functionality with efficient light-to-heat conversion efficiency (up to 72%) upon 808 nm excitation [38] (Fig. 12.4 (ii)). After 330 s of 2 W/cm^2 irradiation, the temperature of solution of 20 mg/ml concentration of nanoparticles in chloroform reached 45 °C. The authors discussed also the issue related to the fact the heating with such NPs occurs along the photoexcitation path within tissue. They proposed the solution known from radiotherapies, where two (or more) subthreshold therapeutic beams meet deeply within tissues and the curing threshold (e.g., sufficient highly localized heating) is reached and feedback controlled in this small confined volume, to limit side effects to normal tissues. They have also discussed the issues related to the fact the heater and thermometers are combined within the same NP. This is particularly important during in vivo treatments, where fluctuations of photoexcitation intensity caused by heterogeneous and variable tissue composition make the ultimate hyperthermia treatment a challenging task.

Photothermal properties of other Nd^{3+}-doped nanocrystals (YVO_4:Nd^{3+}) were also investigated by Kolesnikov et al. and the maximal increase of temperature (around 14 °C) for excitation power 0.9 W was reported for 0.6% of Nd^{3+} [77]. However, when dopant concentration increases (facilitating interionic non-

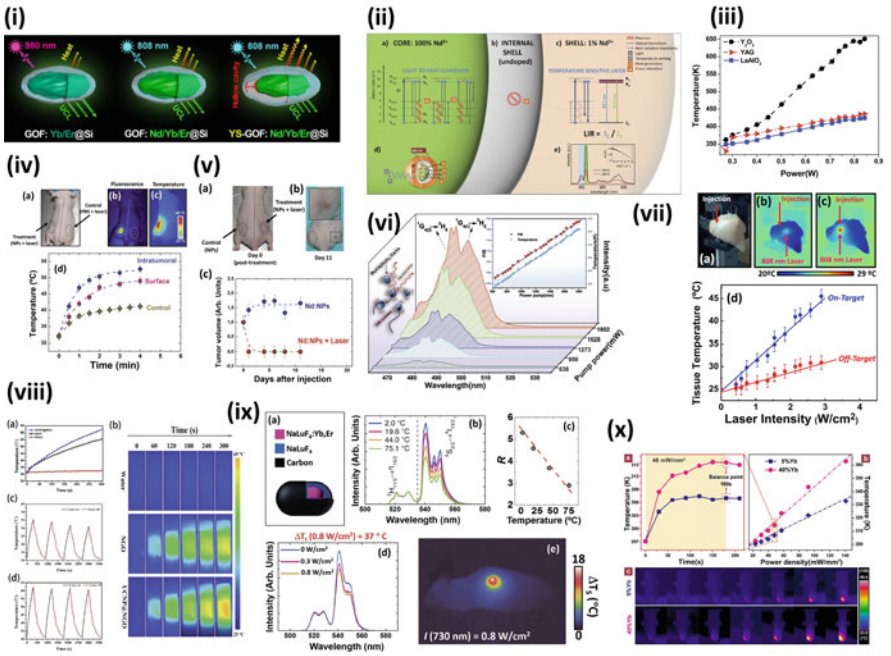

Fig. 12.4 Light-induced heating in lanthanide-doped compounds. (**i**) Models of the core–shell GOF: Yb^{3+}/Er^{3+}@Si and GOF:$Nd^{3+}/Yb^{3+}/Er^{3+}$@Si nanoparticles as well as yolk–shell microcapsules YS-GOF:$Nd^{3+}/Yb^{3+}/Er^{3+}$@Si for light-to-heat and light-to-UC conversion [36]. (**ii**) Schematic design of 100Nd@Y@1Nd single nanoparticle heater/label/thermometer [38], (**iii**) Comparison of temperature increase under excitation at 980 nm for Yb^{3+}/Tm^{3+} co-doped Y_2O_3, YAG, and $LaAlO_3$ phosphors [80]. (**iv**) (a) Optical image of a representative mouse with two tumors. A solution of "dense" Nd:LaF_3 NPs was injected only in the left-side tumor whereas the right-side one was used as a control. (b, c) Infrared fluorescence and thermal images of the same mouse under 808 nm (4 W/cm^2) laser irradiation, respectively. (d) The time evolution of intratumoral temperature [75]. (**v**) (a) Optical image of a representative mouse with two tumors 9 left-side control, right-side irradiated with a 808 nm laser beam (4 W/cm^2)), both injected with a solution containing Nd:LaF_3 NPs. (b) Optical image of the same mouse taken 11 days after treatment. The size evolution of both treated and control tumors is included in (c) [75]. (**vi**) The UCL spectra of the blue bands $^1G_{4(1)}/^1G_{4(2)}$-$^3H_6$ of Tm^{3+} with different pumping power. Inset: temperature (K) and FIR as a function of laser pump power in $Ba_5Gd_8Zn_4O_{21}$:Yb^{3+}/Tm^{3+}[81]. (**vii**) (a) Optical imaging of the chicken breast used for ex vivo photothermal experiments with Nd^{3+}:LaF_3 NPs. (b) and (c) correspond to the thermal images of the chicken breast when illuminated with an 808 nm laser beam (1.5 W/cm^2) without and with spatial overlap with the injection of Nd^{3+}:LaF_3 NPs (off- and on-target situations, respectively). (d) Surface tissue temperature as a function of the 808 nm laser intensity when the beam is illuminating the tissue and the injection (off- and on-target) [76]. (**viii**) (a) Temperature elevation and (b) IR thermal images of water, NGO and UCNP@NGO at various irradiation times upon NIR irradiation; the temperature change of (c) NGO and (d) UCNP@NGO over four laser ON/OFF cycles [82]. (**ix**) Temperature-controlled photothermal therapy with hybrid nanostructures (HNP). (a) Schematic representation of the HNPs designed for simultaneous in vivo thermal sensing and heating. (b) Emission spectra (generated by the $NaLuF_4$:Er^{3+},Yb^{3+} core under 980 nm optical excitation as obtained at different temperatures. (c) Calibration curve of the core sensing unit showing the temperature dependence of the intensity ratio R under excitation at 980 nm. (d) Two photon excited emission spectra generated

radiative interaction), the enhancement of temperature rise for the same excitation power range increases up to 30 °C for 4.8% of Nd^{3+}. Therefore, del Rosal et al. reported extremely high light-to-heat conversion efficiency (72%) in ultrasmall $NdVO_4$ nanocrystals (2.4 nm). The ex vivo experiments on chicken breast with these nanoparticles revealed that even as low excitation density as 0.8 W/cm^2 of 808 nm excitation allowed to increase the nanoparticles' temperature by 14 °C [77]. Additional in vivo experiments confirmed that $NdVO_4$ nanoparticles reveal promising feature as an efficient photothermal agents. This non-radiative depopulation mechanism is ubiquitous in other ions beyond Nd^{3+} such as Yb^{3+}/Er^{3+}, Dy^{3+}, and Sm^{3+}. Xu et al. reported that the photothermal effect can be enhanced by co-doping Sm^{3+} to $NaY(WO_4)_2$:Nd^{3+}. By introducing the 5% of Sm^{3+}, the maximal temperature induced by 2.4 A of laser diode current was 10 °C higher (70 °C) in respect to the singly Nd^{3+}-doped phosphor. This effect was explained in terms of higher probability of interionic non-radiative energy transfer between co-dopants [78]. Lozano-Gorrín et al. have shown that nanocrystalline $Y_3Ga_5O_{12}$ doped with Nd^{3+} and co-doped with Er^{3+},Yb^{3+} can be successfully used as a nanoheating platform, which leads to the overcoming of diathermia (3 W/mm^2 and 15 W/mm^2, respectively), hyperthermia (3.8 W/mm^2 and 21 W/mm^2, respectively) and thermal ablation (4.8 W/mm^2 and 26 W/mm^2, respectively) temperature threshold at relatively low excitation densities of 808 and 920 nm excitation, respectively [79].

Zhang et al. presented effective photothermal conversion in $NaYF_4$:Er^{3+}/Yb^{3+} @$NaYF_4$:Tm^{3+}/Yb^{3+} core–shell NPs synthesized via typical thermal decomposition method, where $NaYF_4$:Tm^{3+}/Yb^{3+} shell was designed as nanoheater for heat generation and $NaYF_4$:Er^{3+}/Yb^{3+} core was designed as nanothermometer for probing temperature [84]. The light-to-heat conversion was examined under 808 and 980 nm excitation wavelength. In addition, the behavior of solvents in which the tested nanoparticles were suspended in order to evaluate the efficiency of heat generation in nanoparticles was checked. They confirmed the applicability of examined materials in photothermal conversion under 808 and 980 nm co-excitation. A different approach was shown by Li et al. [82] where $NaLuF_4$:Yb^{3+}, Er^{3+} up-converting nanoparticles (UCNP) were mixed with nano-oxide graphene (NGO) (Fig. 12.4 (viii)). Initial characterization of these materials was made with photothermal efficiency and photothermal conversion efficiency measurements, using irradiation with an 808 nm (2.0 Wcm^{-2}) for 5 min with monitoring of the system temperature. It was shown that after irradiation time, the temperature of UCNP@NGO reached higher value (63 °C) in respect to the NGO counterpart

Fig. 12.4 (continued) by the HNPs incorporated into a tumor in a nude mouse obtained after a 3-minute long 730 nm laser irradiation at three different power densities. (e) Infrared thermal image of the treated mouse after 730 nm laser irradiation for 3 min at a power density of 0.8 W/cm^2 [83]. (**x**) Laser-induced heating effect of YF_3: 0.5%Tm^{3+}, xYb^{3+} ($x = 5$ and 40%) versus time ($P = 48$ mW/mm^2) (a) and power density ($t = 180$ s) (b) as well as the corresponding power-dependent thermo-images (c) collected with the infrared thermal camera under 980 nm excitation [39]

(55 °C). The estimated light-to-heat conversion efficiency for UCNP@NGO was equal to 40%, while for NGO it reached only 35%. Additionally, UCNP@NGO revealed higher photostability after several irradiation cycles than NGO confirming their better performance as a photothermal agent. The photothermal ablation ability of free NGO and UCNP@NGO on the 4T1 cells was confirmed by using inverted fluorescence microscopy imaging. The UCNP@NGO group indicated near-total cell damage via a photothermal effect, which was much higher than the free NGO. The apoptosis rate of the cells reached 73.6% in free NGO and 99.2% in the UCNP@NGO. In turn, temperature of the tumor injected with UCNP@NGO rapidly increased to ~63 °C after 5 min, which was 10 °C higher than for free NGO. In vitro and in vivo studies revealed that UCNP@NGO nanoparticles possessed excellent biocompatibility, efficiently ablated cancerous cells via photothermal effect and could act as a promising agent for the in vivo photothermal therapy of tumors. Dey et al. [85] presented a novel approach in which Y_2O_3 co-doped Er^{3+}–Yb^{3+} and Eu^{3+}–Er^{3+}–Yb^{3+} upon 980 nm were examined. In the case of the Er^{3+}–Yb^{3+} co-doped Y_2O_3 phosphor, temperature changed from 317 K to 347 K for 7.01–55.84 W/cm^2 pump power density respectively. In turn, in Eu^{3+}–Er^{3+}–Yb^{3+} co-doped Y_2O_3, the same values of pump power density caused temperature change from 301 K to 403 K. Another material, i.e., YVO_4:Er^{3+}/Yb^{3+} nanoparticles were proposed by Mahata et al. [86]. The examined materials were synthesized by the hydrothermal route with the addition of ethylene glycol responsible to make spherical shape of particles. The authors observed that the temperature of the powder increased from 315 to 460 K as pump power at 980 nm increased from 13.18 to 50.45 W/cm^2. Dey et al. [87] indicated that 1%Er^{3+}/2%Yb^{3+} co-doped La_2O_3 nanocrystals are proper for laser-induced optical heating. They used 980 nm laser irradiation and for pump power densities from 108 to 1560 mW detected temperature changes from 301 K to 370 K, respectively. Later, another group of researchers performed analysis of 1%Er^{3+}/2%Yb^{3+} co-doped La_2O_3 nanocrystals [88]. The authors examined the influence of dopant concentration on up-conversion luminescence and revealed the best amount for further optical sensing and optical heating study. Due to heat generation, the temperature of the sample increased from 300 K to 340 K at increased excitation density from 7.08 to 26.19 W/cm^2. The cytotoxicity determination on HeLa cells confirmed that even for the highest dosage of 100 μg/ml cell viability was higher than 80%. One another material is sodium gadolinium molybdate nanocrystals ($Na_{0.5}Gd_{0.5}MoO_4$:Er^{3+}/Yb^{3+}), which was analyzed in terms of optical heating applications by Du et al. [37]. To study thermal effect induced by laser, the UC spectra of the $Na_{0.5}Gd_{0.5}MoO_4$:0.01%Er^{3+}/0.11%Yb^{3+} under different pump power from 334 mW to 1032 mW were made. As it was presented by Pandey et al. [89], Er^{3+}/Yb^{3+} co-doped $SrWO_4$-enabled conventional NIR to visible up-conversion emission and the heat generated inside the sample were calculated and they found that the temperature gain was up to ~417 K on increasing pump power up to 1700 mW. Du et al. showed that the increase of the excitation density from 246 mW to 445 mW raised up the temperature from 276 K to 324 K in BIOCl:0.03%Er^{3+} microplates [90]. Different kind of approach was taken by Suo

et al. [36] who examined two types of materials alike core–shell GdOF: RE@SiO_2 (RE = 10%Yb^{3+}/1%Er^{3+} and 1%Nd^{3+}/10%Yb^{3+}/1%Er^{3+}) and yolk–shell GdOF: 1%Nd^{3+}/10%Yb^{3+}/1%Er^{3+}@SiO_2 samples (Fig. 12.4 (i)). According to the obtained results, up-converting yolk–shell microcapsules with thermal sensing and optical heating bifunctions can be potentially used as thermometer heater platforms. The ex vivo experiments on chicken breast revealed that upon 980 nm excitation, temperature rise (22.4 K) was higher than that for the same sample with 808 nm excitation (11.9 K). On the other hand, the yolk–shell structure revealed better suitability for light-to-heat conversion (with temperature increase by 34.1 K). As a result of combining sensitive thermometry and efficient heat generation into one up-converting platform, yolk–shell GdOF: 1%Nd^{3+}/10%Yb^{3+}/1%Er^{3+}@SiO_2 microcapsules could be regarded as a candidates for real-time controlled photothermal therapy. Lu et al. shown that when the 980 nm excitation power increases to 3.78 W, the temperature of $Gd_2(MoO_4)_3$:Er^{3+},Yb^{3+} powder increases to 613 K [91]. An interesting approach was presented by Shao et al. who demonstrated that the rise of temperature of chloroform solution of $NaYF_4$:20%Yb^{3+}/2%Er^{3+}@$NaYF_4$:10%Yb^{3+}/10%Nd^{3+} core–shell nanoparticles (10 mg/mL) after 4 min of 808 nm irradiation (3.6 W/cm^2) may be enhanced by the dye (IR-806) sensitization (increase of temperature by 12 °C in respect to the 4 °C of bare $NaYF_4$:20%Yb^{3+}/2%Er^{3+}@$NaYF_4$:10%Yb^{3+}/10%Nd^{3+} nanocrystals) [92]. However, at longer irradiation time photodegradation of the dye was observed, which resulted in lowering the photoinduced temperature of the solution and ultimately questions the use of such hybrid structures for PTT. Liu et al. reported that for the $NaYbF_4$:1%Er^{3+} microcrystals the heat generated after 5 s of 980 nm irradiation (9.1 W/cm^2) enabled an increase in temperature by 290 °C up to ~307 °C [93]. Suo et al. investigated the ability of YF_3: Tm^{3+}/Yb^{3+} microcrystals for heat generation as a function of Yb^{3+} concentration [94]. After 3 min of 980 nm irradiation, the temperature of microcrystals with 5%Yb^{3+} was increased to 333 K, while for 40%Yb^{3+} it reached 363 K. Moreover, taking the advantage from the fact that emission intensity ratio of Tm^{3+} bands ($^3F_{2,3} \rightarrow {}^3H_6$ at 700 nm and $^3H_4 \rightarrow {}^3H_6$ at 776 nm) can be used for luminescent thermometry, Suo et al. proposed one another all-in-one platform for temperature-controlled heating application. Subsequently, an interesting material showing thermometric and optical heating properties proposed by Suo et al. is Yb^{3+}/Tm^{3+} co-doped $Ba_5Gd_8Zn_4O_{21}$ with various dopant concentrations (Fig. 12.4 (vi)) [81]. The laser-induced heating effect from 278.8 to 321.8 K upon increasing the pump power from 638 to 1802 mW at 980 nm. The results indicate that Yb^{3+}/Tm^{3+} co-doped $Ba_5Gd_8Zn_4O_{21}$ phosphors could be considered as candidates for optical heater and optical temperature sensor, which could not only transfer photon energy into heat but also measure the temperature (with the absolute sensitivity $S_a = 0.3\%/K$). Sun et al. confirmed that also $BaGd_2ZnO_5$:Tm^{3+},Yb^{3+} microcrystalline powder reveal efficient light-to-heat conversion capacity [95]. It was shown that temperature of the powdered phosphor increased linearly with 980 nm excitation density reaching 360 K for 13.45 W/cm^2.

12.4 Polymeric Photothermal Agents

Due to their strong NIR absorption, high light-to-heat efficiency and good photostability the conjugated polymers (CPs) are the most frequently used as a PTT agent [40, 96, 97]. CPs are characterized by delocalized electrons in the polymeric backbone and rapid excitation diffusion [97]. The heat generation in CP nanoparticles bases on the luminescence quenching and the non-radiative vibrational relaxation. A very interesting approach, which shows effective photothermal tumor ablation, both in vitro and in vivo, is a nontoxic porphyrin-containing conjugated polymer (PorCP), being a donor–acceptor structure [96] (D–A), where porphyrin is a donor and benzothiadiazole (BT) is an acceptor (Fig. 12.5).

To facilitate the incorporation of such CP in the cells, the PorCP was encapsulated in polymeric shells and the surface was modified by the use of *Tat* peptide, which caused the formation of PorCP-Tat NPs and the promotion of π–π stacking of porphyrin structure along the polymer chains. This in turn, led to the aggregation, which caused the quenching and non-radiative decay of excitons, entailing high light-to-heat conversion efficiency (63.8%). After 808 nm laser irradiation (0.75 W/cm^2) for 4 min, the temperature of a solution

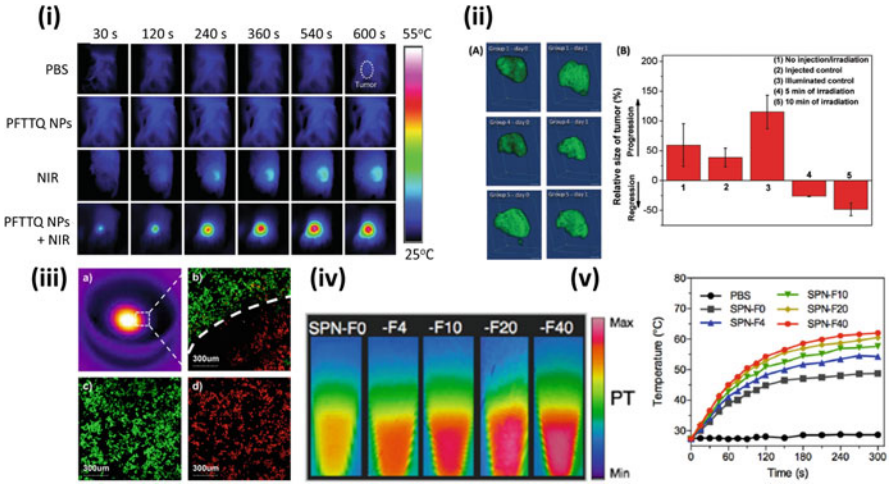

Fig. 12.5 (**i**) IR thermal images of HeLa tumor-bearing mice after treatment with PBS or PFTTQ NPs (1 mg/mL) without laser irradiation, only NIR laser irradiation (808 nm, 0.75 W/cm^2) without NPs, and 1 mg/mL of PFTTQ NPs with laser irradiation (808 nm, 0.75 W/cm^2) at different times [40]. (**ii**) (A) 3D fluorescence images of zebrafish liver tumor groups before and after different treatments for 1 d. (B) The relative tumor volume changes in each group, studied after 1 d of posttreatment ($p < 0.05$) [96] (**iii**) (a) Thermal images of the 4T1 cell culture dish after incubation with Pdot-1 and laser irradiation (0.5 W/cm^2) for 5 min. (b–d) Fluorescence images of cells stained with calcein AM (live cells, green fluorescence) and PI (dead cells, red fluorescence) [97]. (**iv**) In vitro fluorescence, PA, and PT data of SPNs. Quantification of fluorescence [98]. (**v**) The temperature of SPN solutions as a function of laser irradiating time at the power intensity of 0.5 W/cm^2 [98]

of 0.05 mg/mL PorCP-Tat NPs increased from 24 °C to 66 °C. In vitro study was carried out on the HeLa and MDA-MB-231 cancer cells by the use of 5 mg/L of PorCP-Tat NPs under 10 min of 808 nm (0.75 W/cm^2) laser irradiation. This treatment led to the damage of HeLa and MDA-MB-231 cells by 70% and 80%, respectively. In vivo study was performed on zebrafish liver hyperplasia model and showed that the use of 0.75 mg/mL of PorCP-Tat NPs exposed to 808 nm (0.5 W/cm^2) for 10 min caused the ablation of 50% of liver tumor tissues. Another nanomaterial, which revealed very promising heat generation efficiency (65%) are conjugated polymer dots (Pdots) with donor–acceptor construction units, containing diketopyrrolopyrrole (DPP) and various thiophene derivatives, namely monothiophene, thienothiophene, bithiophene, and benzodithiophene, exhibiting wide absorption spectra (600 nm–900 nm) and nontoxic features for living systems [97]. The most efficient heat generation was presented by the Pdots with monothiophene compound (Pdot-1). After 5 min of exposing these materials (50 μg/mL) to 808 laser irradiation (0.5 W/cm^2), the increase of the temperature of the solution up to 61.4 °C was observed. These preliminary results allowed to investigate Pdot-1 both in in vitro and in vivo. The in vitro study showed that the heat generated after 5 min of 808 nm laser irradiation (0.5 W/cm^2) was sufficient to kill 90% of the 4T1 cancer cells, even when the Pdot-1 concentration was less than 25 μg/mL. In vivo study was carried out on 4T1-bearing living mice, which were injected with 0.5 mg/mL (40 μL) of Pdot-1. The living mice were exposed for 5 min to 808 nm laser irradiation (0.5 W/cm^2). As a consequence, the temperature of the tumor rises to 68 °C, causing efficient ablation of 4T1 cells. Another promising photothermal agent, based on the biocompatible conjugated polymeric structure is poly[9,9-bis(4-(2-ethylhexyl)phenyl)fluorene-alt-co-6,7-bis(4-(hexyloxy)phenyl)-4,9-di(thiophen-2-yl)-thiadiazoloquinoxaline] (PFTTQ), encapsulated in 1,2-distearoyl-sn-glycero-3-phosphoethanolamine-N-[methoxy(polyethylene glycol)-2000] matrix (DSPE-PEG$_{2000}$), responsible for creating PFTTQ NPs [40]. The heat was generated via high non-radiative decay rates, leading to the enhancement of the temperature of the solution by 30 °C (up to 52 °C), which occurred after 10 min lasting 808 nm laser excitation (0.75 W/cm^2) of 0.5 mg/mL PFTTQ NPs. These preliminary results permitted the in vitro and in vivo studies, which were carried out on MDA-MB-231 and HeLa cancer cells. The use of 200 μg/mL PFTTQ NPs for in vitro treatment and 808 nm laser (0.75 W/cm^2) for 10 min caused the ablation of more than 80% of MDA-MB-231 and HeLa cancer cells. The in vivo investigation of the efficiency of the PFTTQ NPs PTT agent was done on mice bearing HeLa tumors. Taking advantage of 1 mg/mL (40 μL) and the same irradiation condition the temperature of the tumor cells increased rapidly from 27 °C to 47 °C (within 3 min) and the tumors disappeared in 4 days after treatment.

A novel approach to optical heating exploited the polymeric structure nanomaterials as heat sources based on the biocompatible semiconducting polymer nanoparticles (SPNs) [98]. The SPNs have a binary optical structure consisting of NIR-absorbing semiconducting polymer and an ultrasmall carbon dot (fullerene), which interact with each other leading to the photoinduced electron transfer

(PET). The semiconducting polymer (SP) and the carbon dot, being an optical dopant, are electron donor and acceptor, respectively. When the energy levels between electron donor and acceptor are aligned, the PET is favorable inside the nanoparticle, which causes the fluorescence quenching and enhancement of non-radiative heat generation after light irradiation. The presented new PTT agent include poly[2,6-(4,4-bis(2-ethylhexyl)-4H-cyclopenta-[2,1-b;3,4-b′]dithiophene)-alt-4,7-(2,1,3-benzothiadiazole)] (PCPDTBT) and (6,6)-phenyl-C71-butyric acid methyl ester (PC70BM), being semiconducting polymer and optical dopant, respectively. Moreover, amphiphilic triblock polymer (PEG-b-PPG-b-PEG) was used to increase the hydrophilicity of SPNs. The SP has a relatively narrow energy gap, which ensures strong NIR light absorption, whereas PC70BM is a fullerene, having high electrophilicity. The energy levels of these components were ideally aligned, which enabled the PET to occur between them. In vitro study was carried out by the use of different amount of PC70MB, but the best results were obtained for the 20 w/w% (SPN-F20), using 15 μg/mL of SPNs. After 5 min of 665 nm laser irradiation (0.5 W/cm^2), the temperature of the SPNs solution increased up to about 60 °C. The in vivo study was performed on 4T1 tumor-bearing mice, which were injected with 100 μg/mL of SPN-F20 concentration. 5 minutes of exposing SPN-F20 to 808 nm laser light (0.3 W/cm^2) the tumor temperature reached 62 °C and caused the death of 77.2% of tumor cells. It is worth mentioning that photothermal treatment of cancer to cause the ablation of tumor cells is not the only application of semiconducting polymer nanoparticles (SPNs). They can also be used as a light-to-heat converters for gene therapy, i.e., remotely activate gene expression, where SPNs are introduced to efficiently deliver genes and, more importantly, to spatiotemporally control of their expression in conjunction with heat-inducible promoters [99]. This can be realized by the utilization of NIR-absorbing dendronized semiconducting polymer (DSP). The DSP, obtained via palladium-catalyzed Suzuki polymerization, plays the role of photothermal nanocarrier and intracellular nanotransducer, showing absorption band at 500–900 nm and 44.2% of light-to-heat conversion efficiency upon 808 nm irradiation. The temperature of the DPS solution (concentration of 132 μg/ml) reached 58.8 °C after 480 s of laser exposure (0.67 W/cm^2). DSPs consist of three crucial components, namely the hydrophobic semiconducting backbone (i.e. a NIR photothermal transducer), the cationic third-generation polyamidoamine side chains (PAMAM3) (i.e., a gene vector), and the neutral poly(ethylene glycol) blocks (PEG) (i.e., a water solubility enhancer). The investigated DSPs shown promising properties in terms of biological applications due the possibility of their dissolution in aqueous and buffer solutions, hydrodynamic diameter of about 15 nm, stability of morphology both in ex vivo and in vivo environment. Moreover, they demonstrate lack of cytotoxicity even when used in higher concentration. The mentioned gene expression is regulated by heat shock promoter (HSP70), which in turn is activated by photothermal signal. After electrostatic attraction-based formation of DSP and HSP70 complex, gene release occurs. The 808 nm laser irradiation leads to heat generation by DSP influencing the HSP70 and activates transcription. The promising ex vivo results enables the conduction of in vitro and

in vivo experiment, using 808 nm light on HeLa cells with luciferase genes (pSV40-Luc)—a reporter gene (0.75 W/cm^2 for 30 min) and HeLa cells pellets transfected with DSP/pHSP70-Luc nanocomplexes (0.42 W/cm^2) injected into black living mice, respectively. Both measurements show the feasibility of application of DSP as an intracellular photothermal nanotransducer to remote control of gene expression even in living animals.

Semiconducting polymer can be also applied in the field of neuroscience to precisely control neuronal activity and to define events in specific cells of living tissues, where SPN are investigated in terms of their potential employment as a targeted photothermal activator of neurons and nanomodulator of thermosensitive ions channels in neurons [100]. In 2016, semiconducting polymer nanobioconjugates ($SPNs_{bc}$) was presented possessing specific surface, enabling conjugation with TRPV1 antibody, lack cytotoxicity and an ion permeable polymodal and thermosensitive channel on the plasma membrane of neurons, which can be activated by heat. This channel is responsible for the intercellular Ca^{2+} influx of neutrons and thus SPN by the heat generation influences this mechanism. Presented here SPN consists of poly(cyclopentadithiophene-alt-benzothiadiazole) (SP1) and poly(cyclopentadithiophene-alt-diketopyrrolopyrrole) (SP2), synthesized via Stille polymerization, with the maxima of absorbance at 660 nm and 766 nm, respectively. Moreover, SP1 and SP2 were transferred into water-soluble nanoparticles, with the ~25 nm of hydrodynamic diameters and spherical morphology, by nanocoprecipitation with polystyrene-b-poly(acrylic acid) (PS-PAA), creating SPN1 and SPN2, respectively. After 360 s laser irradiation (1 W/cm^2, nanoparticles concentration = 18 μg/ml) the SPN2 solution in PBS can reach 70 °C with 20% photothermal conversion efficiency, while SP1 shows 30% of photothermal efficiency (heated up to about 50 °C). The ability of SPNs to activate TRPV1 was investigated by the use of mouse neuroblastoma/rat DRG neuron hybrid ND7/23 cells and HeLa cells. SPN2 was able to increase the local temperature up to 43 °C in a fast way (808 nm light, 104 μW/cm^2 for 2 s), activating TRPV1 ion channels and inducing the intercellular Ca^{2+} influx. Moreover, this mechanism is reversibly activated and silenced while switching on and off the 808 nm laser irradiation with 0.5 s interval.

Another conducting polymer, which can be used for photothermal treatment of cancer is PEDOT (poly(3,4-ethylenedioxythiophene), being considered as a biocompatible organic material widely utilized in bioapplications [101]. Light-to-heat generation abilities of two nano-types of PEDOT, i.e., PEDOT:PSS poly(3,4-ethylenedioxythiophene):poly(4-styrene-sulfonate) and PEDOT nanotubes were investigated in terms of ability to ablate tumors, such as RKO and HCT116 colorectal cancer cells. Both materials exhibited no toxicity and absorption in NIR range, with the maxima at 830 nm and 884 nm for PEDOT:PSS and PEDOT nanotubes, respectively. However, PEDOT nanotubes reveal greater absorbance coefficient, which leads to a higher amount of generated heat compared to the PEDOT:PSS nanomaterials. Moreover, PEDOT nanotubes possess greater conjugation length, which causes higher charge mobility and more electrons can be transferred to

phonon bands to enhance heat generation. The 808 nm irradiation (0.6 W/cm^2) for 5 min showed the temperature increase by 16 °C and 8 °C using 0.015 mg/mL of PEDOT nanotubes and PEDOT:PSS nanoparticles, respectively. In vitro studies of both nanomaterials were carried out for the concentration of 0.01 mg/ml, 0.05 mg/ml, and 0.1 mg/ml under 808 nm laser diode irradiation (0.6 W/cm) for 5 min. The result showed that the highest concentration of PEDOT and PEDOT:PSS caused the cellular mortality at 95% and 80% level, respectively. However, after incorporation of 0.05 mg/ml of the materials, the tumor viability is less than 30% and 100%, respectively, which points to the better photothermal therapeutic properties of PEDOT nanotubes. Another in vitro study of PEDOT nanotubes tumor ablation abilities (PEDOT concentration = 0.01 mg/ml, 0.05 mg/ml and 0.1 mg/ml) was carried out on collagen gel tissue phantoms with the tumor environment, where cancer cells were suspended in the collagen gel matrix. It was concluded that the depth of tissue penetration is ranging from 0 to 100 μm for 0.05 mg/ml of concentration (0.6 W/cm^2 of 808 nm). As the PEDOT concentration increased, the tumor cell viability of RKO and HTC116 reduces, achieving the value less than 5% and 40% after 5 min of treatment, respectively.

It is well known that polyaniline nanoparticles can efficiently transfer the light to heat, showing strong absorbance in NIR region, allowing for tumor cell ablation. Different concentrations of PA, having size of 100–240 nm, namely 0.3125, 0.0625, and 0.125 mg/mL were exposed to 808 nm light (0.5 W/cm^2) for 10, 20, 30, 60, 90, 120, and 180 s [102]. As the amount of PA raised, the absorption in the range of 750–1000 nm increased. The photothermal conversion effect, being induced by NIR irradiation caused the enhancement of PA solution (PA concentration = 0.125 mg/ml) up to 67 °C after 180 s. This phenomenon enables the in vitro investigation on HeLa cells, providing the decrease of tumor viability after 2 min of 808 nm irradiation (0.5 W/cm^2). These results led to the creation of new composite structure, in which PA nanoparticles were incorporated into poly(e-caprolactone) and gelatin (PG) to form nanofibrous polyaniline PG fabrics via electrospinning, possessing excellent biocompatibility. The laser irradiation (808 nm, 0.5 W/cm^2) of PA PG fiber pieces for 1, 3, and 5 min caused the temperature enhancement from 25 °C to 54 °C, 76 °C, and 89 °C, respectively. In turn, the in vivo study on polyaniline PG-generated HeLa cells death, showed that after treatment with 808 nm the tumor growth is inhibited in 90%. This phenomenon results from the fact, that PA nanoparticles escape from PG and enter the tumor tissue after PG was swelled by tissue fluid.

12.5 Silicon-Based Photothermal Agents

Silicon-based nanoparticles and especially porous silicon nanoparticles (PSiNPs) possess many unique properties, including excellent biocompatibility, large specific area, easiness in their surface functionalization making them hot research topic for

multimodal cancer therapy. Xia et al. proposed to use polyaniline/PSiNPs (PANI–PSiNPs) nanocomposite as a light-to-heat converting nanoplatform [27]. Authors showed that after 20 min of 808 nm irradiation (1.6 W/cm^2), the temperature of water solution of PANI–PSiNPs (400 μg/mL) increased by 20 °C. Moreover, the excellent photostability of PANI–PSiNPs was confirmed by over 4 heating–cooling cycles. The in vitro (using human umbilical vein endothelial-HUVEC and 4T1 cells) and in vivo (4T1-tumor-bearing mice) experiments revealed good biocompatibility and biodegradability of PANI–PSiNPs. After 48 h of incubation with 200 μg/mL PANI–PSiNPs, both cells cultures revealed viability higher than 80%. In vivo studies revealed that over 28 days, the weight of Balb/C mice was continuously growing indicating the lack of PANI–PSiNPs toxic effect. Moreover, the biodistribution studies of PANI–PSiNPs indicated that 1 day after injection, the nanoparticles were mainly localized in the mononuclear phagocyte system-related organs (liver 19.8 ± 1% ID/g; spleen 20.4 ± 3.6% ID/g). However, after 28 days, the nanoparticles were completely cleared from the body through degradation of the porous silicon into soluble silicic acid followed by excretion from the body. Hong et al. in their comprehensive studies demonstrated that the fragments of porous silicon (PSi) exhibited better light-to-heat conversion performance in respect to other materials under investigations [103]. After 20 min of 808 nm irradiation (300 mW/cm^2), the temperature of PSi increased to almost 80 °C while for other PTT agents under investigation observed light-induced heating was less efficient (~70 °C for TiO_2 nanotubes, ~50 °C for TiO_2 nanoparticles, ~52 °C for Au nanoparticles, ~42 °C for SWCNTs, and ~39 °C for MWCNTs). Additionally, the authors showed that PSi revealed better performance in respect to the crystalline Si, which was attributed to the larger surface-to-volume ratio of porous material. The in vitro test performed on BXPC-3 cells treated with DMSO–PSi colloids pointed out that the temperature increased to 52 °C after 20 min of 1.25 W/cm^2 808 nm irradiation and thus viability of BxPc-3 cells was reduced to 5.7% [104].

Regli et al. showed that the light-to-heat conversion for the Si nanocrystals depends on the nanoparticle size [25]. The increase of photothermal efficiency from 58% for 4 nm NCs to 75% for 8 nm NCs was explained in terms of increasing the probability of non-radiative recombination of electron and holes states. In the case of bulk Si, the heat is generated mainly via Auger processes, which is, however, reduced for small NCs owing to the quantum confinement effects. Additionally, the PTT efficiency may be further enhanced by the shifting of the excitation wavelength toward shorter wavelength (64% for 4 nm NCs upon 488 nm irradiation) (Fig. 12.6).

As noticed by Lee et al., the functionalization of PSi' surface is required for attachment of the cancer markers to PSi [107]. One of the simple ways to provide such functionalization is based on the oxidation of PSi surface leading to PSiO generation. This modification meaningfully reduced the ability of these nanoparticles to convert light into heat. The presented studies indicated that the rise of temperature after 10 min of 808 nm irradiation (600 mW/cm^2) was about 8 °C lower in the case of PSiO (68 °C) in respect to the PSi (75 °C). Furthermore, the in vitro studies showed much lower viability of CT-26 cells incubated with PSi (~40%) comparing to the PSiO (~75%). Xia et al. showed that the efficient photothermal

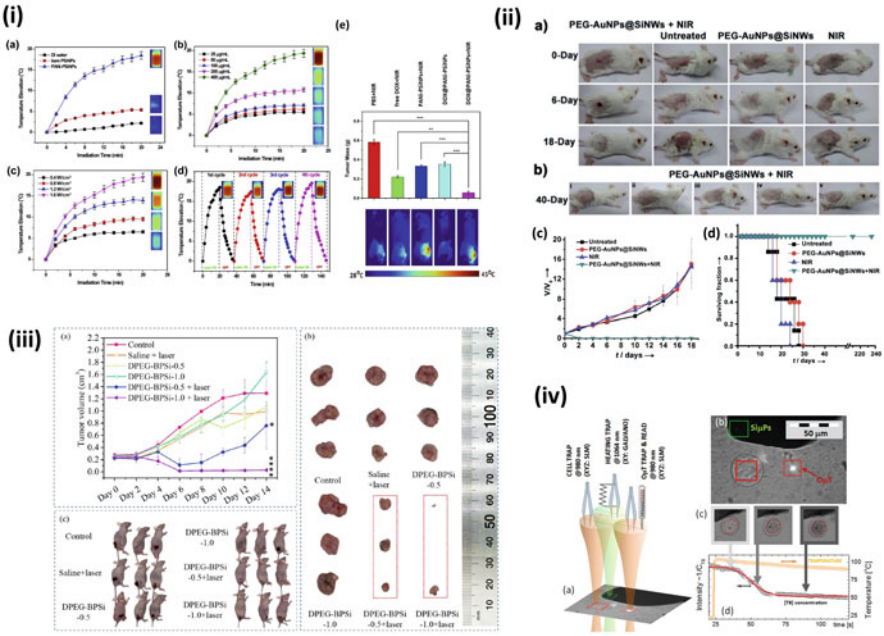

Fig. 12.6 (**i**) T–t curves of (a) DI water, bare PSiNPs (400 μg/mL), and PANi–PSiNPs (400 μg/mL) in aqueous solution under NIR laser irradiation with the power intensity of 1.6 W/cm^2 for 20 min, (b) PANi–PSiNPs solution with different concentration (20, 50, 100, 200, and 400 μg/mL) under NIR laser irradiation with the power intensity of 1.6 W/cm^2 for 20 min, (c) 400 μg/mL PANi–PSiNPs solution under NIR laser irradiation with different power intensity (0.4, 0.8, 1.2, and 1.6 W/cm^2) for 20 min, and (d) photothermal stability of 400 μg/mL PANi–PSiNPs solution under repeated NIR laser irradiation with the power intensity of 1.6 W/cm^2. Their corresponding thermal images were shown in the inset. (e) Five groups of 4T1-tumor-bearing mice exposed to (1) PBS + NIR laser, (2) free DOX + NIR laser, (3) PANi-PSiNPs + NIR laser, (4) only DOX@PANi–PSiNPs, and (5) DOX@PANi–PSiNPs + NIR laser. (e) Thermal imaging of different groups of tumor-bearing mice under NIR laser irradiation and the weight of the tumors harvested from different groups of mice after 14 days [27] (**ii**) Therapeutic effect of the SiNW-based hyperthermia agent. (a) Photos of the mice treated with different means (first column, PEG–AuNPs@SiNWs + NIR; second column, untreated; third column, PEG–AuNPs@SiNWs; fourth column, NIR). (b) Five mice 40 days after photothermal treatment from five independent sets. (c) Tumor growth curves of the 4T1 tumor cell-bearing mice over 18 days. (d) Survival curves of the mice treated with different means (e.g., black line, untreated; red line, PEG–AuNPs@SiNWs; blue line, NIR; green line PEG–AuNPs@SiNWs + NIR) [26]. (**iii**) Antitumor effect of the DPEG-BPSi nanoparticles on nude mice bearing CT 26 tumors. (a) Values of tumor volume are expressed as mean ± SD ($n = 5$). (b) Dissected tumor tissues from the nude mice. (c) Photos of anaesthetized mice at day 14 after treatment [105] (**iv**) (a) Functional scheme of the optical trapping system for single-cell hyperthermia, where 980 nm optical traps (orange cones on (a), red rectangles on (b)) are responsible for gentle trapping the cell as well as trapping/reading of the Optical micro thermometer (OmT), while the 1064 nm optical trap (green cone on (a) and green rectangle on (b)) is responsible for optical trapping/heating with Si microparticles (SimP) and (b) representative microscopic image of the cell, SiμP and OmT being trapped, activated and read. The heat is generated by the SimP heater particle (120 × 80mm) absorbing power from a moveable laser beam of 1064 nm. The scale bar (b) is 50 mm (c) The time-lapse images of the heated cells at 10, 30, and 65 seconds after switching on the heating. (d) Graphs of relative Trypan Blue (TB) accumulation in the dying cell (intensity ~ [TB concentration]$^{-1}$, left axis) and the corresponding temperature (right axis) [106]

effect in PSiNPs may also be favorable for heat-induced anticancer drug release [108]. Therefore, DOX/IR820/NH_2 –PSiNPs nanoplatform was designed with the IR820 dye, which enhances absorption cross section for 808 nm irradiation. As it was demonstrated, the 0.4 mg/mL concentration of DOX/IR820/NH_2–PSiNPs in water led to the increase of temperature by 15 °C after 5 min of 808 nm irradiation (1.6 W/cm^2).

Recently, black porous silicon nanoparticles (BPSi) were shown to be more efficient in converting NIR light (808 nm) into heat than the selected inorganic PCAs such as gold nanoparticles (diameter = 5.0 nm), Fe_3O_4 (diameter = 10 nm), and single-wall carbon nanotubes [105].

12.6 Titanium-Based Photothermal Agents

Titanium dioxide and dehydrogenated titanium dioxide have also recently gained attention as an efficient and biocompatible NIR-activated photothermal agents. Wang et al. demonstrated photothermal therapy in CD133 high expressed pancreatic cancer stem-like cells using black TiO_2 nanoparticles [109] (Fig. 12.7).

The high photothermal conversion efficiency in the water solution of bTiO_2–Gd led to the temperature increase to 70 °C and 55 °C after 10 min of 808 nm irradiation (1.5 W/cm^2) for nanoparticles concentration of 150 μg/mL and 50 μg/mL, respectively. The in vitro studies on Cd133 highly expressing PANC-1 cells indicated that the presence of bTiO_2–Gd–CD133mab led to a significant lowering of the PANC-1 cells number [111]. Another in vitro photothermal treatment was demonstrated on murine colon cancer cells (CT-26) using PVA–TiO_2 nanotubes and 2 W/cm^2 of 808 nm irradiation. The temperature of the colloid reached 45 °C (from 22 °C) after 10 min of irradiation and the cell viability was around 25%, which resulted from necrosis of the most of the cells and about 10% of late apoptosis. Better results were obtained by combining PTT with DOX drug release techniques (4.3% of cell viability). Guo et al. proposed dehydrogenated black TiO_{2-x} nanoparticles as a multifunctional NIR triggered chemo-/photothermic and photothermal agent [41]. It was shown that the absorption cross section of these TiO_{2-x} nanoparticles was fourfold higher for 808 nm wavelength in respect to the TiO_2 counterpart. The photothermal effect was investigated using DOX@TiO_{2-x}@PDA-Cy5.5 nanoplatform upon 808 nm irradiation (1 W/cm^2). After 10 min of irradiation the temperature of water solution of 1 mg/mL of DOX@TiO_{2-x}@PDA-Cy5.5 reached 54 °C. Moreover, it was proved that in in vivo experiments on tumor-bearing mice (MDA-MB-231) the temperature rise induced by using TiO_{2-x}@PDA and DOX@TiO_{2-x}@PDA-Cy5.5 was high enough to generate tumor cell apoptosis after a few minutes of irradiation (53.5 °C and 58.5 °C, respectively). However, 10 days after treatment, the volume of tumor increased again. On the other hand, total vanishing of tumor was observed in the case of DOX@TiO_{2-x}@PDA-Cy5.5 suggesting that the light-induced drug release has beneficial and synergistic impact. Ou et al. proposed to use of Magnéli-phase titanium oxides (Ti_8O_{15}) as a PTT agent

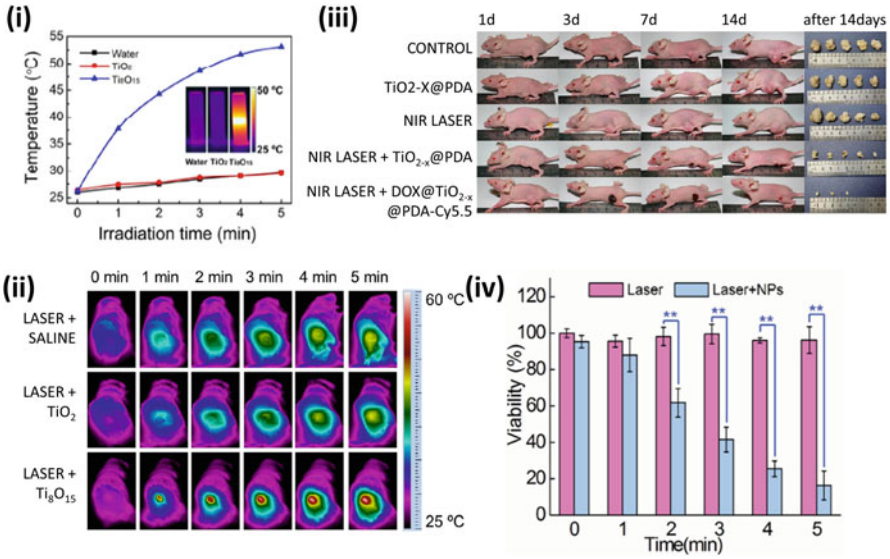

Fig. 12.7 (**i**) The comparison of TiO_2 and Ti_8O_{15} photothermal heating curves. Inset: IR images after laser irradiation at 1 W/cm^2 for 5 min [42]. (**ii**) IR thermal images of tumor-bearing mice. Pictures were taken for the intratumoral injection of saline (upper row), TiO_2 (middle row), and Ti_8O_{15} (lower row) under 808 nm laser irradiation at different time intervals [42]. (**iii**) In vivo antitumor studies using TiO_{2-x}: Representative photographs of mice and tumors [41]. (**iv**) Viability of MCF-7 cells treated with or without 100 μg mL^{-1} H–TiO_2–PEG NPs and 808 nm laser irradiation at 2 W/cm^2 for ≈5 min [110]

of significantly higher light-to-heat conversion efficiency compared to the TiO_2 counterpart [42]. Both in vitro (on 4T1 cancer cells cultures −0.125 mg/mL) and in vivo (mice bearing tumors, 25 μL of 2 mg/mL, dose = 2.5 mg/kg) experiments using 5 min of 808 nm (1 W/cm^2) irradiation revealed advantage of using Ti_8O_{15} over TiO_2. While in the case of the mice group for which intertumoral injection of TiO_2 was used, the average lifespans of ~14 days was observed (during this time tumor reached 1 cm^3), for intertumoral injection of Ti_8O_{15}, the mice were tumor-free 3 days after the treatment and survived. Ren et al. verified the potential application of black hydrogenated TiO_2 (H–TiO_2–PEG) nanoparticles in the in vitro experiments on MCF-7 and 4T1 cells [63]. The viability of both cells groups was reduced to around 20% after 5 min of 808 nm irradiation (2 W/cm^2). Additionally, low cytotoxicity and good biocompatibility of H–TiO_2–PEG allows for in vivo photothermal treatment on tumor-bearing mice. After 5 min of irradiation the temperature of the tumor increased to 52.6 °C enabling ablation of the tumor cells. As it was shown, the necrosis of the cancer cells with the destruction of the tumor vessels took place during the treatment. The survival rate 50 days after treatment using H–TiO_2–PEG nanoparticles was 100%.

12.7 Iron-Based Photothermal Agents

The main advantage of iron-based nanoparticles in the cancer treatment is related to their multimodal functionality, including their magnetic properties (magnetic resonance MR-imaging) and high photothermal efficiency (PTT agents). Oh et al. demonstrated that by using 500 μg/mL of Fe_3O_4@DMSA/DOX nanoparticles, the temperature of their water colloidal solution was elevated to 60 °C after 10 min of 808 (1 W/cm^2) irradiation [112]. This capability to convert light into heat was further used as a trigger for light-stimulated drug release on the MDS-MB-231 cells. After 10 min of laser irradiation almost 80% of apoptotic cells were found. The comparison with the fact that for nanoparticles without DOX the viability was much higher (only around 35% apoptotic cells) allows to deduce that the apoptosis was the effect of bimodal treatment involving PTT and thermally induced drug release therapy combined. Zhao et al. demonstrated that phase-shifted PFH@PLGA/Fe_3O_4 nanoplatforms can be effectively used as PTT agent, which enabled to increase the temperature of the cancer to 60 °C after 12 min of 808 nm irradiation [113]. It was shown that thermal effect of NIR irradiation and the thermoelastic expansion effect of nanocapsule phase transition caused a synergistic effect that induced coagulative necrosis and damage of tumors. Espinosa used Fe_3O_4 nanoparticles as an agents for bimodal magnetic hyperthermia and photothermal treatment [114]. Combining the magnetic hyperthermia (MHT at 520 kHz) and NIR laser (0.3 W/cm^2) induced PTT, the authors were able to increase the temperature of the nanoparticles by 25 °C in respect to the 9 °C for NIR only. This effect enabled to reduce the SKOV3 cells' viability to 15%. Furthermore the in vivo studies showed that NIR irradiation reduced the tumor growth rate by a factor of two, while the total tumor regression was observed after dual treatment. Another example of Fe_3O_4-based PTT agent was APTES-functionalized NIR-activated Fe_3O_4@mSiO_2 hybrid nanocomposite, which was characterized by high biocompatibility and stability in water. Additionally, it revealed reasonable light-to-heat conversion efficiency enabling temperature increase of the water solution to 45 °C after 15 min of 808 nm irradiation (2 W/cm^2). For this excitation density, the KB cells reveal only 15% of viability. The cytotoxic effect of Fe_3O_4 nanoparticles was meaningfully reduced by Shen et al. by the use of carboxymethyl chitosan (CMCTS) as a stabilizing agent [115]. This composite enabled to elevate the temperature of 150 mg/mL solution of Fe_3O_4@CMCTS to 70 °C after 5 min of 808 nm irradiation (2 W/cm^2). It is worth to note that the surface modification does not affect the PTT properties of Fe_3O_4 nanoparticles. The 200 μg/mL of Fe_3O_4@CMCTS led to complete apoptosis of KB cells. The in vivo tumor ablation experiment was performed upon 1.5 W/cm^2 of 808 nm irradiation for 5 min. The temperature of the tumor treated with Fe_3O_4@CMCTS rapidly increased to 50.2 °C after 1 min and further saturated at 52 °C after 5 min of irradiation. The histological examination confirmed that photothermal treatment using these nanoparticles led to total damage of tumor. Another confirmation of highly desirable properties of iron oxide nanoparticles for photothermal therapy was given by Chen et al. in both in vitro and in vivo studies. The studies on the influence of the ligand on the stability and the performance for the

light-to-heat conversion for PEI-, PAA-, and PVA-Fe_3O_4 NPs revealed that although ligand did not affect the heating abilities of the Fe_3O_4, the use of PEI significantly reduced the stability of the colloids and increased the cytotoxicity of the NPs [116].

Saeed et al. demonstrated that Fe_3O_4 nanoflowers (NFs) of the diameter of 70 nm were comparable to photothermal properties of β-TiO_2 [31]. In this case, the increase of temperature of the water solution of Fe–NFs by the 30 °C after 10 min of 808 irradiation (1.3 W/cm^2) was observed. Additionally, the in vivo cancer thermal treatment of mice with MCF-7 cancer cells, confirmed that 15 days after treatment the relative tumor volume decreased while its size increased concurrently 7 times in the control group. One of the most important issues of usage the Fe_3O_4 is the low efficacy of the photothermal therapy related to the easiness they leak from the tumor site [117]. For this reason, Zhang et al. developed a gelatin/Fe_3O_4 composites [118]. The studies on their heating abilities revealed that rise of the temperature by 25 °C can be observed after 180 s of 805 nm irradiation (1.6 W/cm^2) using gel/Fe_3O_4-15 (18.7 mass% of Fe_3O_4 in the final composite) composite. The in vitro studies proved that the total HeLa cancer cells damage can be obtained using the same excitation density. Lin et al. showed that by taking advantage from polydopamine (PDA), the Fe_3O_4@PDA core–shell structure was not only efficient heater (increase of temperature by 25 °C for 0.1 mg/mL after 10 min of 808 nm irradiation, excitation density 2 W/cm^2) but also led to the detection of mRNA [24]. Pazik et al. reported other Fe-based photothermal agent, namely $Mn_{1-x}Ni_xFe_2O_4$ nanocrystals [119]. By the use of 6 nm in diameter nanoparticles (3 mg/mL), the authors observed elevation of temperature by over 60 °C after 18 min of 808 nm irradiation (excitation density 1.5 W/cm^2) (Fig. 12.8).

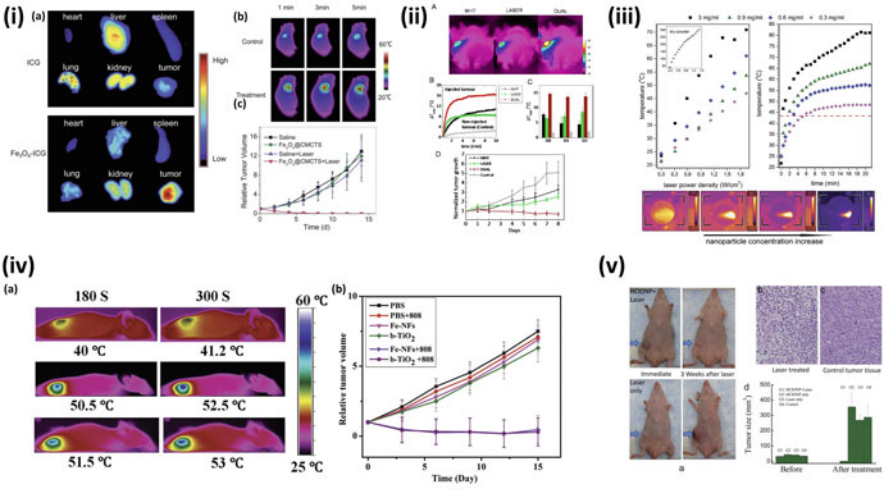

Fig. 12.8 Iron oxide nanoheathers (**i**) Ex vivo fluorescence images of excised organs and tumors after intravenous injection of Fe_3O_4. (a) In vivo photothermal therapy using Fe_3O_4@CMCTS. Thermographic images of saline-injected (control) and Fe_3O_4@CMCTS-injected (treatment) tumor-bearing mice under 808 nm laser irradiation at a power density of 1.5 Wcm^2 with different

12.8 Conclusions

Many different NP systems are claimed to be promising for thermotherapy, but it is not easy to qualitatively compare different materials for biomedical applications. The photothermal conversion efficiency η defined by Eq. (12.1), could become a figure of merit, but it is rarely measured, and it is impossible to judge on different materials based on existing literature (Table 12.1), because many studies do not provide excitation power density, saturation time (i.e., time necessary to reach stable maximum temperature) or other parameters. Other papers show the properties of powders but not colloids, thus the concentration of NPs and the measurement conditions are not homogenous, and definitely judging on PTT efficiency from dry power experiments is not a reliable method, since fundamental light-to-heat conversion efficiency will depend on the aggregation state, porosity, and concentration of NPs—none of these parameters can be measured easily to normalize the obtained results. A simplified approach, which we propose here, enables to quantitatively compare light-to-heat efficiency between different NPs. We considered a normalized value how much excitation intensity (in W/cm^2) is required to increase the temperature of colloidal solution of NPs by 1 °C within 1 second of illumination (Table 12.1 and Fig. 12.9). Further normalizing this efficiency figure of merit, by the concentration of the colloidal solution, gives an overview and the

Fig. 12.8 (continued) times: 1 min, 3 min, and 5 min (b). Volumetric changes of S180 tumors in different groups of mice after irradiation (c) [115]. (**ii**) Thermal images obtained with the IR camera in mice, after intratumoral injection of nanocubes (50 μL at [Fe] = 250 mM), in the left-hand tumor, and after 10 min application of magnetic hyperthermia (MHT, 110 kHz, 12 mT), NIR laser irradiation (LASER, 808 nm at 0.3 W/cm^2), or DUAL (both effects) (a). Corresponding thermal elevation curves for all treatments and for the non-injected tumor in the DUAL condition (b). Average final temperature increase obtained after 10 min (MHT, LASER, and DUAL) on day 0 (1 h after injection) and 1 and 2 days after injection and for non-injected tumors (c). Average tumor growth in nanocube-injected mice exposed to MHT, LASER, and DUAL during the 8 days following the 3 days of treatment (d) [114]. (**iii**) Laser power dependence on $Mn_{1-x}Ni_xFe_2O_4$ ferrite heater nanoparticles dispersion temperature (left) as well as evolution of the sample temperature over time (right). Inset in the left figure shows results achieved for dry powder. Bottom images show concentration effect on dispersion heating ability after 60 s [119]. (**iv**) In vivo PTT: temperature variations in tumor-bearing mice exposed to (top row) Saline group: mice intratumorally (IT) injected and irradiated with 808 nm (0.7 W/cm^2); (middle row) mice IT injected with Fe–NFs and (bottom row) b-TiO_2 NPs (100 mL, 250 mg/mL) and irradiated at 808 nm (0.7 W/cm^2) (a), tumor growth curves for different systems (b) [31]. (**v**) Representative photos of SUM-159 tumor-bearing mice of both immediate and 3 weeks after laser treatment. Laser wavelength 885 nm. Power density 2.5 W cm^2. Irradiation time = 10 min. Arrows point to the tumor sites. H&E staining of tumor tissues from mouse treated with nanoparticles plus laser irradiation (a) and control mouse without any treatment (b). Anti-tumor efficacy of four different groups of mice before and 3 weeks post various treatments. Four groups (5 mice for each group) are magnetic nanocrystals injected mice with laser irradiation (G1), nanocrystals injected mice without laser irradiation (G2), laser-treated mice without injection of nanoparticles (G3), and control mice injected with PBS (G4) (c). (d) [35]

Table 12.1 The comparison of different features of different NIR-activated PTT agents (group: G—graphene-based materials, P—polymeric materials, Ln—lanthanide-doped materials, Si—silicon-based materials, Ti—titanium-based materials, Fe—iron-based materials)

PTT agent	Group	Excitation density (W/cm^2)	ΔT (°C)	NPs concentration	°C/1 W/cm^2/s establishment time	Heating efficiency/ concentration	Comments	Ref.
Graphene @ phthalocyanine	G	3	33 (after 5 min)	10 μg/mL	2.20	0.220000	29% HeLa	[22]
Nano-ICG-GO-FA	G	1	35 (after 10 min	20 μg/mL	3.50	0.175000	10% HeLa	[49]
GO-PEG-folate	G	0.25	11 (after 8 min) in vivo	200 μL/mice; 8 mg/kg	5.50	0.027500	Tumor-inoculated C57BL/J destruction after 14 days	[18]
GO-PEG-PEI	G	2	11 (after 5 min)	10 μg mL	1.10	0.110000	Mice receiving GGIC plus NIR laser treatment showed the smallest tumor volumes, with tumor growth inhibited by ~91%.	[51]
GO-IONP	G	3	35 °C (after 5 min)	40 μg/mL	2.33	0.058300	20% viability BXPC-3 cells	[52]
Fluorinated GO (FGO)	G	(1.6 W)	37.3 (after 1 min)	1 μg mL				[53]
GO_HA (Hyaluronic acid)	G	2	32 (after 10 min)	1 mg/mL	1.60	0.001600	20% B16F1 cells viability	[54]
Supra-CND	G	1	32 (after 10 min)	200 ppm	3.20			[43]
C-dots	G	2	25 (after 10 min)	200 μg/mL	1.25	0.006250	0% viability of HBE cells	[57]
CyCD	G	2	37 (after 10 min)	120 μg/mL	1.85	0.015420	91% CT26 tumor inhibition after 11 days	[59]

N-CND	G	15 mJ/cm^2 (PW)	27 (after 5 min)	20 mg/mL			Total growth inhibition of HepG2 after 14 days	[61]
DA CNDs	G	1.5	30 (after 5 min)	50 μg/mL	4.00	0.080000	13% of HeLa cell viability	[62]
SWCNT-(KFKA)7	G	1.2	22 (after 5 min)	50 μg/mL	3.67	0.073300		[63]
MWCNT	G	1.4	19 (808 nm)	1.5 mg/mL				[47]
			19.6 (980 nm)					
			19.5 (1090 nm)					
SWNT-PEG-TA	G	1	40 (after 5 min)	5 μg/mL	8.00	1.600	20% viability HCC1937	[66]
CNS	G	6	45 (after 10 min)	400 μg/mL	0.75	0.001880	<20% PC-3M-IE8 cells viability	[29]
LaF_3:Nd^{3+}	Ln	2	34 (after 10 min)	0.3% in mass	1.70			[74]
$NaNdF_4$@ $NdYF_4$@ $NaYF_4$:1%Nd^{3+}	Ln	2	25 (after 6 min)	20 mg/mL	2.08	0.000100		[38]
YVO_4:4.8%Nd^{3+}	Ln	1	24	–				[77]
$Y_3Ga_5O_{12}$:Nd^{3+}	Ln	800	42	Powder				[79]
$Y_3Ga_5O_{12}$:Yb^{3+}, Er^{3+}	Ln	5000	46	Powder				[79]
Y_2O_3: Yb^{3+},Tm^{3+}	Ln	P = 0.85 W	358	Powder				[72]
$LaAlO_3$: Yb^{3+},Tm^{3+}	Ln	P = 0.85 W	143	Powder				[72]
YAG:Yb^{3+},Tm^{3+}	Ln	P = 0.85 W	131	Powder				[72]

(continued)

Table 12.1 (continued)

PTT agent	Group	Excitation density (W/cm^2)	ΔT (°C)	NPs concentration	°C/1 W/cm^2/s establishment time	Heating efficiency/ concentration	Comments	Ref.
$NaLuF_4:Yb^{3+},Er^{3+}$ @NGO	Ln	2	30 (after 5 min)	0.5 mg/mL	3.00	0.006000		[82]
$Y_2O_3:Yb^{3+},Er^{3+}Eu^{3+}$	Ln	55	100	Powder				[85]
$Y_2O_3:Yb^{3+},Er^{3+}$	Ln	55	20	Powder				[85]
$YVO_4:Yb^{3+}$, Er^{3+}	Ln	50	130	Powder				[86]
$La_2O_3:Yb^{3+},Er^{3+}$	Ln	26	40	Powder				[88]
$SrWO_4:Yb^{3+},Er^{3+}$	Ln	P = 1.7	120	Powder			Micro	[89]
GdOF: $Nd^{3+}/Yb^{3+}/Er^{3+}@SiO_2$	Ln	7	40	1 mg/mL			53% E coli viability	[36]
$NaYF_4:Yb^{3+}/Er^{3+}$@ $NaYF_4:Yb^{3+}/Nd^{3+}$	Ln	3.6	11 (after 10 min)	10 mg/mL	0.31	0.000030		[92]
YF_3:0.5%Tm^{3+}/40%Yb^{3+}	Ln	4.8	18 (after 3 min)	Micropowder	1.22			[94]
$Ba_5Gd_8Zn_4O_{21}$: Yb^{3+}/Tm^{3+}	Ln	P = 1.8	43	Powder				[81]
POrCP NPs	P	0.75	50 (after 10 min)	0.1 mg/mL	6.67	0.066667	0% HeLa cell viability	[96]
CP1−CP4	P	0.5	35 (after 5 min)	50 μg/mL	14.00	0.280000		[97]
PFTTQ NPs	P	0.75	38 (after 10 min)	400 μg/mL	5.07	0.012670	10% MDA-MB-231 cell viability	[40]
SPNs-F40	P	0.5	32 (after 5 min)	15 μg/mL	12.80	0.853330		[98]
PSiNPs	Si	1.6	19 (after 20 min)	400 μg/mL	0.59	0.001480		[27]
PSi fragments	Si	0.3	58 (after 10 min)	Powder				[103]

DMSO-PSi	Si	1.25	27	–				[104]
Si-NCs	Si	P = 1 W	30 (after 15 min)	4.3 mg/mL				[25]
PSi	Si	0.6	50 (after 10 min)	–	8.33			[107]
PSiO	Si	0.6	43 (after 10 min)	–	7.17			[107]
DOX/IR820/NH 2 -PSiNPs	Si	1.6	15 (after 5 min)	0.4 mg/mL	1.88	0.00469		[108]
bTiO_2-Gd	Ti	1.5	45 (after 10 min)	150 μg/mL	3.00	0.02000	45% cell viability CD133	[109]
PVA-TNT	Ti	2	20 (after 10 min)		1.00			[111]
DOX@TiO_{2-x}@PDA-Cy5.5	Ti	1	24 (after 10 min)	1 mg/mL	2.40	0.00240	35% cell MDA-MB-231 viability	[41]
Ti_8O_{15}	Ti	1	27 (after 5 min)	1 mg/mL	5.40	0.00540	30% cell viability	[42]
Fe_3O_4	Fe	2	40 (after 10 min)	250 μg/mL	2.00	0.00800	70% of MDA-MB-23 cells viability	[112]
Fe_3O_4 nanocubes	Fe	0.3	8 (after 10 min)	12 mM	2.67	0.00022	35% SKOV3 cells viability	[114]
Fe-NFs	Fe	1.3	30 (after 10 min)	200 μg/mL	2.31	0.01154	22% MCF-7 cells viability	[31]
Fe3O4@CMCTS	Fe	2	45 (after 5 min)	150 mg/mL	0.075	0.0000005		
$Mn_{1-x}Ni_xFe_2O_4$	Fe	1.5	60 (after 20 min)	3 mg/mL	2.00	0.00067		[119]

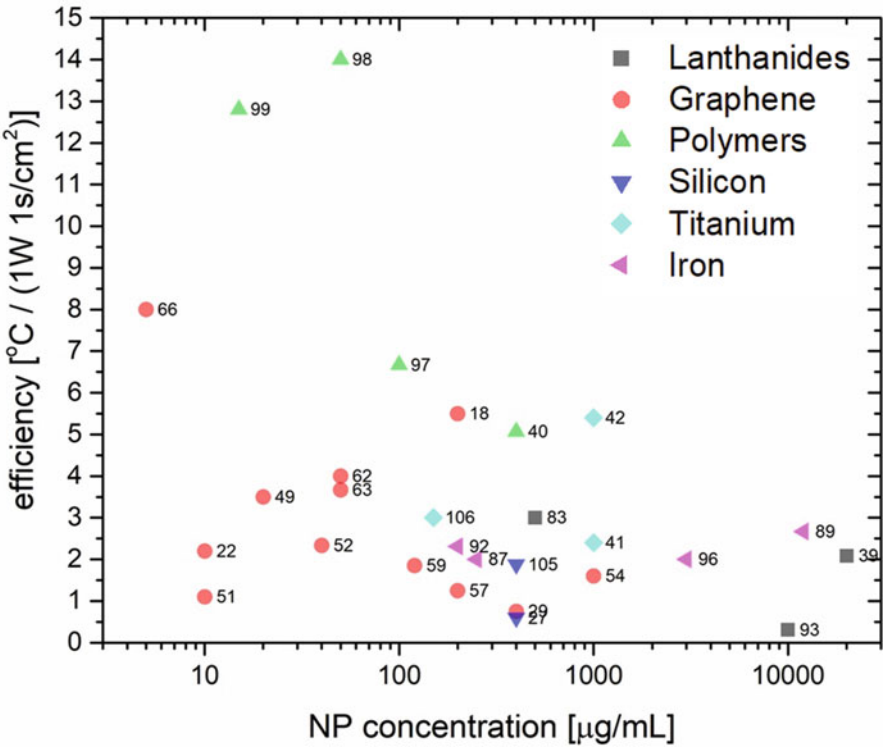

Fig. 12.9 A comparison of light-to-heat efficiencies of different types of NPs versus the NPs dose used. The numbers by the points indicate the reference article. Only those references were shown, which provided enough experimental data to calculate efficiency of light-to-heat generation per single Watt/cm^2 of optical excitation power, per single second of illumination, per μg of NPs per ml of solvent

comparison between different materials. Polymer NPs, which heat up to 35 °C after 5 min of illumination at very low 15 ug/mL concentrations seem to be much better than all other materials. Although similarly small concentrations have been tested with carbon-based materials, such materials display 2, up to over 10 times smaller heating rates. Such comparison shall not be analyzed without careful interpretation. Lanthanide-based NPs, for example, unless conjugated with GO, show very poor light-to-heat efficiency values (although $\eta > 70\%$ was estimated) at very high concentrations, which originates most probably from their low absorption cross section. However, their great potential is the capability to combine heating and optical thermometry within single NP. Another great potential of Ln:NPs is their absorption in NIR, anti-Stokes or NIR-NIR emission, long luminescence lifetimes, and photostability, which all make the high signal to background luminescence detection possible. Moreover, due to narrowband absorption bands, some features of Ln^{3+} (e.g., either luminescence or heating, or a design of Ln-doped NPs) enable to specifically address the given properties, e.g., 800 nm can be used to initiate

light-to-heat conversion in highly, e.g., Nd^{3+}-doped NPs, while 980 can address the luminescence and, e.g., temperature readout without inducing extensive heating. Such features are either impossible or difficult to get with GO-based nanomaterials. Therefore, not only heating efficiency matters in practical implementation of these materials, but also additional features such as easiness of biofunctionalization, reproducibility of photo-physical properties, biosafety, and lack of bio-interactions other than through generated heat, multifunctional properties, etc., which all impact the suitability of such nanotechnology designs for PTT.

For practical hyperthermia, either intratumor injection, passive diffusion or active targeting of tumor with bio-functionalized nanoparticles can be achieved depending on the surface chemistry of HT agents. From these three possibilities, only active targeting shall offer selectivity of HT unlike other options, which also means the exact concentration of heating nanoparticles in such real in vivo therapies is unknown, and will obviously depend on the mechanism of retention, size of the nanoparticles, their surface chemistry, type of tumor, and its vasculature. Despite successful demonstrations of HT on mice tumors after intratumor injection of HTNPs, one shall expect this treatment approach will be sufficient for solid tumors, but not for diffused cancers localized close to delicate tissues (e.g., within head or neck) or close to nerves. For this reason, combining nanoheating with localized, volumetric, subtissue thermometry is important, and safer than disregarding thermometry feedback control. For the same reason, combining nanoheaters and nanothermometry within single nanoparticles is more straightforward and safer than exploiting these two features in two individual nano-species. This combination is especially promising for in vivo experiments, since hyperthermia treatment at extended tissue depths, i.e., up to a few centimeters, may become possible. Volumetric feedback control of hyperthermia treatment by single nanoparticle thermometer and heater is difficult, because (1) the concentration of HTNPs is unknown, (2) local heating within HTNPs may be very high leading to saturation of optical thermometers, (3) heating and luminescence of HTNPs occurs along the whole path of photoexcitation [5].

There are numerous future directions for HT research, and most important one is finding materials, which are as efficient in light-to-heat conversion as possible. Simultaneously, these materials shall enable in either passive (thought saturation of heat generation) or active (through localized temperature 3D subskin, volumetric monitoring) way, to feedback control the amount of heat being deposited in the tissues. Despite numerous successful hyperthermia demonstrations, quantitative measures to compare different materials have to be reported, to let objectively judge on the suitability of these materials for HT:

1. How efficient given nanomaterials are—what stimulus dose (e.g., W/cm^2 optical stimulation intensity in a given time per NPs mg/ml dose) is required to raise the temperature by 1 °C?
2. How safe they are by themselves—do they display inherent chemical primary or secondary toxicity, do they aggregate, how fast the clearance of NPs from the body occurs?

3. How specific the nanoheater platforms are tumor passive or active targeting should be compared with deposition of NPs in normal tissue; lack of side effects to delicate surrounding tissues should be verified as well?

Only finding trustworthy answers to these questions will help to find the most reliable nanomaterials and bring the nanotechnology from laboratories to patients beds.

Acknowledgments A.B. acknowledges the FET Open project that has received funding from the European Union's Horizon 2020 research and innovation programme under grant agreement No. 801305. K.K and K.E acknowledge "High sensitive thermal imaging for biomedical and microelectronic application" project is carried out within the First Team program of the Foundation for Polish Science co-financed by the European Union under the European Regional Development Fund.

References

1. Sun X et al (2008) Nano-graphene oxide for cellular imaging and drug delivery. Nano Res 1:203–212
2. Hu Z, Li J, Huang Y, Chen L, Li Z (2015) Functionalized graphene/C60nanohybrid for targeting photothermally enhanced photodynamic therapy. RSC Adv 5:654–664
3. Gangopadhyay M et al (2015) Coumarin-containing-star-shaped 4-arm-polyethylene glycol: targeted fluorescent organic nanoparticles for dual treatment of photodynamic therapy and chemotherapy. Photochem Photobiol Sci 14:1329–1336
4. Gary-Bobo M et al (2012) Cancer therapy improvement with mesoporous silica nanoparticles combining targeting, drug delivery and PDT. Int J Pharm 423:509–515
5. Marciniak L, Pilch A, Arabasz S, Jin D, Bednarkiewicz A (2017) Heterogeneously Nd3+ doped single nanoparticles for NIR-induced heat conversion, luminescence, and thermometry. Nanoscale
6. Bednarkiewicz A, Wawrzynczyk D, Nyk M, Strek W (2011) Optically stimulated heating using Nd3+ doped NaYF4 colloidal near infrared nanophosphors. Appl Phys B Lasers Opt 103:847–852
7. Roper DK, Ahn W, Hoepfner M (2007) Microscale heat transfer transduced by surface plasmon resonant gold nanoparticles. J Phys Chem C
8. Shibu ES, Hamada M, Murase N, Biju V (2013) Nanomaterials formulations for photothermal and photodynamic therapy of cancer. J Photochem Photobiol C: Photochem Rev 15:53–72
9. Shanmugam V, Selvakumar S, Yeh C-S (2014) Near-infrared light-responsive nanomaterials in cancer therapeutics. Chem Soc Rev 43:6254–6287
10. Bao Z, Liu X, Liu Y, Liu H, Zhao K (2016) Near-infrared light-responsive inorganic nanomaterials for photothermal therapy. Asian J Pharm Sci 11:349–364
11. Hong G, Diao S, Antaris AL, Dai H (2015) Carbon nanomaterials for biological imaging and nanomedicinal therapy. Chem Rev 115:10816–10906
12. Jaque D et al (2014) Nanoparticles for photothermal therapies. Nanoscale 6:9494–9530
13. Cheng L, Wang C, Liu Z (2014) Functional nanomaterials for phototherapies of cancer. Chinese J Clin Oncol 41:18–26
14. Singh R, Torti SV (2013) Carbon nanotubes in hyperthermia therapy. Adv Drug Deliv Rev 65:2045–2060
15. Yang K, Feng L, Shi X, Liu Z (2013) Nano-graphene in biomedicine: theranostic applications. Chem Soc Rev 42:530–547

16. Chen YW, Su YL, Hu SH, Chen SY (2016) Functionalized graphene nanocomposites for enhancing photothermal therapy in tumor treatment. Adv Drug Deliv Rev 105:190–204
17. Qu Y et al (2018) Advancements of graphene-based nanomaterials in biomedicine. Mater Sci Eng C 90:764–780
18. Kalluru P, Vankayala R, Chiang CS, Hwang KC (2016) Nano-graphene oxide-mediated in vivo fluorescence imaging and bimodal photodynamic and photothermal destruction of tumors. Biomaterials 95:1–10
19. Sahu A, Choi WI, Lee JH, Tae G (2013) Graphene oxide mediated delivery of methylene blue for combined photodynamic and photothermal therapy. Biomaterials 34:6239–6248
20. Kim SH et al (2015) In vitro and in vivo tumor targeted photothermal cancer therapy using functionalized graphene nanoparticles. Biomacromolecules 16:3519–3529
21. Gollavelli G, Ling YC (2014) Magnetic and fluorescent graphene for dual modal imaging and single light induced photothermal and photodynamic therapy of cancer cells. Biomaterials 35:4499–4507
22. Jiang B-P et al (2014) Graphene loading water-soluble phthalocyanine for dual-modality photothermal/photodynamic therapy via a one-step method. J Mater Chem B 2:7141–7148
23. Sheng Z et al (2013) Protein-assisted fabrication of nano-reduced graphene oxide for combined in vivo photoacoustic imaging and photothermal therapy. Biomaterials 34:5236–5243
24. Lin LS et al (2014) Multifunctional Fe3O4@polydopamine core-shell nanocomposites for intracellular mRNA detection and imaging-guided photothermal therapy. ACS Nano 8:3876–3883
25. Regli S, Kelly JA, Shukaliak AM, Veinot JGC (2012) Photothermal response of photoluminescent silicon nanocrystals. J Phys Chem Lett 3:1793–1797
26. Su Y et al (2014) Silicon nanowire-based therapeutic agents for in vivo tumor near-infrared photothermal ablation. J Mater Chem B 2:2892–2898
27. Xia B et al (2017) Photothermal and biodegradable polyaniline/porous silicon hybrid nanocomposites as drug carriers for combined chemo-photothermal therapy of cancer. Acta Biomater 51:197–208
28. Peng Z et al (2017) Carbon dots: biomacromolecule interaction, bioimaging and nanomedicine. Coord Chem Rev 343:256–277
29. Miao ZH et al (2016) Glucose-derived carbonaceous nanospheres for photoacoustic imaging and photothermal therapy. ACS Appl Mater Interfaces 8:15904–15910
30. Torti SV et al (2007) Thermal ablation therapeutics based on CNx multi-walled nanotubes. Int J Nanomedicine 2:707–714
31. Saeed M et al (2018) Controllable synthesis of Fe3O4 nanoflowers: enhanced imaging guided cancer therapy and comparison of photothermal efficiency with black-TiO2. J Mater Chem B 6:3800–3810
32. Huang C-C et al (2015) New insight on optical and magnetic Fe_3O_4 nanoclusters promising for near infrared theranostic applications. Nanoscale
33. Marciniak L et al (2016) Water dispersible LiNdP4O12nanocrystals: new multifunctional NIR-NIR luminescent materials for bio-applications. J Lumin 176:144–148
34. Chu M et al (2013) Near-infrared laser light mediated cancer therapy by photothermal effect of Fe3O4 magnetic nanoparticles. Biomaterials 34:4078–4088
35. Chen H et al (2014) Highly crystallized iron oxide nanoparticles as effective and biodegradable mediators for photothermal cancer therapy. J Mater Chem B
36. Suo H, Zhao X, Zhang Z, Guo C (2017) 808 nm light-triggered thermometer-heater upconverting platform based on Nd3+-sensitized yolk-Shell GdOF@SiO2. ACS Appl Mater Interfaces 9:43438–43448
37. Du P, Luo L, Park HK, Yu JS (2016) Citric-assisted sol-gel based Er3+/Yb3+-codoped Na0.5Gd0.5MoO4: a novel highly-efficient infrared-to-visible upconversion material for optical temperature sensors and optical heaters. Chem Eng J 306:840–848

38. Marciniak L, Pilch A, Arabasz S, Jin D, Bednarkiewicz A (2017) Heterogeneously Nd $^{3+}$ doped single nanoparticles for NIR-induced heat conversion, luminescence, and thermometry. Nanoscale 9:8288–8297
39. Suo H et al (2017) All-in-one thermometer-heater up-converting platform YF3:Yb3+,Tm3+ operating in the first biological window. J Mater Chem C 5:1501–1507
40. Geng J et al (2015) Biocompatible conjugated polymer nanoparticles for efficient photothermal tumor therapy. Small 11:1603–1610
41. Guo W et al (2017) TiO2-xbased nanoplatform for bimodal cancer imaging and NIR-triggered chem/photodynamic/photothermal combination therapy. Chem Mater 29:9262–9274
42. Ou G et al (2016) Photothermal therapy by using titanium oxide nanoparticles. Nano Res 9:1236–1243
43. Li D et al (2016) Supra-(carbon nanodots) with a strong visible to near-infrared absorption band and efficient photothermal conversion. Light Sci Appl 5(1–8):e16120
44. Cheng Y et al (2008) Highly efficient drug delivery with gold nanoparticle vectors for in vivo photodynamic therapy of cancer. J Am Chem Soc 130:10643–10647
45. Wei X et al (2018) A designed synthesis of multifunctional carbon nanoframes for simultaneous imaging and synergistic chemo-photothermal cancer therapy. New J Chem 42:923–929
46. Sheng Z et al (2013) Protein-assisted fabrication of nano-reduced graphene oxide for combined in vivo photoacoustic imaging and photothermal therapy. Biomaterials 34:5236–5243
47. Maestro LM et al (2013) Heating efficiency of multi-walled carbon nanotubes in the first and second biological windows. Nanoscale 5:7882
48. Miao W, Shim G, Lee S, Oh YK (2014) Structure-dependent photothermal anticancer effects of carbon-based photoresponsive nanomaterials. Biomaterials 35:4058–4065
49. Wang Y-W et al (2013) Dye-enhanced graphene oxide for photothermal therapy and photoacoustic imaging. J Mater Chem B 1:5762
50. Hu SH, Chen YW, Hung WT, Chen IW, Chen SY (2012) Quantum-dot-tagged reduced graphene oxide nanocomposites for bright fluorescence bioimaging and photothermal therapy monitored in situ. Adv Mater 24:1748–1754
51. Tao Y, Ju E, Ren J, Qu X (2014) Immunostimulatory oligonucleotides-loaded cationic graphene oxide with photothermally enhanced immunogenicity for photothermal/immune cancer therapy. Biomaterials 35:9963–9971
52. Wang S et al (2014) Magnetic graphene-based nanotheranostic agent for dual-modality mapping guided photothermal therapy in regional lymph nodal metastasis of pancreatic cancer. Biomaterials 35:9473–9483
53. Romero-Aburto R et al (2013) Fluorinated graphene oxide; a new multimodal material for biological applications. Adv Mater 25:5632–5637
54. Jung HS et al (2014) Nanographene oxide À hyaluronic acid conjugate for photothermal ablation therapy of skin cancer. ACS Nano 8:260–268
55. Wu M-C, Deokar AR, Liao J-H, Shih P-Y, Ling Y-C (2013) Graphene-based photothermal agent for rapid and effective killing of bacteria. *ACS Nano* 7:1281
56. Hassan M, Gomes VG, Dehghani A, Ardekani SM (2018) Engineering carbon quantum dots for photomediated theranostics. Nano Res 11:1–41
57. Ge J et al (2015) Red-emissive carbon dots for fluorescent, photoacoustic, and thermal theranostics in living mice. Adv Mater 27:4169–4177
58. Geng B et al (2018) NIR-responsive carbon dots for efficient photothermal cancer therapy at low power densities. Carbon N Y 134:153–162
59. Zheng M et al (2016) One-pot to synthesize multifunctional carbon dots for near infrared fluorescence imaging and photothermal cancer therapy. ACS Appl Mater Interfaces 8:23533–23541
60. Ge J et al (2016) Carbon dots with intrinsic theranostic properties for bioimaging, red-light-triggered photodynamic/photothermal simultaneous therapy in vitro and in vivo. Adv Healthc Mater 5:665–675

61. Lee C et al (2016) Biodegradable nitrogen-doped carbon nanodots for non-invasive photoacoustic imaging and photothermal therapy. Theranostics 6:2196–2208
62. Li Y, Zhang X, Zheng M, Liu S, Xie Z (2016) Dopamine carbon nanodots as effective photothermal agents for cancer therapy. RSC Adv 6:54087–54091
63. Hashida Y et al (2014) Photothermal ablation of tumor cells using a single-walled carbon nanotube-peptide composite. J Control Release 173:58–66
64. Zhang M et al (2017) Magnetic and fluorescent carbon nanotubes for dual modal imaging and photothermal and chemo-therapy of cancer cells in living mice. Carbon N Y 123:70–83
65. Mori K, Kawaguchi M, Fujigaya T, Ohno J, Ikebe T (2018) Polymer-coated carbon nanotubes as a molecular heater platform for hyperthermic therapy. J Hard Tissue Biol 27:139–146
66. Han Z, Han X, Wang Z, Wu S, Zheng R (2015) Thioaptamer conjugated single-wall carbon nanotubes in human breast cancer targeted photothermal therapy in-vivo and in-vitro. Int J Clin Exp Med 9:58–68
67. Nair LV, Nagaoka Y, Maekawa T, Sakthikumar D, Jayasree RS (2014) Quantum dot tailored to single wall carbon nanotubes: a multifunctional hybrid nanoconstruct for cellular imaging and targeted photothermal therapy. Small 10:2771–2775
68. Lin Z et al (2015) Photothermal ablation of bone metastasis of breast cancer using PEGylated multi-walled carbon nanotubes. Sci Rep 5:1–10
69. Chen D et al (2014) Photoacoustic imaging guided near-infrared photothermal therapy using highly water-dispersible single-walled carbon nanohorns as theranostic agents. Adv Funct Mater 24:6621–6628
70. del Rosal B et al (2017) Nd3+ ions in nanomedicine: perspectives and applications. Opt Mater (Amst) 63:185–196
71. del Rosal B, Ximendes E, Rocha U, Jaque D (2017) In vivo luminescence nanothermometry: from materials to applications. Adv Opt Mater 5
72. Liu G et al (2016) Investigation into optical heating and applicability of the thermal sensor bifunctional properties of Yb^{3+} sensitized Tm^{3+} doped Y_2O_3, YAG and $LaAlO_3$ phosphors. RSC Adv 6:97676–97683
73. Suo H, Guo C, Li T (2016) Broad-scope thermometry based on dual-color modulation upconversion phosphor Ba5Gd8Zn4O21:Er3+/Yb3+. J Phys Chem C 120:2914–2924
74. Rocha U et al (2016) Real-time deep-tissue thermal sensing with sub-degree resolution by thermally improved Nd3+:LaF3multifunctional nanoparticles. J Lumin 175:149–157
75. Carrasco E et al (2015) Intratumoral thermal reading during photo-thermal therapy by multifunctional fluorescent nanoparticles. Adv Funct Mater 25:615–626
76. Rocha U et al (2014) Nd3+ doped LaF3 nanoparticles as self-monitored photo-thermal agents. Appl Phys Lett 104:053703
77. Kolesnikov IE et al (2017) Nd3+ single doped YVO4 nanoparticles for sub-tissue heating and thermal sensing in the second biological window. Sensors Actuators B Chem 243:338–345
78. Xu S et al (2017) 808 nm laser induced photothermal effect on Sm3+/Nd3+doped NaY(WO4)2 microstructures. Sensors Actuators B Chem 240:386–391
79. Lozano-Gorrín AD et al (2018) Lanthanide-doped Y3Ga5O12 garnets for nanoheating and nanothermometry in the first biological window. Opt Mater (Amst) 84:46–51
80. Liu G et al (2016) Investigation into optical heating and applicability of the thermal sensor bifunctional properties of Yb3+ sensitized Tm3+ doped Y2O3, YAG and LaAlO3 phosphors. RSC Adv 6:97676–97683
81. Suo H et al (2015) Thermometric and optical heating bi-functional properties of upconversion phosphor $Ba_5Gd_8Zn_4O_{21}$:Yb^{3+}/Tm^{3+}. J Mater Chem C 3:7379–7385
82. Li P et al (2018) Lanthanide-doped upconversion nanoparticles complexed with nano-oxide graphene used for upconversion fluorescence imaging and photothermal therapy. Biomater Sci 6:877–884
83. Zhu X et al (2016) Temperature-feedback upconversion nanocomposite for accurate photothermal therapy at facile temperature. Nat Commun

84. Zhang Y et al (2018) Temperature sensing, excitation power dependent fluorescence branching ratios, and photothermal conversion in $NaYF_4:Er^{3+}/Yb^{3+}$@$NaYF_4:Tm^{3+}/Yb^{3+}$core-shell particles. Opt Mater Express 8:1820–1832
85. Dey R, Pandey A, Rai VK (2014) Er3+-Yb3+ and Eu3+-Er3+-Yb 3+ codoped Y2O3 phosphors as optical heater. Sensors Actuators B Chem 190:512–515
86. Mahata MK, Kumar K, Rai VK (2015) Er3+–Yb3+doped vanadate nanocrystals: a highly sensitive thermographic phosphor and its optical nanoheater behavior. Sensors Actuators B Chem 209:775–780
87. Dey R, Pandey A, Rai VK (2014) The Er3+-Yb3+codoped La2O3phosphor in finger print detection and optical heating. Spectrochim Acta – Part A Mol Biomol Spectrosc 128:508–513
88. Sun Z et al (2017) Nanostructured La2O3: Yb3+/Er3+: temperature sensing, optical heating and bio-imaging application. Mater Res Bull 92:39–45
89. Pandey A, Rai VK, Kumar V, Kumar V, Swart HC (2015) Upconversion based temperature sensing ability of Er3+-Yb3+codoped SrWO4: an optical heating phosphor. Sensors Actuators B Chem 209:352–358
90. Du P, Luo L, Yu JS (2017) Tunable color upconverison emissions in erbium(III)-doped BiOCl microplates for simultaneous thermometry and optical heating. Microchim Acta 184:2661–2669
91. Lu H et al (2017) Dual functions of Er3+/Yb3+ codoped Gd2(MoO4)3 phosphor: temperature sensor and optical heater. J Lumin 191:13–17
92. Shao Q et al (2017) Enhancing the upconversion luminescence and photothermal conversion properties of ~800 nm excitable core/shell nanoparticles by dye molecule sensitization. J Colloid Interface Sci 486:121–127
93. Liu G, Wu L, Wei X, Zhang D, Hu L (2018) Investigation on laser-induced heating in NaYbF4:Er3+ for accurate photo-thermal conversion with temperature feedback. Opt Commun 426:418–422
94. Suo H et al (2017) All-in-one thermometer-heater up-converting platform $YF_3:Yb^{3+},Tm^{3+}$ operating in the first biological window. J Mater Chem C 5:1501–1507
95. Sun Z et al (2017) High sensitivity thermometry and optical heating bi-function of Yb3+/Tm3+ co-doped BaGd2ZnO5 phosphors. Curr Appl Phys 17:255–261
96. Guo B et al (2016) A Porphyrin-based conjugated polymer for highly efficient in vitro and in vivo Photothermal therapy. Small 12:6243–6254
97. Li S et al (2016) Near-infrared (NIR)-absorbing conjugated polymer dots as highly effective Photothermal materials for in vivo cancer therapy. Chem Mater 28:8669–8675
98. Lyu Y et al (2016) Intraparticle molecular orbital engineering of semiconducting polymer nanoparticles as amplified theranostics for in vivo photoacoustic imaging and photothermal therapy. ACS Nano 10:4472–4481
99. Lyu Y et al (2017) Dendronized semiconducting polymer as photothermal nanocarrier for remote activation of gene expression. Angew Chemie – Int Ed 56:9155–9159
100. Lyu Y, Xie C, Chechetka SA, Miyako E, Pu K (2016) Semiconducting polymer nanobioconjugates for targeted photothermal activation of neurons. J Am Chem Soc 138:9049–9052
101. MacNeill CM, Wailes EM, Levi-Polyachenko NH (2013) A comparative study of the photothermal efficiency of electrically conducting poly(3,4-ethylenedioxythiophene)-based nanomaterials with cancer cells. J Nanosci Nanotechnol 13:3784–3791
102. Chen Y et al (2015) Polyaniline electrospinning composite fibers for orthotopic photothermal treatment of tumors in vivo. New J Chem 39:4987–4993
103. Hong C, Kang J, Kim H, Lee C (2012) Photothermal properties of inorganic nanomaterials as therapeutic agents for cancer thermotherapy. J Nanosci Nanotechnol 12:4352–4355
104. Hong C, Lee C (2014) In vitro cell tests of pancreatic malignant tumor cells by photothermotherapy based on DMSO porous silicon colloids. Lasers Med Sci 29:221–223
105. Xu W et al (2018) A scalable synthesis of biodegradable black mesoporous silicon nanoparticles for highly efficient photothermal therapy. ACS Appl Mater Interfaces

106. Drobczyński S et al (2017) Toward controlled photothermal treatment of single cell: optically induced heating and remote temperature monitoring in vitro through double wavelength optical tweezers. ACS Photonics 4:1993–2002
107. Lee C, Hong C, Lee J, Son M, Hong SS (2012) Comparison of oxidized porous silicon with bare porous silicon as a photothermal agent for cancer cell destruction based on in vitro cell test results. Lasers Med Sci 27:1001–1008
108. Bing X, Bin W, Zhenyu C, Qi Z, Jisen S (2015) Near-infrared light-triggered intracellular delivery of anticancer drugs using porous silicon nanoparticles conjugated with IR820 dyes. Adv Mater Interfaces 3:1500715
109. Wang S et al (2018) Black TiO2-based nanoprobes for T1-weighted MRI-guided photothermal therapy in CD133 high expressed pancreatic cancer stem-like cells. Biomater Sci
110. Ren W et al (2015) A near infrared light triggered hydrogenated black TiO2 for cancer photothermal therapy. Adv Healthc Mater 4:1526–1536
111. Hong C et al (2012) In-vitro cell tests using doxorubicin-loaded polymeric TiO2 nanotubes used for cancer photothermotherapy. Anti-Cancer Drugs 23:553–560
112. Oh Y, Je JY, Moorthy MS, Seo H, Cho WH (2017) pH and NIR-light-responsive magnetic iron oxide nanoparticles for mitochondria-mediated apoptotic cell death induced by chemo-photothermal therapy. Int J Pharm 531:1–13
113. Zhao Y et al (2015) Phase-shifted PFH@PLGA/Fe_3O_4 nanocapsules for MRI/US imaging and photothermal therapy with near-infrared irradiation. ACS Appl Mater Interfaces 7:14231–14242
114. Espinosa A et al (2016) Duality of iron oxide nanoparticles in cancer therapy: amplification of heating efficiency by magnetic hyperthermia and photothermal bimodal treatment. ACS Nano 10:2436–2446
115. Shen S et al (2013) CMCTS stabilized Fe3O4 particles with extremely low toxicity as highly efficient near-infrared photothermal agents for in vivo tumor ablation. Nanoscale 5:8056
116. Yang J, Fan L, Xu Y, Xia J (2017) Iron oxide nanoparticles with different polymer coatings for photothermal therapy. J Nanopart Res 19:333
117. Hsiao CW et al (2015) Photothermal tumor ablation in mice with repeated therapy sessions using NIR-absorbing micellar hydrogels formed in situ. Biomaterials 56:26–35
118. Zhang J, Li J, Chen S, Kawazoe N, Chen G (2016) Preparation of gelatin/Fe3O4 composite scaffolds for enhanced and repeatable cancer cell ablation. J Mater Chem B 4:5664–5672
119. Pązik R et al (2017) Non-contact Mn1-xNixFe2O4 ferrite nano-heaters for biological applications-heat energy generated by NIR irradiation. RSC Adv 7:18162–18171

Chapter 13
NIR Fluorescent Nanoprobes and Techniques for Brain Imaging

Takashi Jin and Yasutomo Nomura

13.1 Introduction

For in vivo fluorescence imaging, visible-emitting fluorescent probes cannot be applied because of the strong absorption and scattering of visible light by intrinsic chromophores, organelles, and cytoskeleton in cells [1, 2]. Most of the visible-emitting fluorescent probes have been used for in vitro imaging and sensing of biomolecules and organelles using conventional fluorescence microscopes [3, 4]. Compared with visible light (400–700 nm), NIR light (700–1400 nm) allows deeper penetration with reduced absorption and scattering in living tissues [5]. In addition, tissue autofluorescence in the NIR region is much lower than the autofluorescence in the visible region [5]. Thus, NIR fluorescence imaging is widely used for non-invasive visualization of deep tissues in living system [6–9].

So far, conventional NIR region ranging from 700 to 900 nm (1st NIR window) has been used for in vivo imaging [5]. In this NIR region, many kinds of fluorescent probes such as Cy7, ICG, iRFP, and CdSeTe quantum dots (QDs) are commercially available (Fig. 13.1). Recently, NIR fluorescence imaging in the wavelengths of 1000–1400 nm (2nd NIR window) [10–14] has been attracted for clearer deep-tissue imaging at the whole-body level (Fig. 13.2). As the tissue autofluorescence and scattering significantly decrease beyond 1000 nm, 2nd NIR fluorescence

T. Jin (✉)
Laboratory for Nano-Bio Probes, RIKEN Center for Biosystems Dynamics Research, Suita, Japan

Graduate School of Frontier Biosciences, Osaka University, Ibaraki, Japan
e-mail: tjin@riken.jp

Y. Nomura
Laboratory for Nano-Bio Probes, RIKEN Center for Biosystems Dynamics Research, Suita, Japan

Department of Systems Life Engineering, Maebashi Institute of Technology, Maebashi, Japan
e-mail: ynomura@maebashi-it.ac.jp

A. Benayas et al. (eds.), *Near Infrared-Emitting Nanoparticles for Biomedical Applications*, https://doi.org/10.1007/978-3-030-32036-2_13

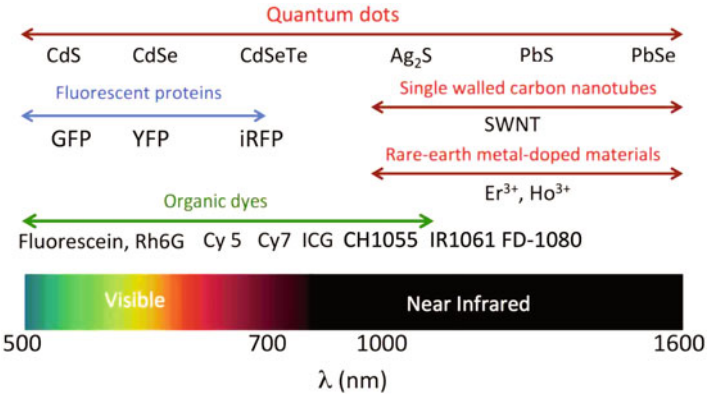

Fig. 13.1 Representative nanoprobes that can be used for bioimaging at the wavelengths of visible and near infrared regions

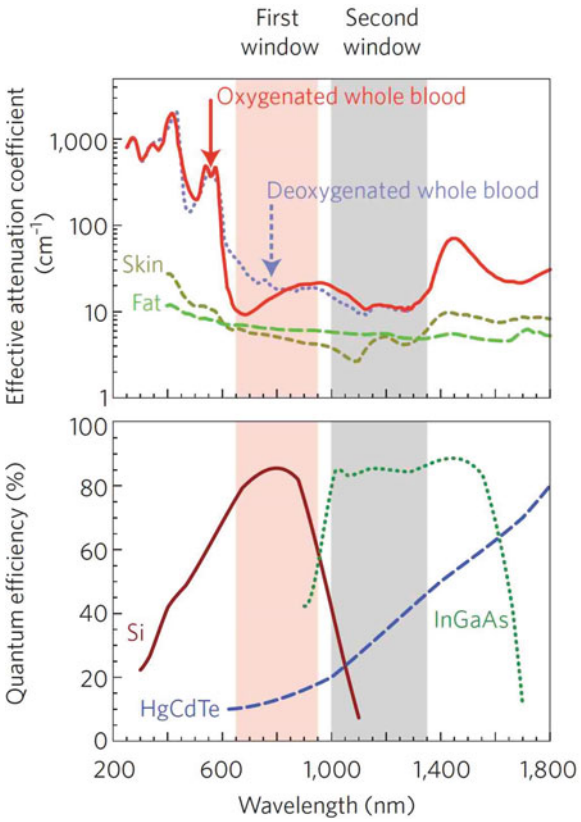

Fig. 13.2 First and second NIR windows in biological tissues. Top: These plots of effective attenuation coefficient (on a log scale) versus wavelength show that absorption and scattering from oxygenated blood, deoxygenated blood, skin, and fatty tissue is lowest in either the first (pink shaded area) or 2nd (grey) NIR window. Bottom: Sensitivity curves for typical cameras based on silicon (Si), indium gallium arsenide (InGaAs) or mercury cadmium telluride (HgCdTe) sensors. Reproduced from ref. [10] with permission from Springer-Nature

imaging offers better spatiotemporal resolution in the deep-tissue imaging [10–12]. Unfortunately, compared with conventional NIR fluorescent probes in the 1st NIR window, NIR fluorescent probes that can be used in the 2nd NIR window are very limited.

During the past 5 years, several types of NIR fluorescent probes such as single-walled carbon nanotubes (SWNTs) [15–32], PbS QDs [33–43], Ag_2S QDs [44–57], and rare earth-doped nanoparticles [58–61] have been developed for in vivo imaging in the 2nd NIR window. Recently, organic dye-based NIR nanoprobes with low toxicities have attracted much attention for deep-tissue imaging in the 2nd NIR window [62–91]. In this chapter, we focus on the synthesis, optical properties, and applications of NIR fluorescent nanoprobes for non-invasive brain imaging in the 2nd NIR window.

13.2 Optical Property of Brain Tissue

In non-invasive fluorescence imaging of brain, autofluorescence, absorption, and scattering by scalp and skull significantly affect the signal-to-background ratios of the fluorescence images. Autofluorescence and absorption result mainly from the intrinsic chromophores such as nicotinamide adenine dinucleotide phosphate (NADP) and flavin in intracellular compartments [92–94]. To get clear NIR fluorescence images of mouse brains, excitation wavelengths are very important to reduce the absorption and autofluorescence by tissues. The detection wavelengths for fluorescence emission are also important to get reduced scattering images.

The absorption spectrum of a mouse brain shows that tissue absorption at the NIR region from 700 to 1400 nm is very low (Fig. 13.3a). The strong absorption at

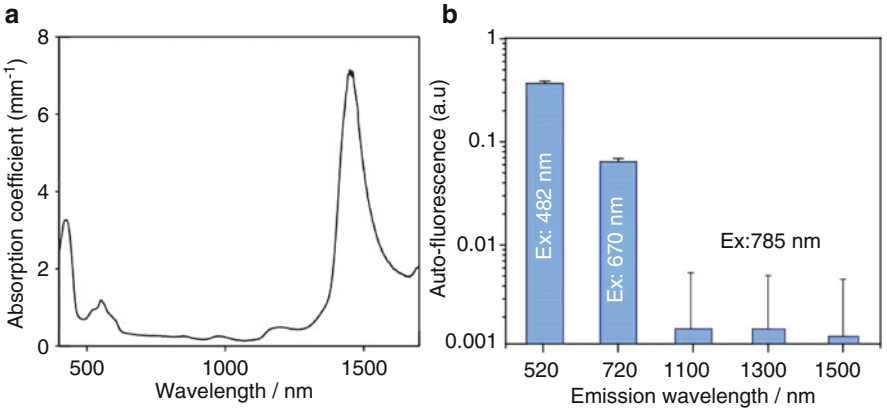

Fig. 13.3 (**a**) Absorption spectrum of a mouse brain. (**b**) Autofluorescence of a mouse brain. The fluorescence at 520 and 720 nm was obtained by excitation at 482 and 670 nm, respectively. The fluorescence at 1110, 1300, and 1500 nm was obtained by excitation at 785 nm. Adapted from ref. [41]

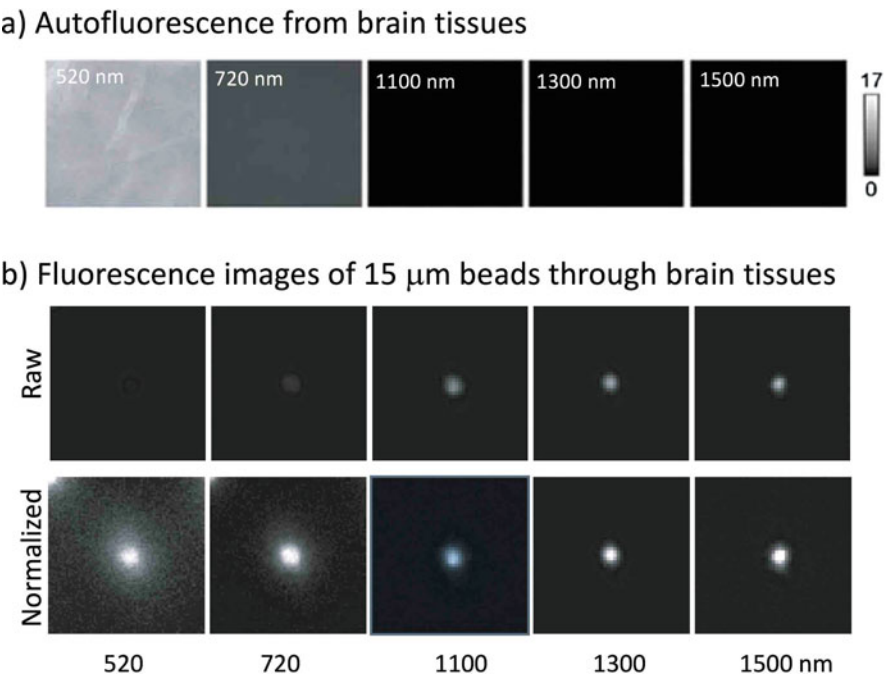

Fig. 13.4 (**a**) Autofluorescence from brain tissues of mice. The autofluorescence at 520 and 720 nm was measured by excitation at 482 and 670 nm, respectively. The autofluorescence over 1000 nm was measured by excitation at 785 nm. (**b**) Fluorescence images of 15 μm beads containing five types of QDs (520, 720, 1100, 1300, and 1500 nm emission) though brain tissues of mice. Thickness of the brain tissues was 100 μm. The intensity of fluorescence emission of each QDs was adjusted to the similar level. Upper images show raw data, and lower images show normalized data. Reproduced from ref. [36] with permission from Royal Society of Chemistry

the visible region less than 600 nm is attributed to the absorption by intrinsic chromophores such as flavin and hemoglobin. The intense absorption at around 1500 nm is due to the absorption by water molecules in the brain tissue. Autofluorescence of the mouse brain strongly depends on the wavelength of excitation (Fig. 13.3b). The intensity of autofluorescence over 1000 nm is very low compared with that of the autofluorescence at 520 and 720 nm. Figure 13.4a shows autofluorescence images (at 520, 720, 1100, 1300, and 1500 nm) of brain tissues. It should be noted that the autofluorescence intensity decreases with increasing the emission wavelength, indicating intrinsic chromophores in tissues are less excited at longer wavelengths. Furthermore, the tissue scattering of NIR fluorescence decreases with increasing the emission wavelength (Fig. 13.4b). These optical properties in the 2nd NIR window allow clearer deep-tissue imaging of brain with high signal-to-background ratios, compared with the imaging performed at the visible and 1st NIR regions.

13.3 NIR Nanoprobes for In Vivo Fluorescence Imaging

13.3.1 Nanomaterial-Based NIR Nanoprobes

SWNTs in the 2nd NIR window the first-reported fluorescent nanoprobes by Dai group for intravital imaging in mice [24]. SWNTs are cylindrical nanotubes (hundred nanometer in length) consisting of graphene layers, and they have a broad emission in the 2nd NIR region [15]. Although raw SWNTs are insoluble to water and their fluorescence quantum yields are very low (<1%), surface functionalization results in water-dispersible and bright SWNTs [24]. So far, several groups have demonstrated the capability of surface-functionalized SWNTs as NIR fluorescent probes for non-invasive imaging of organs, lymph nodes, tumors, and cerebral vessels in mice [25–32]. For biomedical applications, SWNTs have serious problems on their cytotoxicity and difficulty in exclusion from the body [15, 95, 96].

Nanoparticle-based NIR nanoprobes such as Ag_2S QDs, PbS QDs, rare earth-doped nanoparticles are alternative NIR nanoprobes for intravital imaging in the 2nd NIR window (Fig. 13.5). NIR-emitting Ag_2S QDs [44–57], and PbS QDs [33–43]

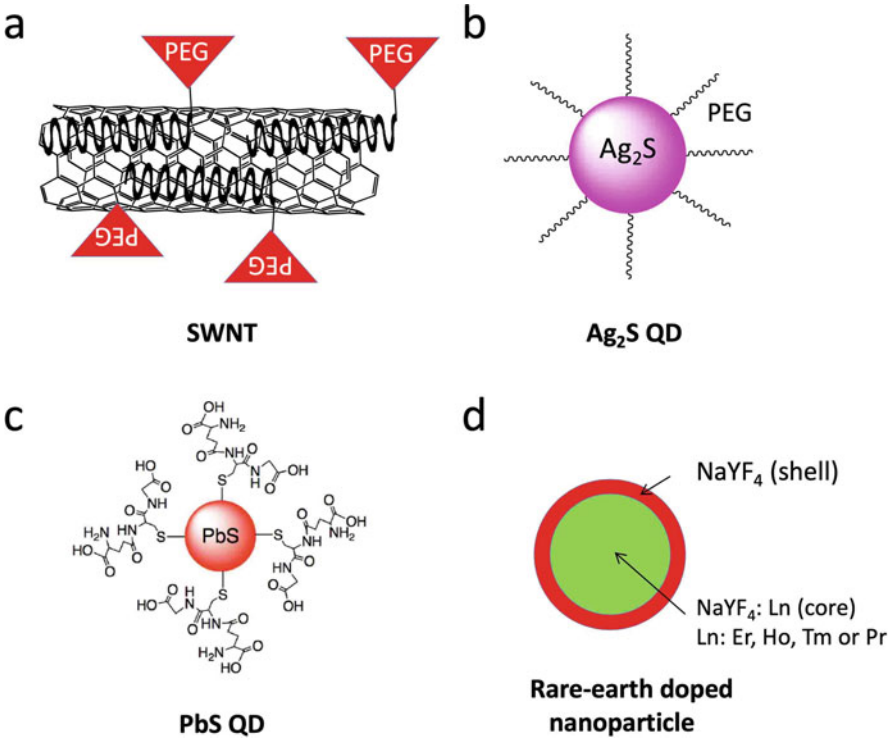

Fig. 13.5 Schematic illustration of typical nanomaterial-based NIR nanoprobes, (**a**) Polyethylene glycol (PEG)-capped SWNT [24], (**b**) PEG-capped Ag_2S QDs [45], (**c**) glutathione-capped PbS QDs [33], and (**d**) rare earth-doped nanoparticle [59]

are semiconductor nanocrystals that have unique optical properties, such as size-dependent tunable emissions, narrow emission bands, high quantum yields, and high resistance to photobleaching. In 2010, Wang group first synthesized NIR-emitting Ag_2S QDs for bioimaging by thermal decomposition of $(C_2H_5)_2NCS_2Ag$ [44]. By optimization of the reaction conditions for preparing QDs, they succeeded in the synthesis of emission tunable Ag_2S QDs with a high quantum yield (ca. 20%) in the wavelength region from 900 to 1200 nm [52]. Furthermore, they demonstrated the capability of the Ag_2S QDs for tumor imaging, in situ tracking of transplanted stem cells, and imaging-guided precise operation of glioma [46, 54–56]. In 2013, our group reported a facile method for preparing water-dispersible PbS QDs, which have tunable emissions from 1000–1400 nm with high quantum yields of 6–12% [33]. As the water-dispersible PbS QDs are capped with glutathione (a natural tripeptide), functionalized QDs with biomolecules such as antibody and peptide are easily prepared. We demonstrated the utility of the PbS QDs for non-invasive visualization of lymph nodes as well as breast tumors in living mice. Furthermore, we synthesized highly bright PbS/CdS QDs with a core/shell structure that emit from 1000 to 1500 nm, and we applied these QDs to non-invasive imaging of cerebral blood vessels in mice [34]. In this work, we found that the signal-to-background ratio in the NIR fluorescence imaging of brain tissue at 1300 nm can be improved 76 times compared to the NIR imaging at 720 nm. In 2013, Moghe group reported rare earth (Er^{3+}, Ho^{3+}, Tm^{3+}, and Pr^{3+})-doped nanoparticles as in vivo shortwave infrared reports for intravital imaging in mice [59]. Other groups also reported rare-earth nanoparticles for organ imaging and cancer early detection [58, 60, 61]. However, biomedical applications of these nanoparticle-based NIR nanoprobes including SWNTs are very limited due to their dose-dependent toxicity [95, 96].

13.3.2 Organic Dye-Based NIR Nanoprobes

Recently, organic dye-based NIR nanoprobes emitting over 1000 nm have been developed as next-generation NIR nanoprobes for intravital bioimaging. Although a variety of NIR organic nanoprobes emitting in the 1st NIR window are commercially available, there are a very limited number of NIR organic nanoprobes that emit over 1000 nm. During a few years, several types of NIR-emitting organic dyes beyond 1000 nm have been reported for bioimaging. Organic dye-based NIR nanoprobes are classified into three types (Fig. 13.6a). Frist type is NIR-dye nanoparticles, where NIR dyes are incorporated into micelles or amphiphilic polymers [62, 63]. Second type is NIR-dye complex, where NIR dyes are conjugated to proteins such as fetal bovine serum [64]. Third type is solely, water-dispersible NIR dyes [65, 67]. To date, these types of organic dye-based NIR nanoprobes have appeared as probes for bioimaging in the 2nd NIR window (Fig. 13.6b). Compared with nanomaterial-based NIR nanoprobes, organic dye-based nanoprobes have well-defined architectures with rapid metabolism and low toxicity [66, 97].

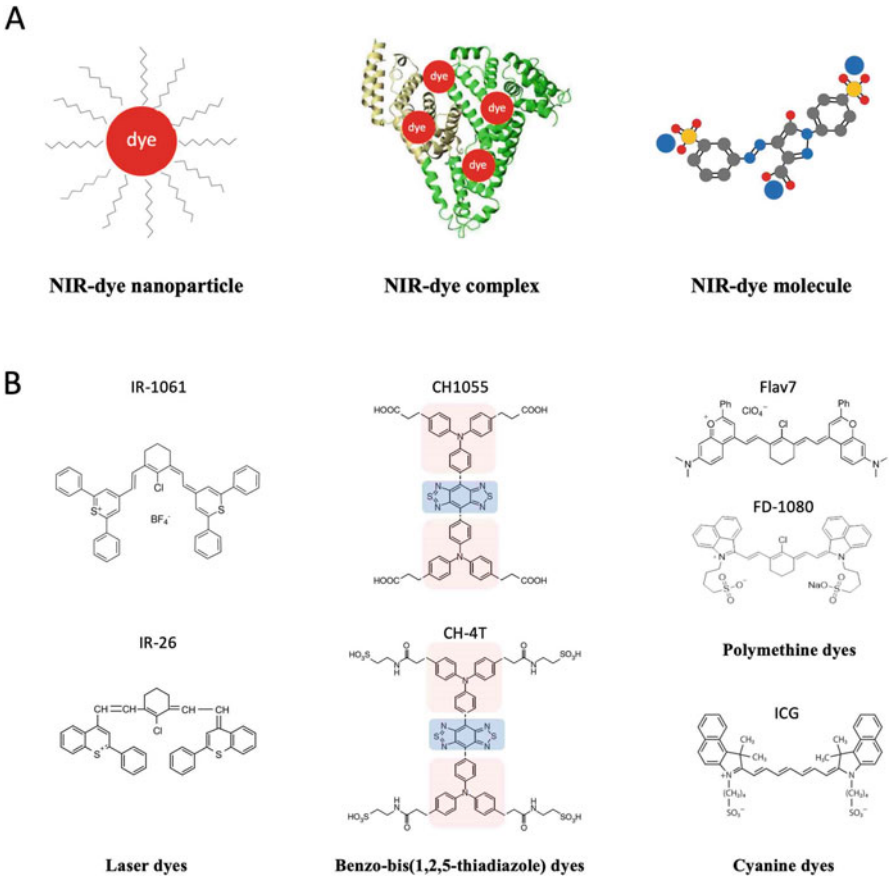

Fig. 13.6 (**a**) Schematic illustration of three types of organic dye-based NIR fluorophore. (**b**) Chemical structures of typical NIR dyes emitting over 1000 nm (laser dyes, benzo-bis (1,2,5-thiadiazole) dyes, polymethine dyes, and cyanine dyes). Blue and pink color show the electron acceptor and donor unit, respectively

In 2013, Dai group reported laser dye, IR-1061 incorporated nanoparticles as a NIR nanoprobe for in vivo imaging [62]. IR-1061 is a commercially available polymethine dye, which is highly hydrophobic and insoluble to water. Thus, they incorporated IR-1061 to nanoparticles consisting of amphiphilic polymer poly (acrylic acid, PAA) and polyethylene glycol-conjugated phospholipid (DSPE-nPEG). The fluorescence quantum yield of the IR-1061 incorporated nanoparticle was 1.8% [62]. They succeeded in performing whole-body imaging of nude mice after intravenous injection of the IR-1061 incorporated nanoparticles. They found the facile excretion of the IR-1061 nanoparticles from the body. Using the similar strategy, Dai group also reported fluorescent copolymer (poly(benzo[1,2-b:3,4-b']difuran-*alt*-fluorothieno-[3,4-b]thiophen, pDA) incorporated nanoparticles as a

NIR nanoprobe and performed ultrafast fluorescence imaging (>25 flames/sec) in the 2nd NIR window [63].

In the design of NIR-emitting nanoprobes, the energy band gap is known to be significantly affected by conjugation length as well as donor–acceptor (D–A) charge transfer in π-conjugated molecules [78]. In 2016, Dai, Cheng and Hong reported a new type of benzo-bis(1,2,5-thiadiazole) NIR-emitting dyes with D–A–D charge structures (Fig. 13.6b) [65, 69, 80]. This type of NIR nanoprobe (CH1055-PEG) emits at approximately 1050 nm with a quantum yield of 0.3% in an aqueous solution [65]. They modified the fluorescence brightness of CH1055 by complexation of its sulfonated derivative (CH-4T) with bovine serum to produce 110-fold increase in NIR fluorescence. They succeeded to perform molecular imaging of tumors in mice using affibody-functionalized CH1055 [65], leading to a possible application of the NIR dye to tumor detection in humans. Their works showed that the brightness of D–A–D dyes can be significantly improved by their composites with proteins. To date, several derivatives of benzo-bis(1,2,5-thiadiazole) nanoprobes have been reported for in vivo tumor imaging and image-guided surgery [68, 78].

In 2017, Sletten group reported flavylium polymethine nanoprobes for near- and shortwave-infrared imaging [79]. They synthesized a new series of polymethine dyes with dimethylamino flavylium heterocycles and found that a flavylium dye (Flav 7) emitting at ca. 1050 nm is 13 times brighter than IR-26 (quantum yield: 0.05). They achieved whole-body imaging of nude mice by intravenous injection of Flav 7 micelles consisting of mPEG-DSPE lipids, suggesting the possible translation of polymethine nanoprobes to optical diagnostics in NIR region over 1000 nm. In 2018, Zhang group reported the synthesis and application of a cyanine dye (FD-1080) that emit at around 1100 nm for deep-tissue high-resolution dynamic bioimaging [67]. The excitation wavelength (1064 nm) of this NIR probe was longer than that (650–980 nm) of previous reported NIR probe. Thus, this NIR probe allowed deeper tissue imaging due to the high penetration of excitation light (1064 nm). The quantum yield of PD-1080 was 0.31% in an aqueous solution and could be increased to 5.94% after combining with fetal bovine serum. This dye is the first-reported NIR nanoprobe that can be excited at the wavelength longer than 1000 nm.

More recently, several groups have found that a commercially available dye, indocyanine green (ICG) with an emission peak of 830 nm can be used to NIR fluorescence imaging in the 2nd NIR window [72, 73, 83, 85]. ICG is the only NIR nanoprobe that is approved by the Food and Drug Administration (FDA) for clinical use in humans. Although the NIR emission of ICG over 1000 nm is very week, its emissions in blood and vasculatures are clearly detected by an InGaAs camera. In 2018, Bawendi and Bruns group showed that ICG can be used as a NIR nanoprobe for in vivo fluorescence imaging over 1000 nm, including intravital microscopy, non-invasive real-time imaging in blood and lymph vessels, imaging of hepatobiliary clearance, and molecular targeted in vivo imaging [73]. In the same year, Annapragada group reported that ICG-incorporated liposomes show higher contrast to noise ratios compared to free ICG in the 2nd NIR window, allowing visualization of hind limb and intracranial vasculatures [72, 83]. Sun and Chen

group reported that the NIR emissions of ICG including IRDye800 and IR-12N3 have the potential to accelerate clinical translation of NIR fluorescence imaging in the 2nd NIR window [85]. While no FDA-approved NIR organic nanoprobes with an emission peak over 1000 nm exist, the emission of ICG may give rapid translation of longer NIR fluorescence to humans in clinical applications.

13.4 NIR Fluorescence Detection System for Brain Imaging

In most of the commercially available in vivo imaging systems, conventional NIR wavelenths ranging from 700 to 900 nm (1st NIR optical window) are used for deep-tissue imaging. This is because the conventional NIR photodetectors (silicon CCD camera) are sensitive in the 1st NIR region, and 1st NIR-emitting probes (e.g., Indocyanine green, Cy 7, and CdSeTe QDs) are commercially available. Although 1st NIR fluorescence imaging is useful for the non-invasive visualization of organs and tissues, its spatial resolution is not enough to observe cellular dynamics. As tissue autofluorescence and scattering significantly decrease with increasing the excitation/emission wavelength, fluorescence imaging in the 2nd NIR region should be very useful to get better spatiotemporal resolution in deep-tissue imaging [10]. However, there are no commercially available imaging systems with high spatiotemporal resolution in the 2nd NIR window.

Our 2nd NIR microscope imaging system is based on the Macro Zoom System with zoom function from 0.63× to 6.3× (Fig. 13.7). Optical system is optimized for VIS, 1st NIR, and 2nd NIR fluorescence imaging. Solid-state lasers for 645, 785, and 978 nm excitation, and emission filters of 1100 ± 25 nm, 1300 ± 25 nm, and 1500 ± 25 nm are equipped to the optical system. A Xe lamp was used as the excitation light source at 482 nm for VIS imaging. A Si EM camera (iXon3, Andor) is used for VIS and 1st NIR fluorescence imaging, and an InGaAs CMOS camera (C10633-34; Hamamatsu photonics) is used for 2nd NIR fluorescence imaging.

Dai group used a high-resolution microscopic system for NIR imaging of brain imaging cerebral vessels (Fig. 13.8) [31]. High-magnification intravital imaging of cerebral vessels was carried out in epifluorescence mode with an 808-nm diode laser (RMPC lasers, 160 mW) as the excitation source and two objective lenses (4× and 10×) for microscopic imaging. The mouse with scalp hair removed was intravenously injected with a solution of SWNTs and placed in a home-made stereotactic platform fixed on a motorized 3D-translational stage that allowed for the digital position adjustment and readout of the mouse relative to the objective. The emitted fluorescence was filtered through a 1000-nm long-pass filter, a 1300-nm long-pass filter, and a 1400-nm short-pass filter to ensure only photons in the 1300–1400 nm.

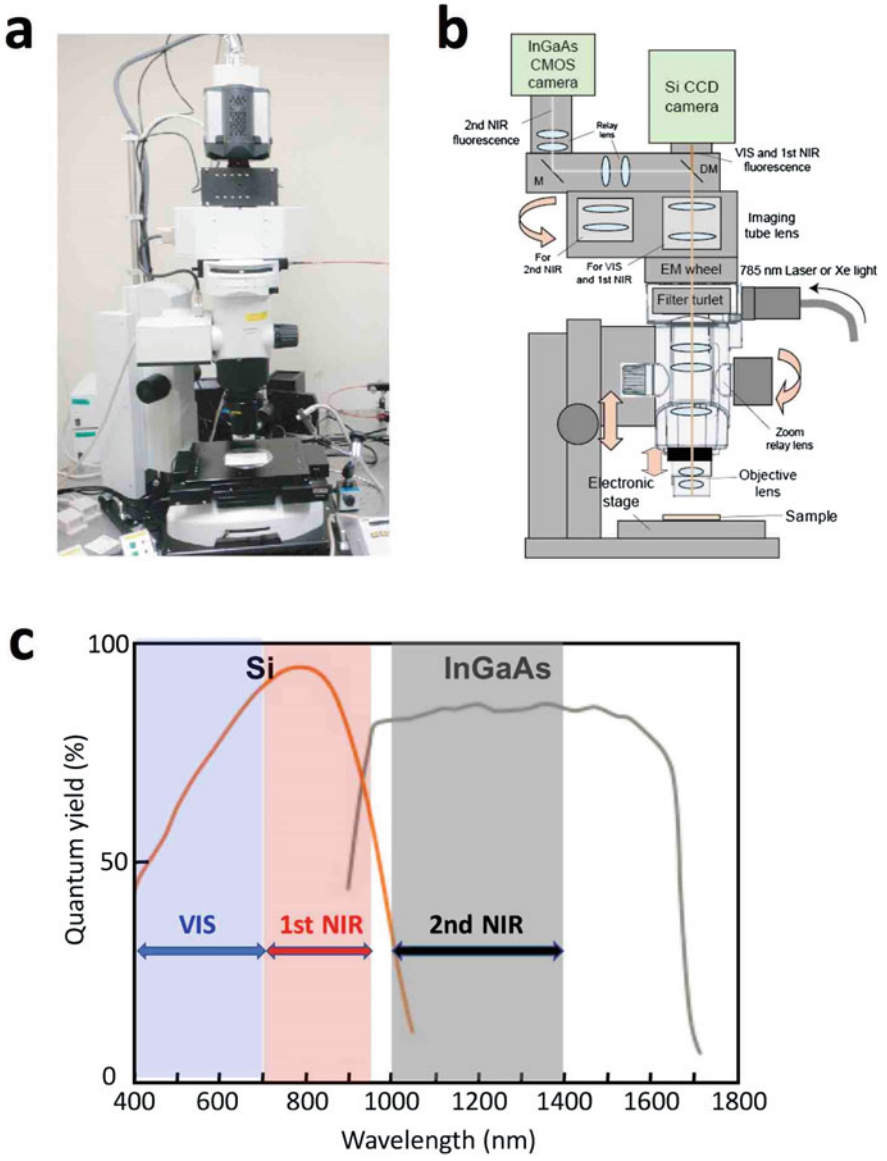

Fig. 13.7 (**a**, **b**) Up-right fluorescence microscope system for in vivo imaging in VIS, 1st NIR, and 2nd NIR region (400–1400 nm). (**c**) Sensitivity curves for typical cameras based on silicon (Si), indium gallium arsenide (InGaAs) sensors. Si and InGaAs cameras are sensitive within the 1st and 2nd NIR windows, respectively

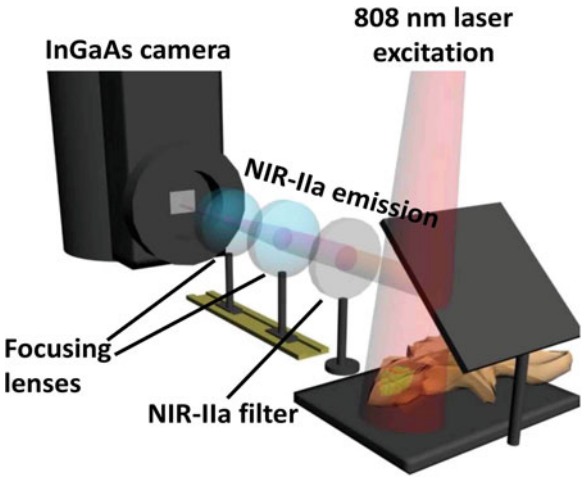

Fig. 13.8 A schematic of NIR fluorescence imaging for non-invasive through-scalp and through-skull brain vascular imaging. NIR-IIa emission: 1300–1400 nm. Reproduce from ref. [31] with permission from Springer-Nature

13.5 Non-invasive Brain Imaging Using NIR Nanoprobes

13.5.1 Cerebral Blood Vessels

13.5.1.1 SWNT Probes

To date, mouse brain imaging has largely relied on magnetic resonance (MR), X-ray computed tomography (CT), and positron emission tomography (PET). However, these imaging modalities have limited spatial resolution and long scanning times. During the past 5 years, a number of reports on non-invasive brain imaging of mice in the 2nd NIR window have appeared using NIR nanoprobes such as SWNTs [31, 98], QDs [34, 41, 99–102], rare earth-doped nanomaterials [104, 105], and organic dyes [65–77, 104–107]. In 2014, Dai et al. first reported 2nd NIR fluorescence imaging of a mouse brain by using (SWNTs) (Fig. 13.9) [31]. They performed through-scalp and through-skull fluorescence imaging of mouse cerebral vasculatures without craniotomy, utilizing the intrinsic photoluminescence of SWNTs in the 1.3–1.4 nm NIR window. They found that reduced photon scattering in the NIR region allowed fluorescence imaging to a depth of >2 mm in mouse brain with sub-10 μm resolution. In this fluorescence imaging, they achieved dynamic NIR fluorescence imaging (5.3 frames/sec) of cerebral blood perfusion.

13.5.1.2 QD Probes

In 2014, our group first reported the non-invasive fluorescence angiography of a mouse head using PbS/CdS QDs in the 2nd NIR window [34]. To date, several types of QDs including PbS QDs, Ag_2S QDs, and InAs QDs have been used for brain imaging in the 2nd NIR window [100–103]. Figure 13.10 shows the fluorescence

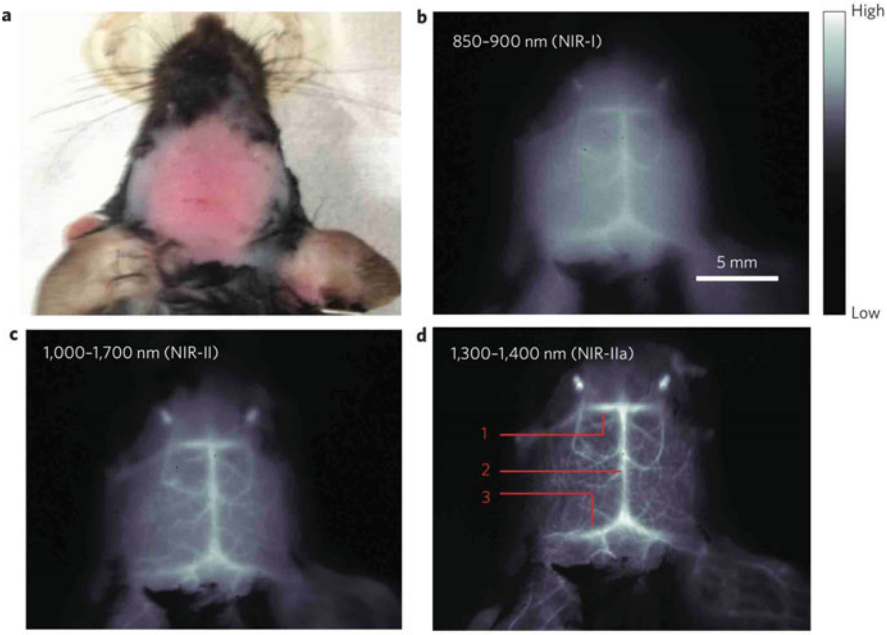

Fig. 13.9 NIR fluorescence imaging of mouse brain vasculatures with SWNT–IRDye800 in different NIR subregions. (**a**), A C57Bl/6 mouse head with the hair removed. (**b–d**), Fluorescence images of the same mouse head in the NIR-I, NIR-II, and NIR-IIa regions. In (**d**), the inferior cerebral vein, superior sagittal sinus, and transverse sinus are labeled 1, 2, and 3, respectively. Reproduced from ref. [31] with permission from Springer-Nature

angiography for a mouse head using bovine serum albumin (BSA)-conjugated VIS, 1st NIR, and 2nd NIR-emitting QDs [34]. The fluorescence images of mouse cerebral vessels were measured by using band-path filters (525, 720, and 1300 nm) after injection of each QDs in a mouse tail vein. Autofluorescence of the mouse body dramatically decreased in the angiography of 2nd NIR images compared with that of the VIS and 1st NIR images. Blood vessels showed a clearer image in the 2nd NIR region due to the higher penetration and lower scattering of the 2nd NIR light in the tissue. The spatial resolution of the fluorescence image of the blood vessels was significantly improved by increasing the imaging wavelength, which also increased the signal-to-background ratio of the 2nd NIR fluorescence images compared with VIS or 1st NIR fluorescence images.

The 2nd NIR fluorescence imaging shows deeper penetration with lower scattering compared with the VIS and 1st NIR fluorescence imaging. Although NIR light over 1000 nm can penetrate across the skin and scalp of the mouse brain, it is difficult to determine the precise value of brain imaging depth in living mice. Figure 13.11 shows the imaging depth for an isolated mouse brain. Visualization depth for the cerebral blood vessels was evaluated by measuring z-stacked images for the isolated brain. In our NIR imaging system, maximum depth for the visualization

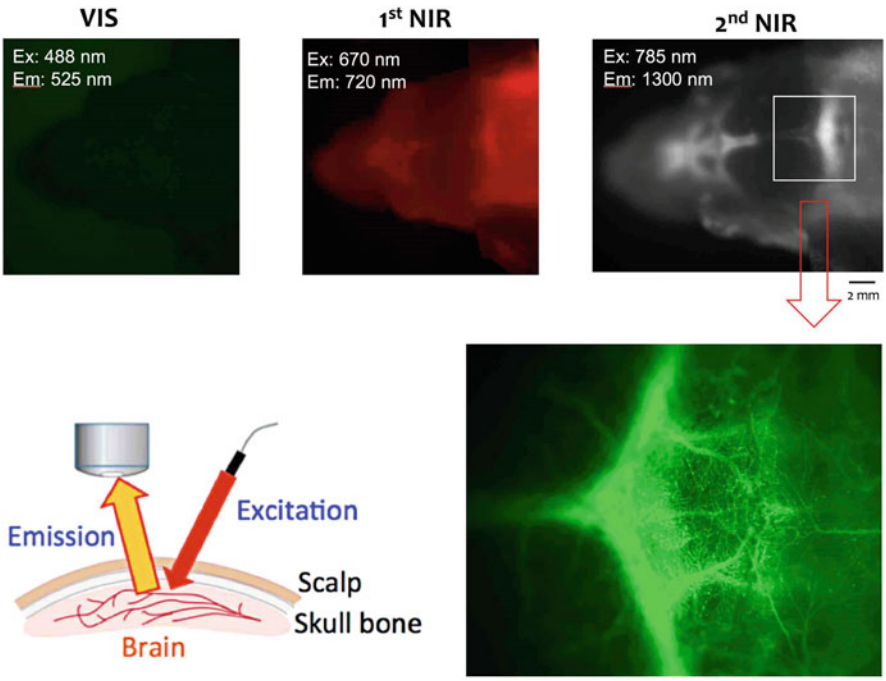

Fig. 13.10 Fluorescence angiography of a mouse head. The images show its Vis (520 nm), 1st NIR (720 nm), and 2nd NIR (1300 nm) fluorescence angiographies, where excitation wavelengths are 488 nm, 670 nm, and 785 nm, respectively. CdSe/ZnS QDs, CdSeTe/CdS QDs, PbS/CdS QDs were used for fluorescence imaging at 525, 720, and 1300 nm, respectively. Reproduced from ref. [34]. Copyright (2014) with permission of Royal Society of Chemistry

of the fine structure of cerebral blood vessels was determined to be ca. 1.6 mm. For a brain of living mouse, we can perform NIR fluorescence imaging of cerebral blood vessels with high spatial resolution. Figure 13.12 shows non-invasive NIR fluorescence images of cerebral blood vessels of a nude mouse after injection of PbS QDs via a tail vein. Immediately after injection of the QDs, strong NIR fluorescence signals were detected and clear images of the cerebral blood vessels could be taken. Although the intensity of the NIR fluorescence signals was gradually decreased, the NIR fluorescence images of the cerebral blood vessels could be taken for ca. 5 minutes post-injection of the PbS QDs. In this brain imaging, we could observe small blood capillaries with a spatial resolution of ca. 10 μm.

13.5.1.3 Rare-Earth Nanoprobes

Rare earth (Er^{3+})-doped nanoprobes can also be used for brain imaging in the NIR window beyond 1500 nm [104, 105]. In general, with increasing the emission wavelength in fluorescence imaging, tissue scattering of the emission light is

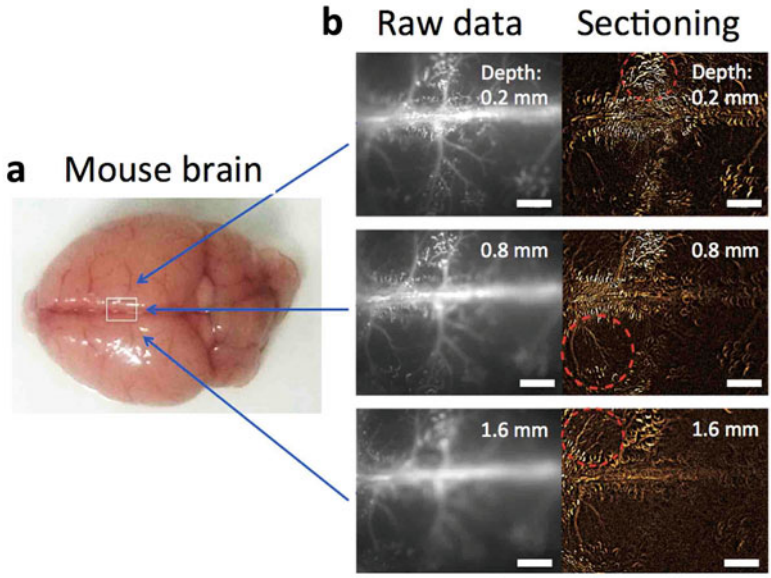

Fig. 13.11 (**a**) Bright-field image of a mouse brain perfused by PbS QDs. (**b**) Raw fluorescence images and sectioning images at the depth of 0.2 mm, 0.8 mm, and 1.6 mm from the surface. The sectioning image was obtained from a raw image minus its previous and next image. Red circles with dotted lines show cerebral blood vessels appearance after sectioning. Scale bar: 1 mm. Adapted from ref. [41]

decreased. Thus, fluorescence imaging beyond 1500 nm would give clearer images of the brain compared with the imaging wavelength in the 2nd NIR region. Zhong et al. reported Er/Ce co-doped $NaYbF_4$ nanocrystals for in vivo fluorescence imaging in the NIR region between 1500 and 1700 nm [104]. This Er/Ce co-doped nanoprobe shows bright emission at 1550 nm under 980 nm excitation. In this probe, Ce doping suppresses the upconversion pathway while boosting down conversion by ninefold to produce bright 1550 nm emission. The authors reported that the quantum yield of this rare-earth nanoprobe was 0.27–2.73% with a highest value among reported down conversion rare earth-doped nanomaterials, leading to fast in vivo cerebrovascular imaging with a 20 ms exposure time in the NIR region between 1500 and 1700 nm (Fig. 13.13).

13.5.1.4 Organic Dye Nanoprobes

Very recently, much attention has been paid to organic dye-based NIR nanoprobes for in vivo imaging in the 2nd NIR window due to their low toxicities and rapid clearance from the body [62–77, 106, 107]. The safety of NIR fluorescent probes is crucial for the application of 2nd NIR fluorescence imaging to biomedical and clinical fields. The fluorescence brightness of organic dye-based NIR nanoprobes

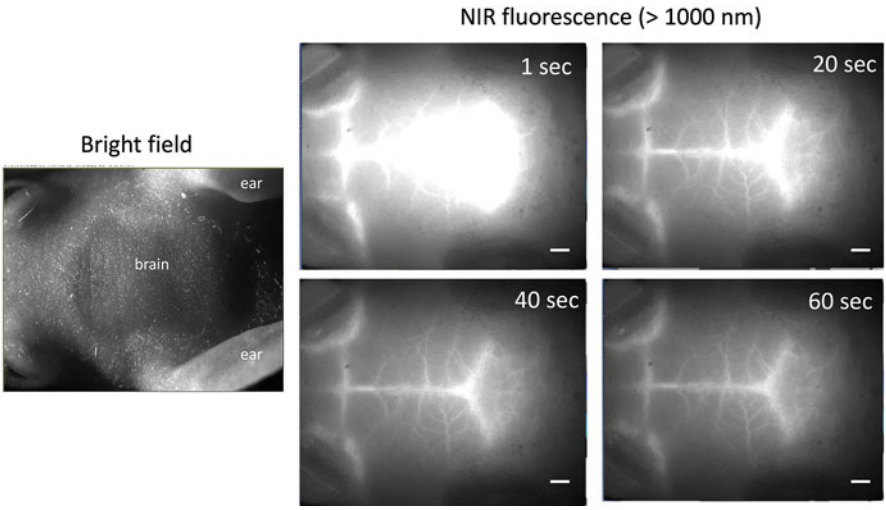

Fig. 13.12 NIR fluorescence images of cerebral blood vessels in a nude mouse. NIR fluorescence images were taken 1 s, 20 s, 40 s, and 60 s post-injection of PbS QDs (200 μL, 2 μM) through a tail vein. Excitation: 670 nm, Emission >1000 nm. Laser power; 25 mW/cm^2. Exposure time: 100 ms. Scale bar: 1 mm. Adapted from ref. [12]. Copyright (2018) The Electrochemical Society

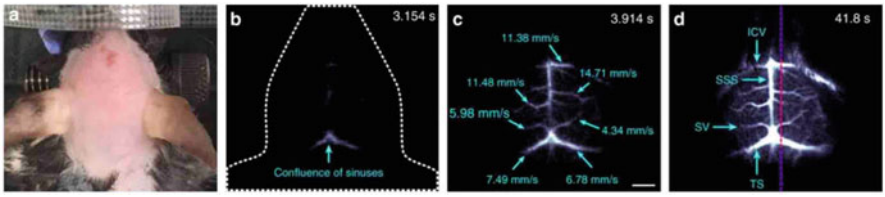

Fig. 13.13 Fast in vivo brain imaging with Er-doped nanoprobes in the 2nd NIR region. (**a**) Color photograph of a C57Bl/6 mouse preceding NIR fluorescence imaging. (**b**–**d**) Time-course NIR brain fluorescence images (exposure time: 20 ms) showing the perfusion of Er-doped nanoprobes into various cerebral vessels. Reproduced from ref. [104] with permission from Springer-Nature

is lower than that of nanomaterial-based NIR nanoprobes because of the smaller extinction coefficients of organic dyes. To overcome the low fluorescence brightness, several efforts have been made to increase the fluorescence brightness of organic dye-based NIR probes.

Wan et al. reported a bright organic NIR nanoprobe (p-FE) for three-dimensional imaging of cerebral vasculatures [66]. They encapsulated an organic NIR dye (FE) in the hydrophobic interior of an amphiphilic polymer, poly (styrene-co-chloromethyl styrene)-graft-poly(ethylene glycol) (PS-*g*-PEG), to produce a bright and biocompatible NIR nanoprobe (size: 12 nm) that can be used for the fluorescence imaging in the 2nd NIR window. The fluorescence quantum yield of p-FE in aqueous environment was ca. 16.5%. With this bright organic NIR nanoprobe, non-invasive ultrafast in vivo NIR imaging of cerebral blood vessels with a short

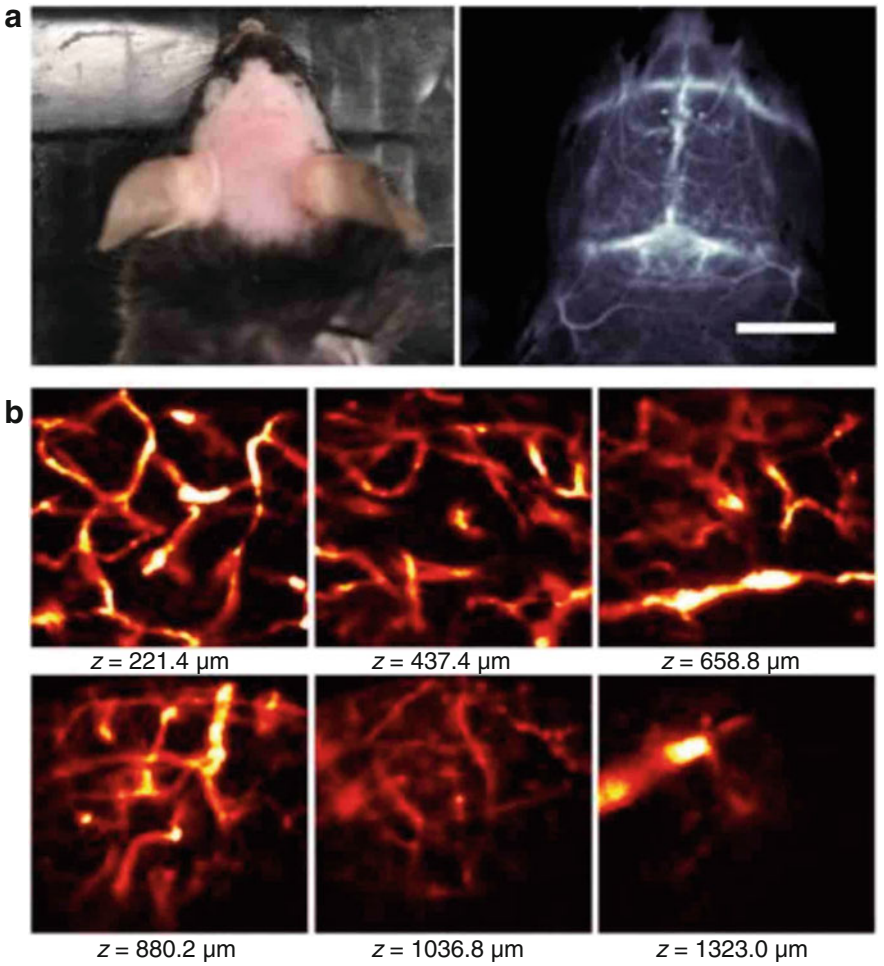

Fig. 13.14 (**a**) Photo and wide-field NIR-II epi-fluorescence imaging of the brain in a mouse injected with p-FE (808 nm excitation, emission >1200 nm) with an exposure time of 5 ms. (**b**) Ex vivo confocal imaging of brain in a mouse injected with p-FE (785 nm excitation, emission >1100 nm, laser power ~30 mW, PMT voltage ~500 V). Reproduced from ref. [66] with permission from Springer-Nature

exposure time of 2–5 ms was achieved (Fig. 13.14). In addition, the bright organic NIR nanoprobe enabled three-dimensional NIR fluorescence imaging of cerebral blood vessels using a confocal imaging system.

13.5.2 Brain Tumors

NIR fluorescence imaging is useful for the non-invasive visualization of brain tumors as well as cerebral blood vessels in living mice. In 2016, Antaris et al. reported a small NIR dye (CH1055) for mouse brain imaging in the 2nd NIR window [65]. They synthesized a small molecule (CH1055, 0.97 kDa) and PEGylated CH1055 (8.9 kDa) and showed the capability of these NIR organic nanoprobes for orthotopic glioblastoma brain tumor imaging. They used an orthotopic glioblastoma brain tumor-bearing mouse by implanting U87MG cells in the mouse brain at a depth of 4 mm with the left hemisphere (Fig. 13.15a, b). Once the brain tumor reached a diameter of 2–3 mm, they intravenously injected PEGylated CH1055 (100 μg) to the mouse and observed NIR fluorescence from the tumor at periodic time points over next 3 days. They observed that 6 h post-injection, the tumor was clearly visible during high magnification of NIR fluorescence (>1200 nm) imaging (Fig. 13.15c). After 24 h, the tumor was clearly visible with a tumor-to-normal tissue ration of 4.25 when using a whole-body imaging system (Fig. 13.15d). In

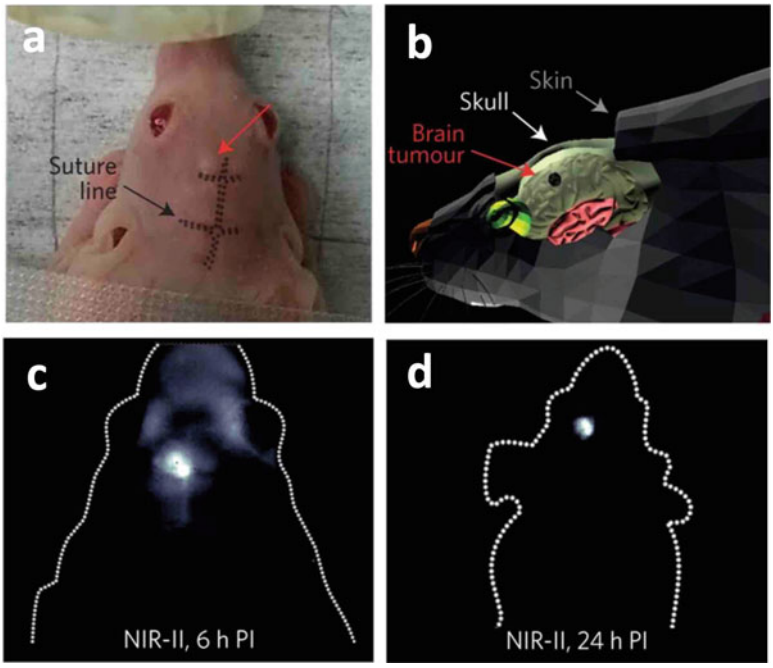

Fig. 13.15 (**a**) Color photograph of a nude mouse preceding high-magnification NIR-II imaging, with an outline over suture lines. (**b**) Graphic representation demonstrating the location of a U87MG orthotopic glioblastoma brain tumor under both the scalp and skull. (**c**, **d**) High-magnification NIR-II fluorescence imaging (1200 nm long-pass filter, 800 ms) showing strong tumor fluorescence detectable through both the scalp and skull 6 h post-intravenous injection. Reproduced from ref. [65] with permission from Springer-Nature

this study, the accumulation of PEGylated CH1055 to a brain tumor was attributed to passive tumor uptake via the enhanced permeation and enhanced (EPR) effect [108]. Recently, Tian et al. reported the fluorescence imaging of a glioblastoma brain tumor by using active tumor uptake of RGD peptide-conjugated NIR dye (IR-BEMC6P@RGD) [76]. They detected strong tumor fluorescence (>1300 nm) through scalp/skull at 12 h post-injection.

13.5.3 Cerebrovascular Disorders

NIR fluorescence imaging can be also used for the visualization of the pathophysiological state of blood vessels in sepsis. Thrombosis in cerebral blood vessels is induced by administration of lipopolysaccharide (LPS) to mice (Fig. 13.16a). Heparin is used as an inhibitor of blood coagulation [109–111]. The magnified images with the scalp removed (Fig. 13.16b) of blood vessels, showed septic clots (i.e., thrombosis), and the number of clots was increased by administration of LPS. The administration of heparin resulted in the suppression of the number of clots (Fig. 13.16b and c). Figure 13.16d shows the immunohistochemistry for an LPS-administrated brain slice, indicating the formation of clots in cerebral blood vessels. The blood coagulation was quantified by enzyme-linked immunosorbent assays (ELISA) (Fig. 13.16e). Thrombin–antithrombin complex (TAT) is a valid biomarker for disseminated intravascular coagulation [112]. After administration of LPS, averaged TAT values were significantly increased, and the level of TAT was recovered by heparin administration. This study suggests that 2nd NIR fluorescence imaging is useful for the detection of thrombosis in an LPS-injected mouse.

13.6 Summary and Outlook

In this chapter, we presented recent progress in NIR fluorescent nanoprobes and techniques for brain imaging in the 2nd NIR window. During the past 5 years, a variety of the NIR nanoprobes have been synthesized, and the proof of principle studies on their capabilities for non-invasive brain imaging have been performed. The pioneer work by Dai group using SWNTs has proven the advantages of NIR fluorescence imaging of brain tissues in the 2nd NIR window [31]: deeper penetration, reduced scattering, and low-autofluorescence in deep-tissue imaging. Nanomaterial-based NIR nanoprobes such as Ag_2S QDs, PbS QDs, and rare earth-doped nanoparticles have also contributed to prove their superior properties for brain imaging. Although the nanomaterial-based NIR nanoprobes such as SWNTs cannot be applied to clinical fields because of their cytotoxic properties, these NIR nanoprobes should be very useful for the study of cancer cell metastasis, immune/inflammatory response, and stem cell dynamics in the animal level.

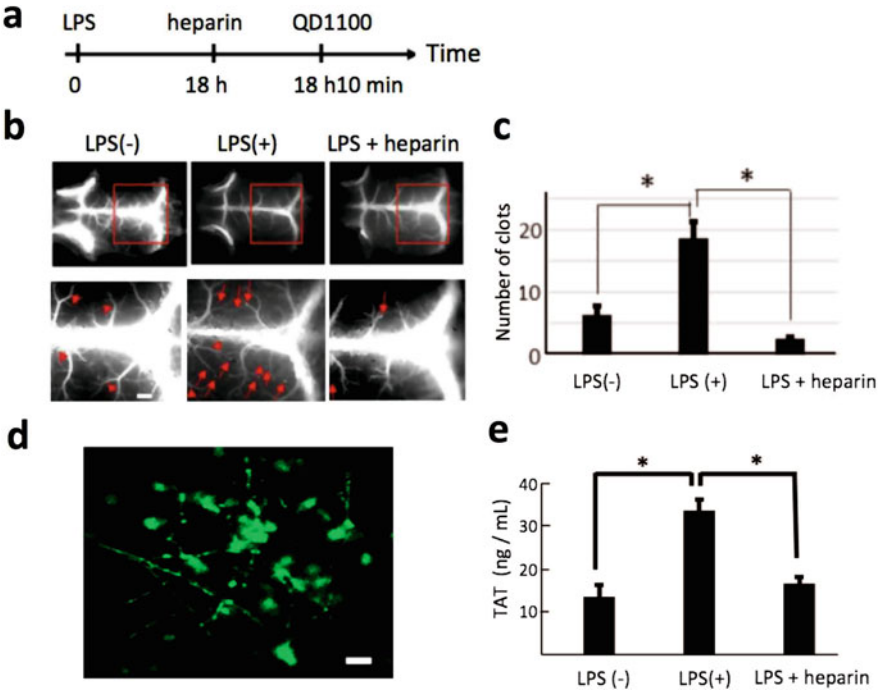

Fig. 13.16 (**a**) Time course of the experimental procedure for LPS and heparin administration. (**b**) NIR fluorescence images (>1000 nm) of cerebral blood vessels before and after administration of LPS (LPS (−) and LPS (+)) and the image followed by additional administration of heparin (LPS + heparin), with scalp removed. Lower panel shows the magnification of the images shown by red rectangular. Red arrowheads show clots. Scale bars: 1 mm. (**c**) Statistical analyses of the clots in the cerebral vessels. (**d**) Immunofluorescence staining of LPS-treated cerebral blood vessels, where anti-fibrinogen antibody (Alexa FLuor 488) was used for staining of fibrinogen. Fibrinogen helps the formation of blood clots. Scale bar: 10 μm. (**e**) ELISA assays for TAT in blood plasma. Adapted from ref. [41]

For biomedical and clinical applications in humans, the NIR nanoprobes must be rapidly metabolized and excluded from the body. The renal filtration threshold for rapid clearance via urine excretion is known as ca. 5 nm [113]. In this regard, smaller organic dye nanoprobes are suitable as NIR probes for fluorescence imaging in humans. In a few years, researchers have developed several types of NIR-dye nanoprobes that emit over 1000 nm [62–91]. These organic NIR nanoprobes have shown the possible application of NIR intravital imaging to biomedical fields. Notably, recent studies showed that the FDA-approved NIR dye, ICG can be used to perform in vivo NIR imaging over 1000 nm. This finding permits the rapid translocation of 2nd NIR-emitting organic dyes (>1000 nm) in the clinical fields.

In the practical use of the 2nd NIR-emitting organic dyes in the clinical fields, high brightness and safety are necessary as optical contrast agents. At the same time, highly sensitive NIR imaging system with a high spatiotemporal resolution should

also be developed for the clinical use such as non-invasive visualization of blood vessels and tumors. At present, except for conventional NIR imaging system (700–900 nm for animals, there is no NIR fluorescence (>1000 nm) imaging system for humans [114]. In the near future, by developing highly sensitive 2nd NIR-emitting organic dyes and intravital imaging system, NIR fluorescence imaging in the 2nd NIR window will be an indispensable tool for non-invasive imaging in biomedical and clinical fields [115].

Acknowledgements The authors thank Setsuko Tsuboi, Sayuri Yamada and Satoko Masa for their help with manuscript preparation.

References

1. Liu H, Beauvoit B, Kimura M, Chance BJ (1996) Dependence of tissue optical properties on solute-induced changes in refractive index and osmolarity. J Biomed Opt 1:200–211
2. Lim YT, Kim S, Nakayama A, Stott NE, Bawendi MG, Frangioni JV (2003) Selection of quantum dot wavelengths for biomedical assays and imaging. Mol Imaging 2:50–64
3. Terai T, Nagano T (2008) Fluorescent probes for bioimaging applications. Curr Opin Chem Biol 12:515–521
4. Joo C, Balci H, Ishitsuka Y, Buranachai C, Ha T (2008) Advances in single-molecule fluorescence methods for molecular biology. Annu Rev Biochem 77:51–76
5. Weissleder R (2001) A clearer vision for *in vivo* imaging. Nat Biotechnol 19:316–317
6. Zhang RR, Schroeder AB, Grudzinski JJ, Rosenthal EL, Warram JM, Pinchuk AN, Eliceiri KW, Kuo JS, Weichert JP (2017) Beyond the margins: real-time detection of cancer using targeted fluorophores nanoprobes. Nat Rev Clin Oncol 14:347–364
7. Namikawa T, Sato T, Hanazaki K (2015) Recent advances in near-infrared fluorescence-guided imaging surgery using indocyanine green. Surg Today 45:1467–1474
8. Liu Z, Yang K, Lee ST (2011) Single-walled carbon nanotubes in biomedical imaging. J Mater Chem 21:586–598
9. Aswathy RG, Yoshida Y, Maekawa T, Kumar DS (2010) Near-infrared quantum dots for deep tissue imaging. Anal Bioanal Chem 397:1417–1435
10. Smith AM, Mancini MC, Nie S (2009) second window for *in vivo* imaging. Nat Nanotechnol 4:710–711
11. Shi L, Sordillo LA, Rodriguez-Contreras A, Alfano R (2016) Transmission in near-infrared optical windows for deep brain imaging. J Biophotonics 9:38–43
12. Tsuboi S, Yamada S, Nakane Y, Sakata T, Yasuda H, Jin T (2018) Water-soluble near-infrared fluorophores emitting over 1000 nm and their application to in vivo imaging in the second optical window (1000-1400 nm). ECS J Solid State Sci Technol 7:R3093–R3101
13. Shi L, Alfano R (eds) (2017) Deep imaging in tissue and biomedical materials. Pan Stanford Publishing, Singapore
14. Hemmer E, Acosta-Mora P, Mendez-Ramos J, Fischer S (2017) Optical nanoprobes for biomedical applications: shining a light on upconverting and near-infrared emitting nanoparticles for imaging, thermal sensing, and photodynamic therapy. J Mater Chem B 5:4365–4392
15. Pan J, Li F, Choi JH (2017) Single-walled carbon nanotubes as optical probes for bio-sensing and imaging. J Mater Chem B 5:6511–6522
16. Cherukuri P, Bachilo SM, Litovsky SH, Weisman RB (2004) Near-infrared fluorescence microscopy of single-walled carbon nanotubes in phagocytic cells. J Am Chem Soc 126:15638–15639

17. Lefebvre J, Austing DG, Bond J, Finnie P (2006) Photoluminescence imaging of suspended single-walled carbon nanotubes. Nano Lett 6:1603–1608
18. Crochet J, Clemens M, Hertel T (2007) Quantum yield heterogeneities of aqueous single-wall carbon nanotube suspensions. J Am Chem Soc 129:8058–8059
19. Leeuw TK, Reith RM, Simonette RA, Harden ME, Cherukuri P, Tsyboulski DA, Beckingham KM, Weisman RB (2007) Single-walled carbon nanotubes in the intact organism: near-ir imaging and biocompatibility studies in drosophila. Nano Lett 7:2650–2654
20. Liu Z, Cai W, He L, Nakayama N, Chen K, Sun X, Chen X, Dai H (2007) *In vivo* biodistribution and highly efficient tumour targeting of carbon nanotubes in mice. Nat Nanotechnol 2:47–52
21. Jin H, Heller DA, Strano MS (2008) Single-particle tracking of endocytosis and exocytosis of single-walled carbon nanotubes in NIH-3T3 cells. Nano Lett 8:1577–1585
22. Welsher K, Liu Z, Daranciang D, Dai H (2008) Selective probing and imaging of cells with single walled carbon nanotubes as near-infrared fluorescent molecules. Nano Lett 8:586–590
23. Jin H, Heller DA, Sharma R, Strano MS (2009) Size-dependent cellular uptake and expulsion of single-walled carbon nanotubes: single particle tracking and a generic uptake model for nanoparticles. ACS Nano 3:149–158
24. Welsher K, Liu Z, Sherlock SP, Robinson JT, Chen Z, Daranciang D, Dai H (2009) A route to brightly fluorescent carbon nanotubes for near-infrared imaging in mice. Nat Nanotechnol 4:773–780
25. Welsher K, Sherlock SP, Dai H (2011) Deep-tissue anatomical imaging of mice using carbon nanotube fluorophores in the second near-infrared window. Proc Natl Acad Sci U S A 108:8943–8948
26. Hong G, Lee JC, Robinson JT, Raaz U, Xie L, Huang NF, Cooke JP, Dai H (2012) Multifunctional *in vivo* vascular imaging using near-infrared II fluorescence. Nat Med 18:1841–1846
27. Yi H, Ghosh D, Ham MH, Qi J, Barone PW, Strano MS, Belcher AM (2012) M13 phage-functionalized single-walled carbon nanotubes as nanoprobes for second near-infrared window fluorescence imaging of targeted tumors. Nano Lett 12:1176–1183
28. Robinson JT, Hong G, Liang Y, Zhang B, Yaghi OK, Dai H (2012) *In vivo* fluorescence imaging in the NIR-II with long circulating carbon nanotubes capable of ultra-high tumor uptake. J Am Chem Soc 134:10664–10669
29. Diao S, Hong G, Robinson JT, Jiao L, Antaris AL, Wu JZ, Choi CL, Dai H (2012) Chirality enriched (12,1) and (11,3) single-walled carbon nanotubes for biological imaging. J Am Chem Soc 134:16971–16974
30. Ghosh D, Bagley AF, Na YJ, Birrer MJ, Bhatia SN, Belcher AM (2014) Deep, noninvasive imaging and surgical guidance of submillimeter tumors using targeted M13-stabilized single-walled carbon nanotubes. Proc Natl Acad Sci U S A 111:13948–13953
31. Hong G, Diao S, Chang J, Antaris AL, Chen C, Zhang B, Zhao S, Atochin DN, Huang PL, Andreasson KI, Kuo CJ, Dai H (2014) Through-skull fluorescence imaging of the brain in a new near-infrared window. Nat Photon 8:723–730
32. Bisesi JH, Ngo T, Ponnavolu S, Liu K, Lavelle CM, Afrooz AR, Saleh NB, Ferguson PL, Denslow ND, Sabo-Attwood T (2015) Examination of single-walled carbon nanotubes uptake and toxicity from dietary exposure: tracking movement and impacts in the gastrointestinal system. Nanomaterials 5:1066–1086
33. Nakane Y, Tsukasaki Y, Sakata T, Yasuda H, Jin T (2013) Aqueous synthesis of glutathione-coated PbS quantum dots with tunable emission for non-invasive fluorescence imaging in the second near-infrared biological window (1000–1400 nm). Chem Commun 49:7584–7586
34. Tsukasaki Y, Morimatsu M, Nishimura G, Sakata T, Yasuda H, Komatsuzaki A, Watanabe TM, Jin T (2014) Synthesis and optical properties of emission-tunable PbS/CdS core–shell quantum dots for *in vivo* fluorescence imaging in the second near-infrared window. RSC Adv 4:41164–41171

35. Tsukasaki Y, Komatsuzaki A, Mori Y, Ma Q, Yoshioka Y, Jin T (2014) A short-wavelength infrared emitting multimodal probe for non-invasive visualization of phagocyte cell migration in living mice. Chem Commun 50:14356–14359
36. Corricelli M, Depalo N, Carlo ED, Fanizza E, Laquintana V, Denora N, Agostiano A, Striccoli M, Curri ML (2014) Biotin-decorated silica coated PbS nanocrystals emitting in the second biological near infrared window for bioimaging. Nanoscale 6:7924–7933
37. Sasaki A, Tsukasaki Y, Komatsuzaki A, Sakata T, Yasuda H, Jin T (2015) Recombinant protein (EGFP-protein G)-coated PbS quantum dots for *in vitro* and *in vivo* dual fluorescence (visible and second-NIR) imaging of breast tumors. Nanoscale 7:5115–5119
38. Benayas A, Ren F, Carrasco E, Marzal V, del Rosal B, Gonfa BA, Juarranz A, Sanz-Rodriguez F, Jaque D, Garcia-Sole J, Ma D, Vetrone F (2015) PbS/CdS/ZnS quantum dots: a multifunctional platform for in vivo near-infrared low-dose fluorescence imaging. Adv Funct Mater 25:6650–6659
39. Wu K, Zhang J, Fan S, Li J, Zhang C, Qiao K, Qian L, Han J, Tang J, Wang S (2015) Plasmon-enhanced fluorescence of PbS quantum dots for remote near-infrared imaging. Chem Commun 51:141–144
40. Jin T, Imamura Y (2016) Applications of highly bright PbS quantum dots to non-invasive near-infrared fluorescence imaging in the second optical window. ECS J Solid State Sci Technol 5:R3138–R3145
41. Imamura Y, Yamada S, Tsuboi S, Nakane Y, Tsukasaki Y, Komatsuzaki A, Jin T (2016) Near-infrared emitting PbS quantum dots for *in vivo* fluorescence imaging of the thrombotic state in septic mouse brain. Molecules 21:1080
42. Chen J, Kong Y, Wang W, Fang H, Wo Y, Zhou D, Wu Z, Li Y, Chen S (2016) Direct water-phase synthesis of lead sulfide quantum dots encapsulated by β-lactoglobulin for *in vivo* second near infrared window imaging with reduced toxicity. Chem Commun 52:4025–4028
43. Kong Y, Chen J, Fang H, Heath G, Wo Y, Wang W, Li Y, Guo Y, Evans SD, Chen S, Zhou D (2016) Highly fluorescent ribonuclease-A-encapsulated lead sulfide quantum dots for ultrasensitive fluorescence *in vivo* imaging in the second near-infrared window. Chem Mater 28:3041–3050
44. Du Y, Xu B, Fu T, Cai M, Li F, Zhang Y, Wang Q (2010) Near-infrared photoluminescent Ag_2S quantum dots from a single source precursor. J Am Chem Soc 132:1470–1471
45. Hong G, Robinson JT, Zhang Y, Diao S, Antaris AL, Wang Q, Dai H (2012) *In vivo* fluorescence imaging with Ag_2S quantum dots in the second near-infrared region. Angew Chem Int Ed 51:9818–9821
46. Jiang P, Tian ZQ, Zhu CN, Zhang ZL, Pang DW (2012) Emission-tunable near-infrared Ag_2S quantum dots. Chem Mater 24:3–5
47. Zhang Y, Hong G, Zhang Y, Chen G, Li F, Dai H, Wang Q (2012) Ag_2S quantum dot: a bright and biocompatible fluorescent nanoprobe in the second near-infrared window. ACS Nano 6:3695–3702
48. Jiang P, Zhu CN, Zhang ZL, Tian ZQ, Pang DW (2012) Water-soluble Ag_2S quantum dots for near-infrared fluorescence imaging *in vivo*. Biomaterials 33:5130–5135
49. Yang HY, Zhao YW, Zhang ZY, Xiong HM, Yu SN (2013) One-pot synthesis of water-dispersible Ag_2S quantum dots with bright fluorescent emission in the second near-infrared window. Nanotechnology 24:055706
50. Zhang Y, Zhang Y, Hong G, He W, Zhou K, Yang K, Li F, Chen G, Liu Z, Dai H, Wang Q (2013) Biodistribution, pharmacokinetics and toxicology of Ag_2S near-infrared quantum dots in mice. Biomaterials 34:3639–3646
51. Zhang Y, Liu Y, Li C, Chen X, Wang Q (2014) Controlled synthesis of Ag_2S quantum dots and experimental determination of the exciton bohr radius. J Phys Chem C 118:4918–4923
52. Gui R, Wan A, Liu X, Yuan W, Jin H (2014) Water-soluble multidentate polymers compactly coating Ag_2S quantum dots with minimized hydrodynamic size and bright emission tunable from red to second near-infrared region. Nanoscale 6:5467–5473

53. Li C, Zhang Y, Wang M, Zhang Y, Chen G, Li L, Wu D, Wang Q (2014) *In vivo* real-time visualization of tissue blood flow and angiogenesis using Ag_2S quantum dots in the NIR-II window. Biomaterials 35:393–400
54. Chen G, Tian F, Li C, Zhang Y, Weng Z, Zhang Y, Peng R, Wang Q (2015) *In vivo* real-time visualization of mesenchymal stem cells tropism for cutaneous regeneration using NIR-II fluorescence imaging. Biomaterials 53:265–273
55. Li C, Li F, Zhang Y, Zhang W, Zhang XE, Wang Q (2015) Real-time monitoring surface chemistry-dependent *in vivo* behaviors of protein nanocages via encapsulating an NIR-II Ag_2S quantum dot. ACS Nano 9:12255–12263
56. Chen J, Kong Y, Wo Y, Fang H, Li Y, Zhang T, Dong Y, Ge Y, Wu Z, Zhou D, Chen S (2016) Facile synthesis of β-lactoglobulin capped Ag_2S quantum dots for *in vivo* imaging in the second near-infrared biological window. J Mater Chem B 4:6271–6278
57. Wu Q, Zhou M, Shi J, Li Q, Yang M, Zhang Z (2017) Synthesis of water-soluble Ag_2S quantum dots with fluorescence in the second near-infrared window for turn-on detection of Zn(II) and Cd(II). Anal Chem 89:6616–6623
58. Kamimura M, Kanayama N, Tokuzen K, Soga K, Nagasaki Y (2011) Near-infrared (1550 nm) *in vivo* bioimaging based on rare-earth doped ceramic nanophosphors modified with PEG-b-poly(4-vinylbenzylphosphonate). Nanoscale 3:3705–3713
59. Naczynski DJ, Tan MC, Zevon M, Wall B, Kohl J, Kulesa A, Chen S, Roth CM, Riman RE, Moghe PV (2013) Rare-earth-doped biological composites as *in vivo* shortwave infrared reporters. Nat Commun 4:2199
60. Zevon M, Ganapathy V, Kantamneni H, Mingozzi M, Kim P, Adler D, Sheng Y, Tan MC, Pierce M, Riman RE, Roth CM, Moghe PV (2015) CXCR-4 targeted, short wave infrared (SWIR) emitting nanoprobes for enhanced deep tissue imaging and micrometastatic cancer lesion detection. Small 11:6347–6357
61. Shao W, Chen G, Kuzmin A, Kutscher HL, Pliss A, Ohulchanskyy TY, Prasad PN (2016) Tunable narrow band emissions from dye-sensitized core/shell/shell nanocrystals in the second near-infrared biological window. J Am Chem Soc 138:16192–16195
62. Tao Z, Hong G, Shinji C, Chen C, Diao S, Antaris AL, Zhang B, Zou Y, Dai H (2013) Biological imaging using nanoparticles of small organic molecules with fluorescence emission at wavelengths longer than 1000 nm. Angew Chem Int Ed 52:13002–13006
63. Hong G, Zou Y, Antaris AL, Diao S, Wu D, Cheng K, Zhang X, Chen C, Liu B, He Y, Wu JZ, Yuan J, Zhang B, Tao Z, Fukunaga C, Dai H (2014) Ultrafast fluorescence imaging in vivo with conjugated polymer fluorophores in the second near-infrared window. Nat Commun 5:4206
64. Antaris AL, Chen H, Diao S, Ma Z, Zhang Z, Zhu S, Wang J, Lozano AX, Fan Q, Chew L, Zhu M, Cheng K, Hong X, Dai H, Cheng Z (2017) A high quantum yield molecule-protein complex fluorophore for near-infrared II imaging. Nat Commun 8:15269
65. Antaris AL, Chen H, Cheng K, Sun Y, Hong G, Qu C, Diao S, Deng Z, Hu X, Zhang B, Zhang X, Yaghi OK, Alamparambil ZR, Hong X, Cheng Z, Dai H (2016) A small-molecule dye for NIR-II imaging. Nat Mater 15:235–242
66. Wan H, Yue J, Zhu S, Uno T, Zhang X, Yang Q, Yu K, Hong G, Wang J, Li L, Ma Z, Gao H, Zhong Y, Su J, Antaris AL, Xia Y, Luo J, Liang Y, Dai H (2018) A bright organic NIR-II nano fluorophore for three-dimensional imaging into biological tissues. Nat Commun 9:1171
67. Li B, Lu L, Zhao M, Lei Z, Zhang F (2018) An efficient 1064 nm NIR-II excitation fluorescent molecular dye for deep-tissue high-resolution dynamic bioimaging. Angew Chem Int Ed 57:7483–7487
68. Zhang XD, Wang H, Antaris AL, Li L, Diao S, Ma R, Nguyen A, Hong G, Ma Z, Wang J, Zhu S, Castellano JM, Wyss-Coray T, Liang Y, Luo J, Dai H (2016) Traumatic brain injury imaging in the second near-infrared window with a molecular fluorophore. Adv Mater 28:6872–6879
69. Shou K, Qu C, Sun Y, Chen H, Chen S, Zhang L, Xu H, Hong X, Yu A, Cheng Z (2017) Multifunctional biomedical imaging in physiological and pathological conditions using a NIR-II probe. Adv Funct Mater 27:1700995

70. Guo B, Sheng Z, Kenry Hu D, Lin X, Xu S, Liu C, Zheng H, Liu B (2017) Biocompatible conjugated polymer nanoparticles for highly efficient photoacoustic imaging of orthotopic brain tumors in the second near-infrared window. Mater Horiz 4:1151–1156
71. Jiang Y, Upputuri PK, Xie C, Lyu Y, Zhang L, Xiong Q, Paramanik M, Pu K (2017) Broadband absorbing semiconducting polymer nanoparticles for photoacoustic imaging in second near-infrared window. Nano Lett 17:4964–4969
72. Bhavane R, Starosolski Z, Stupin I, Ghaghada KB, Annapragada A (2018) NIR-II fluorescence imaging using indocyanine green nanoparticles. Sci Rep 8:14455
73. Carr JA, Franke D, Caram JR, Perkinson CF, Saif M, Askoxylakis V, Datta M, Fukumura D, Jain RK, Bawendi MG, Bruns OT (2018) Shortwave infrared fluorescence imaging with the clinically approved near-infrared dye indocyanine green. Proc Natl Acad Sci U S A 115:4465–4470
74. Kurbegovic S, Juhl K, Chen H, Qu C, Ding B, Leth JM, Drzewiecki KT, Kjaer A, Cheng Z (2018) Molecular targeted NIR-II probe for image-guided brain tumor surgery. Bioconjug Chem 29:3833–3840
75. Qi J, Sun C, Li D, Zhang H, Yu W, Zebibula A, Lam JWY, Xi W, Zhu L, Cai F, Wei P, Zhu C, Kwok RTK, Streich LL, Prevedel R, Qian J, Tang BZ (2018) Aggregation-induced emission luminogen with near-infrared-II excitation and near-infrared-I emission for ultradeep intravital two-photon microscopy. ACS Nano 12:7936–7945
76. Tian R, Ma H, Yang Q, Wan H, Zhu S, Chandra S, Sun H, Kiesewetter DO, Niu G, Liang Y, Chen X (2019) Rational design of a super-contrast NIR-II fluorophore affords high-performance NIR-II molecular imaging guided microsurgery. Chem Sci 10:326–332
77. Ding F, Li C, Xu Y, Li J, Li H, Yang G, Sun Y (2018) PEGylation regulates self-assembled small-molecule dye-based probes from single molecule to nanoparticle size for multifunctional NIR-II bioimaging. Adv Healthc Mater 7:e1800973
78. Sun Y, Qu C, Chen H, He M, Tang C, Shou K, Hong S, Yang M, Jiang Y, Ding B, Xiao Y, Xing L, Hong X, Cheng Z (2016) Novel benzo-bis(1,2,5-thiadiazole) fluorophores for *in vivo* NIR-II imaging of cancer. Chem Sci 7:6203–6207
79. Cosco ED, Caram JR, Bruns OT, Franke D, Day RA, Farr EP, Bawendi MG, Sletten EM (2017) Flavylium polymethine fluorophores for near- and shortwave infrared imaging. Angew Chem Int Ed 56:13126–13129
80. Sun Y, Ding M, Zeng X, Xiao Y, Wu H, Zhou H, Ding B, Qu C, Hou W, Er-Bu A, Zhang Y, Cheng Z, Hong X (2017) Novel bright-emission small-molecule NIR-II fluorophores for *in vivo* tumor imaging and image-guided surgery. Chem Sci 8:3489–3493
81. Zhu S, Yang Q, Antaris AL, Yue J, Ma Z, Wang H, Huang W, Wan H, Wang J, Diao S, Zhang B, Li X, Zhong Y, Yu K, Hong G, Luo J, Liang Y, Dai H (2017) Molecular imaging of biological systems with a clickable dye in the broad 800- to 1,700-nm near-infrared window. Proc Natl Acad Sci U S A 114:962–967
82. Feng Y, Zhu S, Antaris AL, Chen H, Xiao Y, Lu X, Jiang L, Diao S, Yu K, Wang Y, Herraiz S, Yue J, Hong X, Hong G, Cheng Z, Dai H, Hsueh AJ (2017) Live imaging of follicle stimulating hormone receptors in gonads and bones using near infrared II fluorophore. Chem Sci 8:3703–3711
83. Starosolski Z, Bhavane R, Ghaghada KB, Vasudevan SA, Kaay A, Annapragada A (2017) Indocyanine green fluorescence in second near-infrared (NIR-II) window. PLoS One 12:e0187563
84. Sun Y, Zeng X, Xiao Y, Liu C, Zhu H, Zhou H, Chen Z, Xu F, Wang J, Zhu M, Wu J, Tian M, Zhang H, Deng Z, Cheng Z, Hong X (2018) Novel dual-function near-infrared II fluorescence and PET probe for tumor delineation and image-guided surgery. Chem Sci 9:2092–2097
85. Zhu S, Hu Z, Tian R, Yung BC, Yang Q, Zhao S, Kiesewetter DO, Niu G, Sun H, Antaris AL, Chen X (2018) Repurposing cyanine NIR-I dyes accelerates clinical translation of near-infrared-II (NIR-II) bioimaging. Adv Mater 30:1802546
86. Lin J, Zeng X, Xiao Y, Tang L, Nong J, Liu Y, Zhou H, Ding B, Xu F, Tong H, Deng Z, Hong X (2019) Novel near-infrared II aggregation-induced emission dots for *in vivo* bioimaging. Chem Sci. 10:1219–1226

87. Sheng Z, Guo B, Hu D, Xu S, Wu W, Liew WH, Yao K, Jiang J, Liu C, Zheng H, Liu B (2018) Bright aggregation-induced-emission dots for targeted synergetic NIR-II fluorescence and NIR-I photoacoustic imaging of orthotopic brain tumors. Adv Mater 30:1800766
88. Tang Y, Li Y, Hu X, Zhao H, Ji Y, Chen L, Hu W, Zhang W, Li X, Lu X, Huang W, Fan Q (2018) "Dual lock-and-key"-controlled nanoprobes for ultrahigh specific fluorescence imaging in the second near-infrared window. Adv Mater 30:1801140
89. Shou K, Tang Y, Chen H, Chen S, Zhang L, Zhang A, Fan Q, Yu A, Cheng Z (2018) Diketopyrrolopyrrole-based semiconducting polymer nanoparticles for *in vivo* second near-infrared window imaging and image-guided tumor surgery. Chem Sci 9:3105–3110
90. Lu X, Yuan P, Zhang W, Wu Q, Wang X, Zhao M, Sun P, Huang W, Fan Q (2018) A highly water-soluble triblock conjugated polymer for *in vivo* NIR-II imaging and photothermal therapy of cancer. Polym Chem 9:3118–3126
91. Zhu S, Herraiz S, Yue J, Zhang M, Wan H, Yang Q, Ma Z, Wang Y, He J, Antaris AL, Zhong Y, Diao S, Feng Y, Zhou Y, Yu K, Hong G, Liang Y, Hsueh AJ, Dai H (2018) 3D NIR-II molecular imaging distinguishes targeted organs with high-performance NIR-II bioconjugates. Adv Mater 30:1705799
92. Georgakoudi I, Jacobson BC, Müller MG, Sheets EE, Badizadegan K, Carr-Locke DL, Crum CP, Boone CW, Dasari RR, Van Dam J, Feld MS (2002) NAD(P)H and collagen as in vivo quantitative fluorescent biomarkers of epithelial precancerous changes. Cancer Res 62:682–687
93. Zipfel WR, Williams RM, Christie R, Nikitin AY, Hyman BT, Webb WW (2003) Live tissue intrinsic emission microscopy using multiphoton-excited native fluorescence and second harmonic generation. Proc Natl Acad Sci U S A 100:7075–7080
94. Gallas JM, Eisner M (1987) Fluorescence of melanin-dependence upon excitation wavelength and concentration. Photochem Photobiol 45:595–600
95. Ema M, Gamo M, Honda K (2016) A review of toxicity studies of single-walled carbon nanotubes in laboratory animals. Regul Toxicol Pharmacol 74:42–63
96. Park EJ, Roh J, Kim SN, Kang MS, Lee BS, Kim Y, Choi S (2011) Biological toxicity and inflammatory response of semi-single-walled carbon nanotubes. PLoS One 6:e25892
97. Jin T, Tsuboi S, Komatsuzaki A, Imamura Y, Muranaka Y, Sakata T, Yasuda H (2016) Enhancement of aqueous stability and fluorescence brightness of indocyanine green using small calix[4]arene micelles for near-infrared fluorescence imaging. Med Chem Commun 7:623–631
98. Diao S, Blackburn JL, Hong G, Antaris AL, Chang J, Wu JZ, Zhang B, Cheng K, Kuo CJ, Dai H (2015) Fluorescence imaging in vivo at wavelengths beyond 1500 nm. Angew Chem Int Ed 54:14758–14762
99. Li C, Cao L, Zhang Y, Yi P, Wang M, Tan B, Deng Z, Wu D, Wang Q (2015) Preoperative detection and intraoperative visualization of brain tumors for more precise surgery: a new dual-modality MRI and NIR nanopobe. Small 11:4517–4525
100. Franke D, Harris DK, Chen O, Bruns OT, Carr JA, Wilson MW, Bawendi MG (2016) Continuous injection synthesis of indium arsenide quantum dots emissive in the short-wavelength infrared. Nat Commun 7:12749
101. Bruns OT, Bischof TS, Harris DK, Franke D, Shi Y, Riedemann L, Bartelt A, Jaworski FB, Carr JA, Rowlands CJ, Wilson MWB, Chen O, Wei H, Hwang GW, Montana DM, Coropceanu I, Achorn OB, Kloepper J, Heeren J, So PTC, Fukumura D, Jensen KF, Jain RK, Bawendi MG (2017) Next-generation *in vivo* optical imaging with short-wave infrared quantum dots. Nat Biomed Eng 1:0056
102. Zamberian F, Turyanska L, Patane A, Liu Z, Williams HEL, Fay MW, Clarke PA, Imamura Y, Jin T, Bradshaw TD, Thomas NR, Grabowska AM (2018) Stable DHLA–PEG capped PbS quantum dots: from synthesis to near-infrared biomedical imaging. J Mater Chem B6:550–555
103. Zebibula A, Alifu N, Xia L, Sun C, Yu X, Xue D, Liu L, Li G, Qian J (2018) Ultrastable and biocompatible NIR-II quantum dots for functional bioimaging. Adv Funct Mater 28:1703451

104. Zhong Y, Ma Z, Zhu S, Yue J, Zhang M, Antaris AL, Yuan J, Cui R, Wan H, Zhou Y, Wang W, Huang NF, Luo J, Hu Z, Dai H (2017) Boosting the down-shifting luminescence of rare-earth nanocrystals for biological imaging beyond 1500 nm. Nat Commun 8:737
105. Deng Z, Li X, Xue Z, Jiang M, Li Y, Zeng S, Liu H (2018) A high performance Sc-based nanoprobe for through-skull fluorescence imaging of brain vessels beyond 1500 nm. Nanoscale 10:9393–9400
106. Guo B, Sheng Z, Hu D, Liu C, Zheng H, Liu B (2018) Through scalp and skull NIR-II photothermal therapy of deep orthotopic brain tumors with precise photoacoustic imaging guidance. Adv Mater 30:e1802591
107. Liu W, Wang Y, Han X, Lu P, Zhu L, Sun C, Qian J, He S (2018) Fluorescence resonance energy transfer (FRET) based nanoparticles composed of AIE luminogens and NIR dyes with enhanced three-photon near-infrared emission for *in vivo* brain angiography. Nanoscale 10:10025–10032
108. Kim TH, Mount CW, Dulken BW, Ramos J, Fu CJ, Khant HA, Chiu W, Gombotz WR, Pun SH (2012) Filamentous, mixed micelles of triblock copolymers enhance tumor localization of indocyanine green in a murine xenograft model. Mol Pharm 9:135–143
109. Slofstra SH, van 't Veer C, Buurman WA, Reitsma PH, Ten Cate H, Spek CA (2005) Low molecular weight heparin attenuates multiple organ failure in a murine model of disseminated intravascular coagulation. Crit Care Med 33:1365–1370
110. Ding R, Zhao D, Guo R, Zhang Z, Ma X (2011) Treatment with unfractionated heparin attenuates coagulation and inflammation in endotoxemic mice. Thromb Res 128:e160–e165
111. Li R, Tong J, Tan Y, Zhu S, Yang J, Ji M (2015) Low molecular weight heparin prevents lipopolysaccharide induced-hippocampus-dependent cognitive impairments in mice. Int J Clin Exp Pathol 8:8881–8891
112. Wada H, Wakita Y, Nakase T, Shimura M, Hiyoyama K, Nagaya S, Deguchi H, Mori Y, Kaneko T, Deguchi K, Fujii J, Shiku H (1996) Increased plasma-soluble fibrin monomer levels in patients with disseminated intravascular coagulation. Am J Hematol 51:255–260
113. Choi HS, Liu W, Misra P, Tanaka E, Zimmer JP, Ipe BI, Bawendi MG, Frangioni JV (2007) Renal clearance of quantum dots. Nat Biotechnol 25:1165–1170
114. Li C, Wang Q (2018) Challenges and opportunities for intravital near-infrared fluorescence imaging technology in the second transparency window. ACS Nano 12:9654–9659
115. Schnermann MJ (2017) Chemical biology: organic dyes for deep bioimaging. Nature 551:176–177

Index

A. Benayas et al. (eds.), *Near Infrared-Emitting Nanoparticles for Biomedical Applications*, https://doi.org/10.1007/978-3-030-32036-2

Q